ELECTRO-ELASTICITY SENSING IN AXIALLY-LOADED CONCRETE USING
RECYCLED STEEL RESIDUALS AS FUNCTIONAL FILL

by

David Bryant Scott

A dissertation submitted to the faculty of
The University of North Carolina at Charlotte
in partial fulfillment of the requirements
for the degree of Doctor of Philosophy in
Infrastructure and Environmental Systems

Charlotte

2018

Approved by:

_____
Dr. Shen-en Chen

_____
Dr. Janos Gergely

_____
Dr. Brett Tempest

_____
Dr. Peng Wang

_____
Dr. Thomas Nicholas

ii

ABSTRACT

DAVID BRYANT SCOTT. Evaluation of Discrete Sensing Materials in Concrete using Recycled and Graded Steel Shavings. (Under the direction of DR. SHEN-EN CHEN)

Self-sensing concrete is embedded with electrostrictive materials that provides indications of strain based on variations in electrical conductivity, or its inverse, resistance. Previous works includes embedded material that vary in size from nano-scale (a thousand times smaller than the diameter of a human hair) to as large as a coarse human hair. Materials used for creating self-sensing concrete include carbon tubes, graphite, crystals, or ceramics that are added in a solid phase to the other raw materials used to create concrete. Currently, these enhancing materials used to create self-sensing concrete are uniformly distributed while the concrete is being mixed. Research, testing, and analysis described herein investigates how steel shaving waste (or recycled steel residuals) of different sizes and aspect ratios (dust and fiber) can be segregated (graded) and mixed within fresh concrete to enhance its ability to be self-sensing. The study includes the development of concrete using the recycled steel residuals (RSR) for a specific application – nuclear power plants. To prevent disaster, nuclear power generation facilities utilize heavily reinforced, mass concrete, which presents a challenging scenario for conventional nondestructive evaluation (NDE) techniques. In this study, instead of developing a specific NDE technique(s) to be externally applied to the concrete, the proposed study will focus on exploring a fundamental understanding of the physics of electron flow through concrete that has incorporated recycled steel. Goals for this work

include developing a structural health monitoring technique, as an alternative to nondestructive evaluation, by formulating the concrete material to itself become a sensor and transmitting data about the level of strain of the self-sensing concrete. This study will begin with review of existing embedded sensor technologies used for structural health monitoring of reinforced concrete to detect common types and levels of material degradation. This portion of the study will include providing aid to decision makers using decision making techniques – decision tree analysis and analytical hierarchy process. Following this, relationships between resistance, resistivity, Poisson's ratio, modulus of elasticity (Young's modulus), and orthogonal spatial representation will be theoretically developed. The theoretical development will also include continuum theory to relate axial stress with three-dimensional deformation as a function of Poisson's ratio and shear modulus of concrete materials shaped as cylindrical specimens. Final stages of the study is empirical. It includes axial compression testing of concrete specimens and measuring the variations in strain and correlating strain with changes in electrical conductivity. The empirical testing includes concrete with varying mixture designs developed using criteria from the American Concrete Institute (ACI) and ASTM International, load concentrations of recycled steel residuals, and undergoing monotonic loading. The theoretical and experimental research reconciled electric, elastic, and material characterizations of concrete with recycled steel residuals; and, it showed that electric conductivity/resistivity is affected by strain and that an electro-elastic relationship exists in concrete containing recycled steel residuals.

ACKNOWLEDGMENTS

You've become very special to me, and I'm grateful to also call you a friend. Finally, to the most important persons in my life with whom the good Lord has blessed me to partner. Esther-Elaine, Eden Lily, and Evangeline Love, the Lord has placed you in my life, and you are the reason that I wish for my days to be long and filled with time together; you give me so much joy. I'm forever grateful for your patience with me during this pursuit and am proud to be called your husband and father. And to my God and Lord Savior Jesus Christ, thank you for giving so abundantly beyond all that I could ask and think.

DEDICATION

To my beautiful and patient wife, Esther-Elaine, and our dear daughters, Eden Lily and Evangeline Love.

TABLE OF CONTENTS

LIST OF TABLES

LIST OF FIGURES

LIST OF ABBREVIATIONS

AAR   Alkali-Aggregate Reactivity (Reaction)

ACI   American Concrete Institute

ACR   Alkali-Carbonate Reactivity (Reaction)

AE   Acoustic Emissions

AFNOR   Association Française de Normalisation

AHP   Analytical Hierarchy Process

ANSYS   Analysis System (software)

ASM   Autonomous Sensing Materials

ASR   Alkali-Silica Reactivity (Reaction)

ASTM   American Standard for Testing and Materials International

BSI   British Standards Institute

DEF   Delayed Ettringite Formation

EPRI   Electric Power Research Institute

ETDR   Electrical time-domain reflectometry

ETS   Embedded and/or Topical Sensors

FHWA   Federal Highway Administration

FO   Fiber Optics

IAEA   International Atomic Energy Agency

ISO   International Standards Organization

LIDAR   Light Distance and Ranging

LR	Leak Rate
LTO	Long Term Operations
MWCNT	Multi-walled Carbon Nano Tubes
NACE	National Association of Corrosion Engineers
NCS	Nuclear Concrete Structures
NDE	Nondestructive Evaluation
NEA	Nuclear Energy Agency
RADAR	Radio Distance and Ranging
RSR	Recycled Steel Residuals
SAR	Synthetic Aperture Radar
SHM	Structural Health Monitoring
SWCNT	Single-walled Carbon Nanotube
TRL	Technical Readiness Level

CHAPTER 1 INTRODUCTION

Concrete is arguably the most important construction material in the world and is utilized in every developed country. It is also plagued with deterioration through a variety of different mechanisms – chemical related, construction induced, steel degradation, environmentally induced, and excessive strain. Degradation of concrete leads to trillions of dollars spent annually to inspect for, design, and execute repairs. These repairs are equally needed within the electric utility industry. More specifically, the nuclear power industry consists of aged plants that experience the aforementioned degradation mechanisms; and, nuclear power for commercial production of energy consists of many plants under construction that provide opportunity to use modern concrete mixture designs to help reduce the likelihood of near- and long-term degradation of the material. To make matters worse, nuclear power plants consists of extremely robust and heavily reinforced mass concrete elements. These members are also sometimes lined with steel; and, the significant mismatch of acoustic impedance (high to low) reduces the investigation of the concrete condition to nearly impossible extremes (Electric Power Research Institute 2013).

Innovative and alternative materials to embed into concrete have previously been proposed to create smart concrete that improves the mechanical properties of the structural element (Scott, D.B. 2015). Embedded materials can be used to detect the occurrence or approaching onset of damage to plain and reinforced concrete resulting from excessive strain. More specifically, the detection technique indicates strain through changes in measurable electrical conductivity of the concrete. The measurement of changes in electrical conductivity becomes more achievable through the nearly ubiquitous distribution

of particles having electrostrictive properties. This has been called *self-sensing concrete* or *autonomous sensing materials (*ASMs*).* Unique to the testing described here is the testing of innovated functional filler which utilizes recycled steel residuals (RSRs). The research described herein provides a review of existing embedded and topical sensor technology; a decision strategy for selecting sensors; theoretical derivation of germane relationships between resistance, resistivity, strain, and load; and empirical results of testing specimens using recycled steel residuals.

Problem Statement and Purpose

Given the information from the previous subsection, the question is begged, "do recycled steel residuals provide opportunity to create self-sensing concrete to determine levels of concrete strain as a function of changes in electrical conductivity/resistance?" If so, "is there a concentration of RSR which provides better indication of strain through changes in electrical conductivity/resistance?" The research explores the opportunity to utilize recycled steel particles which have electrostrictive properties in order to detect existing and approaching damage of reinforced concrete.

Hypothesis

Autonomous sensing using recycled steel residuals that are infused into concrete mixtures can offer strain detection of reinforced concrete.

Research Significance

Though reinforced concrete is used broadly for construction, it is prone to cracking. Concrete cracking is caused by a variety of reasons and some of these cracks may be prevented. By identifying existing or pending cracks in a timely manner, excessive damage

can potentially be prevented or, at least, stunted. The infrastructure throughout much of the world has aged considerably. There is a large amount of deterioration which has occurred or will continue to occur as structures utilizing reinforced concrete continue to age. Consequently, repair and/or replacement of reinforced concrete structures – buildings, bridges, and roads – will continue to increase in the coming years and decades. Detrimentally, there are insufficient funds and manpower to engage in all of the needed repairs of reinforced concrete. This is evident in the reports of low quality infrastructure in the United States of America (America's Infrastructure GPA 2015) and other countries with aged infrastructure. According to (America's Infrastructure GPA 2015), grades for these infrastructures – buildings, bridges, and so on – are Cs and Ds. For the sake of public safety, these structures will either need repair or will be subject to full demolition and reconstruction. Though there have been efforts and progress in reclaiming processed concrete, demolishing existing and rebuilding new concrete structures will be very taxing on the environment and financially costly. The environmental dangers of demolishing existing concrete structures include airborne and water-bound impurities. Furthermore, rebuilding new concrete structures rely upon draining natural resources – stone and water. Equally important, and maybe more damaging, is the refining of natural resources to create cement – the key ingredient in concrete for binding. This cement refining produces and emits a reported five (5) percent of the world's carbon dioxide emissions (Hendriks, C.A., et al. 2003).

As such, the opportunity to significantly reduce the damage incurred by replacing concrete is very important. An optimum method of achieving this is by preventing the

onset of damage. Currently, evaluations of concrete predominantly require being physically present at the structure to utilize a variety of nondestructive evaluation (NDE) techniques – ground penetrating RADAR, impact echo, impulse response, shear wave tomography, coring, half-cell potential, and resistivity (ACI Committee 228; Scott, D.B 2013; Scott D.B., et al 2013; Scott D.B. 2015). More recently, remote sensing has become more popular which relies upon the strategic placement of embedded and/or topical sensors (ETSs) – strain gauges, fiber optics (FO), acoustic emission (AE), maturity probes, crack monitors, coaxial cables, temperature gauges, electrochemical sensors (Scott D.B., et al 2013). Beyond traditional nondestructive testing and discrete sensors, there is an opportunity to turn the concrete into a sensor which can potentially be achieved using RSR. For this research RSR will be included in the reinforced concrete through modifying the mixture properties. If the material of the concrete has the potential of indicating existing or approaching strain which is excessive, then preventing damage is more possible.

Using RSR allows the concrete to become its own sensor, making it self-sensing. The important property of the RSR is its electrostrictive nature. Electrostrictive property is the ability of a material to change in electrical resistance based on a change in shape (i.e., the material becomes more or less electrically resistant as the material lengthens or compresses, respectively). Previous work on creating self-sensing concrete utilized ASM with varying sizes – nanoscale (a thousand times smaller than the diameter of a human hair), or it may be as big and coarse as a human hair (Li, H., Xiao, H., Ou, J., 2004; Scott D.B. 2015). Sometimes the materials consist of tubes made from carbon and sometimes the material is a crystal or ceramic (Kholkin, A.K., 2009). The concrete becomes the

4

sensor, because the electrostrictive material is mixed in with other concrete constituents – cement, water, rocks, and sand. Autonomous sensing materials are usually very durable and usually matches or exceeds the concrete life. The benefits of smart materials embedded in new materials and structures include improved structural performance, reduced maintenance, and increased sustainability. These benefits may be achieved through planning and utilizing ASMs and provide opportunity to improve structural strength, ductility, usability, and reduced costs (Sreekala, R., Muthumani, K. 2009). The materials used to embed in concrete is expensive, though prices have reduced significantly (Pammi, S., et al. 2003; Sreekala, R., Muthumani, K. 2009). Fortunately, relative to cement content, a small percentage of the material can be used to achieve the desired sensing property of the concrete member and system. None the less, cost is restrictive and commencement of self-sensing concrete will be slow. The inclusion of these materials will likely be in small, strategic areas. This would include areas of small repair, small grout areas such as at post-tension anchors, or appropriate areas for a structural member where cracking is more likely.

Test Plan and Methods

To determine the success of using RSR for creating self-sensing concrete, the research described herein included literature review, theoretical development of mathematical relationships, and empirical testing. The literature review is focused on how engineers and scientists are currently performing structural health monitoring (SHM) on concrete using discrete placement of ETS. Next, a selection strategy is offered to provide aid for determining the best sensing system for a given applications. Determining theoretical changes in strain as a function of electrical resistance requires understanding

between the mechanical deformation of concrete as a function of load along with changes in resistance as a function of material properties – namely, resistivity – and physical dimensions of the members or specimens being tested. Therefore, Chapter 4 includes the development of the theoretical relationships between resistance, strain, resistivity, and Poisson's ratio. Additionally, continuum theory is used to show the relationship between axial compressive loads on specimens with the deformation that occurs in that member. Finally, Chapter 5 and Chapter 6 includes description and results from empirical testing. The testing is of concrete cylinders and columns. The specimens have varied shape (circle and square cross sections), size (4- and 6-in. diameters and sides), mixture designs, and RSR concentrations (0%, 0.5%, 1%, 1.6%, and 2%). Mixture proportioning will follow industry standards, rationale, and best practices found in published literature by the American Concrete Institute (ACI) and ASTM International (ASTM). Additionally, concrete plastic and hardened properties will be tested in general accordance with ASTM standards – slump, air content, density, compressive strength, and modulus of elasticity. Specimens will also include embedded electrodes with external connection for inputting alternating-current (AC) electricity through the concrete and the measuring electrical potential across a known distance. The chapters herein describe nascent stages of research needed to indicate the viability of self-sensing concrete using RSR. Research results are reported within five articles submitted to peer-reviewed journals. Discussion, conclusions, and additional details of the research are also included.

Dissertation Outline

Following this introduction, the dissertation herein includes chapters and appendix. The chapters consist of to-be-published, peer-reviewed journal articles. Chapter 2 is an article highlighting literature review performed on damage and degradation mechanisms that are unique to reinforced concrete for commercial nuclear power plants. Chapter 2 also includes literature review of embedded and topical sensors used for structural monitoring of concrete. Chapter 3 discusses decision analysis tools that can be used as an aid for engineers to determine a suitable type of sensor for concrete applications. The article also includes an example of how this tool can be specifically used to test a model of post-tensioned reinforced concrete beam that has been thermally loaded in a beyond design basis accident such as a main steam line break or a loss of coolant accident. Chapter 4 provides an abbreviated derivation of the mathematical relationships between resistance, resistivity, and strain as a function of uniaxial loading of a concrete specimens. Loading and displacement are based on continuum theory of the concrete specimen. Chapter 5 includes experimental methods and results of standard sized concrete specimens – 4x8-in. and 6x12-in. cylinders. The experiment consisted of measuring changes in voltage and resistance as a function of changes in uniaxial strain. The results are characterized as the electro-elastic relationship between strain and resistance. Similar to Chapter 5, Chapter 6 includes additional, and more extensive, electro-elastic experiments for concrete column specimens – 6x6x20-in. The specimens were loaded with different concentrations of recycled steel residuals – 0%, 0.5%, 1%, and 2% - and then axially loaded in compression. The electro-

elasticity results are discussed. The report appendix includes software code, select photos of specimens, and results from mechanical and electro-elastic testing.

CHAPTER 2 INNOVATIVE CONCRETE SENSING TECHNOLOGIES FOR NUCLEAR POWER PLANTS

Abstract

Nondestructive evaluation has been used to investigate construction and aging of concrete structures for the nuclear power industry. Like non-nuclear reinforced concrete structures, mechanisms causing reduced concrete serviceability include chemical and physical attacks. However, nuclear concrete often have unique structural characteristics which increase the proclivity towards degradation and inhibit inspection using traditional NDE techniques. Modern embedded sensing technologies can provide opportunities for the in-depth evaluation of nuclear, reinforced concrete. This paper offers an assessment of emerging embedded and surficial sensor techniques and critically evaluates sensor applicability for concrete structures used in the nuclear power industry.

Introduction

Nondestructive evaluation (NDE) has been used for the investigation and evaluation of nuclear concrete structures (NCS) for decades (Naus 2007). Nuclear structures consisting of reinforced concrete are, in general, unique to most commercial structures. Examples of nuclear related reinforced concrete structures are cooling fluid intakes, cooling towers, containments, spent-fuel pools, and dry-cask storage. Applications of NDE include investigation of aging effects of concrete containments at nuclear power plants for chemical attacks, physical attacks, and degradation factors such as leaching, alkali-aggregate reactions, freeze-thaw, fatigue, vibration, corrosion, elevated temperature, and others (Power Reactor Information System 2015).

The configuration and sensitivity of certain parts of these structures necessitates limited access to perform NDE. Furthermore, the nuclear industry utilizes copious composite structures (e.g.; steel-lined concrete containments, dry-cask storage and spent fuel pools) which further limit direct NDE access to the concrete structure. At times, this limitation restricts testing to be performed on only one side of the component or is further stunted by an array of penetrations which inhibit the ability to perform NDE. Finally, nuclear structures are robust, containing thick structural members and large concentrations of reinforcing steel and the access timing (many elements of a nuclear, reinforced concrete structure are only accessible during outages) are additional critical element associated with maintenance inspection. The combination of these hindrances creates significant complications for conventional NDE and high-fidelity investigations for nuclear applications.

ACI 228.2R (ACI Committee 228 1998) divides traditional NDE techniques into several broad categories: visual, stress waves, nuclear, magnetic and electrical, penetrability, infrared thermography, and RADAR. Other than visual evaluation, these techniques require the imputation of energy into the concrete element, and, subsequently, measuring the responses of the element. These techniques have been directly used in the past on NCSs experiencing delamination in an extent-of-damage survey (Scott, D 2013; Muenow RA 1988; Kim, Kim, Seo, et al. 2002). The techniques may be used to indicate corrosion potential of reinforcement, cracking strength, Young's Modulus, voids, bond repair, delamination, honeycomb, member thickness, etc. These techniques may be used singularly or in tandem. More recently, innovative technologies such as microwave holography (Ghasr T, LePape Y, Scott DB, et al. 2015) or air coupling (instead of direct contact) ultrasound devices (Kee, Fernandez-Gomez, Zhu 2011; Bhardwaj MC 2009) have been developed. Along with traditional NDE, these techniques are often-used tools to provide data on condition assessment of nuclear concrete structures (Clayton, Hileman 2012). NDE practices for general concrete applications are well established and documented (La Plaine Cedex Association de Normalisation (AFNOR) 2005; Non-Destructive Tests on Hardened Concrete 2004; Technical Committee B/517 2004; Nuclear Energy Agency 2002; Fedearly Highway Admininstration 2001; ASTM Committee C09 2002; ASTM Committee C09 2010; Sreekla R, Muthamani K 2009; Withey, Vemura, Bachilo, et al. 2012; Li H, Xiao H, Ou J 2004; Kim DJ, Lee C, Chang H, et al. 2011; Shen B, Yang X, Li Z 2006).

Alternatively, a suite of innovative sensing techniques is emerging which may supplement or, in some cases, replace traditional NDE (Suchanek WL, Riman RE 2009). These techniques include using sensors made up of single-walled carbon nanotubes (Yang M, Dai J 2012; Abu-Yosef AE, Pasupathy P, Wood SL, et al. 2012), piezoelectric ceramic, fiber optics, and electrochemical (Yao Y, Tung S-T E, Glisic B 2014). These sensors are topical (Yang M, Dai J 2012) or embedded (Abu-Yosef AE, Pasupathy P, Wood SL, et al. 2012). Interrogation of these sensors may require contact or be remote (Renshaw J, Guimaraes M, Scott DB 2013). They have been shown to indicate material strength during and after curing, structural strain, and crack development (ACI Committee 201 2008).

These embedded and/or topical sensors (ETS) may be able to overcome limitations unique to NCS. The following offers considerations which may be made for the upcoming and continued advancements in sensing technologies and application of these technologies to NCS. There are also external sensing techniques with devices detached from the monitored structures including radio detection and ranging (RADAR), light detection and ranging (LIDAR), infrared thermography, synthetic aperture RADAR (SAR), etc. But they are outside of the scope of this paper.

Damage and degradation of reinforced concrete

Source of damage induced into NCS varies: Whether under construction, nearing end-of-service, or somewhere in between, nuclear structures may potentially have damaged conditions that need to be investigated. At the time of this writing, there are 57 new nuclear power plants under construction and at the same time, hundreds of operating plant structures proceed to age throughout the world. Majority of the world's 448 reactors are

older than 20 years – more than half of the typical 40-year license age (Power Reactor Information System 2015). Figure 2-1 shows the aging nuclear plant population. At the end of 2012, fifteen units in the US had been in operation for at least 40 years and license-extension applications are regularly submitted to extend use beyond the original 40-year licenses.

Evaluation of nuclear concrete structures must include inspection of in-service structures, forming a technical basis for continued operation, and determining necessary remedial action to extend service of these nuclear assets. Table 2-1 offers an inventory of potentially damaging mechanisms for reinforced concrete, which can be differentiated into environmental, construction, and extreme operations. The compilation of images in Figure 2-2 indicates the varying ways degradation is revealed.
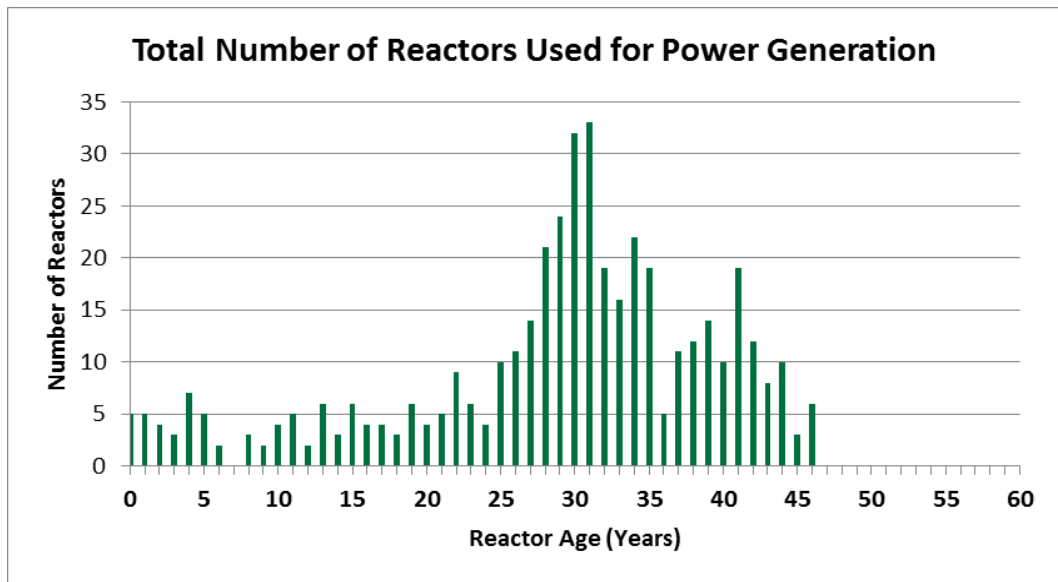
Figure 2-1
Global Age of Nuclear Reactors Used for Energy (data from [Power Reactor Information System 2015])
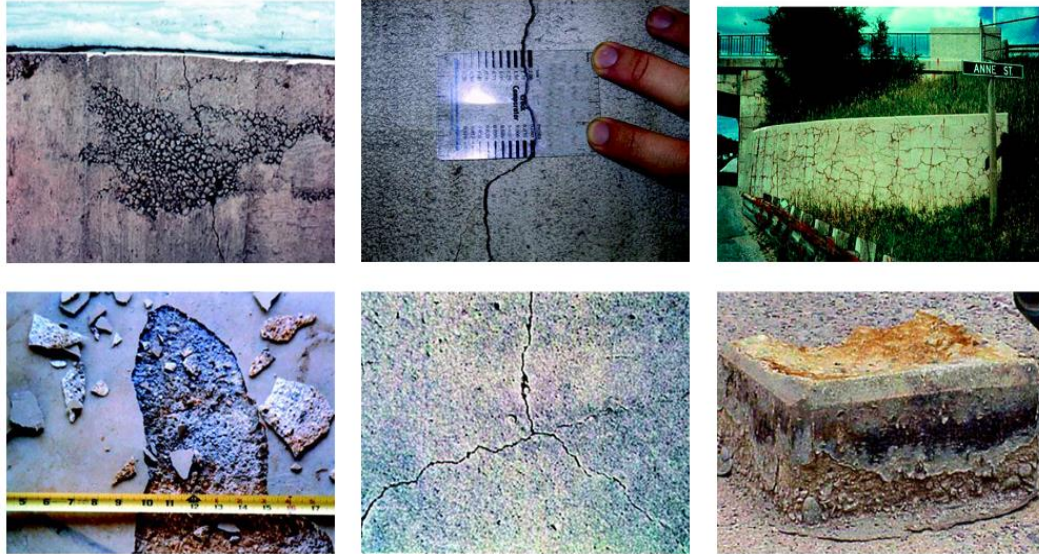
Figure 2-2
Degradation Mechanisms for Reinforced Concrete (ACI Committee 222 2001)

Table 2-1
Defect and Mechanism Inventory

Defect Category	Defect Type/Impetus	Life-cycle stage it may occur	Defect scope (structural/material)
Environment Induced	Alkali-aggregate reactivity (AAR)	Intermediate, LTO (long term operations)	Material
	Carbonation	Intermediate, LTO	Material
	Chloride Ingress	Intermediate, LTO	Material
	Deformed bar reinforcement corrosion	Intermediate, LTO	Material
	Corrosion of steel liner	Intermediate, LTO	Material
	Delayed Ettringite Formation (DEF)	Intermediate, LTO	Material
	Irradiation	LTO	Material
	Radiation	New-build, Intermediate, LTO	Material
	Sulfate Attack	Intermediate, LTO	Material

Construction Induced	Crack	New-build, Intermediate, LTO	Structural and Material
	Delamination	New-build, Intermediate, LTO	Structural
	Freeze-thaw	New-build, Intermediate, LTO	Material
	Honeycomb/void	New-build, Intermediate, LTO	Structural
	Shrinkage	New-build, Intermediate, LTO	Material
Steel Related	Creep	Intermediate, LTO	Structural
	Debonding of liner and steel	New-build, Intermediate, LTO	Structural
	Fatigue	LTO	Structural
	Lack of bond at Nelson studs	New-build, Intermediate, LTO	Structural
	Rupture of tendon and/or tendon heads	New-build, Intermediate, LTO	Structural
Extreme Operation (Or other)	Coating Failure	New-build, Intermediate, LTO	Material
	Fire	New-build, Intermediate, LTO	Material
	High temperature exposure	Intermediate, LTO	Material
	Inclusions (embedded during construction)	New-build, Intermediate, LTO	Structural
	Missile Impact	New-build, Intermediate, LTO	Structural
	Moisture intrusion	New-build, Intermediate, LTO	Material

	Thermal differentials	New-build	Material
	Leak Rate Failure	New-build, Intermediate, LTO	Structural
	Erosion and/or abrasion	Intermediate, LTO	Material

Environment Induced Problems

Many of the defects identified in Table 2-1 are further complicated by the unique characteristics of NCS. For example, corrosion in metals may result in volumetric increases, which produces additional stress on surrounding concrete and significantly cracks and weakens the concrete (NACE TG 400 2012). Concrete spalling often ensues. Metal corrosion is, in part, environmentally induced, and is especially critical for NCSs because of the massive amount of embedded steel arrangements.

In addition, nuclear related structures use heavy amounts of or are often near large bodies of water in order to cool the heat generated from nuclear processes. This water sometimes includes chlorides which were used to treat the water; or, the plant is near the sea which introduces a harsh chloride environment. The ingress of chlorides into the concrete will be a catalyst for corrosion of reinforcing steel. In addition to the proclivity towards corrosion of reinforcing steel, chemical attack may occur such as in the form of alkali-aggregate reactivity. Alkali-aggregate reactivity is subcategorized into two forms, namely: alkali-silica reaction or alkali-carbonate reaction. Environmentally induced degradation may be stunted through the use of coatings 'consisting of paints, mortars, liquefied rubbers, and resins' (Mindess S, Young JF, Darwin D 2004). Nonetheless,

improper selection of coatings or exposure to extreme conditions may still lead to peeling, blistering, or flaking.

Construction Induced Problems

Many concrete related problems started at the construction phase and includes honeycombing, internal voids, and cracking oriented perpendicular and/or parallel to the concrete surface. The thick members of NCS are prone to excessive temperature differentials between concrete core and surface areas, thus, may result in delayed ettringite formation potentially leading to map cracking. Map cracking is a series of interconnected cracks that encompass large concrete surface areas and is especially significant for mass concrete found in NCS.

Heavy reinforcement and use of prestressed tendons are also problematic for NCS. Many concrete nuclear structures are reinforced with post-tension tendons that extend both horizontally (hoop tendons) and vertically. Tendons are designed to keep concrete in compression which requires the tendons to endure very high stresses, resulting in tendon stretch and leads to concrete cracking and tendon rupture. Debonding between the concrete and steel may occur between the composite materials due to shrinkage or external loading. The areas of debonding are more susceptible to having intrusion of contaminants which leads to degradation.

Steel Related Problems

In recent years, there have been steel alternatives which have been utilized to reinforce concrete. However, steel, either deformed bar steel or high-tension tendons, remains the material of choice to provide greater tensile capacity for concrete.

Unfortunately, the use of steel provides additional degradation mechanisms which induce a range of issues from aesthetic considerations to structural failure. The most common degradation issue associated with steel is corrosion as described above. ACI (American Concrete Institute) defines corrosion as the destruction of metal by chemical, electrochemical, or electrolytic reaction within its environment (NACE TG 400 2012). Corrosion can be initiated through several means: chlorides found in the concrete, carbonation, stray current, and, in some cases, galvanic induction through localized dissimilar metals (ASTM Committee C09 2002; Mindess S, Young JF, Darwin D 2004; ACI Committee 349 2002). At best if corrosion were to occur then it will eventually protrude through pores and joints at the surface and be an eye-sore. It is usually reddish, brown in color and may protrude as hardened flakes or a gel-like by product. More importantly, corrosion of a high-stressed tendon could cause sudden collapse of a structure. Corrosion products, during the chemical reaction, replaces the consumed steel with a larger volume of corroded material. The increased volume produces additional stress on surrounding concrete and significantly cracks and weakens the concrete. Traditional testing of corrosion involves electrochemical techniques which are used to indicate potential rate of corrosion, which does not provide evidence of the extent of corrosion that has previously occurred. One opportunity for research is to investigate the ability of non-destructive testing techniques, to determine corrosion extents.

Additional degradation mechanisms associated with steel reinforcement within concrete is creep, lack of bond (during or post construction), fatigue, and rupture (Mindess S, Young JF, Darwin D 2004). These are all related to the mechanical relationship between

the reinforcing steel and concrete when loaded. They are heavily affected by design and construction practices. For instance, if a tendon anchor has insufficient cover then the anchor will be overcome by the stress transferred from the tendon and will violently release. Alternatively, concrete is susceptible to creep when subjected to long-term loading. This may occur whether with post-tension and prestressed structures or regularly reinforced concrete structures.

<u>Extreme Operation Conditions</u>

According to ACI 349.3R (ACI Committee 349 2002), neutron irradiation affects the crystalline structure of the cement matrix and the mechanical properties of reinforcing steel such that the ductility of the steel is reduced (William K, Xi Y, Naus D, et al. 2013). It is reported that radiation exposures $>10^{10}$ rads of gamma can result in significant increase in concrete volume and reduction in strength (Fillmore DL 2004).

For nuclear power plants, steam is generated by harnessing the extreme heat developed through nuclear reactions between radioactive materials. Temperatures reach hundreds of degrees Fahrenheit (>315 °C). These high thermal loads desiccate and reduce the elasticity of concrete. Additionally, prolonged exposure to high temperatures may cause loss of ductility to post-tension tendons found in NCS. Leak Rate (LR) tests are typically required for verification of the pressure or leakage limited boundaries of nuclear containment structures (U.S. Nuclear Regulatory Commission 2014).

Mechanics associated with nuclear structures

The initiation of the damages associated with nuclear concrete described previously are mostly characterized as material damage and not considered as structural damage.

Hence, classical mechanical descriptions of material damages such as fracture, fatigue, and corrosion, can be applied. Mechanical descriptions of material damages are based on the constitutive behaviors of materials as described in Table 2-2. Some of the constitutive models may be rate dependent. The constitutive models rely primarily on the assumption of a continuum and the material properties such as elastic constants can be described as spring elements and dashpots. Damage parameters associated with constitutive models require measurements such as deformation rate (in case of plastic or inelastic deformations), stress fields and crack tip opening and fracture process zone (in case of fracture), etc. (Barbero EJ, De Vivo L 2001; Budianski B, O'Connell RJ 1975).

Pre-existing defects that can help qualify damage at a later stage may also be essential. For example, the extent of micro-cracking in concrete and initial an-isotropy of material. In damage mechanics, these are described as internal variables. The damage affects the constitutive behavior, and the changes in internal variables become an essential requirement for the sensors. For example, (Barbero EJ, De Vivo L 2001) defines the extent of microcracks within a material as an internal damage variable and calling it microcrack density distribution. Rules of evolution must be defined to describe the pre-existing damage that was initiated and then increases; these can be described as constitutive damage laws. Correlation between constitutive material constants and damage variables to traditional sensor measurements such as strain gauges and displacement gauges, have been well defined. However, the new sensing techniques described in the following have not been defined.

Table 2-2
Mechanical Behavior Characterizing Material Damage

Linear Elastic	Hypoelastic	Hyperelastic	Viscoelastic	Plastic
Isotropic	Nonlinear	Large Strain	Time-Dependent	Irreversible
Non-Isotropic	Reversible	Rubber Elastic	Temperature	Rate Dependent
Orthotropic	Isotropic/Non-isotropic	Stretch		

Embedded and/or Topical Sensors

Technologies utilizing ETS include sensors made up of carbon nanotubes (Pammi S, Brown C, Datta S, et al. 2003), nano-oxides, piezoelectric ceramic, fiber optics (Fallon RW, Zhang L, Everall LA, et al. 1969-1973, 1988), and more. The following sections introduce some specific ETS technologies. It is important to identify the stage of development of a sensor in order to ensure proper application for concrete. Table 2-3 provides a summary of sensor technology that may be used for various defects and degradation mechanisms for reinforced concrete highlighted in Table 2-1. Table 2-3 indicates sensor type, resulting measurement, and characteristics. These sensors identified herein may be topical or embedded. Interrogation of these sensors may require contact or remote detectors. Also, it can be observed that the sensor technology indicated here requires electrical connectivity; therefore, it is very important to consider using components that are durable when embedded in harsh NCS environments. These sensors can indicate material strength during and after curing and structural strain. The range and sensitivity levels found in Table 2-3 are not intended to indicate exhaustive information of existing sensor technology. It is intended to provide general reference of these levels.

Figure 2-3 provides a basic rubric of NCS characterization based on likely concrete defects and available ETS technologies. The following sections detail the different types of sensors which may be utilized in/on NCSs.

<u>Fiber Optics</u>

Fiber optic (FO) sensors are popular sensors for structural monitoring because of their increased reliability, autonomy, ease of installation, and increased measurement quality (Fallon RW, Zhang L, Everall LA et al. 1969-1973, 1998). Fiber optics may be used as a single strand or in a bundle; additionally, fibers may be classified as short gauge (discrete) or long gauge (distributed). They have good sensitivity and resolution with the ability to measure in the level of microns and are resilient to relatively high temperatures (Glisic B 2007). However, FO sensors with this high-temperature resilience may require expensive materials such as gold. Often, FO sensors are used to provide a measurement across 20 mm or less. Distributed FO sensors are used to cover distances up to kilometers (Mrad N, Li H 2009). Depending on the FO sensor, they can be used to indicate a variety of physical parameters: temperature, pressure, strain, displacement, rotation, magnetic/electric field, and corrosion. They measure through different means and are classified as intensity-based fiber optic sensors, interference-based point sensors, polarization-based sensors, and Bragg Grating-based fiber optic strain gauges (Huston D 2011). In (Nunes, Olivieri, Kato, Luiz, Braga 2007), the authors measured strain ranging 'from 1,000 to 3,000 $\mu\varepsilon$ for temperatures as low as -253 °C.'

Fiber Optic sensors are especially ideal for NCS since they are not influenced by the electric saturation of the surrounding environment and will not be affected by chemical

attacks because they are essentially chemically inert. However, the placement and installation of FO sensors can be a challenge for existing NCS in areas where the concrete is not directly accessible.

<u>Carbon Nanotube Composite Coatings and Modified Concrete</u>

Carbon nanotube composite coatings consist of very small tubes of bonded carbon atoms. The bond between adjacent carbon atoms is covalent (sharing of electrons between atoms) and the tubes may be open-end or closed-end. The atoms are predominantly linked in a hexagonal shape with the closed-end tubes having a pentagonal shape near the ends (Wille K, Loh KJ 2010). Single cylinder tubes are labeled at SWCNT (single-walled carbon nanotubes); however, multiple tubes may be concentrically placed within each other and are labeled as MWCNT (multi-walled carbon nanotubes). The diameters are in the nanometer range with lengths up to several centimeters. Carbon nanotubes have the 'highest strength-to-weight ratio' of any known material with a total strength reported to be up to 150 GPa (Wille K, Loh KJ 2010). As such, they have reinforcing functions for the material in which they are embedded. The sensitivity of carbon nanotubes are reported to vary depending on the application. Carbon nanotubes can be used as a functional filler material of a coating that can then be applied topically. As a coating, it can be used to indicate the strain occurring in the substrate on which the coating is applied. This occurs because the electronic structure of the carbon nanotubes changes when the material stretches and compresses. In (Li H, Xiao H, Ou J 2004), the authors indicate that SWCNT using fluorescence spectra will 'reveal axial strains below 0.1%' which is sufficient for large-scale objects. A limitation of the application of this highly functioning coating is

23

systemic to all coating systems, which is the sufficiency of the bond between the coating and the substrate. Debonding characterized as peeling, scaling, or osmotic blistering will limit the benefit of the coating impregnated with carbon nanotubes.

Coatings containing carbon nanotubes were previously written about as a means whereby strain could be passively measured using changes in luminescence according to strain of the coating. Similar to this and the piezoelectric nanoparticles, carbon nanotubes may be dispersed within a concrete mix which will allow strain to be measured. One of the benefits of carbon nanotubes is that it has superior piezoelectric properties over traditional piezo-ceramic materials (Pammi S, Brown C, Datta S, et al. 2003). Historically, the biggest challenge with using carbon nanotubes is its tendency to coagulate which prevents it from fully dispersing within a binding matrix. Anti-covalent techniques are reported to degrade mechanical properties of the carbon nanotubes yet other techniques have shown to successfully provide long-term suspension and dispersion. Carbon nanotubes are expensive and a business case would be need to be established for applying carbon nanotubes throughout an entire NCS. Therefore, application of carbon nanotube would likely be through discretely patching strategically placed areas of the modified concrete mixture.

Piezoresistive Fibers

Fiber polymers were first used to reinforce concrete in the 1950s with more regular uses beginning in the 1980s (Muchaidze I, Pommenrenke D, Chen G 2011). Embedding fiber materials having piezoelectric properties into concrete will give it additional reinforcement (increasing its strength and stiffening) and improve its self-sensing functionality. Besides polymers, these materials can consist of graphite, carbon, steel (ACI

Committee 440 2007). When used in a bulk manner (i.e. the fibers are expected to be fully dispersed in the concrete) the fibers are randomly oriented. The random orientation of the fibers allows ubiquitous and isotropic strengthening and stiffening of the concrete while the use of piezoresistive material allows the self-sensing properties to be achieved (Han B, Yu X, Ou J 2014). Wang and Chung, in (Wang X, Chung DDL 1998), suggest that piezoresistive fibers may be used as a coating composite with an epoxy as a binder. When used in this manner the orientation of the fibers are in the plane of the thin coating. They may also be used as a sensor system with other piezoresistive materials where six-mm long fibers and copper gauze were embedded in a cement-based material (Han B, Guan X, Ou J 2006). Given the varying materials that can be used as piezoresistive fibers and the high temperatures found within areas of NCSs, thermal conductivity of the bulk material should be considered. Heat transfer through the member may have affect (positive or negative) on the exhaust of heat in the case of an accident. Or given the larger nature of these fibers, expansion of the material within the concrete may need to be offset by induced air-entraining admixtures as part of the concrete mixture design.

Piezoelectric Acoustic Emissions

Techniques involving acoustic emission sensors consist of measuring the elastic waves produced during a mechanical event – strain or fracture – with relatively low sensitivity (Sakamoto WK, Higuti RT, Tiago MM 2009; Marin-French P, Martin T, Tunnicliffe DL, et al. 2002; Qin, Peng, Ren, et al. 2009). Though these sensors are passive, a network of these sensors can indicate the location of an 'event' through triangulation. A traditional AE sensor consists of piezoelectric ceramic or crystal; however, composite

sensors are also used. In (Marin-French P, Martin T, Tunnicliffe DL, et al. 2002), the authors suggest that piezoelectric material is not compatible with the concrete in which it is embedded and the use of composite sensors is more superior. The sensor to which they refer is a composite consisting of piezoelectric rods embedded in cement. The cement phase of the composite provides low acoustic impedance and dielectric constant yet the embedded ceramic offers the traditional piezoelectric effects found in like-kind smart materials. Acoustic emission sensors often have a narrow band of frequency to be measured which sometimes doesn't correlate with the frequency of the 'mechanical event' of the concrete and is difficult to distinguish between vibrations occurring from the normal operation of the plant.

Skin-Type Sensor

Metal oxides may be used in a solid state as a thermistor because of the Arrhenius relationship between temperature and electrical conductivity. In previous experimentation, these oxides are mixed and then screen printed onto a substrate where they are sintered at a temperature up to a little more than 1,200 °C (Park K, Bang DY 2003). The sintering temperature and oxide composition affect the electrical properties of the sensor. None-the-less, the embedment of these thermistors can provide a value indication of concrete core and surface temperatures to determine the likelihood of delayed ettringite formation or excessive temperature differentials. Similarly, sensors may be applied in a thin patch-like manner (Zhang 2005).

Self-Sensing Concrete

Traditionally, strain is measured through the adhesion of a strain gage on the surface of a material. Self-sensing concrete allows embedment of nanoparticles with piezoelectric and/or electrostrictive properties to be dispersed throughout a concrete material (Agari Y 2009). The nanoparticles consist of various materials that include piezoelectric crystals, piezoelectric ceramic, composite of ceramic and polymer piezoelectric, graphite, carbon, steel (Kholkin AK, Kiselev DA, Kholkine LA, et al. 2009). This material may be used as part of a concrete mixture at proportions on the order of three to ten percent (Shen B, Yang X, Li Z 2006) of the cement content. Because of its ubiquitous nature within the concrete component, the strain range and sensitivity would theoretically be bound only by the limitation of the host material, in this case concrete. Once cracked to prevent connectivity, there would be a loss or, at best, reduction of strain sensitivity and accuracy (Pacheo-Torgal F, Gonzalez J, Jalali S 2011). As the hardened concrete is strained the electrical properties (conductivity/resistivity) of the concrete can be measured to indicate the level and type of strain which is occurring. For NCS with heavy congestion of reinforcing steel and the need to indicate strain through changes in electrical conductivity, placement of the electrodes to interrogate the conductivity of the bulk material will have small tolerances. The measuring mechanism is not only sensitive to strain but also to the conductivity of the NCS steel which pose difficulty in indicating the disparate causes of changes in electrical resistance.

Electrochemical Sensors

As discussed above, the corrosion of reinforcing steel is an electrochemical process (Muralidharan S, Ha TH, Bae JH, et al. 2006). The process requires the development of a

corrosion cell which includes an anodic area (where electrons are lost), cathodic area (where electrons are gained), metallic path (for concrete this is usually reinforcing steel), and an electrolytic path (concrete matrix lacking passivity) (Vennesland Ø, Raupach M, Andrade C 2007; Poursaee A, Weiss WJ 2009). Sensors and sensing techniques used to identify corrosion may be topical or embedded and can include varying techniques called potentiostatic linear polarization resistance, galvanostatic pulse polarization, potentiodynamic cyclic polarization, galvanostatic polarization, and electrochemical impedance spectroscopy (Andrade C, Sanchez J, Castillo A, et al. 2011). Depending on the technique, sensors require direct access to the reinforcing steel being measured or, at a minimum, electrical connectivity to the steel. Interpretation of electrochemical sensors are often difficult and care should be taken when performing analysis test results (Andrade C, Sanchez J, Castillo A, et al. 2011). Traditional electrochemical sensors are not developed to experience the high temperature environment that may be found in parts of nuclear power plants; so, the sensors used in this manner should be upfitted to be more robust or strategically placed away from high-temperature zones.

<u>Coaxial Cables</u>

Coaxial cables are used with varying material configurations and they usually consist of two layers of conductive material, one of which is spirally bound; and, they both sandwich another dielectric material (Muchaidze I, Pommenrenke D, Chen G 2011). The spiral nature of a portion of the cable is what sets it apart from most coaxial cables and is what helps provide its ability to become a sensor rather than a simpler transmitter of signal. They have been utilized for crack detection and corrosion monitoring on a variety of

28

structural members (Green GG, Belarbi A, Chen G, et al. 2005). For crack detection its primary mode of indication is electrical time-domain reflectometry (ETDR) which provides indication of strain (Sun S, Pommenrenke D, Drewiniak JL, et al. 2012). The strain is indicated because of discontinuities along the cable as portions of the spiral bound cable are stretched apart. It has also been placed near reinforcing steel found in concrete where corrosion was induced. The cable undergoes the same corrosion as the reinforcing steel and the pitting stifles the connectivity of the cable and indicates the corrosion. It should be noted that sensitivity and resolution of the sensor is a function of cable length. The cable lengths for most NCS applications is expected to be very long and stunt sensitivity and resolution. Additionally, there is no indication that the pitting location of the coaxial cables can be located, only that signal disruption is present. However, since corrosion of concrete reinforcing steel causes a large amount of damage to structures and further development of this technology would be very rewarding.

Table 2-3
Comparison of Different ETS Technologies

Sensor Type	Measurement	Range/Sensitivity	Application Issues
Fiber optics	Temperature, strain, corrosion, or stress	Up to several thousand microns, >300 °C (Fallon RW, Zhang L, Everall LA et al. 1969-1973, 1998; Glisic B 2007; Mrad N, Li H 2009; Huston D 2011; Nunes, Olivieri, Kato, Luiz, Braga 2007)	Heavy reinforcement environment will restrict placement; sensitive to mechanical vibration during concrete placement
Carbon nanotube composite coating	Strain	Unknown on actual structures (Withey, Vemura, Bachilo, et al. 2012)	Surface coatings are unable to detecting embedded issues.
Piezoresistive fibers	Stress	0.05% strain (Shen B, Yan Z, Li Z 2006;	Connectors are required.

		Suchanek WL, Riman RE 2009)	
Piezoelectric AE	Acoustic emissions energy, distance	1.5 mJ, 12 cm distance (Sakamoto WK, Higuti RT, Tiago MM 2009; Marin-French P, Martin T, Tunnicliffe DL, et al. 2002)	Detection depth is questionable; useable frequency range is questionable.
Skin-type sensor	Temperature	Up to 1200 °C (Park K, Bang DY 2003)	Surface indication only.
Polymer modified self-sensing concrete	Strain	Potentially unlimited (Agari Y 2009)	Radioactivity tolerance; heat tolerance; reinforcing steel compatibility; accuracy of damaged concrete is unknown.
Carbon nanotube modified concrete	Strain	Potentially unlimited (Pacheco-Torgal F, Gonzalez J, Jalali S 2011)	Durability
Electrochemical	Electron flow and chemical changes	(Vennesland Ø, Raupach M, Andrade C 2007)	Corrosion of reinforcing steel and internal chemistry of concrete; accuracy due to variations in concrete and environment.
Coaxial Cables	Strain and electron flow	Varied (Muchaidze I, Pommenrenke D, Chen G 2011)	Corrosion and cracking.
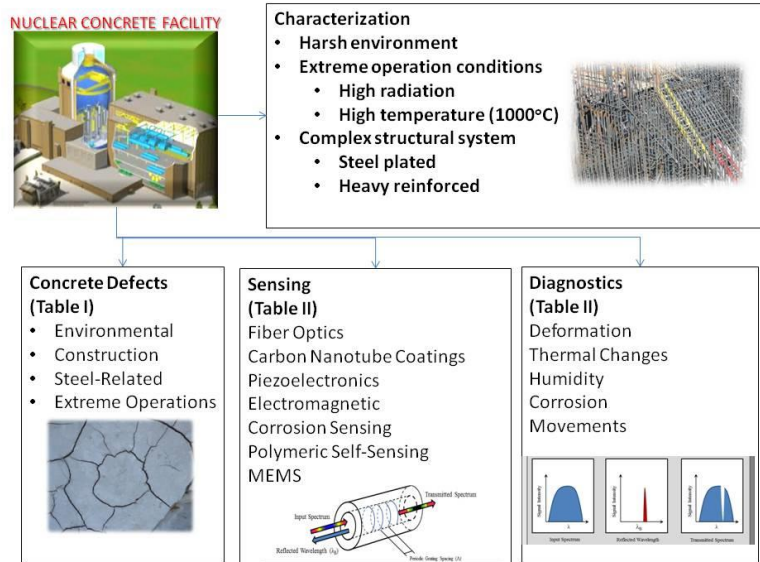
Figure 2-3
Schematic of Sensing Applications for NCS Evaluation

Technology Readiness and Discussion

Table 2-3 indicates different sensor types, resulting measurement, and characteristics and may be topical or embedded. Interrogation of these sensors may require contact or remote detectors. Also, it can be observed that the indicated sensor technology requires electrical connectivity; therefore, it is very important to consider using components that are durable when embedded in harsh NCS environments. These sensors can indicate material strength during and after curing and structural strain. The range and sensitivity levels found in Table 2-3 are not intended to indicate exhaustive information of existing sensor technology but, instead, provides general reference of these levels. Figure 2-3 provides a basic rubric of NCS characterization, likely concrete defects, and available ETS technologies.

Several of the sensors are made up of robust materials that can be discretely placed in concrete and act as functional fillers that are dispersed ubiquitously within the concrete. However, as previously noted, some of these sensors are still limited to being interrogated only by connecting through cables. As such, placement of sensors and their associated connections must be strategically placed in areas that are distant or shielded from high temperatures and radiation loading. Fortunately, areas of high radiation loadings is limited to a few distinct areas of the NCS; and, there are many areas and large amounts of concrete used for NCS that do not experience the harsh loading and temperature conditions. Areas of high radiation dose includes the pedestal for the reactor pressure vessel, shield containment walls, and dry cask storage containers (Electric Power Research Institute 2011).

Conclusion

Due to challenging characteristics including mass materials, extensive steel reinforcements, potential exposures to high temperature and radiation, application of NDT sensing for NCS extends beyond typical NDE sensor capabilities and innovative sensing technologies are needed. This paper brings awareness of the recent embedded and/or topical sensors (ETS) technologies into the nuclear industry. Identified ETS technologies include fiber optics, carbon nanotube composite coatings, piezoresistive fibers, piezoelectric acoustic emissions, skin-type sensors, self-sensing modified concrete, electrochemical sensors and coaxial cables. The topological advantages of these sensors stem from the fact that they are capable of being embedded or surficial, periodically or continuously monitored, and physically accessible or remotely monitored. However, for

actual NCS applications, additional considerations such as signal interrogation methods should be robust for the hush environment. Nonetheless, many ETS technologies have high potential for unconventional applications such as for NCS systems.

Acknowledgement

References

Abu-Yosef AE, Pasupathy P, Wood SL, et al. Detection of Multiple Corrosion Thresholds in Reinforced Concrete Structures Using Passive Sensors. Smart Structures, In Gyekenyesi AL, editor. SPIE 8347, Smart Structures. SPIE. April 5, 2012.

ACI Committee 201. ACI 201.1R-08, Guide for Conducting a Visual Inspection of Concrete in Service. Farmington Hills (MI): American Concrete Institute; 2008.

ACI Committee 222. ACI 222R-01, Protection of Metals in Concrete Against Corrosion. Farmington Hills (MI): American Concrete Institute; 2001.

ACI Committee 228. ACI 228.2R, Nondestructive Test Methods for Evaluation of Concrete in Structures. Farmington Hills (MI): American Concrete Institute; 1998.

ACI Committee 349. ACI 349.3R, Evaluation of Existing Nuclear Safety-Related Concrete Structures. Farmington Hills (MI): American Concrete Institute; 2002.

ACI Committee 440. ACI 440R-07, Report on Fiber Reinforced Polymer (FRP) Reinforcement for Concrete Structures. Farmington Hills (MI): American Concrete Institute; 2007.

ACI Committee 515. ACI 515.2R-13 Guide to Selecting Protective Treatments for Concrete. Farmington Hills (MI): American Concrete Institute; 2013.

Agari, Y. Functionally Graded Polymer Blend. In: Schwartz M, editor. Smart Materials. Boca Raton (FL): CRC Press; 2009. 3.

American Concrete Institute (ACI). Concrete Terminology, ACI CT-13. Farmington Hills (MI): ACI; 2013.

Andrade C, Sanchez J, Castillo A, et al. Interpretation of Corrosion Monitoring from Embedded Sensors. In: 15th International Conference on Structural Health Monitoring of Intelligent Infrastructure, SHMII-5; December 11-15, 2011: 1-7.

ASTM Committee C09. Standard Test Method for Pulse Velocity Through Concrete. West Conshohocken (PA): ASTM International; 2002.

ASTM Committee C09. Standard Practice for Evaluation the Condition of Concrete Plates Using Impulse-Response Method. West Conshohocken (PA): ASTM International; 2010.

Barbero EJ, De Vivo L. A Constitutive Model for Elastic Damage in Fiber-Reinforced PMC Laminae. International Journal of Damage Mechanics SAGE. January, 2001; 10: 73-93.

Bhardwaj MC. Noncontact Ultrasonic Testing and Analysis of Materials. In: Schwartz M, editor. Smart Materials. Boca Raton (FL): CRC Press; 2009: 9.3.

Budiansky B, O'Connell RJ. Elastic Moduli of a Cracked Solid. International Journal of Solid Structures. June 27, 1975; 12 (2): 1281-1297.

Clayton and Hileman. Light Water Reactor Sustainability Nondestructive Evaluation for Concrete Research and Development Roadmap. Oak Ridge (TN): Oak Ridge National Laboratory; 2012.

Fallon RW, Zhang L, Everall LA, et al. All-Fiber Optical Sensing System: BG Sensor Interrogated by Long-Period Grating. Measurement Science Technology. December, 1998; No. 9 (12): 1969-1973.

Federal Highway Administration (FHWA). Prediction of Chloride Penetration in Concrete. McLean (VA): FHWA; 2001.

Fillmore, DL. Report INEEL/EXT-04-02319, Literature Review of the Effects of Radiation and Temperature on the Aging of Concrete. Idaho Falls (ID): NEEL; 2004.

Ghasr T, LePape Y, Scott DB, et al. Holographical Microwave Imaging of Corroded Steel Bars in Concrete. ACI Mater J. January-February, 2015; 112(1): 115-124.

Glisic, B. Fibre Optic Methods for Structural Health Monitoring. West Sussex (UK): John Wiley & Sons Ltd.,: 2007.

Greene GG, Belarbi A, Chen G, et al. Distributed Coaxial Cable Crack Sensors for Crack Mapping in RC. Tomizuka M, editor. Proceedings of SPIE Vol. 5765, Smart Structures and Materials. 2005; Bellingham, WA: 407-418.

Han B, Guan X, Ou, J. Electrode Design, Measuring Method and Data Acquisition System of Carbon Fiber Cement Paste Piezoresistive Sensors. Science Direct, Sensors and Actuators A. 2006; No. 135: 360-369.

Han B, Yu X, Ou J. Self-Sensing Concrete in Smart Structures. New York (NY): Elsevier Inc.: 2014.

Huston D. Structural Sensing, Health Monitoring, and Performance Evaluation. Boca Raton (FL): CRC Press / Taylor and Francis Group, LLC: 2011.

Institution of Structural Engineers (ISE). Structural Effects of Alkali-Silica Reaction. London (UK): ISE, SETO Ltd.; 1992.

Kee, Fernandez-Gomez, Zhu. Evaluating surface-breakage cracks in concrete using air-coupled sensors. ACI Mater J. September-October, 2011; 108(5): 558-565.

Kholkin AK, Kiselev DA, Kholkine LA, et al. Piezoelectric and Electrostrictive Ceramics Transducers and Actuators. In: Schwartz M, editor. Smart Materials. Boca Raton (FL): CRC Press; 2009. 9.1.

Kim DJ, Lee C, Chang H, et al. Embedded Piezoelectric Sensor-Based Real-Time Strength Monitoring during Curing Process of Concrete. SPIE 7981, Sensors and Smart Structures Technologies for Civil, Mechanical, and Aerospace Systems. April 14, 2011; San Diego, CA.

Kim, Kim, Seo, et al. Feasibility Study of the IE-SASW Method for Nondestructive Evaluation of Containment Building Structures in Nuclear Power Plants. Nucl Engin and Des. January 23, 2002; 219: 97-110.

La Plaine Cedex Association de Normalisation (AFNOR). Methodology for Qualification on Non-Destructive Tests. La Plaine Cedex (FR): AFNOR; 2005.

Li H, Xiao H, Ou, J. A Study on Mechanical and Pressure-Sensitive Properties of Cement Mortar with Nanophase Materials. Cem and Concr Res. 2004; 34: 435-438.

Marin-Franch P, Martin T, Tunnicliffe DL, et al. PTCa/PEKK Piezo- Composites for Acoustic Emission Detection. Science Direct, Sens and Actuators A 99. 2002; No. 99(3): 236-243.

Mindess S, Young JF, Darwin D. Concrete. Upper Saddle River (NJ): Pearson Education, Inc.; 2004.

Mrad N, Li H. Fiber Optic Systems: Optical Fiber Sensor Technology. In: Schwartz M, editor. Smart Materials. Boca Raton (FL): CRC Press; 2009. 14.1.

Muchaidze I, Pommenrenke D, Chen G. Steel Reinforcement Corrosion Detection with Coaxial Cable Sensors. Tomizuka M, Yun CB, Giurgiutiu V, et al., editors. Proceedings of SPIE Vol. 7981, Sensors and Smart Structures Technologies for Civil, Mechanical, and Aerospace Systems (79811L-1); 2011.

Muenow RA. Field Proven NDT Methods for Evaluation of Damage and Repair of Nuclear Facilities. Nuclear Plant Journal. 1988; 6: 81-82, 89.

Muralidharan S, Ha TH, Bae JH, et al. A Promising Potential Embeddable Sensor for Corrosion Monitoring Application in Concrete Structures. Measurement. 2006; 40: 600-606.

NACE TG 356. Stray-Current Induced Corrosion in Reinforced and Prestressed Concrete Structures. Houston (TX): NACE International; 2010

NACE TG 400. SP0112, Corrosion Management of Atmospherically Exposed Reinforced Concrete Structures. Houston (TX): NACE International; 2012

Naus, DJ. Report No. ORNL/TM-2007/191, Inspection of Nuclear Power Plant Structures – Overview of Methods and Related Applications. Oak Ridge (TN); 2007.

Non-Destructive Tests on Hardened Concrete. Geneva (CH): International Standards Organization (ISO); 2004.

Nuclear Energy Agency (NEA). Electrochemical Techniques to Detect Corrosion in Concrete Structures in Nuclear Installations. Vienna (Austria): NEA; 2002.

Nunes, Olivieri, Kato, Luiz, Braga. FBG sensor multiplexing system based on the TDM and fixed filters approach. Science Direct, Sensor and Actuators, A. 2007; 138: 341-349.

Pacheco-Torgal F, Gonzalez J, Jalali S. Sustainable Monitoring of Concrete Structures: Strength and Durability Performance of Polymer-Modified Concrete. International J of Sustainable Energy. 2011; First article, 1-5.

Pammi S, Brown C, Datta S, et al. Concepts for Smart Nanocomposite Materials. Smart Materials, Structures, and Systems, SPIE 5062; 2003; 5062: 629-636.

Park K, Bang DY. Electrical Properties of Ni-Mn-Co-(Fe) Oxide Thick-Film NTC Thermistors Prepared by Screen Printing. J. Mater Sci Mater Electronics. 2003; No. 14: 81-87.

Poursaee A, Weiss WJ. An Automated Electrical Monitoring System (AEMS) to Assess Property Development in Concrete. Automation in Constr. 2009; 19: 485-490.

Power Reactor Information System (PRIS) [Internet]. Geneva (CH): International Atomic Energy Agency (IAEA). [cited June 2015]. Available from: https://www.iaea.org/pris/.

Qin, Peng, Ren, et al. Application of cement-based piezoelectric composites in acoustic emission detection for concrete. In: Jinsong L, Anand K, Asundi, et al., editors. Proceedings of SPIE Vol. 7493, Second International Conference on Smart Materials and Nanotechnology in Engineering; 2009, p. 1-9.

Renshaw J, Guimaraes M, Scott DB. Thermographic Inspection of Massive Concrete Structures. Proceedings of the 2013 QNDE Conference; 2013; p 978-984.

Sakamoto WK, Higuti RT, Tiago MM. Piezoelectric Composite Film for Acoustic Emission Detection. Ultrasonics Symp, IEEE. September 20-23, 2009; Rome: 1487-1490.

Scott, D. Internal Inspection of Reinforced Concrete for Nuclear Structures Using Shear Wave Tomography. Energy Convers and Manag.; 2013; 74: 582-586.

Shen B, Yang X, Li Z. A Cement-Based Piezoelectric Sensor for Civil Engineering Structure. Materials and Structures. 2006; 1-5.

Sreekala R, Muthamani, K. Structural Applications of Smart Materials. In: Schwartz M, editor. Smart Materials. Boca Raton (FL): CRC Press; 2009. 4.

Suchanek WL, Riman RE. Intelligent Synthesis of Smart Ceramic Materials. In: Schwartz M, editor. Smart Materials. Boca Raton (FL): CRC Press; 2009. 2.

Sun S, Pommerenke D, Drewniak JL, et al. Signal Loss, Spatial Resolution, and Sensitivity of Long Coaxial Crack Sensors. Shih-Chi Liu, editor. Proceedings of SPIE Vol. 5391, Smart Structures and Sensors. 2012; Bellingham, WA: 786-797.

Technical Committee B/517. Concrete - Determination of Ultrasonic Pulse Velocity. Brussels (BE): British Standards Institute (BSI); 2004.

U.S. Nuclear Regulatory Commission (USNRC). U.S. Nuclear Regulatory Commission Regulations: Title 10, Code of Federal Regulations. Washington, DC (USA): USNRC; 2014.

Vennesland Ø, Raupach M, Andrade C. RILEM TC 154-EMC, Electrochemical Techniques for Measuring Corrosion in Concrete – Measurements with Embedded Probes. Materials and Structures. 2007; 40: 745-758.

Wang X, Chung, DDL. Short Carbon Fiber Reinforced Epoxy Coating as a Piezoresistive Strain Sensor for Cement Mortar. Science Direct, Sensors and Actuators. 1998; No. 71: 208-212.

Wille K, Loh KJ. Nanoengineering Ultra-High-Performance Concrete with Multiwalled Carbon Nanotubes. Transportation Research Records. 2010; 2142: 119-126.

William K, Xi Y, Naus D, et al. Review of the Effects of Radiation on Microstructure and Properties of Concretes Used in Nuclear Power Plants. Washington DC (USA): US Nuclear Regulatory Commission (USNRC); 2013.

Withey, Vemuru, Bachilo, et al. Strain Paint: Noncontact Strain Measurement Using Single-Walled Carbon Nanotube Composite Coatings. Nano Lett, Am Chem Soc. June 13, 2012; 12: 3497-3500.

Yang M, Dai J. Review on Optical Fiber Sensors with Sensitive Thin Films. Photonic Sensors. October 21, 2012; 2 (1): 14-28.

Yao Y, Tung S-T E, Glisic B. Crack Detection and Characterization Techniques - An Overview. Struct. Control and Health Monitoring. February, 2014, 21; 1387-1413.

Zhang. Piezoelectric Paint Sensor for Real-time Structural Health Monitoring. In: Tomizuka M, editors. Proceedings of SPIE Vol. 5765, Smart Structures and Materials; 2005; Bellingham, WA: p. 1095-1103.

CHAPTER 3 DECISION CONSIDERATIONS FOR STRUCTURAL HEALTH MONITORING DESIGN FOR NUCLEAR REINFORCED CONCRETE

Abstract

Structural health monitoring (SHM) has been suggested for monitoring reinforced concrete structures at nuclear plants through embedded, surficial, or attached sensors that identify changes of important concrete parameters including strain, temperature, stress, and vibration. Because of the vast number of available techniques, it is always a challenge in selecting an appropriate sensor and sensor-system for specific concrete structures in various loading and environmental conditions. In nuclear facilities, there are unique considerations including high temperatures and radiation that do not exist in residential and other commercial concrete structures. To illustrate the challenges of detecting thermal changes in nuclear concrete, a thermal analysis of a nuclear reinforced concrete model is conducted. This paper examines the different aspects of SHM sensor strategy and selection, and it recommends a multi-criteria decision approach to provide decisive direction for the most appropriate sensor to utilize for structural monitoring.

Keywords: decision analysis, nondestructive evaluation (NDE), nuclear reinforced concrete, nuclear concrete structures (NCS), sensors, structural health monitoring (SHM)

Introduction

Nuclear facilities utilized a significant amount of reinforced concrete structural elements. Examples of nuclear related, reinforced concrete structures are cooling fluid intakes, cooling towers, containments, spent-fuel pools, and dry-cask storage. Traditional nondestructive evaluation (NDE) has been used for the investigation and evaluation of nuclear concrete structures (NCS) for decades (Naus 2009). NDE has been used to investigate aging effects of concrete containments at nuclear power plants for problems including chemical attacks, physical attacks, and degradation factors such as leaching, alkali-aggregate reactions, freeze-thaw, fatigue/vibration, corrosion, elevated temperature, and others (IAEA 2002, Scott 2013). NDE devices and associated techniques have been documented in Malhotra & Carino (2004), technical reports (AFNOR 2005, Internatinal Standards Organization, 2004, IAEA 2002 and 2005, Technical Committee B/517, EPRI 2000, Committee on the Safety of Nuclear Installations 2002, NACE TG055, 2008, Federal Highway Administration, 2001, Hola & Schabowicz 2010, and ASTM standards (Committee G01 2009, Committee C09 2004, Committee C09 2010 and Committee C09 2002), etc. Beyond these publications there are copious journal articles and trade publications on NDE techniques. Some recent NDE advancements are progressing including microwave holography to detect steel corrosion (Ghasr et al. 2015) or air coupling (instead of direct contact) devices to the test surface (Kee et al. 2011 and Bhardwaj, 2009).

One of the key challenges regarding traditional NDE techniques is the requirement for personnel to be "hands-on" to operate the equipment at the specific location of the

reinforced concrete member which is being investigated, which may be difficult and may expose inspectors to hazardous working environment. More recently, embedded and advanced sensors are being used to initiate, supplement, and/or replace traditional NDE testing strategies and plans. These advanced sensors include fiber optics, piezoresistive fibers, nano-scale composites, nanotube modified concrete, and electrochemical based sensors, etc. This is especially pertinent for nuclear facilities because the unique configuration and the sensitivity issues of certain parts of these structures necessitating limited access to perform NDE. The combination of multiple hindrances creates significant complications for NDE and high-fidelity investigations for nuclear applications.

Structural health monitoring (SHM) typically refers to the use of embedded or automated sensor systems to evaluate a structure without personnel being present. SHM techniques include using sensors made up of single-walled carbon nanotubes (Withey et al. 2012), nano-oxides (Li et al. 2004), piezoelectric ceramic (Kim et al. 2011, Shen and Li 2006, Suchanek and Riman 2009), fiber optics (Yang and Dai, 2012), and electrochemical sensors. These sensors may be topical (Withey et al. 2012) or embedded (Li et al. 2004) and the interrogation of these sensors may be contact-based or may be remote (Abu-Yosef et al. 2012). They have been shown to indicate material strength during and after curing (Kim et al. 2011 and Park and Kim, 2011), structural strain (Li et al. 2004), and crack development (Yao et al. 2014). Given the copious types of sensors and properties, the engineer needs to decide the appropriate sensors and sensing technology for the particular application.

This paper suggests a simple decision-making approach to determine the right sensor to be utilized in a nuclear facility. Parameters considered in decision making include material properties, mechanical properties, and loading, etc. To understand the challenges in nuclear reinforced concrete, numerical modeling of nuclear reinforced concrete member is used to determine the requirements for sensor sensitivities.

Damage Mechanisms and Sensor Selection

The first step in sensor selection is to profile the damage scenarios and failure mechanics of the target structure. Reinforced concrete has a multitude of damages and degradation mechanisms which affect its performance. Table 3-1 summarizes possible damage/degradation mechanisms pertaining to NCS' structural elements including embedded reinforcements. The reduction in NCS structural integrity may be material-related (either concrete or steel reinforcement) and/or structurally-induced and may occur during placement of the concrete or due to long-term use. Hence, many of the identified problems in Table 3-1 are time-dependent processes and can impact sensor selection and sensing strategy design.

Obviously, the location of the specific structural element within the nuclear power facility dictates the likely induced damage/damages to the structure. Regardless of the location, the potential for reinforced concrete to be damaged increases for nuclear facilities because of the size of the structural members, the heavy congestion of reinforcing steel, the exposure to nuclear radiation, and the exposure to high temperatures.

<u>Sensor Considerations</u>

The initiation of the damages associated with nuclear concrete described in Table 3-1 are mostly characterized as material and interface damages and little on structural damages. Hence, classical mechanical descriptions of material damages such as fracture,

Table 3-1

Different Problems Associated with Nuclear Reinforced Concrete

Problem	Description
Alkali-aggregate reactivity (AAR)	A chemically-induced reaction that is subcategorized as alkali-carbonate reaction (ACR) and alkali-silica reaction (ASR); it occurs as a result of certain types of cement reacting, deleteriously, with the silica and/or carbon in the aggregate of the concrete.
Carbonation	A chemical process which can cause broad surface damage, micro-cracking, and shrinkage. American Concrete Institute (ACI) defines carbonation as "reaction between carbon dioxide and a hydroxide or oxide to form a carbonate, especially in cement paste, mortar, or concrete." (American Concrete Institute, 2013)
Chloride ingress	Chlorides are sometimes environmentally induced or purposefully applied. They may be the result of being near large bodies of salt water or applied on icy areas. Chloride ingress is a common cause for corrosion of reinforcing steel found in concrete.
Coating failure	A common focus in nuclear concrete structures and failure modes may consist of peeling, blistering, or flaking. "Coatings may consist of paints, mortars, liquefied rubbers, and resins." (ACI Committee 350, 2004) A loss of coating function may lead to rapid loss of concrete integrity.
Corrosion	Electrochemical phenomenon in which the steel reinforcement sheds electrons and deteriorates while the same reinforcing steel gains section volume due to the deposit of an iron oxide. (ACI Committee 222, 2001)
Cracks and voids	May occur both perpendicular or parallel to the surface and may result from insufficient vibration of the concrete during placement, inadequate design, overstress of the concrete while in plastic or hardened states, restraint, etc.
Creep	The contraction, expansion, flexural, and/or torsional deformations of concrete as a result of sustained load.
Debonding of liner and/or steel	Large portions of nuclear structures consist of composite materials where the concrete is lined with steel that is near one-inch thick. Debonding may occur when shrinkage of the concrete or external loading causes unplanned separation between the materials.

Delamination	A specific type of crack that is generally oriented parallel to the concrete surface which may be caused due to improper curing of the concrete, insufficient transverse reinforcement across a section, or creep.
Delayed ettringite formation (DEF)	Another chemically-induced damage mechanism in which an expansive gel is produced around the concrete aggregate during continued strength gain and induces excessive stress and strain on the concrete which then succumbs to cracking.
Fatigue	The condition in which cracking and breaking occurs due to the repeated and cyclical application of a load which is usually occurring at high frequencies.
Fire exposure	In some causes fire exposure (and other means of high temperature for that matter) may cause a variety of damage such as surficial dehydration, spalling, strength loss, reduction of elasticity, and potentially full loss of structural integrity. "More severe fires and thermal exposure can produce differential expansion between the steel reinforcement and concrete and the loss of bond between the concrete and the reinforcement." (ACI Committee 349, 2002)
Freeze-thaw	The expansion of internal moisture when it freezes while in hardened concrete. The expansion may cause extensive cracking.
High-energy impact	This may be a cause of significant damage due to internal or external impact from objects must be resisted. These objects may act like missiles which may cause concrete damage on small and large scales.
High-temperature exposure	Potentially in excess of 600 F (315 C), the high temperatures found in nuclear facilities reduces the material strength, modulus, and durability of the concrete causing it to desiccate and become brittle.
Irradiation	The reduction of concrete mechanical strength or durability due to neutron irradiation.
Inclusion	The introduction of unwanted material that may be cast within structural concrete. The presence of contents such as gloves, lumber, plastic, etc. creates inferior concrete which is prone to cause failure, corrosion, and/or degradation.
Leaching	The extrusion of minerals from concrete as a result of flowing or penetrating moisture. "If this leaching progresses without mitigation, the leaching process can produce a loss of mechanical properties, such as compressive strength and modulus of elasticity." (ACI Committee 349, 2002)
Leak rate failure	A leak test which is required for verification of the pressure or leakage limited boundaries of nuclear containment structures according to Appendix J to Title 10, Part 50 of the Code of Federal Regulations (U.S. Nuclear Regulatory Commission, 2014). The leak tests determine the ability of the structure to maintain positive, internal pressure.
Loss of post-tension tension	The rupture or excessive elongation of a tendon or the slippage of a tendon between it and the surrounding concrete in which structural failure may eventually result.

Map cracking	A particular type of cracking that usually occurs due to chemically-induced damage mechanisms (e.g., delayed ettringite formation, alkali-aggregate reaction); the name was established because the array and pattern of cracking appears to be similar to road lines on a map.
Shrinkage	Defined by ACI as a "decrease in either length or volume of a material resulting from changes in moisture content or chemical changes." (American Concrete Institute, 2013) The phenomenon may cause cracking during instances when the concrete is restrained to prevent the shrinkage.
Sulfate attack	A chemical process which occurs when a compound called monosulfoaluminate (C_4ASH_{12}) detrimentally reacts with sulfates to form ettringite ($C_6AS_3H_{32}$). Ettringite being expansive may lead to cracking and deterioration of the concrete.
Thermal differential	The temperature difference between two internal locations within concrete. A common problem in mass concrete, thermal differential could lead to cracking because the thermal gradient creates differential expansion and contraction.

fatigue, and corrosion, can be applied. Mechanical description of damages is important for the interpretation of the extent of damage as a function of the services life. Mechanical description of material damages is typically based on the constitutive behaviors of materials as described in Table 3-2. The constitutive models rely primarily on the assumption of a continuum and the material properties, such as elastic constants, can be described as spring elements and dashpots. Damage parameters associated with constitutive models require measurements such as deformation rate (in case of plastic or inelastic deformations), stress fields and crack tip length (in case of fracture), etc. (Barbero & Lonetti 2002)

Pre-existing defects that can be associated with damage at a later stage may also be essential. For example, the extent of micro-cracking in concrete and the initial anisotropy of a material. In damage mechanics, these are described as internal variables. The ability to determine the damage affects, constitutive behavior, and changes in internal variables

become an essential requirement for the extent of sensing system design including the number of sensors and the coverage area. Rules of evolution must be defined to describe the pre-existing damage that was initiated and then increases; these can be described as the constitutive damage laws (Budiansky-O'Connell 1976). Correlation between the constitutive material constants and damage variables to the traditional sensor

Table 3-2
Mechanical Behavior Characterizing Material Damage

Linear Elastic	Hypoelastic	Hyperelastic	Viscoelastic	Plastic
Isotropic	Nonlinear	Large strain	Time-dependent	Irreversible
Non-isotropic	Reversible	Rubber elastic	Temperature	Rate dependent
Orthotropic	Isotropic / Non-isotropic	Stretch		

measurements such as strain gauges and displacement gauges, have been well defined. However, the new sensing techniques incorporated in SHM schemes have not been defined.

It is important to acknowledge the varying aspects of embedded sensor applications for nuclear power plants in order to devise strategy for the placement of sensors. First, one must consider whether the effect detected at an isolated location is a valuable enough indication of the effect across an entire member. For example, if strain across an entire member is required then a distributed system with possibly multiple strain gauges may be warranted. On the other hand, a fully distributed sensor system (i.e. the straining detection is continuous across the entire length of the sensor such as in Brillouin –type continuous

fiber optic sensors) may not be as valuable as distributed discrete sensors which may provide multi-directional strain indications.

Additional items to consider are wired versus wireless data communications. The sensors and the sensor connections will, at times, need to be radiation hardened and/or resilient against high thermal loading (as indicated in the following section). It is not good enough to cavalierly place sensors on/in an NCS member. Sensor direction, placement frequency, type, resolution and sensitivity must accommodate difficult configurations, compatibility of varying materials, and radiation and thermal loading found at a nuclear power plant. Sensor resolution and sensitivity together determines the damage detectability of the sensor to the target issue.

Modeling Example of Thermal Stress Propagation in NCS

To illustrate the unique NCS thermal sensing scenarios, heat transfer within an NCS member is modeled using ANSYS (Goodman 2011, Smith 2011). NCS concrete containments contain reinforcement meshes in two orthogonal directions and often contain post-tensioned tendons. In addition, shear stirrups, lap or mechanical splices, and anchor embeds are added to the concrete matrix congestion (Figure 3-1). Hence, the model consists of a heavily reinforced concrete beam (24 in. x 48 in. x 192 in.) (Figure 3-2). The upper portion of the member contains a single row of reinforcement (compression face). The bottom side (tension face) of the member contains two layers of reinforcement. A tendon duct and bundle are located near the bottom face using an unbonded, post-tensioning system. The hatching shown in Figure 3-1 between the tendon bundle and duct wall represents a corrosion inhibitor.

Figure 3-2 shows the numerical model subjected to thermal transient stressing with an external thermal loading which increased from 70 °F to 700 °F at a rate of 0.1 °F/s. The transient, internal thermal effects are then determined while a maximum thermal loading of 700 °F was sustained for 72 hours. Figure 3-2 shows the results from the damaged beam and undamaged beam at 12 hours of heat transfer loaded from the bottom. To simulate corrosion, the bottom tendon is cut at the mid-section. The results indicate
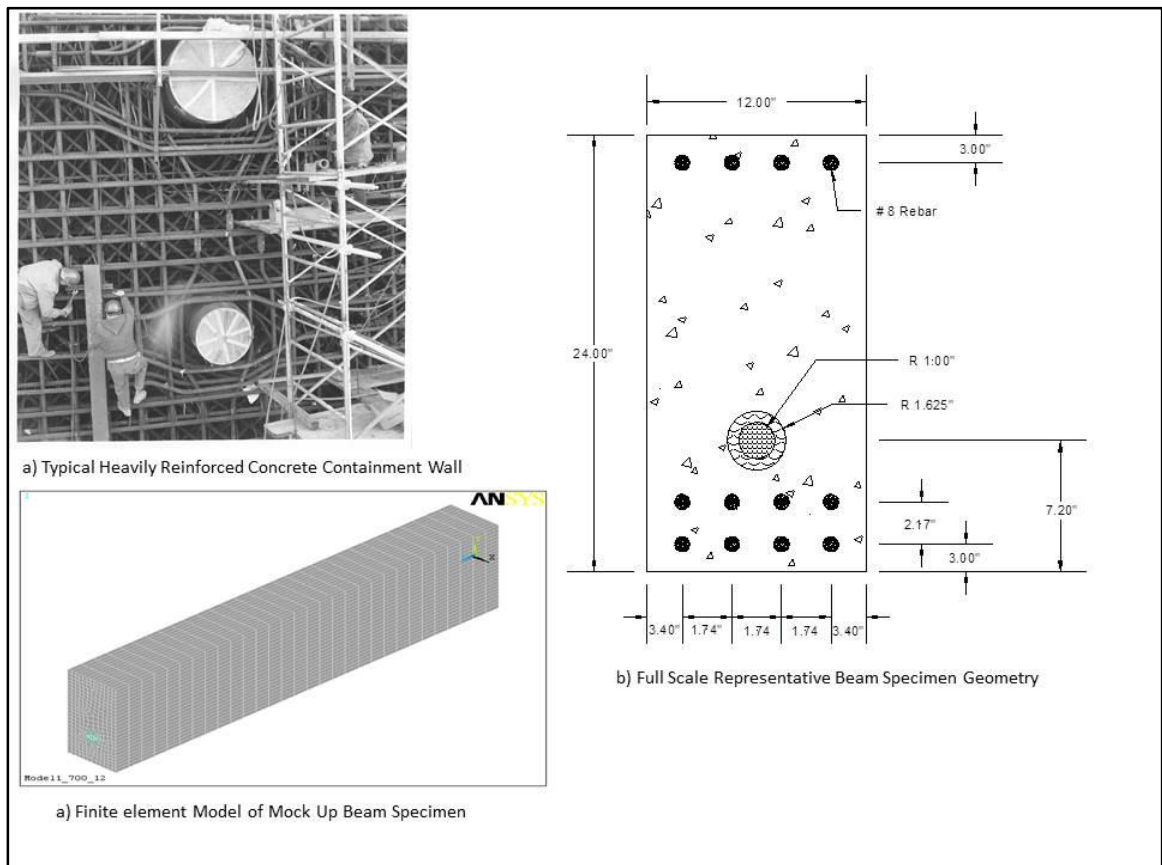

a) Typical Heavily Reinforced Concrete Containment Wall

a) Finite element Model of Mock Up Beam Specimen

b) Full Scale Representative Beam Specimen Geometry

Figure 3-1
FE Modeling of Mock-Up NCS Beam: a) Typical NCS Construction; b) Full-Scale
Mock-Up Beam Design; and c) Finite Element Model (Goodman, 2011)
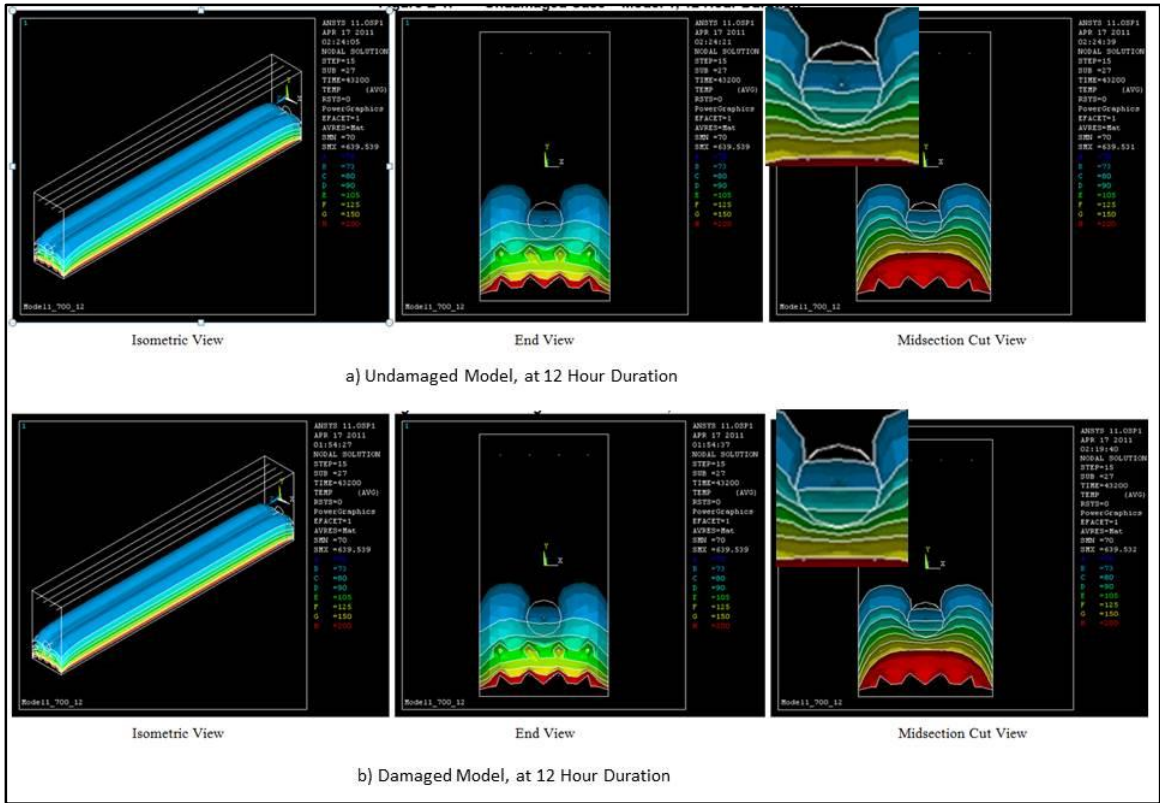
Figure 3-2
Temperature Distribution for Damaged and Undamaged Beams at 12 Hours (Goodman, 2011)

only a slight change in stress profile with tendon temperature at the maximum effect only reaching approximately 90.5 °F (undamaged case) and approximately 88.5 °F (damaged case). Figure 3-3 shows the temperature variation along the tendons for both undamaged and damaged cases. The thermal effect is even less significant at the top of the beam (which took several hours before the heat reaches the top of the beam).

Numerical modeling of the NCS can be a viable and cost-saving approach for the proper selection of placement and networking of embedded or topical SHM sensors. As such, mathematical models of the concrete at various stages of its strain are beneficial for an effective sensor regimen. An important conclusion from the model is that sensing in
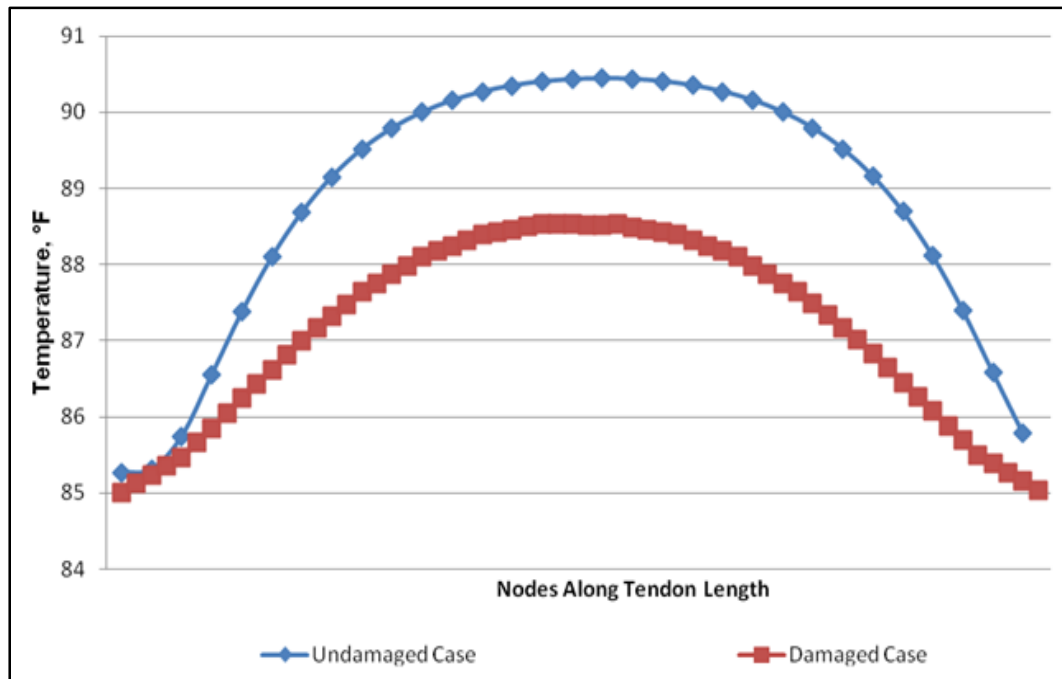
Figure 3-3
Temperature Variation along the Tendons for Undamaged and Damaged Cases (Smith, 2011)

NCS may require sensors to be close to the heat source – hence, a strategically placed sensing system would be required. Additionally, the sensors must be designed with steady data streaming with robust wires which will need to be durable such that the extreme heat simulated in this model does not destroy the sensing system through loss of connectivity.

Similar models of composites have been utilized in which the material is characterized as a continuum "cast in a consistent thermodynamic framework that automatically satisfies the thermodynamic restrictions" (Barbero & Lonetti 2001 and 2002, Barbero, Greco, and Lonetti, 2005). The different stages of strain referred to above consist of models which characterize concrete while it is elastic, plastic, fractured, and healing. Some sensors may still be effective even after the concrete has fractured. However, most sensors will require the concrete to remain uncracked in order to maintain effectiveness.

For instance, self-sensing concrete using piezoelectric nanoparticles have indicated changes in strain through changes in electrical conductivity/resistance in the concrete, which may require maintaining electrical connectivity throughout a failure process. Credible studies are needed to test the level of cracking (which a concrete could undergo) while still maintaining enough material of a monolith. None the less, the level of concrete strain and the extent at which sensors will be effective should be determined prior to the design of the SHM network.

Traditional NDE techniques include visual, stress waves, nuclear, magnetic and electrical, penetrability, infrared thermography, and radar – all require energy imputation and measure the subsequent mechanical, electrical, or particle wave responses of the structure (Fallon et al. 1998). Similarly, current potential SHM techniques require energy imputation and measurement of specific responses (Li et al. 2006, Withey et al. 2012, Pammi et al. 2003, Wang and Chung 1998, Han et al. 2007, Sakamoto et al. 2009). Some recent sensor advancements include air coupled systems and topometric (scanning) systems, etc. (Kee et al. 2011). However, these techniques, including visual, are not always achievable due to the complexities and hindrances highlighted above.

Decision Analysis Options for Sensor Selection

In this section, a decision analysis is conducted for the purpose of selecting the right SHM sensor to be used for an NCS. As shown by the numerical model, decision analysis requires that the engineer decides on the relevant and critical parameters and selection criteria. The selection criteria may include cost, life expectancy, remote monitoring, self-

sustainment, reliability, robustness, accuracy, ease of deployment/placement, and maintenance.

Decision analysis techniques may consist of a single criterion or of multiple criteria. A single-criteria decision analysis technique compares multiple options with a given criterion and make a decision according to that single criteria. One example of single-criteria decision analysis technique is the decision tree analysis, which is a graphical and quantitative technique used to solve a properly developed decision analysis problem. It primarily consists of decision nodes, uncertainty nodes, connecting branches, alternatives, probabilities, outcomes, consequences, and expected values, etc. (Clemen and Reilly 2014). It includes possible decision options between selected alternatives which best accommodate fundamental objectives made by the decision maker. For single criteria analysis, a decision tree is established and then "rolled back" to determine the decision with the highest expected value.

Although single-criteria analysis is valuable, most scenarios will require meeting multiple design criteria. Multi-criteria decision trees also include the same components as noted above and are also rolled back. However, multi-criteria decision trees require additional operations for proper comparison of alternatives. Multi-criteria decision analysis requires: 1) scaling of different criteria and 2) subjective weighting of the criteria. Scaling adjusts the data such that all of the values consist of like-kind units. The weighting is the subjective valuing of the criteria to ensure that the criteria is being appropriately considered relative to each other. Common units for the criteria must be developed in order for comparisons to be made. This is typically accomplished by using percentages.

Due to the concrete complexity, this study will focus on a multi-criteria analysis approach for sensor selection of sensors. Multi-criteria analysis includes weighting the importance of the varying criteria which allows decision makers to provide subjective importance to the various criteria. Weighting will always be subjective and can be catered to the management needs of an NCS. For instance, given the nature of nuclear power plants and emphasis on safety, a particular management of an NCS could value cost far lower than sensor resolution.

Similar to decision tree analysis, analytical hierarchy process includes objective and subjective means to establish decisions to select the best-case sensor or sensor strategy for NCS. The Analytic Hierarchy Process (AHP), is an effective tool for dealing with complex decision making, and it aids the decision maker to set priorities and make the best decision. This process reduces complex decisions to a series of pairwise comparisons (Wu et al. 2012). Also, the AHP incorporates a useful technique for checking the consistency of the decision maker's evaluations, thus reducing the bias in the decision making process.

To make a decision in an organized manner the decision is distilled to the following steps. First, the problem must be defined. The decision analysis problem requires the decision maker(s) to determine the best option given the circumstances and available data. As such, the problem must be defined and consist of:

- an objective (e.g., select the best sensor),
- criteria (e.g, cost, detectability, robustness, accuracy, etc.), and
- alternatives (e.g., Sensor A, Sensor B, Sensor C, etc.).

Next, a pairwise comparison of the criteria is made. This involves subjectively determining the importance (e.g., prioritizing) of each criterion relative to each other. As

previously noted, the criteria for sensors may include robustness, accuracy, resolution, remote monitoring, cost, etc. This prioritizing utilizes matrix operations. It may be displayed in a table, but comparisons are mathematically made using the geometric mean (eigenvalues is also used for comparison of the criteria). The pairwise comparison is performed using a scale, which must be consistent throughout the analysis and is discussed in more detail in the following section.

Multi-Criteria Analytical Hierarchy Process

To demonstrate the AHP for an NCS sensor selection process, an example problem assuming three SHM sensor scenarios is presented: Table 3-3 shows the parameters (input data) assumed for the example problem involving three sensors (A, B, and C). For this example, a scale of 1 to 5 is used and is associated with value inequality. Number 1 indicates the criteria which are being compared has equal value, and 5 will indicate the criteria has extremely unequal values, such that:

1 (Equal) → 2 (Moderate) → 3 (Strong) → 4 (Very Strong) → 5 (Extreme Unequal)

As mentioned above, the AHP analysis utilizes the geometric mean (X_n) of the ranking values. The following formula for the geometric mean is specific to the example of this paper because comparison of three ranking values is being made. This formula is made generic by replacing the "3" with a variable.

$$\overline{X_3} = \sqrt[3]{X_1 * X_2 * X_3} \qquad\qquad (1)$$

Once the geometric mean is determined then each criteria is scaled according to the sum of the geometric means. The pairwise comparison is then made between the criteria.

Following the comparison between the criteria, additional pairwise comparisons are made for the options according to each criteria. For instance, in this example scenario Sensor A, Sensor B, and Sensor C is compared with "cost" as a criterion. This pairwise comparison will determine the preference of each alternative (Sensors A, B, or C) over another as they relate to a specific criterion. The analysis is then completed by

Table 3-3
Example Input Data for Mock Decision Analysis

Sensor label	Cost per sensor ($)	Robustness scenario	Detectability scenario
Sensor A	200	The sensor is able to resist the potential temperature and radiation shielding but the connection is not hardened against radiation flux.	Sensor indicates a highly resolved concrete inclusion and provides the location and extent of damage.
Sensor B	600	Both the sensor and the connections fail under operating temperatures and radiation flux.	Sensor indicates the location of damage within concrete, but is unable to indicate the extent of damage.
Sensor C	1,000	The sensor and connections are able to resist high temperatures and radiation flux.	Sensor indicates damage but is not able to characterize neither location nor extent of damage.

multiplying the matrix and selecting the highest rated option. (An additional step may include performing a cost-benefit analysis but this article assumes cost is included as a criteria and therefore the additional cost-benefit analysis is not necessary.)

The final step of the AHP process includes matrix multiplication. The first matrix will consist of the values derived from the pairwise comparisons of the different alternatives. Note that the first matrix may not be a square matrix. It will only be a square matrix if the number of alternatives matches the number of criteria. This matrix will be

multiplied by a column vector consisting of the values derived in the first pairwise comparison between ranking values. The number of rows of the column vector is equal to the number of criteria for the decision. The resulting column vector will have the highest value indicating the selected alternative.

Example of Analytical Hierarchy Process

The AHP discussed above generates the solution to complex, multi-criteria decision problems with the associated criteria, options, and values for the selection of sensors for NCS. The example includes three brands of sensors that are used for an evaluation of reinforced concrete in a nuclear facility. The decision objective is "selection of the best sensor for an NCS based on three criteria – cost, robustness, and detectability." Inputs for the decision analysis is provided in Table 3-3. The cost criteria is used to allow the decision to compare the different sensor alternatives according to the total cost of the sensor. Additional criteria include robustness and detectability. Robustness is important for NCS because of the harsh environment to which the sensors may be exposed – temperature and radiation loading. Sensor detectability is associated with the probability of detection of each sensor and is functions of the sensor resolution and sensitivity. As indicated in the finite element modeling, the ad hoc sensor must be able to detect the changes in the NCS material.

Following defining the objective, the pairwise comparison of the before-mentioned three criteria is then performed. This is a matrix which can be successfully illustrated using Table 3-4. For calculating the geometric mean and the normalized mean, the ratios are treated as fractions and algebraically calculated. As seen in Table 3-4, the values along the

diagonal are one because the comparisons are made with the same criteria. However, as indicated in Table 3-4, comparing different criteria can show the imbalance of importance between the criteria. In this example, cost is considered four times more important than the robustness and five times more important than the detectability. Table 3-5 through Table 3-7 are the pairwise comparisons of each alternative as they relate to the three criteria. As such, Table 3-5 evaluates Sensor A, Sensor B, and Sensor C relative to cost. Table 3-6 and Table 3-7 evaluate the three sensors relative to robustness and detectability, respectively.

Table 3-4
Pairwise Comparison of Three Criteria Used for AHP

	Cost	Robustness	Resolution	Geometric Mean	Normalized Mean
Cost	1/1	4/1	5/1	2.71	0.69
Robustness	1/4	1/1	1/2	0.50	0.12
Resolution	1/5	2/1	1/1	0.74	0.19
			SUM	3.95	1.00

Table 3-5
Pairwise Comparison of Three Alternatives Relative to Cost

COST					
	Sensor A	Sensor B	Sensor C	Geometric Mean	Normalized Mean
Sensor A	1/1	5/3	5/1	2.03	0.54
Sensor B	3/5	1/1	4/1	1.34	0.36
Sensor C	1/5	1/4	1/1	0.37	0.10
			SUM	3.74	1.00

Table 3-6
Pairwise Comparison of Three Alternatives Relative to Robustness

ROBUSTNESS					
	Sensor A	Sensor B	Sensor C	Geometric Mean	Normalized Mean
Sensor A	1/1	5/3	3/5	1.00	0.28
Sensor B	3/5	1/1	1/5	0.49	0.14
Sensor C	5/3	5/1	1/1	2.03	0.58
			SUM	3.52	1.00

Table 3-7
Pairwise Comparison of Three Alternatives Relative to Detectability

DETECTABILITY					
	Sensor A	Sensor B	Sensor C	Geometric Mean	Normalized Mean
Sensor A	1/1	3/1	5/1	2.47	0.65
Sensor B	1/3	1/1	5/3	0.82	0.22
Sensor C	1/5	3/5	1/1	0.49	0.13
			SUM	3.78	1.00

Finally, for this example, a 3x3 matrix is multiplied with a column vector of three rows. The square matrix is indicative of the values calculated as the normalized mean and the column vector values are from the normalized mean column of Table 3-5 through Table 3-7:

$$\begin{matrix} 0.54 & 0.28 & 0.65 \\ 0.36 & 0.14 & 0.22 \\ 0.10 & 0.58 & 0.13 \end{matrix} * \begin{matrix} 0.69 \\ 0.12 \\ 0.19 \end{matrix} \qquad (2)$$

For completeness, the matrix calculation is provided and shown in the following bullets.

- Sensor A = 0.54*0.69 + 0.28*0.12 + 0.65*0.19 = **0.53**

- Sensor B = 0.36*0.69 + 0.14*0.12 + 0.22*0.19 = **0.31**

- Sensor C = 0.10*0.69 + 0.58*0.12 + 0.13*0.19 = **0.16**

Based on the objective, criteria, options, and comparisons of the example scenario, Sensor A is selected as the best choice for the NCS system.

Discussion

In this paper, simple SHM sensing decision making strategies are discussed that can be used to formulate the appropriate selection of the sensor for the detection and/or monitoring of germane degradation mechanisms for an NCS system. The steps of the proposed strategy are summarized in Figure 3-4.
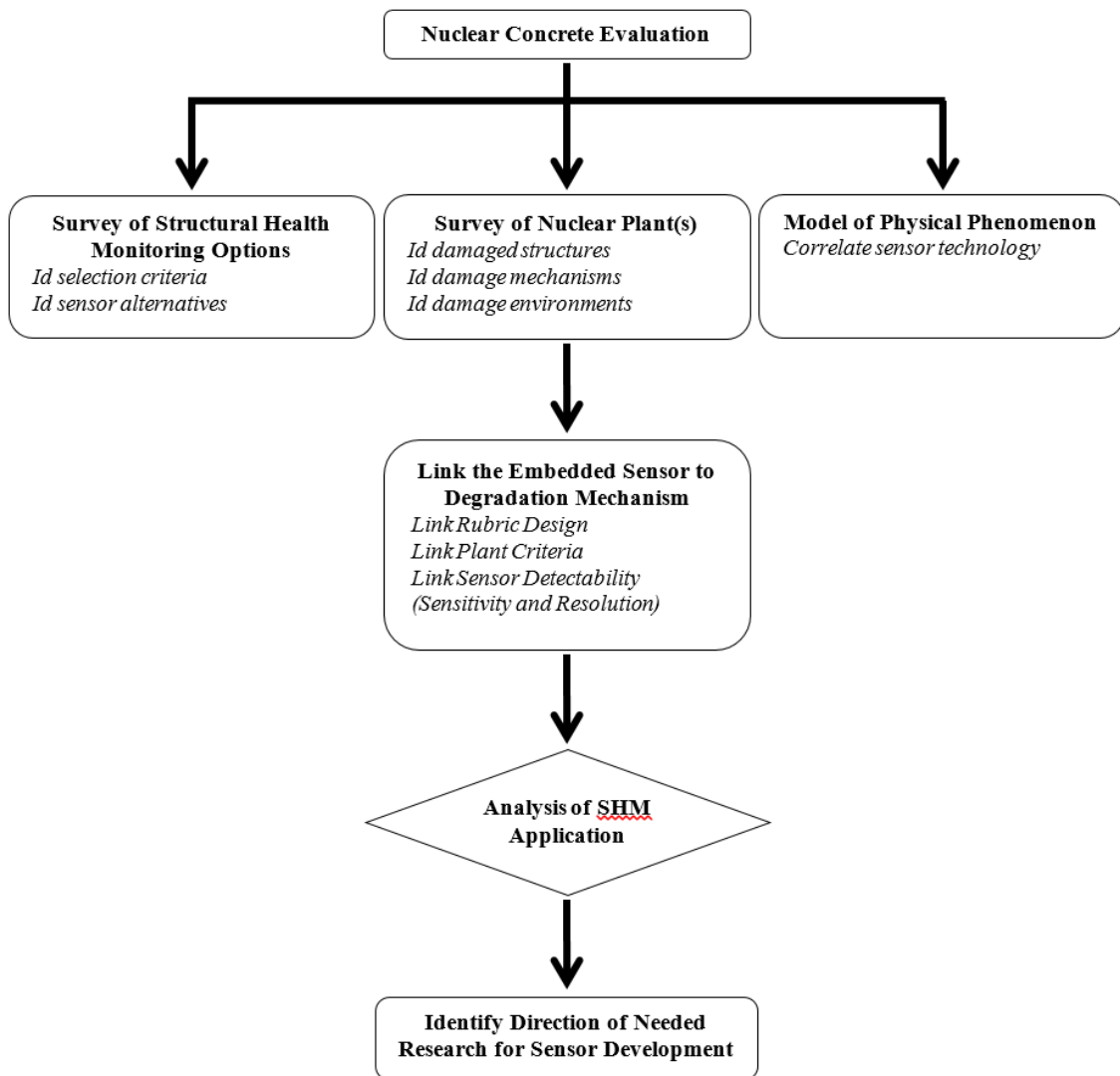
Figure 3-4 Flow Chart of Specifying Sensor Regimen for Structural Monitoring and Damage Detection

The strategy may be employed in a site-specific and/or degradation-specific manner. The initial step consists of an evaluation of the NCS at a nuclear power plant. Many times this evaluation is perceived as an inventory of existing defects or degradation mechanism, but just as important is the inventory of areas with a proclivity towards a specific time of degradation. For instance, an investigation which identifies a reinforced concrete structure having shallow cover and is located near a coast area with intermittent on/off shore winds should be noted to be prone towards reinforcing steel corrosion even if the corrosion is not yet evident. Following this is a survey of other sites with similar conditions and environments to study the concrete condition, structural durability, and mitigation strategies. Next is to review and list the available sensors which address the degradation mechanism identified as existing or likely to exist.

To aid in selecting the type of ad hoc sensor, a numerical model (much like the one presented in this paper) can be deployed to determine the necessary level of sensor resolution and sensitivity required, the spacing between sensors, and the strategic location of sensors for the SHM system. Reviewing the likely degradation mechanisms and the available sensor types are then analyzed to strategically identify the most appropriate solution to the applicable degradation mechanism.

Not discussed in this paper, but is necessary to new sensor technologies is the technology maturity of the sensing technique. It is possible to assign a technical readiness level (TRL) for each sensor technology. Depending on the TRL the direction of future research and level of investment is crafted, vetted, and amended. For an existing nuclear facility, a low TRL level technology is unlikely to befit the needs of the NCS.

Conclusion

Nuclear concrete structures are subject to a variety of degradation mechanisms which are mechanical and chemical in nature (Table 3-1). Sensors can be used to monitor the onset or progression of this noted degradation. Due to challenging characteristics, application of NDE sensing for NCS extends beyond sensor capabilities. As such, sensors used for SHM must be used, but the existing suite of sensors available have limitations and must be catered to specific types of degradation and environmental conditions. Good decision about the sensor type and sensor strategies are critical. The decision process should include multiple types of analysis. Numerical simulation techniques, such as finite element modelling, can help determine the necessary sensor resolution and placement location for detection of NCS damages.

Decision analysis techniques can then be used to help determine the appropriate ad hoc sensor for the NCS scenario. Two techniques which were highlighted in this article are multi-criteria decision tree and analytical hierarchy process. An analytical hierarchy process was developed for a hypothetical scenario which consisted of the selection of a sensor based on the criteria cost, robustness, and sensor detectability.

Disclaimer

The views, opinions, and findings reflected in this publication are the responsibility of the authors only and do not represent official policy or position of EPRI and Duke Energy.

References

Abu-Yosef, AE, Pasupathy, P, Wood, SL and Neikirk, DP, 2012. "Detection of Multiple Corrosion Thresholds in Reinforced Concrete Structures Using Passive Sensors," Smart Structures, SPIE, 8347.

ACI Committee 222, 2001. ACI 222R-01, Protection of Metals in Concrete Against Corrosion. Farmington Hill: American Concrete Institute.

ACI Committee 349, 2002. ACI 349.3R, Evaluation of Existing Nuclear Safety-Related Concrete Structures. Farmington Hill: American Concrete Institute.

ACI Committee 350, 2006. ACI 350-06, Code Requirements for Environmental Engineering Concrete Structures and Commentary. Farmington Hill: American Concrete Institute.

AFNOR, 2005. Methodology for Qualification on Non-Destructive Tests La Plaine Cedex Association de Normalisation (AFNOR)

American Concrete Institute, 2013. Concrete Terminology, ACI CT-13, American Concrete Institute. Farmington Hill: American Concrete Institute.

ASTM Committee C09, 2002. Standard Test Method for Pulse Velocity Through Concrete West Conshohocken PA ASTM International

ASTM Committee C09, 2004. Standard Test Method for Measuring P-Wave Speed and the Thickness of Concrete Plates Using the Impact-Echo Method West Conshohocken PA ASTM International

ASTM Committee C09, 2010. Standard Practice for Evaluation the Condition of Concrete Plates Using Impulse-Response Method the West Conshohocken PA ASTM International

ASTM Committee G01, 2009. Standard Test Method for Corrosion Potentials of Uncoated Reinforcing Steel in Concrete West Conshohocken PA ASTM International

Barbero, Greco, and Lonetti, 2005. Continuum Damage-healing Mechanics with Application to Self-healing Composites, International Journal of Damage Mechanics, 2005; 14; 51; January 2005; pp. 51-81

Barbero and Lonetti, 2001. Damage Model for Composites Defined in Terms of Available Data, 2001

Barbero and Lonetti, 2002. An Inelastic Damage Model for Fiber Reinforced Laminates, 2002

Barbero and Vivo, 2001. A Constitutive Model for Elastic Damage in Fiber-Reinforced PMC Laminae, 2001

Bhardwaj, 2009. Noncontact Ultrasonic Testing and Analysis of Materials. M. Schwartz=editor. Smart Materials. 2009. Chapter 9.3. Boca Raton. CRC Press.

Budiansky and O'Connel, 1976. Elastic Moduli of a Cracked Solid 1976 International Journal of Solid Structures, 1281-97

Clemen, R T, & Reilly, T, 2014. Making Hard Decisions with Decision Tools, 3rd Edition. Mason, OH: South-Western, Cengage Learning.

Committee on the Safety of Nuclear Installations, 2002. Electrochemical Techniques to Detect Corrosion in Concrete Structures in Nuclear Installations Vienna Nuclear Energy Agency

Electric Power Research Institute, 2000. Experimental Validation of Concrete Effects on Guided Waves in Plates Charlotte Electric Power Research Institute

Fallon, RW, Zhang, L, Everall, LA, Williams, JAR, Bennion, I, 1998. "All-Fiber Optical Sensing System: BG Sensor Interrogated by Long-Period Grating," Meas. Sci. Tech., 9, pp 1969-1973.

Federal Highway Administration, 2001. Prediction of Chloride Penetration in Concrete McLean Federal Highway Administration

Ghasr, LePape, Scott, and Zoughi, 2015. Holographical Microwave Imaging of Corroded Steel Bars in Concrete. ACI Materials Journal

Goodman, AQ, 2011. "Design and Modeling of Concrete Specimen for Non-Destructive Testing of Typical Nuclear Containment (Part I – Design and Modeling)" Project Report, UNC Charlotte.

Han, B, Guan, X, Ou, J, 2007. "Electrode Design, Measuring Method and Data Acquisition System of Carbon Fiber Cement Paste Piezoresistive Sensors," Sensors and Actuators A, 135, pp 360-369.

Hola and Schabowicz, 2010. State-of-the-Art Non-Destructive Methods for Diagnostic Testing of Building Structures - Anticipated Development Trends Archives of Civil and Mechanical Engineering.

International Atomic Energy Agency, 2002. Guidebook on Non-Destructive Testing of Concrete Structures Vienna International Atomic Energy Agency.

International Standards Organization, 2004. Non-Destructive Tests on Hardened Concrete Geneva ISO.

International Atomic Energy Agency, 2005. Non-Destructive Testing for Plant Life Assessment Vienna International Atomic Energy Agency.

International Atomic Energy Agency, 2015. IAEA, 2015, Power Reactor Information System.

Kee, Fernandez-Gomez, and Zhu, 2011. Evaluating surface-breakage cracks in concrete using air-coupled sensors. ACI Materials Journal. 2011. pp 558-565.

Kee, SH, Fernandez-Gomez, E, & Zhu, J, 2011. Evaluating surface-breaking cracks in concrete using air-coupled sensors. ACI Materials Journal, pp 558-565.

Kim, Lee, Chang, and Park, 2011. Kim, D., Lee, C., Chang, H., & Park, S. (2011). Embedded Piezoelectric Sensor-Based Real-Time Strength Monitoring during Curing Process of Concrete. Smart Structures.

Li, E, Wang, X, Zhang, C, 2006. "Fiber Optic Temperature Sensor Based on Interference of Selective Higher-Order Modes," Applied Physics Letter 89, 091119.

Li, H, Xiao, H and Ou, J, 2004. "A Study on Mechanical and Pressure-Sensitive Properties of Cement Mortar with Nanophase Materials," Cement and Concrete Research, 34, pp 435-438.

Malhotra and Carino, 2004. Handbook on nondestructive testing of concrete, 2nd edition, 2004. CRC Press.

NACE TG055, 2008. Inspection Methods for Corrosion Evaluation of Conventionally Reinforced Concrete Structures Houston NACE International

Naus, DJ, 2009. "Inspection of Nuclear Power Plant Structures – Overview of Methods and Related Applications," Report: ORNL/TM-2007/191, Oak Ridge National Laboratory.

Pammi, S, Brown, C, Datta, S, Kirikera, GR, Schulz, MJ 2003. "Concepts for Smart Nanocomposite Materials," Smart Structures, SPIE, 5062, pp 629-636.

Park and Kim, 2011. Ubiquitous Piezoelectric Sensor Network (UPSN)-Based Concrete Curing Monitoring for Construction 2011 Modern Telemetry, pp 75-92.

Sakamoto, WK, Higuti, RT and Tiago, MM, 2009. "Piezoelectric Composite Film for Acoustic Emission Detection," Ultrasonics Symposium, IEEE, 20-23 Sept. Rome, pp 1487-1490.

Scott, 2013. Internal Inspection of Reinforced Concrete for Nuclear Structures Using Shear Wave Tomography. Energy Conversion and Management. pp. 582-586

Shen and Li, 2006. A Cement-Based Piezoelectric Sensor for Civil Engineering Structure 2006 Materials and Structures 1-5

Smith, JD, 2011. "Design and Modeling of Concrete Specimen for Non-Destructive Testing of Typical Nuclear Containment (Part II – Model Validation)" Project Report, UNC Charlotte.

Suchanek and Riman, 2009. Intelligent Synthesis of Smart Ceramic Materials. Book editor: Schwarz, M; Smart Materials; 2009; chapter 2; Boca Raton; CRC Press

Technical Committee B/517, Concrete, 2004. Testing Concrete - Determination of Ultrasonic Pulse Velocity Brussels British Standards Institute

U.S. Nuclear Regulatory Commission, 2014. U.S. Nuclear Regulatory Commission U.S. Nuclear Regulatory Commission Regulations: Title 10, Code of Federal Regulations

Wang, X and Chung, DDL, 1998. "Short Carbon Fiber Reinforced Epoxy Coating as a Piezoresistive Strain Sensor for Cement Mortar," Sensors and Actuators, 71, pp 208-212.

Withey, Vemuru, Bachilo, Nagarajaiah, and Weisman, 2012. Withey, P., Vemuru, V., Bachilo, S., Nagarajaiah, S, Weisman, R, 2012. Strain Paint: Noncontact Strain Measurement Using Single-Walled Carbon Nanotube Composite Coatings. Nano Letters, 3497-3500.

Wu, W., Kou, G., Peng, Y., & Ergu, D., 2012. Improved AHP-Group Decision Making for Investment Strategy Selection. Technological and Economic Development of Economy, 299-316.

Yang and Dai, 2012. Review on Optical Fiber Sensors with Sensitive Thin Films. Photonic. 2012. 14-28.

Yao, Tung, and Glisic, 2014. Crack Detection and Characterization Techniques - An Overview, 2014. Structural Control and Health Monitoring published online

CHAPTER 4 ELECTRO-ELASTIC AND CONTINUUM MECHANICAL RELATIONSHIPS FOR STRAIN QUANTIFICATION USING ELECTRIC RESISTIVITY MEASUREMENTS

Abstract

Self-sensing concrete consists of embedded, electrically conductive materials allowing the enhanced concrete electrical properties for measurements and correlation to mechanical strains. This paper offers simple electromechanical correlations so that measurement technique can be designed to study the effects of different types of embedded additive materials. An example of the one-dimensional axial behaviors of a concrete element along with electric field derivations is presented. A measurement approach is presented to demonstrate how the concrete specimen will be loaded in compression and the correlation between load, strain, and change in resistance.

Keyword: continuum theory, recycled steel residuals, resistivity, self-sensing concrete, structural health monitoring (SHM)

Introduction

Infrastructure throughout much of the United States has aged considerably. Consequently, repair and/or replacement of reinforced concrete structures (buildings, bridges, and roads alike) will continue to increase in the coming years and span across multiple industries including the nuclear power plant structures. Approximately half of the 99 operating units are beyond their original design license of 40 years in the United States (Scott et al. 2013, IAEA 2018). The types of damage mechanisms typical to nuclear concrete include construction-related issues (cracking, delamination, cold-joints, honeycombs); environmentally-induced attack (alkali-aggregate reaction, carbonation, chloride ingress); extreme operations (high thermal differentials, missile impact, fire, abrasion); and steel-related issues (tendon rupture, corrosion, fatigue).

Inspection of concrete structures is traditionally performed using nondestructive evaluation techniques requiring the inspector to be physically present at the structure and may require visual inspection coupled with testing methods such as ground penetrating radar, impact echo, impulse response, shear wave tomography, coring, half-cell potential, and resistivity, etc. (ACI 1998, Scott 2013). However, traditional testing methods need sensors capable of reaching into the complex nuclear concrete element for damage detection.

Recent interests in self-sensing technologies using embedded smart materials have the potential of turning concrete into sensors that can help overcome many deficiencies faced by traditional testing techniques. This is achieved using a variety of materials with electrostrictive properties to create autonomous sensing structural members (Chung 2002,

67

Li et al. 2004, Han et al. 2014, Scott 2015). The underlying assumption is if the constituents of the concrete include material which has the potential of indicating existing or approaching strain that is excessive, then prevention of damage is more possible.

To achieve self-sensing in concrete, the sensing-enabling material is embedded in the concrete mixtures to create a functional concrete material. The embedded material may vary in shape (particles, tubes, fibers), size (nanoscale to centimeters), and material (carbon, steel slag, nickel, graphite, crystal or ceramic) (Han et al. 2014, Kholkin 2009, Wille and Loh 2010, Sreekala and Muthumani 2009, Pammi et al. 2003). The objective is to expedite the measurability of material resistance to either damages or external load induced stressing. Self-sensing concrete requires the marriage between two physical quantities: mechanical stress and electric properties.

This paper offers a simple elastic correlation between the multi-physical quantities for the self-sensing concrete for strain quantification. The derivations are borrowed largely from electro-elasticity and continuum mechanics. An example of a uni-directional compressed concrete beam is also provided.

Mathematical Derivations

The self-sensing concrete is assumed to be able to pass an electric current through a homogeneous material and use the detection of changes in the electric properties of concrete to determine material changes. It is also assumed that with internal changes, the concrete will experience a change in electric properties. We further assume that certain element is added to the concrete to make it more conductive, so that the measurements can

be amplified. We first investigate the formulation of electric properties (resistance and resistivity) in the self-sensing concrete.

Resistance and Resistivity

Though low when compared to other materials, concrete has a measurable level of conductivity: When current is passed through the concrete an electrical field, V (V/m), develops in the concrete. The electrical current is equivalent to the resistivity (ρ, V-m) multiplied by the current density (J, amps/cm2) (Sears and Zemansky 1970). This relationship can be written with the variables in indicial notation.

$$V_i = \rho_{ij} J_j \tag{1}$$

where V and J being first-order tensors and ρ is a second order tensor with i and j representing indices of a Cartesian coordinate system and therefore are equal to x_1, x_2, or x_3 (Fig. 1).
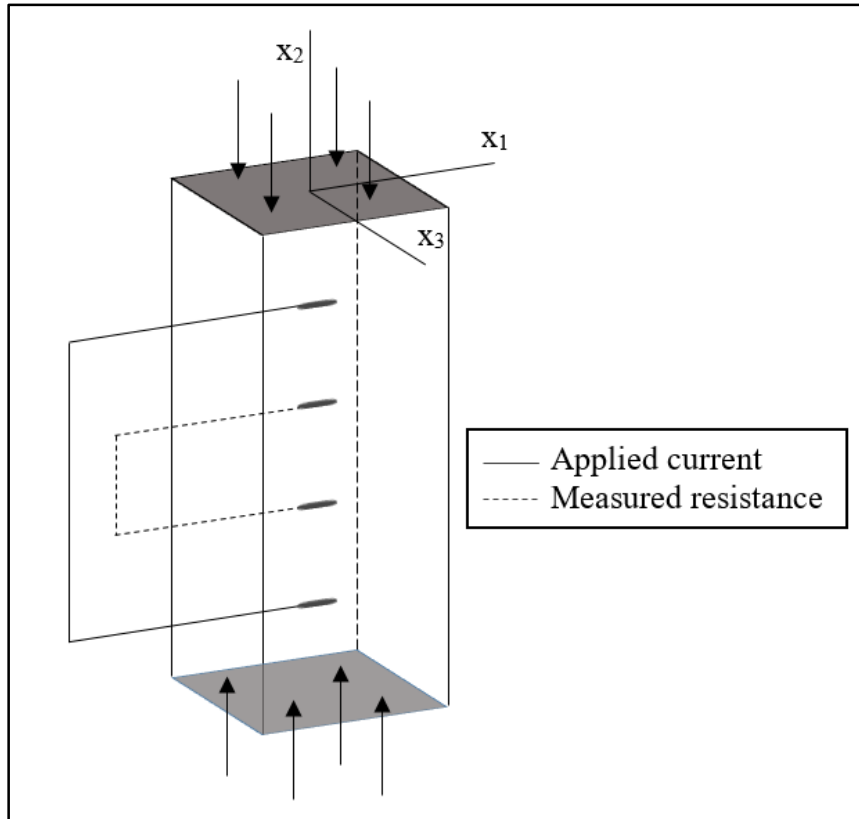
Figure 4-1
Test Specimen Schematic under Axial Compression with Electric Measurement

There are three components in concrete that may have varying levels of electrical properties – aggregate, binding agent, and interfacial transition zone between the hydrated cement and aggregate. For study of the bulk electrical properties of concrete, concrete is assumed as a single electrical element and having an electrical path across the concrete element. Using embedded electrodes, important macro resistivity properties of the concrete material are determinable. For measuring changes in concrete strain through changes in electrical measurements, the right side of Eq. 1 can be integrated to create the relationship between the geometry and electrical properties of the material utilizing an elemental length of ds dotted with J (capitalized bold indicates vector field).

70

$$\rho_{ij}J_j \cdot ds_j \tag{2}$$

The vector directions of ds and J are parallel and, therefore, reduces the dot product:

$$\rho \frac{I}{A} ds \tag{3}$$

where the current density is rewritten as a function of the current (I) and the sectional area (A). Assuming constant uni-directional current, Eq. 3 can be integrated across the length of the element (from arbitrary position a to b):

$$I \int_{b}^{a} \frac{\rho}{A} ds \tag{4}$$

The integral of Eq. 4 is the resistance, R (in ohms). Ohm's law is developed when combining Eq. 4 and Eq. 1. Solving for the integral across the element length (L) gives:

$$R = \frac{\rho L}{A} \tag{5}$$

<u>Relationship between Strain, Resistance, and Resistivity</u>

Because bulk property is assumed, Eq. 5 represents a homogeneous material with a constant cross section and is electrically isotropic and is a fundamental equation used by researchers for its strain and resistance/resistivity relationship. However, a theoretical relationship between measured resistance/resistivity and strain is not readily available in literature on this subject. This relationship between strain and resistance/resistivity is derived using three-dimensional Cartesian coordinate system as shown in Fig. 1 with the top-center as the origin (0, 0, 0). Rewriting Eq. 5 to remove the quotients and applying the product rule gives:

$$\rho * dx_2 + x_2 * d\rho = R * d(x_1 x_3) + x_1 x_3 dR \tag{6}$$

where

$$d(x_1 x_3) = x_1 dx_3 + x_3 dx_1 \tag{7}$$

and x is the positional coordinate system with $x_1 x_3$ representing the member cross-sectional area. Hence, Eq. 7 is the product rule applied to the derivative of the product of x_1 and x_3. Subsequently, strain in the direction of axial length can be related to the dimensional changes in x_1 and x_3 directions using Poisson's ratio (v). The change in length is assumed to be due to axial compression along the x_2-direction such that:

$$\frac{dx_1}{x_1} = \frac{dx_3}{x_3} = -v\frac{dx_2}{x_2} \tag{8}$$

Eq. 8 can be rewritten in terms of dx_1 and dx_3 and then plugged into Eq. 7 to give:

$$d(x_1 x_3) = -(x_1 x_3)v\frac{dx_2}{x_2} - (x_1 x_3)v\frac{dx_2}{x_2} = -2(x_1 x_3)v\frac{dx_2}{x_2} \tag{9}$$

Eq. 6 is then divided by $\rho * x_2$ and combined with Eq. 5 and Eq. 9 to indicate the change in resistance:

$$\frac{d\rho}{\rho} = \frac{dR}{R} - \frac{dx_2}{x_2} - \frac{2v*dx_2}{x_2} \tag{10}$$

Rearranging Eq. 10 and define strain (ε) as $\frac{dx_2}{x_2}$, we get:

$$\varepsilon = \frac{1}{(1+2v)} * (\frac{dR}{R} - \frac{d\rho}{\rho}) \tag{11}$$

The variations of Equation 11 indicate the definition of axial strain for these specimens (ε) and, though not the derivation, a variation of Eq. 15 can be found in (Han et al. 2014). This is an important equation and shows that both resistance and resistivity values (and with Poisson's ratio known) must be measured in test specimens if one desires to directly calculate strain. It is also important to note that both quotients on the right side are unitless and that this equation is applicable to any material and geometry provided that the geometry has a uniform cross section. For concrete, scientists have dismissed the strain

term and measure resistance to report fractional changes in resistivity as a percentage of the static resistivity of a material.

Compression Loading and Displacement

As proof-of-concept, a concrete column loaded in compression with an electric measurement set up is considered and is shown in Fig. 1. An alternating electric current is applied through the electrodes placed near the ends of the column and the changes in electrical potential will be measured across pairs of electrodes near the midway point of the column. Continuum mechanics theory is used to characterize the loading and mechanical response of the concrete column, assuming the column to be frictionless, homogeneous, and isotropic. The column is further assumed as a "short column," with unidirectional compression failure (i.e., with no buckling). For short columns, the first order buckling load will be one to two orders of magnitude greater than the compression load.

Given the orientation of the column relative to the coordinate system (Fig. 1), the compression tensor (C) is given with the axial compression load $(-C^+)$ in the 2-2 position of the matrix indicating it is on the x_2 face and along the x_2 direction:

$$[C] = \begin{bmatrix} 0 & 0 & 0 \\ 0 & -C^+ & 0 \\ 0 & 0 & 0 \end{bmatrix} \tag{12}$$

According to Hooke's Law, the cross-sectional strain in each Cartesian direction is:

$$\varepsilon_{11} = \varepsilon_{33} = \frac{-\nu(-C^+)}{E} \tag{13}$$

73

The strain (ε_{ij}) in the x_2 direction and the displacements in x_1 and x_3 directions are associated by Poisson's ratio (v) and modulus of elasticity (E), and can be generalized for displacement (u) in all three directions (Mase et al. 2010) as:

$$2\varepsilon_{ij} = u_{i,j} + u_{j,i} = \frac{\partial u_i}{\partial x_j} + \frac{\partial u_j}{\partial x_i} \tag{14}$$

and

$$\varepsilon_{ii} = \frac{\partial u_i}{\partial x_i} \tag{15}$$

Eq. 14 and 15 can be expanded with the condition that C_{21}, C_{12}, C_{31}, C_{13} are each equal to zero, then the corresponding strains in each of those directions are also equal to zero. Given the boundary conditions as:

$$\frac{\partial u_1}{\partial x_1} = \varepsilon_{11} = \frac{-v(-C^+)}{E} \tag{16}$$

$$\frac{\partial u_2}{\partial x_2} = \varepsilon_{22} = \frac{-C^+}{E} \tag{17}$$

$$\frac{\partial u_3}{\partial x_3} = \varepsilon_{33} = \frac{-v(-C^+)}{E} \tag{18}$$

Integrating gives:

$$u_1 = \frac{-v(-C^+)}{E} x_1 + y(x_2) \tag{19}$$

$$u_2 = \frac{-C^+}{E} x_2 + f(x_1, x_3) \tag{20}$$

$$u_3 = \frac{-v(-C^+)}{E} x_3 + z(x_2) \tag{21}$$

which produces three functions of integration: $y(x_2), f(x_1, x_3), and\ z(x_2)$. With μ being the shear modulus of the concrete, these functions of integration can be further reduced with proper assumptions such as symmetry:

74

$$\varepsilon_{21} = \varepsilon_{12} = \frac{C_{21}}{2\mu} = 0 \tag{22}$$

and

$$\frac{\partial u_2}{\partial x_1} + \frac{\partial u_1}{\partial x_2} = 0 \tag{23}$$

$$\frac{df}{dx_1} + \frac{dy}{dx_2} = 0 \tag{24}$$

Eq. 24 can be rewritten and equate to a variable ω_0 and get:

$$\frac{df}{dx_1} = -\frac{dy}{dx_2} = \omega_o \tag{25}$$

Splitting these two equations apart and integrating each in the respective x_1 and x_2 directions gives:

$$f(x_1) = \omega_o x_1 + a \tag{26}$$

$$y(x_2) = -\omega_o x_2 + b \tag{27}$$

Eq. 22, 23, 28, and 29 are combined to yield the following mechanical relationships:

$$u_1(x_1, x_2) = \frac{-v(-c^+)}{E} x_1 - \omega_o x_2 + b \tag{28}$$

$$u_2(x_1, x_2) = \frac{-c^+}{E} x_2 + \omega_o x_1 + a \tag{29}$$

Eq. 28 and Eq. 29 are the displacement functions where a and b are shown to be zero at the locations where x_1 and x_2 equal to zero. From symmetry, u_1 is equal to u_3. Assuming further that the angular rotation at each end of the specimen is zero ($\omega_0 = 0$). As such, displacements in the x_1, x_2, and x_3 directions are characterized by:

$$u_1 = \frac{v(-c^+)}{E} x_1 \tag{30}$$

$$u_2 = \frac{-c^+}{E} x_2 \tag{31}$$

75

$$u_3 = \frac{v(-C^+)}{E} x_3 \tag{32}$$

Conclusion

In this paper, a first order electromechanical correlation has been derived to describe the behavior of a hypothetical "smart" concrete that can self-sense the strain conditions as a function of resistance and resistivity values. Through measuring electrical properties, the concrete structural and material state-of-health can be evaluated. Such a method is suggested to replace traditional nondestructive evaluation. The correlation for a uni-directionally loaded short column member is provided as an example, which can be extended to describe the behaviors of more complex elements and loading schemes. The simplistic correlations assume that the concrete is homogeneous and that the added conductive element is uniformly distributed throughout the concrete material.

The germane mathematical relationships are derived utilizing electro-elasticity and continuum mechanics to offer the physical phenomenon to measure the effectiveness of recycled steel residuals to create self-sensing concrete. The theoretical relationship is applicable to any material and geometry given that the cross section is uniform and the loading is axial. Assumptions such as uniform distribution of electrostrictive materials and inter-conductivity following a straight path, are also implicitly made. These assumptions are critical and the results of the theoretical relationships above need to be determined experimentally. The selection of a measuring device is critical to the accuracy of measurements.

Finally, the presence of possible steel reinforcing bars or prestressed tendons within real-life concrete structure can significantly change the electric properties and additional

derivations are needed to modify the equations to accommodate different material conditions.

Disclaimer

The views, opinions, and findings reflected in this publication are the responsibility of the authors only and do not represent official policy or position of EPRI.

References

ACI (American Concrete Institute). (1998). "Nondestructive Test Methods for Evaluation of Concrete in Structures Committee." *ACI 228.2R-98*, Farmington Hills, MI.

Chung, D.D.L. (2002). "Electrical Conduction Behavior of Cement-Matrix Composites," *Journal of Materials Engineering and Performance,* Vol. 11(2), 194-204.

Han B., Yu X., and Ou J. (2014). *Self-Sensing Concrete in Smart Structures*, Elsevier Inc., Oxford, UK.

IAEA. (2018). *Power Reactor Information System*. International Atomic Energy Agency [https://www.iaea.org/PRIS/CountryStatistics/CountryDetails.aspx?current=US] (Last accessed Jan. 04, 2018).

Kholkin, A. K. (2009). "Piezoelectric and Electrostrictive Ceramics Transducers and Actuators". In M. Schwartz, *Smart Materials* (Ch. 9.1), CRC Press, Boca Raton, FL.

Konsta-Gdoutos M.S., and Aza C.A. (2014). "Self sensing carbon nanotube (CNT) and nanofiber (CNF) cementitious composites for real time damage assessment in smart structures." *Cement and Concrete Composites*, 53, 162-169.

Li H., Xiao H., Ou J. (2004). "A Study on Mechanical and Pressure-Sensitive Properties of Cement Mortar with Nanophase Materials." *Cement and Concrete Research,* 34, 435-438.

Mase G.T., Smelser R.E., and Mase G.E. (2010). *Continuum Mechanics for Engineers, Third Edition*, CRC Press, Boca Raton, FL.

Pammi, S., Brown, C., Datta, S., Kirikera, G., Schulz, M.J. (2003). "Concepts for Smart Nanocomposite Materials." *Proc., Smart Materials, Structures, and Systems*, SPIE Vol. 5062, 629-636.

Scott, D.B., Goodman, A., Smith, J.D., Chen, S. (2013). "Applications of New Sensing Technologies for Reinforced Concrete Related to Nuclear Facilities: Considerations and Potentials." In F. Chang (Editor) *Proc., Structural Health Monitoring 2013*. Stanford University, Palo Alto, CA, 710-716.

Scott, D.B. (2013). "Internal Inspection of Reinforced Concrete for Nuclear Structures Using Shear Wave Tomography." *Energy Conversion and Management*, Vol. 74, 582-586.

Scott, D.B. (2015). "From Dumb Rocks to Smart Materials: Self-Sensing and Self-Healing Concrete." *EPRI Technology Insights*, 3002005597, Palo Alto, CA.

Sears, F.W., and Zemansky, M.W. (1970). *University Physics, Fourth Edition*, (Ch. 28), Addison-Wesley Publishing Company Inc., Reading, MA.

Sreekala, R., and Muthumani, K. (2009). "Structural Application of Smart Materials," In M. Schwartz, *Smart Materials* (Ch. 4), CRC Press, Boca Raton, FL.

Wille, K. A., and Loh K.J. (2010). "Nanoengineering Ultra-High-Performance Concrete with Multiwalled Carbon Nanotubes." *Journal of the Transportation Research Board*, Washington, DC.

CHAPTER 5 STRAIN ASSESSMENT OF SMART CONCRETE USING COST-EFFECTIVE RECYCLE STEEL RESIDUALS

Abstract

In recent years, engineers and scientists have performed laboratory testing to determine changes in strain of cement-based specimens using electric-based measuring methods. The advancements offers opportunity to develop a new category of structural health monitoring for reinforced concrete. However, traditional functional filler used to create the smart concrete is not cost effective and reduces likelihood of acceptance. As a cost-effective alternative, recycled steel residual materials is considered and described in this paper. Recycled steel residuals procured as waste from a steel mill is distributed in concrete mixtures. Concrete cylinder test specimens – 4x8-in. and 6x12-in. – are cast and used to measure changes in electric resistance as a function of time, load, and strain. The findings indicate that recycled steel residuals may be used to create the smart concrete but that additional testing should be performed.

Keywords: concrete, nondestructive evaluation (NDE), recycled steel residual (RSR), resistance, resistivity, strain, structural health monitoring (SHM)

Introduction

Nondestructive evaluation (NDE) has been used for the investigation and evaluation of concrete structures including defects and aging effects of concrete for problems including chemical attacks, physical attacks, and degradation factors such as leaching, alkali-aggregate reactions, freeze-thaw, fatigue/vibration, corrosion, elevated temperature, and others (ACI Committee 228 1998, Scott D. 2013). Traditional NDE techniques such as ultrasound, dye penetrant, impact-echo and nuclear methods, require personnel to be "hands-on" and physically close to the structure in order to perform the tests. More recently, in-situ sensors with integrated diagnostic systems are being used to initiate, supplement, and/or replace traditional NDE as part of structural health monitoring (SHM) strategy. SHM techniques utilize sensors to periodically evaluate the structure without personnel being present. Sensors may be permanently attached to the structure and signals may be transmitted wirelessly to a remote station for analysis.

More recently, a variation of SHM has been explored: "self-sensing concrete" utilizes embedded functional fillers as being a mixture component to develop sensing capabilities within the concrete – turning the concrete into a sensor (Wang X, Chung DDL 1998; Li X., Xiao, H, Ou, J 2004). Functional fillers that have been experimented to turn concrete "smart" include single-walled carbon nanotubes (Withey, et al. 2012), nano-oxides (Li X., Xiao, H, Ou, J 2004), piezoelectric ceramic (Kim, et al. 2011; Shen, Li 2006; Suchanek, Riman 2009), fiber optics (Yang, Dai 2012) and electrochemical, etc. These sensors can be topical (Withey, et al. 2012) or embedded (Li X., Xiao, H, Ou, J 2004). The objectives of this new SHM strategy is to modify concrete material with functional

materials to allow autonomous sensing. They have been shown to indicate material strength during and after curing (Kim, et al. 2011; Park, Kim 2011), structural strain (Li X., Xiao, H, Ou, J 2004), and crack development (Yao, et al. 2014).

In most cases the autonomous sensing material is included in the concrete through modifying the mixture properties. The important property of the autonomous sensing material is its electrostrictive nature. Electrostrictive property is the ability of a material to change in electrical properties based on a change in shape (i.e., the material becomes more or less electrically resistant as the material lengthens or compresses, respectively). The proposed autonomous sensing material may vary in size – from nanoscale to centimeter scale (Li X., Xiao, H, Ou, J 2004; Kholkin, Kiselev, Khokine 2009; Wille, Loh 2010; Sreekala, Muthamani 2009; Pammi, et al. 2003). Previously proposed autonomous materials consist of particles, tubes, or fibers made from carbon, steel slag, nickel, graphite; and, sometimes the material is a crystal or ceramic. In most cases, these materials provide concrete with measurable self-sensing capabilities; however, they are also very costly to the point of being prohibitive. For instance, it is reported by (Pammi, et al. 2003) that the high costs of smart nanomaterials prevent its practical use. More specifically to ceramics, (Suchanek, Riman 2009) indicated that newer techniques are needed and preferred for cost reductions in order to promote wide-spread development of ceramics for sensing (Suchanek, Riman 2009). In (Sreekala, Muthamani 2009), the author highlights that costs to manufacturer smart materials has reduced, but that those costs were still impeding wide-spread use.

Alternatively, the use of recycled steel shavings (recycled steel residuals) can be a cost-effective material that produce an equally capable concrete material (that is also environmentally sustainable). Given this and in summary, the use of recycled steel residuals has the potential ability to 1) act as a functional filler providing self-sensing capability for concrete; 2) provide thermal conductivity needed if thermal shock occurs resulting from a loss-of-coolant accident or main steam line break in a nuclear power plant; and/or 3) reduce steel waste and improve the environment.

To determine the feasibility of using recycled steel shavings as functional fill for concrete, laboratory testing of steel-shaving-modified concrete cylinders have been tested under compression following ASTM procedures (ASTM C31 2015, ASTM C39 2003, ASTM G57 2012). Testing was performed on 4x8-in. cylinders using varying concentrations of recycled steel residuals – 0%, 0.5%, and 1% - by volume. The equivalent amount of coarse aggregate was reduced to offset the additional recycled steel residuals as suggested by ACI guidance (ACI Committee 544 2008). Measurements determining resistance were taken of the 4x8-in. cylinders under no-load and axially-loading conditions. The research team elected to perform additional testing on a 6x12-in. cylinder that contained 1.6% concentration of recycled steel residuals, by volume. Additional information about the experimental design and results follows.

Theoretical Considerations

The functional filler modified concrete is designed to enhance its electrorestrictive properties. The intent is to quantify the mechanical strain of the concrete using changes in the electric resistance of the concrete material as described by (Li, Xiao, Ou 2004).

$$R = \frac{\rho L}{A} \tag{1}$$

Eq. 1 establishes a fundamental relationship between resistance and resistivity. Using applicable assumptions of bulk electrical properties of concrete and calculus manipulation, Eq. 2 shows an important relationship relating both resistance and resistivity axial strain.

$$\rho * dx_2 + x_2 * d\rho = R * d(x_1 x_3) + x_1 x_3 dR \tag{2}$$

Using additional calculus and algebra, a more elegant version of Eq. 2 is given in Eq. 3.

$$\varepsilon = \frac{1}{(1+2\nu)} * \left(\frac{dR}{R} - \frac{d\rho}{\rho}\right) \tag{3}$$

The relationship aligns well with findings found in (Li, Xiao, Ou 2004; Konsta-Gdoutos, Aza 2014) in which a variety of materials maintain linear relationships between strain and changes in relative resistance/resistivity, albeit at varying slopes. However, previous studies have not included recycled steel residuals as proposed herein. The proposed recycled steel residuals range in size and shape between fibrous (high length-to-width/thickness ratio) and fine (dust-like) particles.

Additionally, concrete develops electrical polarizations when direct current is applied to it (ASTM G57 2012, Rajabipour 2006) and has been previously observed in concrete specimens by the authors (resistance measurements in other concrete specimens indicated that the resistance was not stable and changes based on the level of polarization which developed in the system). The types of polarizations that develop when using DC input is described by (Rajabipour 2006) as being dipole polarization (similar to groupings of bar magnets), atomic polarization (charged atoms that repel and attract), electronic polarization (change in the orbital path of an electron around a nucleus), interfacial

84

polarization (charges developed at grain boundaries between particles that may bond together), and at interfaces between the negative charges of a solid and the positive ions of the liquid phase of a material.

Experimental Setup

<u>General</u>

For the testing described in this paper, cylinders were impregnated with different concentrations of recycled steel residuals. Because of the considerable variation in size and aspect ratios of the recycled steel residuals, the material was graded and the mixture consisted of a specified proportioning between material retained and passing through a No. 8 sieve (Figure 5-1).
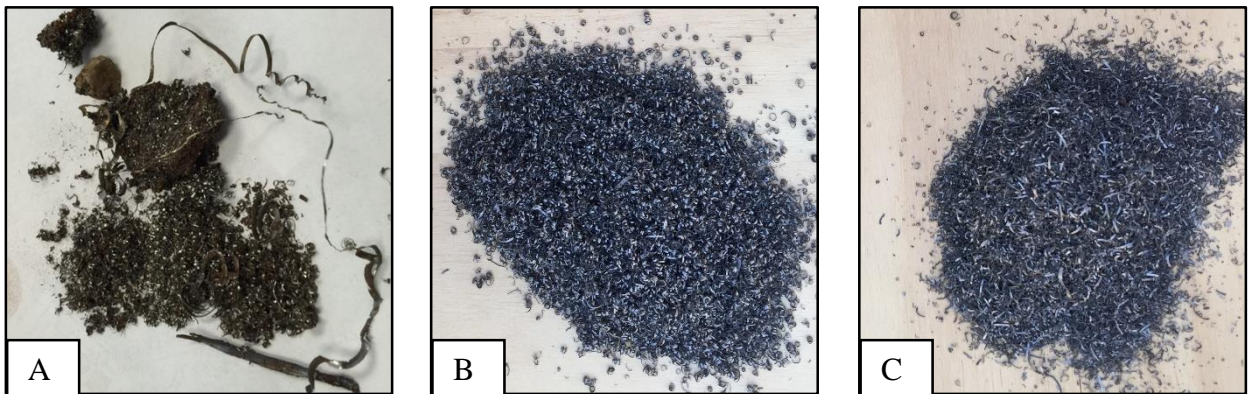
Figure 5-1
Recycled Steel Residuals in Raw Form (A), Retained on No. 8 Sieve (B), and Passing Through No. 8 Sieve (C)

In general, cylinder sizes and casting was done according to ASTM C31 and tested in accordance with ASTM C39 (ASTM C31 2015, ASTM C39 2003). Both 4x8-in. and 6x12-in. cylinders were made and tested. Two important deviations from ASTM standards were purposeful to accommodate the needs of the resistance testing. First, the cylinders

were not wet cured, but were covered only with plastic to help prevent small shrinkage cracking at the top surface. No wet curing through submersion was performed because the conductivity of the material was not to be influenced by external moisture filling the pore spaces of the cylinder. Second, four electrodes were placed within the concrete cylinder. These electrodes consisted of Gauge 10, copper-stranded, insulated wire. One-inch length of insulation was removed from the wire and the exposed section was positioned to be cast at the cross-sectional center of the cylinder(s). The external connections to the wire remained insulated until after concrete placement was completed. The electrodes for like-kind specimens were the same length with 1 in. (25 cm) at the cross-sectional midpoint of the cylinder. Four electrodes were equivalently spaced across the length of the cylinders (Figure 5-2). The theoretical basis for the electrode placement is the test setup described in ASTM G57 (sometimes called the Wenner test) used to determine resistivity of soil (ASTM G57 2012). To combat polarization, alternating current (AC) was applied to the outer electrodes and changes in electrical potential was measured across the inner electrodes. This was performed while loading the specimens in compression.

For loading, a neoprene cap was placed on the bottom of the cylinder and a rubber spacer was added to the top. Using a MASTECH® MS8268 multimeter, it was determined that no electrical connectivity was present between cylinder and the compression machine. A non-adjustable power supply was used to input 25.5 volts, 650 mA of alternating current (AC) at 60 Hz. Using the test scheme similar to (ASTM G57 2012), the potential difference between the inner pair of electrodes was measured. Measurements were performed using a National Instruments [TM] NI 9205 having 32, single-ended spring load channels with a

sampling rate up to 250 kS/s. The software program was created to measure potential values up to +/- 10 volts, for a 100 readings at 1000 S/s. The following sections provides increased detail about the testing of the 4x8-in. and 6x12-in. cylinders.
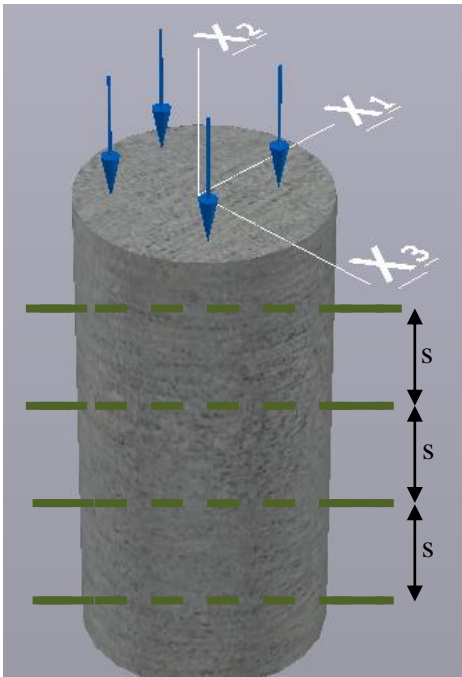
Figure 5-2
Image of Specimen used for Resistance Testing

Experimental Setup for 4x8-in. Cylinder Testing

Testing on the 4x8-in. cylinders was performed to: 1) compare concrete mixtures with and without recycled steel residuals, 2) provide clarity about the early effects of hydration and curing on the changes in electrical conductivity, and 3) determine potential effects of mixture design on conductivity. To perform such tests, multiple batches were made with varying concentrations of recycled steel residuals and cast into 4x8-in. cylindrical specimens in accordance with ASTM C31 (ASTM C31 2015). The concentration of recycled steel residuals were 0.0%, 0.5%, and 1.0% based on total volume

of the mixture (Table 5-1). One specimen of each concentration was made with electrodes. The outer and inner pair of electrodes were one and three inches, respectively, from each cylinder end giving the distance between the electrodes to be two inches. Companion cylinders were cast for each concentration of recycled steel residuals. A 2.5-ft^3, drum, single-speed, rotational mixing unit was used to batch the material. Mixture of the concrete and introduction of the recycled steel residuals was performed in general accordance with ASTM C 192 (ASTM C 192 2002). The specimens were covered with a 6-mil polyethylene sheet for curing.

Table 5-1
Concrete Mixture Design and Batch Weights of 4x8-In. Cylinder

		Concentration of Recycled Steel Residuals		
		0%	0.5%	1.0%
Mixture Component	Yd^3-Mix Design, lbs.	1.5-ft^3 Batch Weights, lbs.	1.5-ft^3 Batch Weights, lbs.	1.5-ft^3 Batch Weights, lbs.
Cement	662	36.8	36.8	36.8
Water	328	18.2	18.2	18.2
Coarse aggregate, No. 67	1,726	95.9	95.9	95.9
Fine aggregate	1,170	65	65	65
RSR (Retained on No. 8 sieve)	Varied	0	1.40	1.95
RSR (Passing through No. 8 sieve)	Varied	0	1.40	1.95

As noted previously, the test setup is to be consistent with that found in ASTM G57 where an alternating current is applied to the outer two electrodes and the potential between the two inner electrodes are measured (ASTM G57 2012). The input consisted of 25.5

volts at 60 Hz. and a current of 650 mA. Ten static voltage measurements were taken of each cylinder at 1, 3, 5, 7, 10, 14, 21, and 28 days after the creation of the specimens.

Experimental Setup for 6x12-in. Cylinder Testing

Additional testing occurred with a single 6x12-in. cylinder to empirically determine the relationship between strain and resistance. Initial testing consisted of a single cylinder with embedded electrodes (Figure 5-2). Cylinder dimensions were 6Dx12 inches; it was made in general accordance with ASTM C31. The outer and inner pair of electrodes were two and 3.5 inches, respectively, from each cylinder end giving the distance between the inner electrodes to be five inches. The concrete was hand mixed and consisted of the mix design weights found in Table 5-2. As indicated previously (Figure 5-1), the shape and size of the raw recycled steel residuals are varied. To characterize the material, it was mechanically sieved using a multi-tray shaker in general accordance of standard processes for aggregate gradations (ASTM C33 2013). The majority of sieved material was retained on the pan and the No. 8 sieve. The graded material used for the mixture consisted of a 2:1 ratio of "pan" and No.-8 materials. The recycled steel residuals was then washed with water and air dried. The specimen mixture was calculated for a 0.2-cubic-foot batch.

Table 5-2
Concrete Mixture Design of 6x12-In. Cylinder

Mixture Component	Mix Design, lbs. (per cubic yard)	Batch Weights, lbs. (0.2 ft^3 batch)
Cement	630	4.7
Water	285	1.9
Coarse aggregate, No. 89	1515	11.4
Fine aggregate	1509	11.2
RSR (Retained on No. 8 sieve)	70	0.52
RSR. (Passing through No. 8 sieve)	140	1.04

After seven days, the cylinder mold was stripped from the cylinder and the specimen placed in a concrete compression machine with the capability to adjust loading rates. Compressive strength of the specimen was not known. The cylinder was loaded monotonically and electric potential measurements were taken at 100 psi increments from 0 to 600 psi, inclusive. The loading rate was congruent with the compressive strength loading requirements of ASTM C39 (ASTM C39 2003). The testing was repeated when the specimen was 28-days old with the specimen taken to failure. The waveform and the maximum values of the potential was recorded. For this cylinder, neither modulus of elasticity (E) nor Poisson's ratio (v) was measured. However, based on similar mixture designs, estimates of E and v were used for the results and were calculated according to the assumed values found in ACI 318 (ACI Committee 318 2011).

Results

Testing of 4x8-in. Cylinder

Table 5-3 provides the low, high, average, and standard deviation values of the calculated resistances of the ten measurements of each specimen at each age. Figure 5-3

provides a plot of the average resistance values as a function of days after casting. Both

the table and plot are insightful. First, given the low standard deviation of the ten

measurements, the electric-based measurements are very consistent. Second, as expected,

the presence of recycled steel residuals provides a reduction in electrical resistance of the

material. Second, as expected, the resistance is reducing as a function of time. Third,

unexpectedly, there does not appear to be a significant difference in resistance between the

concrete specimen with 0.5% and 1.0% concentration of recycled steel residuals.

Table 5-3
Resistance (ohms) of 4x8-In. Cylinders

Days After Casting	Maximum			Minimum			Average			Standard Deviation		
	0%	0.5%	1.0%	0%	0.5%	1.0%	0%	0.5%	1.0%	0%	0.5%	1.0%
1	10.83	8.51	9.18	10.69	8.40	9.09	10.79	8.46	9.15	0.047	0.034	0.026
3	10.90	8.39	8.75	10.82	8.32	8.69	10.85	8.37	8.72	0.026	0.026	0.017
5	11.14	7.98	8.40	10.98	7.95	8.26	11.09	7.97	8.31	0.059	0.007	0.050
7	10.84	7.44	7.71	10.76	7.35	7.65	10.82	7.41	7.69	0.024	0.024	0.024
10	10.58	6.98	7.22	10.49	6.84	7.19	10.53	6.91	7.20	0.036	0.045	0.008
14	10.11	6.44	6.71	9.99	6.37	6.68	10.08	6.42	6.70	0.035	0.027	0.013
21	9.55	5.83	6.19	9.50	5.77	6.19	9.54	5.81	6.16	0.013	0.018	0.032
28	9.31	5.55	5.96	9.26	5.48	5.96	9.28	5.53	5.94	0.021	0.020	0.018
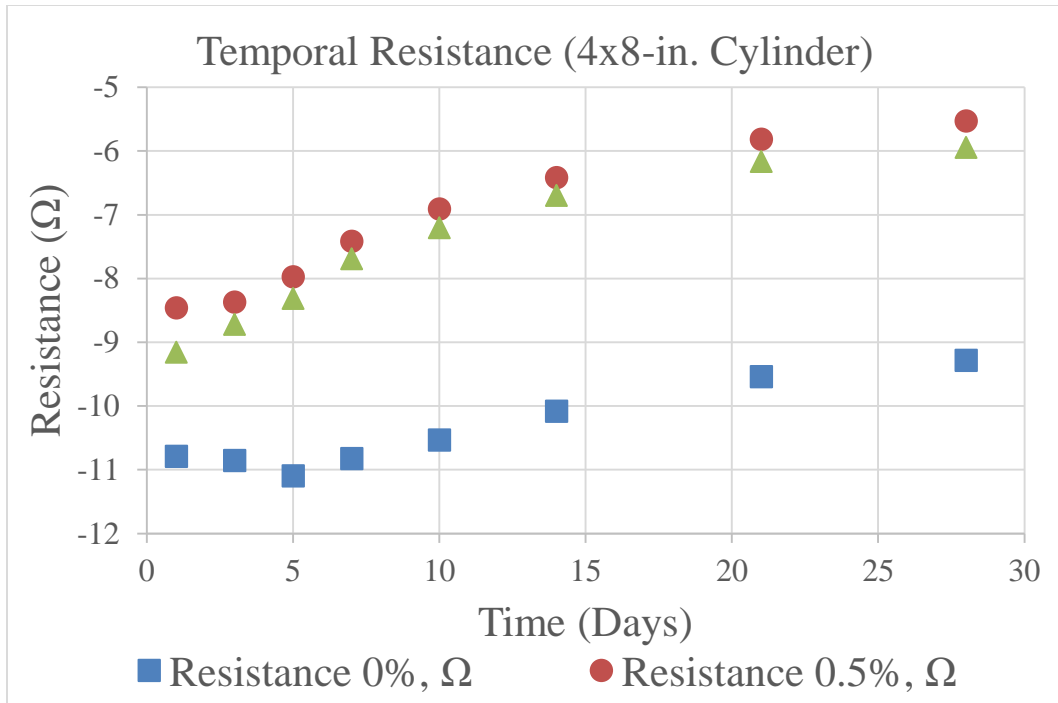
Figure 5-3
Resistance Measurements as a Function of Days after Curing

At 28 days after casting, the specimens were loaded in compression while resistance measurements were taken at pre-determined load intervals. Data related to the physical properties and peak stress resisted by each of the three specimens are given (Table 5-4). As noted previously, AC current (25.5 V, 650 mA, 60 Hz.) was applied at the outer electrodes and the potential across the inner electrodes were measured. Potential measurements were retrieved at 200 psi intervals. The load rate was approximately 75 to 100 pounds per second. Unbonded caps with neoprene pads were used at the top and bottom of the cylinder. Figure 5-4 indicates the change in resistance as a function of a calculated strain using modulus of elasticity.

Table 5-4
Plastic and Hardened Properties of 4x8-In. Specimens

	Concentration of Recycled Steel Shavings		
	0%	**0.5%**	**1.0%**
Height, in.	7.92	7.97	8.07
Diameter, in.	4.02	4.03	4.03
Area, in.^{2}	12.70	12.73	12.73
Weight, lbs.	8.48	8.52	8.78
Density, pcf	145.60	145.17	147.69
Peak Load, psi	2,540	3,030	3,110
Modulus of Elasticity[†], psi	2,872,710	3,137,590	3,178,740
Failure Type	Type 5[*]	Type 5[*]	Type 5[*]

[†]Modulus of Elasticity was calculated based on ACI 318 of 57,000*(f$_c$')$^{0.5}$ (ACI Committee 318 2011)
[*]Type 5 is a side fracture which is noted in (ASTM C39 2003) as being common with unbonded caps
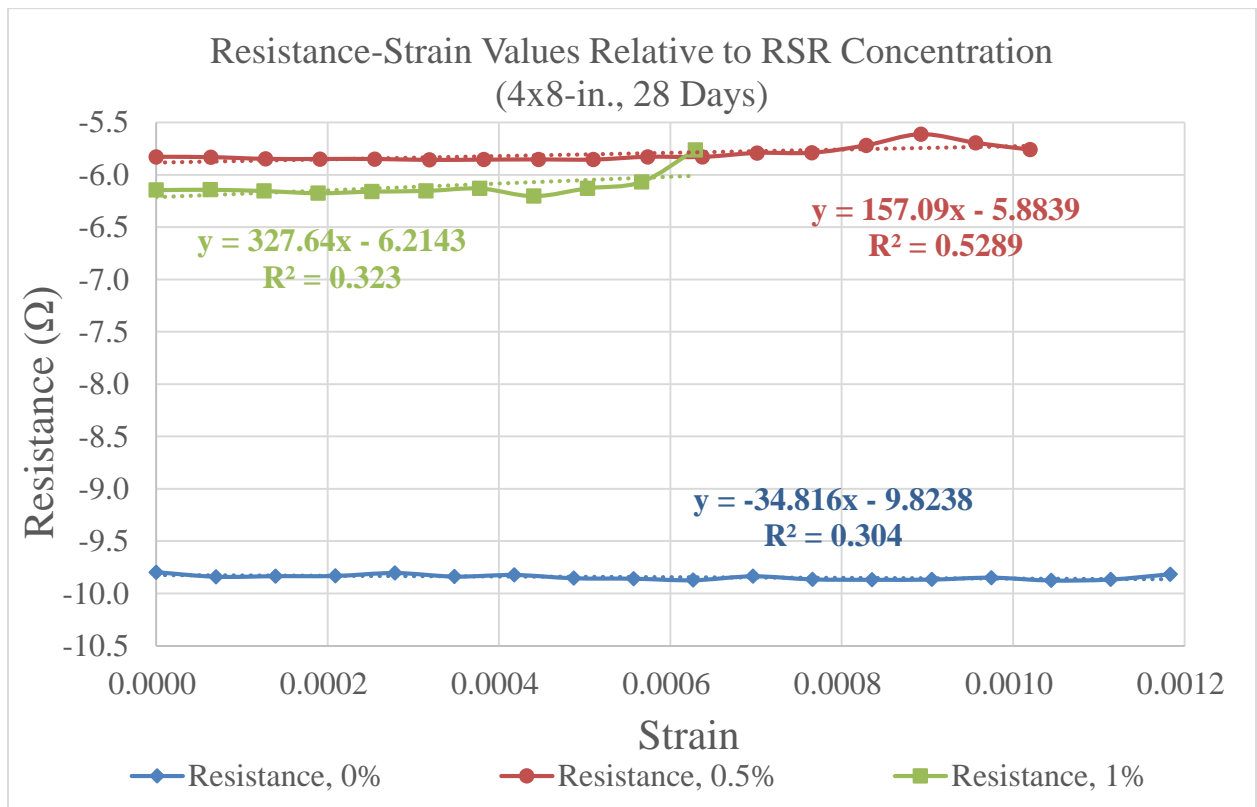
Figure 5-4
Resistance versus Strain (4x8-In. Cylinders, 28 Days)

Results of 6x12 Cylinder Testing

Results of the testing provided insights of particular interest. Figure 5-5 indicates the compiled seven-day, monotonic measurements. As can be seen, the waveforms are not aligned because the signals were positioned differently at each starting point of sampling. When using the extreme minimum or maximum value and plotted as a function of load, it is clearer that resistance of the material increased as compressive loading increased (Figure 5-6). This indicated that changes in conductivity is measurable and observable. However, according to the previous studies referenced above, the theoretical relationship of material strain-resistance is expected to be linear. Based on a linear regression, seven-day data show a linear relationship with a calculated coefficient of determination (R-squared) value of 0.80 (Figure 5-6).
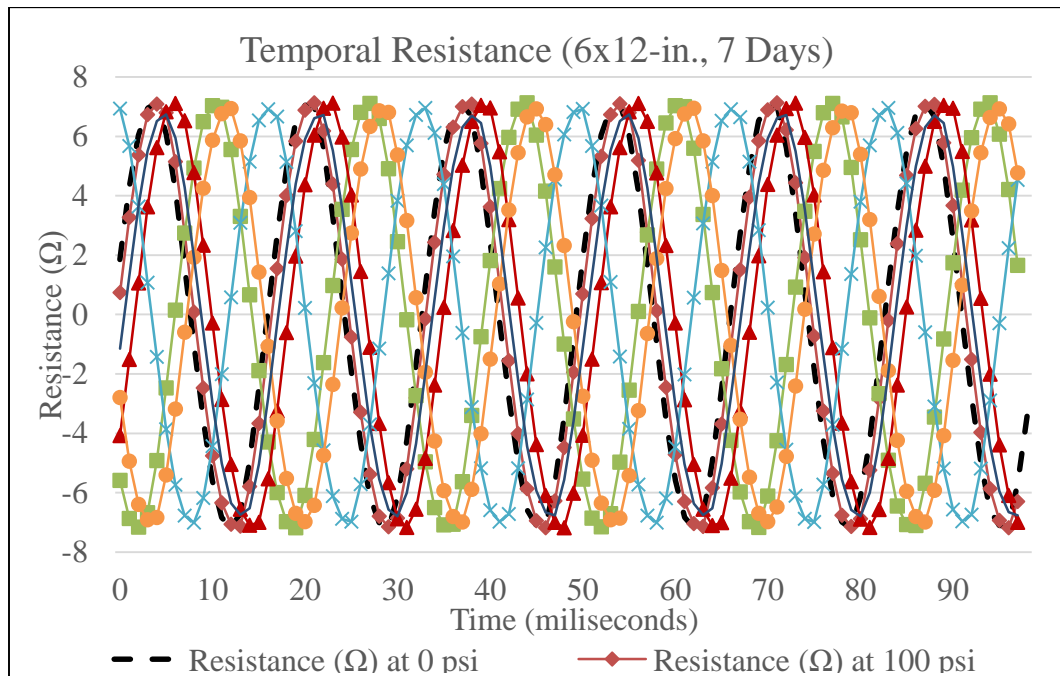
Figure 5-5
Concrete Resistance versus Time (6x12-In. Cylinder, 7 Days)
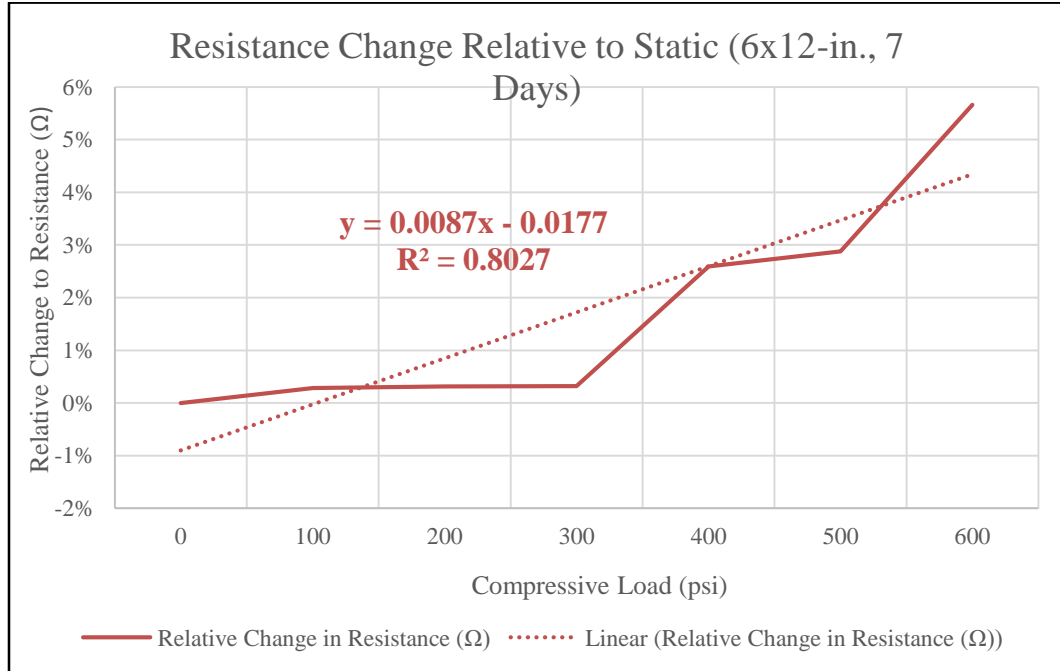
Figure 5-6
Relative Change in Resistance (6x12-In. Cylinder, 7 Days)

For completeness, the raw data for the test results when the cylinder was 28-days old is also provided (Figure 5-7). The electric measurements were taken at compressive loading of zero through 97% of the maximum compressive load at 200 psi intervals. Data is plotted in three approximate segments: 0% to 10%, 10% to 60%, and 60% to 97%. The linear regression noted above is applied to each of the segments. Two very important observations can be seen in Figure 5-7. To maintain electrical isolation between the compression machine and cylinder, a rubber pad was placed at one cylinder end (Figure 5-8). After load to failure, the rubber pad was observed to have had significant strain in the axial direction. Given this, it is very likely that the first multiple data points (four +/-) represent strain in the rubber pad rather than strain in the cylinder. This observation

explains for the low R-squared value. Second, the final data point is closely approaching the point of cylinder failure. Micro-cracking is likely considerable at this point and will have a significant effect on concrete resistance. So, the analysis of the 28-day, resistance-strain curve can legitimately be limited to the points after the first few data points and before the last few data points.
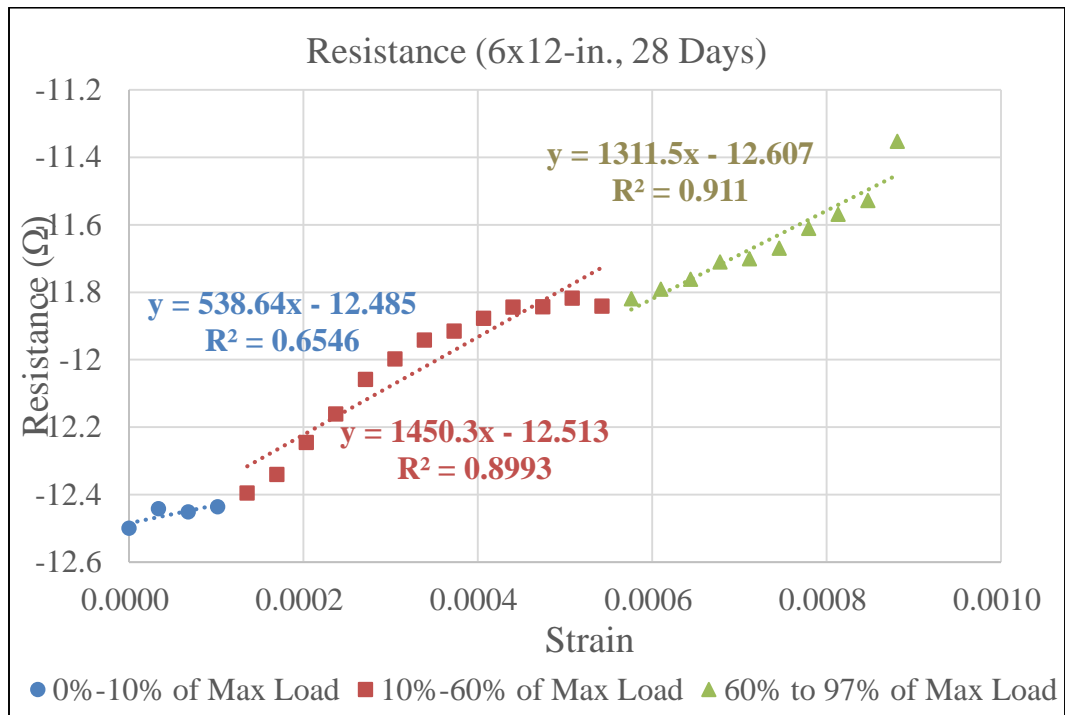
Figure 5-7
Calculated Resistance versus Strain (6x12-In. Cylinder, 28-Days)

Finally, Figure 5-9 indicates the resistance values measured at 7 and 28 days after the specimen was created. There is a measurable difference in resistance between 7 and 28 days. This indicates that the continued curing of the concrete will affect the measurable resistance. Previous studies by others (Backe, et al. 2001; Rajabipour 2006) have shown that electrical properties change as changes in cementitious microstructure occurs as

96

cement cures. Specifically stated in (Backe, et al. 2001), conductivity declines significantly during the hydration process of a cement slurry. The replacement of water within the matrix pores will take more than 28 days to complete a phase transition into solid hydration products (Mindess, Young, Darwin 2004). The pore solution consists of a variety of different ionic species – soluble alkalis and gypsum – and the moisture will remain in solution for approximately 90 days depending on the pore size and matrix structure (Mindess, Young, and Darwin 2004). Additionally, the slope of the linear best-fit line is much greater for the measurements taken at 28 days than at 7 days. This suggests that hydration moisture stunts the observable measurements of resistance as a function of strain. Therefore, the age of specimens must be taken into consideration when using electric-based techniques when using it to indicate strain.
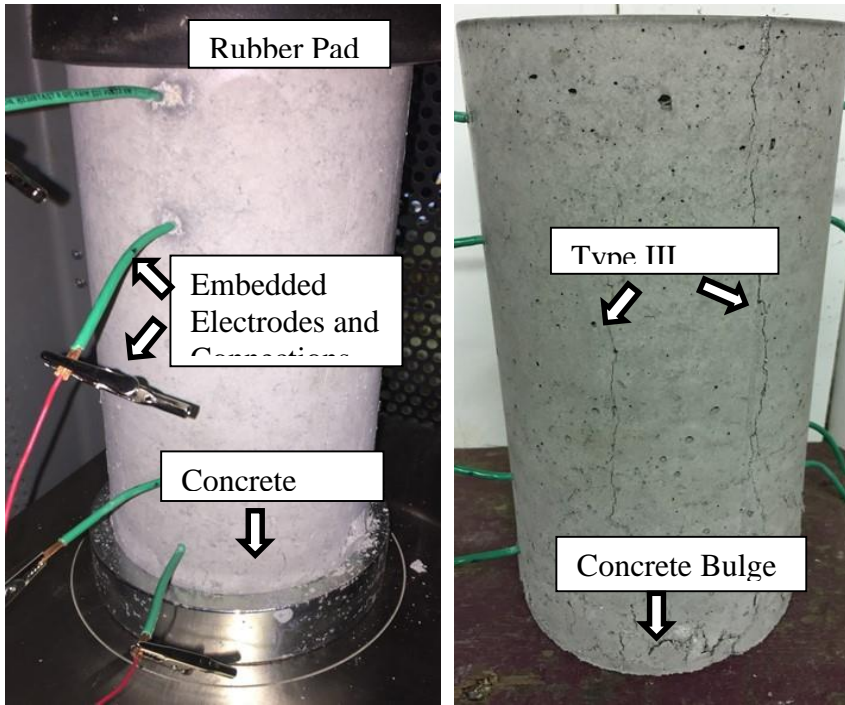
Figure 5-8
Cylinder After Elasto-Electric Testing (6x12-In. Cylinder, 28-Days)
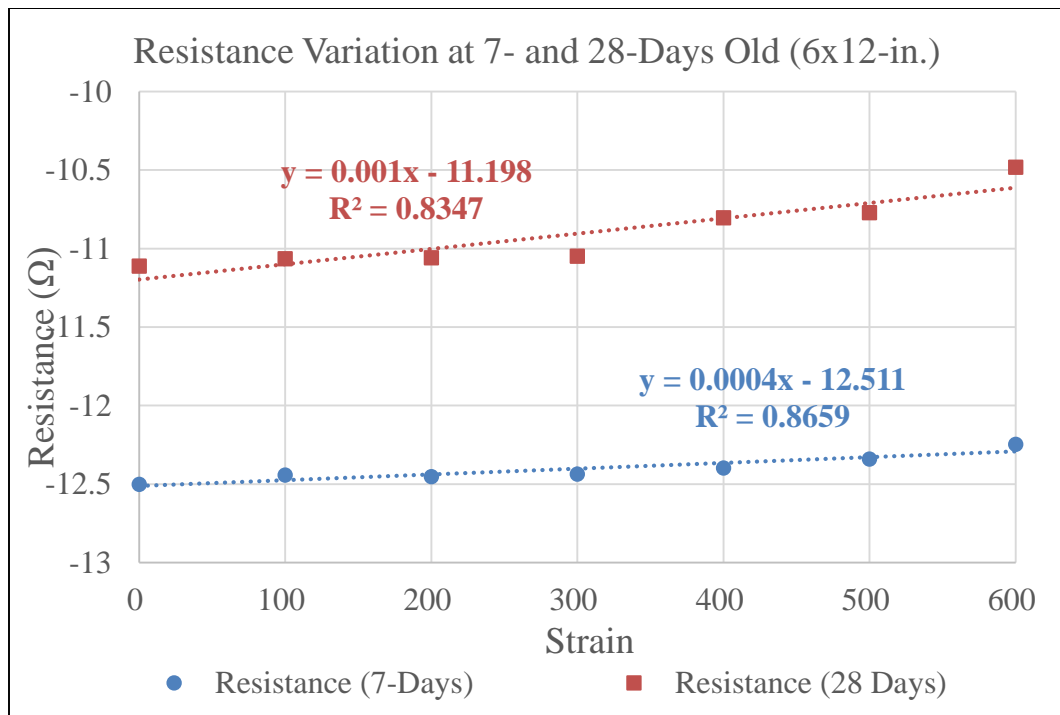
Figure 5-9
Resistance Variation at 7- and 28-Days after Casting (6x12-In. Cylinder)

Discussion

There was some inconsistency in the test results to note. The 6x12-in. cylinder indicated a distinct change in electrical conductivity in the material as the concrete cylinder was being compressed. The increase in resistance was approximately 10% of the original static value, and this, in spite of a loss in transferred loading due to significant strain in the rubber pad at the top of the cylinder. In contrast, the 4x8 cylinder did not have a change in resistance as a function of strain. The changes in resistance for all three cylinders with varying concentrations of recycled steel residuals – 0%, 0.5%, and 1% - were nearly zero. It appears that the inconsistency is a result of the mixture designs and aggregate-to-specimen size ratio. The 6x12 cylinder consisted of a No. 89 stone which has a maximum nominal size of 3/8 to 1/2 in. (ASTM C33 2013). The 4x8 cylinder consisted of a No. 67 stone which has a maximum nominal size of 3/4 to 1 in. (ASTM C33 2013). The aggregate behaves like an insulator and the current flowing through the cylinder follows the more conductive path around the aggregate through the cement matrix of the material. The larger aggregate being used in the smaller cylinder appears to have restricted the electrical connectivity through a more tortuous path. This is also supported by the similar level of conductivity found in the 4x8 cylinder with 0.5% and 1% concentration of recycled steel residuals. (That is, the 1% concentration did not have an increase in conductivity when compared to the 0.5%-concentration cylinder.) This suggests that the conductivity of the cylinders is affected by the insulating aggregate. As such, future concrete specimens should include larger specimen-to-aggregate size ratios.

Additionally, electrically isolating materials between the specimen and compression machine should be of low modulus. A neoprene pad, potentially a viscoelastic material, or other type of capping material are good options to distribute and accommodate slight irregularities at the ends of the specimens as recommended in germane standards (ASTM C39 2003). During testing, the connectivity (or lack of connectivity) should be confirmed using a multimeter. Also, for the reported study here, strain is being theoretically calculated using recommended relationships between yield strength and modulus of elasticity (ACI Committee 318 2011). Actual strain will likely be different from that calculated using theory (Electric Power Research Institute 2016). To better determine strain, companion specimens should be used to find modulus of elasticity and Poisson's. Additionally, strain should be directly measured on the specimens.

Finally, input current for the study reported here was fixed at 25.5 V (AC), 650 mA, and 60 Hz. Variability in load, current, and/or frequency will allow consistency to applicable standards for this type of testing (ASTM G57 2012) and provide opportunity to learn more about the phenomenon being tested. Additionally, this study established that changes in strain affects changes in electrical resistance of a material when impregnated with recycled steel residuals. As such, it is possible to detect differences in strain at different cross-sectional locations of a specimen. Therefore, it would be informative if multiple pairs of inner electrodes were placed and each pair simultaneously measured while loading the specimen.

Conclusion

In this study, the use of recycled steel residuals (steel shavings) as a cost-effective method of creating self-sensing, smart concrete was explored. A 6x12-in. cylinder containing 1.6% recycled steel residuals was tested by compressing the cylinder and regularly measuring the potential within the concrete when a 25.5 V (AC), 650 mA, 60 Hz current was applied to the specimen. The measurements indicated that strain is sometimes detectable using resistance measurements within the concrete. It is deduced that a deciding factor in electric-based strain detection is the specimen-to-aggregate ratio. This was surmised because the 4x8-in. cylinders did not show a correlation between strain and resistance. The research team concludes that the larger aggregate in the smaller specimens did not allow the electrical resistance to be dictated by the strain of the cement matrix but was instead a function of the path around the larger aggregate within the specimen.

References

ACI Committee 228, 1998. ACI 228.2R, Nondestructive Test Methods for Evaluation of Concrete in Structures. Farmington Hills (MI): American Concrete Institute; 1998.

ACI Committee 318, 2011. ACI 318-11, Building Code Requirements for Structural Concrete. Farmington Hill: American Concrete Institute.

ACI Committee 544, 2008. ACI 544.3R-08, Guide for Specifying, Proportioning, and Production of Fiber-Reinforced Concrete. Farmington Hill: American Concrete Institute.

ASTM C31, 2015. "Standard Practice for Making and Curing Concrete Test Specimens in the Field." ASTM C31/C31M – 15a, West Conshohocken, PA.

ASTM C33, 2013. "Standard Specification for Concrete Aggregates." ASTM C33/C33M – 13, West Conshohocken, PA.

ASTM C39, 2003. "Standard Test Method for Compressive Strength of Cylindrical Concrete Specimens." ASTM C 39/C 39M, West Conshohocken, PA. ASTM International, 2003.

ASTM C192, 2002. "Standard Practice for Making and Curing Concrete Test Specimens in the Laboratory." ASTM C192/C192M – 02, West Conshohocken, PA.

ASTM G57, 2012. "Standard Test Method for Field Measurement of Soil Resistivity Using the Wenner Four-Electrode Method." ASTM G57 – 06 (Reapproved 2012), West Conshohocken, PA.

Backe, K.R., Lile, O.B., Lyomov, S.K., 2001. "Characterizing Curing Cement Slurries by Electrical Conductivity." SPIE Drilling & Completion, pp 201-207.

Electric Power Research Institute, 2016. *Advanced Nuclear Technology: Evaluation of Self-Consolidating Concrete Mixtures and Structural Members: Phase 1*. EPRI, Palo Alto, CA: 2016. 3002007567

Kim, Lee, Chang, and Park, 2011. Kim, D., Lee, C., Chang, H., & Park, S. (2011). Embedded Peizoelectric Sensor-Based Real-Time Strength Monitoring during Curing Process of Concrete. Smart Structures.

Kholkin AK, Kiselev DA, Kholkine LA, et al. Piezoelectric and Electrostrictive Ceramics Transducers and Actuators. In: Schwartz M, editor. Smart Materials. Boca Raton (FL): CRC Press; 2009. 9.1.

Konsta-Gdoutos M.S., and Aza C.A., 2014. "Self sensing carbon nanotube (CNT) and nanofiber (CNF) cementitious composites for real time damage assessment in smart structures."

102

Mindess S, Young JF, Darwin D. Concrete. Upper Saddle River (NJ): Pearson Education, Inc.; 2004.

Li, H, Xiao, H and Ou, J, 2004. "A Study on Mechanical and Pressure-Sensitive Properties of Cement Mortar with Nanophase Materials," Cement and Concrete Research, 34, pp 435-438.

Pammi, S, Brown, C, Datta, S, Kirikera, GR, Schulz, MJ, 2003. "Concepts for Smart Nanocomposite Materials," Smart Structures, SPIE, 5062, pp 629-636.

Park and Kim, 2011. Ubiquitous Piezoelectric Sensor Network (UPSN)-Based Concrete Curing Monitoring for Construction 2011 Modern Telemetry 75-92

Rajabipour, F., 2006. "Insitu Electrical Sensing and Material Health Monitoring in Concrete Structures," Thesis, Purdue University, UMI Number 3259972.

Scott, D. Internal Inspection of Reinforced Concrete for Nuclear Structures Using Shear Wave Tomography. Energy Convers and Manag.; 2013; 74: 582-586.

Shen and Li, 2006. A Cement-Based Piezoelectric Sensor for Civil Engineering Structure 2006 Materials and Structures 1-5

Suchanek and Riman, 2009. Intelligent Synthesis of Smart Ceramic Materials. Book editor: Schwarz, M; Smart Materials; 2009; chapter 2; Boca Raton; CRC Press

Sreekala R, Muthamani, K., 2009. Structural Applications of Smart Materials. In: Schwartz M, editor. Smart Materials. Boca Raton (FL): CRC Press; 2009. 4.

Suchanek WL, Riman RE, 2009. Intelligent Synthesis of Smart Ceramic Materials. In: Schwartz M, editor. Smart Materials. Boca Raton (FL): CRC Press; 2009. 2.

Wille K, Loh, KJ, 2010. Nanoengineering Ultra-High-Performance Concrete with Multiwalled Carbon Nanotubes. Transportation Research Records. 2010; 2142: 119-126.

Wang X, Chung, DDL, 1998. Short Carbon Fiber Reinforced Epoxy Coating as a Piezoresistive Strain Sensor for Cement Mortar. Science Direct, Sensors and Actuators. 1998; No. 71: 208-212.

Withey, Vemuru, Bachilo, Nagarajaiah, and Weisman, 2012. Withey, P., Vemuru, V., Bachilo, S., Nagarajaiah, S, Weisman, R, 2012. Strain Paint: Noncontact Strain Measurement Using Single-Walled Carbon Nanotube Composite Coatings. Nano Letters, 3497-3500.

Yao, Tung, and Glisic, 2014. Crack Detection and Characterization Techniques - An Overview 2014 Structural Control and Health Monitoring published online

Yang and Dai, 2012. Review on Optical Fiber Sensors with Sensitive Thin Films. Photonic. 2012. 14-28.

CHAPTER 6 ASSESSMENT OF RECYCLED STEEL RESIDUALS AS FUNCTION FILL IN AXIALLY LOADED CONCRETE COLUMN FOR STRAIN DETECTION

Abstract

This paper describes the design of a self-sensing concrete column using recycled steel residuals (RSR) as functional fill and the testing of the column under slow-rate cyclic loading. The RSR modified concrete has the advantage of sustainably using the otherwise waste material from steel fabrication process. Two columns (one without and one with 2% of RSR by volume) were fabricated in the lab and load tested in cyclic axial compression. The columns are connected to an alternating current power source and have three electrode sets each for electric property measurements. The results indicate that the 2% specimen can accurately detect the loading and unloading processes using electric-based measurements to calculate resistance. Based on the test results, empirical linear equations are derived to correlate the mechanical and electrical behaviors.

Keywords: axial compression, electro-elasticity, recycled steel residuals, resistance and strain relations, self-sensing concrete, strain detection

Introduction

Self-sensing concrete or autonomous sensing concrete is a subject matter that has drawn significant attention in recent years (Wang et al. 1998, Li et al. 2004, Han et al. 2014). The technology focuses on modifying concrete material with added sensing functionalities, which is a significant contrast to traditional nondestructive testing/evaluation (NDT/E) or structural health monitoring (SHM) technologies that depend on the application of extraneous sensors to concrete structures (ACI 1998, Malhotra and Carino 2003). For some concrete structures, traditional NDE has application limitations that include requiring being at the concrete, with some areas not accessible by sensors and sensor transmittants. Furthermore, NDT sensors provide only localized data that may not be representative of the health state of the entire structure. Hence, to supplement conventional inspections and offset some of these limitations, there is growing emphasis to develop self-sensing or smart concrete.

Specifically, self-sensing concrete is a concrete material technology that has the ability to indicate strain (and potential damages) based on changes in the electrical properties of the concrete (Wang et al. 1998). Researchers have used materials with electrostrictive properties that is ubiquitously embedded throughout the concrete mixture and is infused with the concrete during and after hydration and final setting of the concrete. In most cases, electrodes are either embedded or attached to the surface (Han et al. 2014). The embedded electrodes usually consist of a perforated plate, mesh, or loop. Loading and strains are then applied to the concrete to detect the changes in electrical properties to indicate the change in material strain (Li et al. 2004 and Han et al. 2014). Several

embedded functional materials have been experimented with including single-walled carbon nanotubes, piezoelectric ceramic, electrochemicals, etc., most of which are costly and most of the previous work in this realm has been on small samples containing little to no coarse aggregate and, in some cases, no fine aggregate (Li, et al. 2004, Suchanek and Riman. 2009). As a result, to date this technique has only maintained a low technical readiness level (TRL).

In this paper, recycled steel residual is suggested as an alternative functional material to make concrete self-sensing. To demonstrate the method, compression tests have been performed on a concrete column that contains 2% of the recycled steel residual by volume. The concrete column was axially loaded, and the results are presented herein and includes a theoretical summary of the monitoring technique for self-sensing concrete.

Theoretical Basis of Self-Sensing Concrete

The recycled steel residuals are procured waste products from steel fabricator shops, which may consist of steel shavings of various sizes and with significant amount of metal dust particles. Depending on the number of jobs, a typical steel fabricator may generate several pounds of such wastes per day, which are either sent to steel mills to be re-melt for new metal parts or go straight to landfills. By suggesting the recycling and use of these steel residuals as functional materials for self-sensing concrete, a more sustainable approach to these materials is presented here.
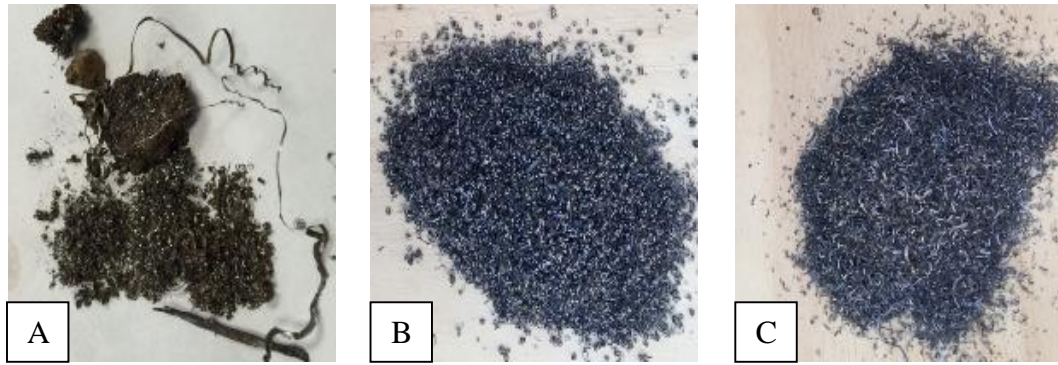
Figure 6-1
Recycled Steel Residuals in: A) Raw Form, B) Retained on No. 8 Sieve, and C) Passing through No. 8 Sieve

Figure 6-1a shows the recycled steel materials, which may be in different degrees of rust and may be coated with oil that is used for cooling during metal forming processes. Hence, some work may be needed to process the material. Figure 6-1b and 6-1C show the same material after being washed and sieved. To ensure consistency, homogeneity, and workability of the modified concrete, only certain sizes of the material should be blended into the concrete mix.

The theory to support the placement of the electrodes comes from the Wenner test method and other electric methods to indicate resistivity of a material across a given section geometry and length (ASTM G57 2012; Konsta-Gdoutos and Aza 2014; Han, Yu, Ou 2014). It should be noted that electric properties such as resistivity tests have been used extensively in the NDT of concrete and geophysical investigations – in most cases, these investigations adopt a four-probe approach (US EPA and Geophysics). The reduction in electrical potential can be measured at any two points along the material and, given a known distance between the points, the resistivity of the material can be measured as follows:

108

$$\rho = \frac{R*A}{L} = \frac{V*A}{I*L} \tag{1}$$

where ρ = resistivity (ohms-in., ohms-cm), R = resistance (ohms), A = cross-sectional area (in.^{2}, cm^2), L = distance between the two inner electrodes of measurement (in., cm), V = potential drop (volts), I = applied current (amps).

Equation 1 is established and applied for the Wenner probe test method to determine the electrical resistance of soil. To indicate the suitability of material, laboratory experiments can be performed by sending a current through soil of a known length and cross section. The electrical potential difference between two inner connections are measured. Using this and the geometry of the box, material resistivity can be calculated.

In the study described herein, embedded electrodes will impart the current (at the outer electrodes) and measure the potential differences within the concrete (across pairs of inner electrodes). The specimen will be loaded axially and in compression. A relationship between the mechanical result (strain) of loading the specimen and changes in electric properties within the concrete – resistance and resistivity – will be measured. The relationship is described as the electro-elastic parameter of the specimen and can be presented as:

$$\varepsilon\,(1+2v) = (\frac{dR}{R} - \frac{d\rho}{\rho}) \tag{2}$$

where ε = strain and v = Poisson's ratio.

Experimental Setup

Axial Test Sensing

The raw recycled steel residuals were processed by sieving the material to determine the approximate fineness and approximate distribution of particle sizes. Large portions of

109

the material passed through a No. 8 sieve (Figure 6-1(C)). Given the approximate size distribution between the material retained on the No. 8 sieve and that passing through it, the recycled steel residuals was proportioned as 2:1 (passing-through:retained-on No. 8) after passing through a No. 4 sieve above the No. 8. The material was cleaned using water under pressure. Additional "cleaning" may be required to produce recycled steel residuals that are suitable for concrete as a functional filler. For instance, degreasing may be necessary to process the material such that potential chemicals will not impede the electrical conductivity of the material. The chemicals may also affect other plastic and hardened properties of the concrete. As noted in the introduction, electrical conductivity of concrete is a function of the cement matrix and the free space between the aggregates and the matrix; hence, an understanding of how the recycled steel residuals will affect these parameters and, consequently, electric conductivity is also investigated.

The concentration of recycled steel residuals used in the studied concrete mixtures is based on ACI 544 publication (ACI 544.3R 2008). Concrete mixture designs are based on ACI 211 (ACI 211.1R 2009, ACI 211.3R 2009) and trial batches were developed both with and without recycled steel residuals. Plastic and hardened properties of the various mixtures are tested and reported here. For resistance testing, prisms (columns) are 6x6x20 in. (150x150x500 mm) which is consistent with the dimensions specified in the ASTM C78 and C1609 (ASTM C78 2015 and ASTM C1609 2012). The prisms will be axially loaded with the long dimension being up/down. Given these dimensions, the first order buckling load is one to two orders of magnitude greater than the compression load to be used for the compression tests. Therefore, the column is determined to be a "short column,"

with unidirectional compression failure (i.e., with no buckling) if loaded to failure. Nonetheless, strain will be measured using surface mounted gages on two planes of the column to determine if eccentricity of the loading develops.

Besides attaching strain gages to the concrete surface, the testing will include measuring changes in electrical conductivity as a function of axial load and strain. Electrical conductivity measurements will be taken by embedded electrodes. Electrode placement in the concrete columns is shown in Figure 6-2. Prior to loading the specimen, the data acquisition device was connected to the electrodes such that a current is supplied to create a circuit using the outer electrodes (Figure 6-2(B)). An electrical bond breaker was placed between the load contacts and the specimen. To prevent polarization of the concrete, alternating current (AC) was imparted into the concrete through the outer electrodes (Rajabipour 2006).

Insulated wires were placed through the forms and the wire insulation stripped at the location where electrical resistance were measured (Figure 6-3(A)). Electrodes consist of 10 Ga., stranded copper with 24-mil insulation. The length of the electrodes protruding through the wires were equivalent and the exposed length of wire was one inch. The forms were ¾ in. thick to prevent bulging of the forms during creation of the specimens. Initial curing included covering the specimens with plastic to retain moisture. Companion cylinders consisted of 4x8-in. for strength testing and 6x12-in. for testing modulus of elasticity.
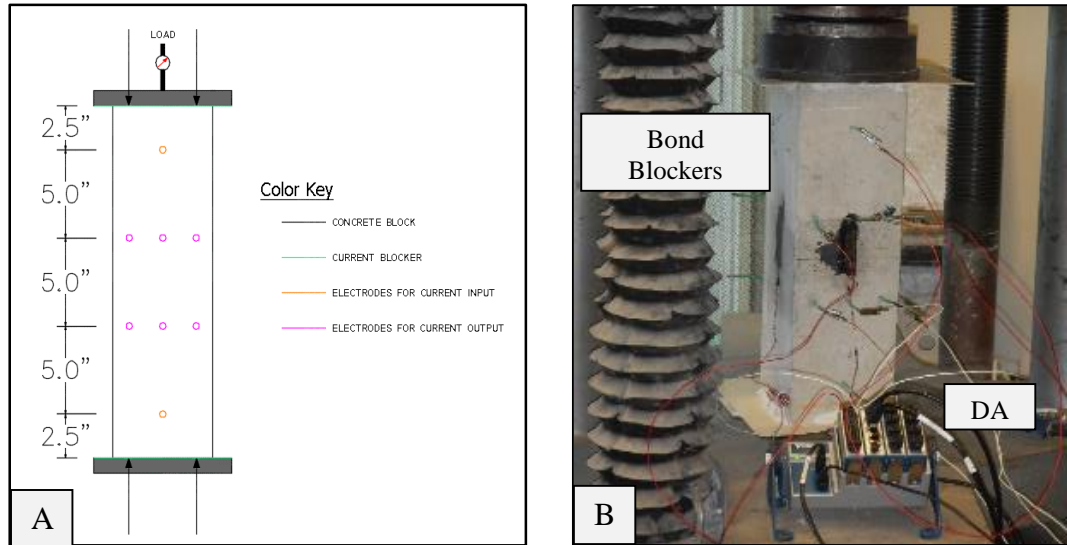
Figure 6-2

Proposed (A) and Actual (B) Test Specimen (6x6x20-in.) for Electro-Elastic Testing
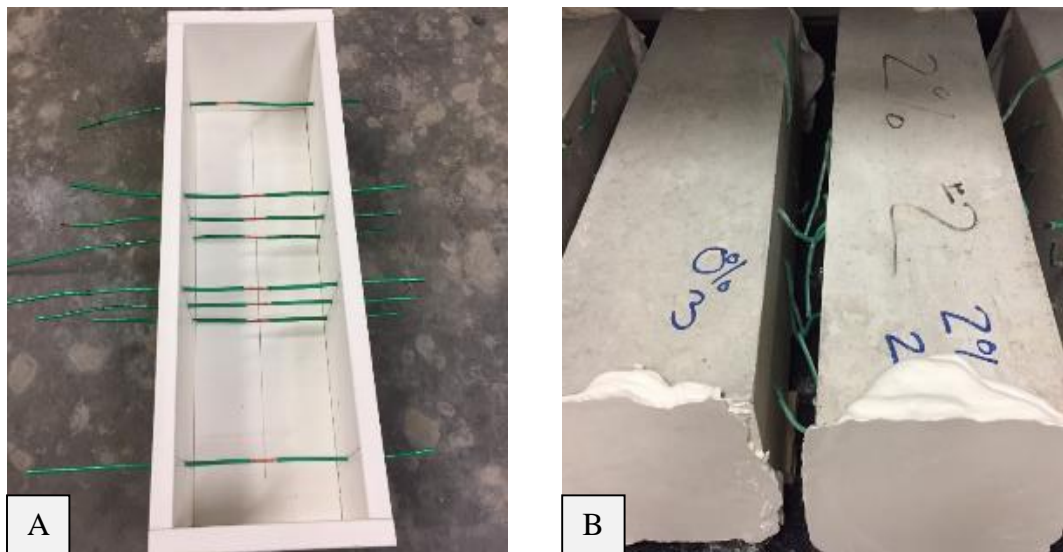
Figure 6-3

Specimen Mold for Columns (A) and Demolded Columns with Plaster Caps (B)

The placement of the electrodes is intended to indicate changes in electrical conductivity as the concrete compresses. Load eccentricity will be verified by the attached strain gages on two adjacent planes of the concrete columns and will be oriented axially. Electric current was applied at the electrodes near the column ends and pass through the

cross-section of the column. Changes in conductivity were measured across three pairs of the electrodes at the exposed wires. Figure 6-4 indicates the expected relationship between current flow, equipotential lines, and placement of electrodes for the proposed specimens for this study. As shown in Figure 6-4, there will be three pairs of electric potential measurements indicated in the following sections as left, middle, and right measurements, respectively.
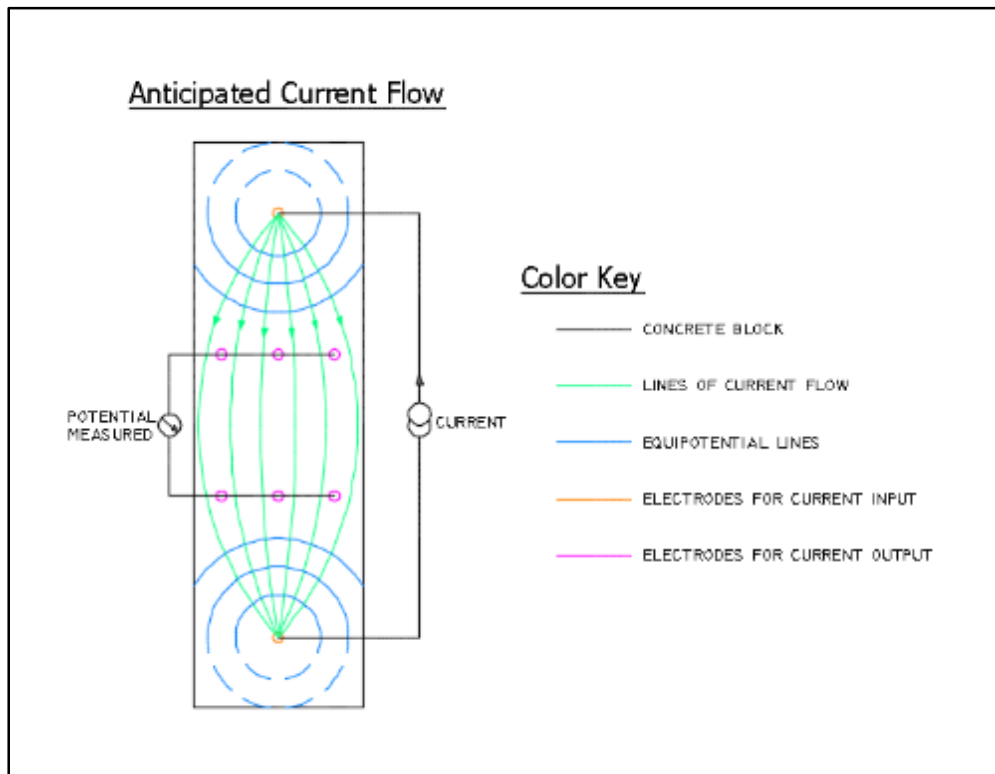
Figure 6-4
Anticipated Current Flow and Locations of Electric Potential Measurements

Concrete Mixture Design

Mixture proportioning and concentrations of recycled steel residuals was developed according to ACI 211 and 544 (ACI 211.1R 2009, ACI 211.3R 2009, ACI 544.1R 1996). Sieve analysis of the fine and coarse aggregates was first performed. The aggregate was characterized according to ASTM C33 ASTM C 33 2003]. A dry-rodded unit weight of the coarse aggregate was measured (ASTM C125 2016). To help prevent a reduction in workability and maintain consistent parameters, all mixtures had a w-cm ratio of 0.45. Additionally, two types of admixtures were used to reduce the likelihood of slump loss – water reducer (WR, Type A) and high-range water reducer (HRWR, Type F) (ACI 212.3R 2010, ASTM C 494 2004). For this project, the coarse and fine aggregates were reduced according to the corresponding volume of added steel. The reduction in coarse and fine aggregates was approximately equivalent, by volume. The concrete was mixed according to ASTM C94 and ASTM C192 ASTM C 94 2004, ASTM C 192 2002).

Two mixture designs were developed and corresponded with recycled-steel-residual ratios of 0 and 2% relative to bulk volume. Table 6-1 indicates the concrete mixtures used for the column testing of this project and the theoretical plastic properties and mixture designations. It should be noted that ACI 544 recommends a maximum concentration of steel fibers to be 1% (ACI 544.3 2008). Based on preliminary studies and values in static electrical conductivity tests of the preliminary test members, one of the mixtures included a higher concentration – 2% – than recommended by ACI 544. The proportioning of mixtures to include a graded recycled steel residual was a result of the findings of the preliminary test mixtures which produced material with significantly reduced workability.

114

Table 6-1
Concrete Mixtures for Specimen Creation

Mixture Component/Parameter	0.0%	2.0%
Cement, lbs.	98.0	98.0
Water, lbs.	41.5	41.5
Coarse aggregate, lbs.	236.3	229.6
Fine aggregate, lbs.	248.0	240.8
Recycled steel residuals, lbs. (Retained on No. 8 sieve)	0.0	13.7
Recycled steel residuals, lbs. (Passing through No. 8 sieve)	0.0	27.3
Water-reducer (Type A), mL (oz. per 100 wt.)‡	86.8 (2.9)	86.8 (2.9)
Water-reducer (Type F), mL (oz. per 100 wt.)†	34.7 (1.2)	34.7 (1.2)
Assumed Entrapped Air, %	1.5	1.5
Batch size, ft^3	4.2	4.2
Theoretical plastic density, pcf	148.5	155.0
w-cm ratio	0.45	0.45
RSR ratio by volume of mixture, %	0	2.0
Fine-to-coarse aggregate ratio	1.03	1.03

‡ Type A, water-reducing admixture may adjust based on observations during mixing.
† Type F, water-reducing admixture may adjust based on observations during mixing.

Plastic and Hardened Properties

Testing for plastic properties includes unit weight (ASTM C138 2001), slump (ASTM C143 2003), air content (ASTM C231 2004), and temperature (ASTM C1064 2004). For testing the hardened properties of the concrete, 6x12-in. cylinders were made. The cylinders are instrumented with two compressometers. One compressometer is oriented to indicate axial strain, the other is oriented to indicate radial strain. The first loading occurs to seat the collars of the compressometers. Loading rates for the testing is to remain between 30 and 40 psi (ASTM C469 2002). The load values and strains are recorded at the various stages indicated in ASTM C469. The values were recorded and calculations for modulus of elasticity and Poisson's ratios were performed.

Two trial batches were performed and concrete workability measured. The trial batches were performed on March 5, 2017. The mixture designs used for the trials batches are shown in Table 6-2. A specific gravity value of 7.8 was used for the recycled steel residuals. A loss of workability was indicated when recycled steel residuals were placed in the concrete mixture.

Table 6-2
Batch Weights of Trial Concrete Mixtures Based on RSR Concentration

Mixture Component and Plastic Property	No RSR	With RSR
Cement, lbs.	46.7	46.7
Water, lbs.	19.2	19.2
Coarse Aggregate, lbs.	114.8	112.2
Fine Aggregate, lbs.	116.4	113.7
Recycled Steel Residuals, lbs.	0.0	15.6
MRWR Admixture, mL (oz./cwt)	96.6 (7)	96.6 (7)
Batch Size, ft^3	2.0	2.0
Assumed Entrapped Air, %	1.5	1.5
Theoretical Plastic Density, pcf	148.5	153.7
w-cm Ratio	0.45	0.45
Slump, in.	6	3

Self-Sensing Measurements

Each column test involves three cycles between minimum and maximum values and the number of voltage measurements is approximately 20 measurements per loading cycle. The loading range is set between 10% and 60% of the concrete strength based on the 6x12-in. companion cylinders. At 100 pounds per second, the loading rate was slower than recommended by ASTM C39 (ASTM C39 2003). Voltage measurements are recorded in a National Instrument (NI) data logger NI 9205 with three parallel differential channels at a sampling rate of 1000 S/s and with a maximum voltage reading of 10 V. One-hundred samples will be taken over six cycles of the 60 Hz. voltage input equivalent to 25.5 V at

116

650 mA. The same data logger is used to record strain using two channels of a NI 9237 having a minimum sampling rate of approximately 1620 S/s.

Results

Figure 6-5 shows the loading histories as stress-strain curves for both the 0% and 2% columns. Testing was repeated on the 2% specimen, hence, Figure 6-5b shows two response curves. The second load test was done one week after the first test to determine the repeatability of the measurements. Figure 6-6 shows the time histories of the strain and the voltage measurements (three pairs for each specimen) for the 0% and 2% specimens (Test 1). These raw data show that the concrete with 2% filler material has correlation with the strain loading; on the other hand, the concrete column without RSR has no visible trend in electric responses. Therefore, the following data analysis will only be performed on 2% specimen. Other specimens with 2% concentration of recycled steel residuals also showed indication of correlation between strain and changes electric potential, but results and analysis for those specimens will not be reported here due to space limitations.
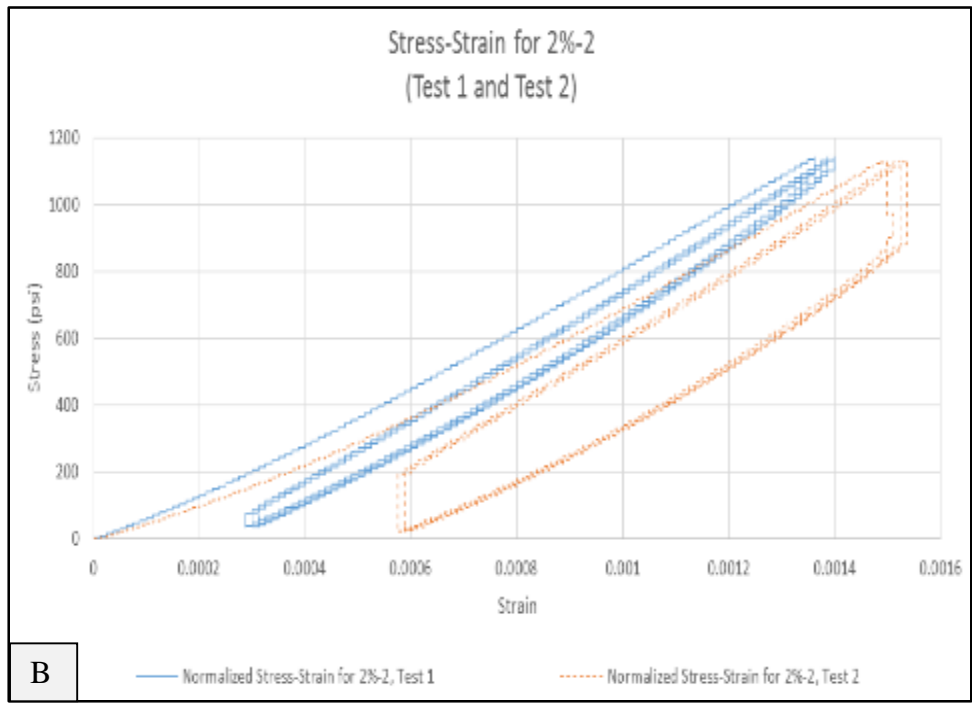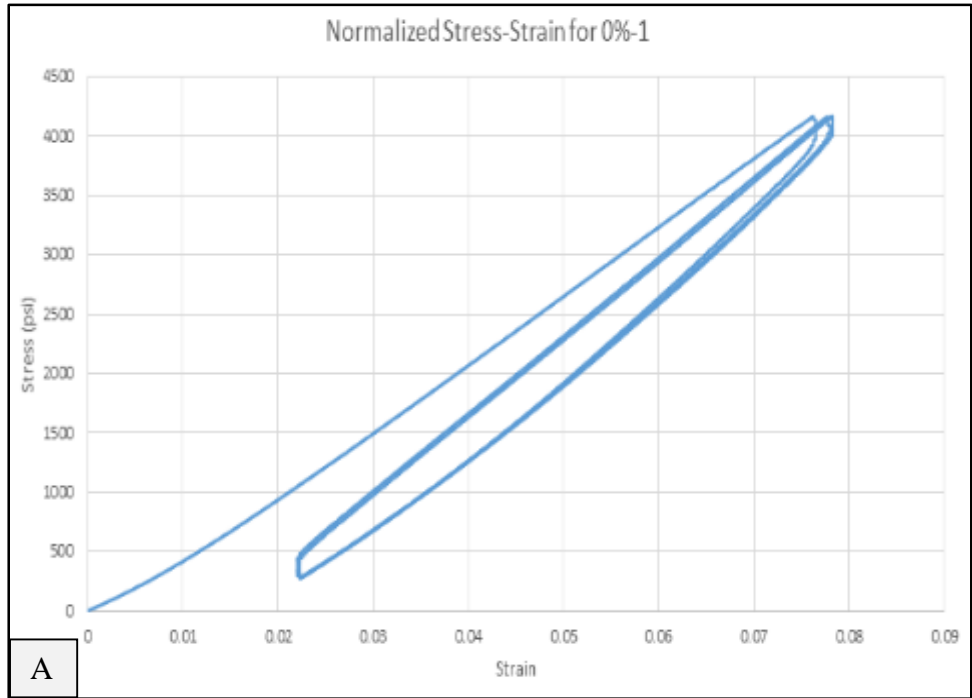
Figure 6-5
Stress Strain Curves Showing Multiple Loading Cycles: 0% (A) and 2% (B) for Both
Test 1 and Test 2
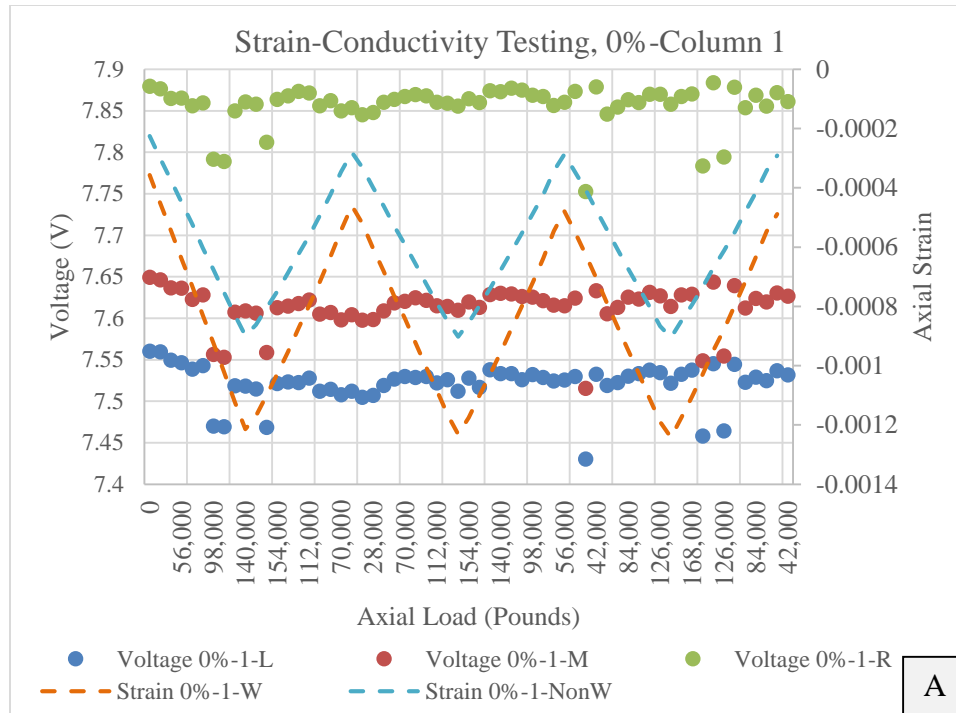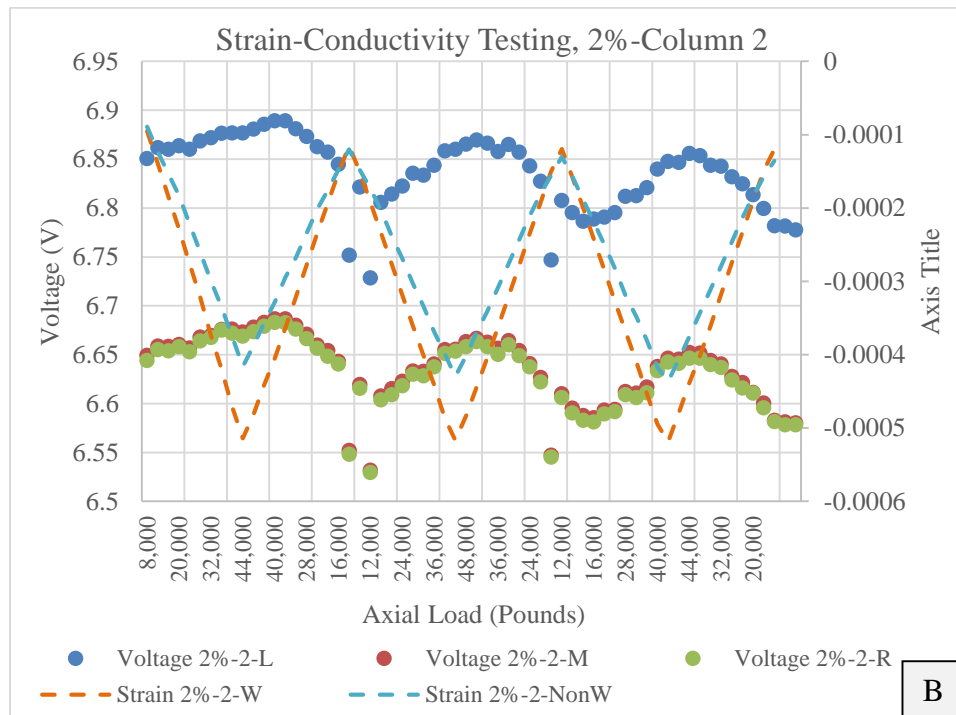
Figure 6-6
Strain and Voltage Measurements Time History (as a Function of Load) for 0%
Specimen (A) and 2% Specimen First Test (B)

To quantify the correlation between electric measurements and mechanical strain, the response histories of all three electrode sets and the strain measurements are first reviewed. Figure 6-7 shows the first load test response histories for the 2% specimen, and it shows the time histories have slight deviation between all three measurements – left, middle, and right electrode sets. Similarly, Figure 6-8 shows the second load test response histories of the electric properties and the strain. Figures 6-7 and 6-8 are plotted as resistance ratio ($\frac{\Delta R}{R_o}$) versus strain history. The resistance ratio was used exclusively because the resistivity term ($\frac{\Delta \rho}{\rho_o}$) found in Eq. 2 contains both electrical and mechanical components. Additionally, the resistivity represents the specimen's dimension which dominates over the changes in electrical potential. Therefore, it was prudent to narrow the correlation to only mechanical and electrical properties as shown in Figures 6-7 and 6-8.
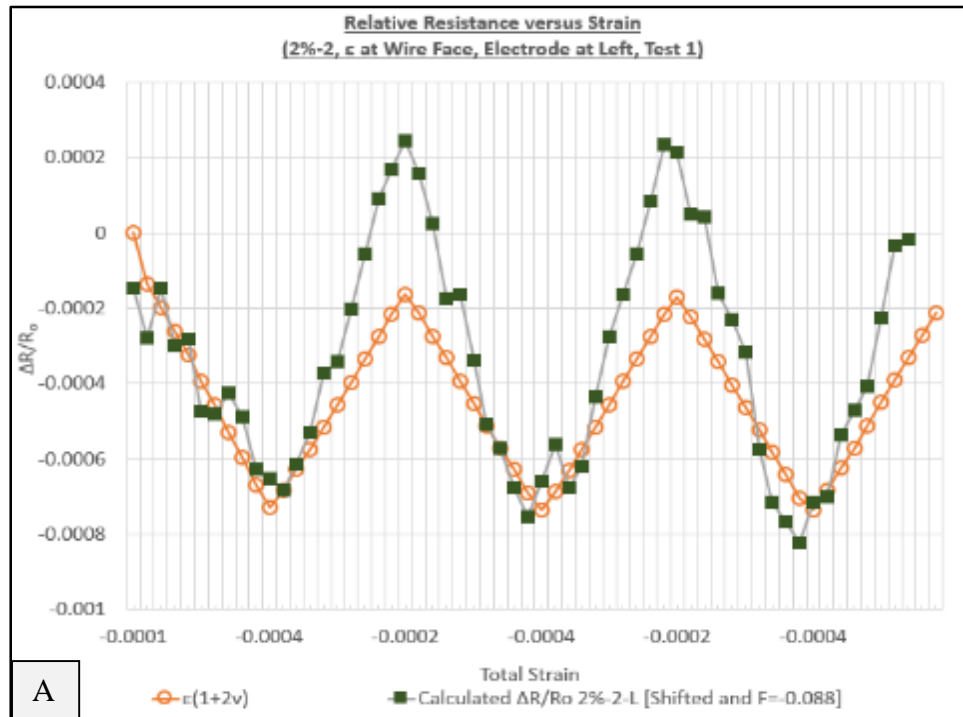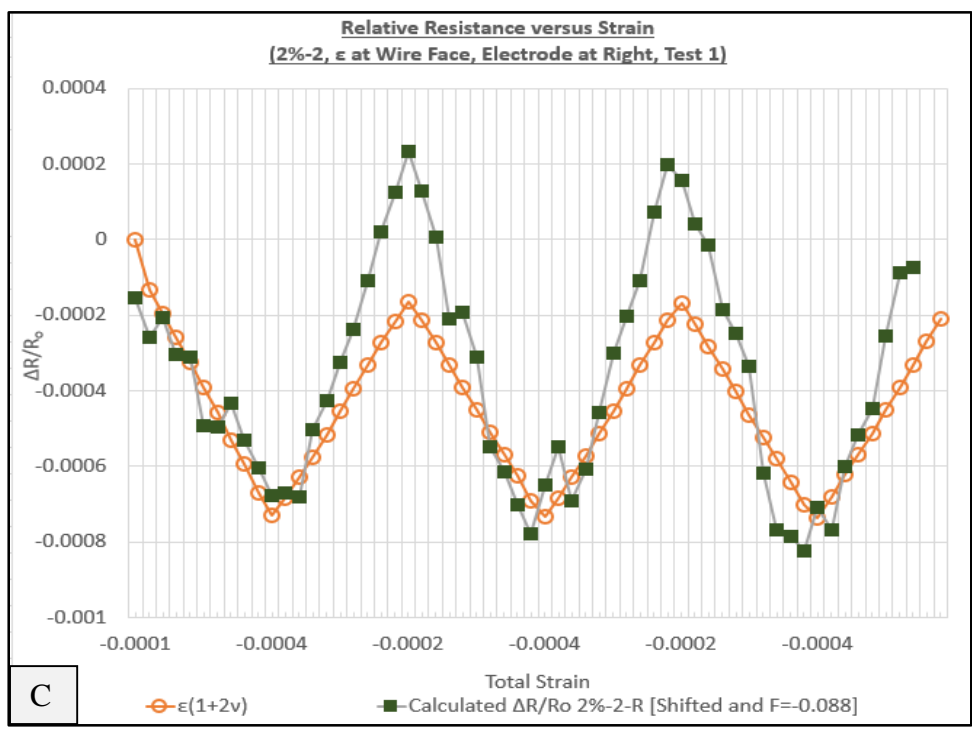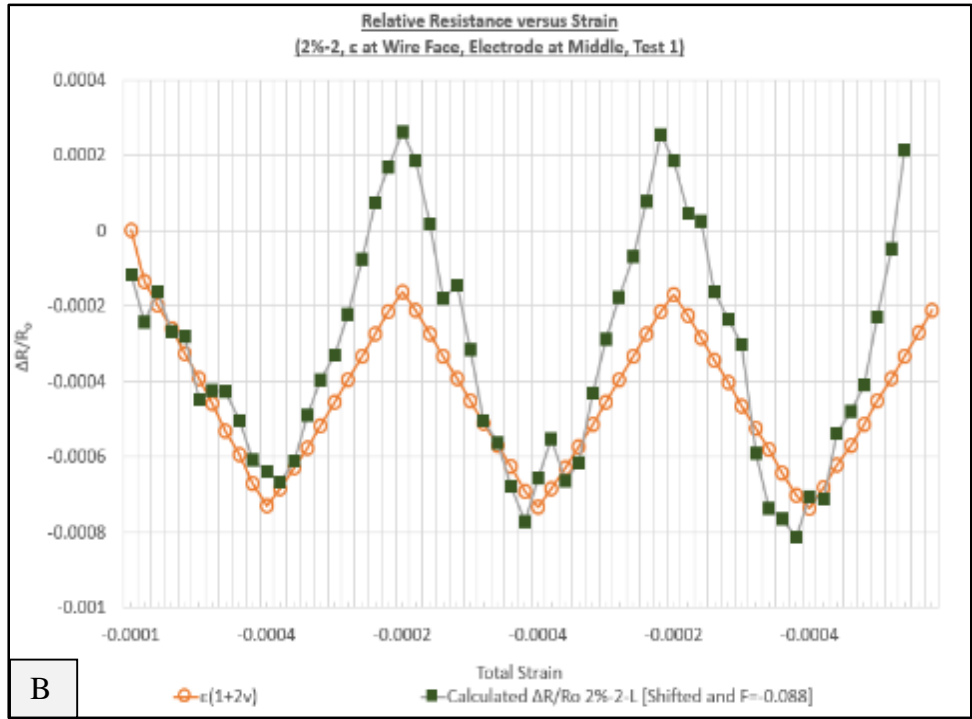
Figure 6-7
Strain and Resistance Measurements Time History for 2% Specimen Load Test 1: Left
Electrode (A), Middle Electrode (B), and Right Electrode (C)

Relative Resistance versus Strain (2%-2, ε at Wire Face, Electrode at Left, Test 2)

A

ε(1+2v)   —■—Calculated ΔR/Ro 2%-2-L [Shifted and F=-0.020]

Relative Resistance versus Strain (2%-2, ε at Wire Face, Electrode at Middle, Test 2)

B

ε(1+2v)   —■—Calculated ΔR/Ro 2%-2-M [Shifted and F=-0.020]

122
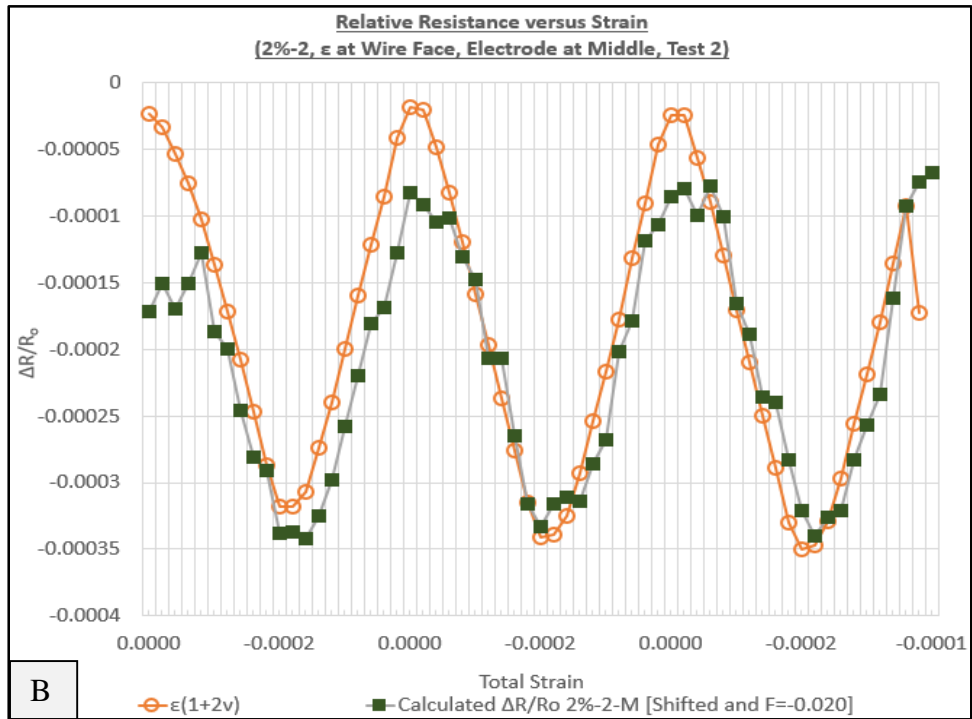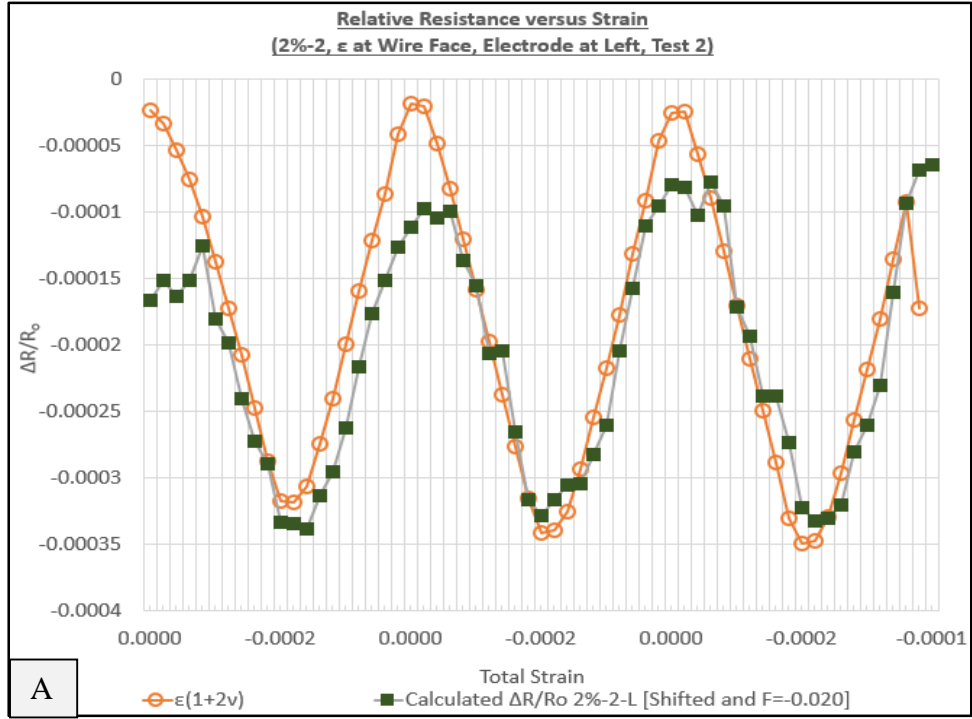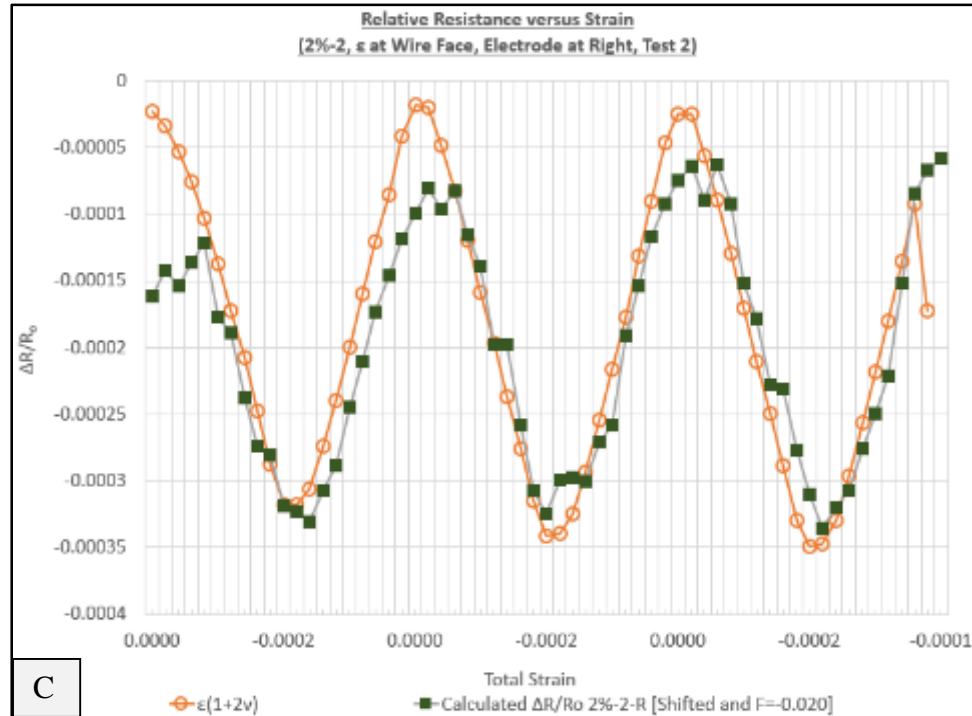
Figure 6-8
Strain and Resistance Measurements Time History for 2% Specimen Load Test 2: a) Left
Electrode, b) Middle Electrode and c) Right Electrode

To establish the electro-elastic correlation, the resistance calculations were made
from the voltage measurements and compared to the measured strain. Each electric
resistivity ratio plot is segregated into six linear curves and plotted against the
corresponding strain and a straight line is determined from the average values. Figure 6-9
and Figure 6-10 each show three plots for left, middle, and right electrode set and for load
Test 1 and Test 2, respectively. Also shown in each plot is the linear best-fit line for each
case. The straight lines are presented so that they will converge at the origin of each
coordinate system and are shown to be offset from the curves because the test results have
not been normalized. Also the strains (x-axis) have been defined as negative to indicate
compression. To develop the linear relationship, slope adjustment was made on the right

123

side of Eq. 2, similar to a gage factor for a strain gage. The value of the slope adjustment is provided in the legend of the plots and is hereby called $\mathcal{F}$ (elasto-electric factor) and is defined as:

$$\varepsilon \, (1 + 2v) = \mathcal{F}(\frac{\Delta R}{R}) \qquad (3)$$

Eq. 3 replaces Eq. 2 and $\mathcal{F}$ can be experimentally determined for different concrete mix designs.

A best fit value is determined for each load test and for each electrode set. Respectively for Test 1 and Test 2, Figures 6-11 and 6-12 show a total of six different plots of measured strain and computed strain relations using Eq. 3. The measured strains are linear relations between the X and Y axes of each plot and the measured strain curves represent the best fit line with different $\mathcal{F}$ values shown in the legend for each plot. Figure 6-11 shows the $\mathcal{F}$ absolute value ranges from 0.065 to 0.068 and Figure 6-12 shows the $\mathcal{F}$ absolute values are more consistent and are equal to 0.026 for Tests 1 and 2, respectively.

125
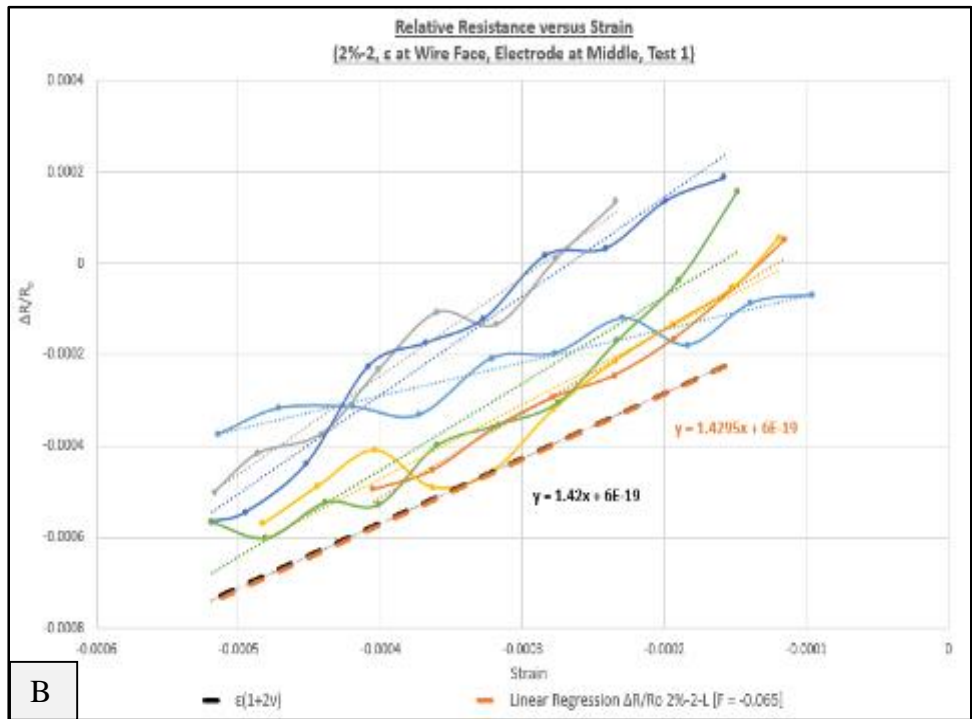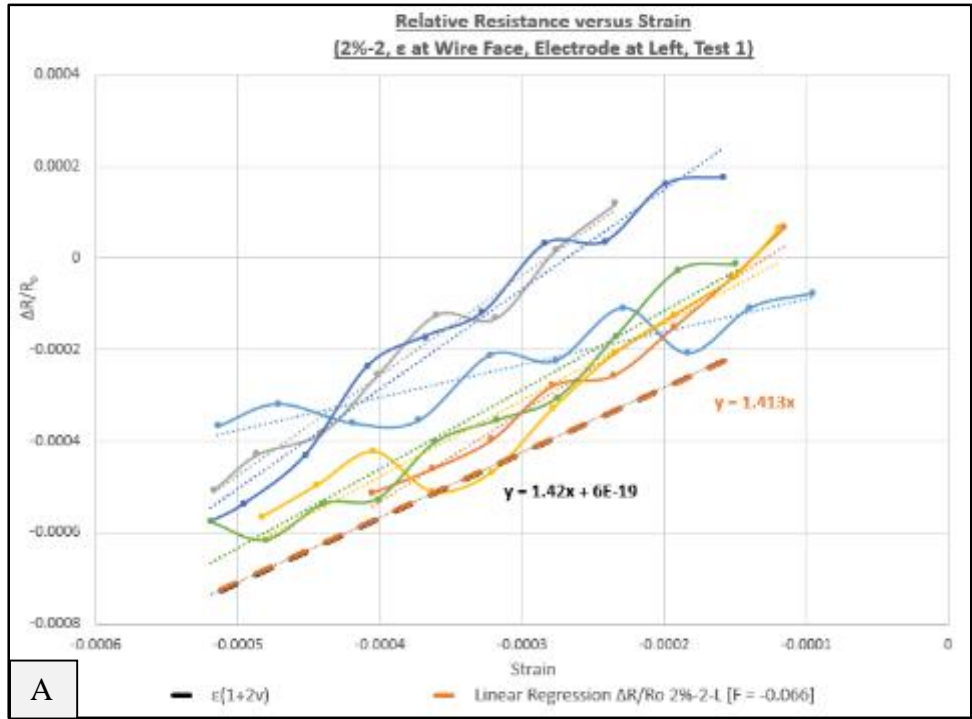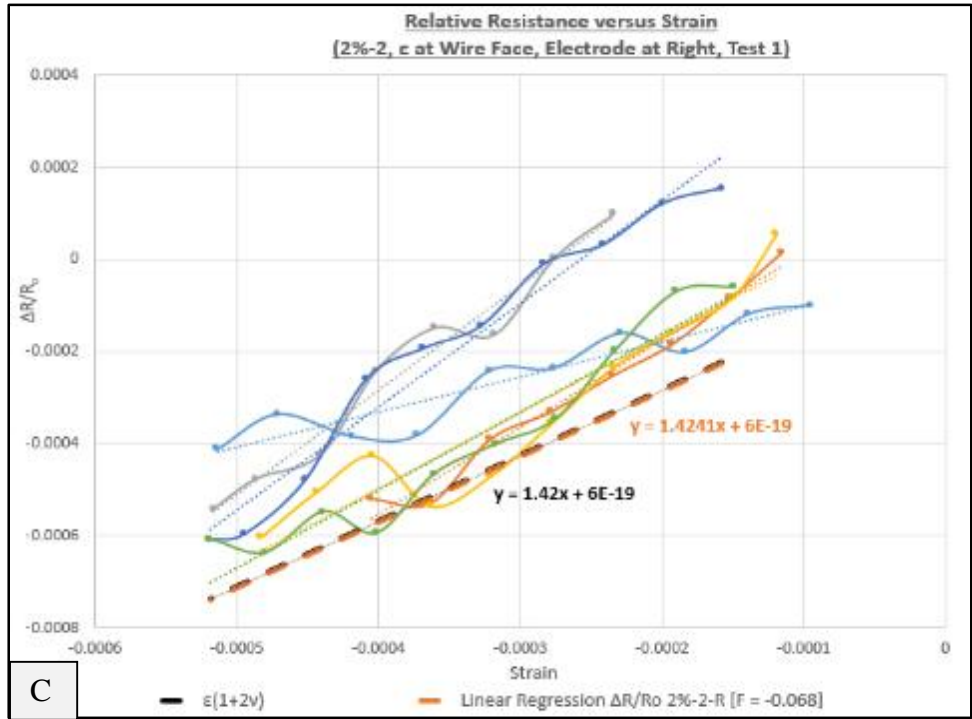
Figure 6-9
Elasto-Electric Parameter X-Y Scatter Plot with Mechanical vs. Electrical Measurements
for Load Test 1 for (a) Left Electrode, b) Middle Electrode and c) Right Electrode)

Relative Resistance versus Strain
(2%-2, ε at Wire Face, Electrode at Left, Test 2)

$y = 1.44x + 6E\text{-}20$

$y = 1.428x + 6E\text{-}20$

ΔR/R₀

Strain

A

— ε(1+2v)   — Linear Regression ΔR/Ro 2%-2-L [F = -0.026]

Relative Resistance versus Strain
(2%-2, ε at Wire Face, Electrode at Middle, Test 2)

$y = 1.44x + 6E\text{-}20$

$y = 1.4498x$

ΔR/R₀

Strain

B

— ε(1+2v)   — Linear Regression ΔR/Ro 2%-2-M [F = -0.026]

127
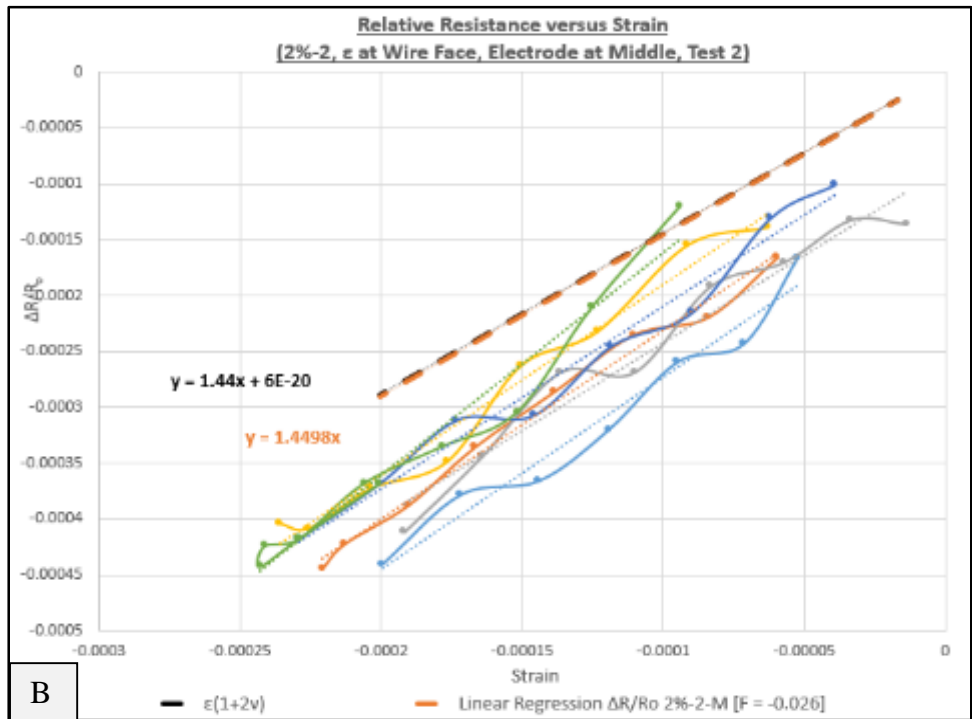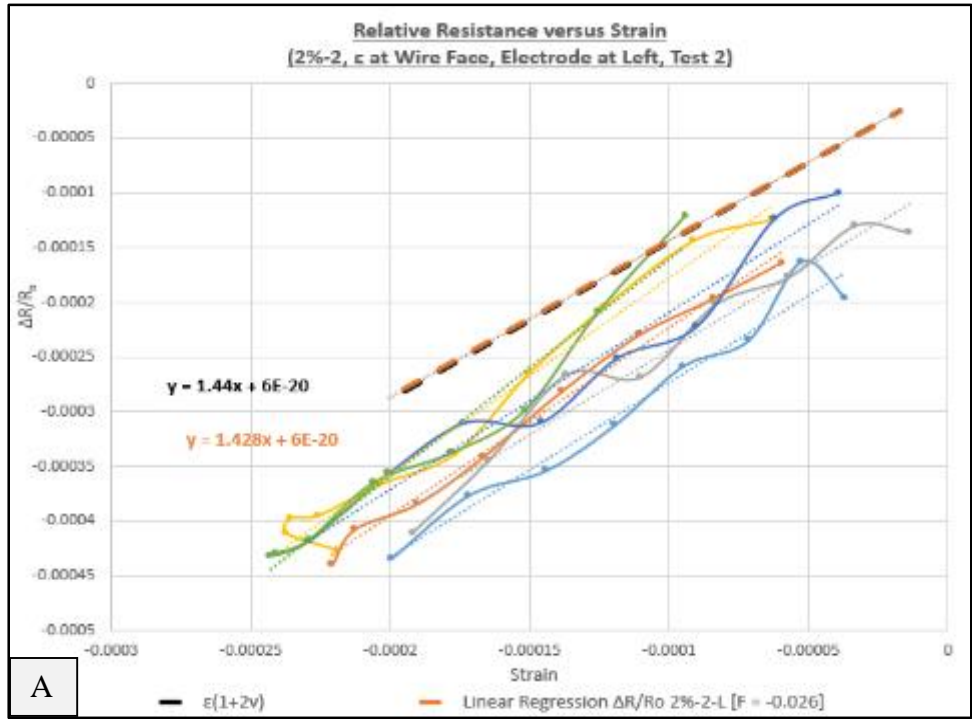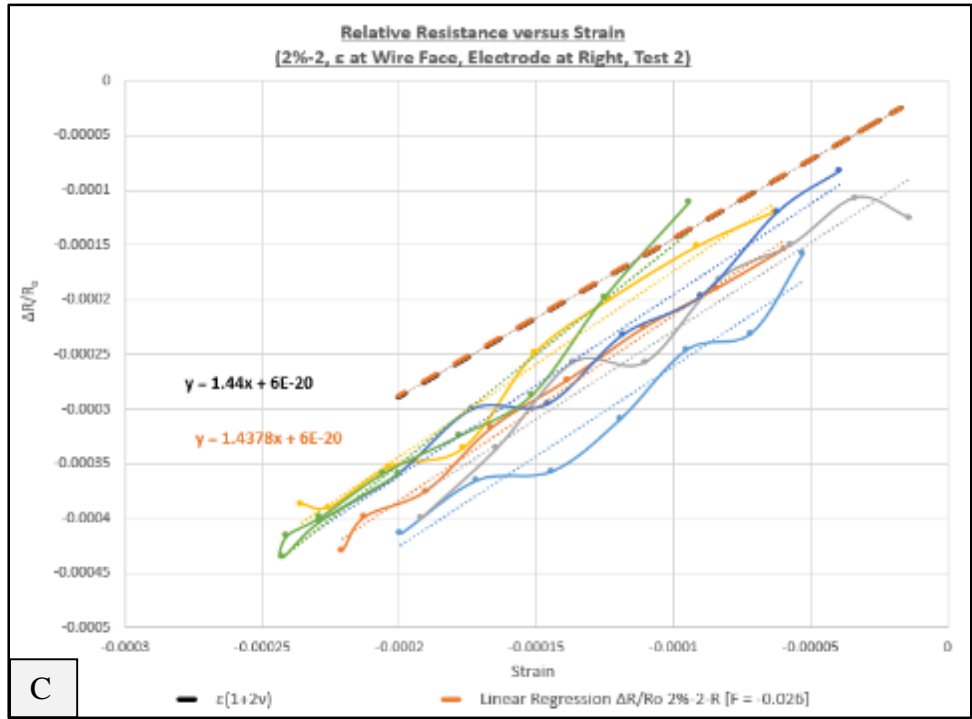
Figure 6-10
Elasto-Electric Parameter X-Y Scatter Plot with Mechanical vs. Electrical Measurements
for Load Test 2 for (a) Left Electrode, b) Middle Electrode and c) Right Electrode)

Comparison of Measured Strain and Derived Elasto-Electric Parameter
(2%-2, ε at Wire Face, Electrode at Left, Test 1)

A — Measured Strain 2%-2-W — Calculated ε = F × (ΔR/Rο) / (1+2ν) [F=-0.066]

y = 0.9951x

y = x

Comparison of Measured Strain and Derived Elasto-Electric Parameter
(2%-2, ε at Wire Face, Electrode at Left, Test 1)

B — Measured Strain 2%-2-W — Calculated ε = F × (ΔR/Rο) / (1+2ν) [F=-0.065]

y = 1.0067x

y = x
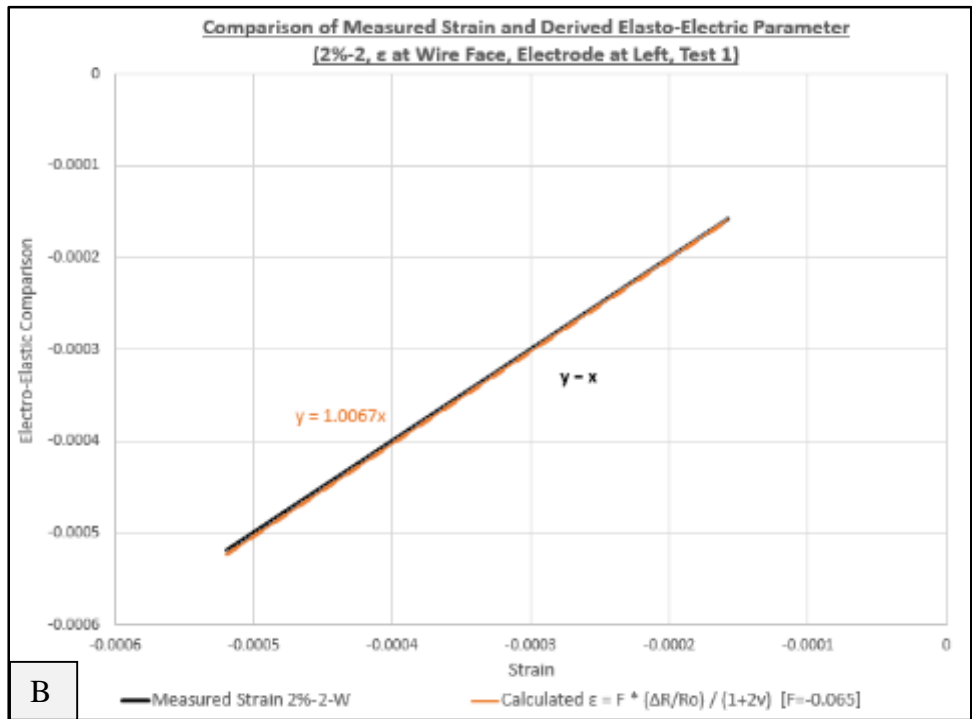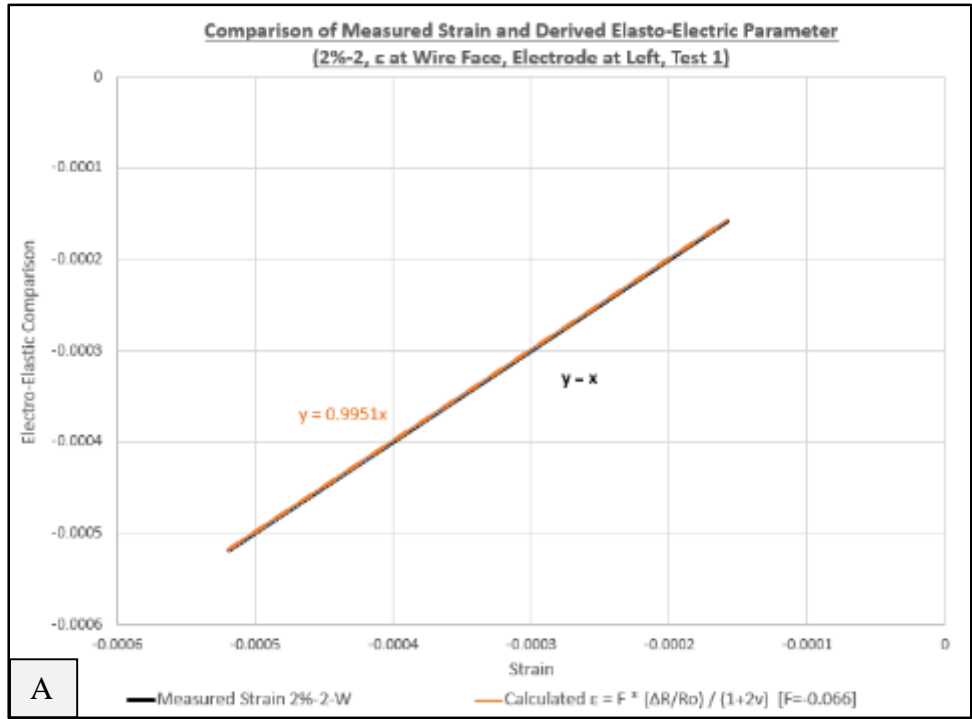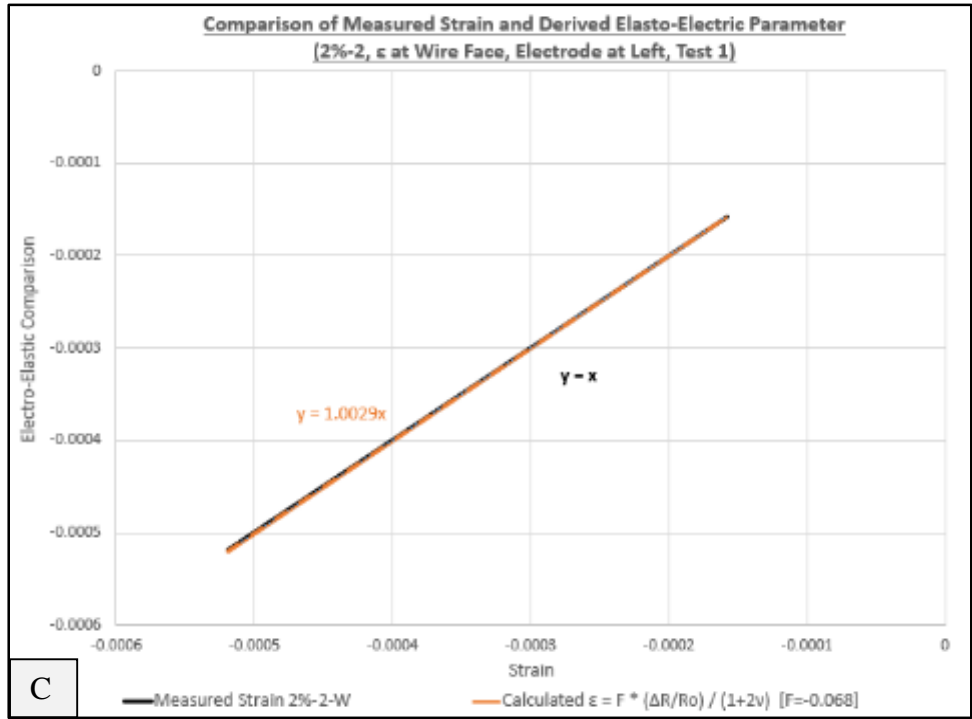
Figure 6-11
Elasto-Electric Relations for Load Test 1 of Left Electrode (A), Middle Electrode (B), and Right Electrode (C) Pairs

130

Comparison of Measured Strain and Derived Elasto-Electric Parameter
(2%-2, ε at Wire Face, Electrode at Left, Test 2)

$y = 0.9916x + 3E\text{-}20$

$y = x$

A   — Measured Strain 2%-2-W   — Calculated ε = F * (ΔR/Ro) / (1+2v) [F=-0.026]

Comparison of Measured Strain and Derived Elasto-Electric Parameter
(2%-2, ε at Wire Face, Electrode at Middle, Test 2)

$y = 1.0068x + 3E\text{-}20$

$y = x$

B   — Measured Strain 2%-2-W   — Calculated ε = F * (ΔR/Ro) / (1+2v) [F=-0.026]
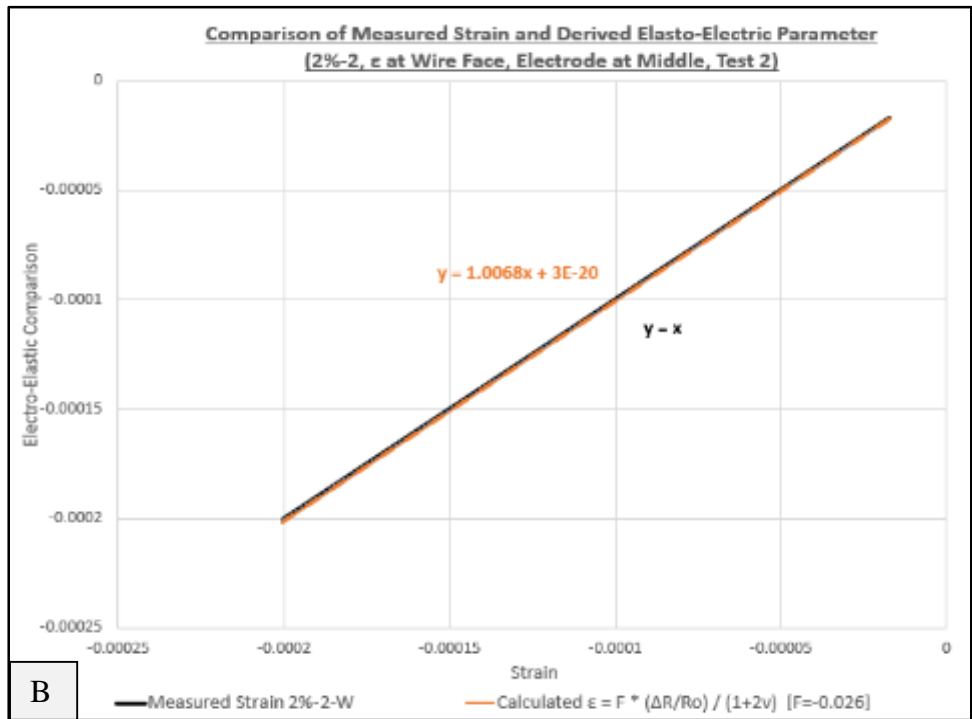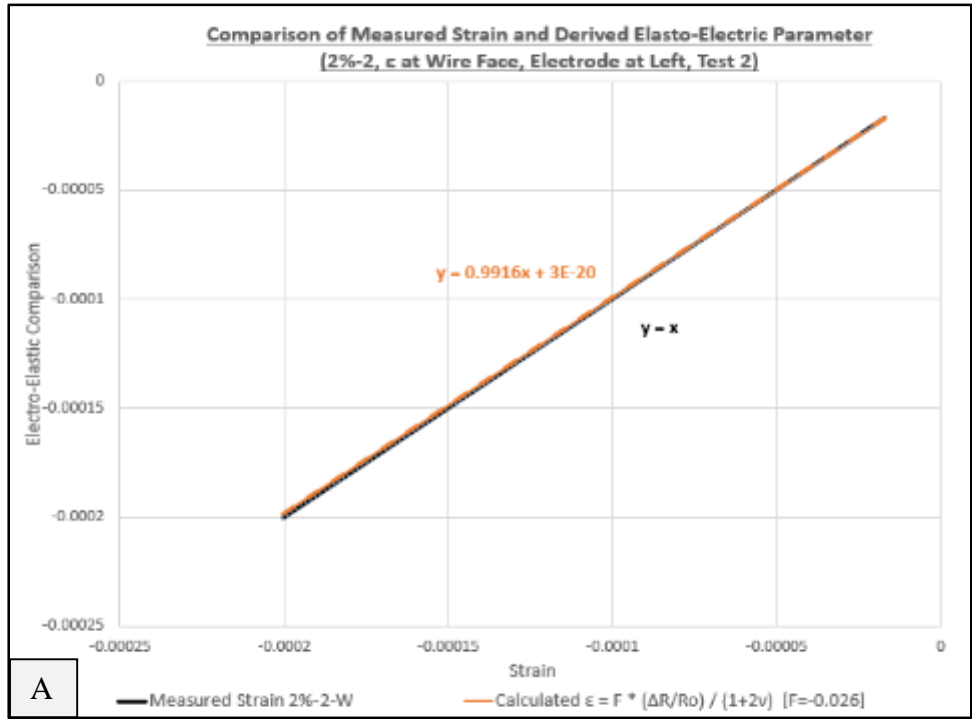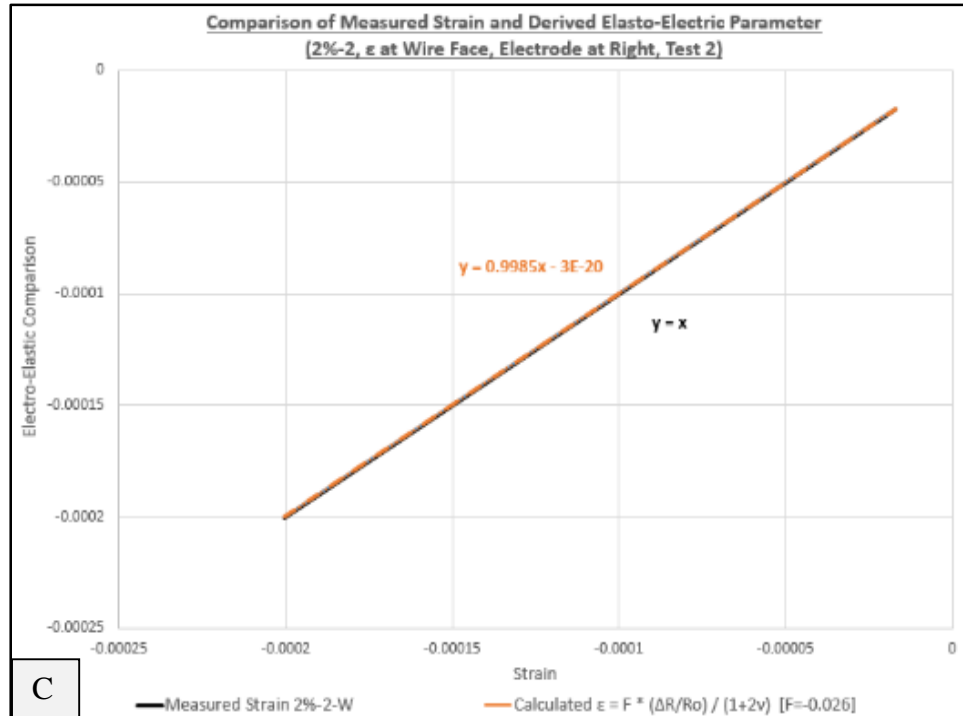
Figure 6-12
Design Elasto-Electric Relations for Load Test 2 of Left Electrode (A), Middle Electrode (B), and Right Electrode (C) Pairs

Discussion

Results from the tests provide interesting information regarding the change in concrete conductivity due to the addition of RSR in the concrete mix. The electric resistance and the strain measurements both show a corresponding trend between the loading/unloading cycles. Two critical observations can be summarized from the testing of the 0% and 2% specimens: 1) there are different mechanical behaviors for the 2% specimen (Figure 6-5), and 2) it is possible to generate a linear correlation to quantify the electro-elastic relationship. First the following section address the issue of material behavior of the 2% specimen.

<u>Loading History Analysis</u>

   Table 6-3 indicates that the plastic properties of the concrete columns were affected

by the introduction of recycled steel residuals. The introduction of recycled steel residuals

cause the air content to increase from 2.5 to 5 times that of the concrete with 0% recycled

steel residuals. Air content partially dictates the level of unit weight in the concrete which

decreased nearly linearly according to the increase in air content. While making the

specimen, off-gassing from the concrete with large bubbles of gas escaping from the top

of the specimens was observed. The evidence of off-gassing and high air content indicates

likely chemical reactions occurred between the hydrating cement and possible grease (oil-

based chemicals) on the recycled steel residuals.

Table 6-3
Plastic Concrete Properties for Each Concrete Mixture Designs

	0.0%	2.0%
Measured Plastic Properties		
Air Content, %	4	20
Unit Weight, pcf	146.1	125.4
Temperature, °F	65	64
Slump, in.	3	3.25

   Given the high air content, it is no surprise that strength and modulus of elasticity

also reduced. Both strength and modulus of elasticity reduced by more than half for the

addition of 2% recycled steel residuals. This also resulted in the different behaviors

between the first and second load tests on the 2% specimen: Test 1 was shown (Figure 6-

5) to provide a similar stress-strain cycles as the 0% specimen, which can be described as

relatively linear during the loading and unloading paths. For Test 2, Figure 6-5 indicates

that the modulus of elasticity of the concrete specimen reduced, rebounding was not

exhaustive, and that there existed a stage during both maximum and minimum loads in which the strain did not change. This interesting observation may indicate a change in the concrete material not unlike a permanent internal consolidation of the material. The result of this material consolidation is a more consistent electro-elastic behavior as indicated by the singular $\mathcal{F}$ factor for Test 2. Table 6-4 summarizes the statistical parameters for both tests and shows that the coefficient of variation is smaller for Test 2 than Test 1. The standard deviations for each of the averaging effects shown in Figures 6-9 and 6-10 are also larger for Test 1 than Test 2, respectively.

Table 6-4
Statistical Comparisons between Test 1 and Test 2 for 2% Specimen

		Calculated $\Delta R/R_o$ 2%-2-R			
		Elasto-Electric Factor	Standard Deviation	Coefficient of Variation	Linear Regression, R^2 Value
Test 1	2%-2; W, L	-0.066	0.000225	0.98	0.68
	2%-2; W, M	-0.065	0.000243	1.02	0.68
	2%-2; W, R	-0.068	0.000226	0.88	0.68
	2%-2; NonW, L	-0.052	0.000177	0.98	0.66
	2%-2; NonW, M	-0.051	0.000177	1.02	0.66
	2%-2; NonW, R	-0.053	0.000177	0.88	0.66
Test 2	2%-2; W, L	-0.026	0.000118	0.45	0.83
	2%-2; W, M	-0.026	0.000119	0.45	0.84
	2%-2; W, R	-0.026	0.000118	0.47	0.84
	2%-2; NonW, L	-0.035	0.000158	0.45	0.78
	2%-2; NonW, M	-0.034	0.000156	0.45	0.79
	2%-2; NonW, R	-0.035	0.000159	0.47	0.78

There was also strain variations between the wire and non-wire faces which indicates eccentricity developed in the column (Figure 6-13). This may be caused by uneven surfaces at each column face or uneven micro-failures of the concrete. It is shown that there is a

smaller deviation between Test 1 strain measurements (Figure 6-13(A)) than that of Test 2 (Figure 6-13(B)).

Another interesting observation associated with the load test is that there is a skew in the voltage measurements during the first test, which may support the assumption of material consolidation. As shown in Figure 6-14, the voltage measurement for Test 1 (Figure 6-14(A)) shows an increasing trend, which is not as obvious as in Test 2 (Figure 6-14(B)). To prove that the voltage measurement skew is not associated with possible increase in material capacitance, a non-loading (static) measurement was conducted on the 2% specimen. Figure 6-15 shows that without any loading on the specimen, the voltage difference of electric current flowing through the specimen remained nearly constant.
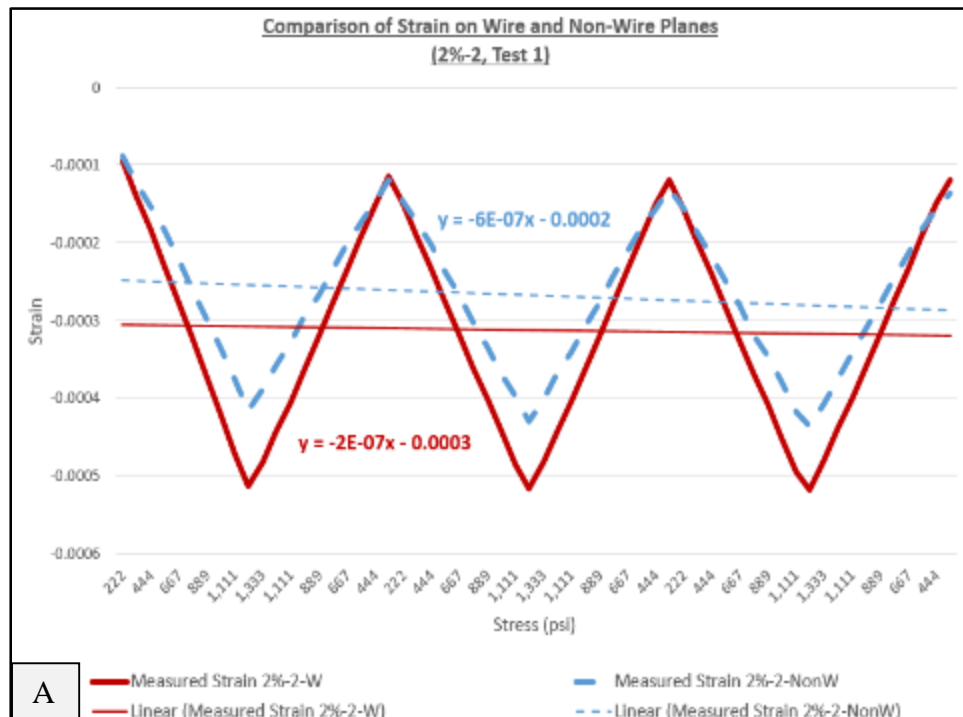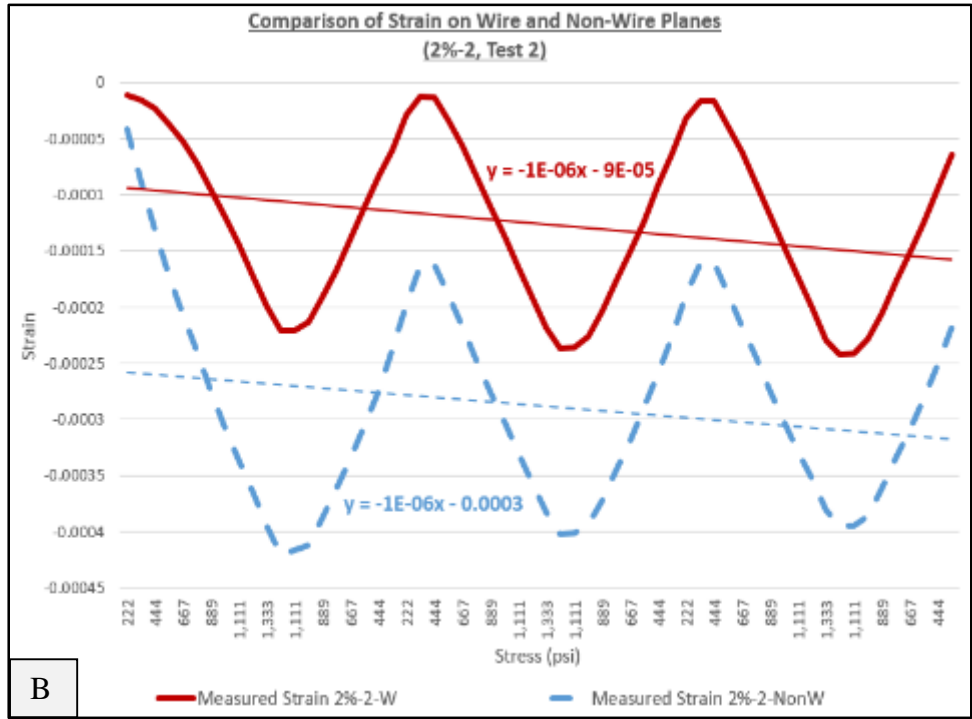
Figure 6-13
Strain Differences between Strain Gauge Measurements of the Wire and Non-Wire Faces
for Test 1 (A) and Test 2 (B)
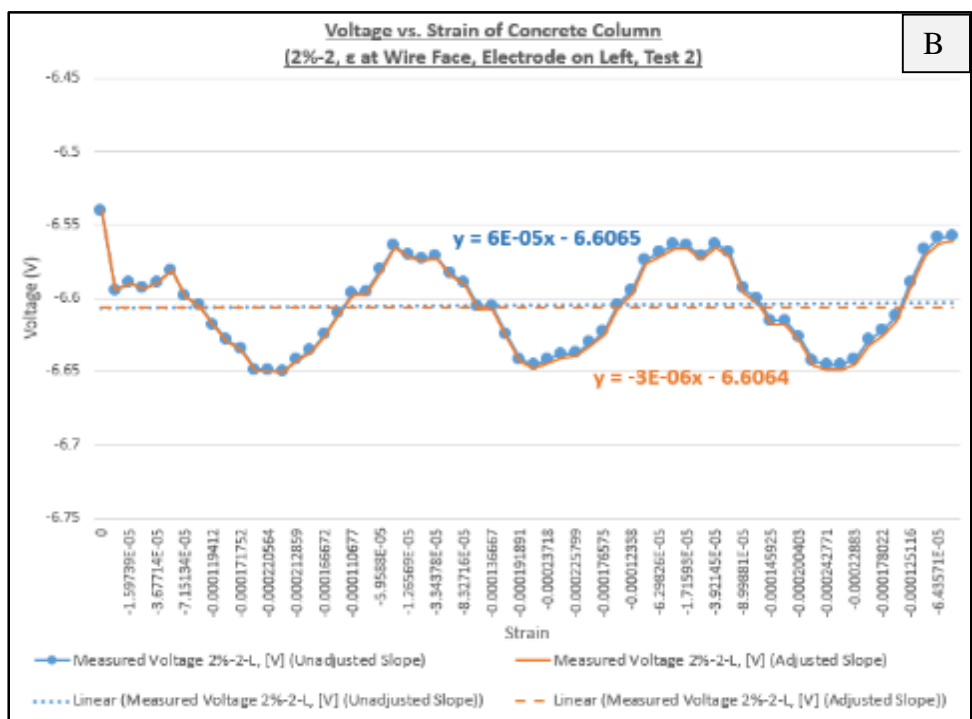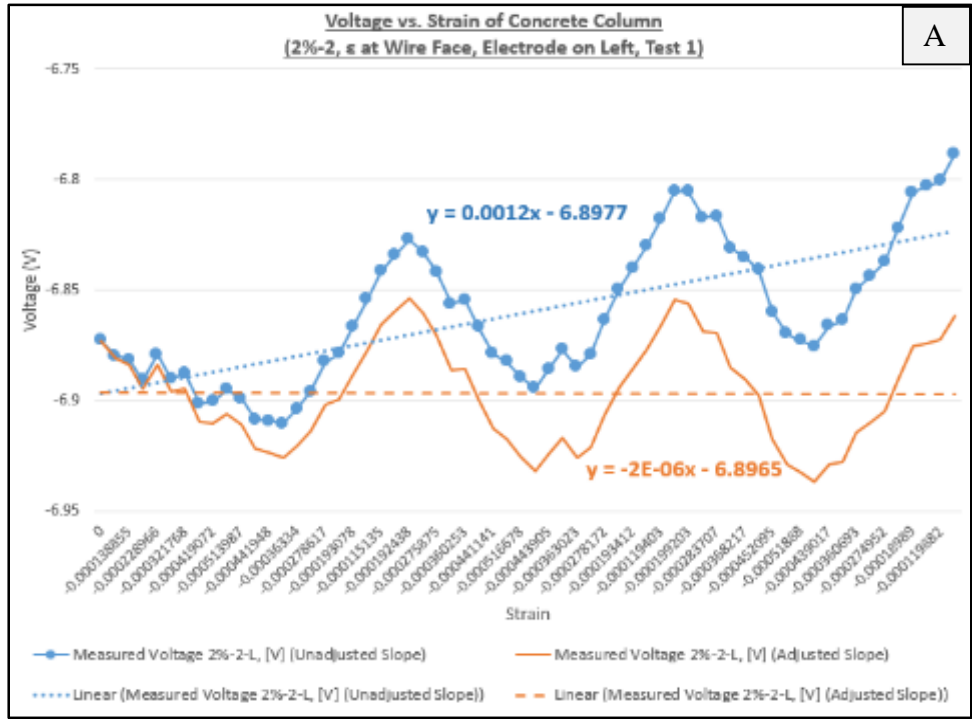
Figure 6-14
Skew in Voltage Measurements for Test 1 (A) and Test 2 (B)
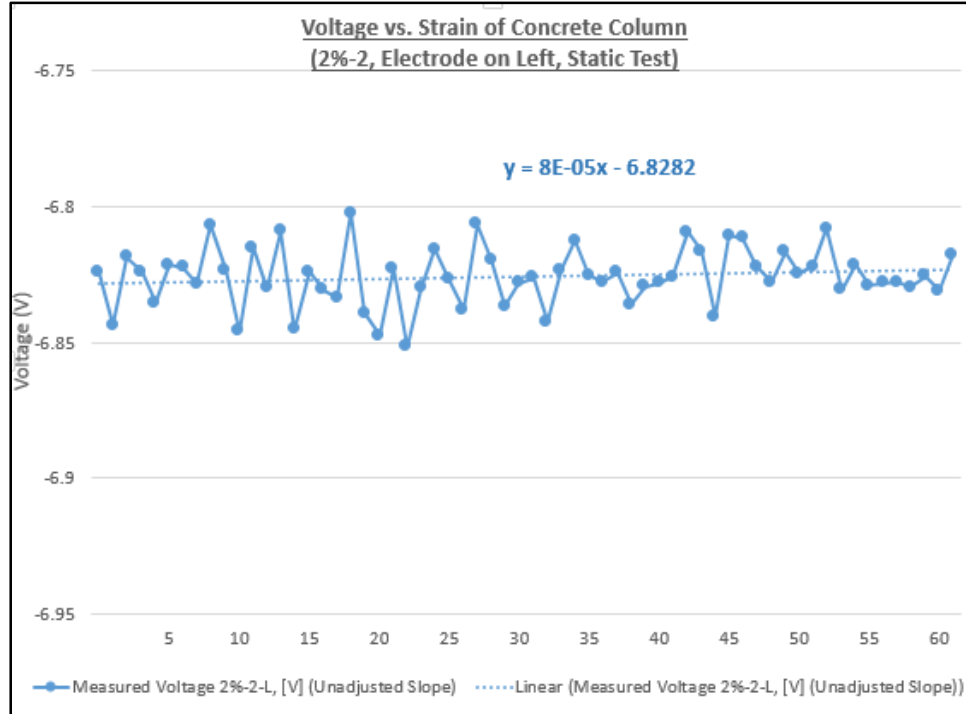
Figure 6-15
Static Voltage Measurements (2%, Column 2, Left Electrode Pair)

Linear Electric-Elasto Relationship

The validation that RSR addition can serve as a functional material for self-sensing of mechanical stressing of concrete is demonstrated in the establishment of the linear correlation as presented in Eq. 3. For the 2% specimen, two equations have been established for both Test 1 and Test 2, Eq. 4 and Eq. 5, respectively. These equations are modified from that of Eq. 3 in order to directly correlate strain and resistance measurements by removing the resistivity term from Eq. 3.

$$\varepsilon \, (1 + 2v) = -0.059(\frac{\Delta R}{R}) \qquad\qquad \text{Eq. 4}$$

$$\varepsilon \, (1 + 2v) = -0.026(\frac{\Delta R}{R}) \qquad\qquad \text{Eq. 5}$$

138

The $\mathcal{F}$ factor for Test 1 is averaged to be -0.059 from all the curves shown in Figure 6-9. Likewise, the $\mathcal{F}$ factor for Test 2 is averaged to be -0.026 from all the curves shown in Figure 6-10. The $\mathcal{F}$ factor needs to be established by conducting tests on full-scale specimens using similar electro-elastic tests for a mix design. It is possible to establish other load test procedures for other mechanical behaviors of concrete structures, such as tension and flexural tests; and the effects of reinforcing steel as a function of distance from the electrode.

In addition, other parameters including plastic and hardened properties of the concrete should be measured and/or observed. Besides the potential benefit of measuring strain through changes in electrical conductivity, the introduction of the reused steel has the potential of causing beneficial and/or detrimental effects to the concrete. For example, the introduction of the added recycled steel residuals might increase the compressive strength and modulus of elasticity of concrete. Alternatively, the recycled steel residuals may cause a lack of workability of the concrete as indicated in some of the preliminary work performed for this study. If that is the case then more consolidation energy will be required for the concrete to be adequately placed in forms during construction.

Conclusion

In this study, recycled steel residuals (RSR) are shown to be useful as a functional fill in concrete to enhance its electrical properties. The outcome is a self-sensing material that can detect the strain responses under loading by electric resistance measurements. Electric-based testing of concrete containing 2% of the recycled steel residuals under cyclic compression test indicates corresponding responses in strain, which is not detected in

concrete specimen without any filler. The test results can also be used to define experimental electro-elastic relations consistent with theoretical equations and to determine a newly introduced term, electro-elastic factor, $\mathcal{F}$.

It is noted that the introduction of recycled steel residuals causes deleterious increase to the air content and mechanical capacity of the 2% concrete specimen. Thus, it is important to ensure that the RSR is fully cleaned. Full scale specimens can be developed according to the process described herein to determine the electro-elastic properties associated with other mechanical behaviors and to derive the calibration factors for different concrete mixtures.

References

ACI Committee 211.1R, 2009. ACI 211.1-91 (Reapproved 2009), Standard Practice for Selecting Proportions for Normal, Heavyweight, and Mass Concrete. Farmington Hill, American Concrete Institute.

ACI Committee 211.3R, 2009. ACI 211.3R-02 (Reapproved 2009), Guide for Selecting Proportions for No-Slump Concrete. Farmington Hill: American Concrete Institute.

ACI Committee 212, 2010. ACI 212.3R, Report on Chemical Admixtures for Concrete. Farmington Hill: American Concrete Institute.

ACI Committee 544, 1996. ACI 544.1R, Report on Fiber Reinforced Concrete. Farmington Hill: American Concrete Institute.

ACI Committee 544, 2008. ACI 544.3R-08, Guide for Specifying, Proportioning, and Production of Fiber-Reinforced Concrete. Farmington Hill: American Concrete Institute.

ASTM C 33/C 33M-03, Standard Specification for Concrete Aggregates, West Conshohocken, PA. ASTM International, 2003.

ASTM C 39/C 39M, Standard Test Method for Compressive Strength of Cylindrical Concrete Specimens, West Conshohocken, PA. ASTM International, 2003.

ASTM C 78/C 78M-15a, Standard Test Method for Flexural Strength of Concrete (Using Simple Beam with Third-Point Loading), West Conshohocken, PA. ASTM International, 2015.

ASTM C 94/C 94M-04, Standard Specification for Ready-Mixed Concrete, West Conshohocken, PA. ASTM International, 2004.

ASTM C125-16, Standard Terminology Relating to Concrete and Concrete Aggregate, West Conshohocken, PA. ASTM International, 2016.

ASTM C 138/C 138M-01a, Standard Test Method for Density (Unit Weight), Yield, and Air Content (Gravimetric) of Concrete, West Conshohocken, PA. ASTM International, 2001.

ASTM C 143/C 143M-03, Standard Test Method for Slump of Hydraulic-Cement Concrete, West Conshohocken, PA. ASTM International, 2003.

ASTM C 192/C 192M-02, Standard Practice for Making and Curing Concrete Test Specimens in the Laboratory, West Conshohocken, PA. ASTM International, 2002.

ASTM C 231/C 231M-04, Standard Test Method for Air Concrete of Freshly Mixed Concrete by the Pressure Method, West Conshohocken, PA. ASTM International, 2004.

ASTM C 469/C 469M-03, Standard Test Method for Static Modulus of Elasticity and Poisson's Ratio of Concrete in Compression, West Conshohocken, PA. ASTM International, 2002.

ASTM C 494/C 494M-04, Standard Specification for Chemical Admixtures for Concrete, West Conshohocken, PA. ASTM International, 2004.

ASTM C 1064/C1064-04, Standard Test Method for Temperature of Freshly Mixed Hydraulic-Cement Concrete, West Conshohocken, PA. ASTM International, 2002.

ASTM C1609/C1609M-12, Standard Test Method for Flexural Performance of Fiber-Reinforced Concrete (Using Beam With Third-Point Loading), West Conshohocken, PA. ASTM International, 2012.

ASTM G57, Standard Test Method for Field Measurement of Soil Resistivity Using the Wenner Four-Electrode Method, West Conshohocken, PA. ASTM International, 2012.

Han B., Yu X., Ou J. (2014) Self-Sensing Concrete in Smart Structures, Elsevier Inc., New York, NY.

Konsta-Gdoutos, MS, Aza, CA (2014) "Self sensing carbon nanotube (CNT) and nanofiber (CNF) cementitious composites for real time damage assessment in smart structures," Cement and Concrete Composites 53, 162-169.

Li, H, Xiao, H and Ou, J, 2004. "A Study on Mechanical and Pressure-Sensitive Properties of Cement Mortar with Nanophase Materials," Cement and Concrete Research, 34, pp 435-438.

Rajabipour, F., 2006. "Insitu Electrical Sensing and Material Health Monitoring in Concrete Structures," Thesis, Purdue University, UMI Number 3259972.

Suchanek and Riman, 2009. Intelligent Synthesis of Smart Ceramic Materials. Book editor: Schwarz, M; Smart Materials; 2009; chapter 2; Boca Raton; CRC Press

US EPA, Environmental Geophysics / Electrical Methods. Retrieved March 30, 2017. Retrieved from
https://archive.epa.gov/esd/archive-geophysics/web/html/electrical_methods.html.

CHAPTER 7 DISCUSSION

As noted in Chapter 1, the concrete industry will benefit from using enhanced concrete to provide autonomous detection of strain. This dissertation provides application to the commercial power industry as an example. The nuclear industry utilizes structures that are designed to withstand extreme conditions such as a main line steam break, loss of coolant accident, heavy seismic loading, or external impact loading (e.g., airplane). The robust nature of the structural designs, however, make inspection with traditional stress waves for nondestructive evaluation to be nearly impossible (Electric Power Research Institute 2013). Alternatives for traditional evaluation techniques is needed for the nuclear power industry that is applicable for both new construction and long-term maintenance.

However, even beyond nuclear power application, findings herein can be easily extrapolated to many industries that utilize concrete. Use of functional fill to provide real-time and timely information about the condition of the concrete needing examination. Experts in concrete have successfully provided similar structural health monitoring using embedded and topical sensors but with some limitations that does not allow ubiquitous function in all structures and in all of the structure. Chapter 5 focused on early testing of small specimens consisting of varying concentrations of recycled steel residuals. There were inconsistencies in the test results to note. The 4x8-in. cylinder showed very little change – nearly zero – in resistance as the concrete cylinders were compressed. It was deduced that one potential cause for this was that the specimens had a very high aggregate-to-specimen-size ratio. The aggregate is expected to have little to no electrical conductivity, so the path of least resistance of flowing electrons would be tortuously

143

circumventing the aggregate. As such, the changes in conductivity will be less dictated by the axial length changes during compression. This idea was also evident when comparing the level of electrical conductivity for the specimens with steel concentrations of 0.5% and 1%. It is rational to expect the level of conductivity to be greater in the specimen with higher steel concentration. Unfortunately, this intuitive conclusion was not evident when comparing electrical potential drop between the inner electrode pairs of the two 4x8-in. specimens. As indicated previously, this suggests that electrical potential is affected by the insulating aggregate and the directness of the matrix path for electrons to pass through.

In contrast, the 6x12-in. cylinder indicated a distinct change in electrical conductivity in the material as the concrete cylinder was being compressed. Though there was compression that occurred in the rubber pad between the cylinder top and compression machine, the change in resistance was approximately 10% relative to the static resistance value when no loading was being applied. For the 6x12-in. specimen, the nominal aggregate size for the concrete mixture was 3/8 to ½ inches – No. 89 stone. This information provided a good lessons-learned to ensure that future testing would include specimens with low aggregate-to-specimen ratios and electrical blocking material with a relatively high modulus and/or very small amount of compressibility. Two more lessons were gathered during the early testing of these specimens. One, strain was calculated using assumptions found in concrete codes published by the American Concrete Institute (ACI Committee 318 2008, ACI Committee 318 2013). Measuring strain directly will provide more accurate understanding of the empirical relationship between compression and electrical resistance. Two, there was no evidence during this early testing, that introduction

of recycled steel residuals causes a degradation in plastic and mechanical properties of the concrete.

Climax for the testing performed for this research consisted of axially loaded concrete columns – 6x6x20-in. One, and unexpectedly, the plastic properties of these specimens and mixtures were drastically affected by the introduction of recycled steel residuals. Air content of the specimens with recycled steel residuals increased 2.5 to 5 times that of the concrete with 0% concentration. As such, the unit weight in the concrete decreased and mechanical properties of the specimens reduced, that is strength and modulus of elasticity was reduced. Based on the observed off-gassing during casting of test specimens, it appears that foreign materials such as aluminum shavings or oil(s) used for steel processing were included in the concrete mixtures and created the increased level of air voids in the concrete.

Given the high air content, both strength and modulus of elasticity reduced by more than half depending on the concentration of recycled steel residuals. In addition to the high air content, the reduction in strength may have been due to negative effects on the cement binding strength. Additional testing should be performed using mortar bars and concrete specimens with similar amounts of air.

However, there was promising electro-elastic results shown with concrete columns containing a steel concentration of 2%. Test 1 of concrete column 2%-1 showed no indication that electrical and mechanical properties (electro-elastic) were correlated (Appendix F). All three pairs of electrodes – left, middle, and right – only indicated a change in voltage potential as a function of time but with no correlation of mechanical

145

strain. However, Test 2 of concrete column 2%-1 provided clear indication that the changes in electrical potential for following the three-cycle pattern of strain that was caused by the axial loading applied to the column. The electro-elastic testing validated the linear nature of resistance and resistivity with strain that was found in previous research and the theoretical relationship between electrical potential and axial strain (Chapter 4 and Appendix A). This observation was even clearer when reviewing the results from column 2%-2.

For analyzing the measured electrical and mechanical properties for column 2%-2, the process included comparing electro-elastic properties that included and excluded the resistivity term of the theoretical relationships derived for this research (Chapter 4 and Appendix A). As highlighted in these derived equations, strain (ε), is equivalent to $\frac{1}{(1+2\nu)} *$ $(\frac{dR}{R} - \frac{d\rho}{\rho})$. However, the final term on the right side of the equation includes both mechanical and electrical changes. Therefore, some analyses found in Appendix G include removing the final term that includes resistivity values. It was determined that the final resistivity (ρ) term dominated the electro-elastic properties and indicated nearly perfect linear correlation. This can be observed in the plots for column 2%-2 (Appendix G). Additionally, and interestingly, correlation between mechanical and electrical properties were observable when comparing *total/overall* changes in electrical potential from the static values, $(\frac{dR}{R_o} - \frac{d\rho}{\rho_o})$, and also when comparing *incremental* changes in electrical potential, $(\frac{dR}{R} - \frac{d\rho}{\rho})$. However, also included in Appendix G is analysis that included the removal of the final resistivity (ρ) term. In these instances, the non-linear variations of

146

electrical properties were clearer and best-fit lines were used to compare the measured changes in electrical potential (and the subsequent resistance calculations) with the mechanical changes in strain.

It is important to recognize that above analysis used conventional definition of resistivity, which may not necessarily be the accurate way to define the intrinsic material property for a dispersive conductor in a non-conductive material. The appropriate definition of resistivity for the functional material-modified, self-sensing concrete should include terms that quantifies the distribution of recycled-steel-residual; the path of current flowing through the material; and, finally, the apparent conductivity of the cement matrix, aggregate, and the recycled steel residuals. Such a definition has not been attempted yet.

Furthermore, as shown in previous chapters, recycled steel residuals exist in different shapes, they can be wire-like and be curly or straight, or in the form of particles. The different shapes, orientations, and/or connectivity between wires within the cement matrix will also dictate the level of electric conductivity within the material. Hence, the material resistivity definition must be more sophisticated than the current simplistic definition based on a homogeneous material.

One approach to define the resistivity of an inhomogeneous material would be to use a combination (in series and/or parallels) of discrete resistors. In such a case, an apparent resistivity term can be derived using Kirchhoff's laws for resistors in a circuit. However, this would require a much more refined test setup, which is not presently available.

In all cases of the analysis, an adjustment parameter, $\mathcal{F}$, was introduced to align the electro-elastic properties imaged in the plots. This factor would be equivalent to a gage

factor used for strain gages. For column 2%-2 and when excluding the resistivity term, an electro-elastic factors ranging -0.068 to -0.051 for Test 1. The electro-elastic factor reduced for Test 2 ranging -0.035 to -0.026. The reduction in the electro-elastic factor is an indication that mechanical damage occurred during Test 1 which increased variability in the electro-elastic results. The electro-elastic factor is far less sensitive to the theorized micro-straining when including the resistivity term. When included the resistivity term, an electro-elastic factor of 5.2 was used for optimum slope alignment based on parametric study. Once aligned, the change in relative and differential (incremental) resistance and resistivity is cyclical and indicative of the changes in strain produced by the compressive loading imparted onto the column. Therefore, analysis that includes or excludes the resistivity term will dictate the level of sensitivity that is capable of being indicated. If a broad understanding of mechanical strain is needed, then including the resistivity term will be sufficient. However, fine indications of micro-cracks within concrete would require excluding the resistivity term because they allow for clearer and observable changes in electrical resistance as a function of the micro-cracking.

CHAPTER 8 CONCLUSION

To support the advancement of structural health monitoring this research explored a more cost-effective alternative to create smart concrete by using recycled steel residuals as function fill. Conclusions of this research follows.

1. Concrete is a major structural material but that undergoes many different types of degradation that may be categorized as chemical, environmental, construction, and, for nuclear power plants, extreme conditions.

2. Traditional nondestructive evaluation techniques have limitations. Embedded and/or topical sensors are used by engineers to offset the limits of structural health monitoring.

3. Decision analysis aids can be used by engineers to determine a suitable structural health monitoring schema for reinforced concrete applications.

4. Previous research to create smart concrete using functional fill has shown some success with materials that are not cost-effective and, therefore, are not practical.

5. Recycled steel residuals, as functional fill, is a more cost-effective method to create smart concrete, but has never been tested.

6. Recycled steel residuals in its raw form is not suitable for concrete application, processing the recycled steel is required.

7. Derivation of fundamental electrical relationships indicate that changes in concrete electrical resistance will indicate strain in concrete. The indicated levels of strain can provide early warning for pending damage and overloading. This has been categorized as one method to create smart concrete.

8. Results indicate that volumetric concentrations of recycled steel residuals of 1.6% effectively provide measurable changes in conductivity that indicates changes in strain. This was observed using 6x12-in. concrete specimens.

9. When using the concrete designs described in Chapter 6, recycled-steel-residual concentrations of 0.5%, 1% and 2%, causes deleterious effects of plastic and hardened concrete properties. More specifically, the air content of specimens were up to 20% and compressive strength was reduced, in some cases, by more than half.

10. Concentrations of 2% provided the best indication that strain is identifiable through changes of electrical resistance.

11. Changes in electrical resistance for column 2, with 2% concentration of recycled steel residuals was repeatable.

12. To closer align a theoretical and experimental relationship between strain and resistance, an adjustment called electro-elastic factor, $\mathcal{F}$, was applied.

13. A test schema that includes using full-size, standard concrete specimens to correlated changes in strain with changes in electrical conductivity can be developed using methods described in this document.

14. Full-size, standard concrete specimens should include a small enough aggregate-to-specimen size ratio such that the insulating aggregate does not stunt the ability to measure changes in electrical conductivity as a function of strain.

15. Additional research should include the following and is detailed further in Chapter 9:

a. reducing the plastic and hardened deleterious effects of imparting recycled steel residuals,

b. discerning compression and tensile strain of flexural members using recycled steel residuals,

c. determining the distance of embedded metals to effect measurements used to develop electro-elastic relationships,

d. determining if recycled steel residuals can provide discernable indications of corrosion activity of steel embedded in concrete.

CHAPTER 9 RECOMMENDED FUTURE RESEARCH

Findings of this research provide precedence and foundation for continued work to learn about using recycled steel residuals as functional fill to develop self-sensing concrete. Also, the findings are valuable, particularly column 2%-2. Just as exciting is the idea of future testing and research to be performed that may also yield valuable information on the viability of recycled steel residuals and the process developed for this research. The following are ideas that should be explored to learn the extent of use for recycled steel residuals.

1. Determine causes of the changes in plastic and hardened properties when mixing recycled steel residuals with conventional concrete mixtures. As an extension of this, it would be valuable to determine processes to prevent deleterious effects of recycled steel residuals to concrete.

2. Also, the test setup described for this research includes three pairs of electrodes by which electrical potential drop was measured. Future testing should include flexural loading onto the specimens such that the pairs of electrodes are used for measuring electrical potential across both compression and tensile fibers of the flexural specimens.

3. Based on the findings of this research, it is rational to conclude that some microcracking was the cause of different rates of change in resistance as a function of load/strain. As such, electro-elastic measuring can be used to measure micro and macro cracking. It is possible that crack propagation can be

measured using time-of-flight-diffraction techniques and studies similar to that used for imputed stress-waves.

4. Another opportunity for research are the effects of embedded steel in concrete. Electric-based techniques such as that described herein are conceivably influenced by surrounding steel (or other) material embedded in concrete. The research idea includes studying the distance between embedded steel and the electrodes used for measuring changes in electrical potential.

5. The electric-based testing used in this study appears to have very good resolution. It would be very interesting to test if the level of resolution could be fine enough to detect corrosion of reinforcing steel. Corrosion is an electrochemical process whereby a corrosion-cell circuit is created with electrons passing through both a metallic path and the surrounding electrolyte. The corrosion process causes this flow of electrons and could potentially be measured using the electric-based techniques described herein.

REFERENCES

ACI Committee 228, 1998. ACI 228.2R, Nondestructive Test Methods for Evaluation of Concrete in Structures. Farmington Hill: American Concrete Institute.

ACI Committee 318, 2008. ACI 318, Building Code Requirements for Structural Concrete (ACI 318-08) and Commentary. Farmington Hills (MI): American Concrete Institute; 2008.

ACI Committee 349, 2013. ACI 349, Code Requirements for Nuclear Safety-Related Concrete Structures (ACI 349-13) and Commentary. Farmington Hills (MI): American Concrete Institute; 2013.

America's Infrastructure G.P.A, retrieved October 25, 2015. http://infrastructurereportcard.org/a/#p/grade-sheet/gpa,

Electric Power Research Institute, 2013. *Nondestructive Evaluation of Steel-Concrete Construction Mockups*. EPRI, Palo Alto, CA: 2013. 3002000294.

Hendriks, C. A., Worrell, E., DeJager, D., Blok, D., Riemer, P., 2003. Emission Reduction of Greenhouse Gases from the Cement Industry, *Greenhouse Gas Control Technologies Conference*, July 2003. www.ieagreen.org.uk.

Kholkin, A. K., 2009. Piezoelectric and Electrostrictive Ceramics Transducers and Actuators. In M. Schwartz, Smart Materials (p. Ch. 9.1). Boca Raton: CRC Press.

Li, H., Xiao, H., Ou, J., 2004. "A Study on Mechanical and Pressure-Sensitive Properties of Cement Mortar with Nanophase Materials," Cement and Concrete Research, 34, 2004, pp 435-438.

Pammi, S., Brown, C., Datta, S., Kirikera, G., Schulz, M. J., 2003. "Concepts for Smart Nanocomposite Materials" in Smart Materials, Structures, and Systems; 2003; SPIE

Scott, D. B., 2013. *Internal Inspection of Reinforced Concrete for Nuclear Structures Using Shear Wave Tomography*, Energy Conversion and Management, 2013, pp. 582-586.

Scott, D. B., Goodman, A., Smith, J. D., Chen, S., 2013. Applications of New Sensing Technologies for Reinforced Concrete Related to Nuclear Facilities: Considerations and Potentials. In F. Chang (Editor), *Structural Health Monitoring 2013*. Paper presented at Structural Health Monitoring 2013, A Roadmap to Intelligent Structures, Stanford University, Palo Alto, California, 10 September (pp. 710-716), DEStech Publications, Inc.

Scott, D. B., 2015. *From Dumb Rocks to Smart Materials: Self-Sensing and Self-Healing Concrete*, EPRI Technology Insights, April, 2015. 3002005597.

Sreekala, R., Muthumani, K., 2009. "Structural Application of Smart Materials," Smart Materials, Chapter 4, M. Schwartz, ed., CRC Press, 2009, Boca Raton, Fl.

Suchanek, W. L., Riman, R. E., 2009. "Intelligent Synthesis of Smart Ceramic Materials," Smart Materials, Chapter 2, M. Schwartz, ed., CRC Press, 2009, Boca Raton, Fl.

APPENDIX A: ELECTRO-ELASTIC AND CONTINUUM RELATIONSHIPS FOR
STRAIN QUANTIFICATION USING ELECTRIC RESISTIVITY MEASUREMENTS

Chapter 4 was submitted to the American Society of Civil Engineers as a "technical note". Word and word-equivalent requirements of the publication is set to a maximum of 3,500. As such, the submitted version is abridged. While developing the theoretical relationships for that submission, an extended-derivation version of the document was developed that included the intermediate steps in the derivations. The larger version also included discussion about polarization developed in concrete when using direct current (DC), the types of polarizations, the benefit of alternating current (AC), the real and imaginary portions of reactance, inductance and capacitance, and electrical impedance spectroscopy (EIS). The following is the unabridged version of the submitted paper and is hereunder submitted for the interested reader.

ELECTRO-ELASTIC AND CONTINUUM MECHANICAL RELATIONSHIPS FOR STRAIN QUANTIFICATION USING ELECTRIC RESISTIVITY MEASUREMENTS

Abstract

Self-sensing concrete consists of embedded materials; the embedded functional fillers make electrical properties of the concrete more measureable as mechanical strain occurs. The embedded material varies in size from nano-scale (a thousand times smaller than the diameter of a human hair) to as large as a coarse human hair; material types of functional fillers are vary – carbon, graphite, crystals, or ceramics. Currently, these enhancing materials used to create self-sensing concrete are uniformly distributed while the concrete is still plastic. A proposed study will investigate how waste steel shavings, called *recycled steel residuals*, of different sizes (dust and fiber) can be segregated (graded) and mixed within concrete to enhance its ability to be *self-sensing*. Goals for this work include determining the benefit of using recycled steel residuals in concrete such that the concrete behaves as a sensor and thereby developing a nondestructive sensing (or structural health monitoring) technique. The technique includes the smart concrete transmitting data about its condition. In the study herein, focus will be on exploring a critical understanding of the for elasto-mechanical and electro-elasticity physics of concrete. The theoretical reconciliation of electric, elastic, and material characterizations of the self-sensing concrete is achieved using resistance and resistivity theory and continuum mechanics of solids. A short column (6x6x20 in.), axially loaded in compression will be used as example of demonstrating the relationship between loading, displacement, and strain. These relationships can then be used for strain-resistance measuring. For completeness, the study

includes the importance of utilizing alternating current for testing, reactance development in concrete, and the potential for conductance and inductance to develop.

158

Introduction

The infrastructure throughout much of the United States has aged considerably. There is a large amount of deterioration which has occurred or will continue to occur as structures utilizing reinforced concrete continue to age. Consequently, repair and/or replacement of reinforced concrete structures – buildings, bridges, and roads – will continue to increase in the coming years. The degradation of concrete structures is equally concerning for the nuclear power industry where the global nuclear-power fleet has been operating for many decades. In the United States, approximately half of the 99 units in operation are beyond their original design license of 40 years (International Atomic Energy Agency 2018, Scott et al. 2013). Reinforced concrete is used abundantly in nuclear power plants; but, the reinforced concrete is subject to a variety of different degradation mechanisms. These types of damage mechanisms include construction-related issues (cracking, delamination, cold-joints, honeycombs); environmentally-induced attack (alkali-aggregate reaction, carbonation, chloride ingress); extreme operations (high thermal differentials, missile impact, fire, abrasion); and steel-related issues (tendon rupture, corrosion, fatigue) (Scott 2013).

Inspection of these nuclear structures is traditionally performed using standard nondestructive evaluation techniques. Evaluations of concrete require an inspector to be physically present at the structure to utilize a variety of nondestructive evaluation techniques – visual, ground penetrating radar, impact echo, impulse response, shear wave tomography, coring, half-cell potential, and resistivity (ACI 1998, Scott 2013, Scott 2015). Remote sensing has become more popular which relies upon the strategic placement of

159

surface-placed and embedded sensors – strain gauges, fiber optics, acoustic emission, maturity probes, crack monitors, coaxial cables, temperature gauges, and electrochemical sensors (ACI 1998). The use of discrete embedded materials provides opportunity to turn the concrete into a sensor. This has been achieved using a variety of materials to create autonomous sensing cement-based specimens/members (Chung 2002, Han et al. 2014, Li et al. 2004). The autonomous sensing material is included in the reinforced concrete through modifying the mixture properties. If the constituents of the concrete include material which has the potential of indicating existing or approaching strain that is excessive, then prevention of damage is more possible. If successful, specifications to include the autonomous sensing material could consist of identifying appropriate concentrations of recycled steel residuals relative to cement or aggregate amounts.

The important property of the autonomous sensing material is its electrostrictive nature. Electrostrictive property is the ability of a material to change in electrical properties based on a change in shape (i.e., the material becomes more or less electrically resistant as the material lengthens or compresses, respectively) (Kholkin 2009). In concrete, autonomous sensing material is embedded in concrete to create an enhanced concrete material that is self-sensing. The proposed autonomous sensing material may vary in size – from nanoscale to centimeter scale (Han et al. 2014, Li et al. 2004, Kholkin 2009, Wille and Loh 2010, Sreekala and Muthumani 2009, Pammi et al. 2003). Previously proposed autonomous materials consist of particles, tubes, or fibers made from carbon, steel slag, nickel, graphite; and, sometimes the material is a crystal or ceramic. As an alternative, *recycled steel residuals* are proposed as an autonomous sensing material and consists as

160

both fibrous and fine (dust-like) particles. As such, use of recycled steel residuals may provide a cost effective alternative to other materials which are used to make "smart" concrete. The use of recycled steel residuals will also reduce waste and thus ensure reducing the environmental impact of steel manufacturing. Additional benefits of using the recycled steel residuals may include improved mechanical properties like strength or thermal conductivity through an increased transfer of heat through the concrete (the transfer of heat through the member will allow the heat to more quickly dissipate and mitigate damage to the concrete).

As indicated previously, autonomous sensing materials have been used to increase the function of concrete. Though a small percentage of the material relative to cement content can be used to achieve the desired sensing property of the concrete member and system, adding the electrostrictive material increases the cost of the concrete because the embedded particles are expensive. For instance, (Pammi et al. 2003) reports that the high costs of smart nanomaterials prevent its practical use (Pammi et al. 2003). More specifically to ceramics, (Suchanek and Riman 2009) indicates that newer techniques are needed and preferred for cost reductions in order to promote wide-spread development of ceramics for sensing (Suchanek and Riman 2009). (Sreekala and Muthumani 2009) highlights that costs to manufacture smart materials have reduced, but that those costs were still impeding wide-spread use.

Alternatively, the (re-)use of steel waste being proposed is low cost and environmentally sustainable, saving steel waste from being sent to landfills. As proposed in this study, the steel shavings are developed during the manufacturing process of other

materials. The steel shavings discussed in this proposal would otherwise be considered waste and would only be reused if a significant amount of reprocessing occurred. However, this proposal is considering the use of steel shavings – recycled steel residuals – in concrete mixes which would not require melting of the waste. This provides a valuable alternate use for the steel and minimize energy spent for processing. This is particularly helpful considering the mass uses of concrete for infrastructure and the use of mass concrete. It is conceivable that small repairs can consist of strategically-placed concrete that contains autonomous sensing materials. However, it is more likely that the use of autonomous sensing materials will be most effective if it makes up an entire structural member. In such cases, the high cost of other, previously-studied self-sensing concrete is currently not cost effective. Therefore, a less expensive alternative could have significant impact on the use of self-sensing concrete through the embedment of recycled steel residuals. Given this and in summary, the use of recycled steel residuals has the potential to: 1) act as a functional filler providing self-sensing capability for the concrete; 2) improve the hardened properties of concrete; and/or 3) reduce steel waste and improve the environment.

Mathematical Derivations to Support Empirical Study

The use of concrete as a smart material is achieved through the embedment of particles to increase the measurability of the material. In the case of embedding steel fibers, changes in strain of the material may be indicated through measurable changes in the resistance of the material. As such, this technology requires a marriage of two disciplines of physics and engineering – electricity and mechanics of materials. The following

provides the germane development of relationships between electricity and mechanics of materials to encourage understanding of the mathematical justification for the work. Mostly, the relationships will begin with continuum theory and will also include specific geometry and physical conditions planned for future study of self-sensing concrete using recycled steel residuals.

Resistance and Resistivity

Though low when compared to other materials, concrete has a measurable level of conductivity. When current is passed through the concrete an electrical field vector (V, V/m), develops in the concrete. The electrical current is equivalent to the resistivity (ρ, V-m) multiplied by the current density (J, amps/cm^2) (Sears and Zemansky 1970). This relationship can be written using continuum theory as seen in Eq. 1 providing the variables in indicial notation.

$$V_i = \rho_{ij}J_j \qquad \text{Eq. 1}$$

with V and J being first-order tensors and ρ is a second order tensor with i and j represent indices of a Cartesian coordinate system and therefore are equal to 1, 2, or 3.

There are three phases in concrete that may have varying levels of electrical properties – aggregate, binding agent, and interfacial transition zone between the hydrated cement and aggregate. For study of the bulk electrical properties of concrete (sometimes called "volume electrical" properties), concrete is assumed as a single electrical element and having an electrical path across the cross section of the concrete element. Using

embedded electrodes, important macro resistivity properties of the concrete material are determinable. For measuring changes in concrete strain through changes in electrical measurements, the right side of Eq. 1 can be integrated to create the relationship between the geometry and electrical properties of the material. Eq. 2 is generated by utilizing an elemental length of ds dotted with J (capitalized bold indicates vector field).

$$\rho_{ij}J_j \cdot ds_j \qquad \text{Eq. 2}$$

The vector directions of ds and J are parallel and therefore reduces the dot product to a simple multiplication that can be re-written as below in Eq. 3, further reducing to the current density as a function of current and cross-sectional area (A).

$$\rho \frac{I}{A} ds \qquad \text{Eq. 3}$$

Eq. 3 can be integrated across the length of the element with current (I) taken out as a constant to develop Eq. 4.

$$I \int_b^a \frac{\rho}{A} ds \qquad \text{Eq. 4}$$

The integral of Eq. 4 is resistance (R, ohms). (Note: Ohm's law is equivalent to combining Eq. 4 and Eq. 1.) Therefore, solving for the integral across a length (L) leads to Eq. 5.

$$R = \frac{\rho L}{A} \qquad \text{Eq. 5}$$

Relationship between Strain, Resistance, and Resistivity

Because the bulk properties is assumed, Eq. 5 represents a homogeneous material that has a constant cross section and is electrically isotropic. As such, Eq. 5 is appropriately applied to concrete though concrete is heterogeneous and can be used to develop an indication of strain as a function of resistance/resistivity. Eq. 5 is a fundamental equation used by researchers to provide indication of changes in resistivity based on measurements of resistance. However, a theoretical relationship between specimen measurements of resistance and strain is not readily available in literature on the subject. To develop the relationship between strain and resistance/resistivity, the coordinate system shown in Figure 1 will be used. The column shown in the figure is oriented in a three-dimensional Cartesian coordinate system with the center of the top of the column being placed at 0,0,0.
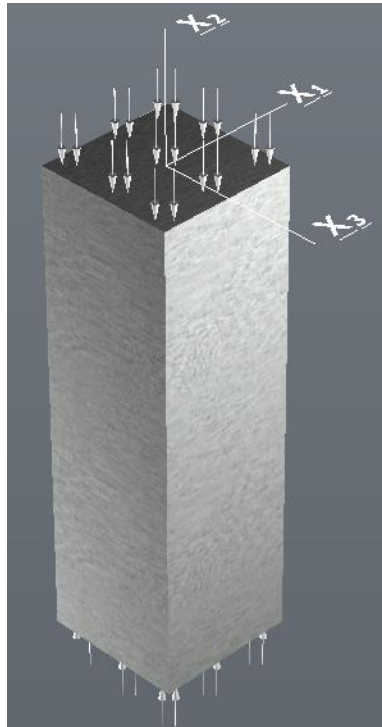
Figure 1
Test Specimen According to Cartesian Coordinate System for 6x6x20 in. Column

After rewriting Eq. 5 to remove the quotient, the product rule is used to give Eq. 6.

$$\rho * dx_2 + x_2 * d\rho = R * d(x_1 x_3) + x_1 x_3 dR \qquad \text{Eq. 6}$$

Each side is then divided by $\rho * x_2$ to create Eq. 7.

$$\frac{dx_2}{x_2} + \frac{d\rho}{\rho} = \frac{R}{\rho x_2} * d(x_1 x_3) + \frac{x_1 x_3}{\rho x_2} * dR \qquad \text{Eq. 7}$$

The right side is then simplified by using Eq. 5 to generate Eq. 8.

$$\frac{dx_2}{x_2} + \frac{d\rho}{\rho} = \frac{d(x_1 x_3)}{x_1 x_3} + \frac{dR}{R} \qquad \text{Eq. 8}$$

Making the cross-section area to be on the $x_1 - x_3$ plane (Figure 1) and then again using the product rule to take the derivative of the area to generate Eq. 9.

$$d(x_1 x_3) = x_1 dx_3 + x_3 dx_1 \qquad \text{Eq. 9}$$

Axial strain causes changes of dimensions in the $x_1 - x_3$ directions according to Poisson's ratio (v). For this study, the change in length is assumed to be axial compression along the x_2-direction to give Eq. 10 and Eq. 11.

$$\frac{dx_1}{x_1} = -\nu\frac{dx_2}{x_2}$$

Eq. 10

$$\frac{dx_3}{x_3} = -\nu\frac{dx_2}{x_2}$$

Eq. 11

Eq. 10 and Eq. 11 can be, respectively, rewritten in terms of dx_1 and dx_3 and then plugged into Eq. 9 to provide Eq. 12.

$$d(x_1x_3) = -(x_1x_3)\nu\frac{dx_2}{x_2} - (x_1x_3)\nu\frac{dx_2}{x_2} = -2(x_1x_3)\nu\frac{dx_2}{x_2}$$

Eq. 12

Finally, Eq. 8 and Eq. 12 can be combined to provide Eq. 13.

$$\frac{dx_2}{x_2} + \frac{d\rho}{\rho} = \frac{dR}{R} - \frac{2(x_1x_3)\nu\frac{dx_2}{x_2}}{x_1x_3}$$

Eq. 13

A couple of further simplifications then provides Eq. 14.

$$\frac{d\rho}{\rho} = \frac{dR}{R} - \frac{dx_2}{x_2} - \frac{2\nu*dx_2}{x_2}$$

Eq. 14

Rearranging Eq. 14 and reducing dx_2/x_2 to strain, Eq. 15 and Eq. 16 can be used to relate resistivity, resistance, and strain.

167

$$\frac{d\rho}{\rho} = \frac{dR}{R} - \frac{dx_2}{x_2}(1+2\nu) \qquad \text{Eq. 15}$$

$$\varepsilon = \frac{1}{(1+2\nu)} * (\frac{dR}{R} - \frac{d\rho}{\rho}) \qquad \text{Eq. 16}$$

Though not the derivation, a variation of Eq. 16 can be found in (Han et al 2014). Eq. 16, relating strain as a function of Poisson's ratio, resistance, and resistivity, is important. It shows that to theoretically calculate strain of any material and of any geometry along a uniform cross section, one must measure both resistance and resistivity and Poisson's ratio must be known. Axial strain (ε) is defined as the change in length divided by the original length, or dx_2/x_2. It is important to note that both quotients on the right side of the equation are unitless along with the strain and Poisson's ratio found in Eq. 16.

The following continues the derivation of the right side to further verify the equality with strain. To start, the following equations will reduce the right-most term ($\frac{d\rho}{\rho}$). Eq. 17 starts with using the product rule on Eq. 5.

$$\frac{d\rho}{\rho} = \left[\frac{x_2}{R*(x_1 x_3)}\right] * \left[\frac{R*d(x_1 x_3)+(x_1 x_3)dR - R*(x_1 x_3)\varepsilon}{x_2}\right] \qquad \text{Eq. 17}$$

Then, Eq. 18 and 19 continue with algebraic manipulations to reduce the formula. Eq. 20 inserts the results from Eq. 19 back into Eq. 17 (the right side of Eq. 16). Eq. 21 further simplifies Eq. 20.

$$\left[\frac{R*d(x_1 x_3) + (x_1 x_3) dR - R*(x_1 x_3)\varepsilon}{R*(x_1 x_3)} \right]$$

Eq. 18

$$\frac{d(x_1 x_3)}{(x_1 x_3)} + \frac{dR}{R} - \varepsilon$$

Eq. 19

$$\frac{1}{(1+2v)} * \left[\frac{dR}{R} - \frac{d(x_1 x_3)}{(x_1 x_3)} - \frac{dR}{R} + \varepsilon \right]$$

Eq. 20

$$\frac{1}{(1+2v)} * \left[\varepsilon - \frac{d(x_1 x_3)}{(x_1 x_3)} \right]$$

Eq. 21

The numerator of the right side of Eq. 21 $d(x_1 x_3)$ has already been solved in Eq. 12 to allow Eq. 21 to be re-written as Eq. 22. Eq. 23 and Eq. 24 continues with algebraic manipulation of the right side of the previous equality (Eq. 16). Eq. 25 shows the final stage of the derivation where the last step leaves the right side of Eq. 16 being strain (ε).

$$\frac{1}{(1+2v)} * \left[\varepsilon - \left[\frac{-2(x_1 x_3) v * dx_2}{(x_1 x_3) * x_2} \right] \right]$$

Eq. 22

$$\frac{1}{(1+2v)} * \left[\varepsilon + \frac{2v * dx_2}{x_2} \right]$$

Eq. 23

$$\frac{1}{(1+2v)} * [\varepsilon + 2v\varepsilon]$$

Eq. 24

$$\frac{1}{(1+2v)} * (1 + 2v)\varepsilon$$

Eq. 25

169

The derivation of Eq. 16 is shown to be true using Eq. 17 through Eq. 25. Based on a review of other literature (Han et al. 2014, Konsta-Gdoutos and Aza 2014), fractional changes in resistivity ($\frac{\Delta\rho}{\rho_o}$, %) is reported as a function of time, strain, or stress. These are reported based on direct measurements of resistance and stress or strain. Resistance is equated to resistivity because the strain for concrete is dismissed as very small; and, thereby negates the ε and ν terms of Eq. 16.

However, it is not always appropriate to theoretically dismiss strain when structural assessments require understanding of the elasto-mechanical condition of the material. Given Eq. 16, to determine strain both resistance and resistivity measurements must be taken continuously or frequently enough to prevent aliasing while uniformly straining the material. This task is difficult. Alternatively, there are two options that can be considered. Either select a material with a very low Poisson's ratio and/or use a geometry with a very small cross section relative to length. In both cases, the resistivity term can be removed from Eq. 16 because the change in cross-section area will be very small while being strained. An additional option is to dismiss the resistivity term and apply a multiplier to the resistance being measured of a specimen.

Compression Loading and Displacement

As part of a proof-of-concept study, empirical data should be gathered to review the relationship between resistance, resistivity, strain, and Poisson's ratio. In the study, a research team will empirically test relationships between strain and changes in electrical current flow in an object. A concrete column can be used, loaded in compression, and then

changes in conductivity/resistance can be measured when a current is applied through the object (Figure 2). To continue with developing the mathematical relationships that may be used, a concrete specimen is assumed to be 6x6x20 in. (150x150x500 mm) with embedded electrodes used to impart alternating electrical current and measure electrical potential (Figure 1 and Figure 2). In this paper, continuum mechanics theory is used to characterize the loading and mechanical response of the specimen. For this derivation, the system is considered frictionless, homogeneous, and isotropic. The column is further assumed as a "short column," and unidirectional compression failure with no buckling. (For short columns, the first order buckling load will be one to two orders of magnitude greater than the compression load.)
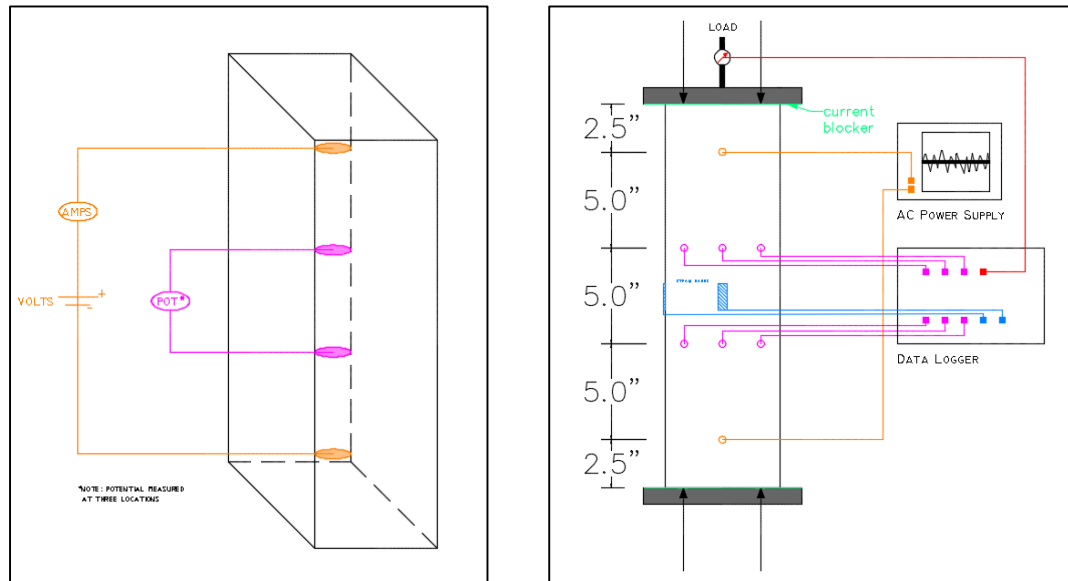
Figure 2
Test Setup of 6x6x20-in. (150x150x500-m) Column

Given the orientation of the column relative to the coordinate system (Figure 1), the compression tensor (C) is given with the axial compression load ($-C^o$) in the 2-2 position of the matrix indicating it is on the x_2 face and along the x_2 direction.

$$[C] = \begin{bmatrix} 0 & 0 & 0 \\ 0 & -C^o & 0 \\ 0 & 0 & 0 \end{bmatrix} \qquad \text{Eq. 26}$$

For the specimen, the strain for the object in each Cartesian directions is given according to constitutive relations in Eq. 27 through 29.

$$\varepsilon_{11} = \frac{-v(-C^o)}{E} \qquad \text{Eq. 27}$$

$$\varepsilon_{22} = \frac{-C^o}{E} \qquad \text{Eq. 28}$$

$$\varepsilon_{33} = \frac{-v(-C^o)}{E} \qquad \text{Eq. 29}$$

Eq. 27 through 29 are constitutive in that Hooke's Law indicates the level of strain (ε_{ij}) in the x_2 direction and the displacements in x_1 and x_3 directions relying on Poisson's ratio (v) and modulus of elasticity (E) of the material. These directional strains have been generalized using continuum mechanics theory as indicated by Eq. 30 and Eq. 31 to show displacement (u) in three directions (Mase 2010).

$$2\varepsilon_{ij} = u_{i,j} + u_{j,i} = \frac{\partial u_i}{\partial x_j} + \frac{\partial u_j}{\partial x_i} \qquad \text{Eq. 30}$$

$$\varepsilon_{ii} = \frac{\partial u_i}{\partial x_i} \qquad \text{Eq. 31}$$

Therefore, given the orientation found in Figure 1, Eq. 32 through 34 apply.

$$\varepsilon_{11} = \frac{\partial u_1}{\partial x_1} \qquad \text{Eq. 32}$$

$$\varepsilon_{22} = \frac{\partial u_2}{\partial x_2} \qquad \text{Eq. 33}$$

$$\varepsilon_{33} = \frac{\partial u_3}{\partial x_3} \qquad \text{Eq. 34}$$

Note, as shown in Eq. 26, C_{21}, C_{12}, C_{31}, C_{13} each equal to zero; therefore, the corresponding strains are equal to zero (i.e., $\varepsilon_{21} = \varepsilon_{12} = \varepsilon_{31} = \varepsilon_{13} = 0$). The equations above (Eq. 27 through 34) can be combined to produce Eq. 35 through 37. Eq. 35 through 37 are integrated with respect to each Cartesian direction to produce Eq. 38 through 40, respectively.

$$\frac{\partial u_1}{\partial x_1} = \varepsilon_{11} = \frac{-v(-C^o)}{E} \qquad \text{Eq. 35}$$

$$\frac{\partial u_2}{\partial x_2} = \varepsilon_{22} = \frac{-C^o}{E} \qquad \text{Eq. 36}$$

$$\frac{\partial u_3}{\partial x_3} = \varepsilon_{33} = \frac{-v(-C^o)}{E} \qquad \text{Eq. 37}$$

$$u_1 = \frac{-v(-C^o)}{E} x_1 + y(x_2) \qquad \text{Eq. 38}$$

$$u_2 = \frac{-C^o}{E} x_2 + f(x_1, x_3) \qquad \text{Eq. 39}$$

$$u_3 = \frac{-v(-C^o)}{E} x_3 + z(x_2) \qquad \text{Eq. 40}$$

The integration produces three functions of integration: $y(x_2), f(x_1, x_3),$ and $z(x_2)$. Prior to reducing these functions of integration and for the sake of simplicity, the column specimen will be adjusted to a two-dimensional column. The results of the two-dimensional column will then be expanded to the three-dimensional object using symmetry. As such, Eq. 41 is true with μ being the shear modulus of the concrete.

$$\varepsilon_{21} = \varepsilon_{12} = \frac{C_{21}}{2\mu} = 0 \qquad \text{Eq. 41}$$

Using Eq. 35 through 40, the following two equations are true.

174

$$\frac{\partial u_2}{\partial x_1} + \frac{\partial u_1}{\partial x_2} = 0 \qquad \text{Eq. 42}$$

$$\frac{df}{dx_1} + \frac{dy}{dx_2} = 0 \qquad \text{Eq. 43}$$

Eq. 43 must be constant and can be rewritten according to Eq. 44 where they both are equated to a variable that is arbitrarily taken to be ω_0.

$$\frac{df}{dx_1} = -\frac{dy}{dx_2} = \omega_o \qquad \text{Eq. 44}$$

Splitting these two equations apart and integrating each in the respective x_1 and x_2 directions gives Eq. 45 and Eq. 46.

$$f(x_1) = \omega_o x_1 + a \qquad \text{Eq. 45}$$

$$y(x_2) = -\omega_o x_2 + b \qquad \text{Eq. 46}$$

Eq. 38, 39, 45, and 46 are combined to yield Eq. 47 and Eq. 48.

$$u_1(x_1, x_2) = \frac{-v(-C^o)}{E} x_1 - \omega_o x_2 + b \qquad \text{Eq. 47}$$

$$u_2(x_1, x_2) = \frac{-C^o}{E} x_2 + \omega_o x_1 + a \qquad \text{Eq. 48}$$

Using Eq. 47 and Eq. 48, a and b are shown to be zero at the locations where x_1 and x_2 equal to zero. Then back to the three-dimensional specimen, symmetry can be used to show that u_1 is equal to u_3. As previously noted, this example derivation is assuming axial loading; and, therefore, the loading should be performed in general accordance with ASTM C39 (ASTM 2016). Therefore, angular rotation at each end of the specimen is assumed to be zero, therefore $\omega_0 = 0$ and, as such, displacements in the x_1, x_2, and x_3 directions are characterized by Eq. 49 through 51. If needed, the total resistance force can be calculated according to Eq. 52 through 54. This provides the relationships between compressive loading stress and displacement (giving strain) for the proposed concrete specimen (Figure 1 and Figure 2). For completeness, derivation of the force resistance of the column is shown in Eq. 52 through Eq. 54.

$$u_1 = \frac{v(-C^o)}{E} x_1 \qquad\qquad \text{Eq. 49}$$

$$u_2 = \frac{-C^o}{E} x_2 \qquad\qquad \text{Eq. 50}$$

$$u_3 = \frac{v(-C^o)}{E} x_3 \qquad\qquad \text{Eq. 51}$$

$$\mathbf{F} = \int C_{22}\, dA\, \hat{e}_2 \qquad\qquad \text{Eq. 52}$$

$$\boldsymbol{F} = C_{22}\, A\, \hat{e}_2 \qquad\qquad\qquad \text{Eq. 53}$$

$$\boldsymbol{F} = -C^o A\, \hat{e}_2 \qquad\qquad\qquad \text{Eq. 54}$$

Effects of Alternating Current

Finally, the electrical derivations in an early section of this article assumed direct current would be applied to the concrete system and therefore utilized material resistance as a representation of impeding electrons. However, concrete develops electrical polarizations when direct current is applied to it (ASTM 2012, Rajabipour 2006) and has been previously observed in concrete specimens by the authors (resistance measurements in other concrete specimens indicated that the resistance was not stable and changes based on the level of polarization which developed in the system). The types of polarizations that develop when using DC input is described by (Rajabipour 2006) as being dipole polarization (similar to groupings of bar magnets), atomic polarization (charged atoms that repel and attract), electronic polarization (change in the orbital path of an electron around a nucleus), interfacial polarization (charges developed at grain boundaries between particles that may bond together), and at interfaces between the negative charges of a solid and the positive ions of the liquid phase of a material. To combat polarization, alternating current (AC) can be used for continued study of concrete specimens. The relationships developed previously are consistent when using AC; however, resistance is replaced with impedance denoted as Z (Eq. 55) because "[c]onceptually, electrical impedance describes the opposition of the material to the flow of an alternating (AC) current" (Rajabipour 2006).

177

Impedance is a function of frequency (f, Hz), angular frequency (ω, rad/sec), time (t, sec), and phase (θ) (Eq. 56 and Eq. 57).

$$V = IZ \qquad \text{Eq. 55}$$

$$V(t) = V_o \cos(\omega t) \qquad \text{Eq. 56}$$

$$I(t) = I_o \cos(\omega t - \theta) \qquad \text{Eq. 57}$$

$$\omega = 2\pi f \qquad \text{Eq. 58}$$

Current (I, amps), is a function of these items but includes a phase shift (θ, radians), which is indicated in Eq. 57. The phase shift of the current indicates the amount of lagging between the voltage and the current. In a system that is dominantly an inductor, the current will lag the voltage. Conversely, if the system is dominantly a capacitor, the voltage will lag the current (Sears and Zemansky 1970).

As noted previously, impedance and resistance have equivalency in Ohm's law. However, impedance (Z, ohms), consists of a real (R, ohms) and imaginary (jX, ohms) parts as indicated symbolically in Eq. 59. The imaginary portion of impedance is a combination of both the inductance and capacitance of the system and the total magnitude of the impedance is given in Eq. 60.

$$\boldsymbol{Z = R + jX} \qquad \text{Eq. 59}$$

$$Z = \sqrt{R^2 + (X_L - X_C)^2}$$
Eq. 60

As previously indicated, these mathematical derivations can support a study of concrete testing with embedded steel shavings. Electrical current can be applied to the concrete and resistance/impedance measurements will be taken of the material. It is interesting to know if the material behaves as a resistor, inductor, or capacitance. Electrical impedance spectroscopy (EIS) can be used to determine this. The EIS testing consists of applying electrical current across a range of frequencies and the resistance/impedance is measured. If the material behaves uniformly with a slope of zero across the sweep of frequencies, then it is considered a resistor. Alternatively, inductance is directly proportional to the AC frequency being applied to the system (Eq. 61). As such, it will linearly increase as the frequency increases according to the magnitude of the inductance. Third, if the material behaves like a capacitor, then the impedance (also called the capacitance reactance) will reduce non-linearly as the frequency increases (Eq. 62) (Sears and Zemansky 1970). Figure 3 shows the behavior of a resistor(s), inductor(s), and capacitor(s).

$$X_L = \omega L$$
Eq. 61

$$X_C = \frac{1}{\omega C}$$
Eq. 62

179
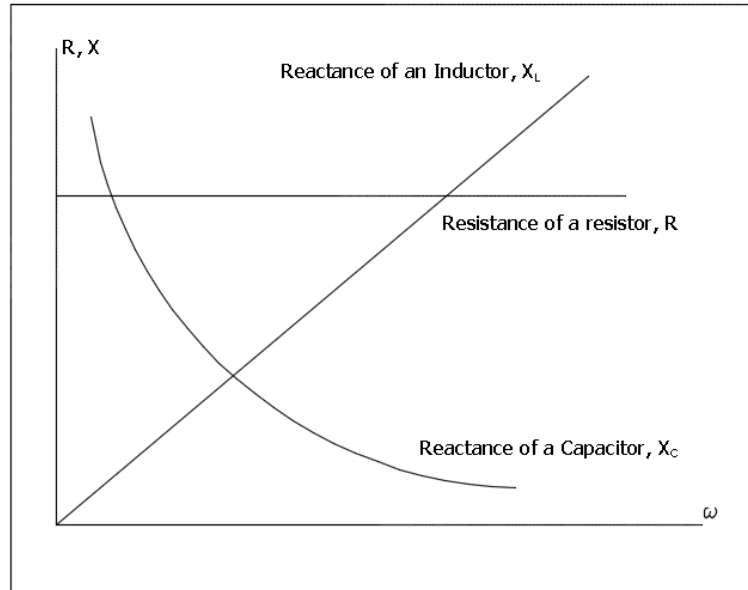
Figure 3
Relationships between angular frequency, reactance, and capacitance (adapted from [Sears and Zemansky 1970])

Conclusion

The existing state of concrete is evaluated using nondestructive evaluation where mechanical and/or electrical energy is being imparted into the concrete and the concrete response is measured to determine internal defects or corrosion of embedded materials. More recently, structural health monitoring is being used to determine the condition of concrete through the embedment of discrete sensors located strategically within a concrete member. Alternatively, it is proposed that concrete becomes its own sensor through a more ubiquitous embedment of smart materials. Smart materials can be used to enhance the concrete electrical properties such that measurable variations in the electrical resistance indicates strain levels within the concrete. A unique, innovative opportunity is to use

recycled steel residuals (shavings) as a less expensive functional filler to create self-sensing concrete.

In this paper, a first order electromechanical correlation has been derived to describe the behavior of a hypothetical "smart" concrete that can self-sense the strain conditions. The correlation is for one-dimensionally loaded short column member, but can be extended to describe the behaviors of more complex elements and loading schemes. The simplistic correlations assume that the concrete is homogeneous and that the added conductive element is uniformly distributed throughout the concrete material. The presence of possible steel reinforcing bars or prestress tendons within the concrete can significantly change the electric properties and additional derivations are needed to modify the equations to accommodate different material conditions.

None the less, the modified concrete can pass electric current through and help evaluate the state of health of the concrete. Such method is suggested to replace traditional nondestructive evaluation or structural health monitoring techniques. By measure the response of the material to mechanical and/or electrical energy to determine internal defects or corrosion of embedded materials.

This paper includes germane mathematical relationships to support the understanding of physics related to empirical testing of concrete enhanced with smart materials. The theoretical relationships utilized electro-elasticity, continuum mechanics, and impedance and reactance to offer the physical phenomenon to measure the effectiveness of recycled steel residuals to create self-sensing concrete. The selection of a measuring device is critical to the accuracy of measurements. The equations derived in

this paper are based on elasto-mechanical and electro-mechanical assumptions – uniform distribution of electrostrictive materials and inter-conductivity follows a straight path. These assumptions are critical and need to be determined experimentally.

References

ACI (American Concrete Institute). (1998). "Nondestructive Test Methods for Evaluation of Concrete in Structures Committee." *ACI 228.2R-98*, Farmington Hills, MI.

ASTM (ASTM International). (2016). "Standard Test Method for Compressive Strength of Cylindrical Concrete Specimens." ASTM C39/C39M – 16, West Conshohocken, PA.

ASTM (ASTM International). (2012). "Standard Test Method for Field Measurement of Soil Resistivity Using the Wenner Four-Electrode Method." ASTM G57 – 06 (Reapproved 2012), West Conshohocken, PA.

Chung, D.D.L. (2002). "Electrical Conduction Behavior of Cement-Matrix Composites," Journal of Materials Engineering and Performance, Vol. 11(2), 194-204.

Han B., Yu X., and Ou J. (2014). *Self-Sensing Concrete in Smart Structures*, Elsevier Inc., Oxford, UK.

International Atomic Energy Agency. (2018). *Power Reactor Information System*. [https://www.iaea.org/PRIS/CountryStatistics/CountryDetails.aspx?current=US] (Jan. 04, 2018).

Kholkin, A. K. (2009). "Piezoelectric and Electrostrictive Ceramics Transducers and Actuators". In M. Schwartz, *Smart Materials* (Ch. 9.1), CRC Press, Boca Raton, FL.

Konsta-Gdoutos M.S., and Aza C.A. (2014). "Self sensing carbon nanotube (CNT) and nanofiber (CNF) cementitious composites for real time damage assessment in smart structures." Cement and Concrete Composites 53, 162-169.

Li H., Xiao H., Ou J. (2004). "A Study on Mechanical and Pressure-Sensitive Properties of Cement Mortar with Nanophase Materials." Cement and Concrete Research 34, 435-438.

Mase G.T., Smelser R.E., and Mase G.E. (2010). *Continuum Mechanics for Engineers, Third Edition*, CRC Press, Boca Raton, FL.

Pammi, S., Brown, C., Datta, S., Kirikera, G., Schulz, M.J. (2003). "Concepts for Smart Nanocomposite Materials." *Proc., Smart Materials, Structures, and Systems*, SPIE Vol. 5062, 629-636.

Poursaee, A. (2011). "Corrosion Measurement Techniques in Steel Reinforced Concrete," Journal of ASTM International, West Conshohocken, PA. ASTM International Vol 8(5).

Rajabipour, F. (2006). "Insitu Electrical Sensing and Material Health Monitoring in Concrete Structures," Thesis, Purdue University, UMI Number 3259972.

Scott, D.B., Goodman, A., Smith, J.D., Chen, S. (2013). "Applications of New Sensing Technologies for Reinforced Concrete Related to Nuclear Facilities:

Considerations and Potentials." In F. Chang (Editor) *Proc., Structural Health Monitoring 2013*. Stanford University, Palo Alto, CA, 710-716.

Scott, D.B. (2013). "Internal Inspection of Reinforced Concrete for Nuclear Structures Using Shear Wave Tomography." Energy Conversion and Management, Vol. 74, 582-586.

Scott, D.B. (2015). "From Dumb Rocks to Smart Materials: Self-Sensing and Self-Healing Concrete." EPRI Technology Insights, 3002005597, Palo Alto, CA.

Sears, F.W., and Zemansky, M.W. (1970). *University Physics, Fourth Edition*, (Ch. 28), Addison-Wesley Publishing Company Inc., Reading, MA.

Sreekala, R., and Muthumani, K. (2009). "Structural Application of Smart Materials," In M. Schwartz, *Smart Materials* (Ch. 4), CRC Press, Boca Raton, FL.

Suchanek, W.L., and Riman, R.E. (2009). "Intelligent Synthesis of Smart Ceramic Materials," In M. Schwartz, *Smart Materials* (Ch. 2), CRC Press, Boca Raton, Fl.

Wille, K. A., and Loh K.J. (2010). "Nanoengineering Ultra-High-Performance Concrete with Multiwalled Carbon Nanotubes." Journal of the Transportation Research Board, Washington, DC.

APPENDIX B: COMPUTER CODE USED FOR EXPERIMENTAL TESTING

During the testing of the 4x8-in. cylinders, 6x12-in. cylinder, and concrete columns, internal electrodes and strain gages were wired to multiple modules for data inquisition and retrieval. The module and chassis was produced by National Instruments. An NI 9205 was used to measure electrical potential between pairs of inner electrodes. The NI 9205 receives up to 10 V, with 16 differential channels for simultaneous testing, and a maximum sampling rate of 250 kS/s. Strain measurements were retrieved using an NI 9237. The NI 9237 is a 4-channel data acquisition device with each channel sampling up to 50 kS/s. It supported quarter-, half-, or full-bridge configurations. Strain gages applied to the concrete columns were three-wire quarter-bridge Wheatstone bridges, so completion of the quarter-bridge required NI 9944 for completion. The minimum sampling rate of the NI 9944 is approximately 1620 S/s. These two modules were housed in the 4-module chassis – cDAQ-9174 for data acquisition. Hardware interfacing was with LabVIEW used to acquire, analyze, and visual data. Two programs were used to simultaneously acquire voltage and strain data. The user interfaces and the block diagrams used for the data acquisition are illustrated below.
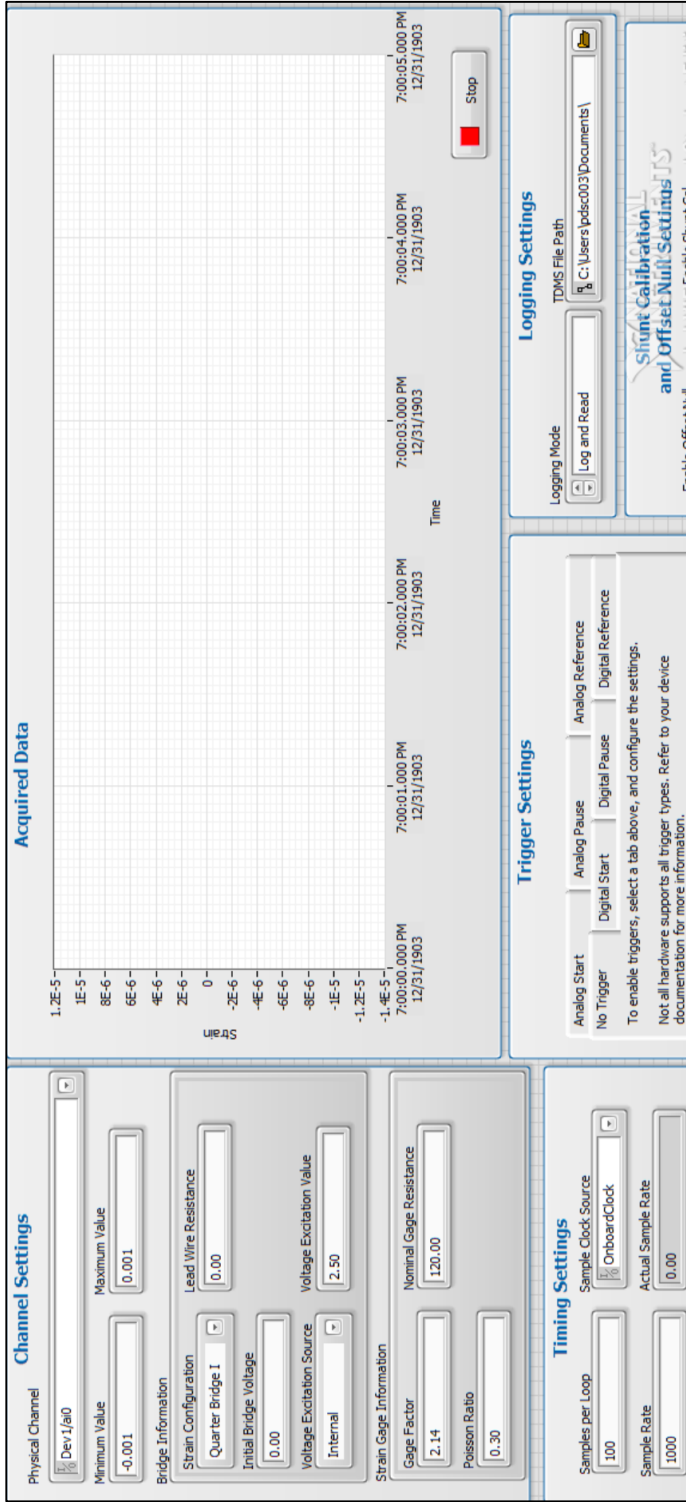
Figure B-1
Front Panel of LabView Interface (Strain)
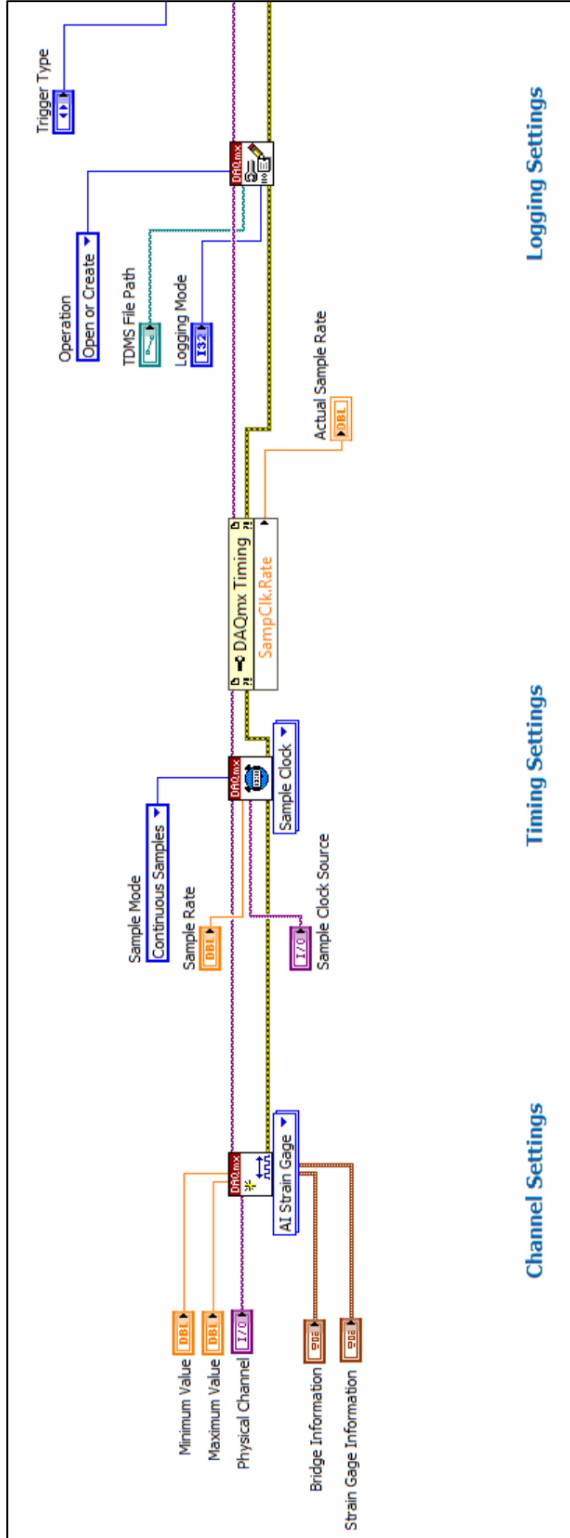
Figure B-2
LabVIEW Block Diagram (Strain: Channel, Timing, and Logging Settings)

"No Trigger", Default

Not all hardware supports all trigger types.
Refer to your device documentation for more information.
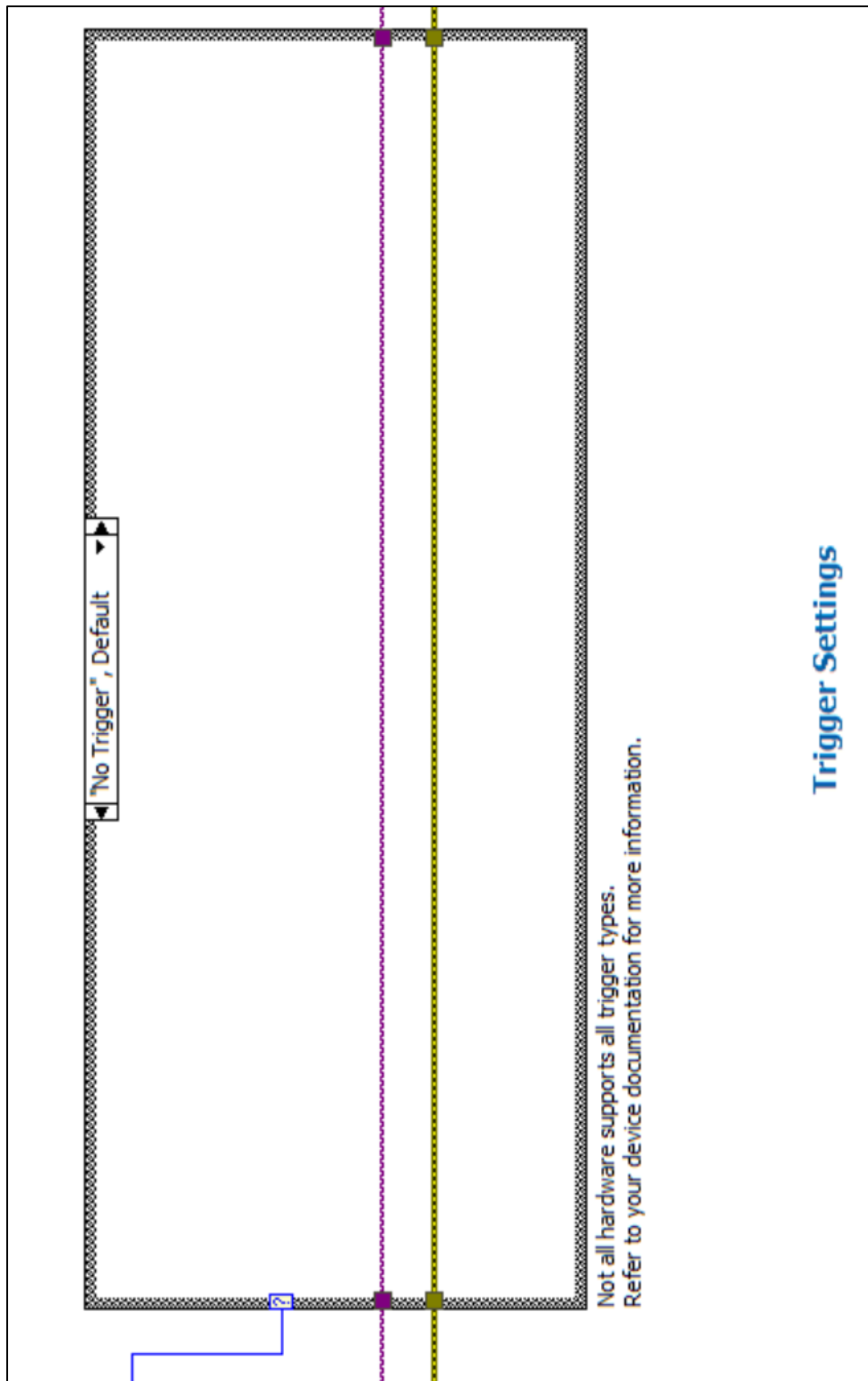
Trigger Settings

Figure B-3
Block Diagram of LabView (Strain: Trigger Settings)
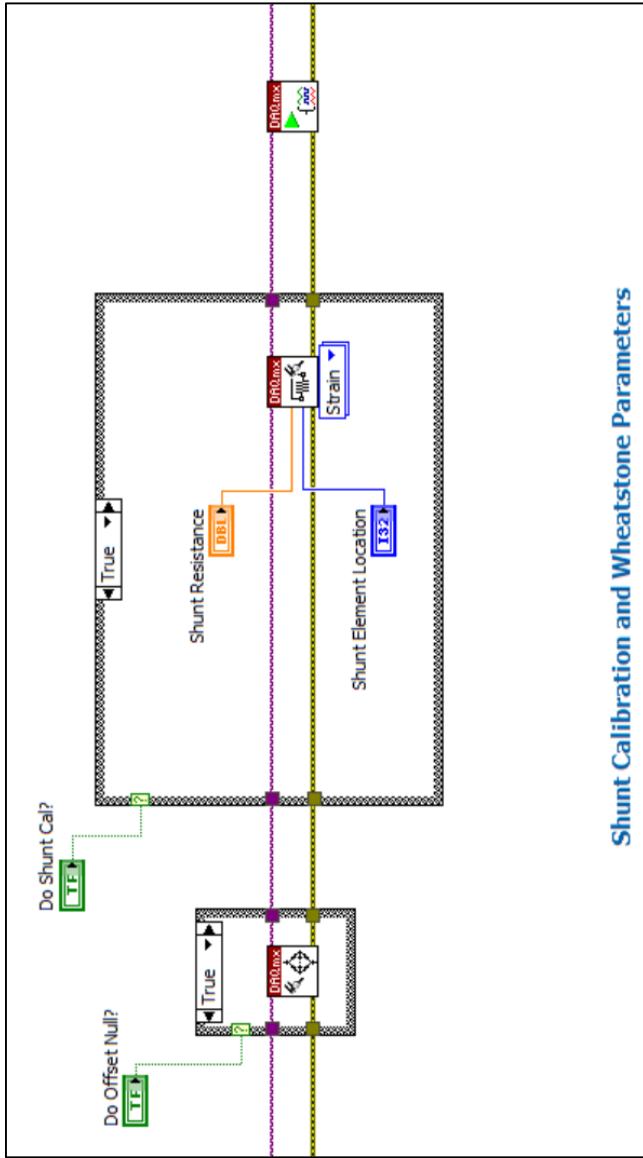
Figure B-4
Block Diagram of LabView (Strain: Shunt Calibration and Wheatstone Parameters)

189
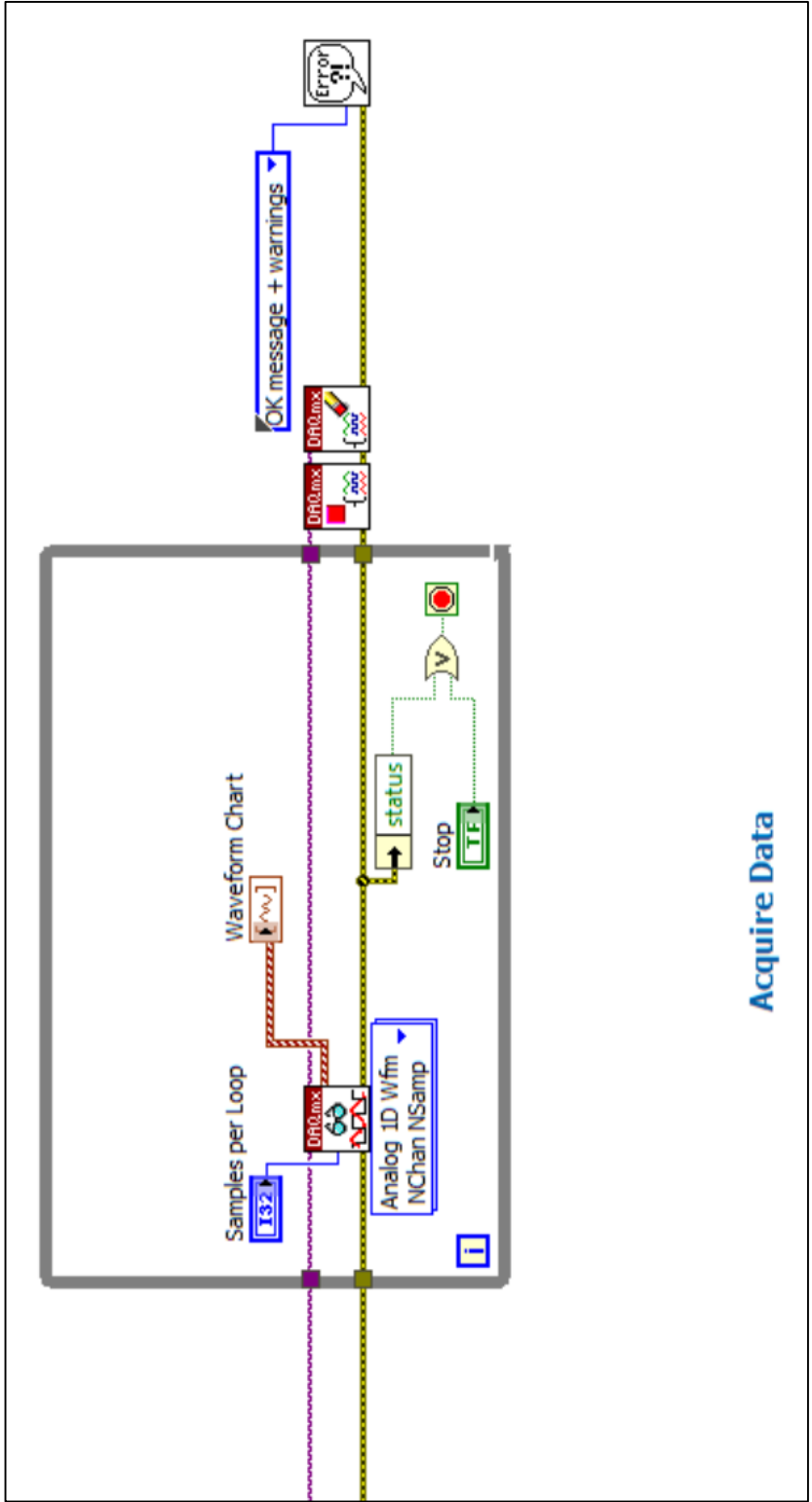
Figure B-5
Block Diagram of LabView (Strain: Acquire Data)
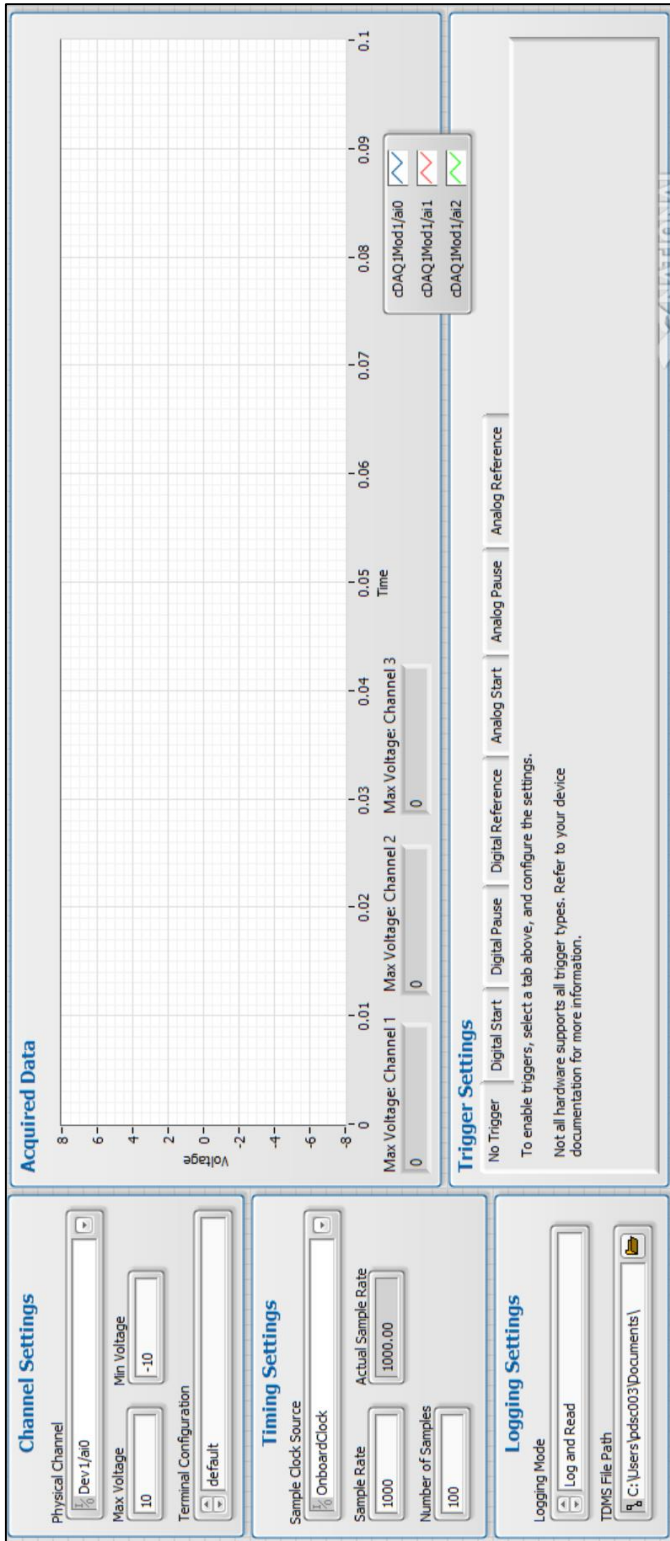
Figure B-6
Front Panel of LabView Interface (Voltage)
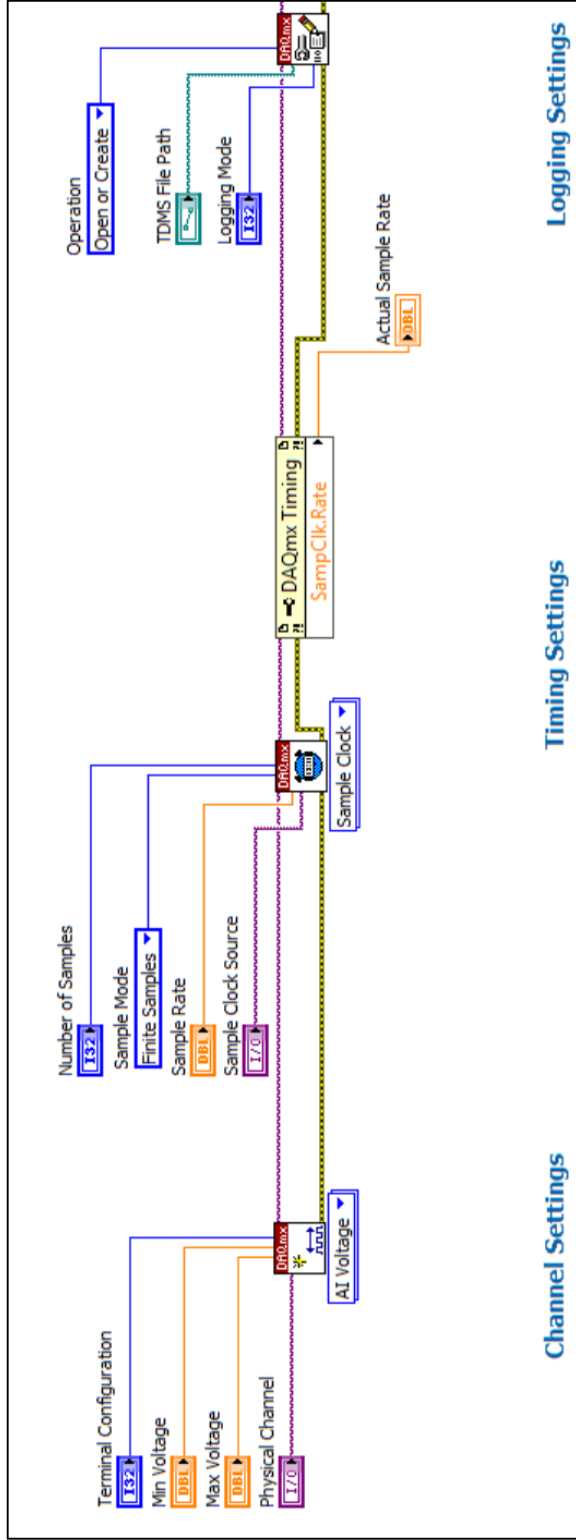
Figure B-7
Block Diagram of LabView Interface (Voltage: Channel, Timing, and Logging Settings)
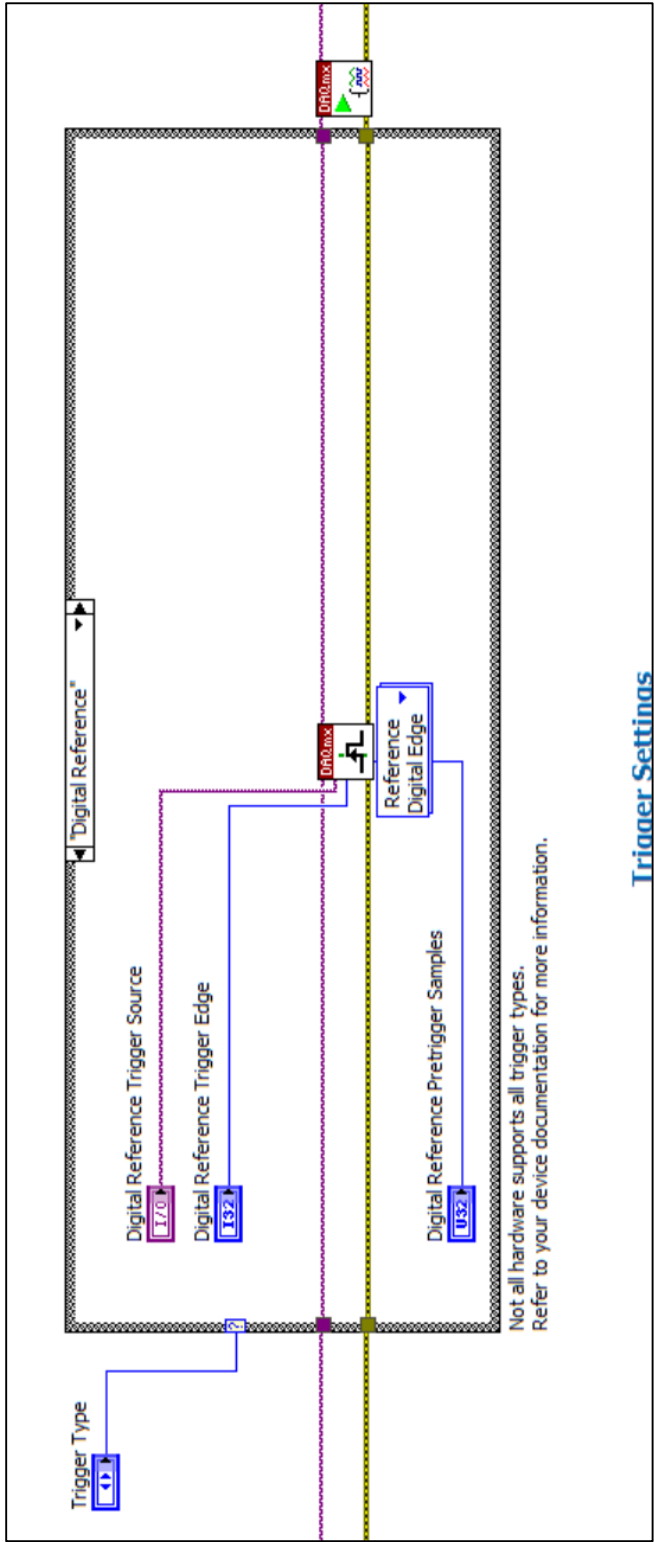
Figure B-8
Block Diagram of LabView Interface (Voltage: Trigger Settings)
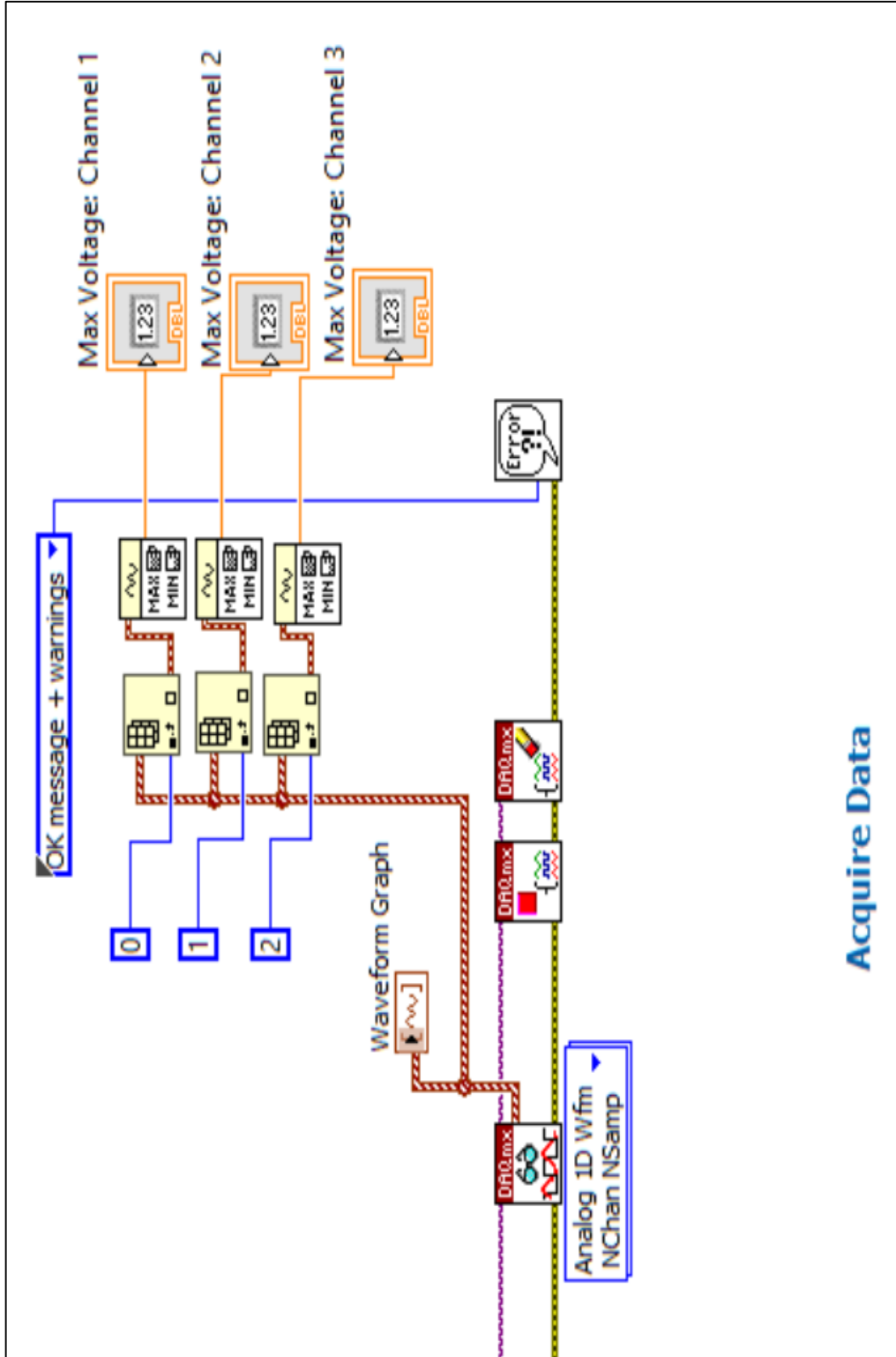
Figure B-9
Block Diagram of LabView Interface (Voltage: Acquired Data)

APPENDIX C: MIX DESIGN FOR CONCRETE SPECIMENS

Mixing and Testing – 6x12-in. Cylinder

Name: David B. Scott
Program: INES
Date: 2017-06
Mixture Id.: 1.6% RSR by Volume

Percentage of RSR = 1.60%
Size of Batch (ft³) = 0.20
Assumed Entrapped Air (%) = 1.5%

Key: Inputs / Outputs

Mixture Design

Component	Specific Gravity	Mass per yard, pounds	Moisture Content, %	Absorption, %	Volume per yard, ft³	Batch volume, ft³	Unadjusted Batch mass, pounds	Moisture adjusted mass, pounds
Cement	3.15	630			3.21	0.02	4.67	4.67
Water	1	285			4.57	0.03	2.11	1.92
CA*	2.64	1515	0.7	0.7	9.19	0.07	11.22	11.22
FA	2.63	1509	2.3	0.6	9.20	0.07	11.18	11.37
RSR	7.8	210			0.43	0.00	1.56	1.56
					27.00			

*Dry Rodded Unit Weight = 97.1 pounds/ft³ per ASTM C29 and FM = 2.73 per ASTM C136. Per 211.1, Weight of CA per yd³ = 0.557*27*100.

Admixture Data

Type	Industry Name	Specific Gravity	Amount, oz/cwt	Amount, ounces/yd³
A	mid-range WR	1.00	7	44.1
Other i				
Other ii				

Theoretical Plastic Data

Plastic Density (pcf)	Relative Yield	FA-CA Ratio	w-cm ratio	RSR ratio by volume, %
153.7	0.99	1.00	0.45	1.6

Plastic Test Data

Batch time	Water held, pounds	Air Content, %	Unit weight, pcf	Temp. °F	Slump, in.
6:30 PM			not measured		

Environmental

Ambient Temp., °F	Relative Humidity, %
72	60

Figure C-1
Mix Design and Batch Proportioning for 6x12 Test Cylinder

Mixing and Testing – 4x8-in. Cylinders

Mixture Component	Yd³-Mix Design, lbs.	Concentration of Recycled Steel Residuals		
		0%	0.5%	1.0%
		1.5-ft³ Batch Weights, lbs.	1.5-ft³ Batch Weights, lbs.	1.5-ft³ Batch Weights, lbs.
Cement	662.4	36.8	36.8	36.8
Water	327.6	18.2	18.2	18.2
Coarse aggregate, No. 67	1,726.2	95.9	95.9	95.9
Fine aggregate	1,170	65	65	65
RSR (Retained on No. 8 sieve)	Varied	0	1.40	1.95
RSR (Passing through No. 8 sieve)	Varied	0	1.40	1.95

Figure C-2
Mix Design and Batch Proportioning for 4x8 Test Cylinders

Mixing and Testing – 6x6x20-in. Columns

Assumed SG for Steel=	7.8	CA Weight for 0% RSR=	1528
Assumed SG for CA=	2.64		

Percent of rsr by volume	Ratio of rsr Volume per Cubic Yard of Concrete	Weight of rsr per Cubic Yard of Concrete (pounds)	Weight of rsr per Cubic Foot of Concrete (pounds)	Reduction of Weight of Coarse Aggregate for RSR (pounds)	Weight of Coarse Aggregate (pounds)
0.0%	0.00	0.0	0.0	0.0	1528
0.2%	0.05	26.3	1.0	8.9	1519
0.4%	0.11	52.6	1.9	17.8	1510
0.5%	0.14	65.7	2.4	22.2	1506
0.6%	0.16	78.8	2.9	26.7	1501
0.8%	0.22	105.1	3.9	35.6	1492
1.0%	0.27	131.4	4.9	44.5	1484
1.2%	0.32	157.7	5.8	53.4	1475
1.4%	0.38	184.0	6.8	62.3	1466
1.6%	0.43	210.3	7.8	71.2	1457
1.8%	0.49	236.5	8.8	80.1	1448
2.0%	0.54	262.8	9.7	89.0	1439
2.2%	0.59	289.1	10.7	97.9	1430
2.4%	0.65	315.4	11.7	106.7	1421
2.6%	0.70	341.7	12.7	115.6	1412
2.8%	0.76	368.0	13.6	124.5	1403
3.0%	0.81	394.2	14.6	133.4	1395

Figure C-3
Concentration Values for RSR by Volume

Name: David B. Scott
Program: INES

Date: 3/17/2017
Mixture Id.: 0% RSR by Volume

Key:
- Inputs
- Outputs
- Batch

RSR (%) = 0.0%
Size of Batch (ft³) = 4.20

Assumed Air Content (%) = 1.5%

Mixture Design

Component	Specific Gravity	Mass per yard, pounds	Moisture Content, %	Absorption, %	Volume per yard, ft³	Batch volume, ft³	Unadjusted Batch mass, pounds	Moisture adjusted mass, pounds
Cement	3.15	630			3.21	0.50	98.00	98.00
Water	1	285			4.57	0.71	44.33	41.45
CA*	2.64	1528	0.13	0.7	9.28	1.44	237.69	236.33
FA	2.63	1567	2.34	0.6	9.55	1.49	243.72	247.96
RSR**	7.8	0	0.2	0.0	0.00	0.00	0.00	0.00

Total Calculated Volume (assumed) = 27.00

*Dry Rodded Unit Weight = 98.6 pounds/ft³ per ASTM C29 and FM = 2.73 per ASTM C136. Per 211.1, Approximate wt. of CA per yd³ = 0.57*27*98.6.

**RSR was proportioned 2:1, material sieved to pan to material retained on No. 8.

Admixture Data

Type	Industry Name	Specific Gravity	Amount, oz./cwt	Amount, ounces/yd³	Amount, ounces/batch	Amount, mL/batch
A	mid-range WR	1.001	3	18.9	2.9	86.8
F	high-range WR	1.001	1.2	7.6	1.2	34.7
Other //						

Theoretical Plastic Data

Relative Yield	FA-CA Ratio	w-cm ratio	RSR ratio by volume, %
0.99	1.03	0.45	0.0

Plastic Test Data

Plastic Density (pcf)	Water held, pounds	Air Content, %	Unit weight, pcf	Temp. °F	Slump, in.
148.5	0	4	146.1	65	3

Batch time: 1:24 PM

Environmental

Ambient Temp., °F	Relative Humidity, %
58	not measured

Figure C-4
Mix Design and Batch Proportioning for 6x620-in. Column (0% RSR Concentration)

Name:	David B. Scott		Date:	3/17/2017			Key:	Inputs
Program:	INES		Mixture Id.:	0% RSR by Volume				Outputs
								Batch

	RSR (%)=	0.5%		Assumed Air Content (%)=	1.5%
	Size of Batch (ft³)=	4.20			

Mixture Design

Component	Specific Gravity	Mass per yard, pounds	Moisture Content, %	Absorption, %	Volume per yard, ft³	Batch volume, ft³	Unadjusted Batch mass, pounds	Moisture adjusted mass, pounds
Cement	3.15	630			3.21	0.50	98.00	98.00
Water	1	285			4.57	0.71	44.33	41.47
CA*	2.64	1518	0.13	0.7	9.21	1.43	236.08	234.73
FA	2.63	1555	2.34	0.6	9.48	1.47	241.88	246.09
RSR**	7.8	66	0.2	0.0	0.14	0.02	10.22	10.24

Total Calculated Volume (assumed)= 27.00

**Dry Rodded Unit Weight = 98.6 pounds/ft³ per ASTM C29 and FM = 2.73 per ASTM C136. Per 211.1, Approximate wt. of CA per yd³ = 0.57*27*98.6.
**RSR was proportioned 2:1, material sieved to pan to material retained on No. 8.

Admixture Data

Type	Industry Name	Specific Gravity	Amount, oz./cwt	Amount, ounces/yd³	Amount, ounces/batch	Amount, mL/batch
A	mid-range WR	1.001	3	18.9	2.9	86.8
F	high-range WR	1.001	1.2	7.6	1.2	34.7
Other II						

Theoretical Plastic Data

Plastic Density (pcf)	Relative Yield	FA-CA Ratio	w-cm ratio	RSR ratio by volume, %
150.1	0.99	1.02	0.45	0.5

Environmental

Ambient Temp., °F	Relative Humidity, %
56	not measured

Plastic Test Data

Batch time	Water held, pounds	Unit weight, pcf	Air Content, %	Temp. °F	Slump, in.
12:42 PM	0	138	10	65	3.25

Figure C-5
Mix Design and Batch Proportioning for 6x620-in. Column (0.5% RSR Concentration)

Key:
| Inputs |
| Outputs |
| Batch |

RSR (%) = 1.0%
Size of Batch (ft³) = 4.20

Assumed Air Content (%) = 1.5%

Mixture Design

Component	Specific Gravity	Mass per yard, pounds	Moisture Content, %	Absorption, %	Volume per yard, ft³	Batch volume, ft³	Unadjusted Batch mass, pounds	Moisture adjusted mass, pounds
Cement	3.15	630			3.21	0.50	98.00	98.00
Water	1	285			4.57	0.71	44.33	41.49
CA*	2.64	1507	0.13	0.7	9.15	1.42	234.35	233.01
FA	2.63	1544	2.34	0.6	9.41	1.46	240.16	244.34
RSR**	7.8	131	0.2	0.0	0.27	0.04	20.44	20.48

Total Calculated Volume (assumed) = 27.00

*Dry Rodded Unit Weight = 98.6 pounds/ft³ per ASTM C29 and FM = 2.73 per ASTM C136. Per 211.1, Approximate wt. of CA per yd³ = 0.57*27*98.6.
**RSR was proportioned 2:1, material sieved to pan to material retained on No. 8.

Admixture Data

Type	Industry Name	Specific Gravity	Amount, oz./cwt	Amount, ounces/yd³	Amount, ounces/batch	Amount, mL/batch
A	mid-range WR	1.001	3	18.9	2.9	86.8
F	high-range WR	1.001	1.2	7.6	1.2	34.7
Other II						

Theoretical Plastic Data

Plastic Density (pcf)	Relative Yield	FA-CA Ratio	w-cm ratio	RSR ratio by volume, %
151.7	0.99	1.02	0.45	1.0

Plastic Test Data

Batch time	Water held, pounds	Air Content, %	Unit Weight, pcf	Temp. °F	Slump, in.
12:00 PM	0	15	131.4	67	6

Environmental

Ambient Temp., °F	Relative Humidity, %
52	not measured

Figure C-6
Mix Design and Batch Proportioning for 6x620-in. Column (1.0% RSR Concentration)

200

Name: David B. Scott
Program: INES

Date: 3/17/2017
Mixture Id.: 0% RSR by Volume

Key:
Inputs
Outputs
Batch

RSR (%) = 2.0%
Size of Batch (ft³) = 4.20

Assumed Air Content (%) = 1.5%

Mixture Design

Component	Specific Gravity	Mass per yard, pounds	Moisture Content, %	Absorption, %	Volume per yard, ft³	Batch volume, ft³	Unadjusted Batch mass, pounds	Moisture adjusted mass, pounds
Cement	3.15	630			3.21	0.50	98.00	98.00
Water	1	285			4.57	0.71	44.33	41.53
CA*	2.64	1484	0.13	0.7	9.01	1.40	230.89	229.57
FA	2.63	1522	2.34	0.6	9.27	1.44	236.71	240.83
RSR**	7.8	263	0.2	0.0	0.54	0.08	40.88	40.97

Total Calculated Volume (assumed) = 27.00

*Dry Rodded Unit Weight = 98.6 pounds/ft³ per ASTM C29 and FM = 2.73 per ASTM C136. Per 211.1, Approximate wt. of CA per yd³ = 0.57*27*98.6.

**RSR was proportioned 2:1, material sieved to pan to material retained on No. 8.

Admixture Data

Type	Industry Name	Specific Gravity	Amount, oz./cwt	Amount, ounces/yd³	Amount, ounces/batch	Amount, mL/batch
A	mid-range WR	1.001	3	18.9	2.9	86.8
F	high-range WR	1.001	1.2	7.6	1.2	34.7
Other ii						

Theoretical Plastic Data

Plastic Density (pcf)	Relative Yield	FA-CA Ratio	w-cm ratio	RSR ratio by volume, %
155.0	0.99	1.03	0.45	2.0

Plastic Test Data

Batch time	water held, pounds	Air Content, %	Unit weight, pcf	Temp. °F	Slump, in.
11:11 AM	0	20	125.4	64	3.25

Environmental

Ambient Temp., °F	Relative Humidity, %
49	not measured

Figure C-7
Mix Design and Batch Proportioning for 6x620-in. Column (2.0% RSR Concentration)

Concrete Demolding

Figure D-1
Demolded Cylinders to be used for Modulus of Elasticity Testing

Figure D-2
Cylinder used for Testing Containing 1% RSR Concentration

Figure D-3
Cylinder used for Testing Containing 2% RSR Concentration

Figure D-4
Demolded Column for Electro-Elastic Testing Containing 2% RSR Concentration

Compression Testing Results – Seven-Day

Figure D-5
Image of failed 4x8 Cylinder with 0.5% RSR Concentration

Figure D-6
Image of Failed 4x8 Cylinder with 2% RSR Concentration

Modulus of Elasticity Testing

Figure D-7
Modulus of Elasticity Setup

Figure D-8
Modulus of Elasticity Testing – 6x12-in. Cylinder

Electro-Elastic Testing
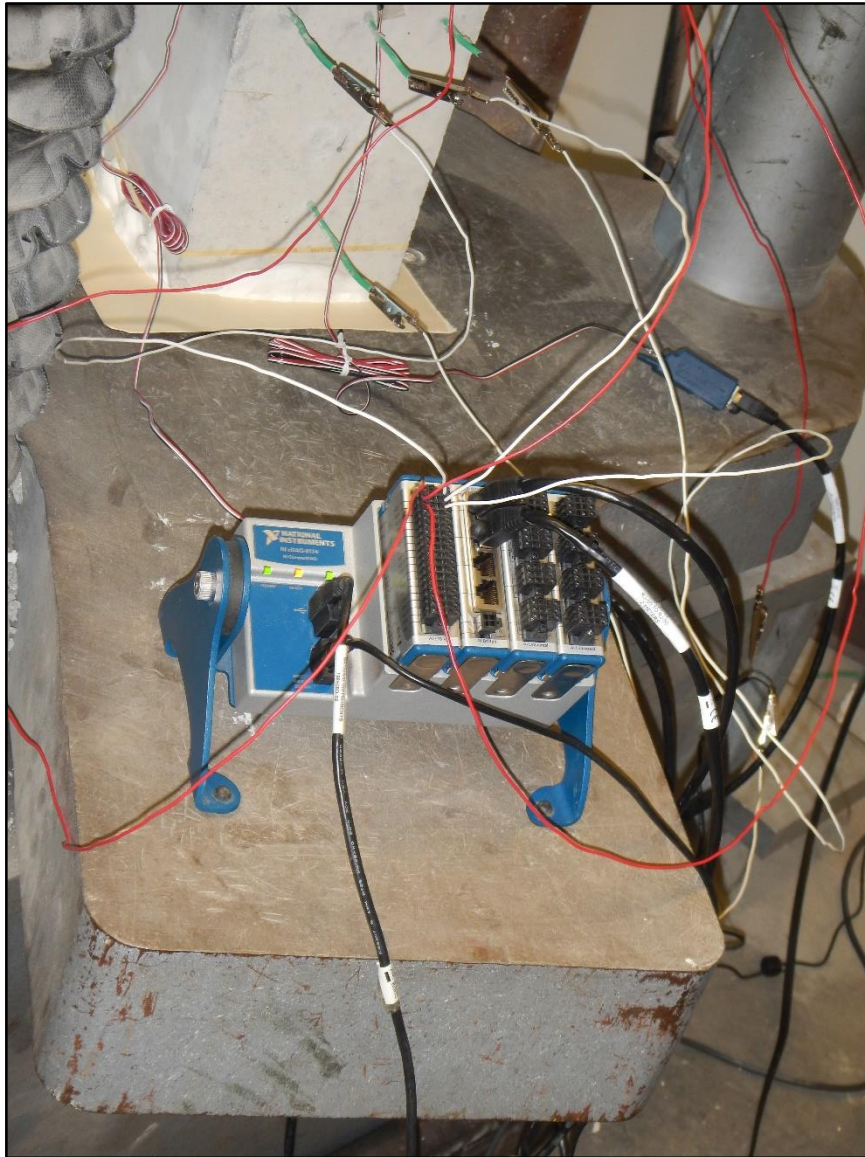
Figure D-9
Data Acquisition Device for Electro-Elastic Testing
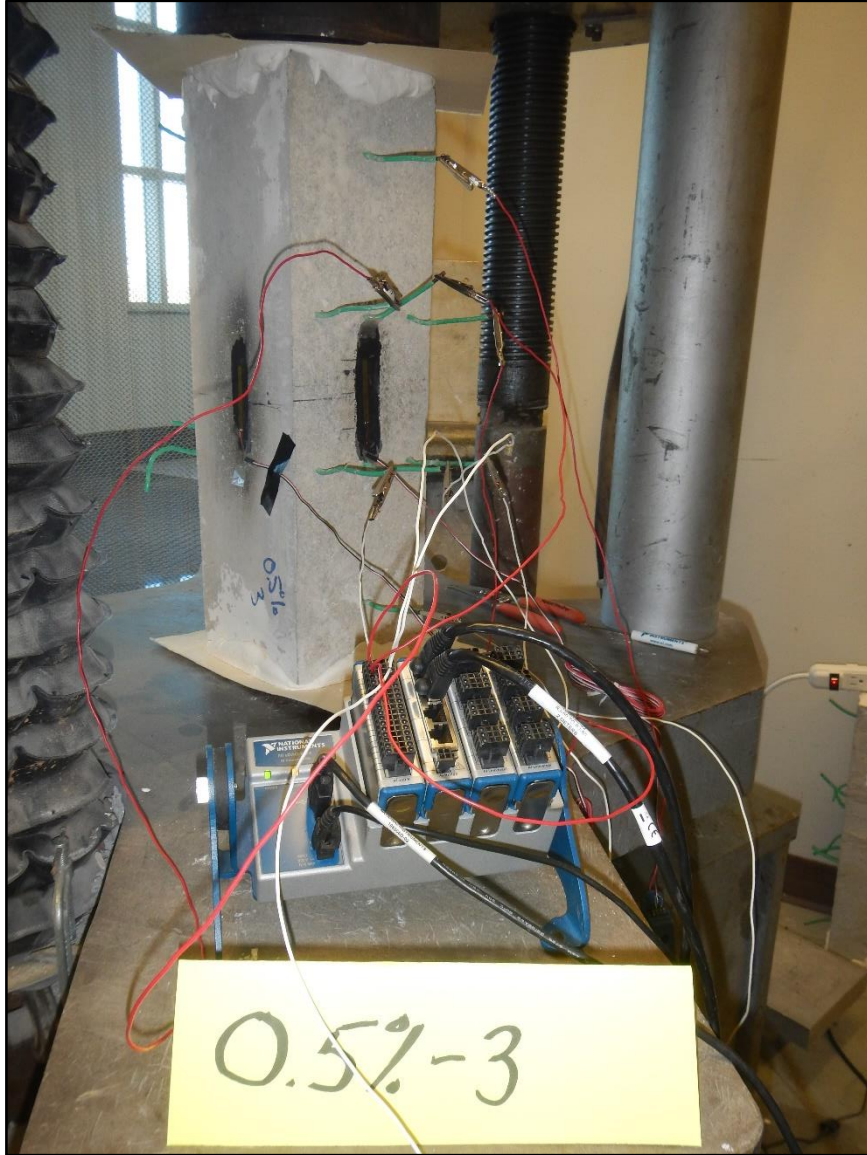
Figure D-10
Electro-Elasticity Testing of Column with 0.5% RSR Concentration
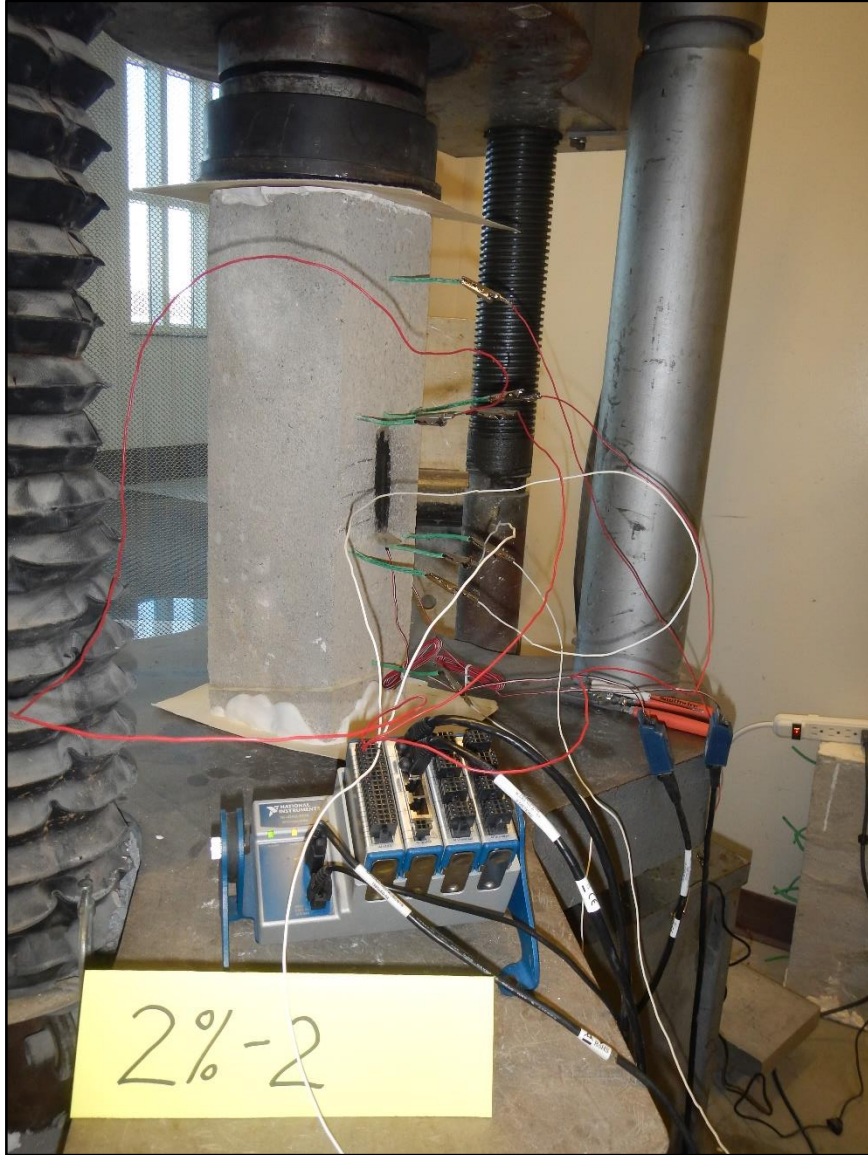
Figure D-11
Electro-Elasticity Testing of Column with 2% RSR Concentration

Physical Properties of Concrete Specimens for Mechanical Testing

2-Day Compressive Strength Testing

RSR%, #	Wt (lbs)	Datum	Dia1 (in.)	Dia2 (in.)	Ave (in.)	Radius (in.)	Area (in.²)	Ht (in.)	Act. Ht. (in.)	Unit Wt.	Load (lbs.)	f'c (psi)	Adj. f'c (psi)	Failure
0, 1	8.525	1.55	5.55	5.55	4	2.00	12.57	9.63	8.08	145.1	51,910	4,131	4,130	cone and shear
0, 2	8.545	1.55	5.54	5.52	3.98	1.99	12.44	9.64	8.09	146.7	62,000	4,984	4,980	cone and split
0, 3	8.565	1.55	5.52	5.54	3.98	1.99	12.44	9.63	8.08	147.2	61,590	4,951	4,950	cone and shear
0.5, 1	7.945	1.55	5.54	5.54	3.99	2.00	12.50	9.83	8.28	132.6	20,290	1,623	1,620	cone and shear
0.5, 2	7.955	1.55	5.53	5.54	3.985	1.99	12.47	9.81	8.26	133.4	19,440	1,559	1,560	cone and shear
0.5, 3	7.925	1.55	5.52	5.56	3.99	2.00	12.50	9.85	8.3	132.0	16,680	1,334	1,330	cone and shear
1, 1	7.535	1.55	5.54	5.52	3.98	1.99	12.44	9.83	8.28	126.4	14,300	1,149	1,150	cone and shear
1, 2	7.615	1.55	5.53	5.53	3.98	1.99	12.44	9.85	8.3	127.4	15,630	1,256	1,260	cone and split
1, 3	7.59	1.55	5.53	5.52	3.975	1.99	12.41	9.84	8.29	127.5	14,640	1,180	1,180	shear
2, 1	7.665	1.55	5.53	5.51	3.97	1.99	12.38	9.82	8.27	129.4	13,050	1,054	1,050	cone and shear
2, 2	7.53	1.55	5.51	5.52	3.965	1.98	12.35	9.78	8.23	128.0	14,390	1,165	1,170	cone and shear
2, 3	7.455	1.55	5.52	5.51	3.965	1.98	12.35	9.79	8.24	126.6	13,110	1,062	1,060	cone and shear

Figure E-1
Measured and Calculated Properties of Concrete Cylinders – 7 Days

28-Day Compressive Strength Testing

RSR%, #	Wt (lbs)	Datum	Dia1 (in.)	Dia2 (in.)	Ave (in.)	Radius (in.)	Area (in.^{2})	Ht (in.)	Unit Wt. (in.3)	Load (lbs.)	Adj. f'_c (psi)	Failure
0, 4	8.535	0	3.972	3.958	3.965	1.98	12.35	7.96	150.1	64,590	5,230	cone and shear
0, 5	8.480	0	3.992	4.008	4.000	2.00	12.57	7.99	145.9	62,490	4,970	cone and shear
0, 6	8.515	0	3.984	4.009	3.997	2.00	12.54	8.02	146.3	66,350	5,290	cone and shear
0.5, 4	7.730	0	4.021	4.015	4.018	2.01	12.68	7.98	132.0	20,550	1,620	cone
0.5, 5	7.745	0	4.004	4.028	4.016	2.01	12.67	7.99	132.2	20,200	1,590	cone
0.5, 6	7.705	0	4.006	4.019	4.013	2.01	12.65	7.96	132.3	20,900	1,650	cone and split
1, 4	7.345	0	4.017	3.996	4.007	2.00	12.61	7.96	126.5	14,000	1,110	cone
1, 5	7.330	0	4.026	3.999	4.013	2.01	12.65	7.98	125.6	16,500	1,300	cone
1, 6	7.405	0	4.008	4.015	4.012	2.01	12.64	8.00	126.6	15,910	1,260	cone and split
2, 4	7.405	0	3.987	4.005	3.996	2.00	12.54	7.95	128.4	15,430	1,230	cone
2, 5	7.485	0	4.000	4.016	4.008	2.00	12.62	7.95	129.0	15,870	1,260	cone
2, 6	7.480	0	4.002	4.009	4.006	2.00	12.60	7.93	129.4	16,470	1,310	cone

Figure E-2
Measured and Calculated Properties of Concrete Cylinders – 28 Days

260 Day Compressive Strength Testing

RSR%, #	Wt (lbs)	Datum	Dia1 (in.)	Dia2 (in.)	Ave (in.)	Radius (in.)	Area (in.^{2})	Ht (in.)	Act. Ht. (in.)	Unit Wt.	Load (lbs.)	f'$_c$ (psi)	Adj. f'$_c$ (psi)	Failure
0, 7	8.375	0	3.960	3.950	3.955	1.98	12.29	8.03	8.03	146.7	88,610	7,213	7,210	cone
0, 8	8.385	0	3.970	4.030	4.000	2.00	12.57	8.01	8.01	143.9	99,160	7,891	7,890	cone and split
0, 9	8.415	0	3.970	3.980	3.975	1.99	12.41	8.03	8.03	146.0	104,570	8,426	8,430	cone
0.5, 7	7.460	0	3.980	3.980	3.980	1.99	12.44	7.98	7.98	129.9	30,760	2,472	2,470	cone
0.5, 8	7.535	0	3.990	4.010	4.000	2.00	12.57	7.99	7.99	129.8	32,860	2,615	2,610	cone
0.5, 9	7.480	0	3.980	3.980	3.980	1.99	12.44	7.98	7.98	130.2	36,255	2,914	2,910	cone
1, 7	7.060	0	3.980	3.990	3.985	1.99	12.47	7.97	7.97	122.7	23,440	1,879	1,880	cone
1, 8	7.085	0	3.980	3.980	3.980	1.99	12.44	7.94	7.94	123.9	23,450	1,885	1,880	cone
1, 9	7.165	0	4.010	3.990	4.000	2.00	12.57	7.99	7.99	123.4	24,620	1,959	1,960	cone
2, 7	7.250	0	3.990	3.970	3.980	1.99	12.44	7.95	7.95	126.7	26,225	2,108	2,110	cone
2, 8	7.125	0	3.980	3.980	3.980	1.99	12.44	7.95	7.95	124.5	28,030	2,253	2,250	cone
2, 9	7.215	0	3.990	3.990	3.990	2.00	12.50	7.99	7.99	124.7	28,980	2,318	2,320	cone

Figure E-3
Measured and Calculated Properties of Concrete Cylinders – 260 Days

Modulus of Elasticity Testing (28-Days)

28-Day Modulus of Elasticity Testing

IS(N), #	Wt (lbs)	Dia1 (in.)	Dia2 (in.)	Ave Dia (in.)	Radius (in.)	Area (in.³)	Ht (in.)	Unit Wt. (in.3)	Ult. Load (lbs.)	f'c (psi)	Rnd. f'c (psi)	Failure Type	$P_{0.00005}$ (lbf)	$P_{40\%}$ (lbf)	$\sigma_{0.00005}$ (psi)	$\sigma_{40\%}$ (psi)	Long. $\varepsilon_{0.00005}$	Long. $\varepsilon_{40\%}$	Radial $\varepsilon_{0.00005}$	Radial $\varepsilon_{40\%}$	Chord MOE (psi)	Poisson's Ratio
0,1	28.455	6.061	6.061	6.061	3.02	28.57	12.04	143.0	154,215	5,398	5,400	shear	7200	61656	252	2159	0.00005	0.000504	0.00000	0.000075	4200000	0.16
0,2	28.485	6.091	6.051	6.061	3.03	28.85	12.00	142.1	149,705	5,189	5,190	shear	7700	59832	267	2075	0.00005	0.000403	0.00000	0.000065	5100000	0.15
0.5, 1	26.015	6.049	6.037	6.043	3.02	28.68	12.05	130.1	47,740	1,665	1,660	cone and split	4500	19096	157	666	0.00005	0.00021	0.00000	0.000032	3200000	0.2
0.5, 2	26.070	6.026	6.026	6.026	3.01	28.52	12.06	131.0	48,990	1,718	1,720	shear	3800	19596	133	687	0.00005	0.000211	0.00000	0.000026	3450000	0.16
1, 1	24.465	6.050	6.025	6.038	3.02	28.63	12.06	122.5	34,370	1,201	1,200	cone	3700	13748	129	480	0.00005	0.000185	0.00000	0.000037	2600000	0.27
1, 2	24.475	6.015	6.054	6.035	3.02	28.60	12.02	123.0	28,835	1,009	1,010	cone	3700	11542	129	404	0.00005	0.000166	0.00000	0.000029	2350000	0.25
2, 1	25.120	6.054	6.035	6.035	3.01	28.51	12.06	126.3	34,675	1,216	1,220	cone	4500	13870	158	487	0.00005	0.000173	0.00000	0.000026	2650000	0.21
2, 1	25.055	6.028	6.040	6.034	3.02	28.60	12.06	125.5	35,275	1,234	1,230	cone	3500	14110	122	493	0.00005	0.000243	0.00000	0.000041	1950000	0.21

Individual Results

Date of Testing: 4/14/2017
Testing technician: David B. Scott, Blake Rigsert, and Ross
Curing method: lime bath
Specimen age: 28 days

Figure E-4
Measured and Calculated Modulus of Elasticity (28-Days)

212

Stress-Strain Data for Specimen 0%,1 at 28 Days After Mixing

Load (lb)	Radial Dial (in.)	Long. Dial (in.)	Long. ε	Radial ε	σ (psi)	$\sigma_{0.00005}$ (psi)	$\sigma_{40\%}$ (psi)	Long. $\varepsilon_{0.00005}$	Long. $\varepsilon_{40\%}$	Radial $\varepsilon_{0.00005}$	Radial $\varepsilon_{40\%}$	slope of σ-ε (psi)
0	0.0000	0.0000	0.00000	0.00000	0	252	2159	0.00005	0.000504	0.00000	7.47E-05	4,282,978
7200	0.0000	0.0008	0.00005	0.00000	252	252	2159	0.00005	0.000504	0.00000	7.47E-05	4,282,978
5000	0.0000	0.0006	0.00004	0.00000	175	252	2159	0.00005	0.000504	0.00000	7.47E-05	4,282,978
10000	0.0000	0.0012	0.00008	0.00000	350	252	2159	0.00005	0.000504	0.00000	7.47E-05	4,282,978
15000	0.0001	0.0018	0.00011	0.00001	525	252	2159	0.00005	0.000504	0.00000	7.47E-05	4,282,978
20000	0.0002	0.0026	0.00016	0.00002	700	252	2159	0.00005	0.000504	0.00000	7.47E-05	4,282,978
25000	0.0003	0.0032	0.00020	0.00002	875	252	2159	0.00005	0.000504	0.00000	7.47E-05	4,282,978
30000	0.0003	0.0038	0.00023	0.00003	1050	252	2159	0.00005	0.000504	0.00000	7.47E-05	4,282,978
35000	0.0004	0.0044	0.00028	0.00003	1225	252	2159	0.00005	0.000504	0.00000	7.47E-05	4,282,978
40000	0.0005	0.0051	0.00032	0.00004	1400	252	2159	0.00005	0.000504	0.00000	7.47E-05	4,282,978
45000	0.0006	0.0058	0.00036	0.00005	1575	252	2159	0.00005	0.000504	0.00000	7.47E-05	4,282,978
50000	0.0007	0.0064	0.00040	0.00005	1750	252	2159	0.00005	0.000504	0.00000	7.47E-05	4,282,978
55000	0.0008	0.0072	0.00045	0.00006	1925	252	2159	0.00005	0.000504	0.00000	7.47E-05	4,282,978
60000	0.0009	0.0077	0.00048	0.00007	2100	252	2159	0.00005	0.000504	0.00000	7.47E-05	4,282,978
65000	0.0010	0.0085	0.00053	0.00008	2275	252	2159	0.00005	0.000504	0.00000	7.47E-05	4,282,978

Legend (left side): Load, Rdg$_R$, Rdg$_L$, ε_L, ε_R, σ, $\sigma_{0.00005}$, $\sigma_{40\%}$, $\varepsilon_{L,0.00005}$, $\varepsilon_{L,40\%}$, $\varepsilon_{R,0.00005}$, $\varepsilon_{R,40\%}$, Slope

Figure E-5
Measured and Calculated Modulus of Elasticity (28-Days, 0% RSR, Column 1)

213
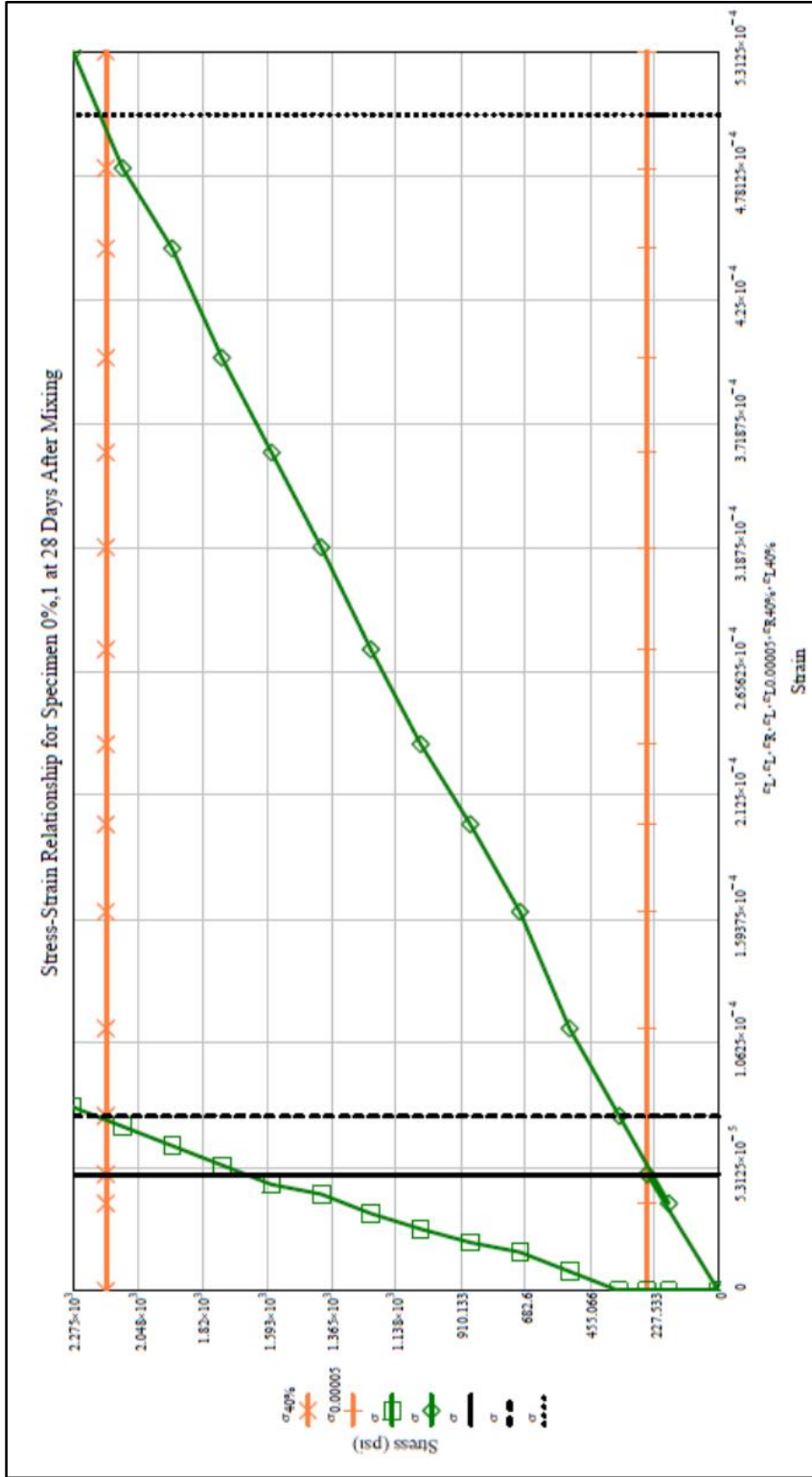
Figure E-6
Measured and Calculated Modulus of Elasticity (28-Days, 0% RSR, Column 1)

Stress-Strain Data for Specimen 0%,2 at 28 Days After Mixing

Load (lb)	Radial Dial (in.)	Long. Dial (in.)	Long. ε	Radial ε	σ (psi)	σ₀.₀₀₀₀₅ (psi)	σ₄₀% (psi)	Long. ε₀.₀₀₀₀₅	Long. ε₄₀%	Radial ε₀.₀₀₀₀₅	Radial ε₄₀%	Slope of σ-ε (psi)
0	0.0000	0.0000	0.00000	0.00000	0	267	2075	0.00005	0.000403	0.00000	6.46E-05	5,149,403
7700	0.0000	0.0008	0.00005	0.00000	267	267	2075	0.00005	0.000403	0.00000	6.46E-05	5,149,403
5000	0.0000	0.0005	0.00003	0.00000	173	267	2075	0.00005	0.000403	0.00000	6.46E-05	5,149,403
10000	0.0000	0.0010	0.00006	0.00000	347	267	2075	0.00005	0.000403	0.00000	6.46E-05	5,149,403
15000	0.0001	0.0015	0.00009	0.00001	520	267	2075	0.00005	0.000403	0.00000	6.46E-05	5,149,403
20000	0.0002	0.0021	0.00013	0.00002	693	267	2075	0.00005	0.000403	0.00000	6.46E-05	5,149,403
25000	0.0002	0.0025	0.00016	0.00002	866	267	2075	0.00005	0.000403	0.00000	6.46E-05	5,149,403
30000	0.0003	0.0031	0.00019	0.00002	1040	267	2075	0.00005	0.000403	0.00000	6.46E-05	5,149,403
35000	0.0004	0.0037	0.00023	0.00003	1213	267	2075	0.00005	0.000403	0.00000	6.46E-05	5,149,403
40000	0.0005	0.0043	0.00027	0.00004	1386	267	2075	0.00005	0.000403	0.00000	6.46E-05	5,149,403
45000	0.0005	0.0048	0.00030	0.00004	1560	267	2075	0.00005	0.000403	0.00000	6.46E-05	5,149,403
50000	0.0006	0.0053	0.00033	0.00005	1733	267	2075	0.00005	0.000403	0.00000	6.46E-05	5,149,403
55000	0.0007	0.0059	0.00037	0.00006	1906	267	2075	0.00005	0.000403	0.00000	6.46E-05	5,149,403
60000	0.0008	0.0064	0.00040	0.00006	2080	267	2075	0.00005	0.000403	0.00000	6.46E-05	5,149,403
65000	0.0009	0.0070	0.00044	0.000007	2253	267	2075	0.00005	0.000403	0.00000	6.46E-05	5,149,403

Figure E-7
Measured and Calculated Modulus of Elasticity (28-Days, 0% RSR, Column 2)
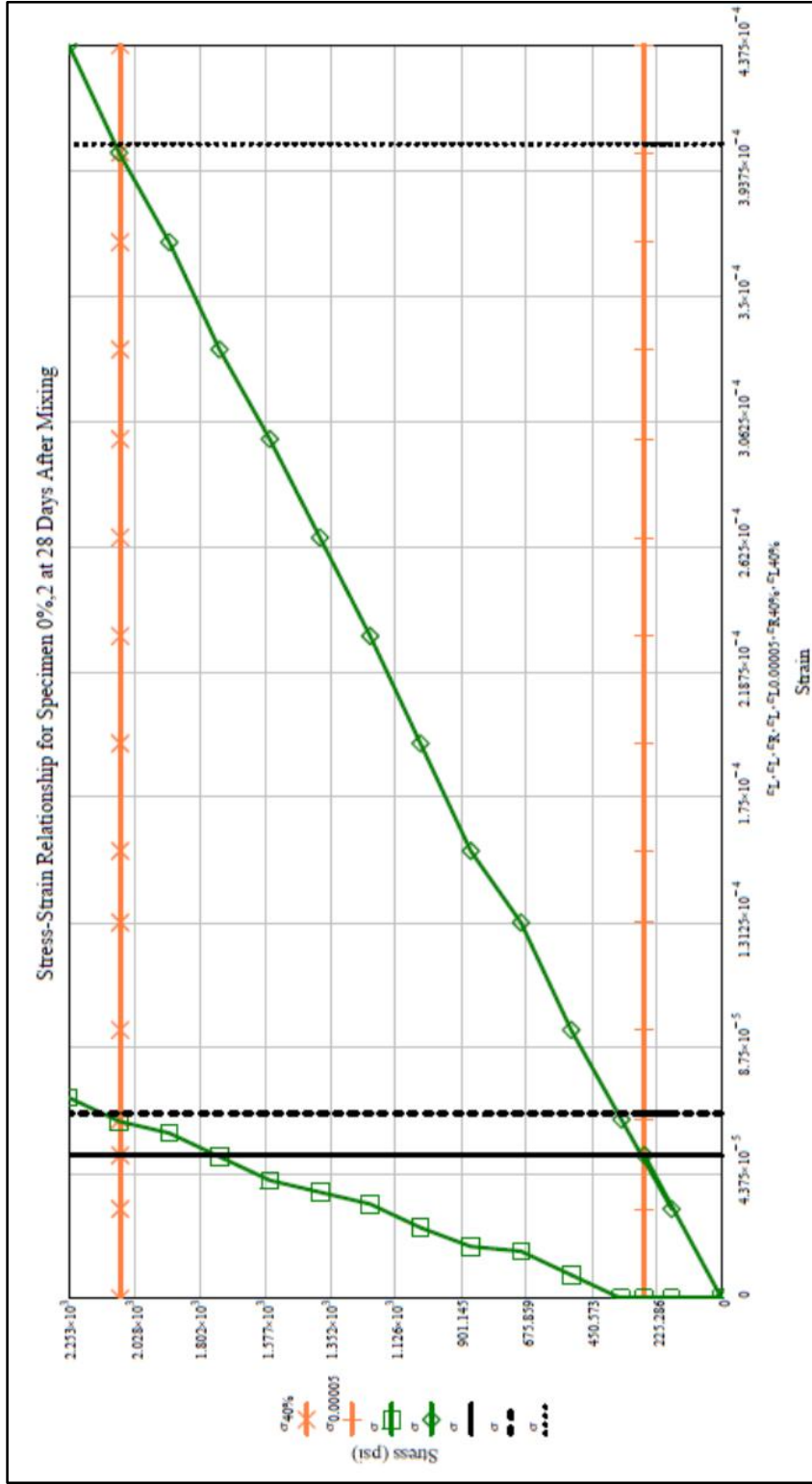
Figure E-8
Measured and Calculated Modulus of Elasticity (28-Days, 0% RSR, Column 2)

216

Stress-Strain Data for Specimen 0.5%,1 at 28 Days After Mixing

Load (lb)	Radial Dial (in.)	Long. Dial (in.)	Long. ε	Radial ε	σ (psi)	σ0.00005 (psi)	σ40% (psi)	Long. ε0.00005	Long. ε40%	Radial ε0.00005	Radial ε40%	Slope of σ-ε (psi)
0	0.0000	0.0000	0.00000	0.00000	0	157	666	0.00005	0.00021	0.00000	3.16E-05	3,169,657
4500	0.0000	0.0008	0.00005	0.00000	157	157	666	0.00005	0.00021	0.00000	3.16E-05	3,169,657
5000	0.0000	0.0009	0.00006	0.00000	174	157	666	0.00005	0.00021	0.00000	3.16E-05	3,169,657
10000	0.0001	0.0017	0.00011	0.00001	349	157	666	0.00005	0.00021	0.00000	3.16E-05	3,169,657
15000	0.0002	0.0025	0.00016	0.00002	523	157	666	0.00005	0.00021	0.00000	3.16E-05	3,169,657
20000	0.0004	0.0034	0.00021	0.00003	697	157	666	0.00005	0.00021	0.00000	3.16E-05	3,169,657
25000	0.0005	0.0044	0.00028	0.00004	872	157	666	0.00005	0.00021	0.00000	3.16E-05	3,169,657

Load
RdgR
RdgL
εL
εR
σ
σ0.00005
σ40%
εL0.00005
εL40%
εR0.00005
εR40%
Slope

Figure E-9
Measured and Calculated Modulus of Elasticity (28-Days, 0.5% RSR, Column 1)

217
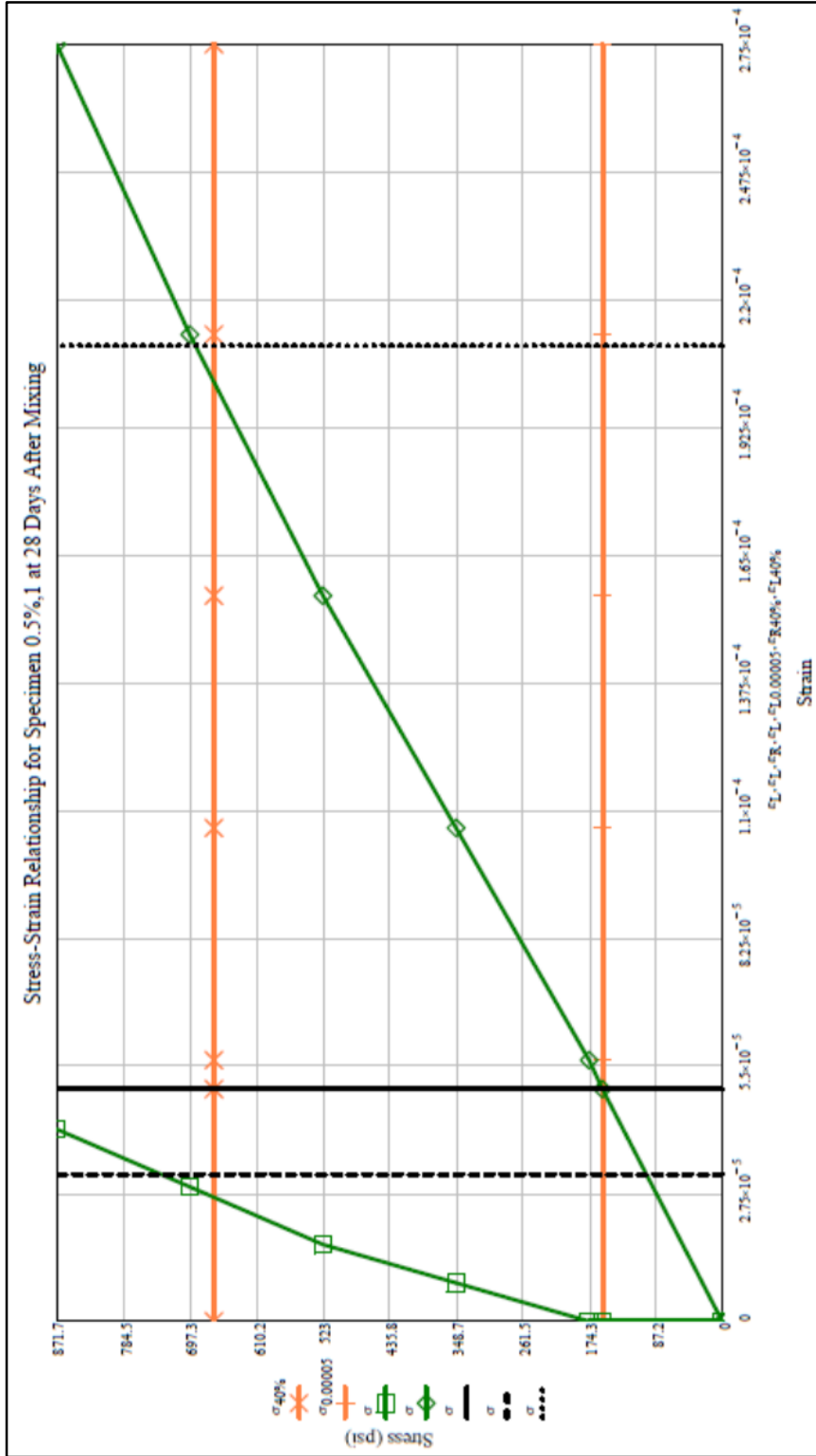
Figure E-10
Measured and Calculated Modulus of Elasticity (28-Days, 0.5% RSR, Column 1)

Stress-Strain Data for Specimen 0.5%, 2 at 28 Days After Mixing

Load (lb)	Radial Dial (in.)	Long. Dial (in.)	Long. ε	Radial ε	σ (psi)	$\sigma_{0.00005}$ (psi)	$\sigma_{40\%}$ (psi)	Long. $\varepsilon_{0.00005}$	Long. $\varepsilon_{40\%}$	Radial $\varepsilon_{0.00005}$	Radial $\varepsilon_{40\%}$	Slope of σ-ε (psi)
0	0.0000	0.0000	0.00000	0.00000	0	133	687	0.00005	0.000211	0.00000	2.6E-05	3,262,237
3800	0.0000	0.0008	0.00005	0.00000	133	133	687	0.00005	0.000211	0.00000	2.6E-05	3,262,237
5000	0.0000	0.0008	0.00005	0.00000	175	133	687	0.00005	0.000211	0.00000	2.6E-05	3,262,237
10000	0.0000	0.0015	0.00009	0.00000	351	133	687	0.00005	0.000211	0.00000	2.6E-05	3,262,237
15000	0.0001	0.0023	0.00014	0.00001	526	133	687	0.00005	0.000211	0.00000	2.6E-05	3,262,237
20000	0.0003	0.0035	0.00022	0.00002	701	133	687	0.00005	0.000211	0.00000	2.6E-05	3,262,237
25000	0.0004	0.0043	0.00027	0.00003	877	133	687	0.00005	0.000211	0.00000	2.6E-05	3,262,237

Figure E-11
Measured and Calculated Modulus of Elasticity (28-Days, 0.5% RSR, Column 2)

219
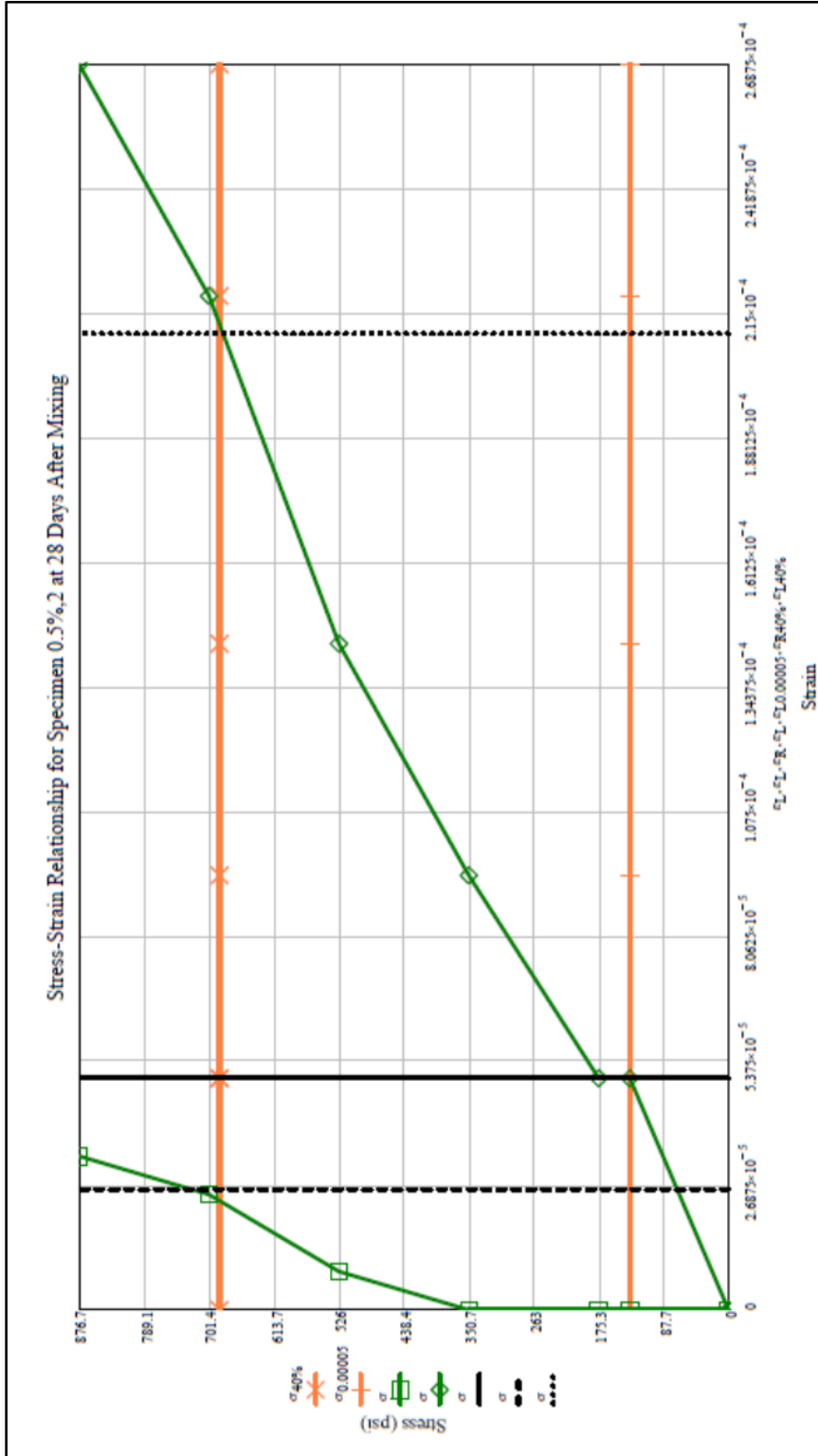
Figure E-12
Measured and Calculated Modulus of Elasticity (28-Days, 0.5% RSR, Column 2)

Stress-Strain Data for Specimen 1%,1 at 28 Days After Mixing

Load (lb)	Radial Dial (in.)	Long. Dial (in.)	Long. ε	Radial ε	σ (psi)	$\sigma_{0.00005}$ (psi)	$\sigma_{40\%}$ (psi)	Long. $\varepsilon_{0.00005}$	Long. $\varepsilon_{40\%}$	Radial $\varepsilon_{0.00005}$	Radial $\varepsilon_{40\%}$	Slope of σ-ε (psi)
0	0.0000	0.0000	0.00000	0.00000	0	129	480	0.00005	0.000185	0.00000	3.7E-05	2,599,425
3700	0.0000	0.0006	0.00005	0.00000	129	129	480	0.00005	0.000185	0.00000	3.7E-05	2,599,425
5000	0.0002	0.0011	0.00007	0.00002	175	129	480	0.00005	0.000185	0.00000	3.7E-05	2,599,425
10000	0.0004	0.0020	0.00013	0.00003	349	129	480	0.00005	0.000185	0.00000	3.7E-05	2,599,425
15000	0.0005	0.0032	0.00020	0.00004	524	129	480	0.00005	0.000185	0.00000	3.7E-05	2,599,425
20000	0.0007	0.0043	0.00027	0.00005	699	129	480	0.00005	0.000185	0.00000	3.7E-05	2,599,425

Load
Rdg$_R$
Rdg$_L$
ε_L
ε_R
σ
$\sigma_{0.00005}$
$\sigma_{40\%}$
$\varepsilon_{L,0.00005}$
$\varepsilon_{L,40\%}$
$\varepsilon_{R,0.00005}$
$\varepsilon_{R,40\%}$
Slope

Figure E-13
Measured and Calculated Modulus of Elasticity (28-Days, 1% RSR, Column 1)

221
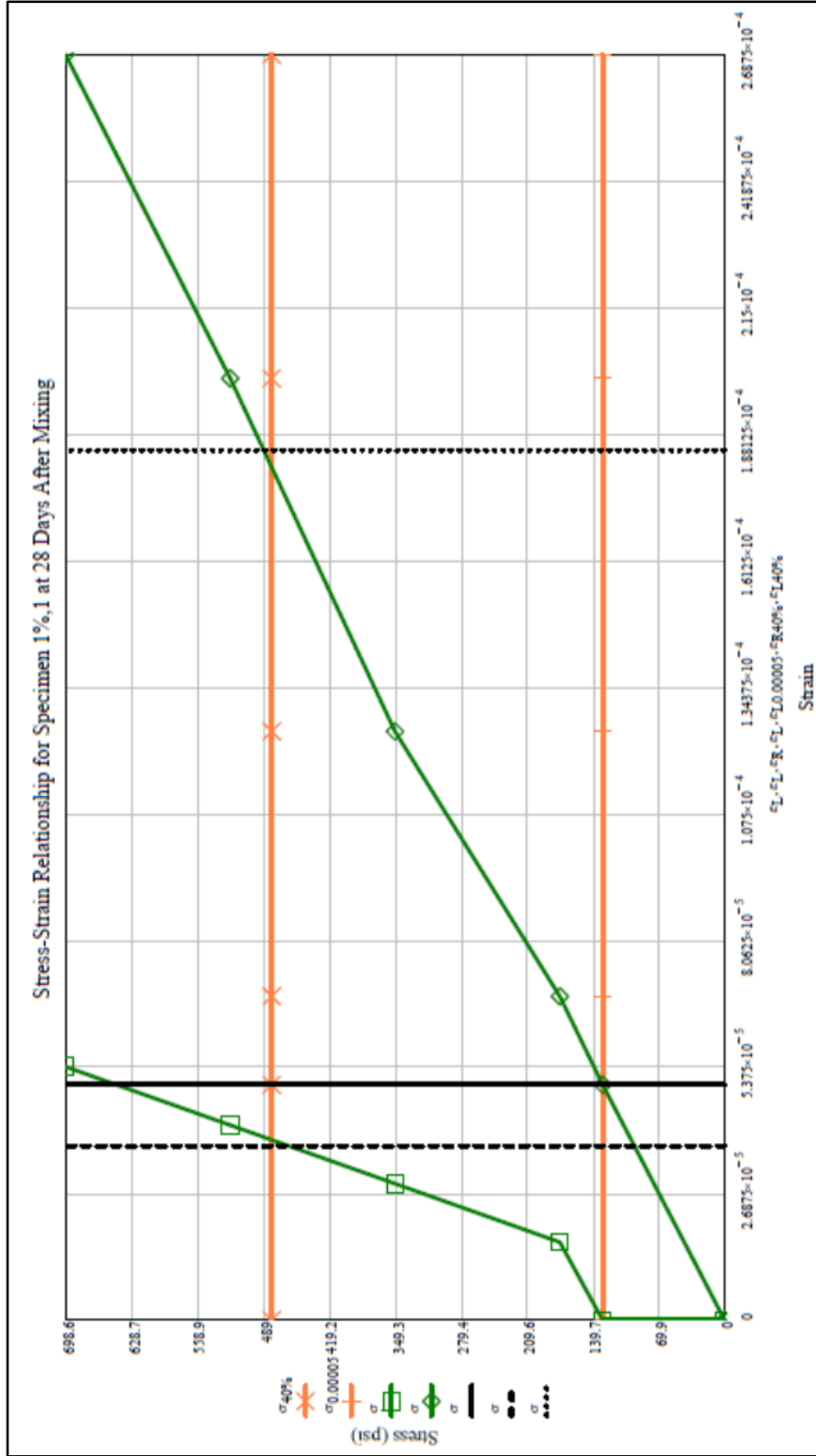
Figure E-14
Measured and Calculated Modulus of Elasticity (28-Days, 1% RSR, Column 1)

Stress-Strain Data for Specimen 1%,2 at 28 Days After Mixing

Load (lb)	Radial Dial (in.)	Long. Dial (in.)	Long. ε	Radial ε	σ (psi)	$\sigma_{0.00005}$ (psi)	$\sigma_{40\%}$ (psi)	Long. $\varepsilon_{0.00005}$	Long. $\varepsilon_{40\%}$	Radial $\varepsilon_{0.00005}$	Radial $\varepsilon_{40\%}$	Slope of σ-ε (psi)
0	0.0000	0.0000	0.00000	0.00000	0	129	404	0.00005	0.000166	0.00000	2.87E-05	2,432,314
3700	0.0000	0.0008	0.00005	0.00000	129	129	404	0.00005	0.000166	0.00000	2.87E-05	2,432,314
5000	0.0002	0.0010	0.00006	0.00001	175	129	404	0.00005	0.000166	0.00000	2.87E-05	2,432,314
10000	0.0003	0.0022	0.00013	0.00002	350	129	404	0.00005	0.000166	0.00000	2.87E-05	2,432,314
15000	0.0005	0.0033	0.00021	0.00004	524	129	404	0.00005	0.000166	0.00000	2.87E-05	2,432,314
20000	0.0006	0.0046	0.00029	0.00005	699	129	404	0.00005	0.000166	0.00000	2.87E-05	2,432,314

Load
Rdε_R
Rdε_L
ε_L
ε_R
σ
$\sigma_{0.00005}$
$\sigma_{40\%}$
$\varepsilon_{L0.00005}$
$\varepsilon_{L40\%}$
$\varepsilon_{R0.00005}$
$\varepsilon_{R40\%}$
Slope

Figure E-15
Measured and Calculated Modulus of Elasticity (28-Days, 1% RSR, Column 2)
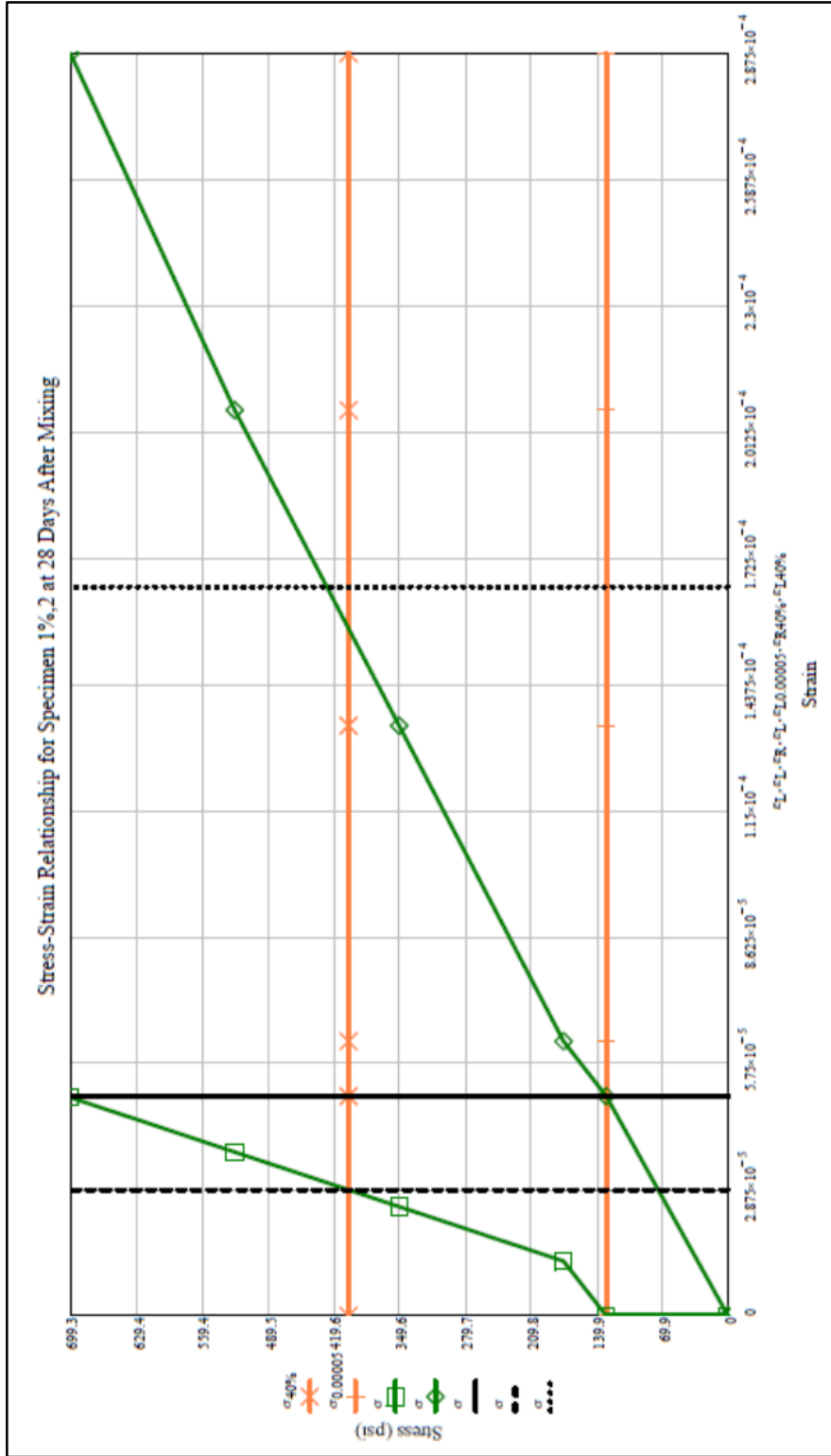
Figure E-16
Measured and Calculated Modulus of Elasticity (28-Days, 1% RSR, Column 2)

Stress-Strain Data for Specimen 2%, 1 at 28 Days After Mixing

Load (lb)	Radial Dial (in.)	Long. Dial (in.)	Long. ε	Radial ε	σ (psi)	$\sigma_{0.00005}$ (psi)	$\sigma_{40\%}$ (psi)	Long. $\varepsilon_{0.00005}$	Long. $\varepsilon_{40\%}$	Radial $\varepsilon_{0.00005}$	Radial $\varepsilon_{40\%}$	Slope of σ-ε (psi)
0	0.0000	0.0000	0.00000	0.00000	0	158	487	0.00005	0.000173	0.00000	2.59E-05	2,806,455
4500	0.0000	0.0008	0.00005	0.00000	158	158	487	0.00005	0.000173	0.00000	2.59E-05	2,806,455
5000	0.0000	0.0010	0.00006	0.00000	175	158	487	0.00005	0.000173	0.00000	2.59E-05	2,806,455
10000	0.0002	0.0018	0.00011	0.00001	351	158	487	0.00005	0.000173	0.00000	2.59E-05	2,806,455
15000	0.0003	0.0030	0.00019	0.00002	526	158	487	0.00005	0.000173	0.00000	2.59E-05	2,806,455
20000	0.0005	0.0040	0.00025	0.00004	702	158	487	0.00005	0.000173	0.00000	2.59E-05	2,806,455

Load
$Rd\varepsilon_R$
$Rd\varepsilon_L$
ε_L
ε_R
σ
$\sigma_{0.00005}$
$\sigma_{40\%}$
$\varepsilon_{L0.00005}$
$\varepsilon_{L40\%}$
$\varepsilon_{R0.00005}$
$\varepsilon_{R40\%}$
Slope

Figure E-17
Measured and Calculated Modulus of Elasticity (28-Days, 2% RSR, Column 1)
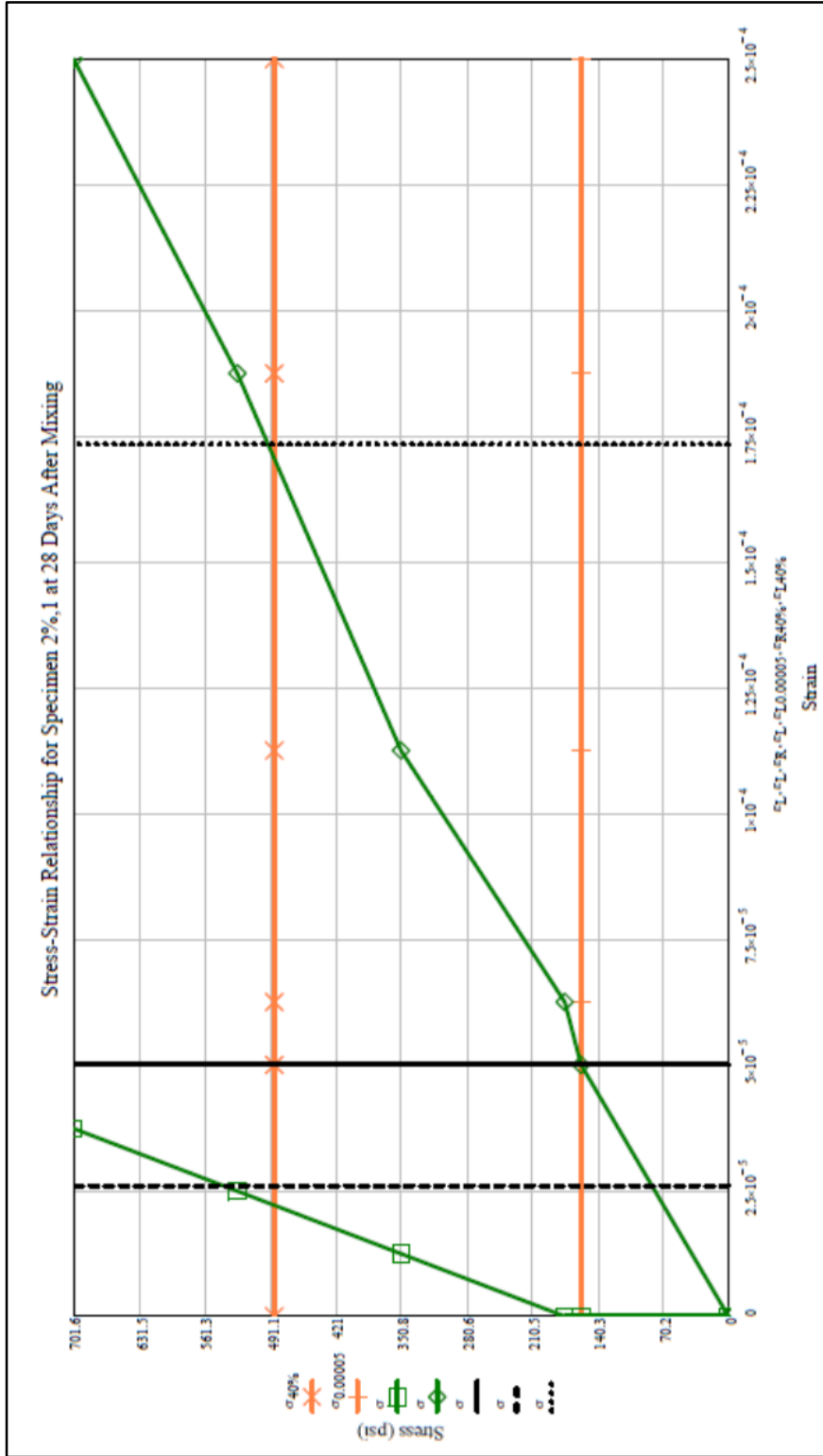
Figure E-18
Measured and Calculated Modulus of Elasticity (28-Days, 2% RSR, Column 1)

Stress-Strain Data for Specimen 2%,2 at 28 Days After Mixing

Load (lb)	Radial Dial (in.)	Long. Dial (in.)	Long. ε	Radial ε	σ (psi)	$\sigma_{0.00005}$ (psi)	$\sigma_{40\%}$ (psi)	Long. $\varepsilon_{0.00005}$	Long. $\varepsilon_{40\%}$	Radial $\varepsilon_{0.00005}$	Radial $\varepsilon_{40\%}$	Slope of σ-ε (psi)
0	0.0000	0.0000	0.00000	0.00000	0	122	493	0.00005	0.000243	0.00000	4.09E-05	2,034,636
3500	0.0000	0.0008	0.00005	0.00000	122	122	493	0.00005	0.000243	0.00000	4.09E-05	2,034,636
5000	0.0002	0.0012	0.00008	0.00002	175	122	493	0.00005	0.000243	0.00000	4.09E-05	2,034,636
10000	0.0003	0.0025	0.00016	0.00002	350	122	493	0.00005	0.000243	0.00000	4.09E-05	2,034,636
15000	0.0006	0.0040	0.00025	0.00005	525	122	493	0.00005	0.000243	0.00000	4.09E-05	2,034,636
20000	0.0007	0.0055	0.00034	0.00006	699	122	493	0.00005	0.000243	0.00000	4.09E-05	2,034,636

Load
$Rd\varepsilon_R$
$Rd\varepsilon_L$
ε_L
ε_R
σ
$\sigma_{0.00005}$
$\sigma_{40\%}$
$\varepsilon_{L0.00005}$
$\varepsilon_{L40\%}$
$\varepsilon_{R0.00005}$
$\varepsilon_{R40\%}$
Slope

Figure E-19
Measured and Calculated Modulus of Elasticity (28-Days, 2% RSR, Column 2)
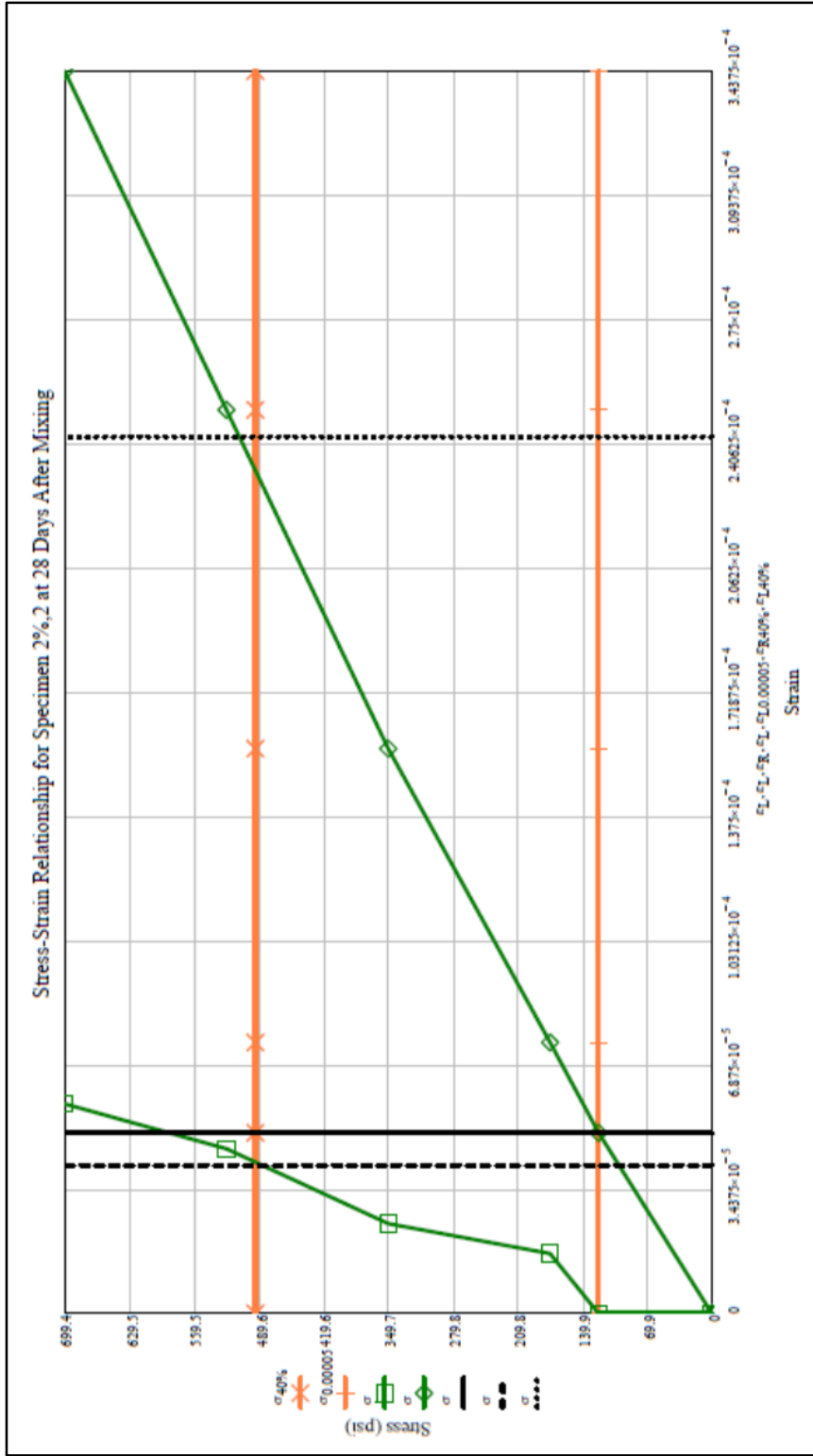
Figure E-20
Measured and Calculated Modulus of Elasticity (28-Days, 2% RSR, Column 2)

Mechanical Testing (260-Day)

260 Day Modulus of Elasticity Testing

RSR#, #	Wt (lbs)	Dia1 (in.)	Dia2 (in.)	Ave Dia (in.)	Radius (in.)	Area (in.²)	Ht (in.)	Unit Wt. (in.3)	Ult. Load (lbs.)	f'c (psi)	Rnd. f'c (psi)	Failure Type	P 0.00005 (lbf)	P 40% (lbf)	σ 0.00005 (psi)	σ 40% (psi)	Long. ε 0.00005	Long. ε 40%	Radial ε 0.00005	Radial ε 40%	Chord MOE (psi)	Poisson's Ratio
0,3	28.100	6.044	6.046	6.045	3.02	28.70	11.95	141.6	216,630	7,548	7,550	cone and shear	9165	86,652	319	3019	0.00005	0.000542	0.00000	0.000125	5500000	0.26
0,4	28.160	6.052	6.046	6.049	3.02	28.74	12.01	141.0	214,810	7,475	7,470	cone and shear	7700	85,924	268	2990	0.00005	0.00051	0.00000	0.000124	5900000	0.27
0.5,3	25.200	6.048	6.054	6.051	3.03	28.76	12.02	125.9	72,250	2,512	2,510	cone	5410	28,900	188	1005	0.00005	0.000301	0.00000	0.000064	3250000	0.25
0.5,4	25.340	6.045	6.056	6.051	3.03	28.75	12.04	126.5	70,440	2,450	2,450	cone	6595	28,176	229	980	0.00005	0.000258	0.00000	0.000047	3600000	0.22
1,3	23.690	6.038	6.048	6.043	3.02	28.68	12.03	118.6	57,455	2,003	2,000	cone	3625	22,982	126	801	0.00005	0.000364	0.00000	0.000063	2150000	0.2
1,4	23.740	6.052	6.040	6.046	3.02	28.71	12.01	119.0	54,920	1,913	1,910	cone	4855	21,968	169	765	0.00005	0.000284	0.00000	0.000036	2550000	0.16
2,3	24.110	6.044	6.032	6.038	3.02	28.63	12.04	120.8	51,280	1,791	1,790	cone	4295	20,512	150	716	0.00005	0.000316	0.00000	0.000057	2150000	0.21
2,4	23.780	6.036	6.046	6.041	3.02	28.66	12.05	118.9	54,905	1,916	1,920	cone	3490	21,962	122	766	0.00005	0.000339	0.00000	0.000067	2250000	0.23

Individual Results

Date of Testing: 12/2/2017
Testing technician: David B. Scott, Ross Newsome
Curing method: lime bath and long period of air exposure
Specimen age: 260 days

ID: 0,3

Load (lb)	Radial Dial (in.)	Long. Dial (in.)
0	0.0000	0.0000
9165		
5000	0.0001	0.0004
10000	0.0002	0.0010
15000	0.0003	0.0014
20000	0.0004	0.0019
25000	0.0004	0.0024
30000	0.0005	0.0029
35000	0.0006	0.0035
40000	0.0007	0.0040
45000		
50000		
55000		
60000		
65000		
70000		

ID: 0,4

Load (lb)	Radial Dial (in.)	Long. Dial (in.)
0	0.0000	0.0000
7700		
5000	0.0001	0.0004
10000	0.0002	0.0009
15000	0.0003	0.0013
20000	0.0003	0.0018
25000	0.0004	0.0023
30000	0.0005	0.0028
35000	0.0006	0.0033
40000	0.0007	0.0038
45000		
50000		
55000		
60000		
65000		
70000		

ID: 0.5,3

Load (lb)	Radial Dial (in.)	Long. Dial (in.)
0	0.0000	0.0000
3410		
5000	0.0001	0.0008
10000	0.0002	0.0016
15000	0.0004	0.0025
20000		
25000		
30000		
35000		
40000		
45000		
50000		
55000		
60000		
65000		
70000		

ID: 0.5,4

Load (lb)	Radial Dial (in.)	Long. Dial (in.)
0	0.0000	0.0000
6595		
5000	0.0001	0.0005
10000	0.0002	0.0014
15000	0.0003	0.0022
20000		
25000		
30000		
35000		
40000		
45000		
50000		
55000		
60000		
65000		
70000		

ID: 1,3

Load (lb)	Radial Dial (in.)	Long. Dial (in.)
0	0.0000	0.0000
3625		
5000	0.0002	0.0014
10000	0.0004	0.0028
15000	0.0005	0.0038
20000		
25000		
30000		
35000		
40000		
45000		
50000		
55000		
60000		
65000		
70000		

ID: 1,4

Load (lb)	Radial Dial (in.)	Long. Dial (in.)
0	0.0000	0.0000
4855		
5000	0.0000	0.0008
10000	0.0001	0.0020
15000	0.0003	0.0031
20000		
25000		
30000		
35000		
40000		
45000		
50000		
55000		
60000		
65000		
70000		

ID: 2,3

Load (lb)	Radial Dial (in.)	Long. Dial (in.)
0	0.0000	0.0000
4295		
5000	0.0001	0.0010
10000	0.0003	0.0023
15000	0.0005	0.0037
20000		
25000		
30000		
35000		
40000		
45000		
50000		
55000		
60000		
65000		
70000		

ID: 2,4

Load (lb)	Radial Dial (in.)	Long. Dial (in.)
0	0.0000	0.0000
3490		
5000	0.0002	0.0012
10000	0.0004	0.0023
15000	0.0006	0.0037
20000		
25000		
30000		
35000		
40000		
45000		
50000		
55000		
60000		
65000		
70000		

Figure E-21
Measured and Calculated Modulus of Elasticity (260-Days)

Stress-Strain Data for Specimen 0%,3 at 260 Days After Mixing

Load (lb)	Radial Dial (in.)	Long. Dial (in.)	Long. ε	Radial ε	σ (psi)	$\sigma_{0.00005}$ (psi)	$\sigma_{40\%}$ (psi)	Long. $\varepsilon_{0.00005}$	Long. $\varepsilon_{40\%}$	Radial $\varepsilon_{0.00005}$	Radial $\varepsilon_{40\%}$	Slope of σ-ε (psi)
0	0.0000	0.0000	0.00000	0.00000	0	251	3019	0.00005	0.000542	0.00000	0.000125	5,574,905
7200	0.0000	0.0008			251	251	3019	0.00005	0.000542	0.00000	0.000125	5,574,905
5000	0.0001	0.0004	0.00003	0.00001	174	251	3019	0.00005	0.000542	0.00000	0.000125	5,574,905
10000	0.0002	0.0010	0.00006	0.00002	348	251	3019	0.00005	0.000542	0.00000	0.000125	5,574,905
15000	0.0003	0.0014	0.00009	0.00002	523	251	3019	0.00005	0.000542	0.00000	0.000125	5,574,905
20000	0.0004	0.0019	0.00012	0.00003	697	251	3019	0.00005	0.000542	0.00000	0.000125	5,574,905
25000	0.0004	0.0024	0.00015	0.00003	871	251	3019	0.00005	0.000542	0.00000	0.000125	5,574,905
30000	0.0005	0.0029	0.00018	0.00004	1045	251	3019	0.00005	0.000542	0.00000	0.000125	5,574,905
35000	0.0006	0.0035	0.00022	0.00005	1220	251	3019	0.00005	0.000542	0.00000	0.000125	5,574,905
40000	0.0007	0.0040	0.00025	0.00006	1394	251	3019	0.00005	0.000542	0.00000	0.000125	5,574,905

Load
Rdg_R
Rdg_L
ε_L
ε_R
σ
$\sigma_{0.00005}$
$\sigma_{40\%}$
$\varepsilon_{L0.00005}$
$\varepsilon_{L40\%}$
$\varepsilon_{R0.00005}$
$\varepsilon_{R40\%}$
Slope

Figure E-22
Measured and Calculated Modulus of Elasticity (260-Days, 0% RSR, Column 3)
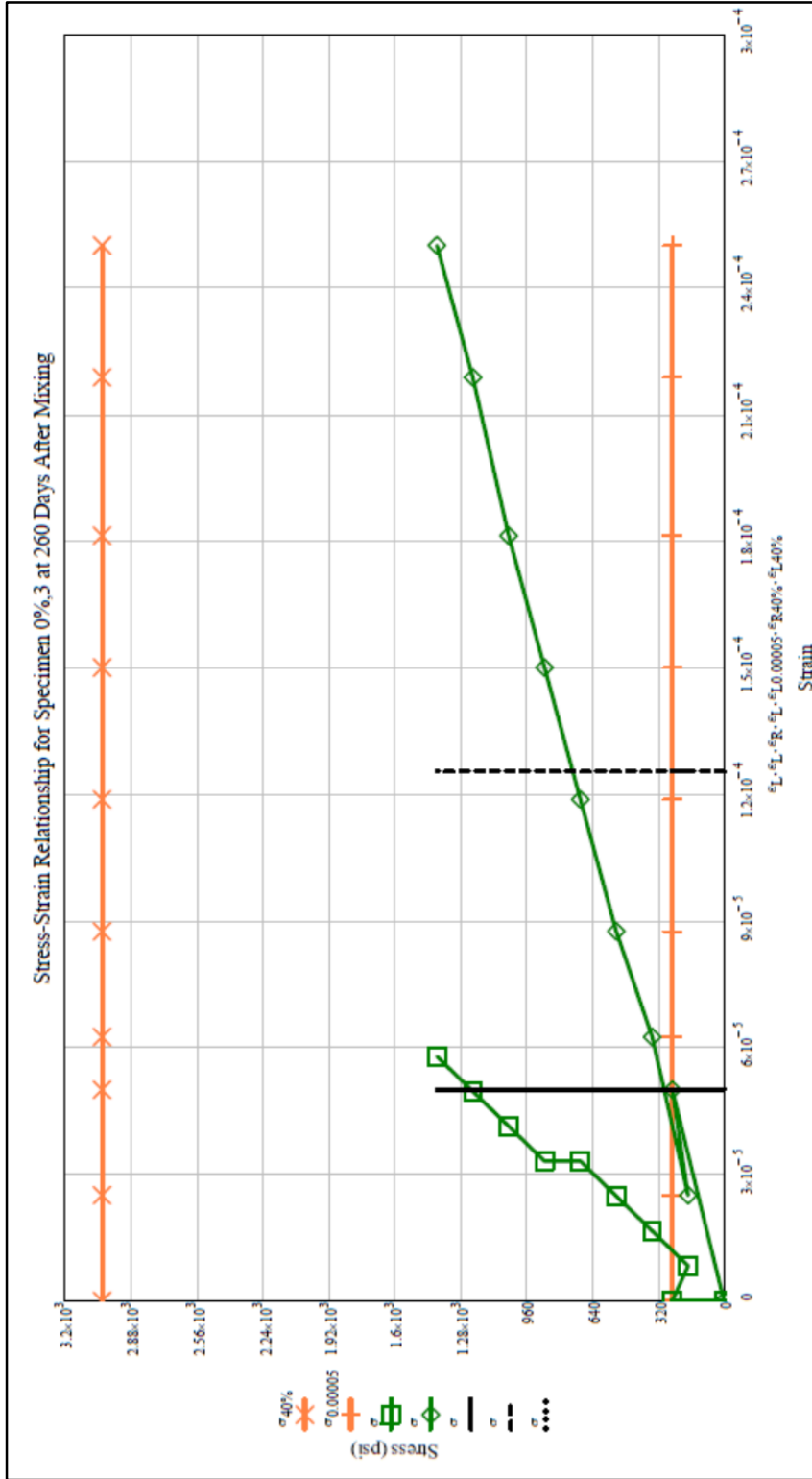
Figure E-23
Measured and Calculated Modulus of Elasticity (260-Days, 0% RSR, Column 3)

Stress-Strain Data for Specimen 0%,4 at 260 Days After Mixing

Load (lb)	Radial Dial (in.)	Long. Dial (in.)	Long. ε	Radial ε	σ (psi)	σ0.00005 (psi)	σ40% (psi)	Long. ε0.00005	Long. ε40%	Radial ε0.00005	Radial ε40%	Slope of σ-ε (psi)
0	0.0000	0.0000	0.00000	0.00000	0	268	2990	0.00005	0.00051	0.00000	0.0001124	5,860,563
7700	0.0000	0.0008	0.00005	0.00000	268	268	2990	0.00005	0.00051	0.00000	0.0001124	5,860,563
5000	0.0001	0.0004	0.00003	0.00001	174	268	2990	0.00005	0.00051	0.00000	0.0001124	5,860,563
10000	0.0002	0.0009	0.00006	0.00002	348	268	2990	0.00005	0.00051	0.00000	0.0001124	5,860,563
15000	0.0003	0.0013	0.00008	0.00002	522	268	2990	0.00005	0.00051	0.00000	0.0001124	5,860,563
20000	0.0003	0.0018	0.00011	0.00002	696	268	2990	0.00005	0.00051	0.00000	0.0001124	5,860,563
25000	0.0004	0.0023	0.00014	0.00003	870	268	2990	0.00005	0.00051	0.00000	0.0001124	5,860,563
30000	0.0005	0.0028	0.00018	0.00004	1044	268	2990	0.00005	0.00051	0.00000	0.0001124	5,860,563
35000	0.0006	0.0033	0.00021	0.00005	1218	268	2990	0.00005	0.00051	0.00000	0.0001124	5,860,563
40000	0.0007	0.0038	0.00024	0.00006	1392	268	2990	0.00005	0.00051	0.00000	0.0001124	5,860,563

Legend: Load, Rd ε_R, Rd ε_L, ε_L, ε_R, σ, $\sigma_{0.00005}$, $\sigma_{40\%}$, $\varepsilon_{L0.00005}$, $\varepsilon_{L40\%}$, $\varepsilon_{R0.00005}$, $\varepsilon_{R40\%}$, Slope

Figure E-24
Measured and Calculated Modulus of Elasticity (260-Days, 0% RSR, Column 4)

Figure E-25
Measured and Calculated Modulus of Elasticity (28-Days, 0% RSR, Column 4)

233

Stress-Strain Data for Specimen 0.5%,3 at 260 Days After Mixing

Load (lb)	Radial Dial (in.)	Long. Dial (in.)	Long. ε	Radial ε	σ (psi)	$\sigma_{0.00005}$ (psi)	$\sigma_{40\%}$ (psi)	Long. $\varepsilon_{0.00005}$	Long. $\varepsilon_{40\%}$	Radial $\varepsilon_{0.00005}$	Radial $\varepsilon_{40\%}$	Slope of σ-ε (psi)
0	0.0000	0.0000	0.00000	0.00000	0	156	1005	0.00005	0.000301	0.00000	6.37E-05	3,338,313
4500	0.0000	0.0008	0.00005	0.00000	156	156	1005	0.00005	0.000301	0.00000	6.37E-05	3,338,313
5000	0.0001	0.0008	0.00005	0.00001	174	156	1005	0.00005	0.000301	0.00000	6.37E-05	3,338,313
10000	0.0002	0.0016	0.00010	0.00002	348	156	1005	0.00005	0.000301	0.00000	6.37E-05	3,338,313
15000	0.0004	0.0025	0.00016	0.00003	522	156	1005	0.00005	0.000301	0.00000	6.37E-05	3,338,313

Load
$Rd_{\varepsilon R}$
$Rd_{\varepsilon L}$
ε_L
ε_R
σ
$\sigma_{0.00005}$
$\sigma_{40\%}$
$\varepsilon_{L0.00005}$
$\varepsilon_{L40\%}$
$\varepsilon_{R0.00005}$
$\varepsilon_{R40\%}$
Slope

Figure E-26
Measured and Calculated Modulus of Elasticity (260-Days, 0.5% RSR, Column 3)

234
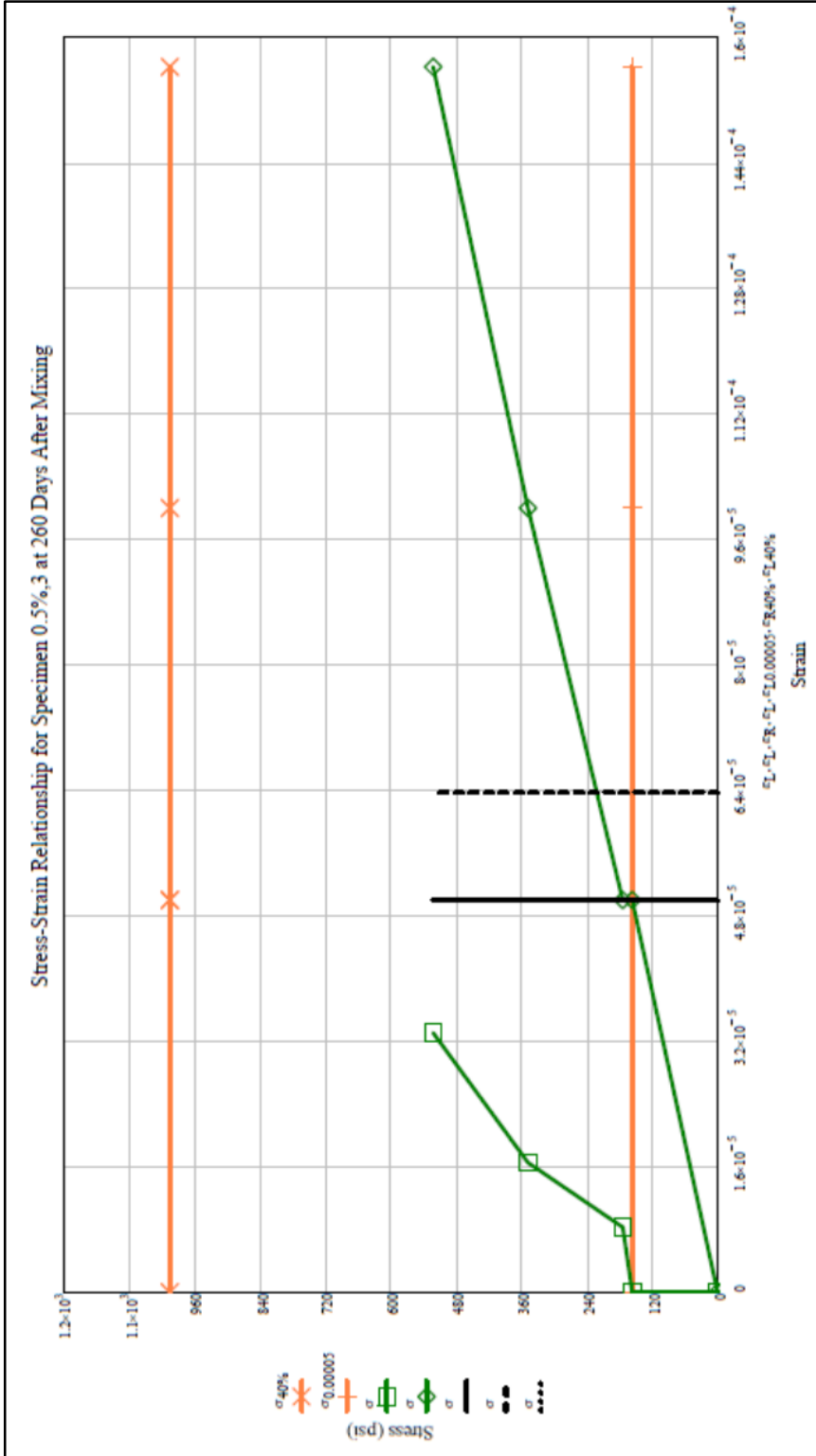
Figure E-27
Measured and Calculated Modulus of Elasticity (260-Days, 0.5% RSR, Column 3)

Stress-Strain Data for Specimen 0.5%,4 at 260 Days After Mixing

Load (lb)	Radial Dial (in.)	Long. Dial (in.)	Long. ε	Radial ε	σ (psi)	$\sigma_{0.00005}$ (psi)	$\sigma_{40\%}$ (psi)	Long. $\epsilon_{0.00005}$	Long. $\epsilon_{40\%}$	Radial $\epsilon_{0.00005}$	Radial $\epsilon_{40\%}$	Slope of σ-ε (psi)
0	0.0000	0.0000	0.00000	0.00000	0	132	980	0.00005	0.000258	0.00000	4.66E-05	3,794,164
3800	0.0000	0.0008	0.00005	0.00000	132	132	980	0.00005	0.000258	0.00000	4.66E-05	3,794,164
5000	0.0001	0.0005	0.00003	0.00001	174	132	980	0.00005	0.000258	0.00000	4.66E-05	3,794,164
10000	0.0002	0.0014	0.00009	0.00002	348	132	980	0.00005	0.000258	0.00000	4.66E-05	3,794,164
15000	0.0003	0.0022	0.00014	0.00002	522	132	980	0.00005	0.000258	0.00000	4.66E-05	3,794,164

Load
RdεR
RdεL
εL
εR
σ
σ0.00005
σ40%
εL0.00005
εL40%
εR0.00005
εR40%
Slope

Figure E-28
Measured and Calculated Modulus of Elasticity (260-Days, 0.5% RSR, Column 4)
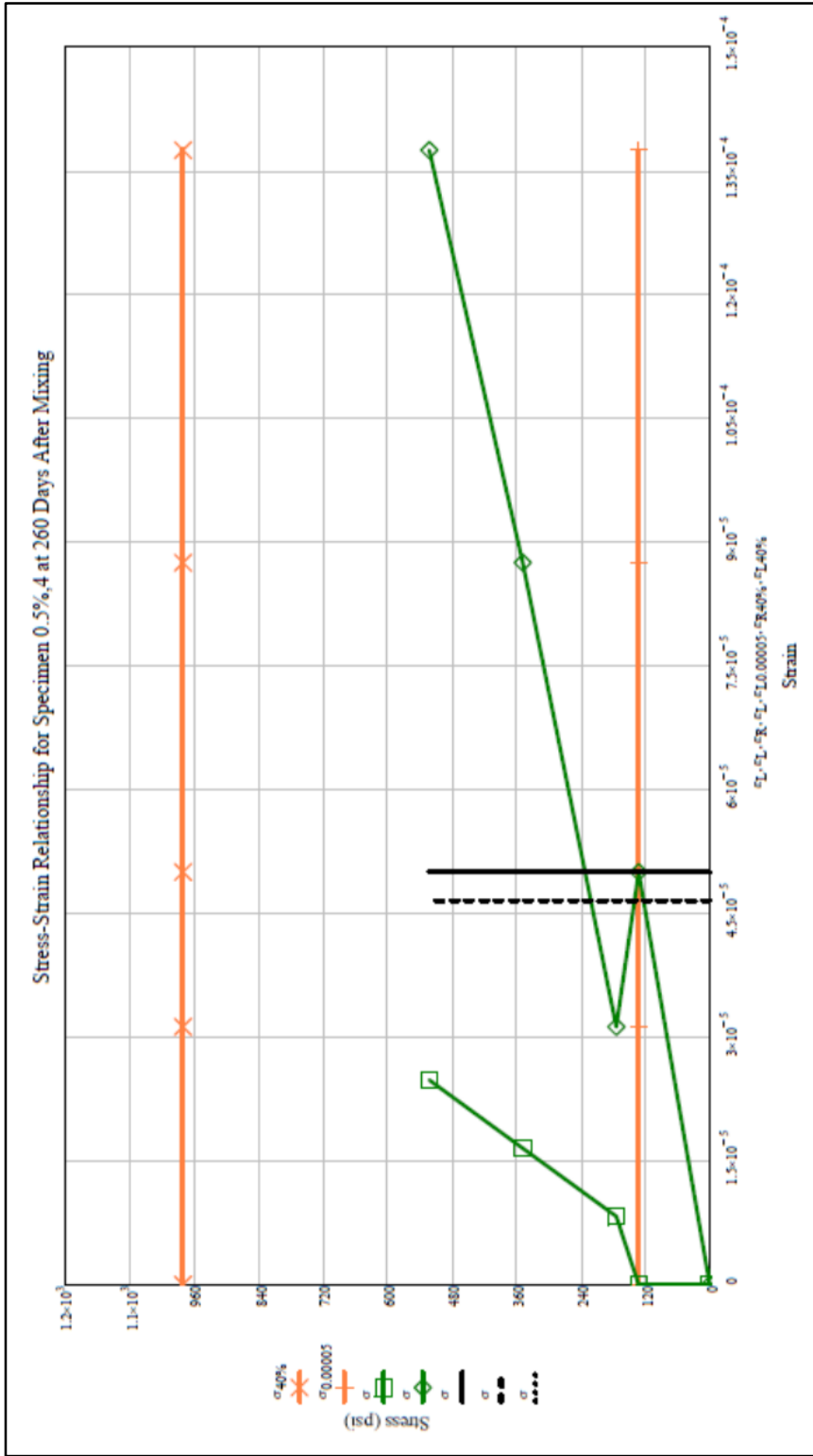
Figure E-29
Measured and Calculated Modulus of Elasticity (260-Days, 0.5% RSR, Column 4)

Stress-Strain Data for Specimen 1%,3 at 260 Days After Mixing

Load (lb)	Radial Dial (in.)	Long. Dial (in.)	Long. ε	Radial ε	σ (psi)	$\sigma_{0.00005}$ (psi)	$\sigma_{40\%}$ (psi)	Long. $\varepsilon_{0.00005}$	Long. $\varepsilon_{40\%}$	Radial $\varepsilon_{0.00005}$	Radial $\varepsilon_{40\%}$	Slope of σ-ε (psi)
0	0.0000	0.0000	0.00000	0.00000	0	129	801	0.00005	0.000364	0.000000	6.34E-05	2,202,077
3700	0.0000	0.0008	0.00005	0.00000	129	129	801	0.00005	0.000364	0.000000	6.34E-05	2,202,077
5000	0.0002	0.0014	0.00009	0.00002	174	129	801	0.00005	0.000364	0.00000	6.34E-05	2,202,077
10000	0.0004	0.0028	0.00018	0.00003	349	129	801	0.00005	0.000364	0.00000	6.34E-05	2,202,077
15000	0.0005	0.0038	0.00024	0.00004	523	129	801	0.00005	0.000364	0.00000	6.34E-05	2,202,077

Load
Rdg$_R$
Rdg$_L$
ε_L
ε_R
σ
$\sigma_{0.00005}$
$\sigma_{40\%}$
$\varepsilon_{L0.00005}$
$\varepsilon_{L40\%}$
$\varepsilon_{R0.00005}$
$\varepsilon_{R40\%}$
Slope

Figure E-30
Measured and Calculated Modulus of Elasticity (260-Days, 1% RSR, Column 3)
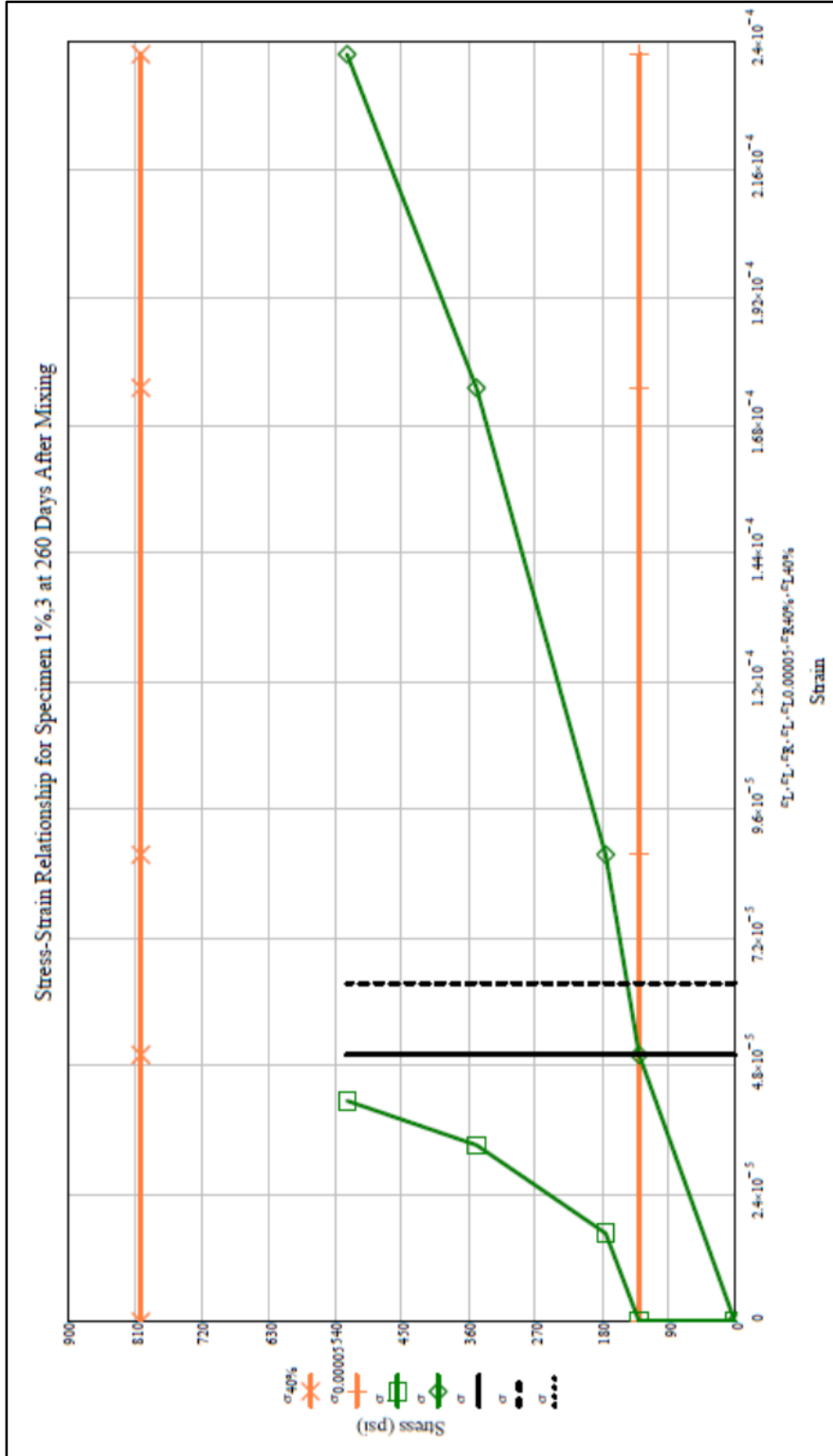
Figure E-31
Measured and Calculated Modulus of Elasticity (260-Days, 1% RSR, Column 3)

Stress-Strain Data for Specimen 1%,4 at 260 Days After Mixing

Load (lb)	Radial Dial (in.)	Long. Dial (in.)	Long. ε	Radial ε	σ (psi)	$\sigma_{0.00005}$ (psi)	$\sigma_{40\%}$ (psi)	Long. $\varepsilon_{0.00005}$	Long. $\varepsilon_{40\%}$	Radial $\varepsilon_{0.00005}$	Radial $\varepsilon_{40\%}$	Slope of σ-ε (psi)
0	0.0000	0.0000	0.00000	0.00000	0	129	765	0.00005	0.000284	0.00000	3.63E-05	2,696,643
3700	0.0000	0.0008	0.00005	0.00000	129	129	765	0.00005	0.000284	0.00000	3.63E-05	2,696,643
5000	0.0000	0.0008	0.00005	0.00000	174	129	765	0.00005	0.000284	0.00000	3.63E-05	2,696,643
10000	0.0001	0.0020	0.00013	0.00001	348	129	765	0.00005	0.000284	0.00000	3.63E-05	2,696,643
15000	0.0003	0.0031	0.00019	0.00002	522	129	765	0.00005	0.000284	0.00000	3.63E-05	2,696,643

Load
$Rd\varepsilon_R$
$Rd\varepsilon_L$
ε_L
ε_R
σ
$\sigma_{0.00005}$
$\sigma_{40\%}$
$\varepsilon_{L0.00005}$
$\varepsilon_{L40\%}$
$\varepsilon_{R0.00005}$
$\varepsilon_{R40\%}$
Slope

Figure E-32
Measured and Calculated Modulus of Elasticity (260-Days, 1% RSR, Column 4)
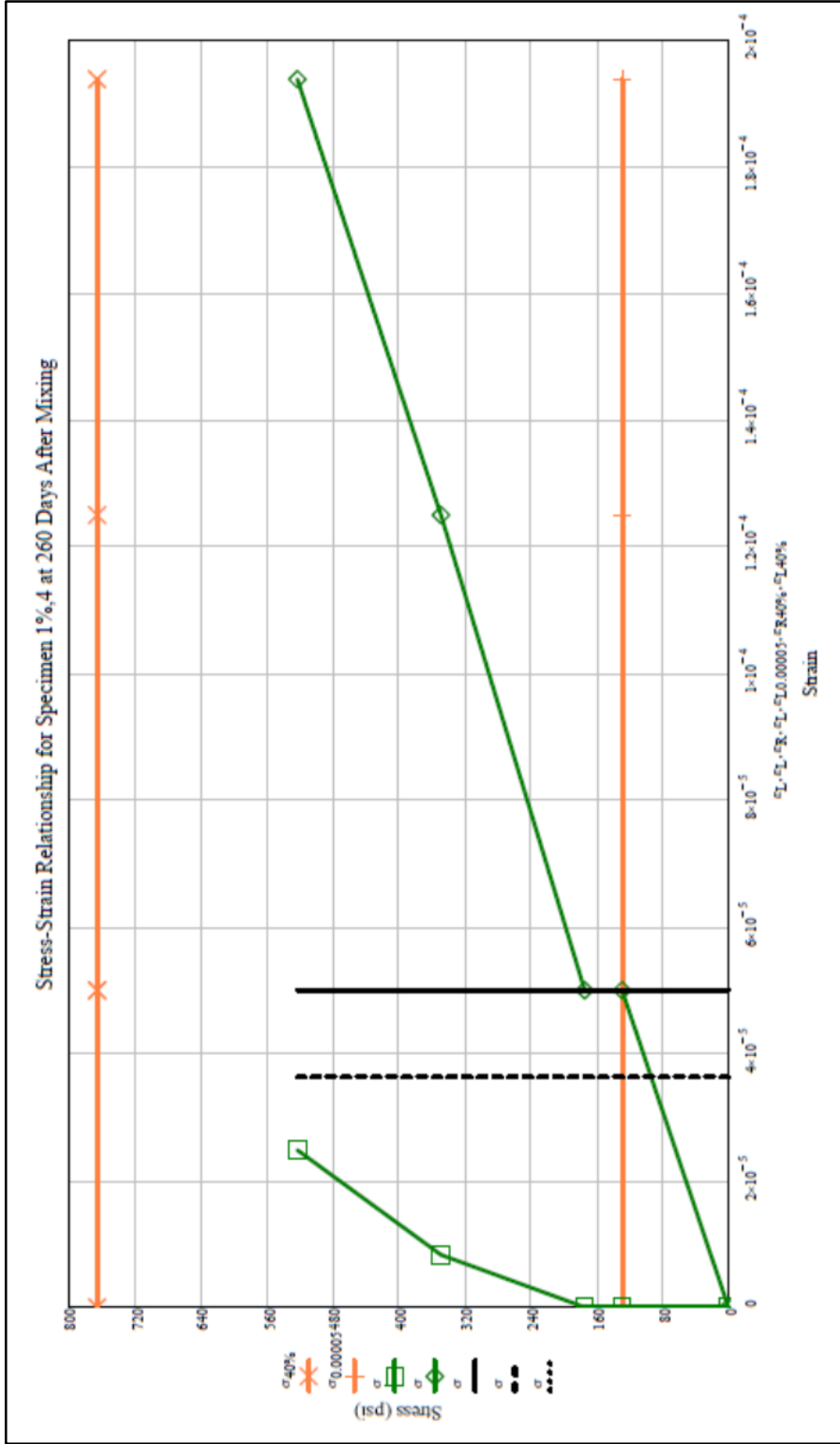
Figure E-33
Measured and Calculated Modulus of Elasticity (260-Days, 1% RSR, Column 4)

Stress-Strain Data for Specimen 2%,3 at 28 Days After Mixing

Load (lb)	Radial Dial (in.)	Long. Dial (in.)	Long. ε	Radial ε	σ (psi)	$\sigma_{0.00005}$ (psi)	$\sigma_{40\%}$ (psi)	Long. $E_{0.00005}$	Long. $E_{40\%}$	Radial $E_{0.00005}$	Radial $E_{40\%}$	Slope of σ-ε (psi)
0	0.0000	0.0000	0.00000	0.00000	0	157	716	0.00005	0.000316	0.00000	5.66E-05	2,265,340
4500	0.0000	0.0008	0.00005	0.00000	157	157	716	0.00005	0.000316	0.00000	5.66E-05	2,265,340
5000	0.0001	0.0010	0.00006	0.00001	175	157	716	0.00005	0.000316	0.00000	5.66E-05	2,265,340
10000	0.0003	0.0023	0.00014	0.00002	349	157	716	0.00005	0.000316	0.00000	5.66E-05	2,265,340
15000	0.0005	0.0037	0.00023	0.00004	524	157	716	0.00005	0.000316	0.00000	5.66E-05	2,265,340

Load
Rdε_R
Rdε_L
ε_L
ε_R
σ
σ_0.00005
σ_40%
ε_L0.00005
ε_L40%
ε_R0.00005
ε_R40%
Slope

Figure E-34
Measured and Calculated Modulus of Elasticity (260-Days, 2% RSR, Column 3)
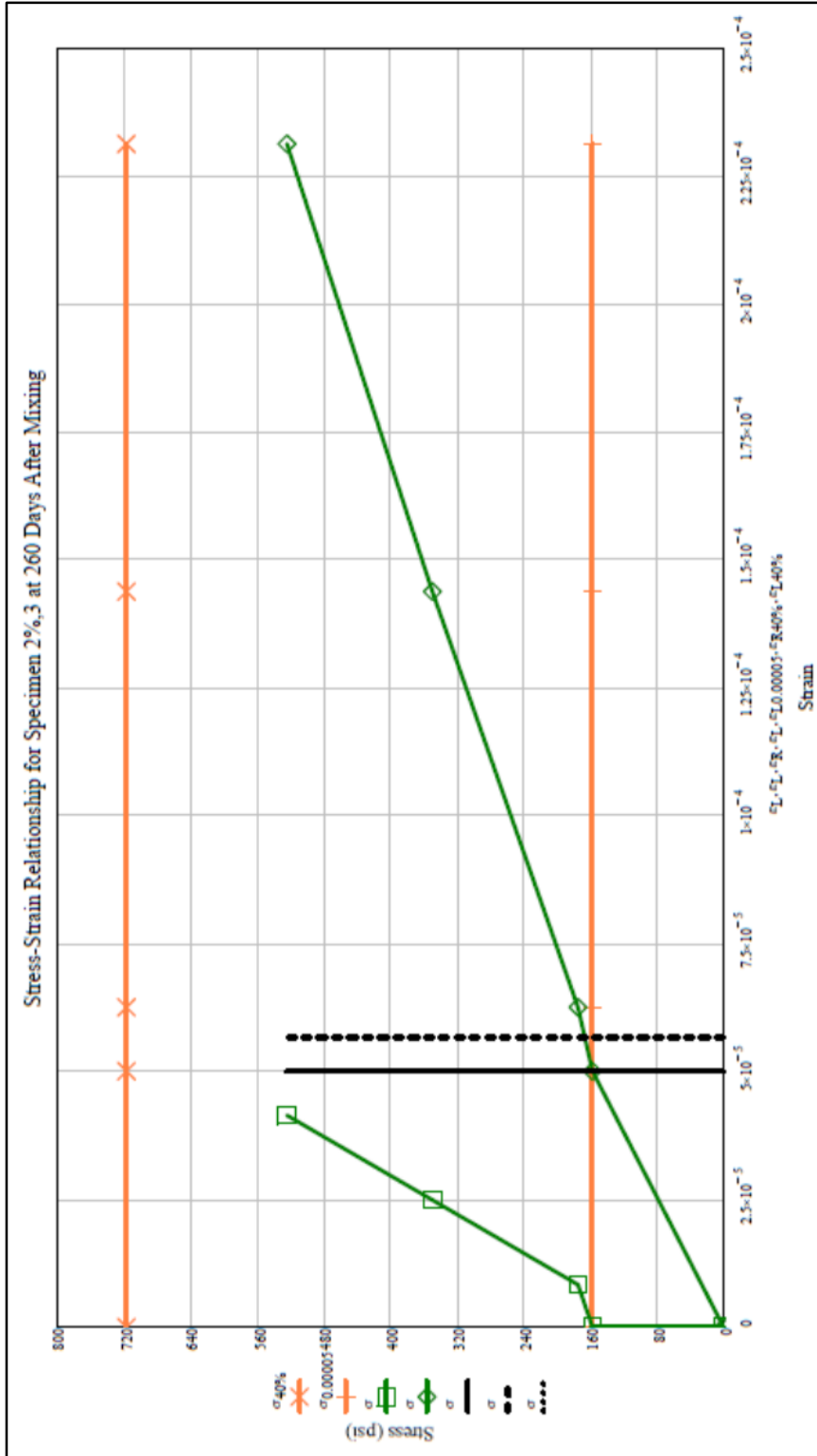
Figure E-35
Measured and Calculated Modulus of Elasticity (260-Days, 2% RSR, Column 3)

Stress-Strain Data for Specimen 2%,4 at 260 Days After Mixing

Load (lb)	Radial Dial (in.)	Long. Dial (in.)	Long. ε	Radial ε	σ (psi)	$\sigma_{0.00005}$ (psi)	$\sigma_{40\%}$ (psi)	Long. $E_{0.00005}$	Long. $E_{40\%}$	Radial $E_{0.00005}$	Radial $E_{40\%}$	Slope of σ-ε (psi)
0	0.0000	0.0000	0.00000	0.00000	0							
3490	0.0000	0.0008	0.00005	0.00000	122	122	766	0.00005	0.000339	0.00000	6.67E-05	2,263,091
5000	0.0002	0.0012	0.00008	0.00002	174	122	766	0.00005	0.000339	0.00000	6.67E-05	2,263,091
10000	0.0004	0.0023	0.00014	0.00003	349	122	766	0.00005	0.000339	0.00000	6.67E-05	2,263,091
15000	0.0006	0.0037	0.00023	0.00005	523	122	766	0.00005	0.000339	0.00000	6.67E-05	2,263,091

Load
$Rd\varepsilon_R$
$Rd\varepsilon_L$
ε_L
ε_R
σ
$\sigma_{0.00005}$
$\sigma_{40\%}$
$\varepsilon_{L0.00005}$
$\varepsilon_{L40\%}$
$\varepsilon_{R0.00005}$
$\varepsilon_{R40\%}$
Slope

Figure E-36
Measured and Calculated Modulus of Elasticity (260-Days, 2% RSR, Column 4)

244
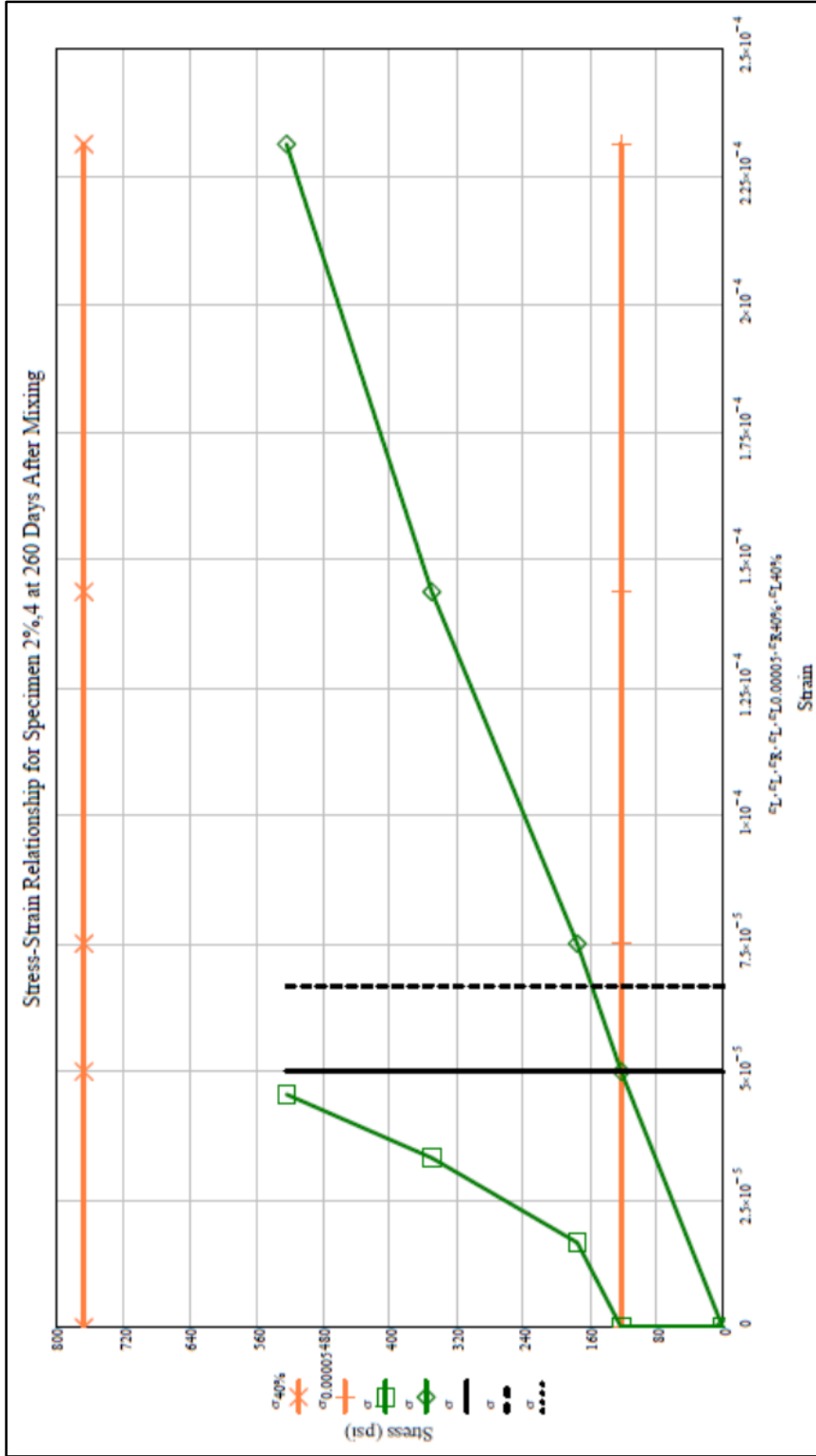
Figure E-37
Measured and Calculated Modulus of Elasticity (260-Days, 2% RSR, Column 4)

APPENDIX F: ELECTRO-ELASTIC TESTING OF CONCRETE COLUMNS AS A FUNCTION OF RECYCLED STEEL RESIDUAL CONCENTRATION

The following includes plots for the testing on the concrete columns. Nomenclature indicates which face of the column on which the strain gage was applied. The first item in the nomenclature represents the volumetric concentration of recycled steel residuals – 0%, 0.5%, etc. The second number represents which column was being tested – 1, 2, or 3. "W" indicates that the strain gage was on the same plane as where the electrodes were protruding from the concrete and was connected to the DAQ leads. "NonW" indicates that the strain gage was applied to the face where electrodes were not protruding. Three pairs of electrodes were measured for this testing and were designated as: "L" for left, "M" for middle, and "R" for right. For example, 1%-2-W-M represents the concrete column containing 1% recycled steel residuals, column number 2, strain gage was applied to the same face from which the electrodes protrude, and the middle pair of electrodes were being measured.

Strain and Resistance (RSR Concentration: 0%, Column 1)
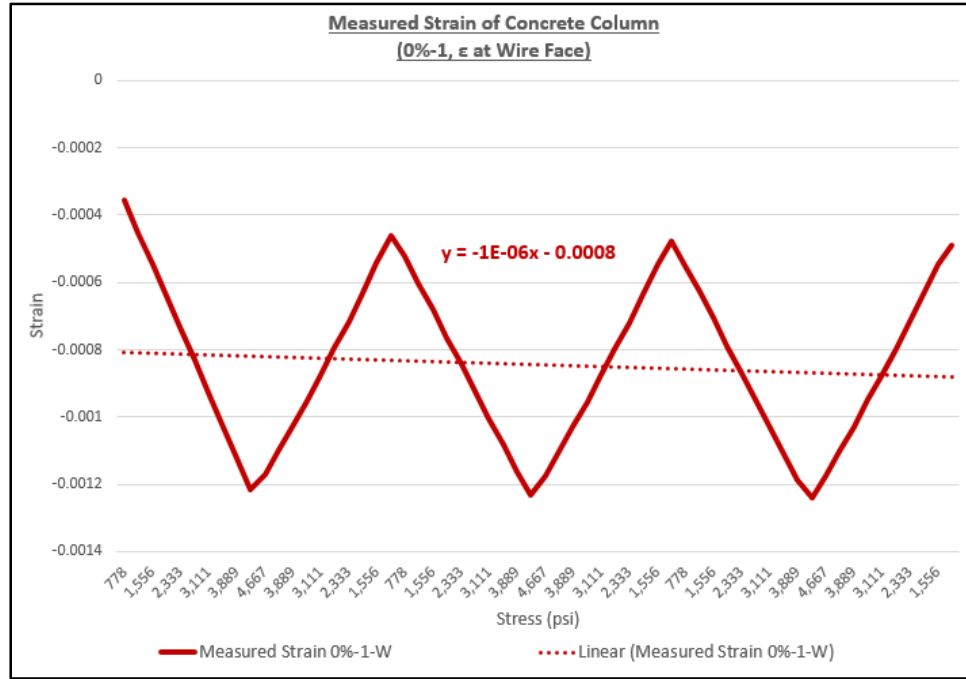
Figure F-1
Strain Measurements (0%, Column 1, Wire Face)
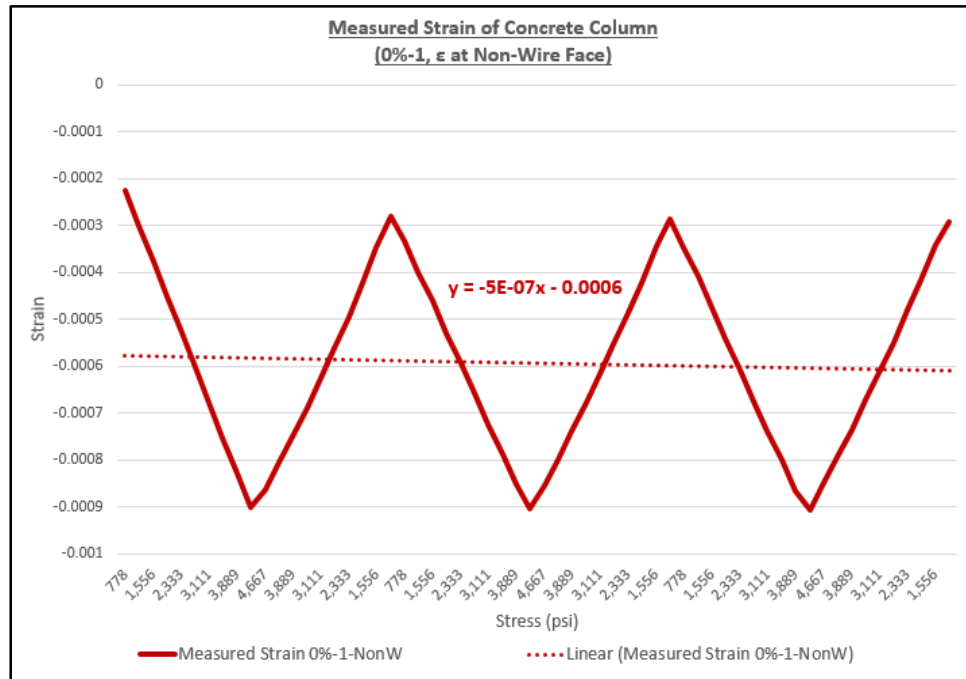
Figure F-2
Strain Measurements (0%, Column 1, Non-Wire Face)
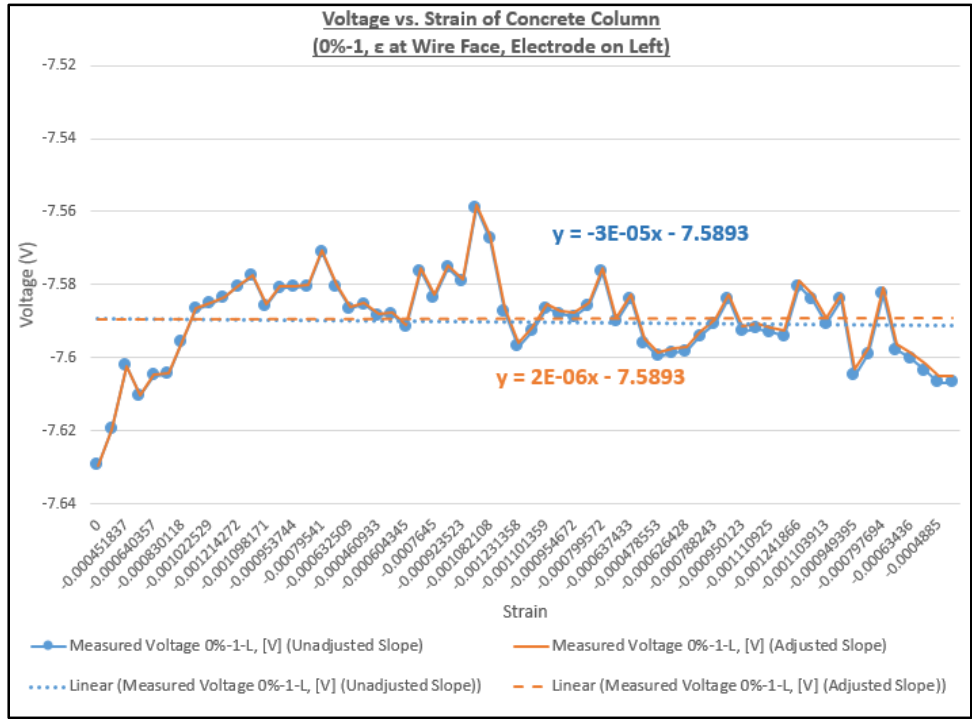
Figure F-3
Voltage Measurements (0%, Column 1, Left Electrode Pair)
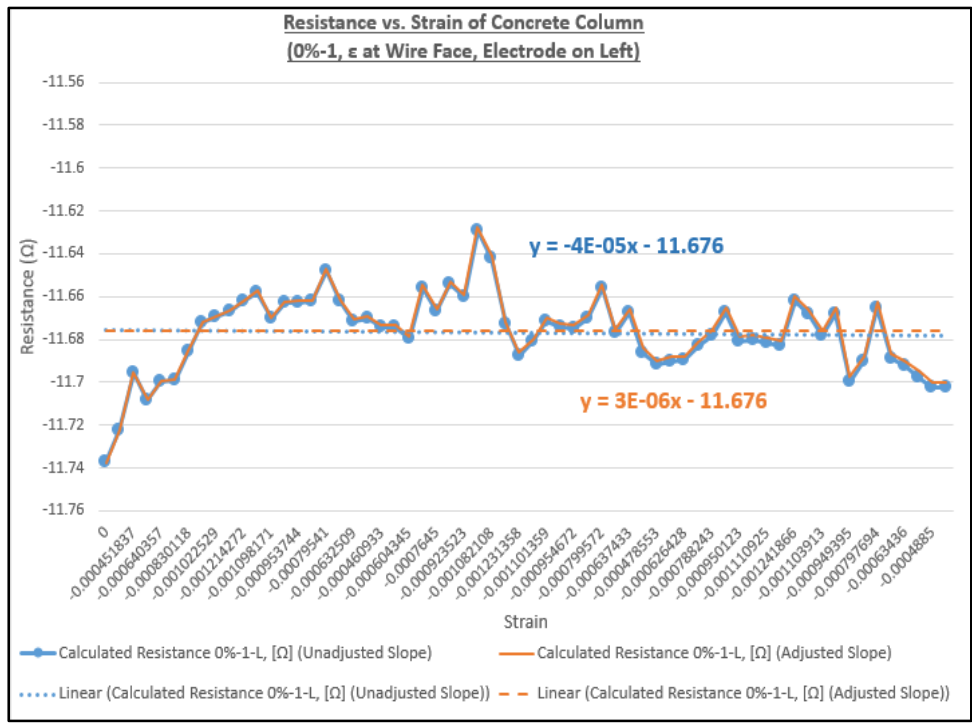
Figure F-4
Calculated Resistance (0%, Column 1, Left Electrode Pair)

248
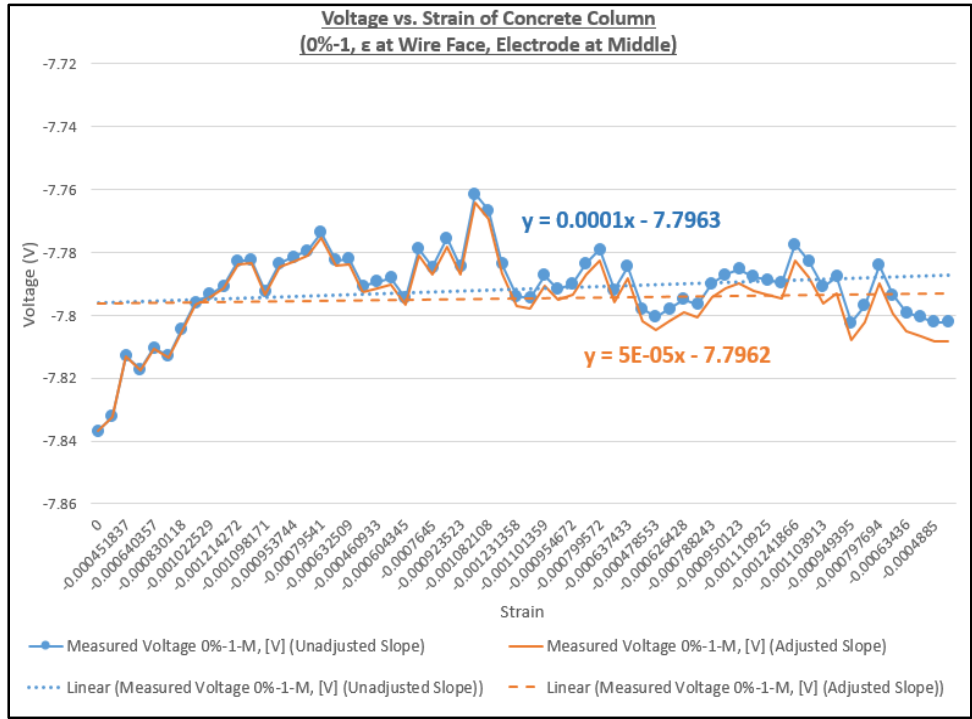
Figure F-5
Voltage Measurements (0%, Column 1, Middle Electrode Pair)
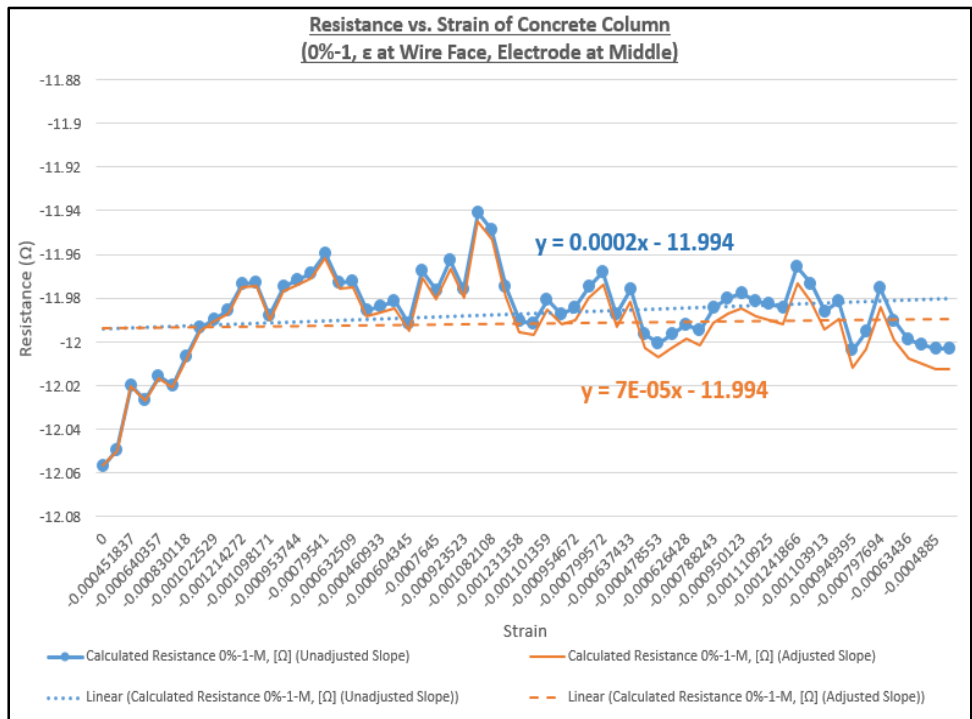
Figure F-6
Calculated Resistance (0%, Column 1, Middle Electrode Pair)
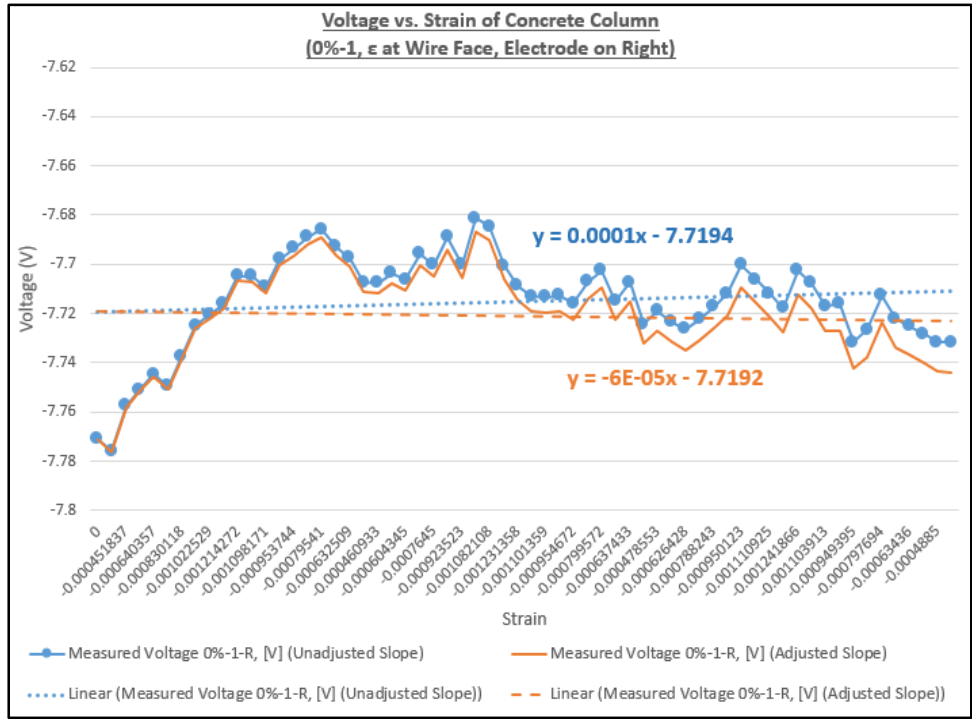
Figure F-7

Voltage Measurements (0%, Column 1, Right Electrode Pair)
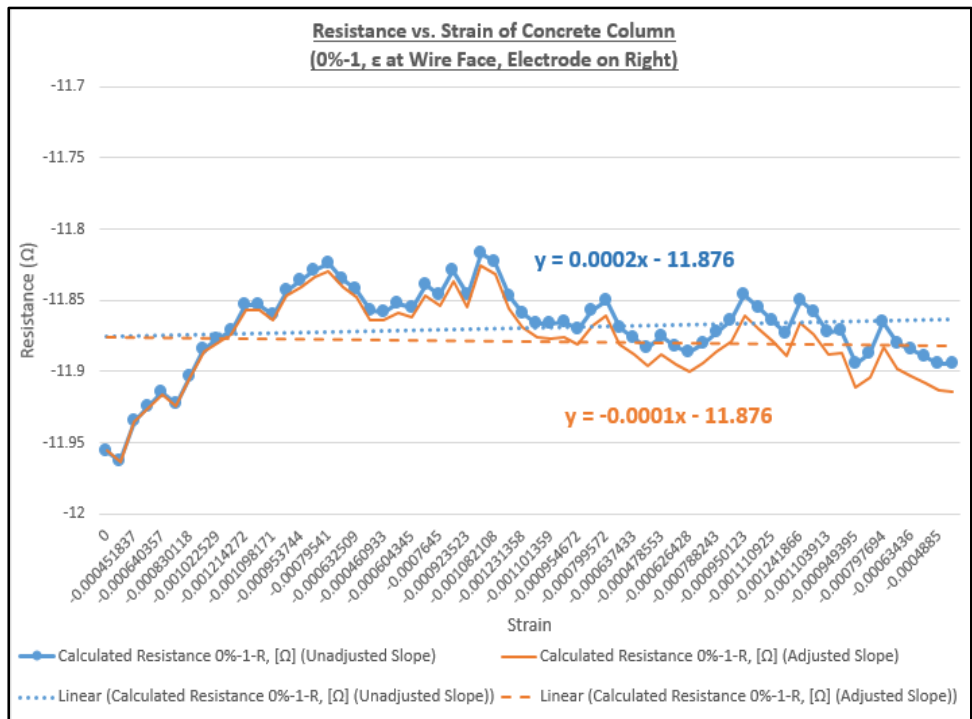
Figure F-8

Calculated Resistance (0%, Column 1, Right Electrode Pair)

Resistance (RSR Concentration: 0%, Column 2)
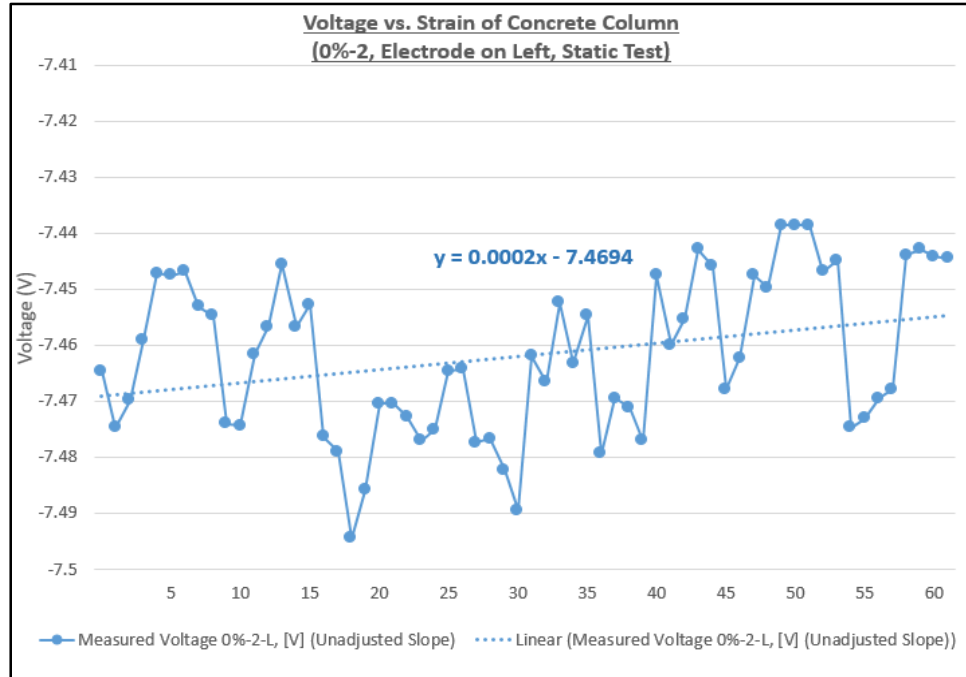
Figure F-9
Static Voltage Measurements (0%, Column 2, Left Electrode Pair)
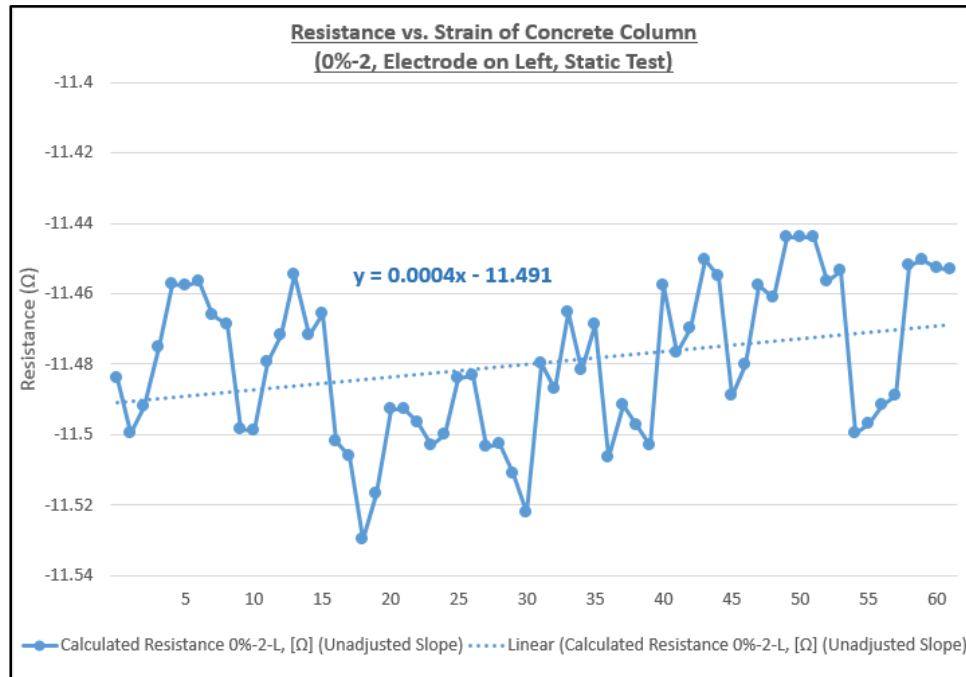
Figure F-10
Static Calculated Resistance (0%, Column 2, Left Electrode Pair)

251
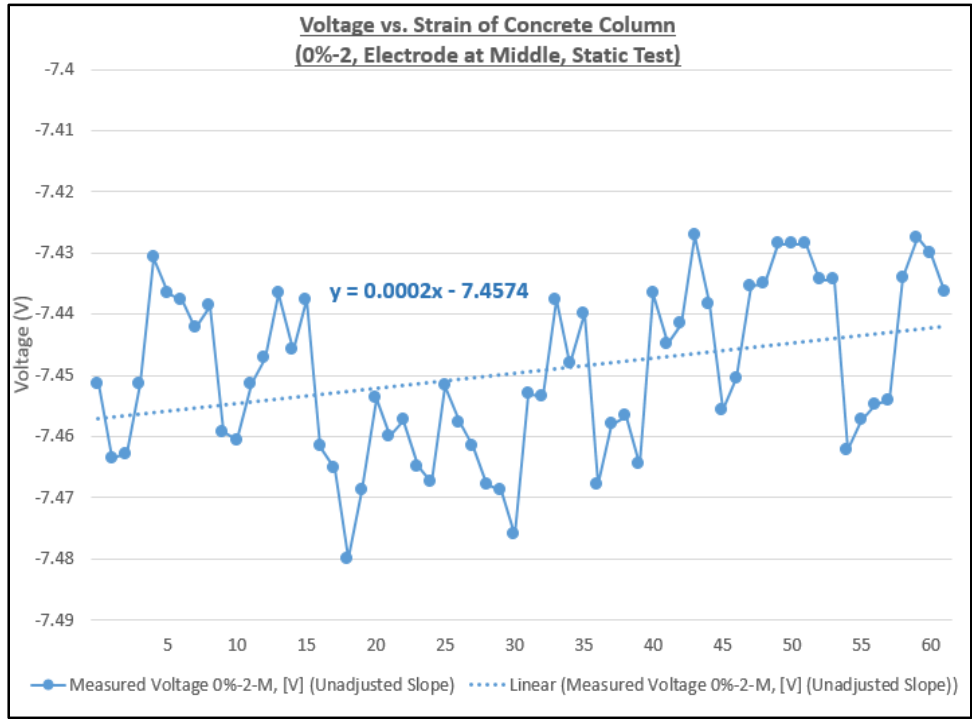
Figure F-11
Static Voltage Measurements (0%, Column 2, Middle Electrode Pair)
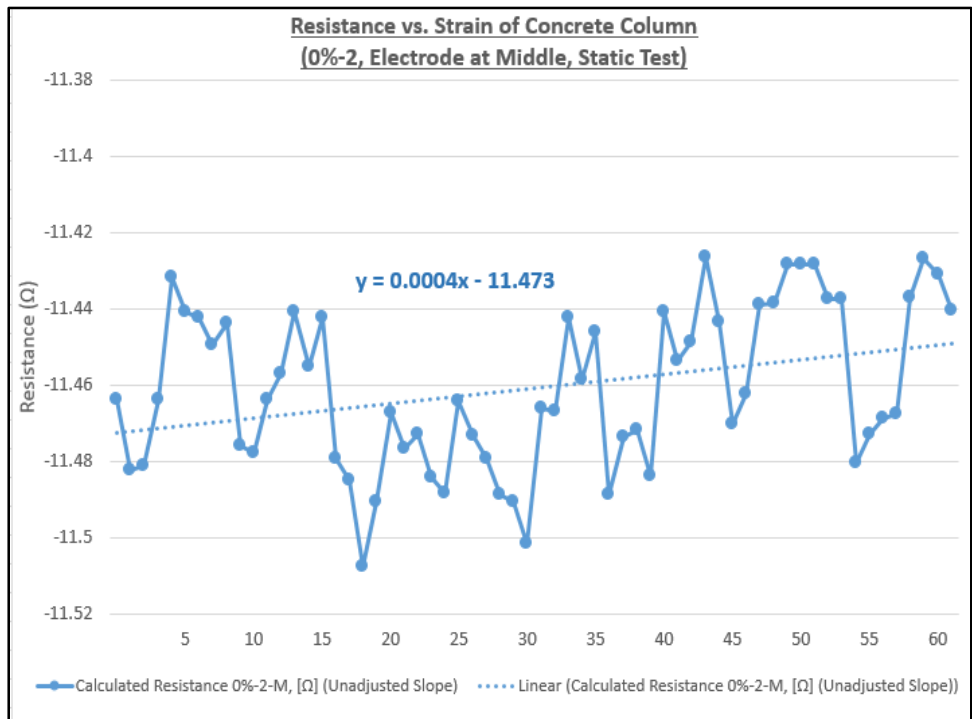
Figure F-12
Static Calculated Resistance (0%, Column 2, Middle Electrode Pair)
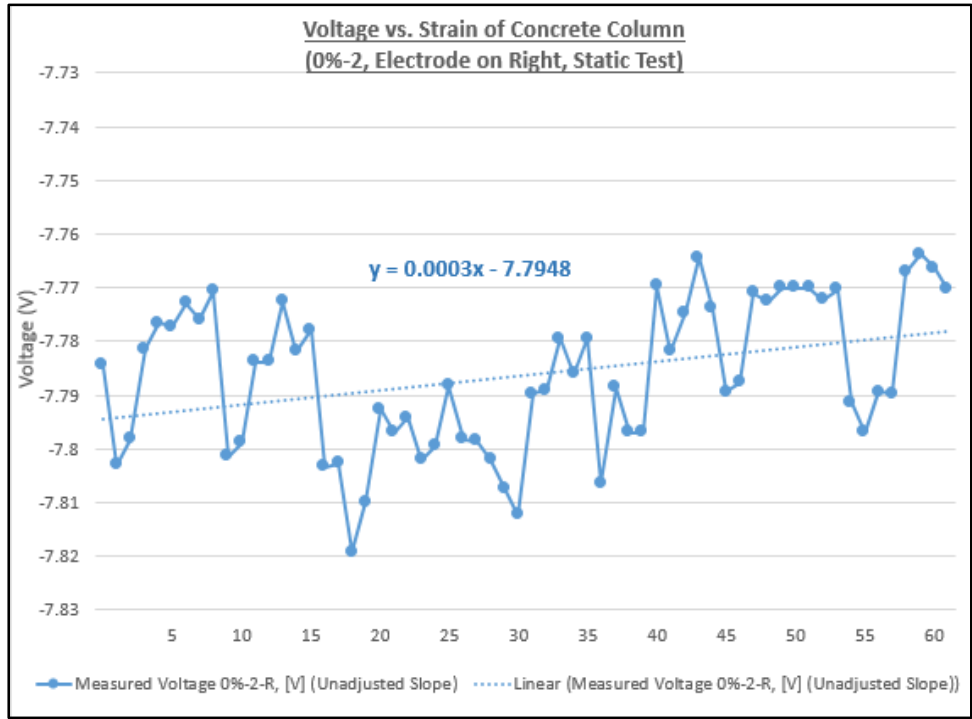
Figure F-13
Static Voltage Measurements (0%, Column 2, Right Electrode Pair)
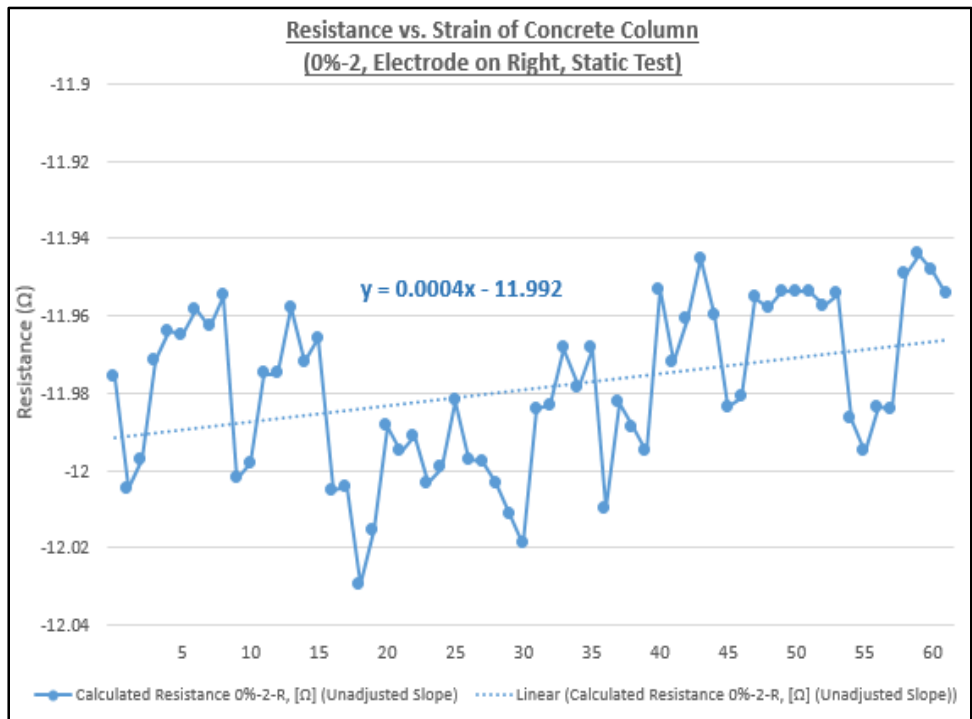
Figure F-14
Static Calculated Resistance (0%, Column 2, Right Electrode Pair)

253

Strain and Resistance (RSR Concentration: 0.5%, Column 1)
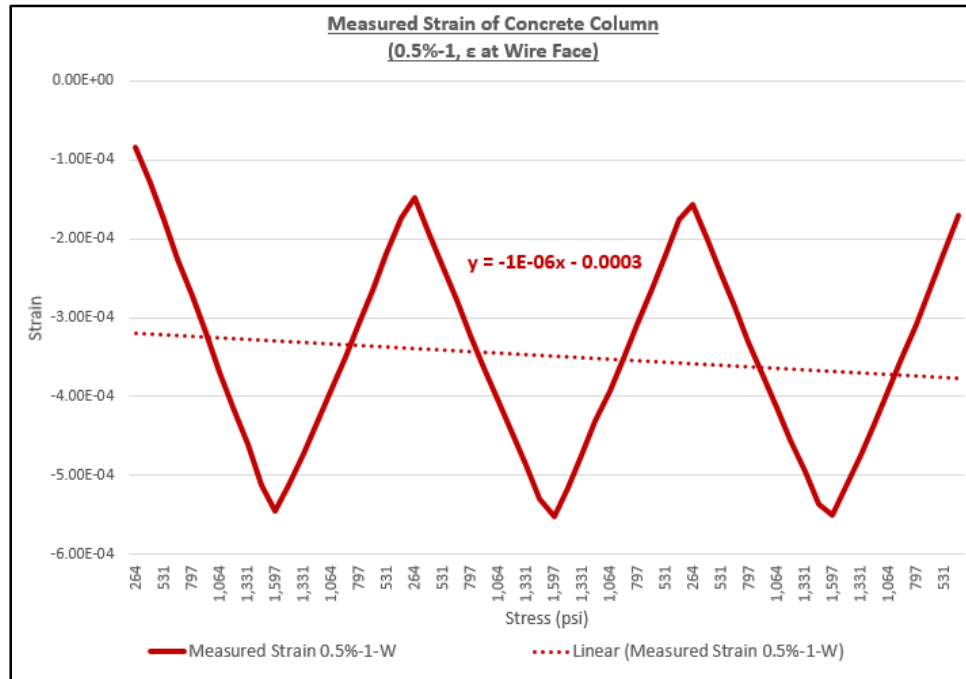
Figure F-15
Strain Measurements (0.5%, Column 1, Wire Face)
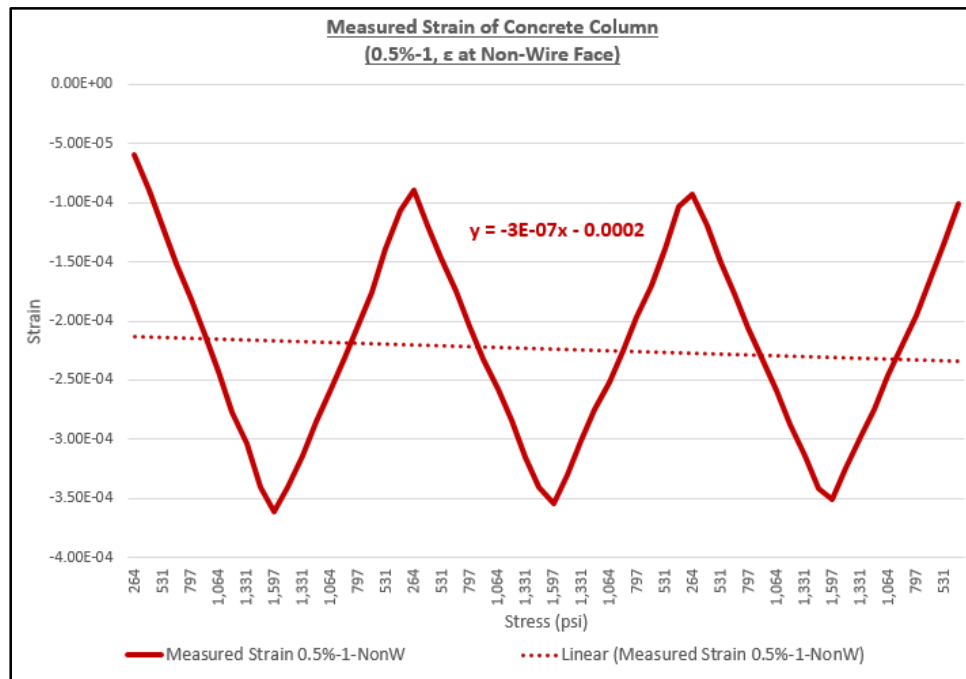
Figure F-16
Strain Measurements (0.5%, Column 1, Non-Wire Face)

254
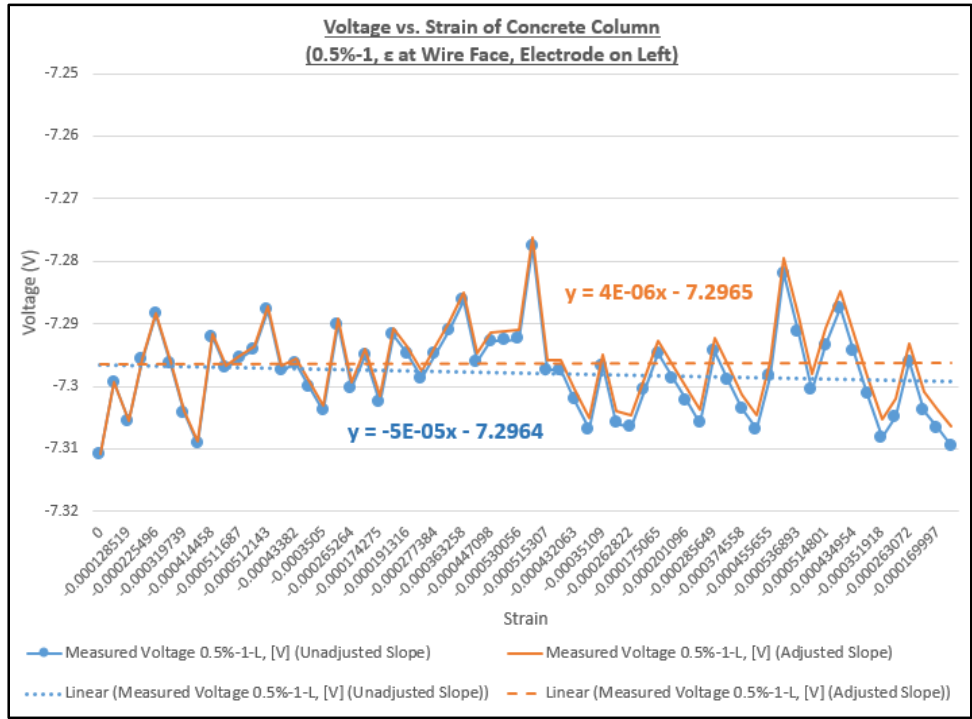
Figure F-17
Voltage Measurements (0.5%, Column 1, Left Electrode Pair)
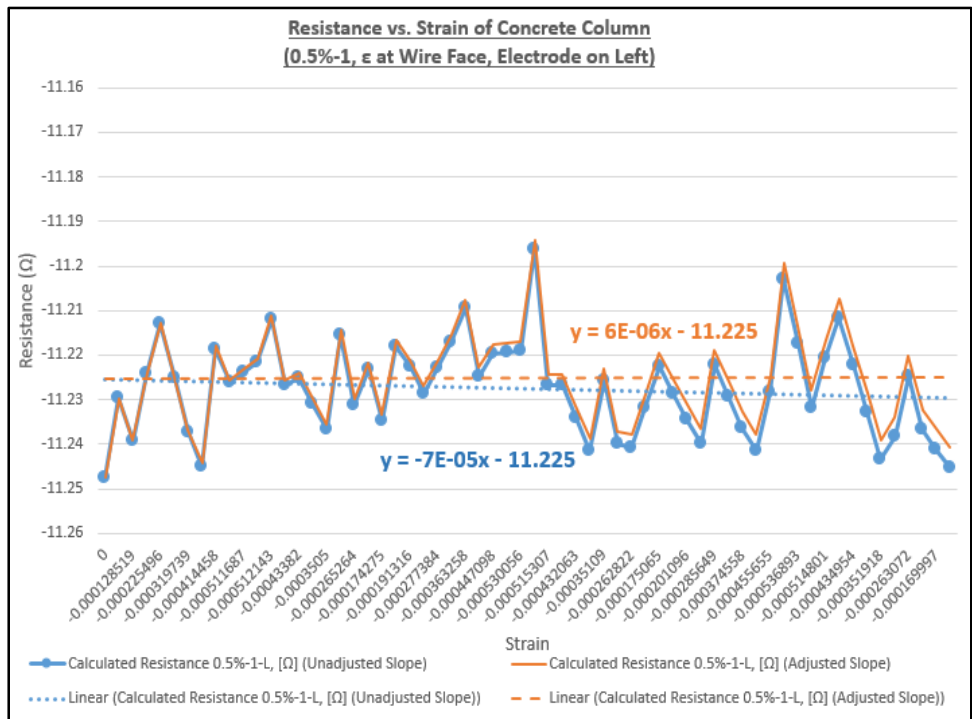
Figure F-18
Calculated Resistance (0.5%, Column 1, Left Electrode Pair)

255
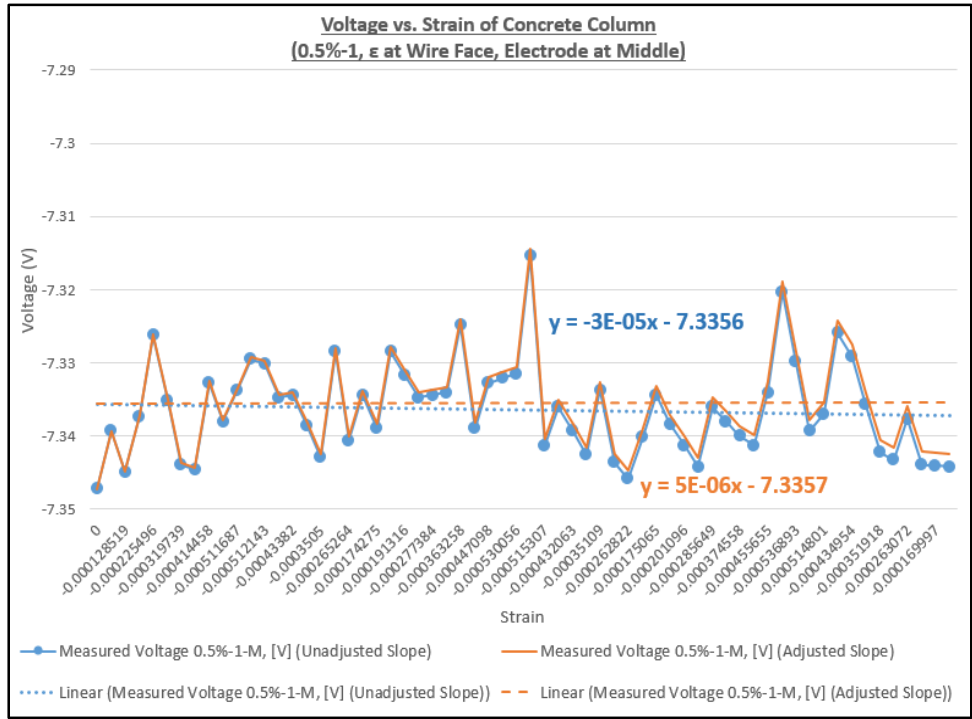
Figure F-19
Voltage Measurements (0.5%, Column 1, Middle Electrode Pair)
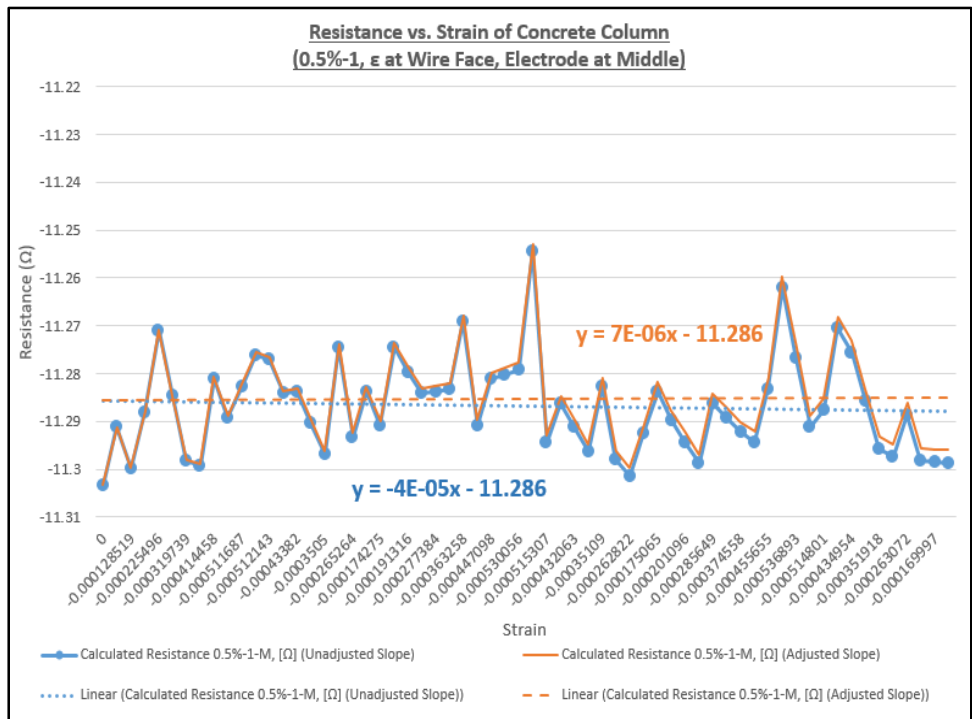
Figure F-20
Calculated Resistance (0.5%, Column 1, Middle Electrode Pair)

256
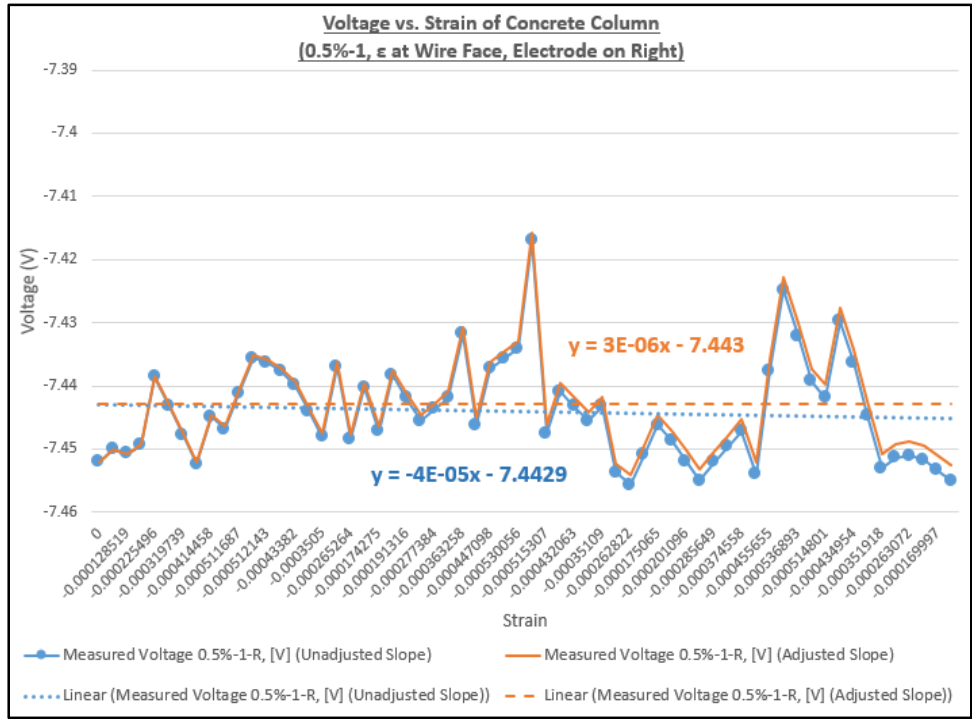
Figure F-21

Voltage Measurements (0.5%, Column 1, Right Electrode Pair)
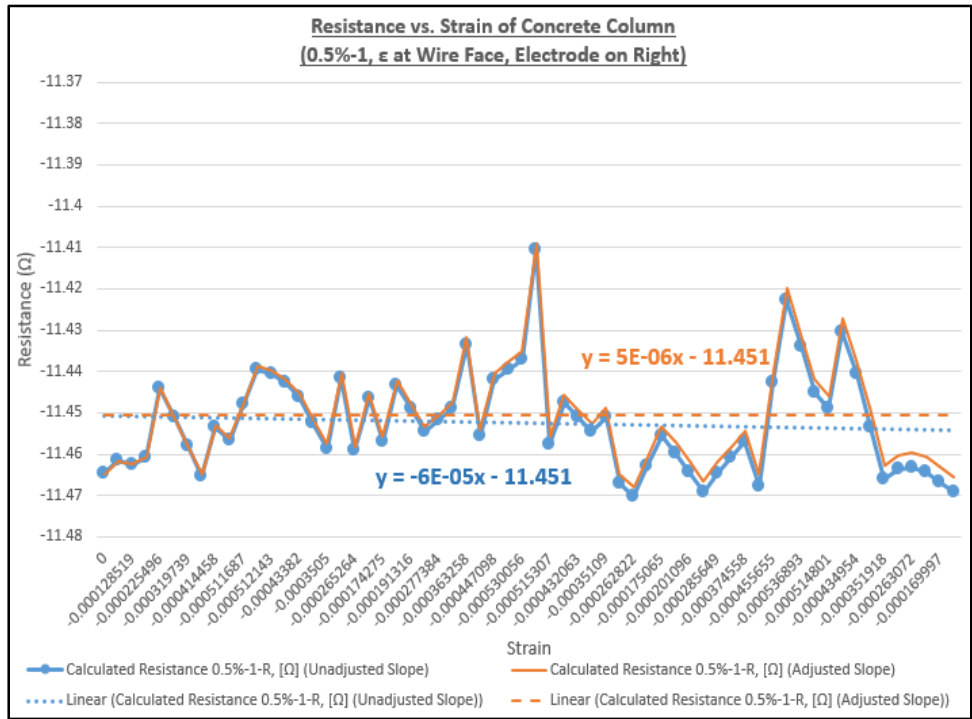
Figure F-22

Calculated Resistance (0.5%, Column 1, Right Electrode Pair)

Strain and Resistance (RSR Concentration: 0.5%, Column 2)
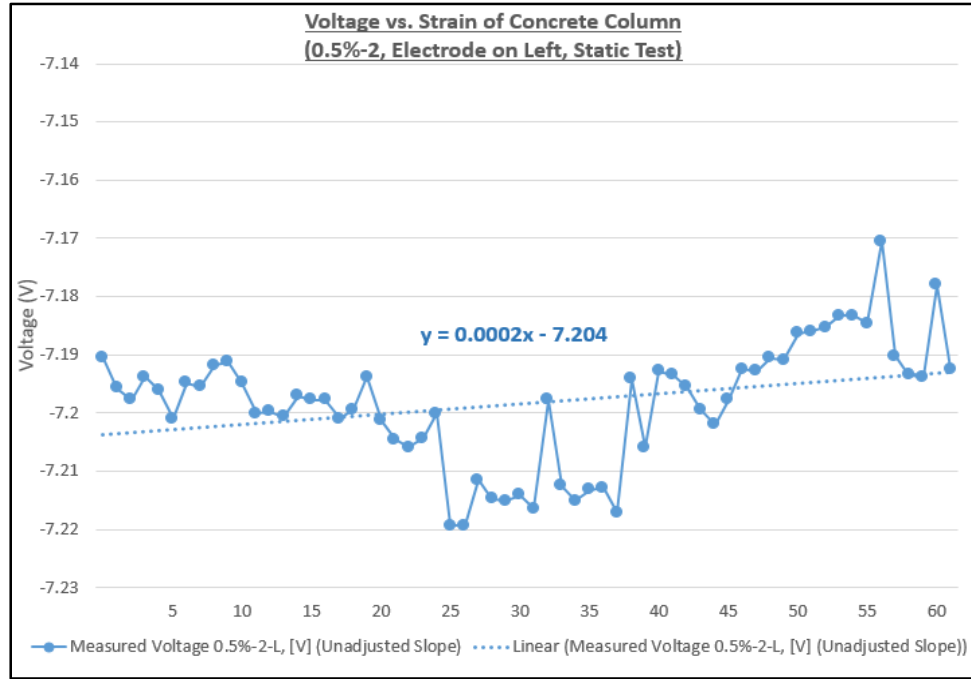
Figure F-23
Static Voltage Measurements (0.5%, Column 2, Left Electrode Pair)
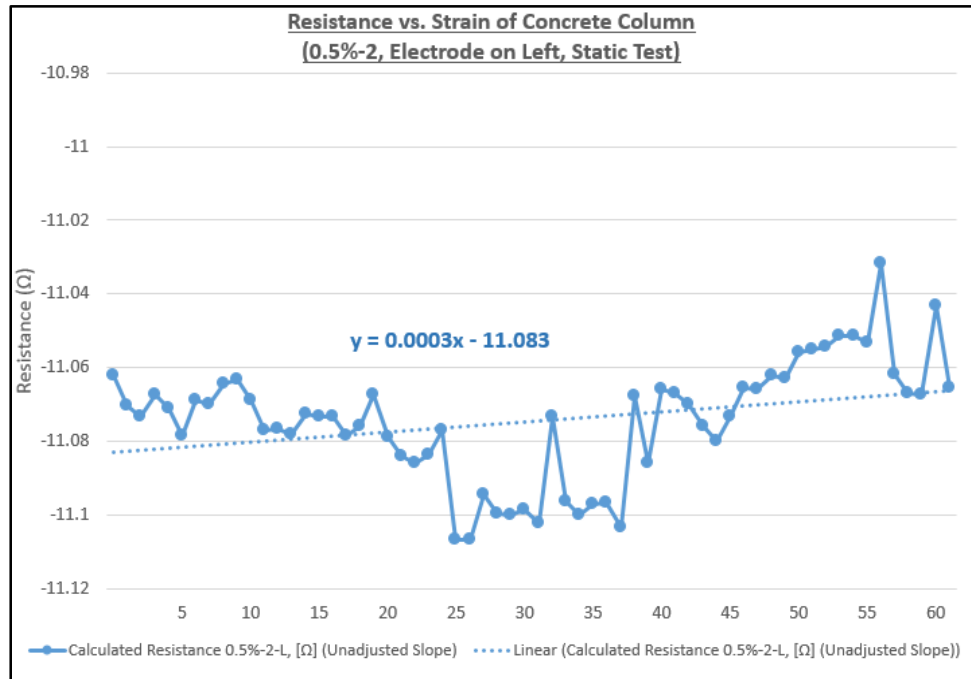
Figure F-24
Static Calculated Resistance (0.5%, Column 2, Left Electrode Pair)
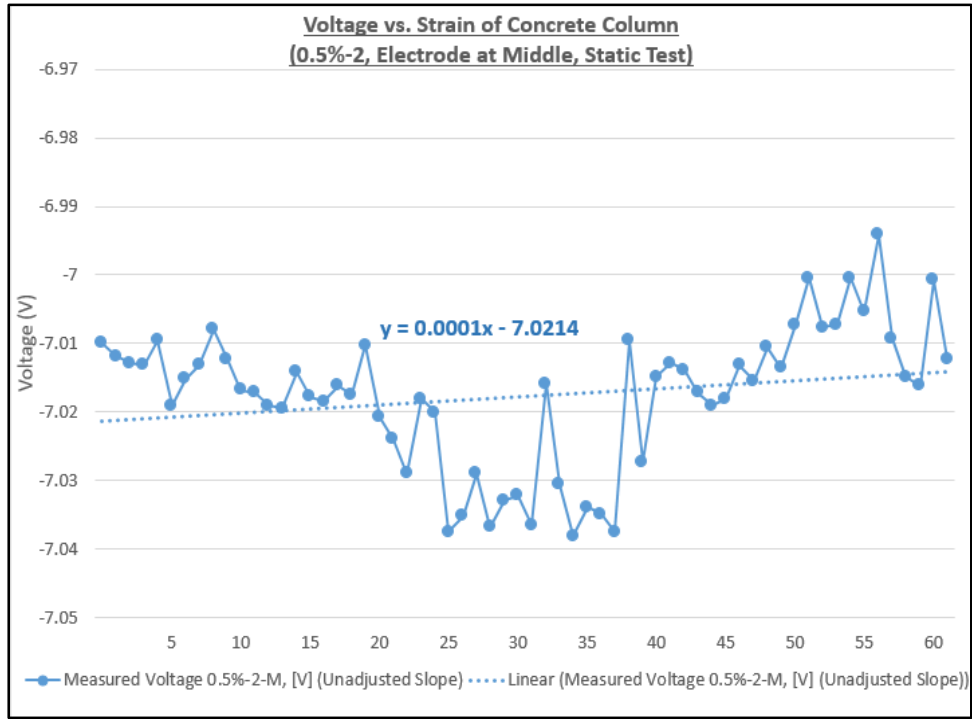
Figure F-25
Static Voltage Measurements (0.5%, Column 2, Middle Electrode Pair)
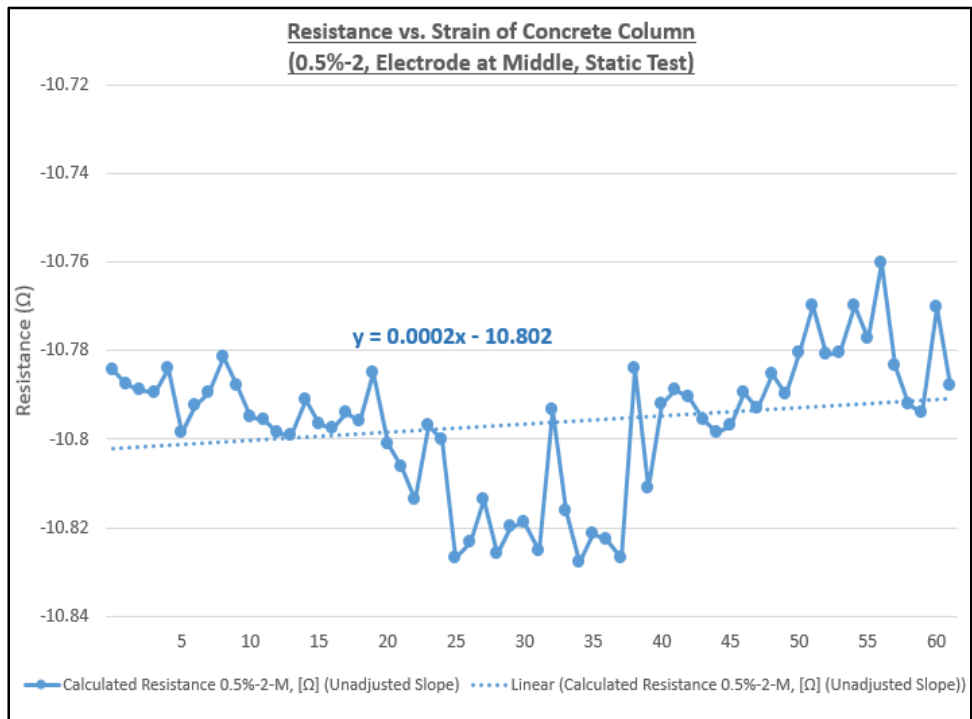
Figure F-26
Static Calculated Resistance (0.5%, Column 2, Middle Electrode Pair)
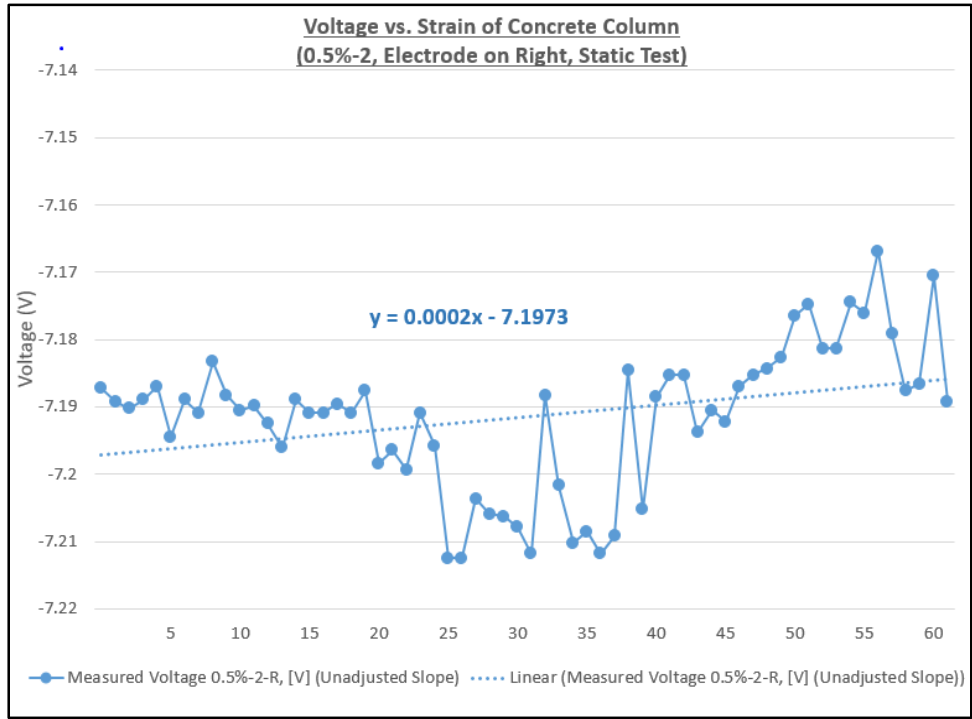
Figure F-27
Static Voltage Measurements (0.5%, Column 2, Right Electrode Pair)
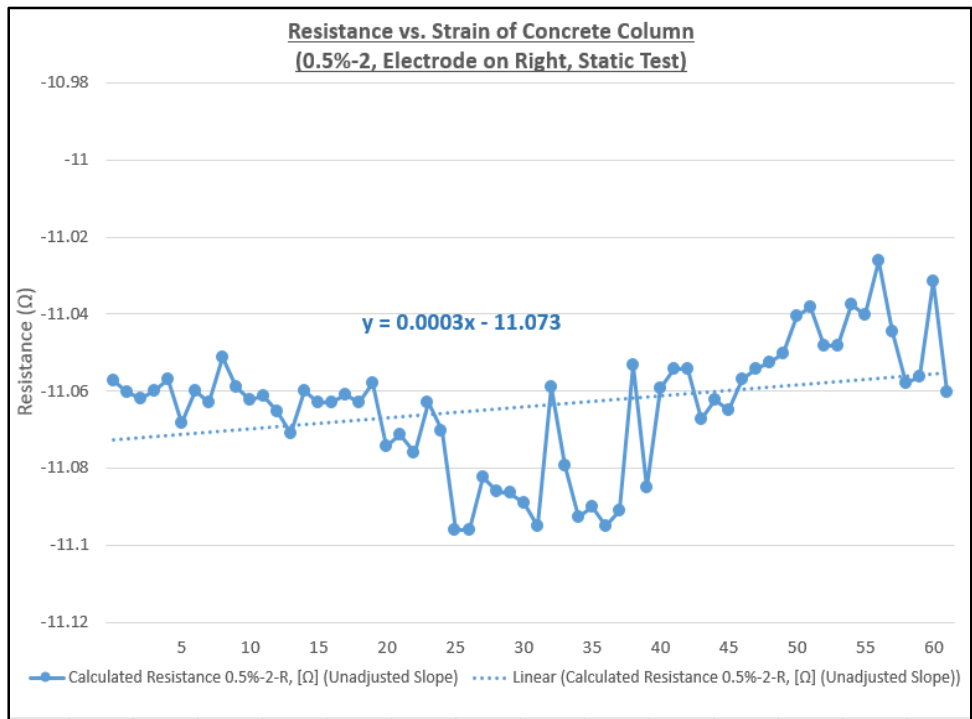
Figure F-28
Static Calculated Resistance (0.5%, Column 2, Right Electrode Pair)

260
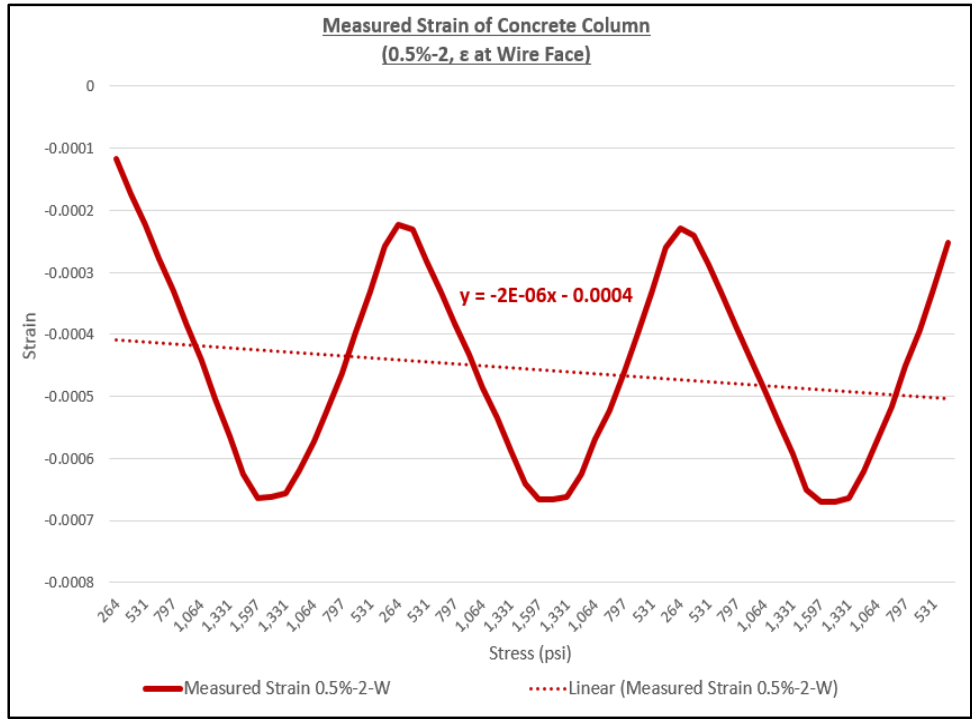
Figure F-29
Strain Measurements (0.5%, Column 2, Wire Face)
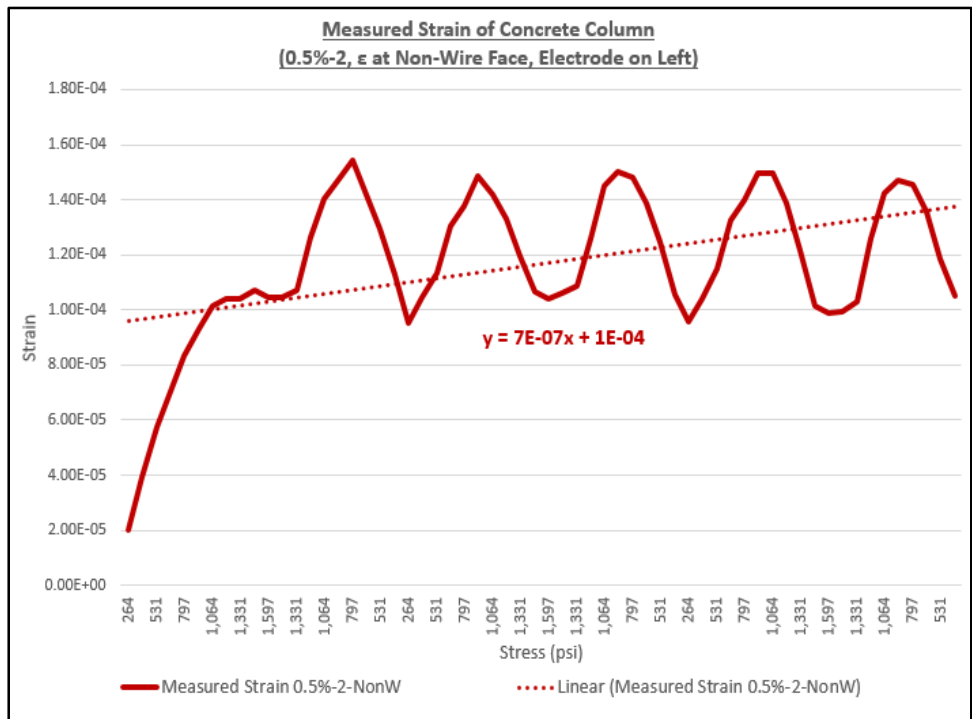
Figure F-30
Strain Measurements (0.5%, Column 2, Non-Wire Face)

261
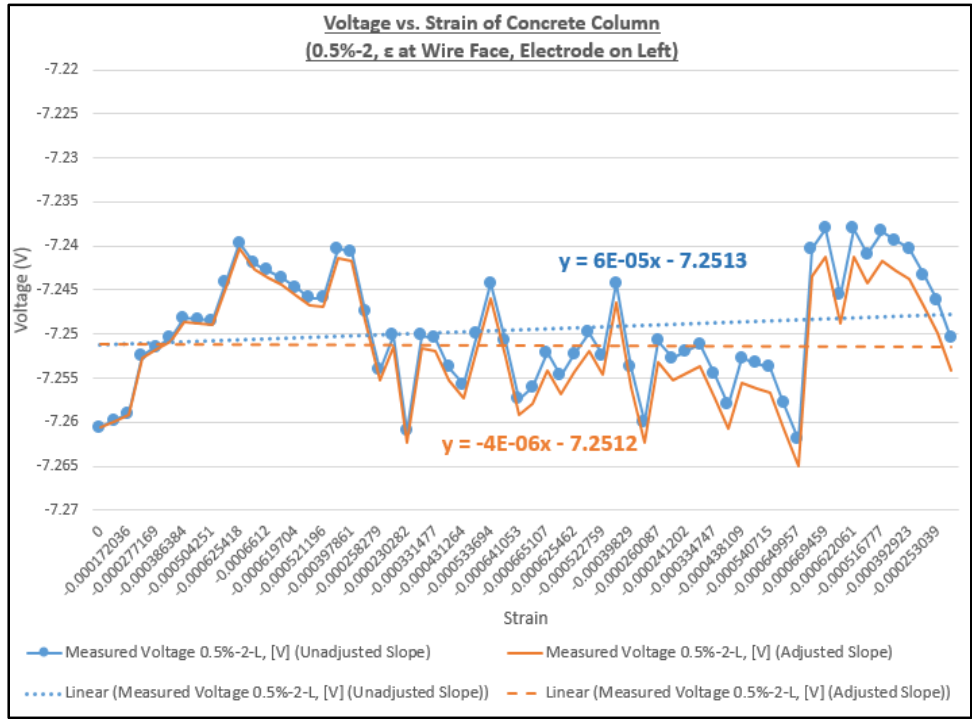
Figure F-31
Voltage Measurements (0.5%, Column 2, Left Electrode Pair)
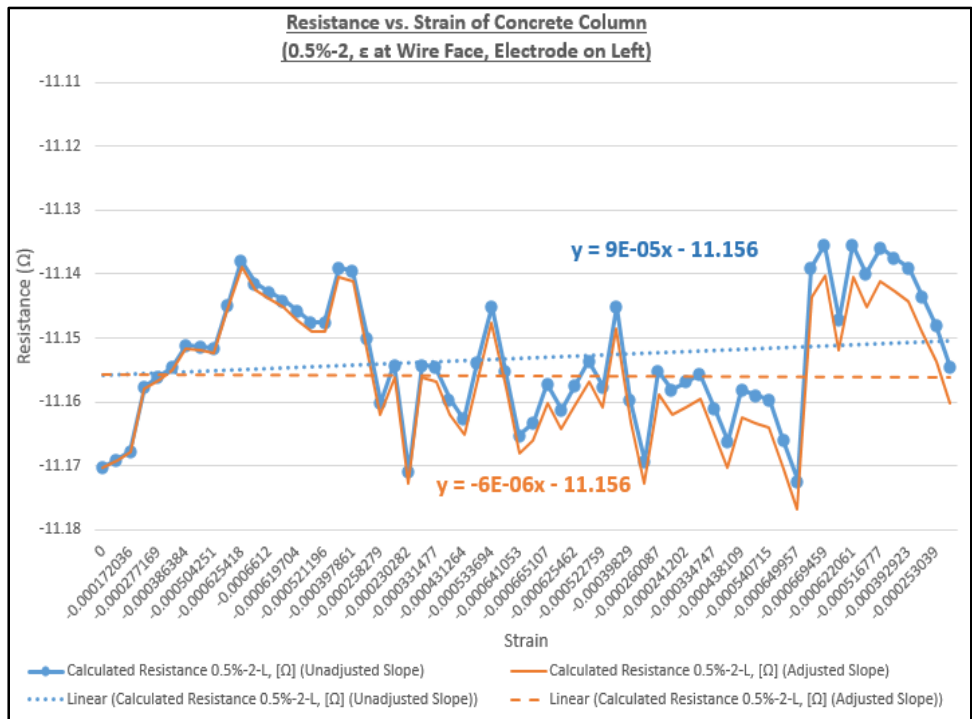
Figure F-32
Calculated Resistance (0.5%, Column 2, Left Electrode Pair)
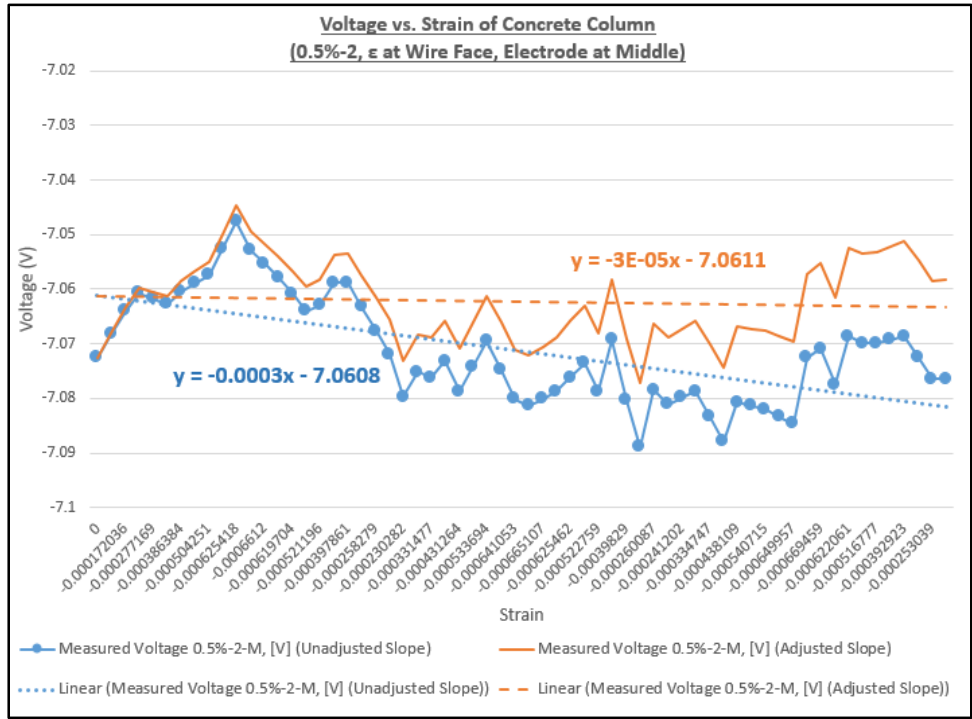
Figure F-33
Voltage Measurements (0.5%, Column 2, Middle Electrode Pair)
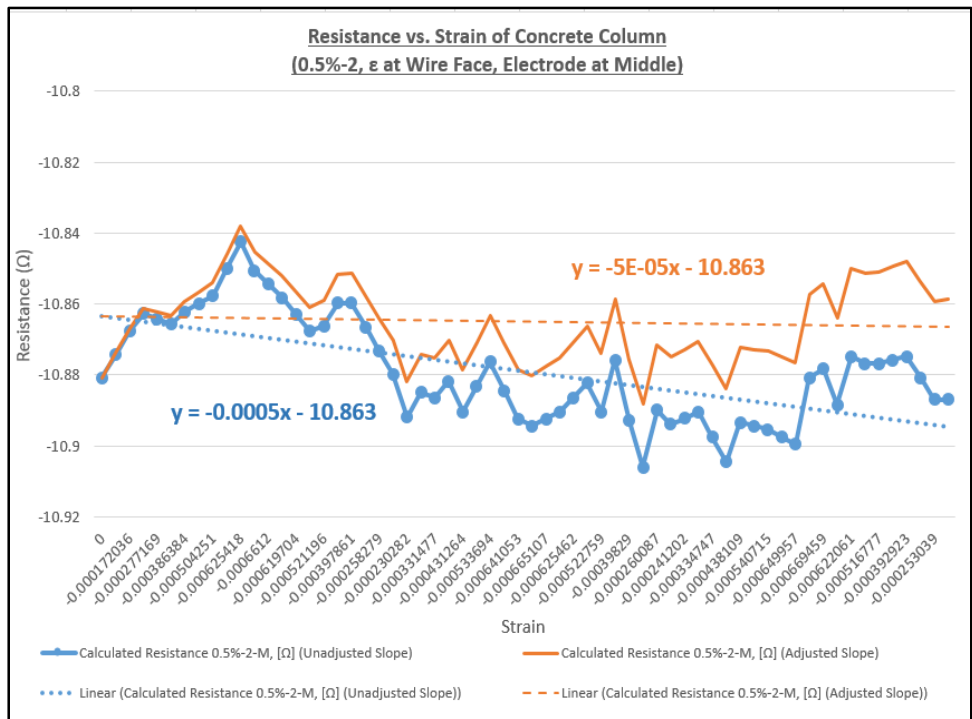
Figure F-34
Calculated Resistance (0.5%, Column 2, Middle Electrode Pair)

263
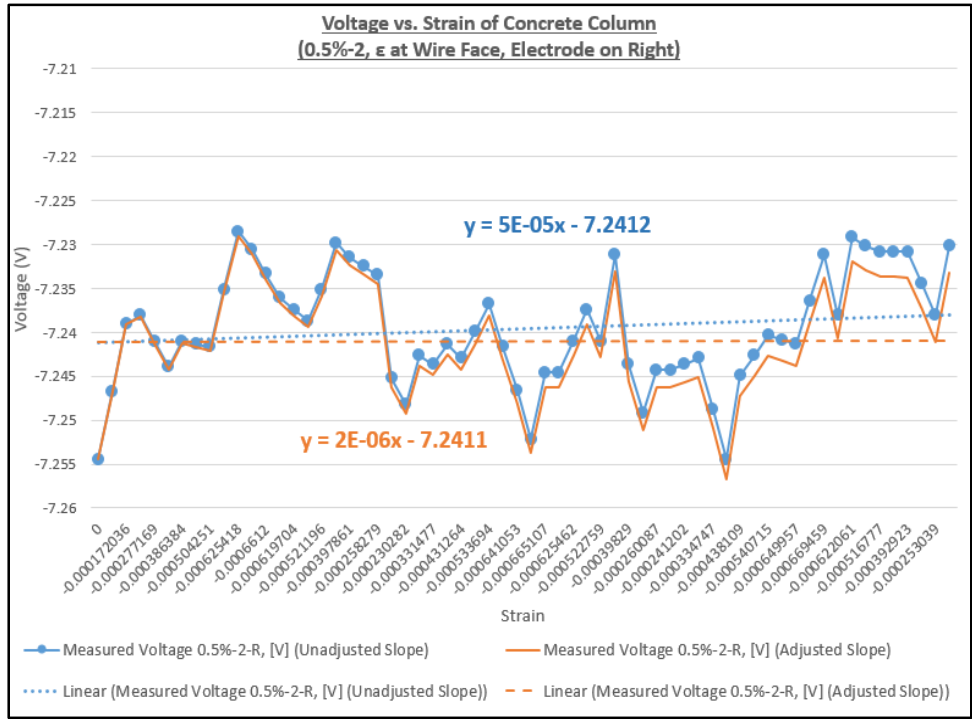
Figure F-35
Voltage Measurements (0.5%, Column 2, Right Electrode Pair)
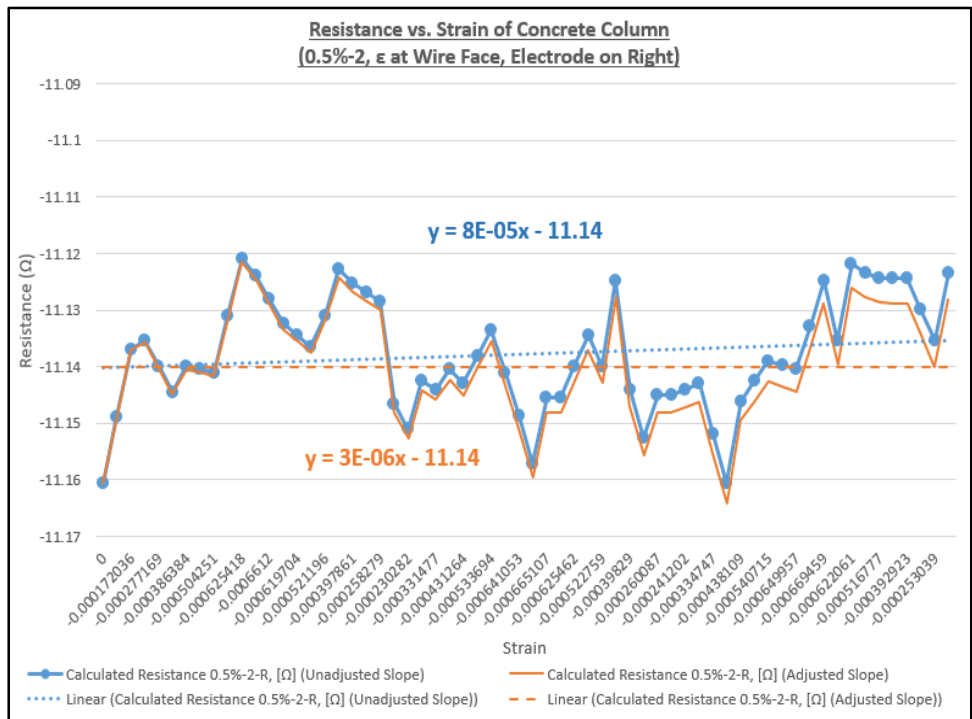
Figure F-36
Calculated Resistance (0.5%, Column 2, Right Electrode Pair)

Strain and Resistance (RSR Concentration: 0.5%, Column 3)
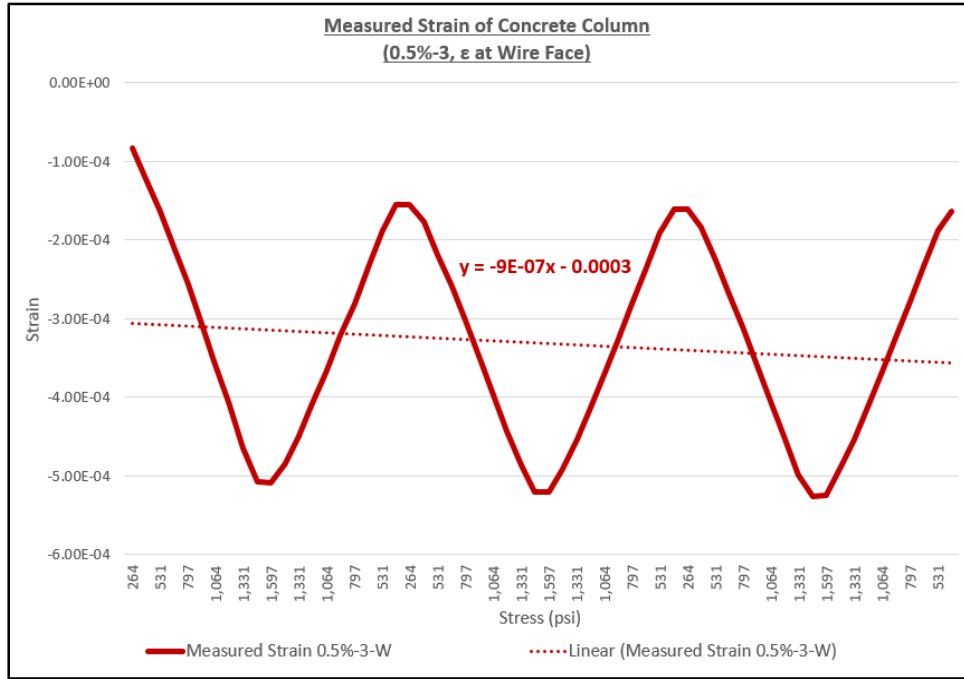
Figure F-37
Strain Measurements (0.5%, Column 3, Wire Face)
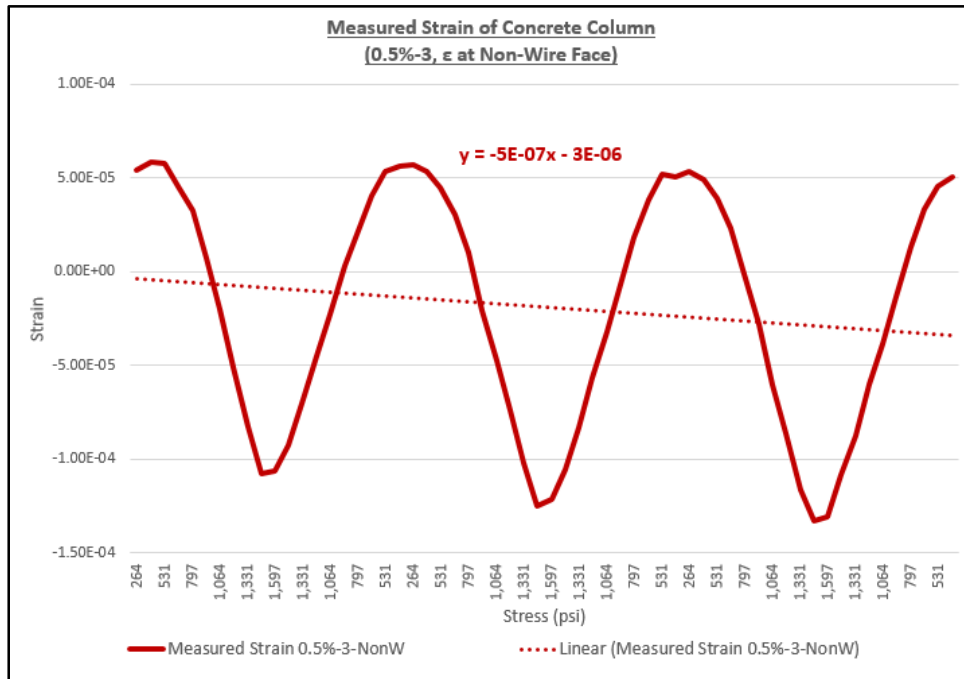
Figure F-38
Strain Measurements (0.5%, Column 3, Non-Wire Face)
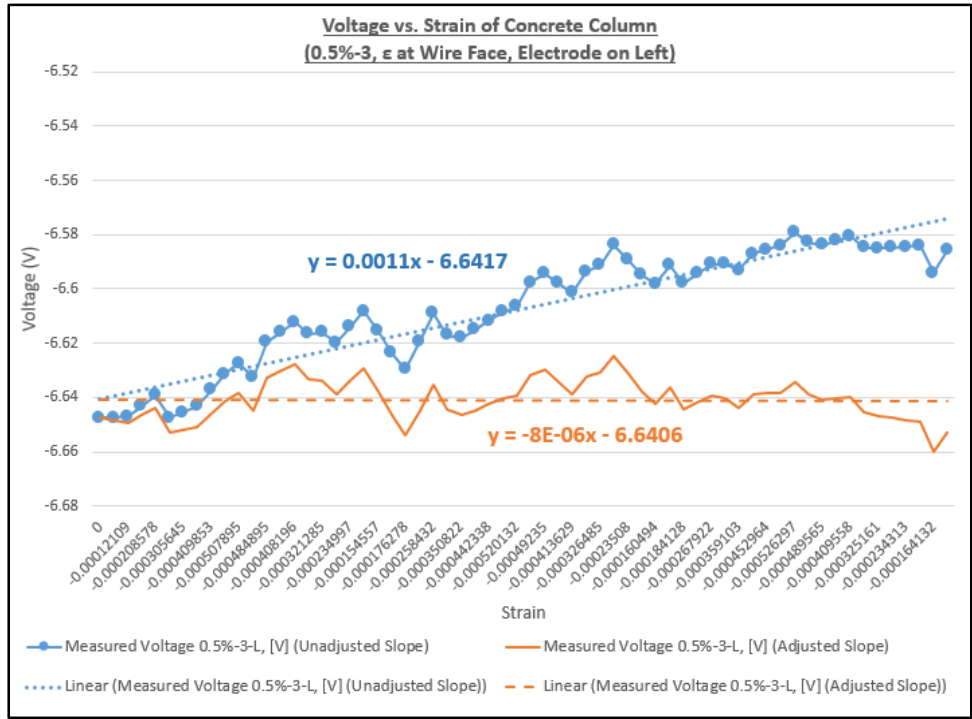
Figure F-39
Voltage Measurements (0.5%, Column 3, Left Electrode Pair)
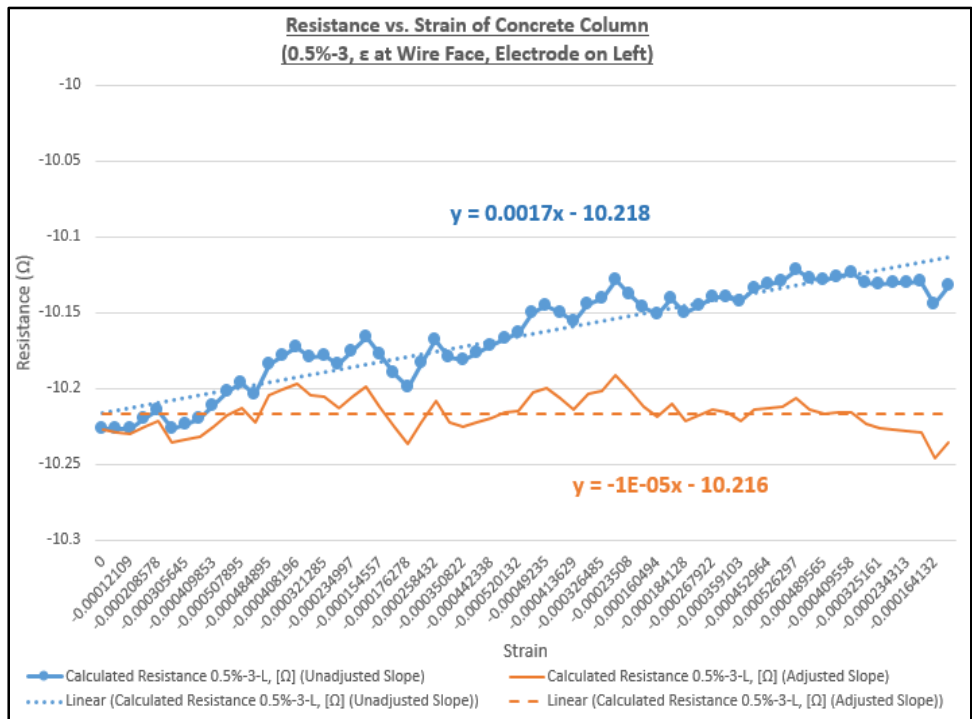
Figure F-40
Calculated Resistance (0.5%, Column 3, Left Electrode Pair)

266
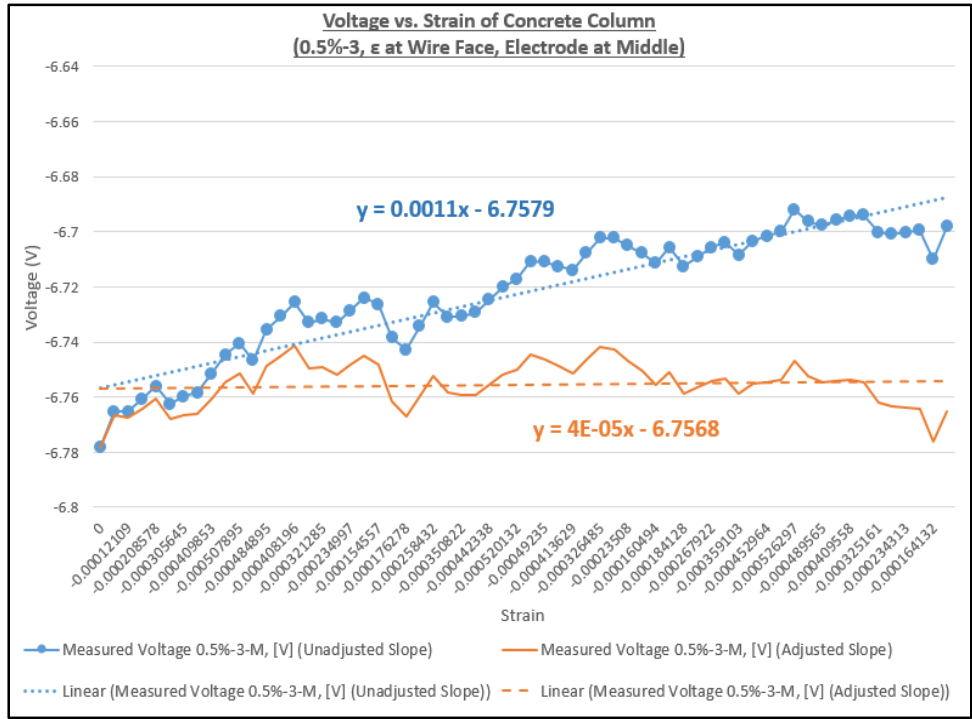
Figure F-41

Voltage Measurements (0.5%, Column 3, Middle Electrode Pair)
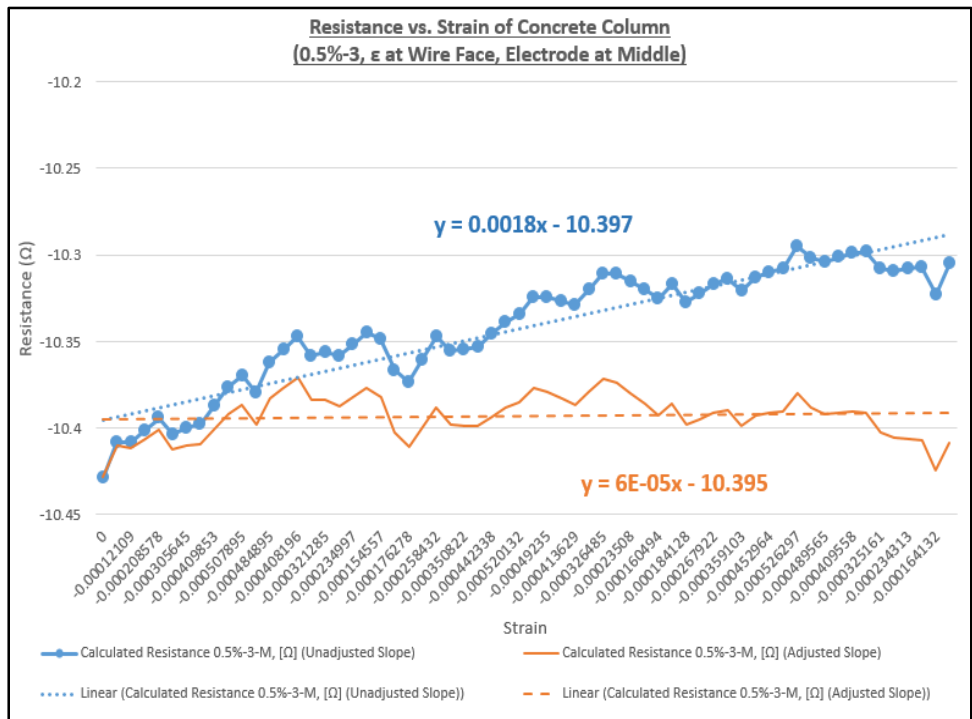
Figure F-42

Calculated Resistance (0.5%, Column 3, Middle Electrode Pair)
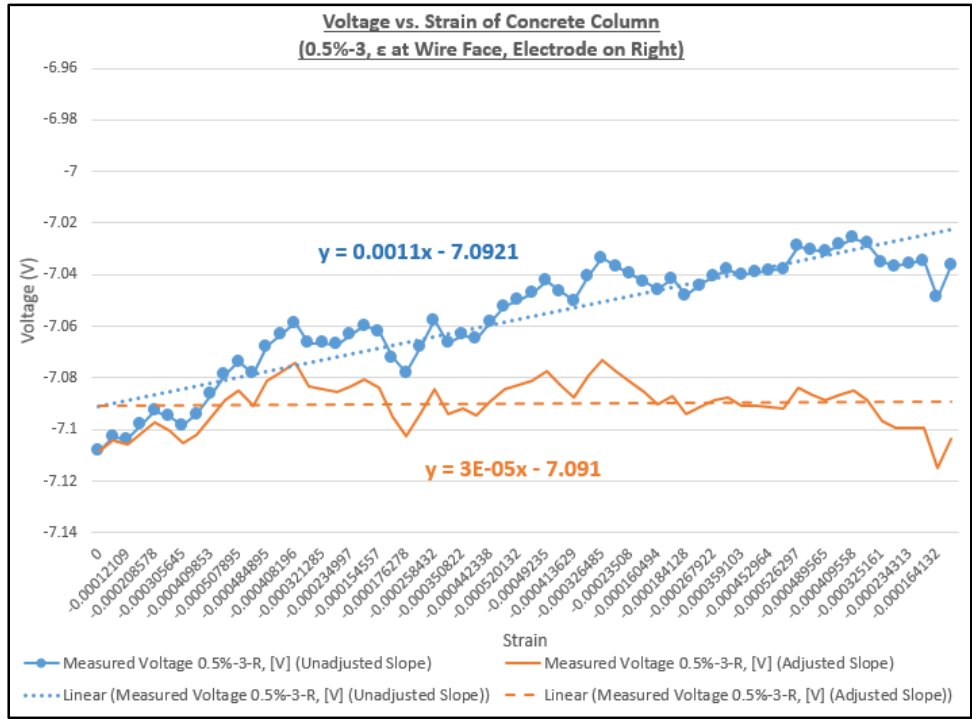
Figure F-43

Voltage Measurements (0.5%, Column 3, Right Electrode Pair)
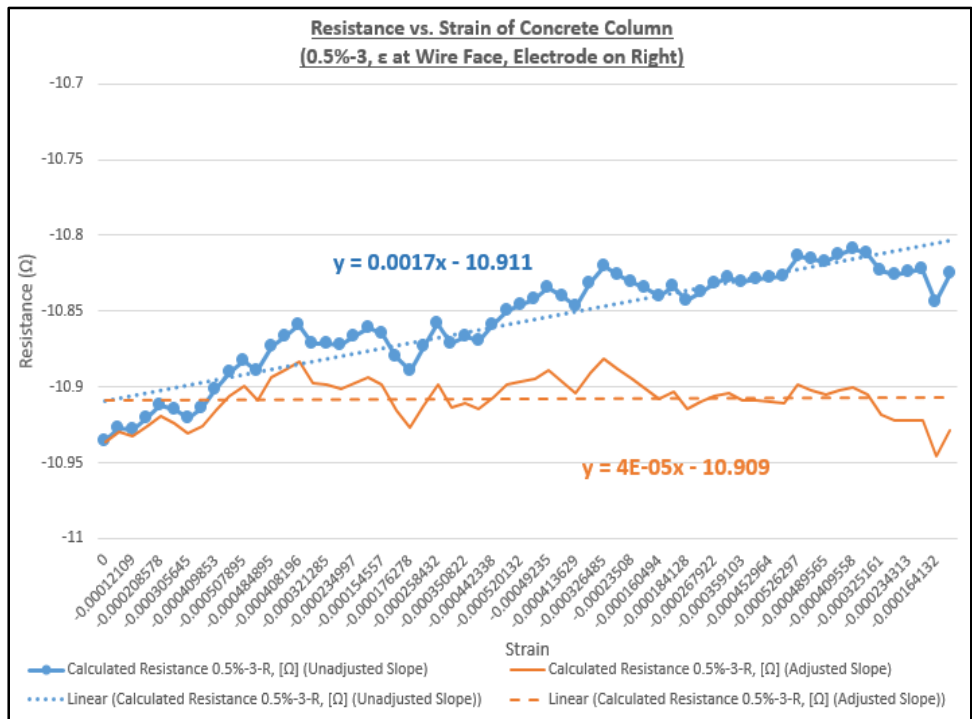
Figure F-44

Calculated Resistance (0.5%, Column 3, Right Electrode Pair)

268

Strain and Resistance (RSR Concentration: 1%, Column 1)
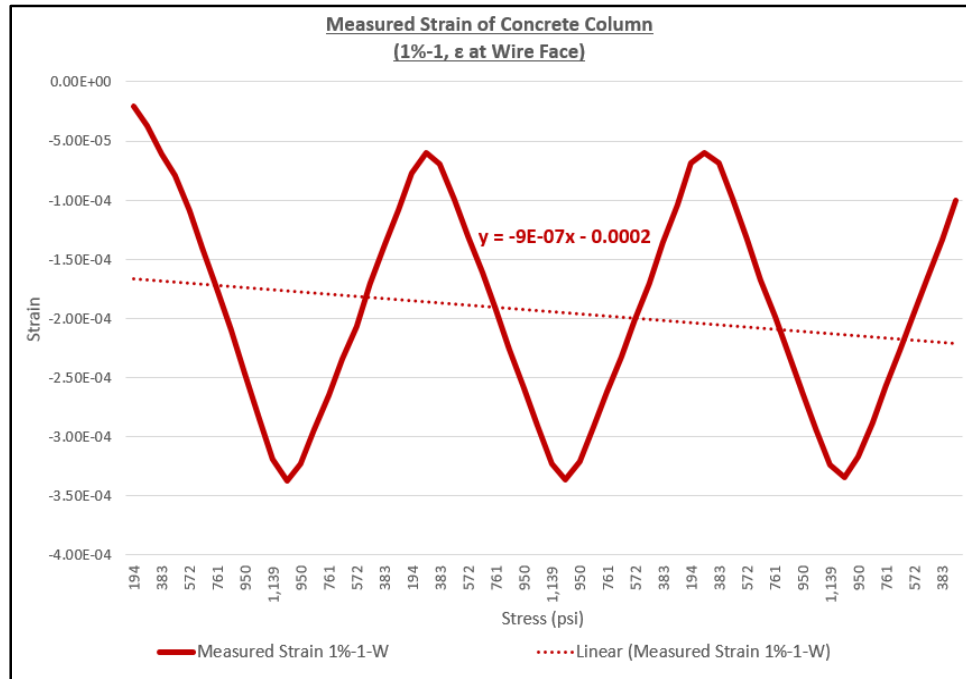
Figure F-45
Strain Measurements (1%, Column 1, Wire Face)
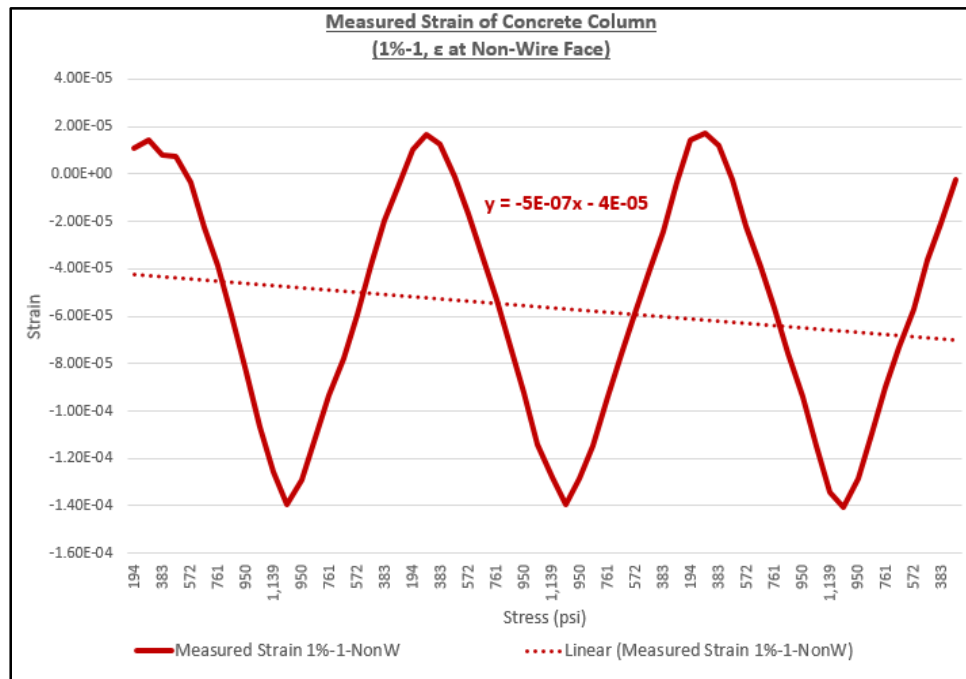
Figure F-46
Strain Measurements (1%, Column 1, Non-Wire Face)

269
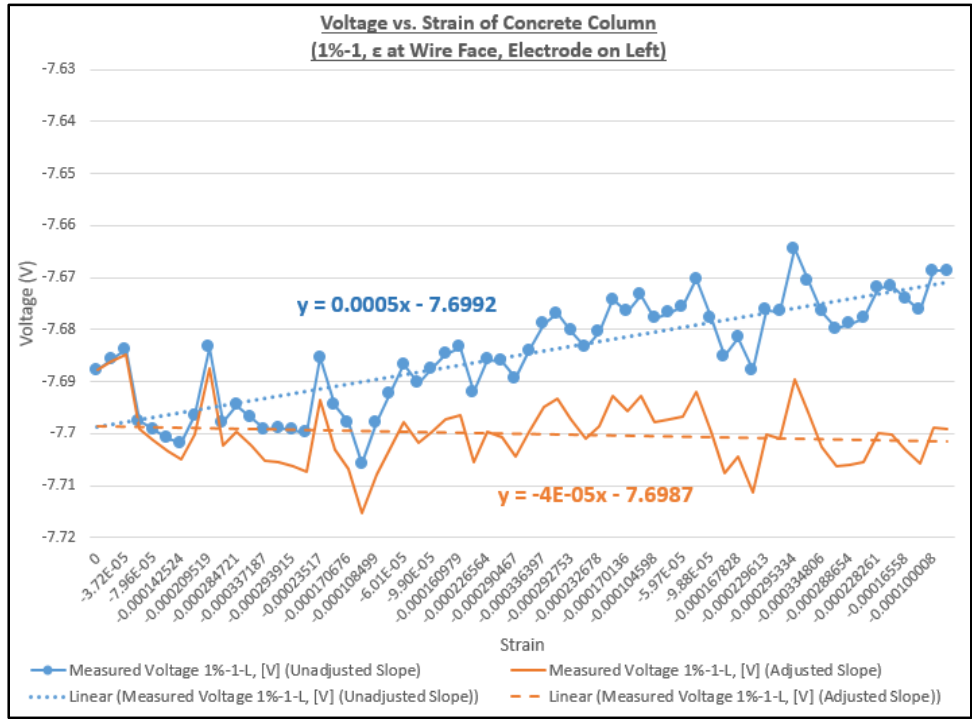
Figure F-47

Voltage Measurements (1%, Column 1, Left Electrode Pair)
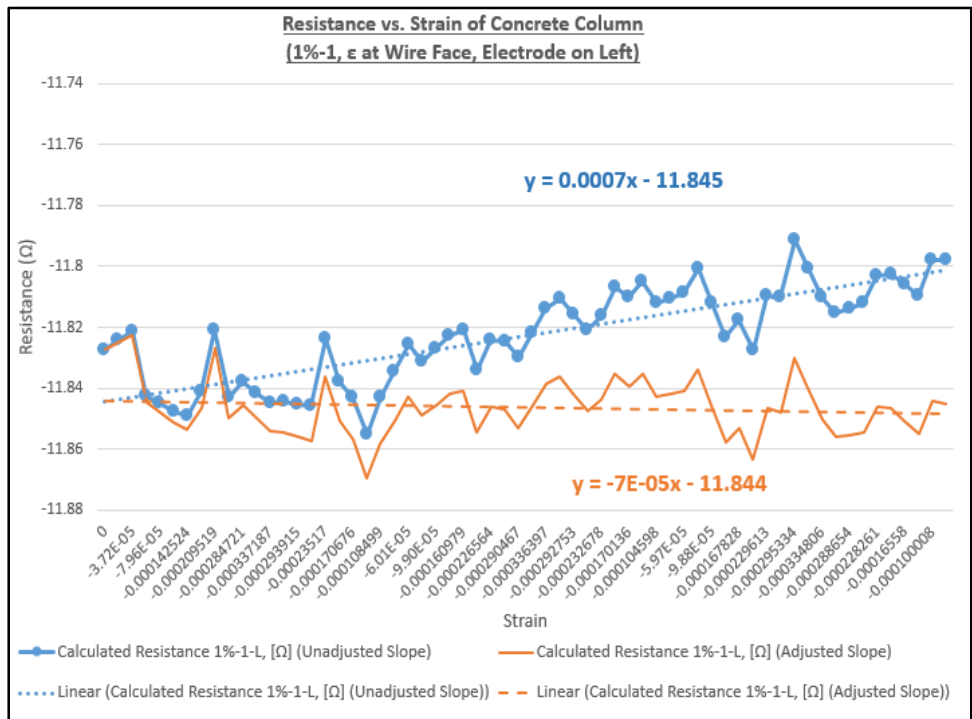
Figure F-48

Calculated Resistance (1%, Column 1, Left Electrode Pair)
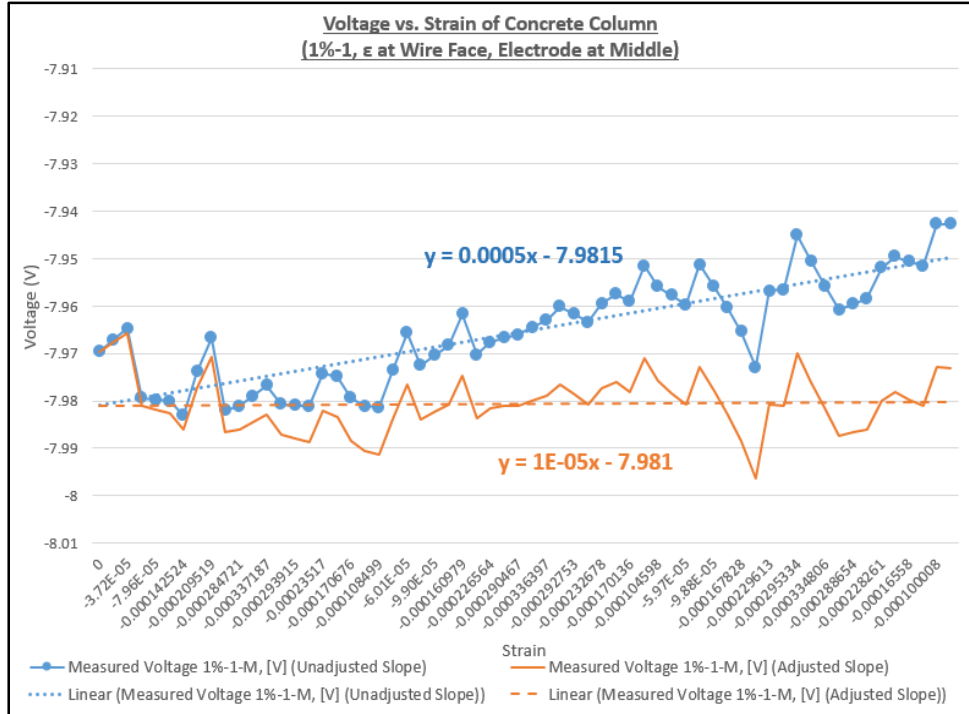
Figure F-49

Voltage Measurements (1%, Column 1, Middle Electrode Pair)
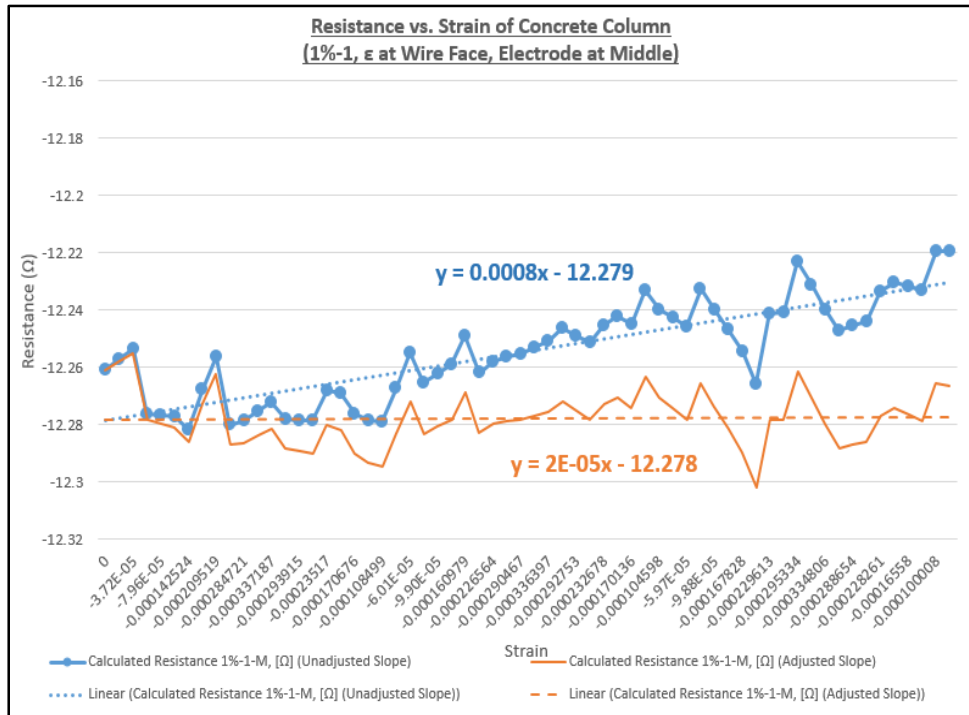
Figure F-50

Calculated Resistance (1%, Column 1, Middle Electrode Pair)
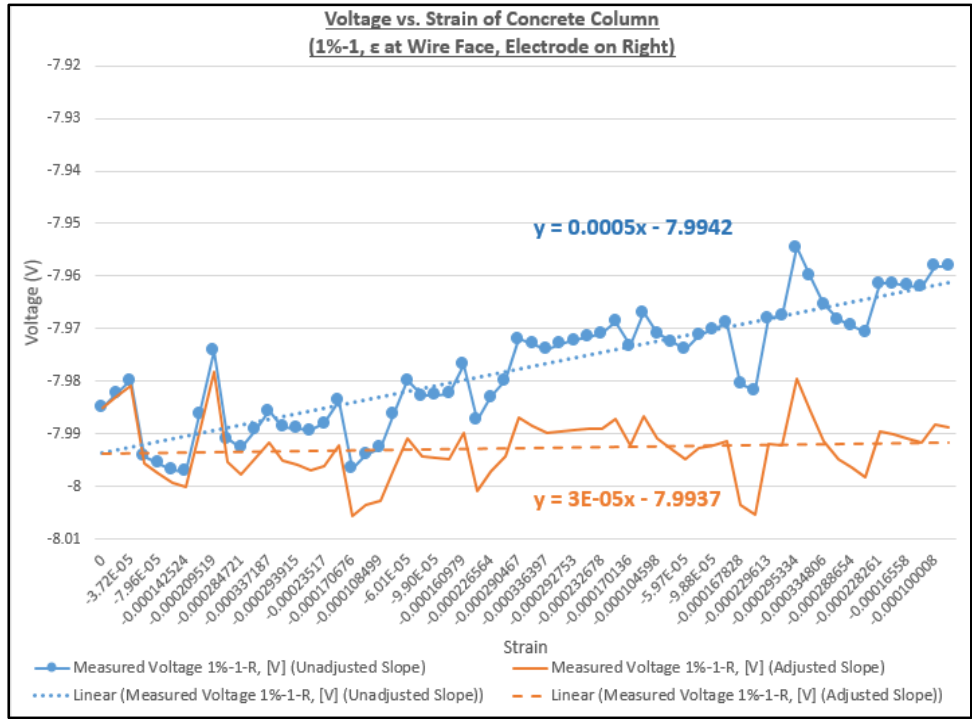
Figure F-51
Voltage Measurements (1%, Column 1, Right Electrode Pair)
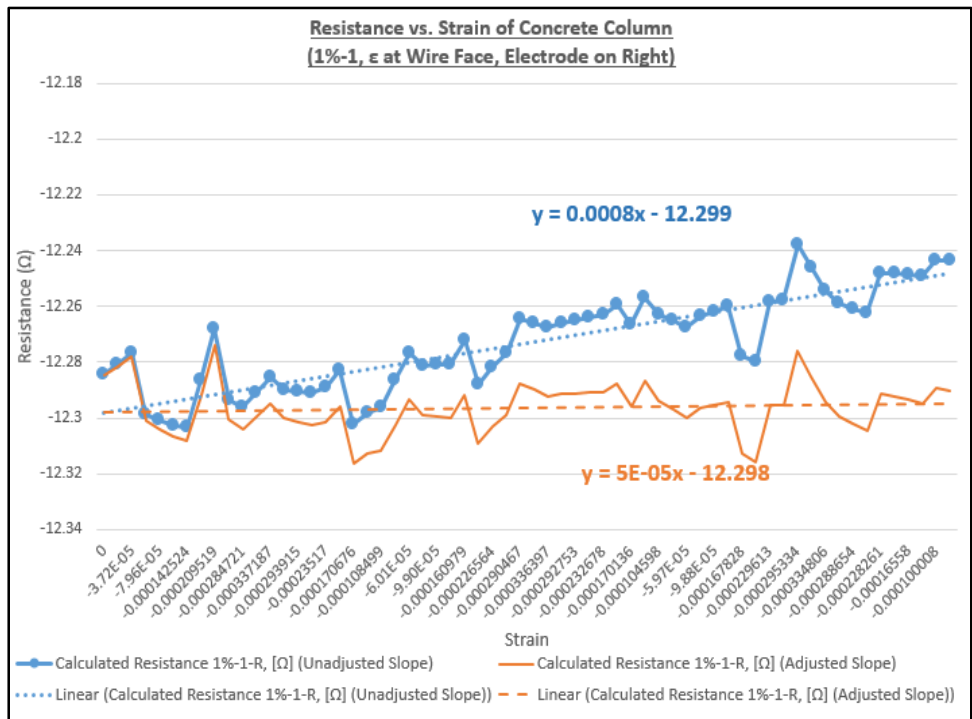
Figure F-52
Calculated Resistance (1%, Column 1, Right Electrode Pair)

Strain and Resistance (RSR Concentration: 1%, Column 2)
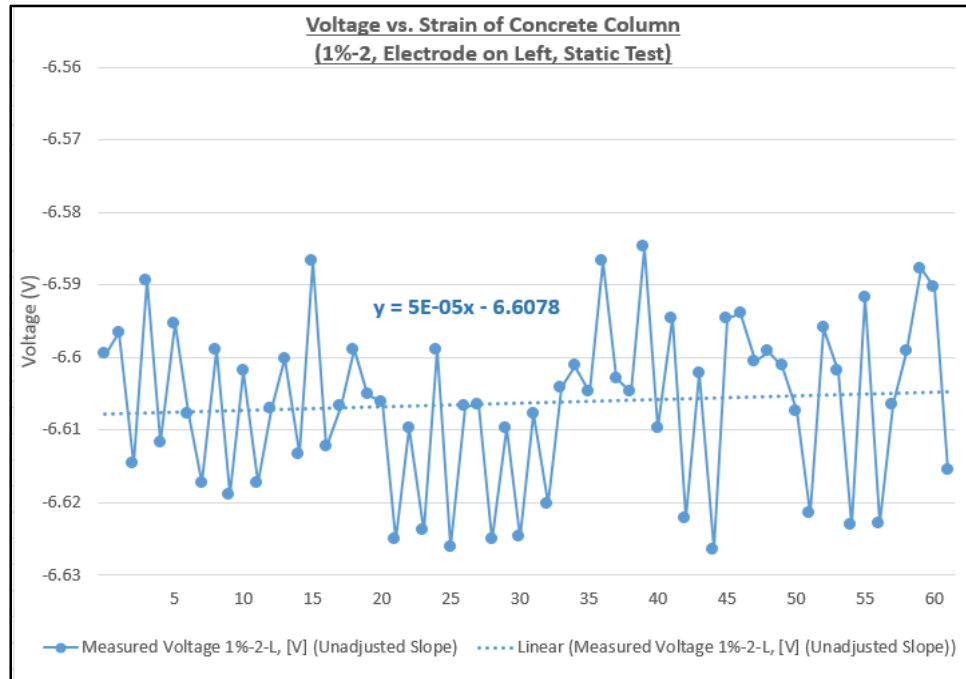
Figure F-53
Static Voltage Measurements (1%, Column 2, Left Electrode Pair)
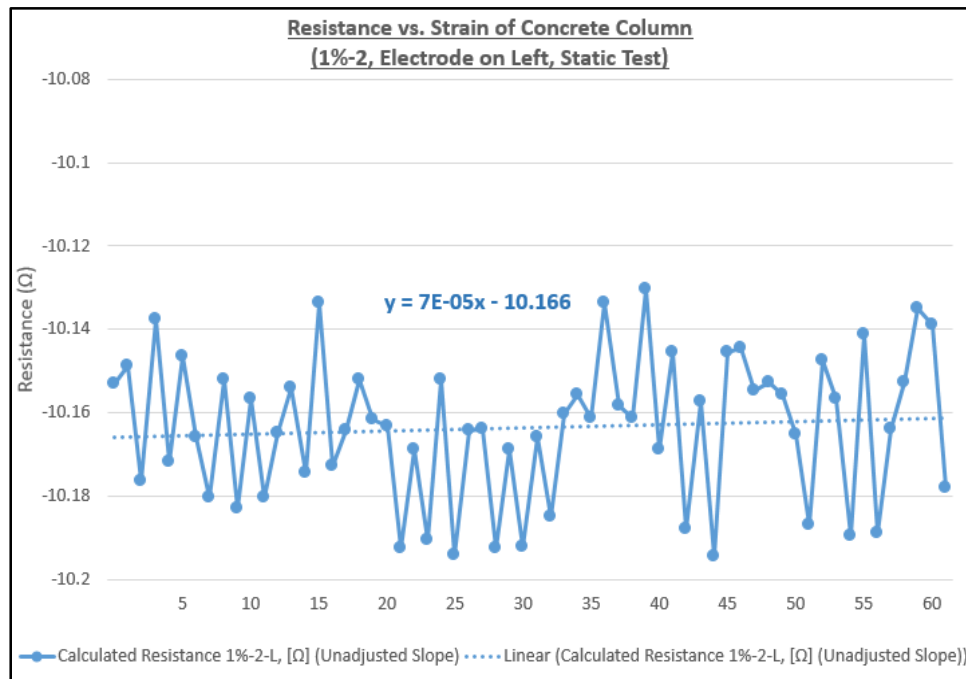
Figure F-54
Static Calculated Resistance (1%, Column 2, Left Electrode Pair)
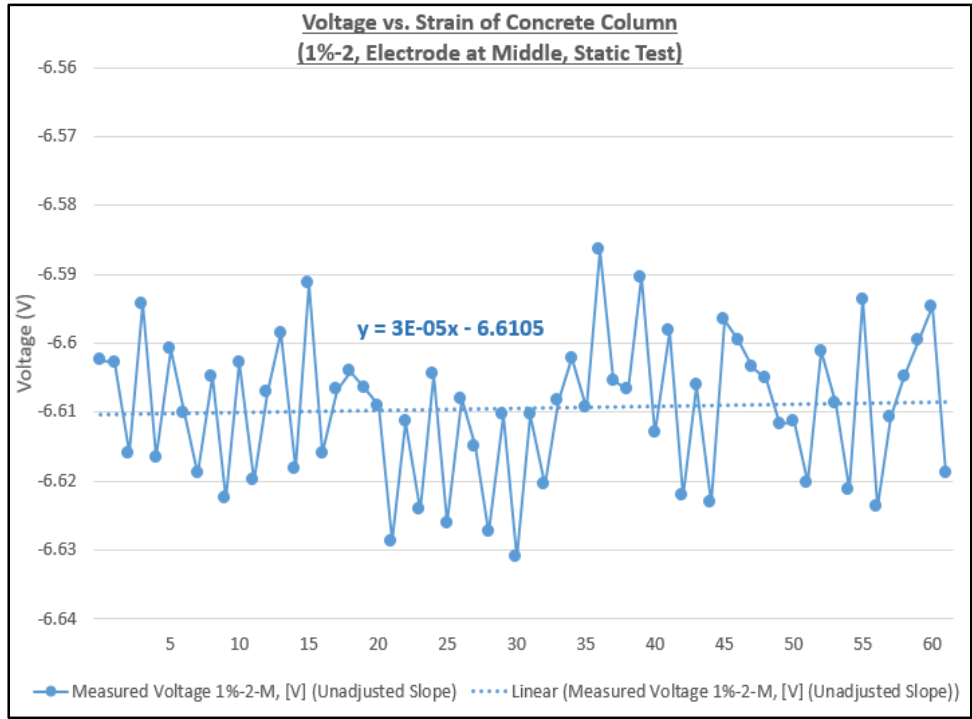
Figure F-55
Static Voltage Measurements (1%, Column 2, Middle Electrode Pair)
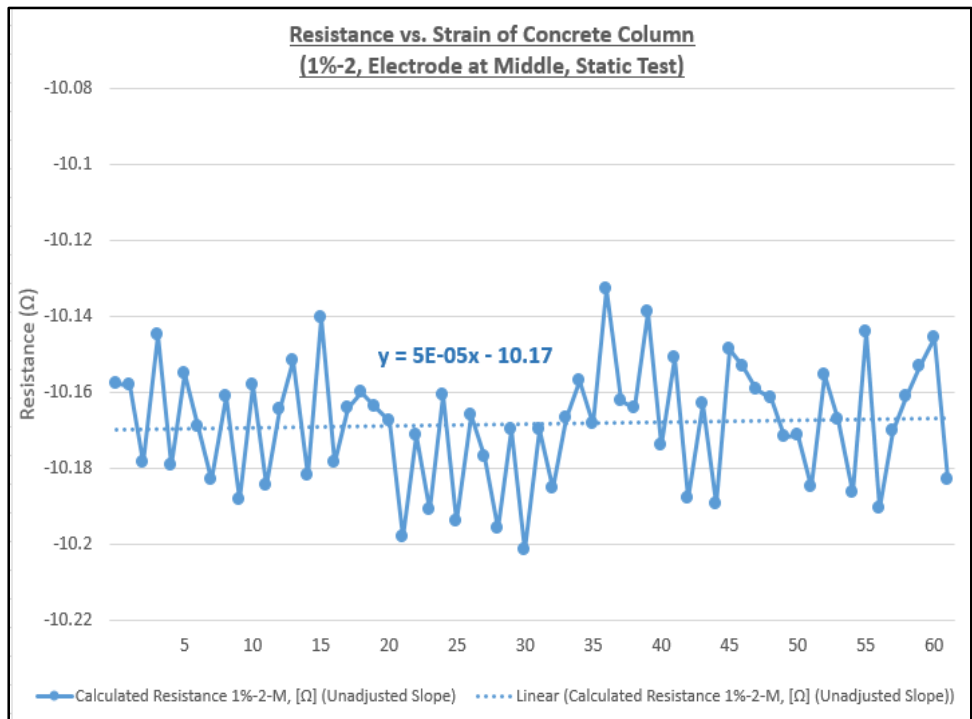
Figure F-56
Static Calculated Resistance (1%, Column 2, Middle Electrode Pair)

274
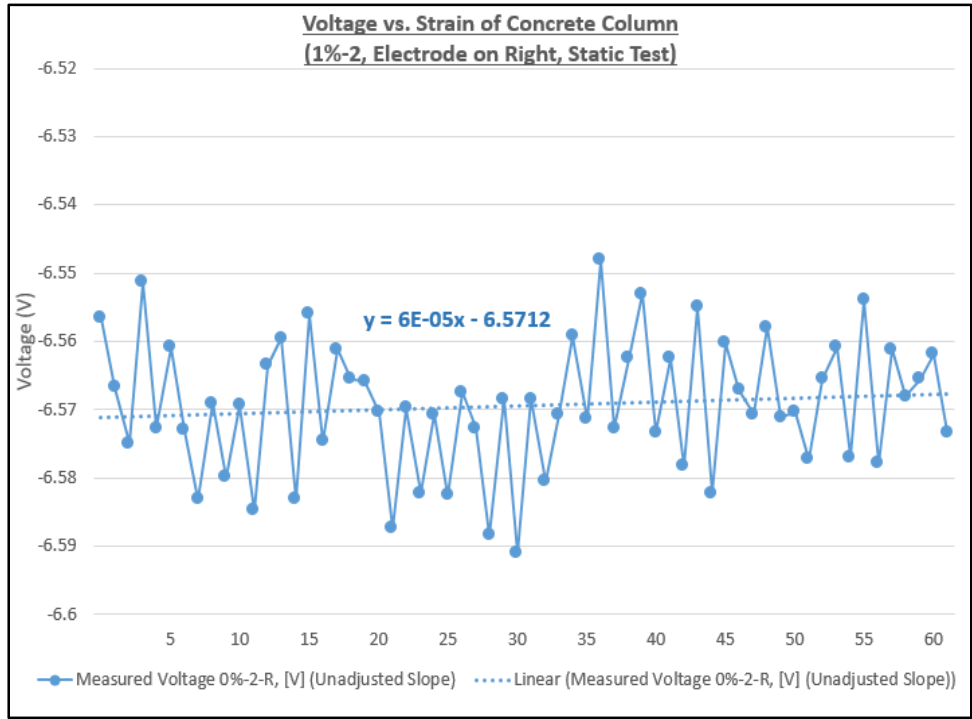
Figure F-57
Static Voltage Measurements (1%, Column 2, Right Electrode Pair)
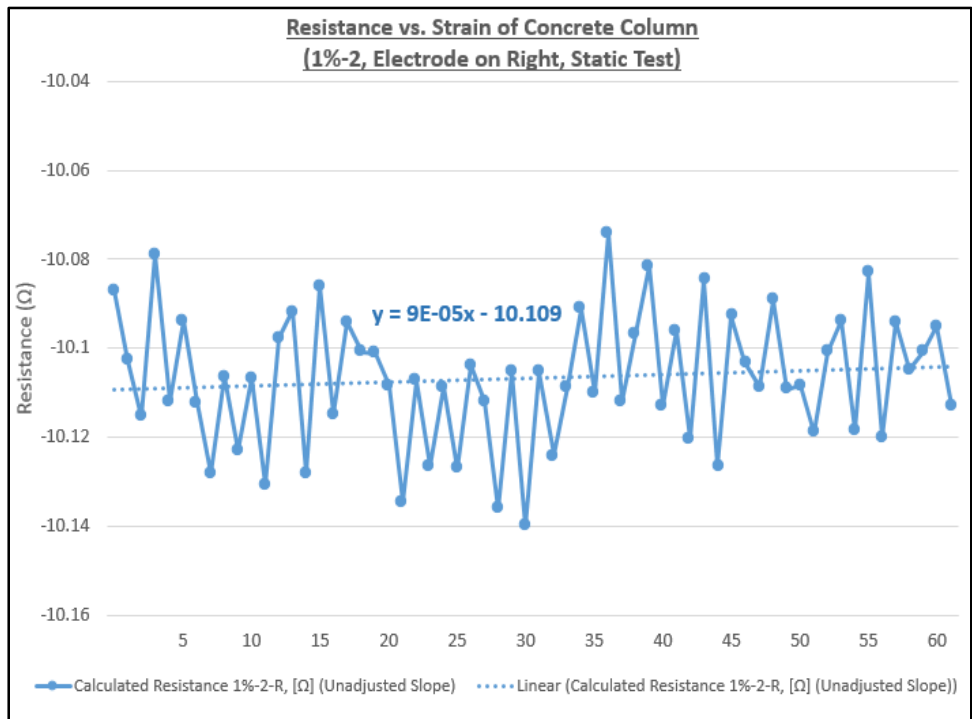
Figure F-58
Static Calculated Resistance (1%, Column 2, Right Electrode Pair)
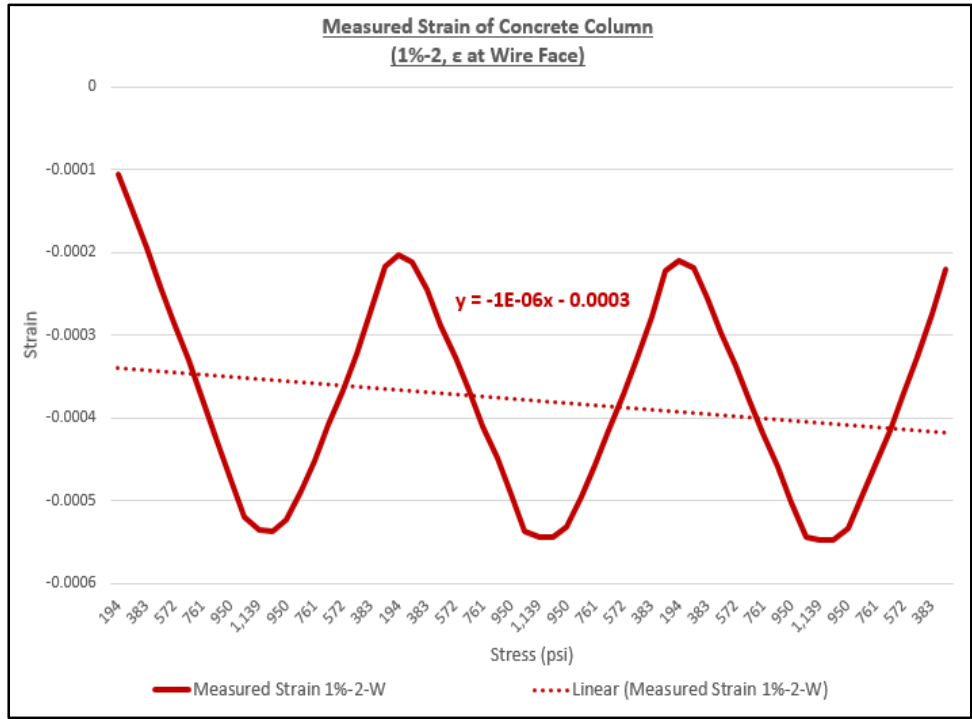
Figure F-59
Strain Measurements (1%, Column 2, Wire Face)
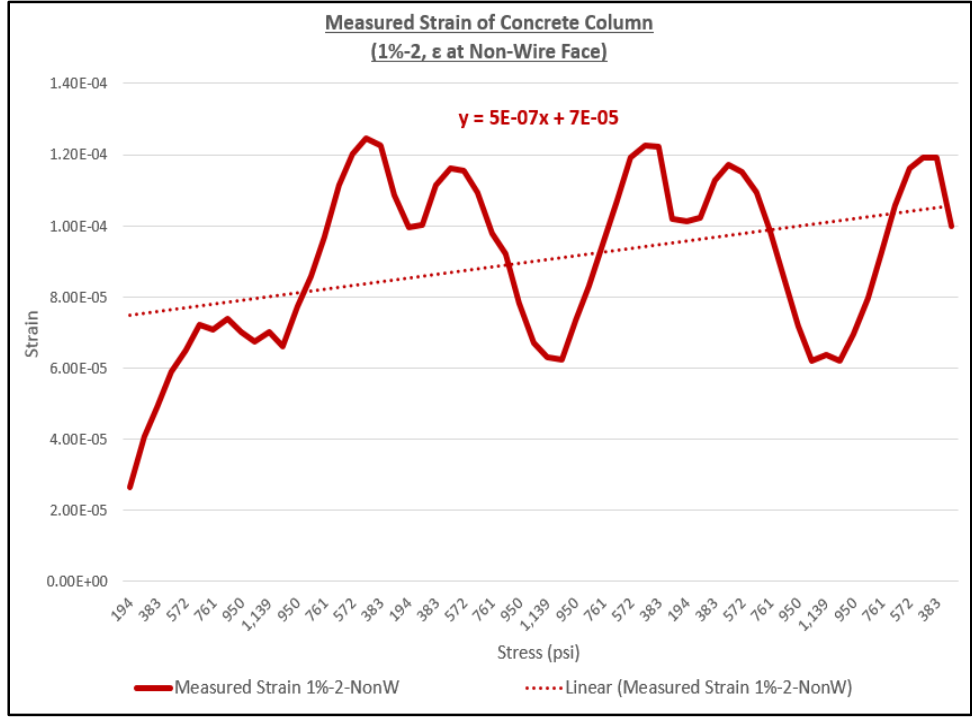
Figure F-60
Strain Measurements (1%, Column 2, Non-Wire Face) *[Strain Gage Appears Faulty]*

276
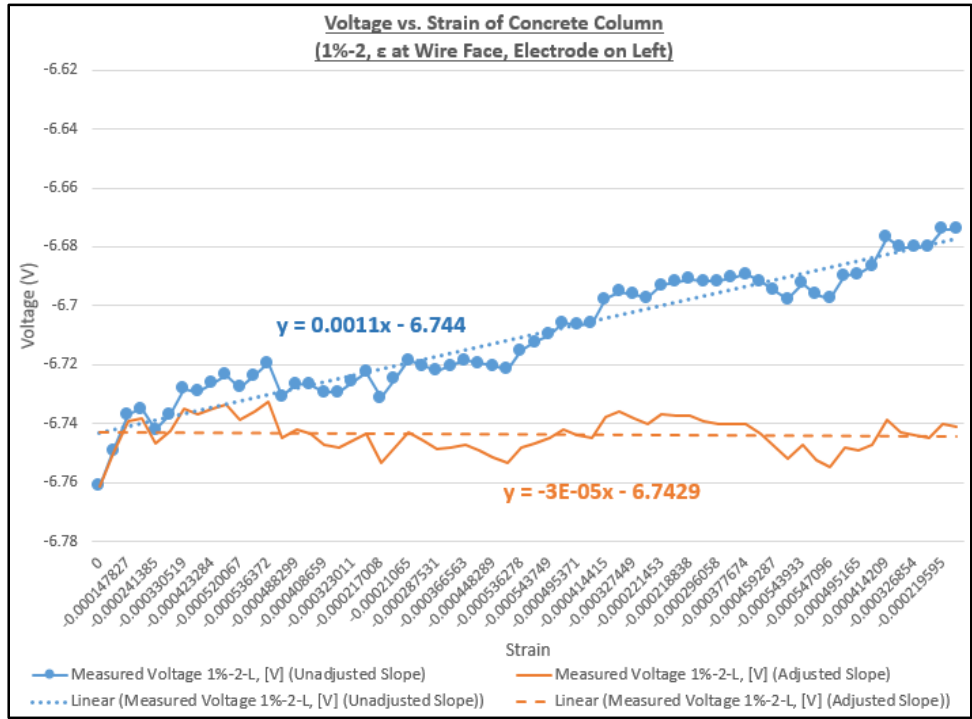
Figure F-61
Voltage Measurements (1%, Column 2, Left Electrode Pair)
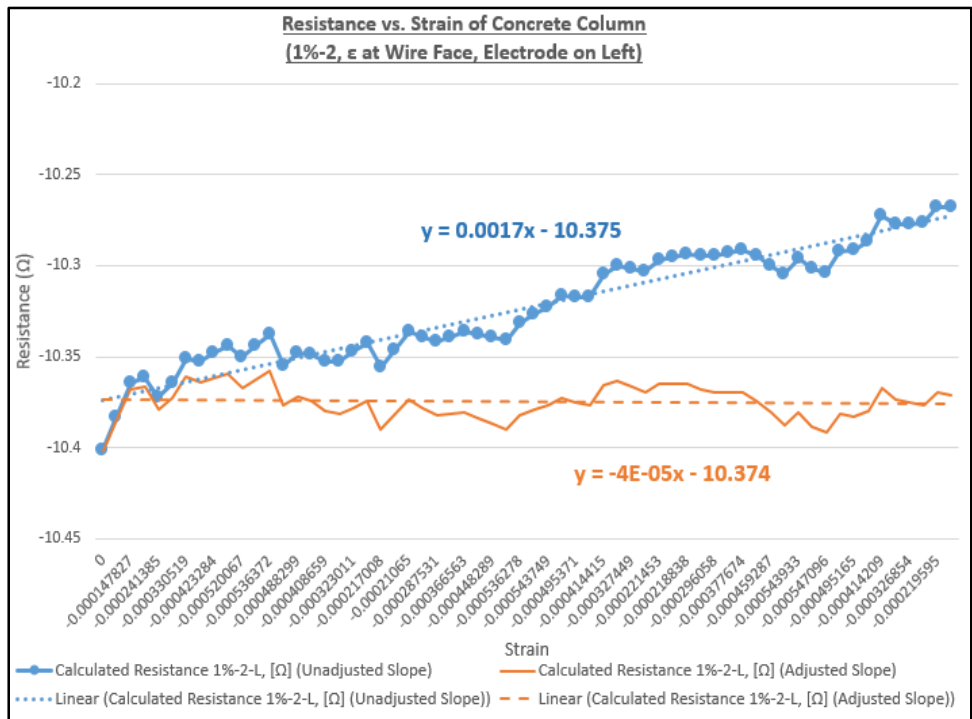
Figure F-62
Calculated Resistance (1%, Column 2, Left Electrode Pair)
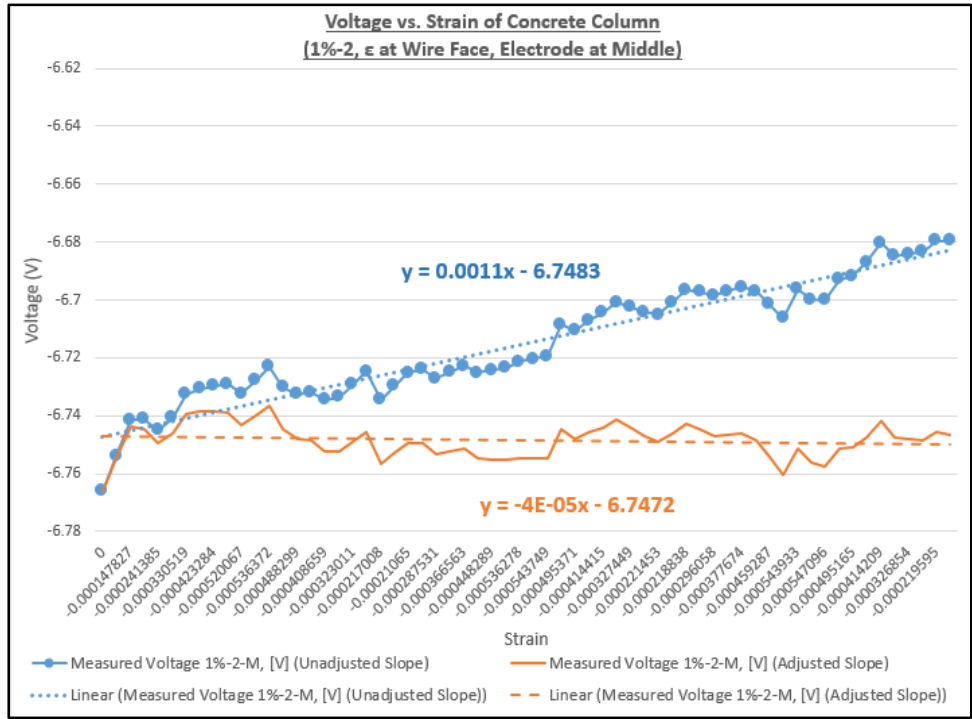
Figure F-63
Voltage Measurements (1%, Column 2, Middle Electrode Pair)
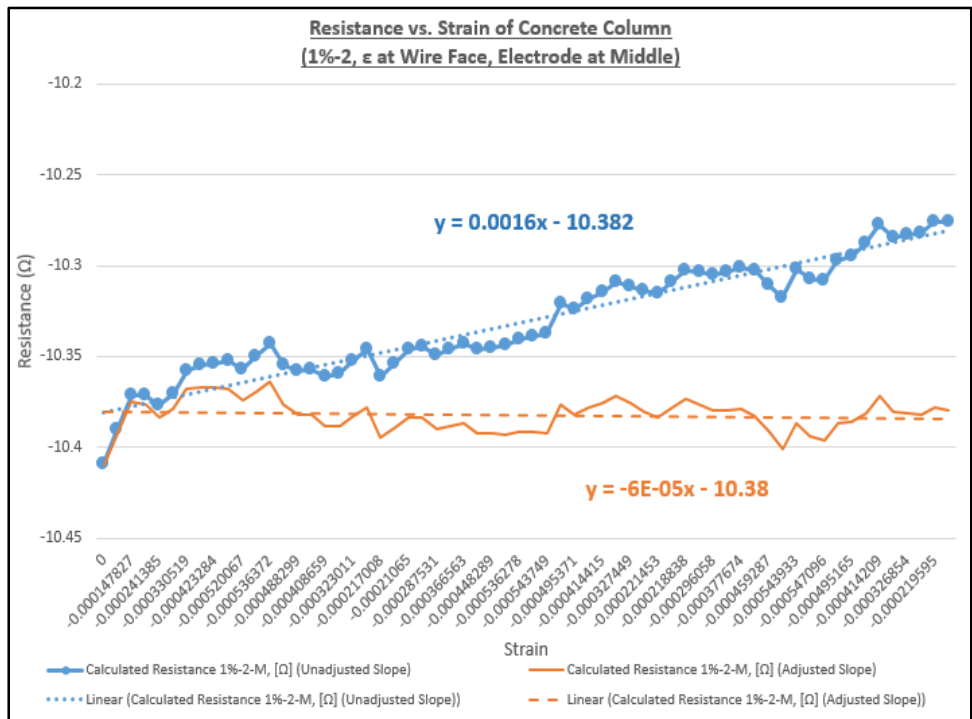
Figure F-64
Calculated Resistance (1%, Column 2, Middle Electrode Pair)

278
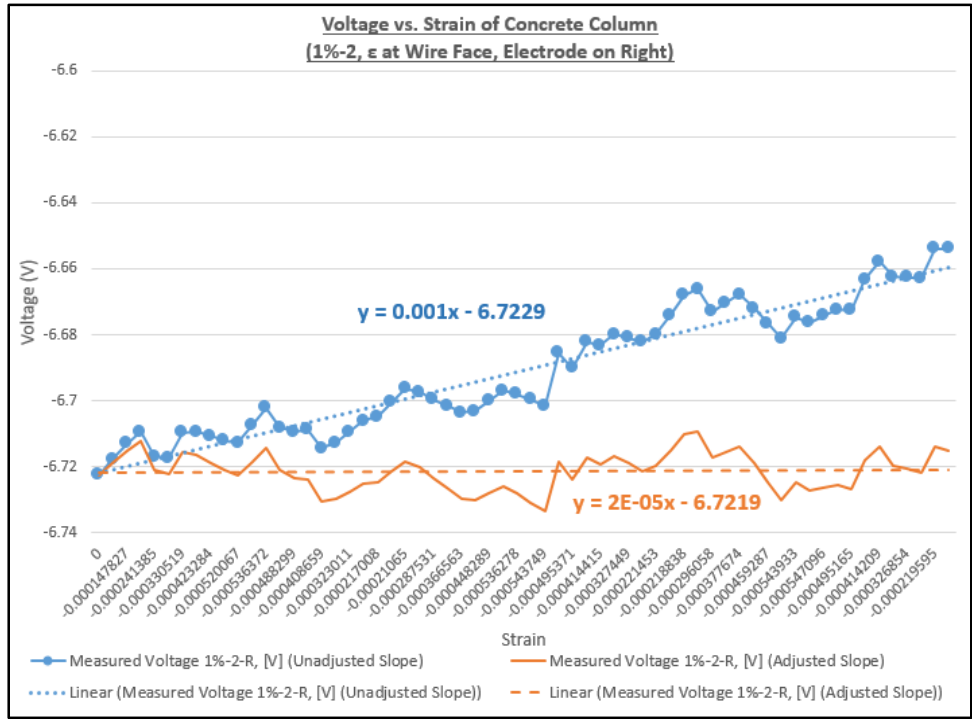
Figure F-65
Voltage Measurements (1%, Column 2, Right Electrode Pair)
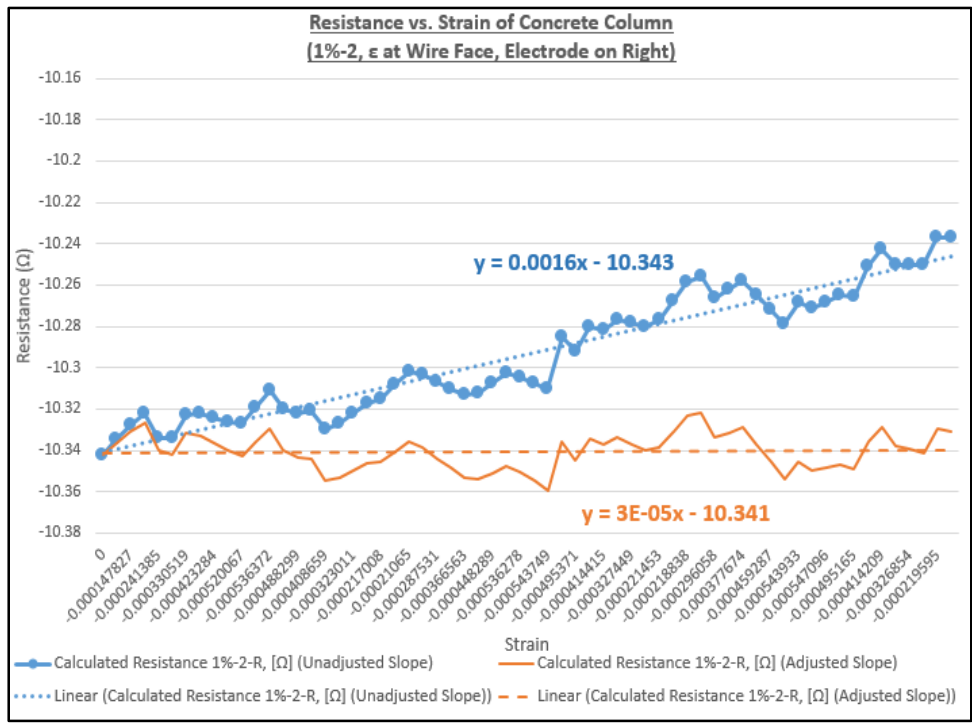
Figure F-66
Calculated Resistance (1%, Column 2, Right Electrode Pair)

Strain and Resistance (RSR Concentration: 1%, Column 3)
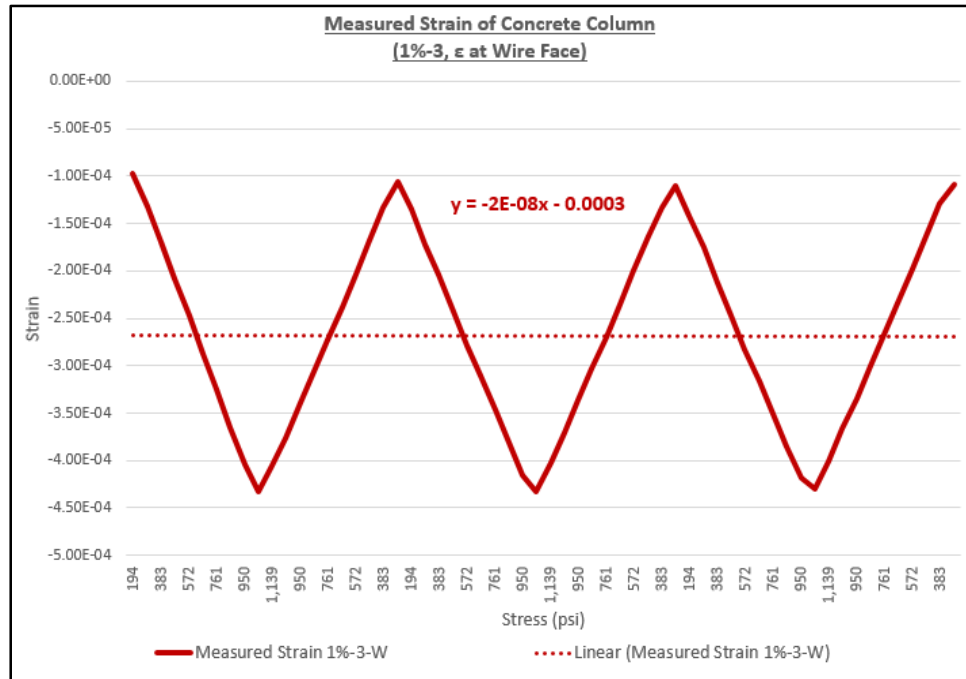
Figure F-67
Strain Measurements (1%, Column 3, Wire Face)
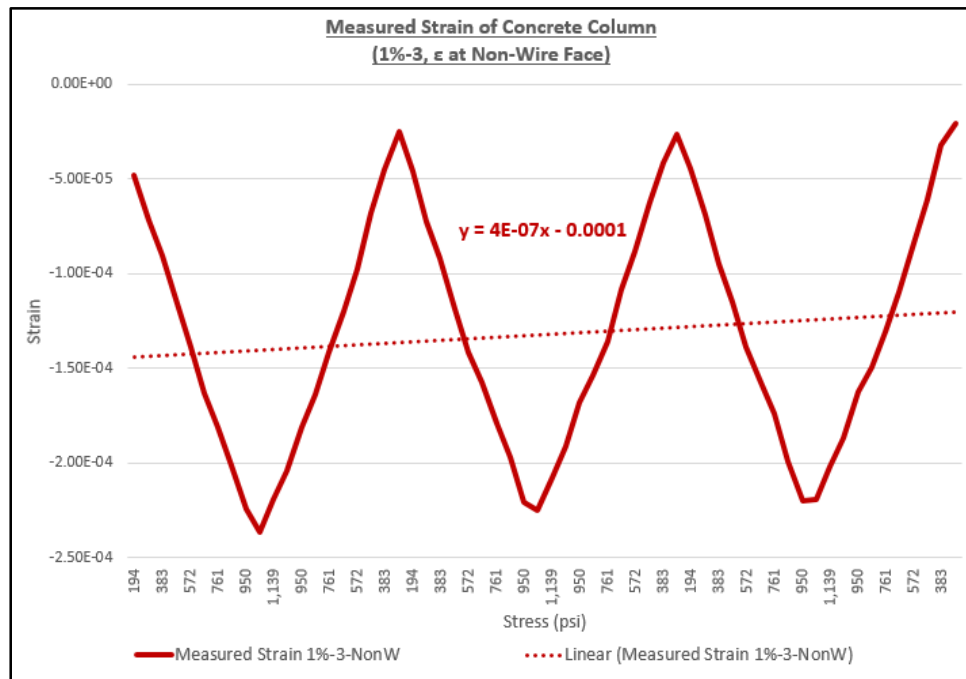
Figure F-68
Strain Measurements (1%, Column 3, Non-Wire Face)

280
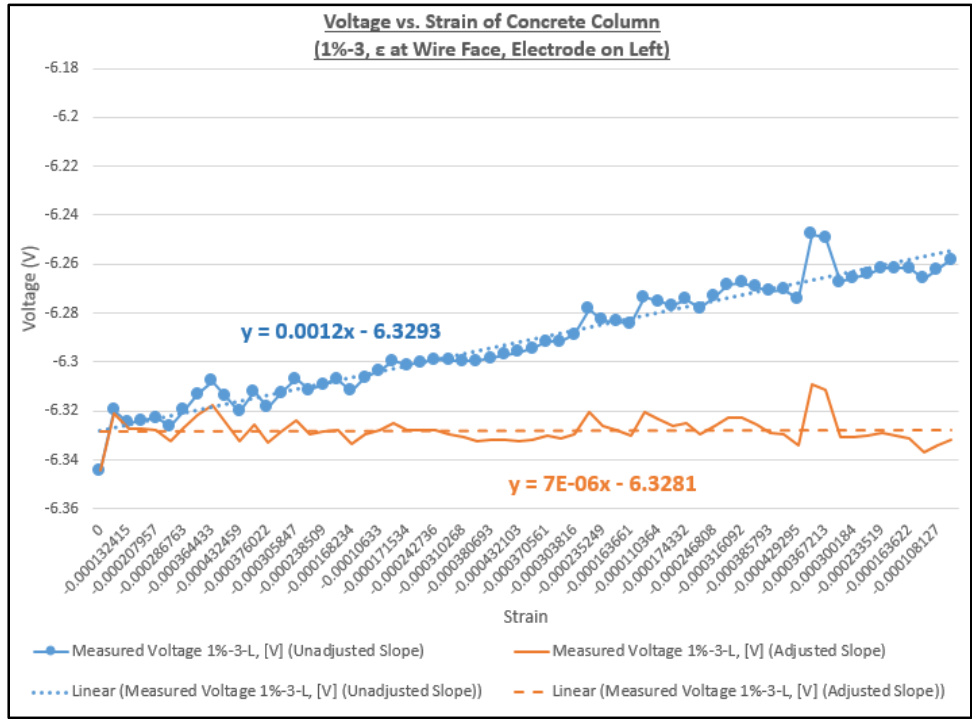
Figure F-69
Voltage Measurements (1%, Column 3, Left Electrode Pair)
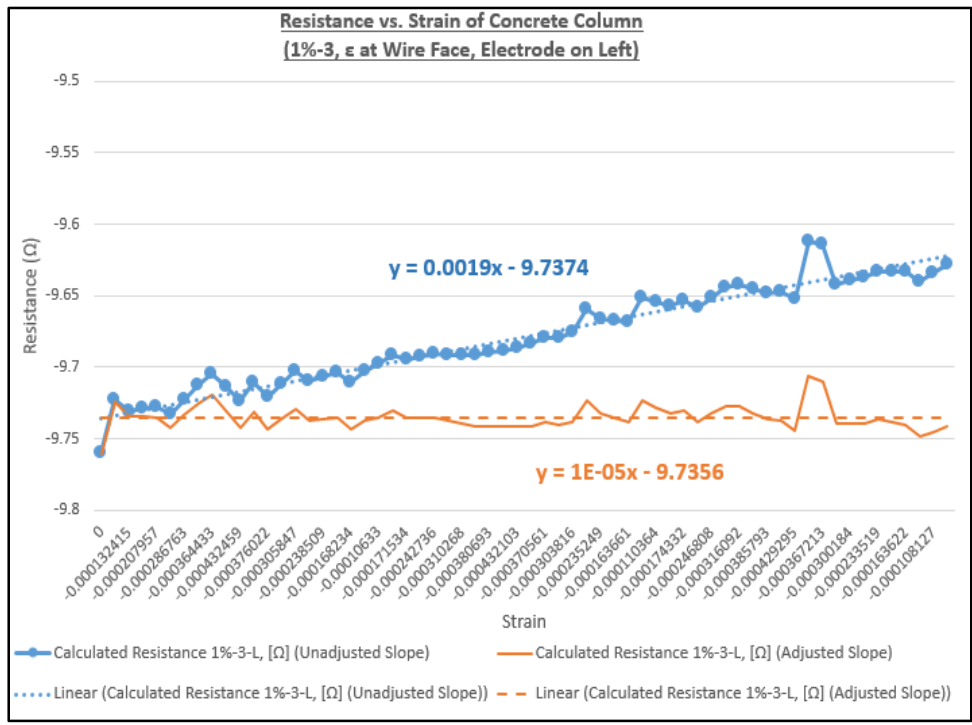
Figure F-70
Calculated Resistance (1%, Column 3, Left Electrode Pair)
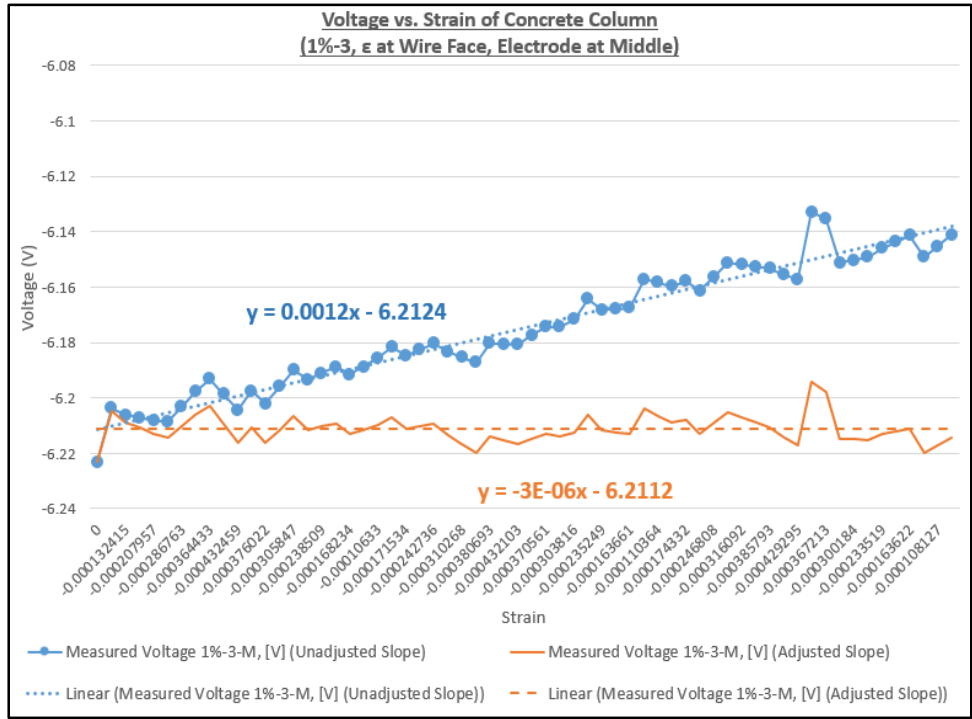
Figure F-71
Voltage Measurements (1%, Column 3, Middle Electrode Pair)
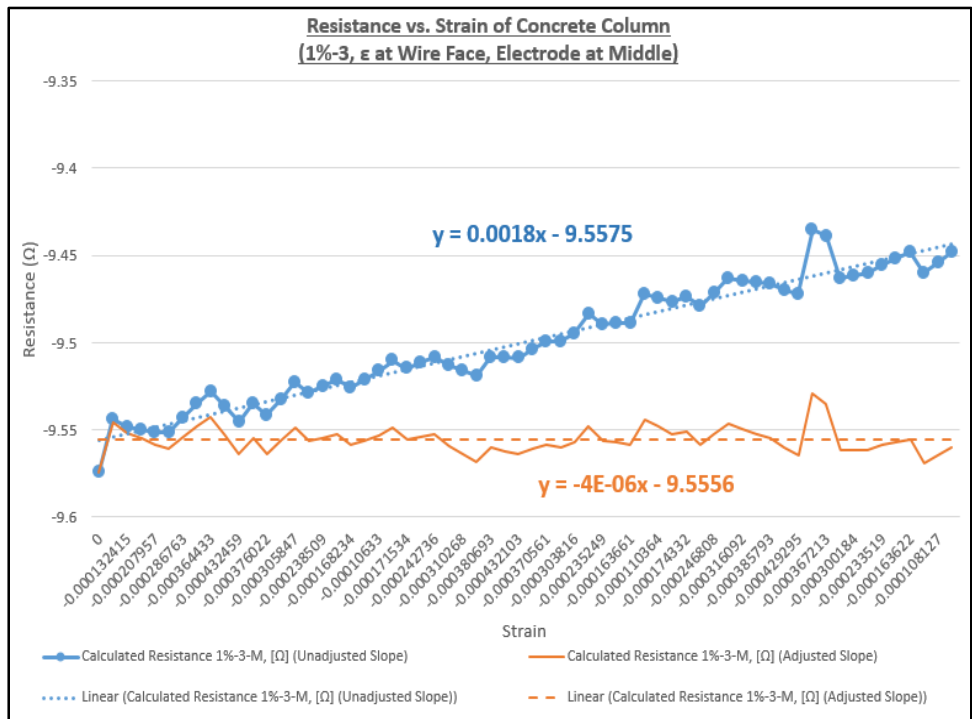
Figure F-72
Calculated Resistance (1%, Column 3, Middle Electrode Pair)

282
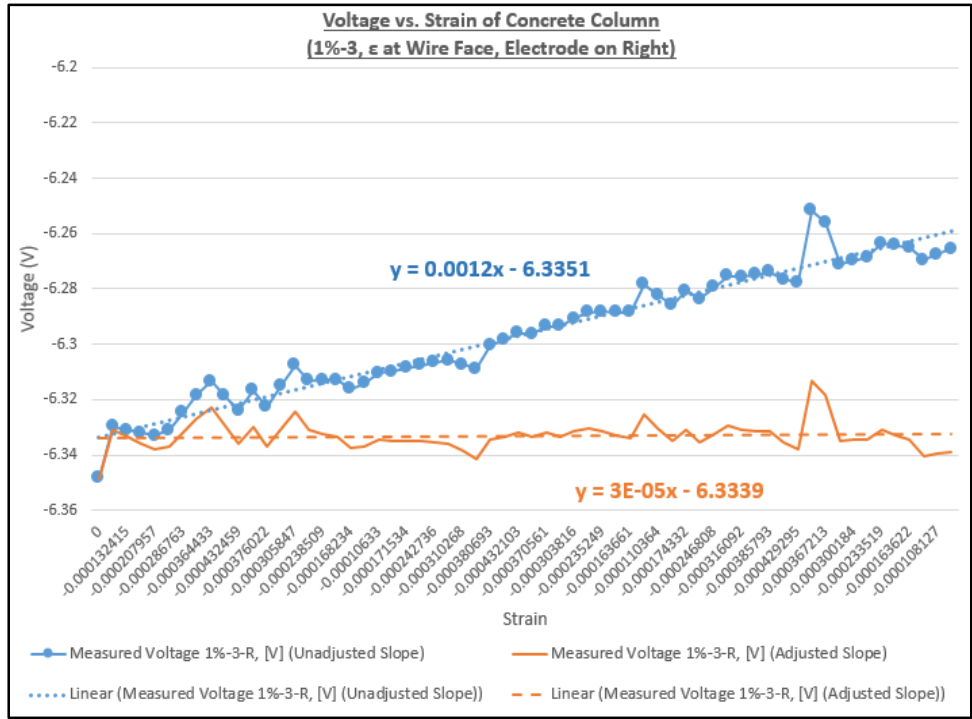
Figure F-73
Voltage Measurements (1%, Column 3, Right Electrode Pair)
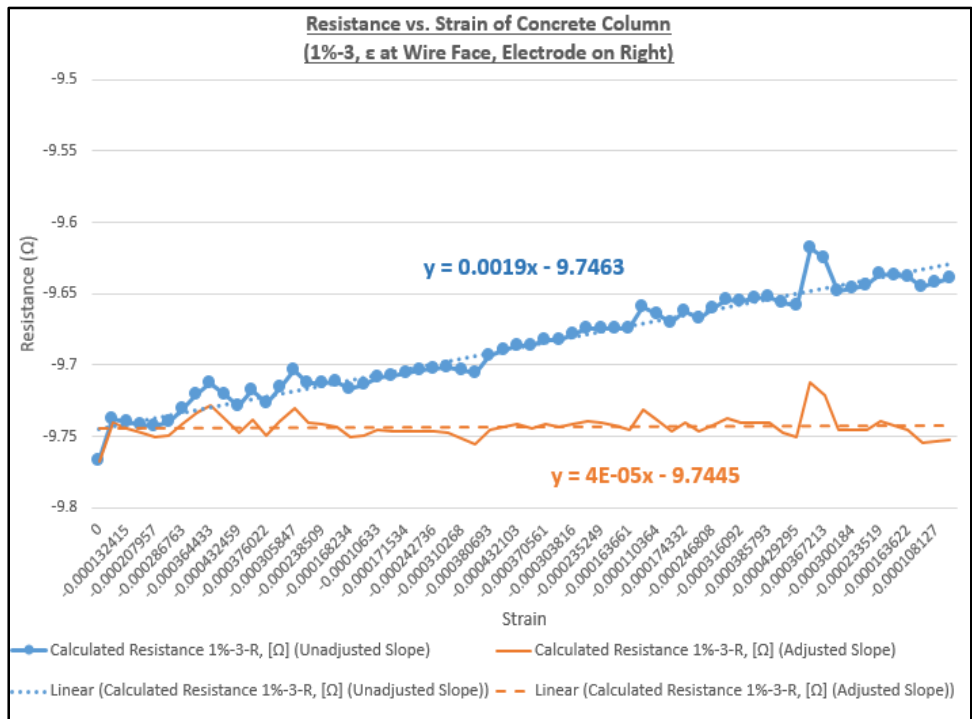
Figure F-74
Calculated Resistance (1%, Column 3, Right Electrode Pair)

Strain and Resistance (RSR Concentration: 2%, Column 1, Test 1)
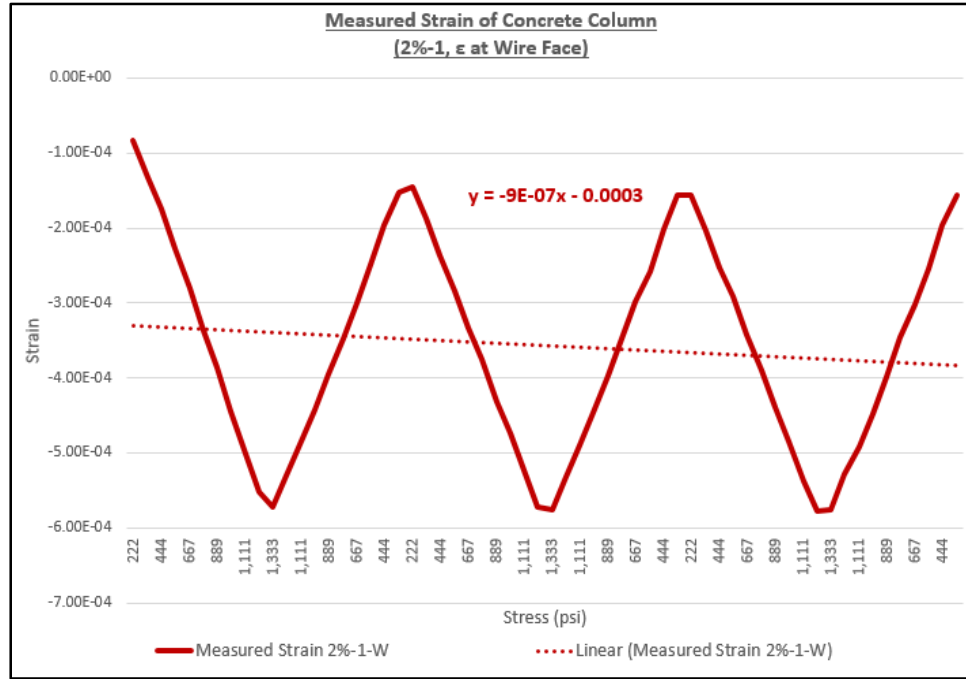
Figure F-75
Strain Measurements (2%, Column 1, Test 1, Wire Face)
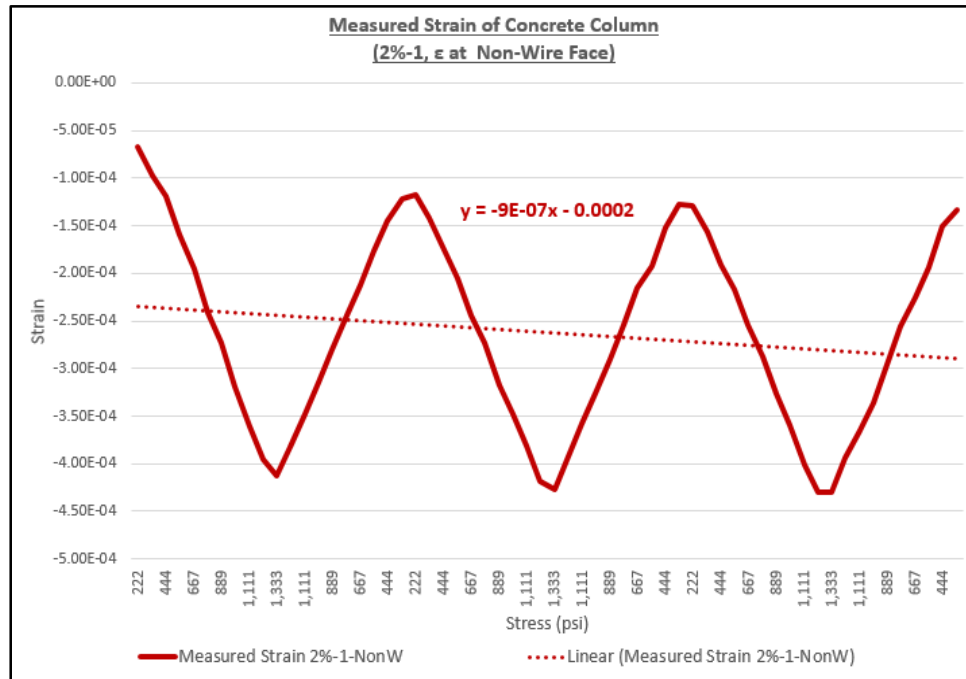
Figure F-76
Strain Measurements (2%, Column 1, Test 1, Non-Wire Face)
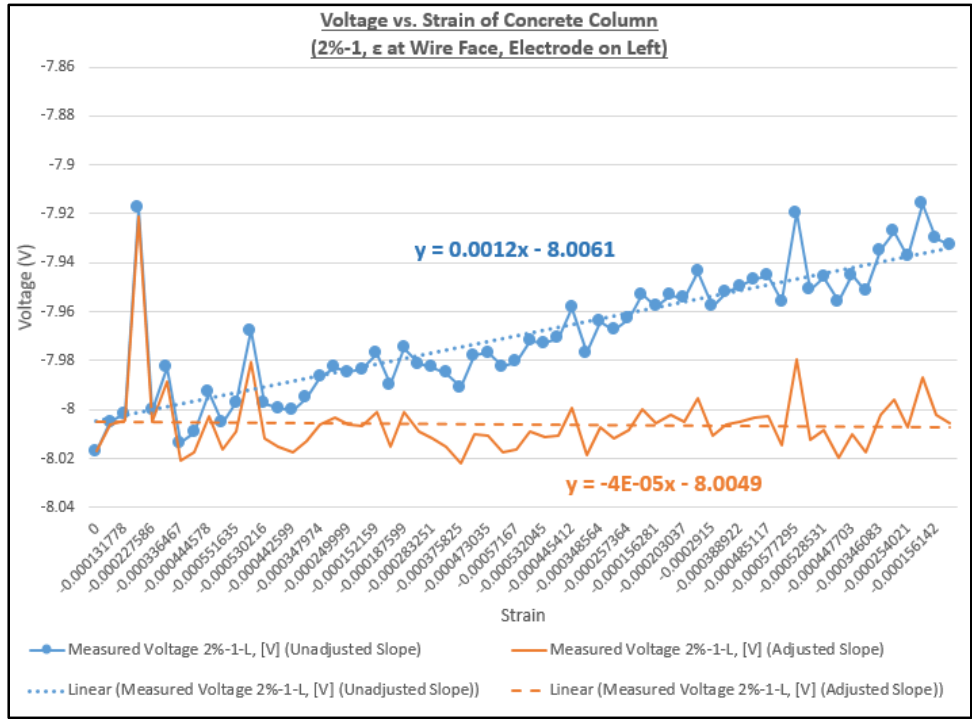
Figure F-77
Voltage Measurements (2%, Column 1, Test 1, Left Electrode Pair)
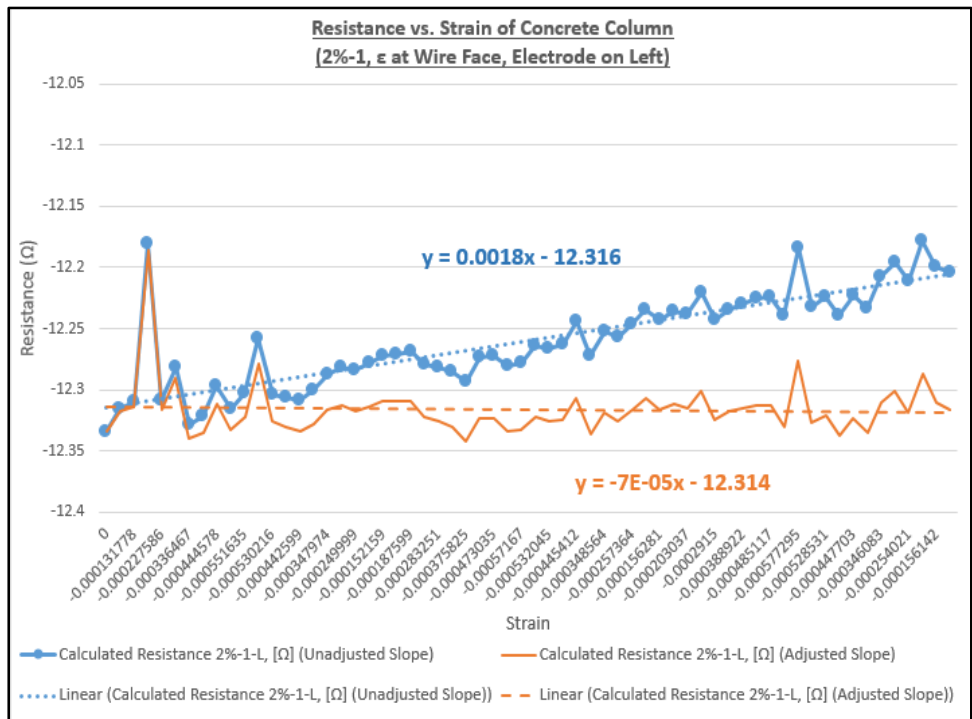
Figure F-78
Calculated Resistance (2%, Column 1, Test 1, Left Electrode Pair)

285
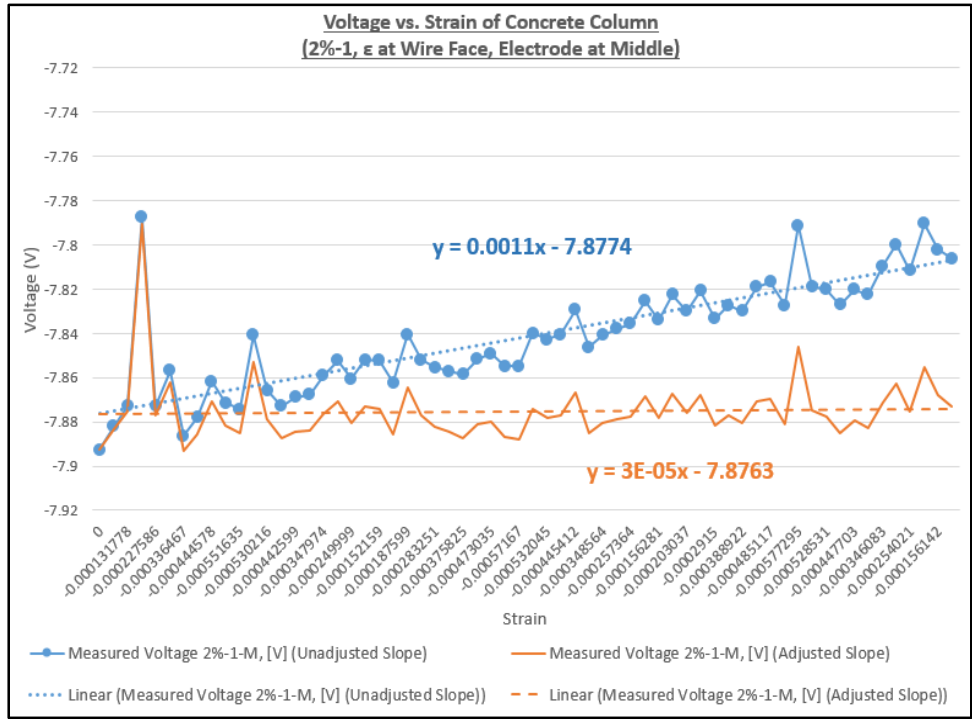
Figure F-79
Voltage Measurements (2%, Column 1, Test 1, Middle Electrode Pair)
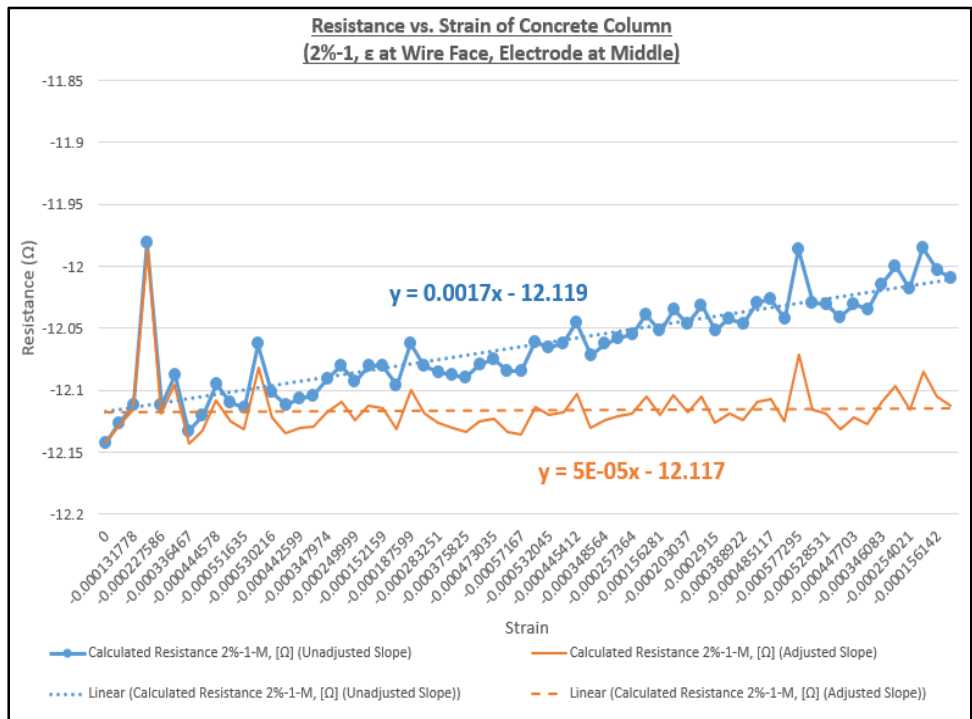
Figure F-80
Calculated Resistance (2%, Column 1, Test 1, Middle Electrode Pair)

286
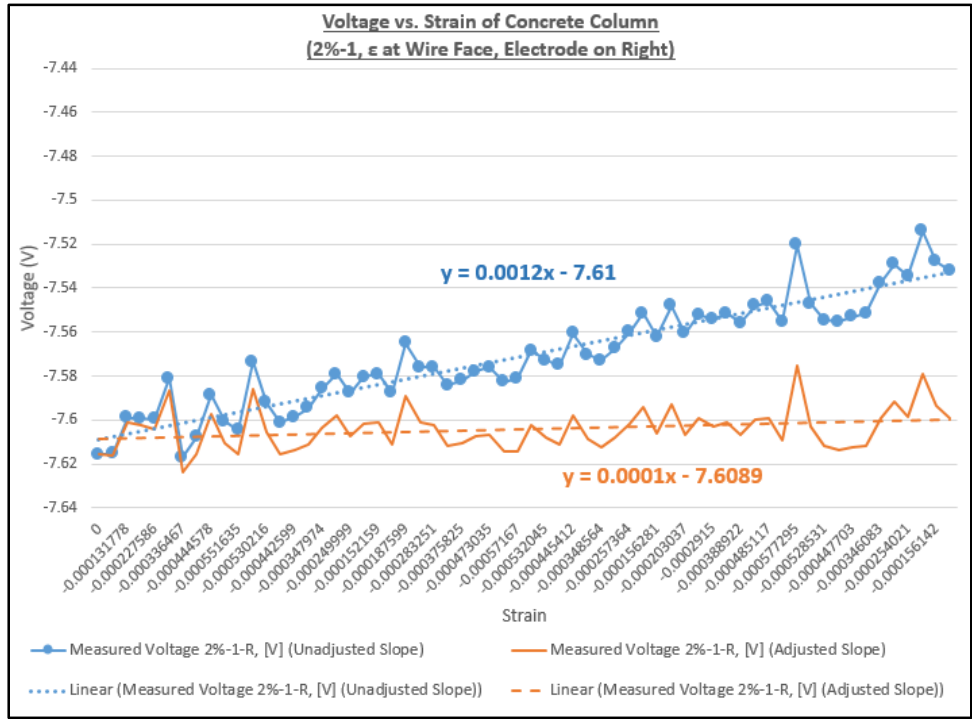
Figure F-81
Voltage Measurements (2%, Column 1, Test 1, Right Electrode Pair)
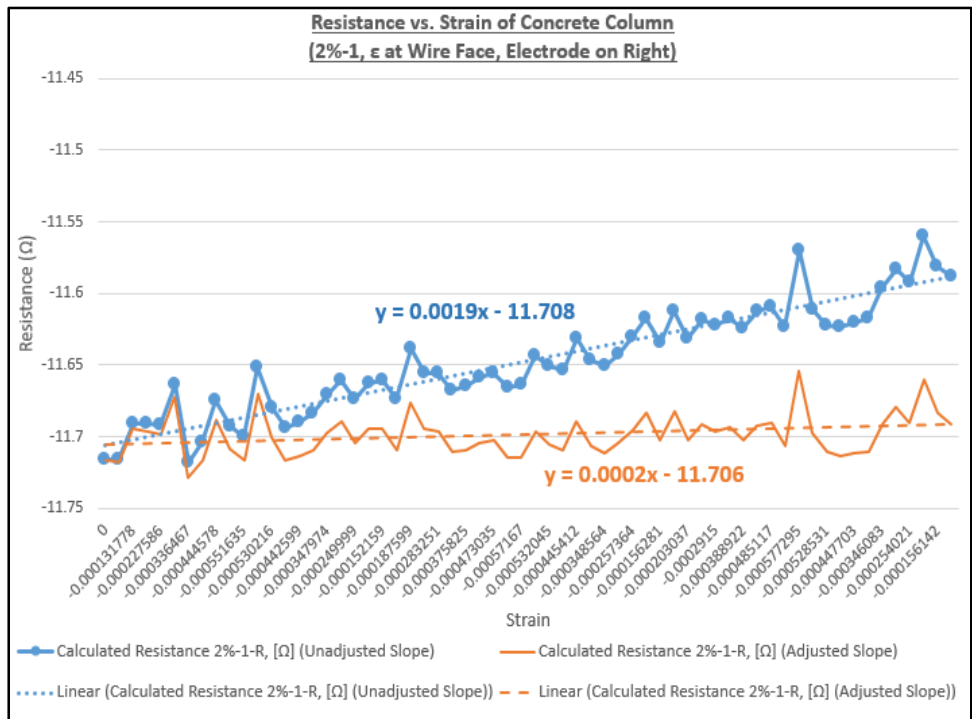
Figure F-82
Calculated Resistance (2%, Column 1, Test 1, Right Electrode Pair)

Strain and Resistance (RSR Concentration: 2%, Column 1, Test 2)
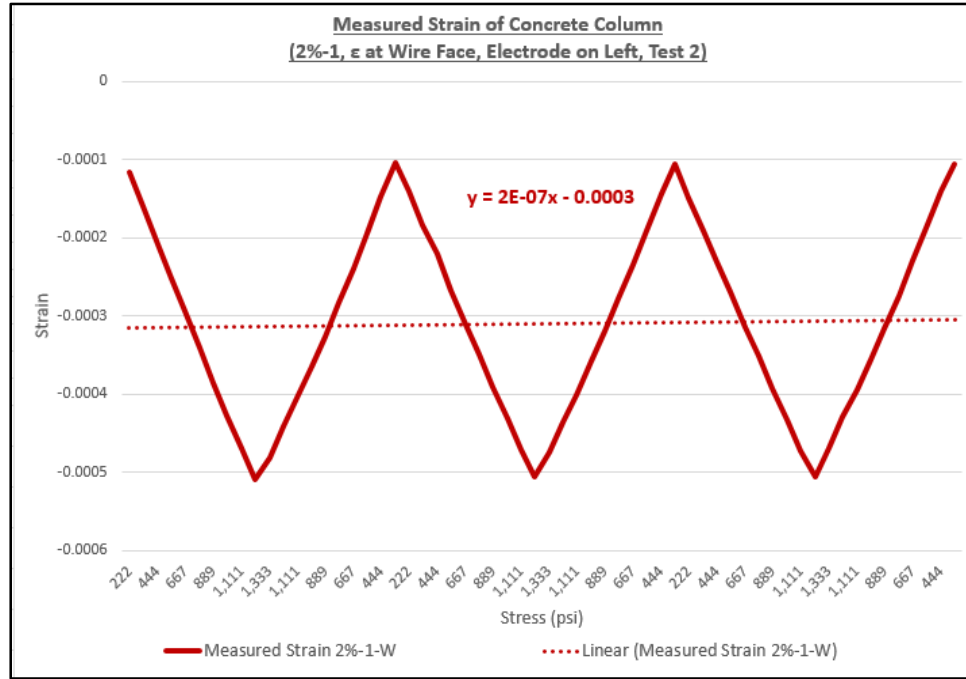
Figure F-83
Strain Measurements (2%, Column 1, Test 2, Wire Face)
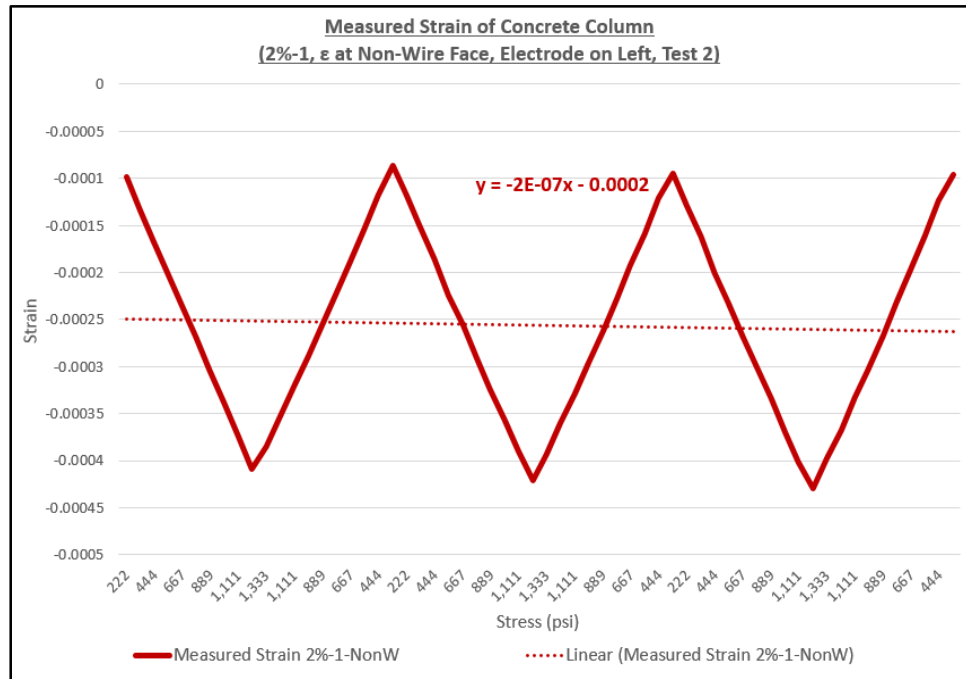
Figure F-84
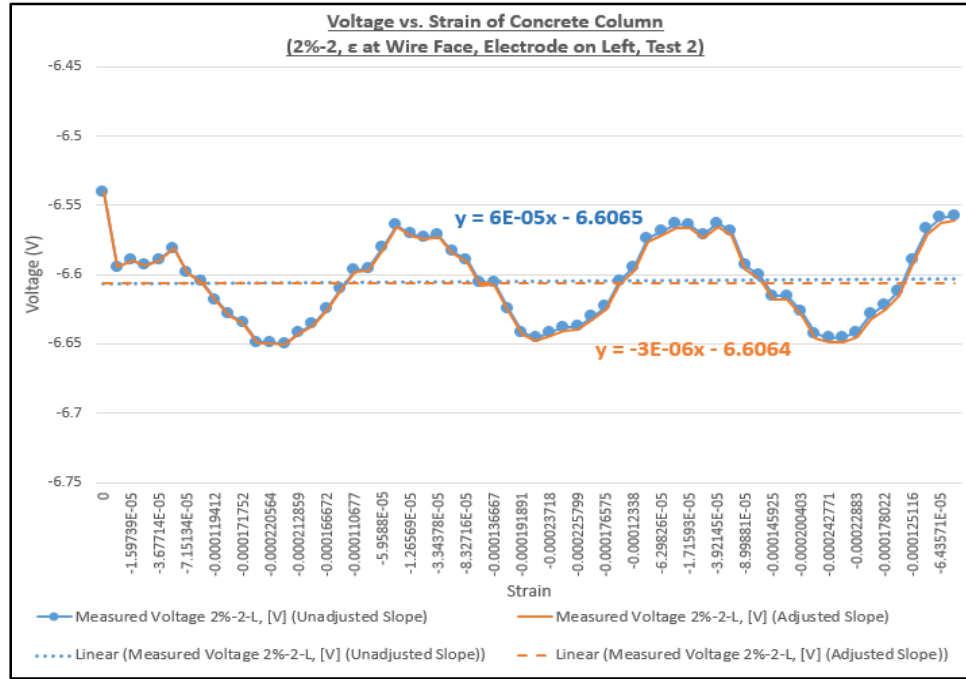Strain Measurements (2%, Column 1, Test 2, Non-Wire Face)
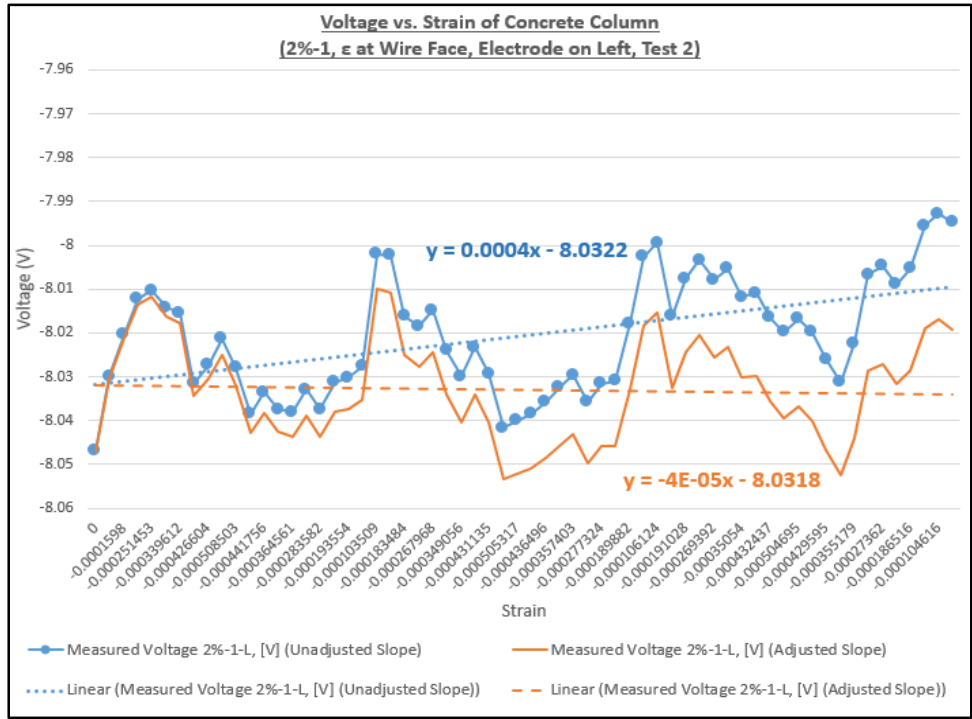
Figure F-85
Voltage Measurements (2%, Column 1, Test 2, Left Electrode Pair)
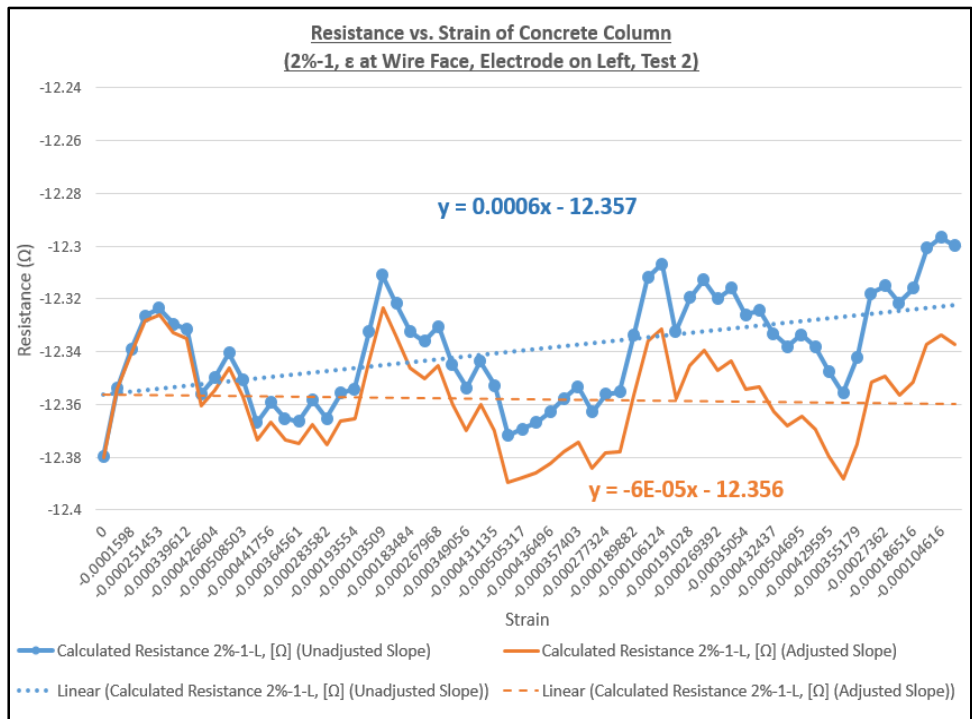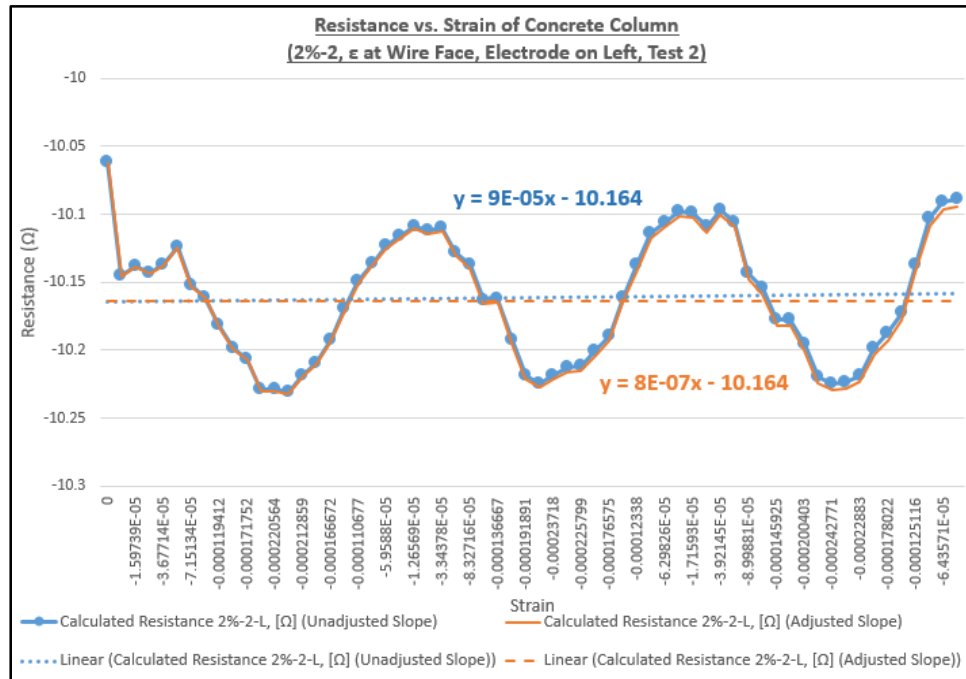

Figure F-86
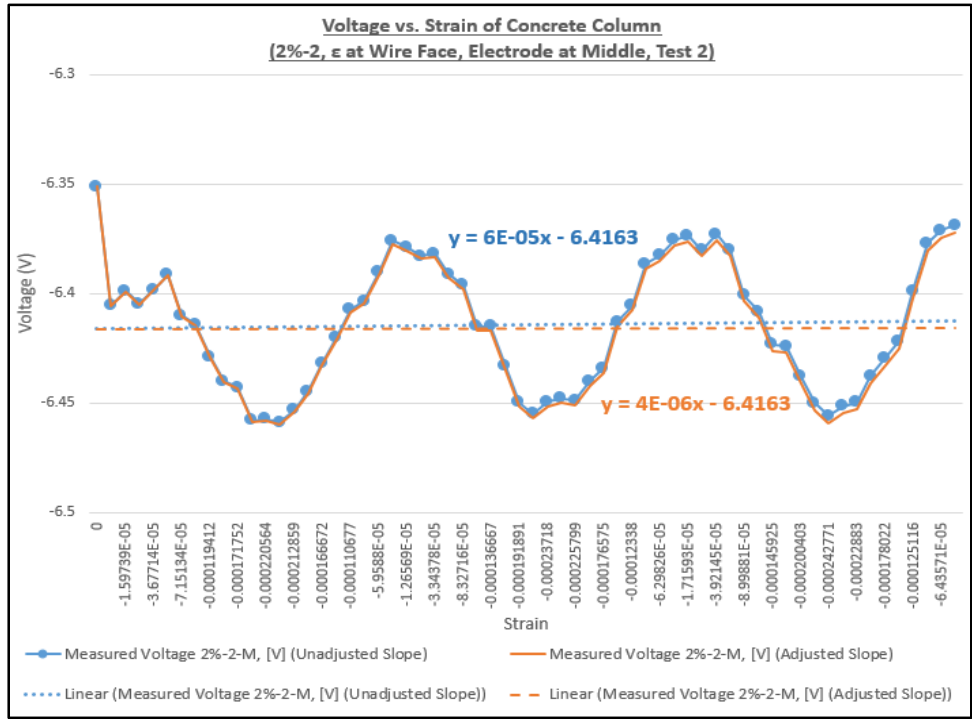Calculated Resistance (2%, Column 1, Test 2, Left Electrode Pair)

289
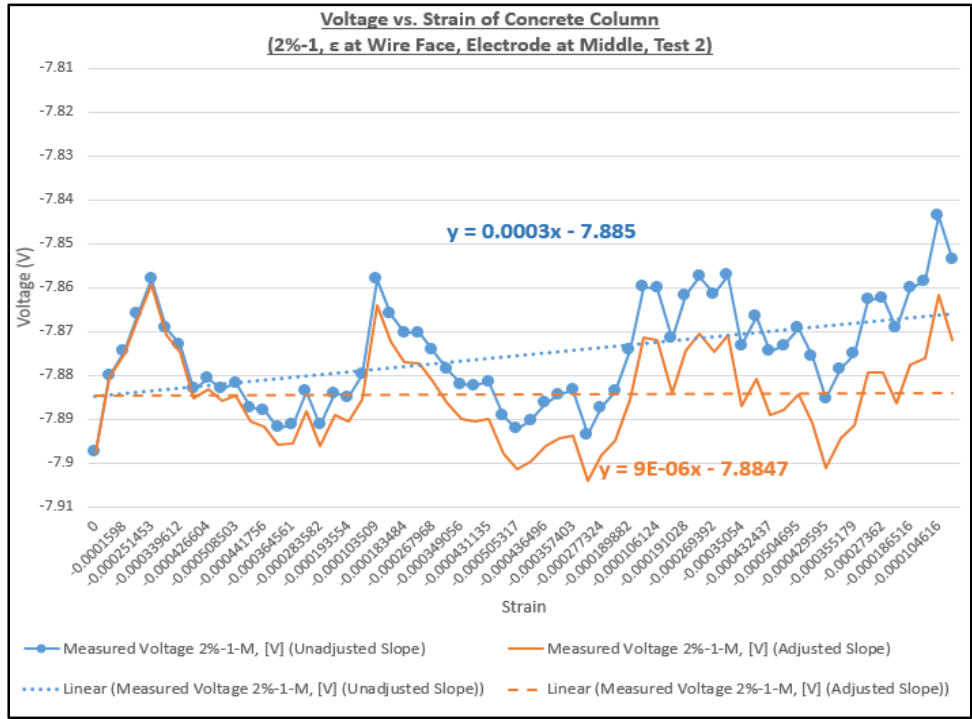
Figure F-87
Voltage Measurements (2%, Column 1, Test 2, Middle Electrode Pair)
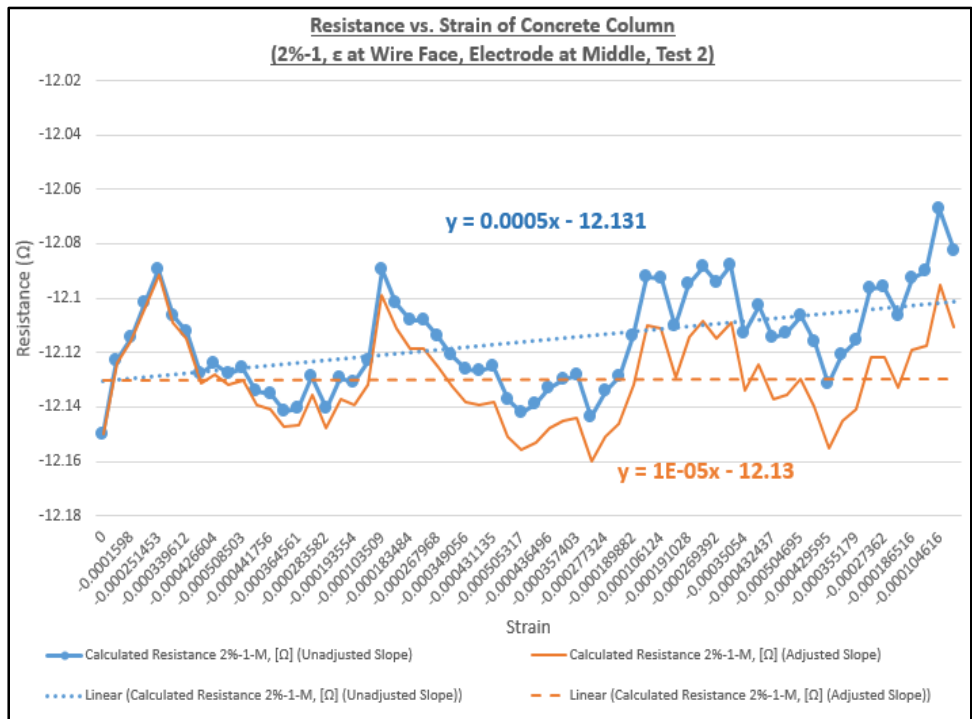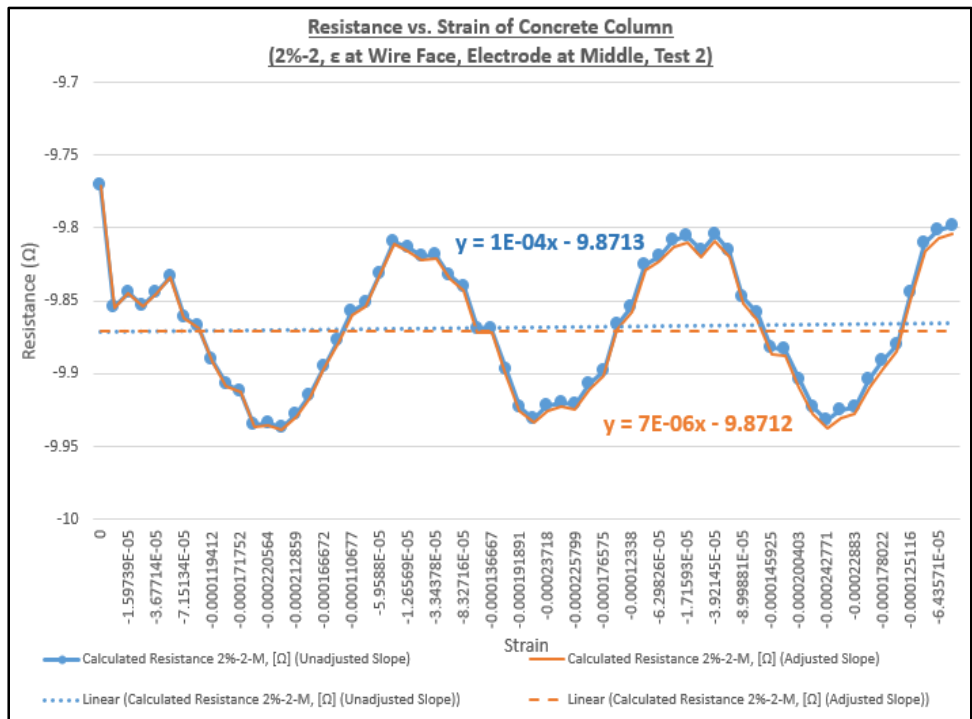

Figure F-88
Calculated Resistance (2%, Column 1, Test 2, Middle Electrode Pair)
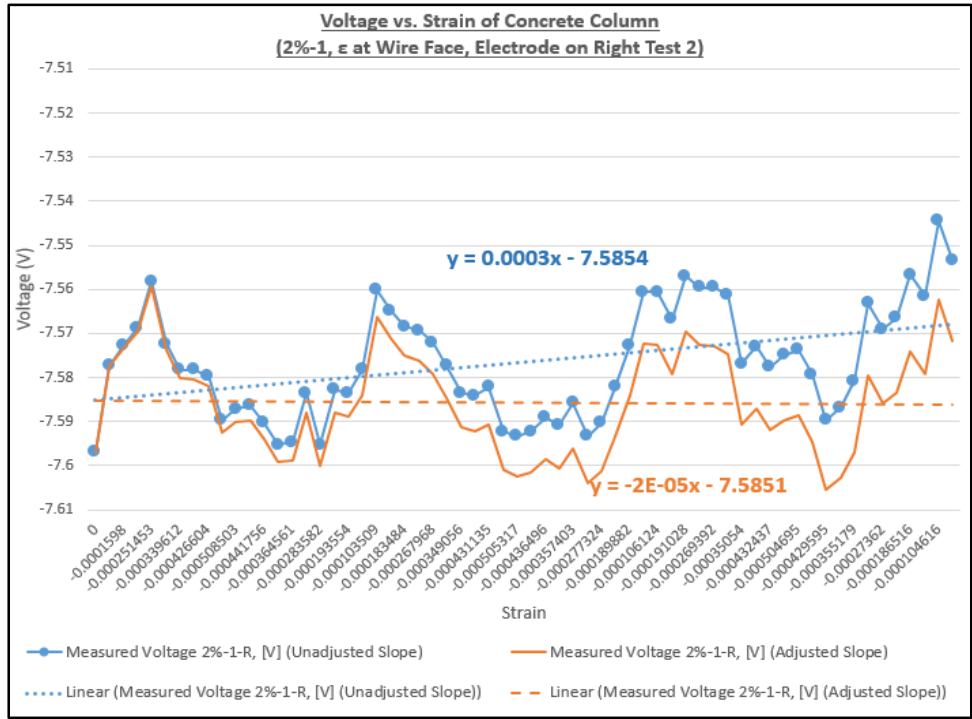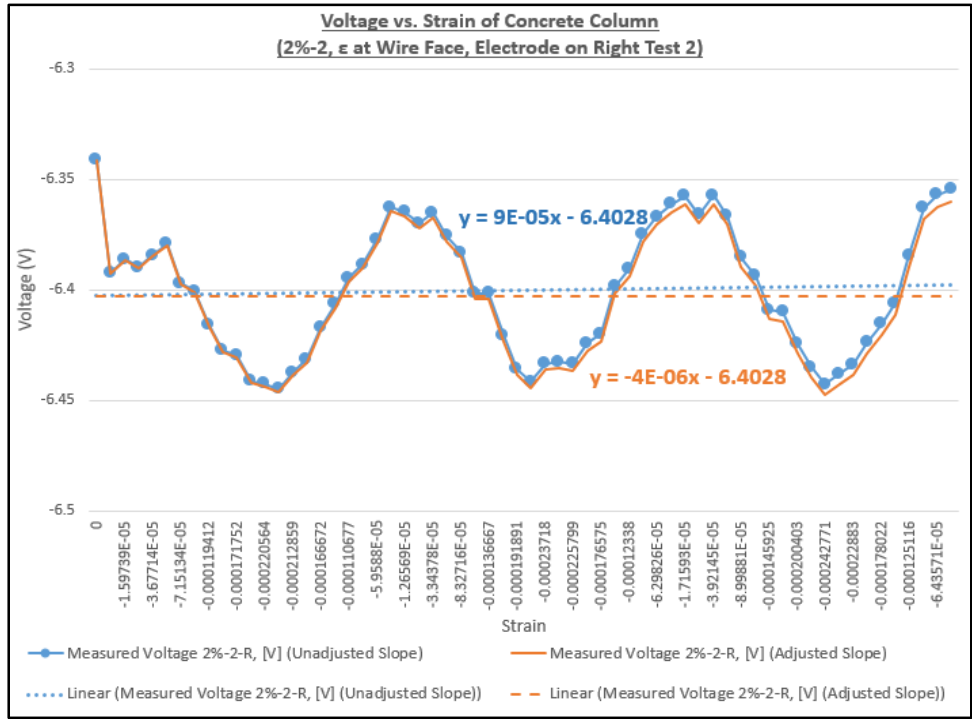
Figure F-89

Voltage Measurements (2%, Column 1, Test 2, Right Electrode Pair)
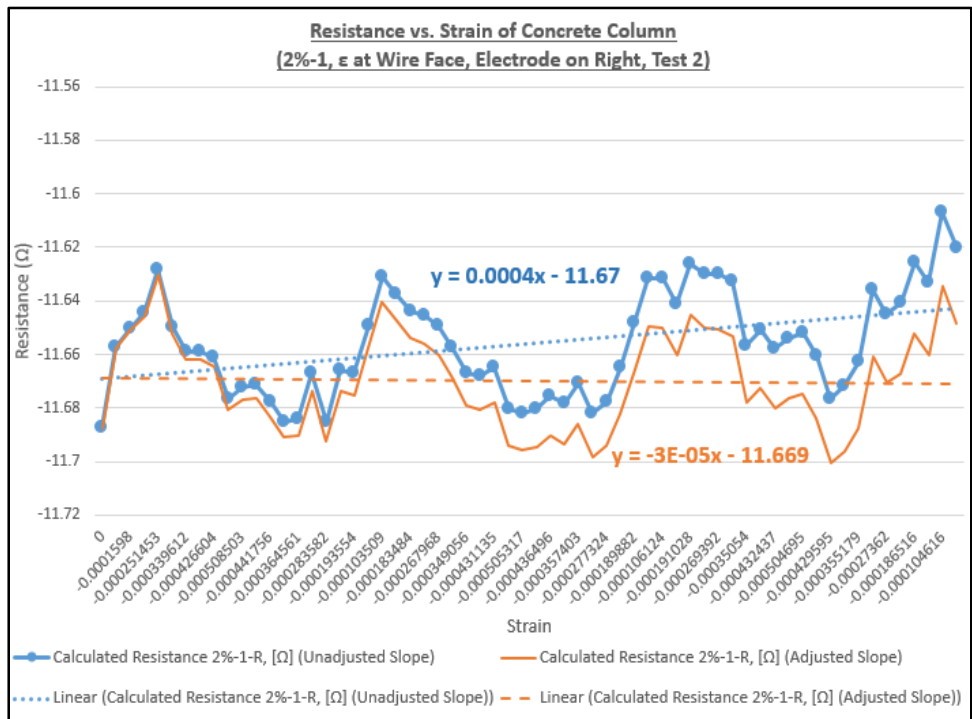
Figure F-90

Calculated Resistance (2%, Column 1, Test 2, Right Electrode Pair)

291

Strain and Resistance (RSR Concentration: 2%, Column 2)

Appendix G has a fuller analysis for column two with two percent concentration of recycled steel residuals.

Strain and Resistance (RSR Concentration: 2%, Column 3, Test 1)
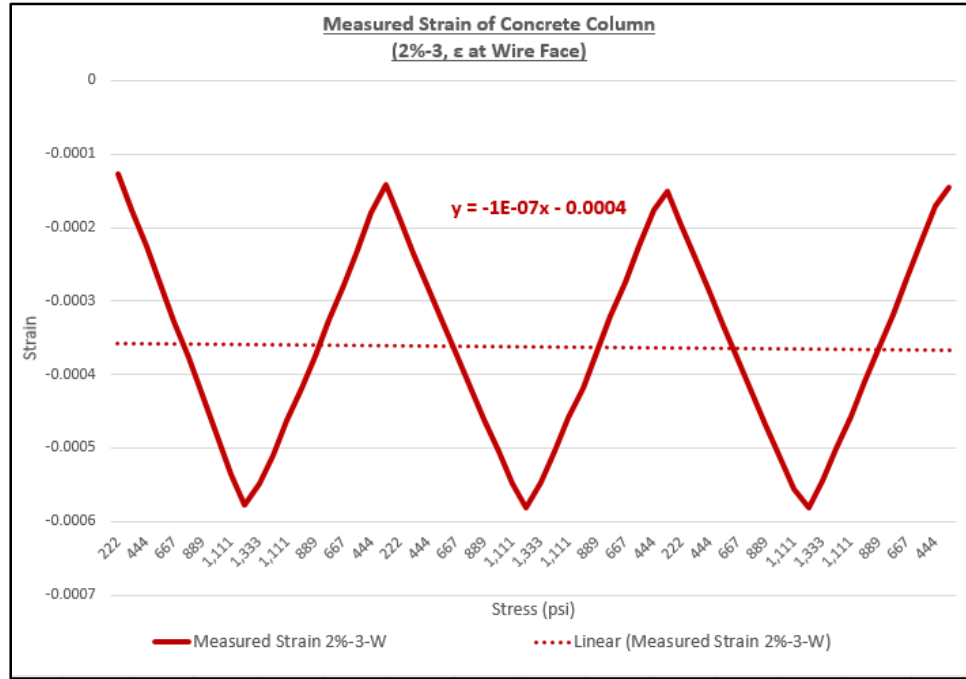
Figure F-91
Strain Measurements (2%, Column 3, Test 1, Wire Face)
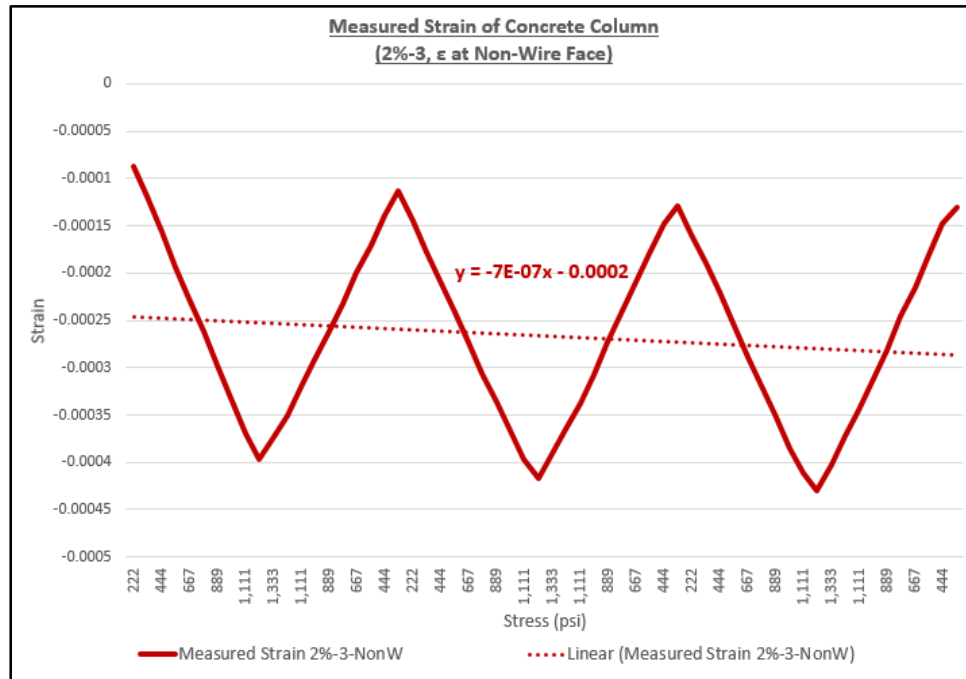
Figure F-92
Strain Measurements (2%, Column 3, Test 1, Non-Wire Face)
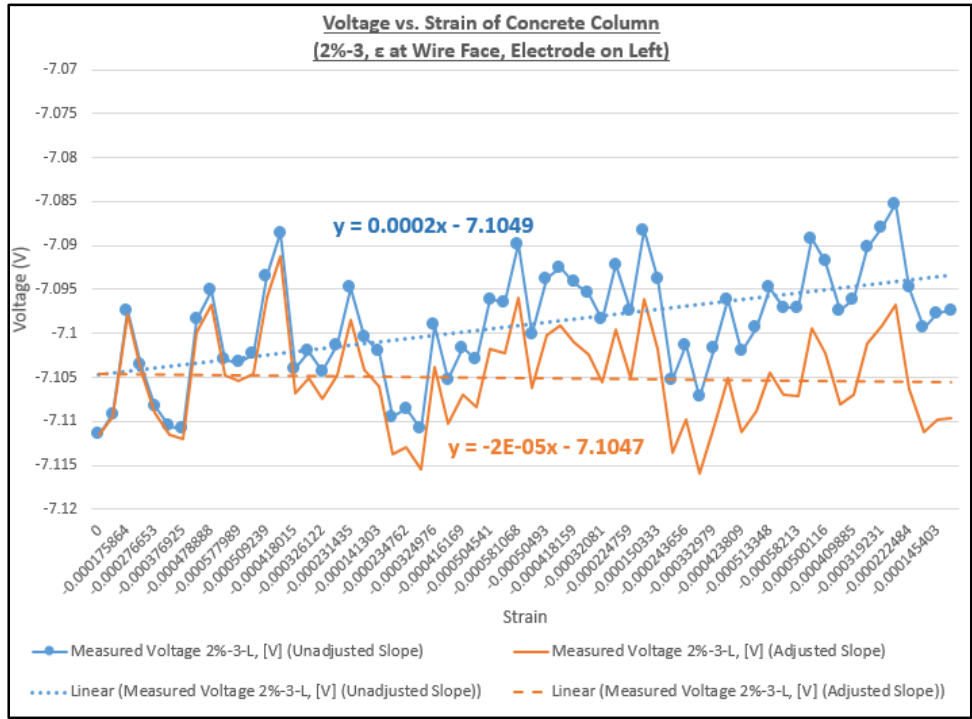
Figure F-93
Voltage Measurements (2%, Column 3, Test 1, Left Electrode Pair)
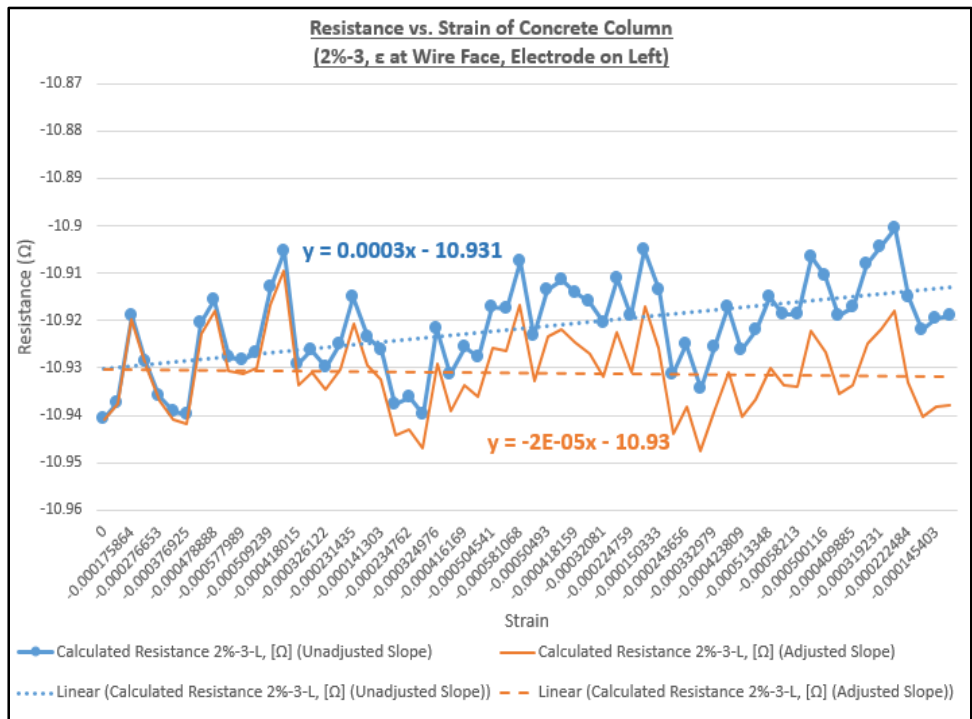
Figure F-94
Calculated Resistance (2%, Column 3, Test 1, Left Electrode Pair)
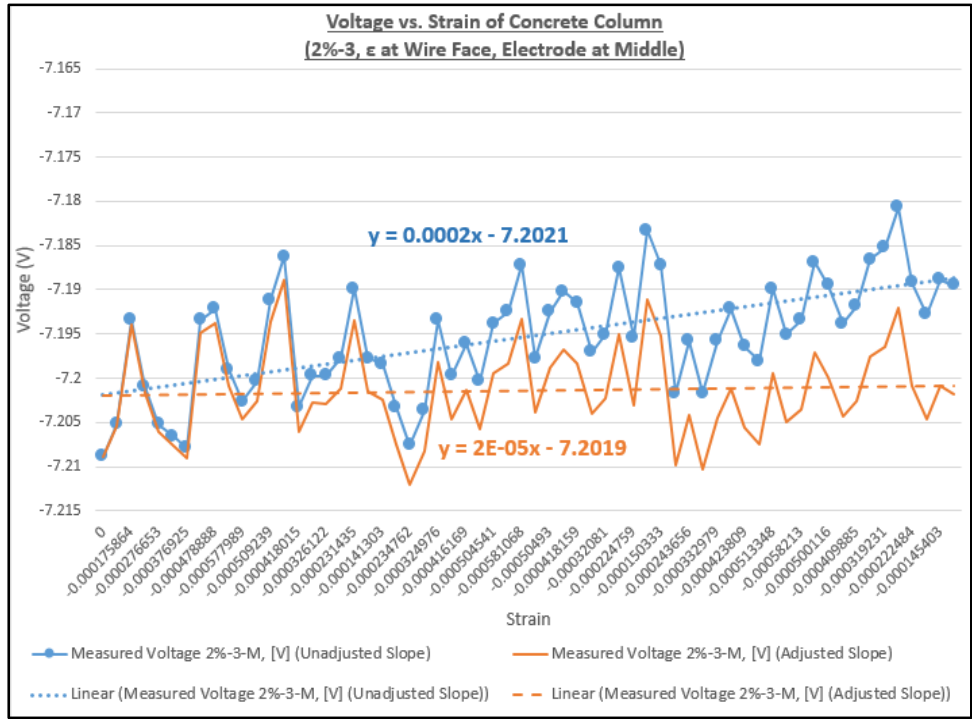
Figure F-95
Voltage Measurements (2%, Column 3, Test 1, Middle Electrode Pair)
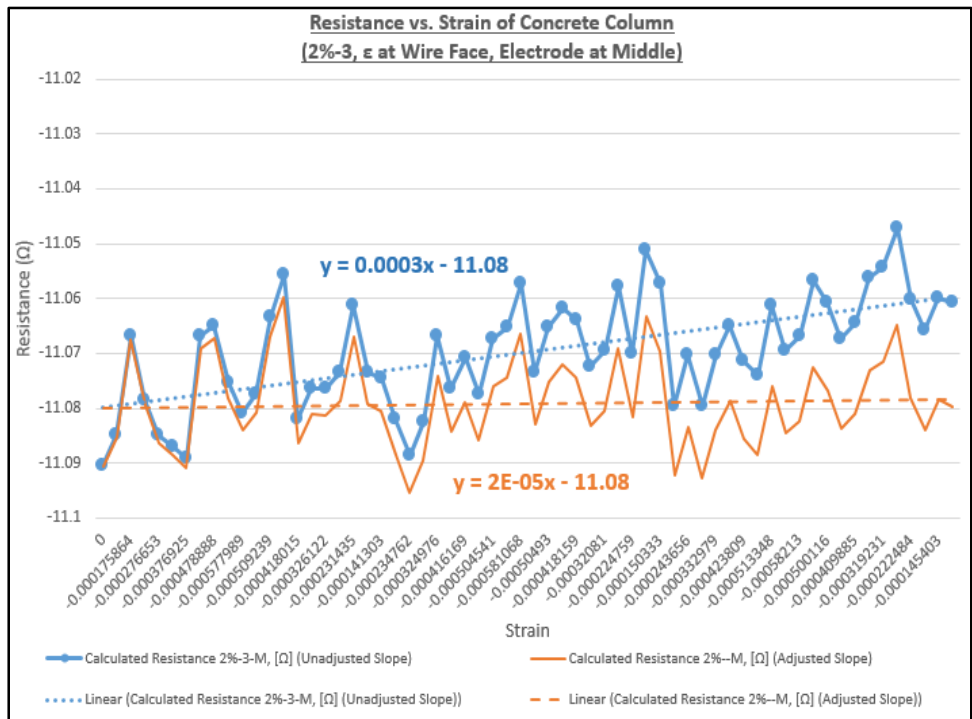
Figure F-96
Calculated Resistance (2%, Column 3, Test 1, Middle Electrode Pair)
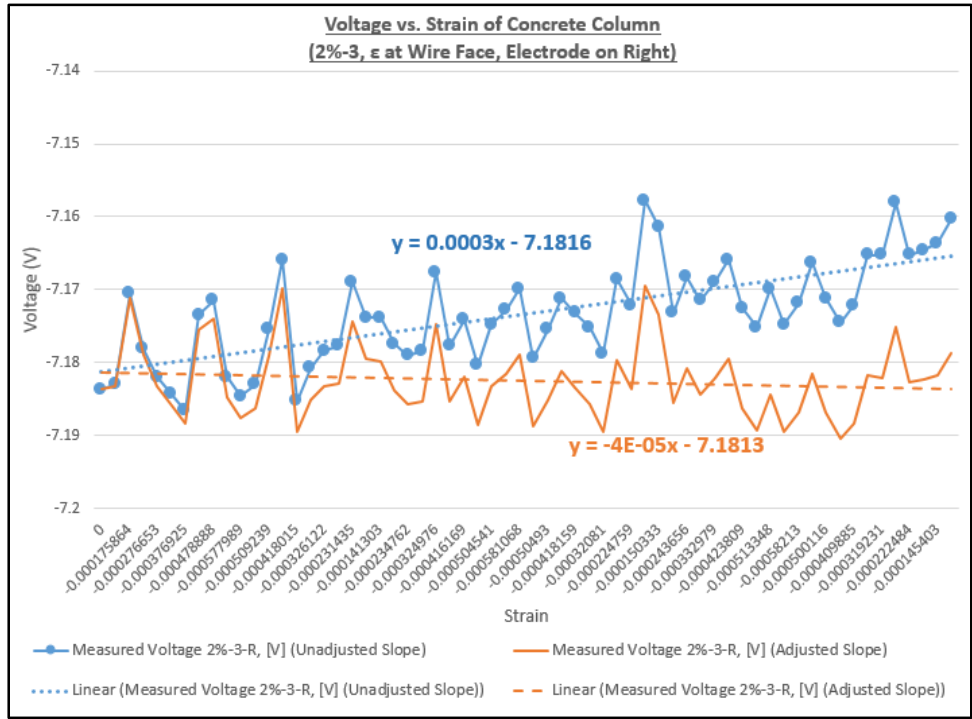
Figure F-97
Voltage Measurements (2%, Column 3, Test 1, Right Electrode Pair)
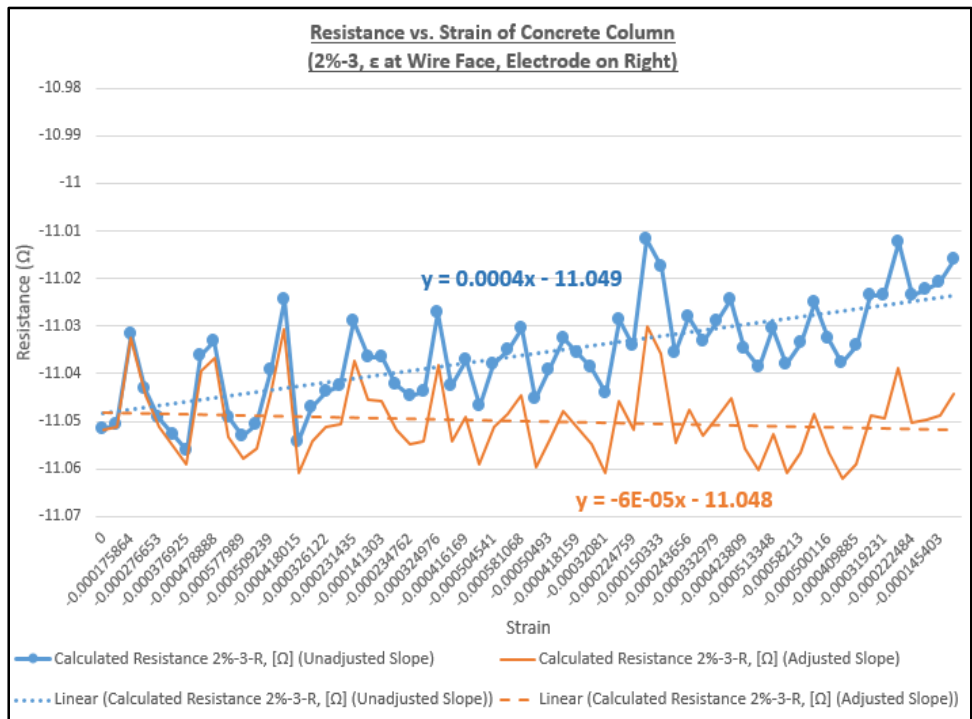
Figure F-98
Calculated Resistance (2%, Column 3, Test 1, Right Electrode Pair)

Strain and Resistance (RSR Concentration: 2%, Column 3, Test 2)
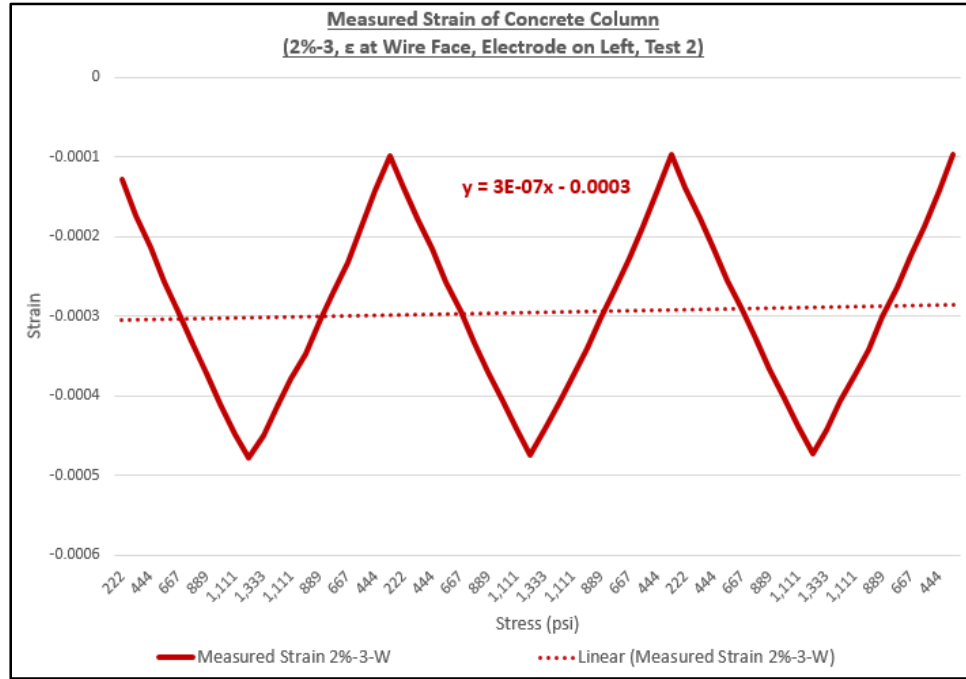
Figure F-99
Strain Measurements (2%, Column 3, Test 2, Wire Face)
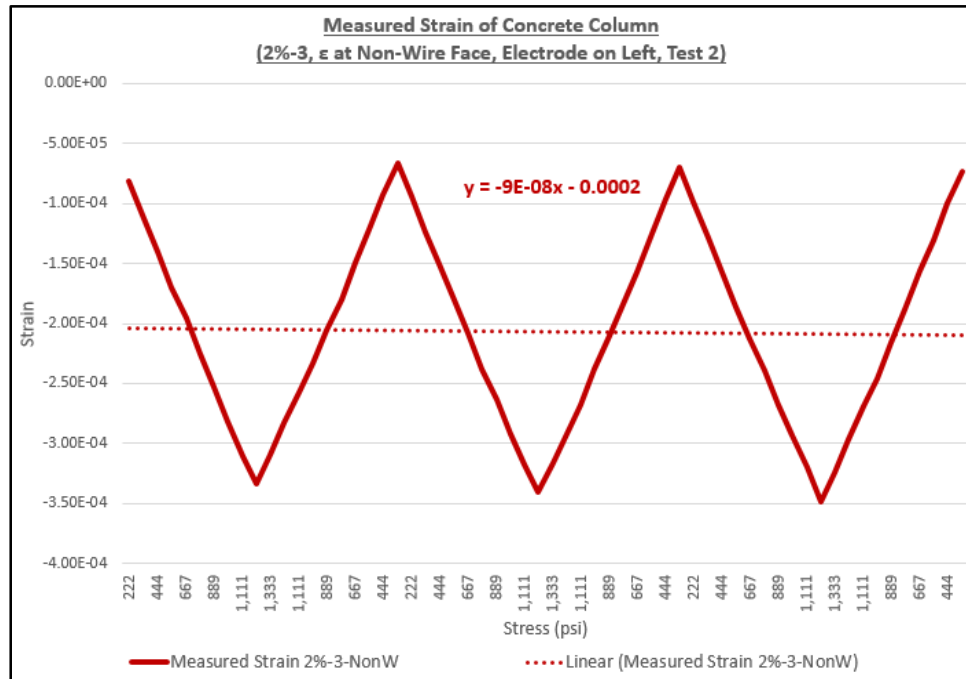
Figure F-100
Strain Measurements (2%, Column 3, Test 2, Non-Wire Face)
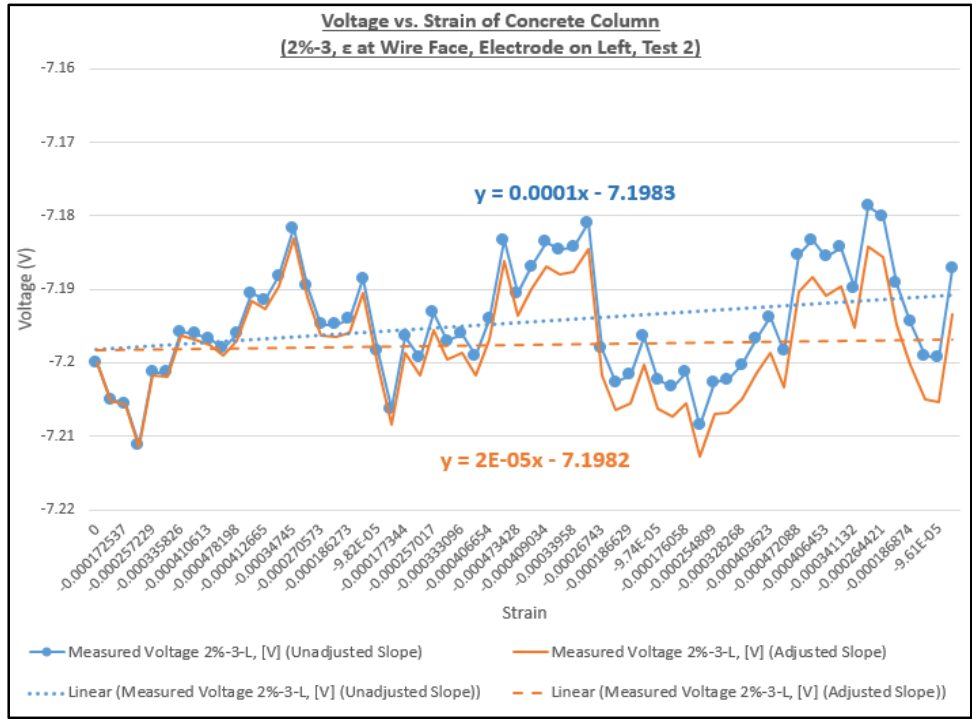
Figure F-101
Voltage Measurements (2%, Column 3, Test 2, Left Electrode Pair)
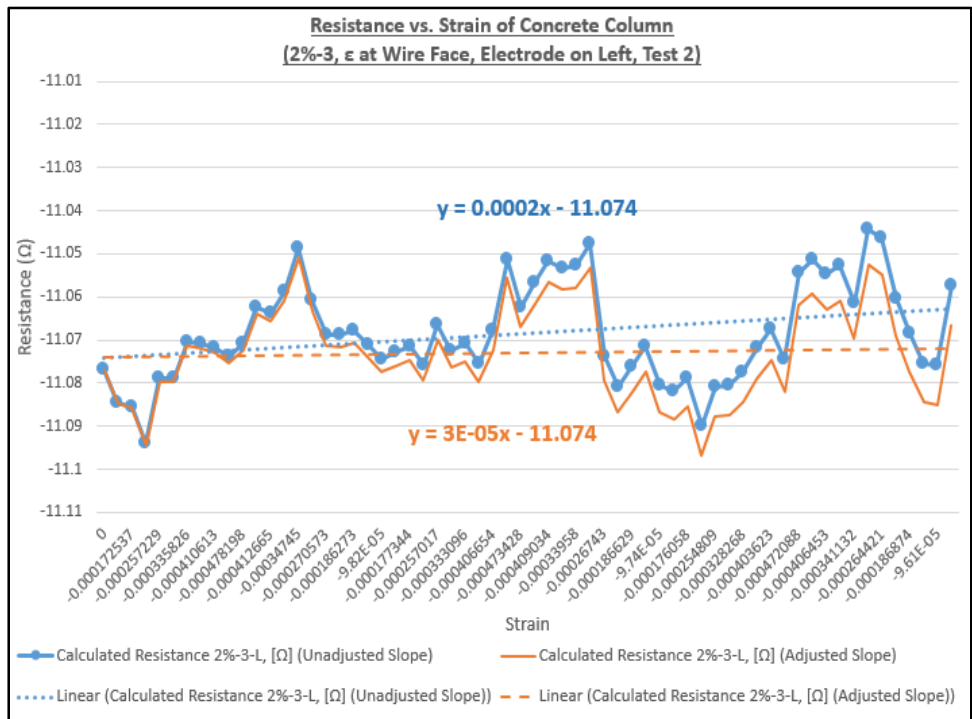
Figure F-102
Calculated Resistance (2%, Column 3, Test 2, Left Electrode Pair)

298
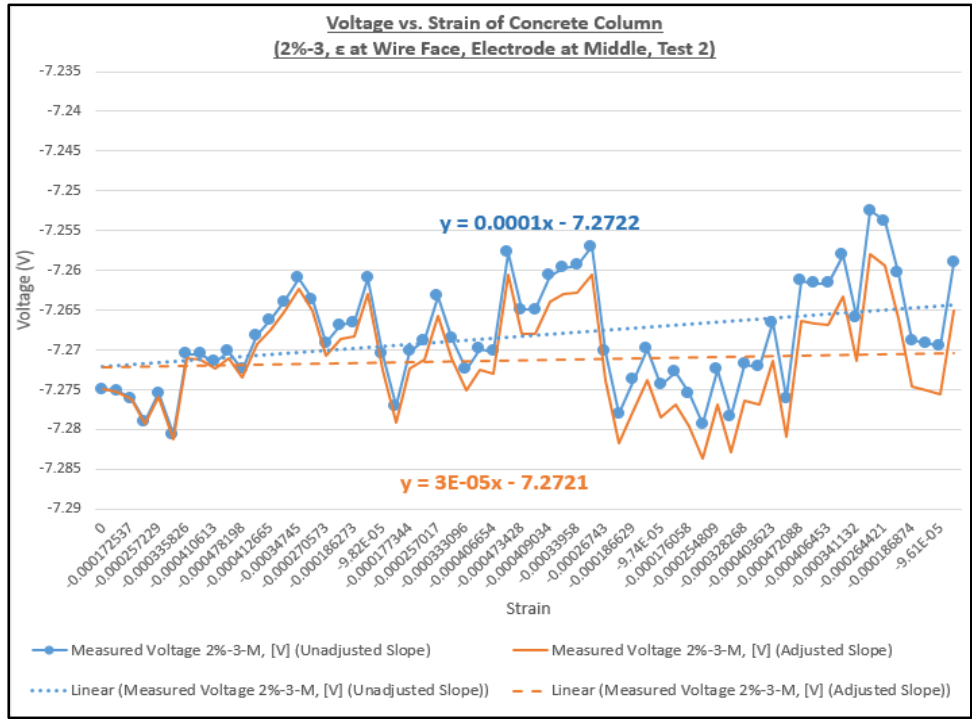
Figure F-103
Voltage Measurements (2%, Column 3, Test 2, Middle Electrode Pair)
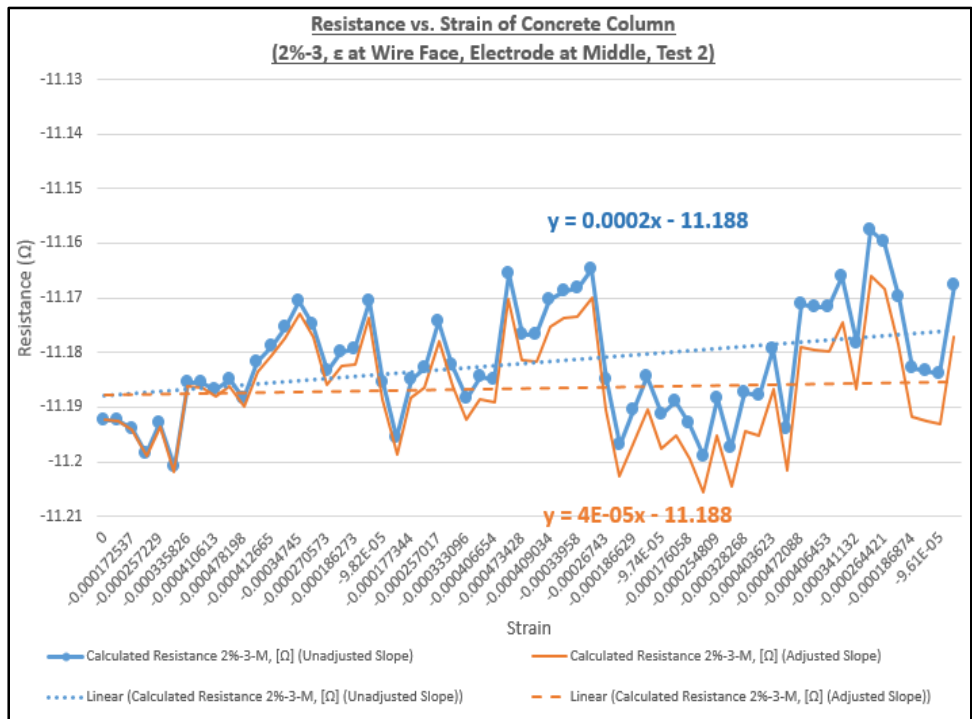
Figure F-104
Calculated Resistance (2%, Column 3, Test 2, Middle Electrode Pair)

299
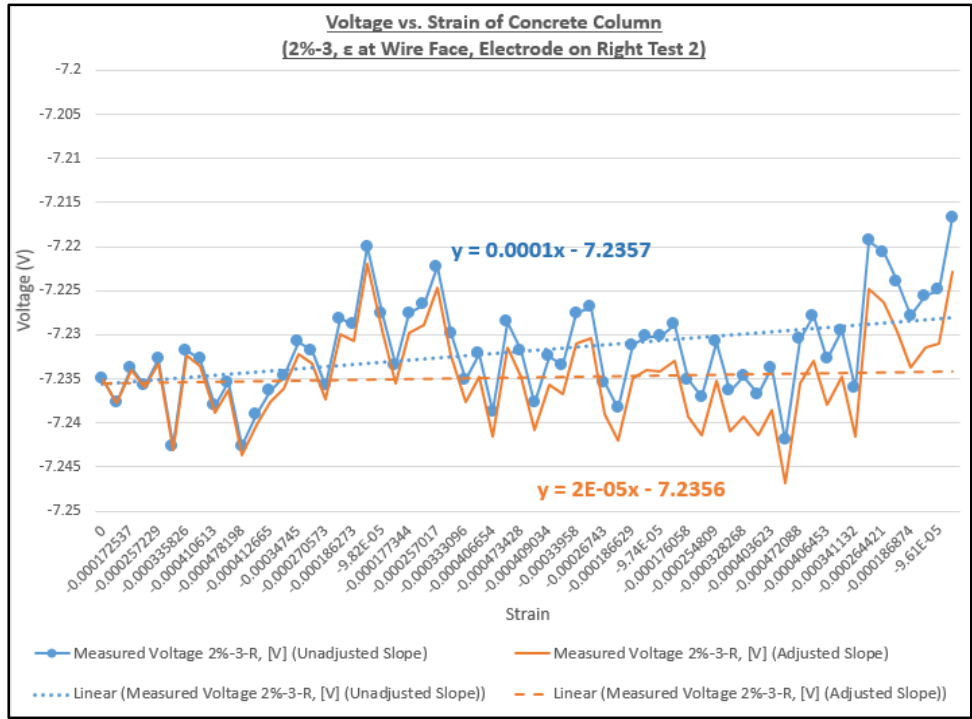
Figure F-105
Voltage Measurements (2%, Column 3, Test 2, Right Electrode Pair)
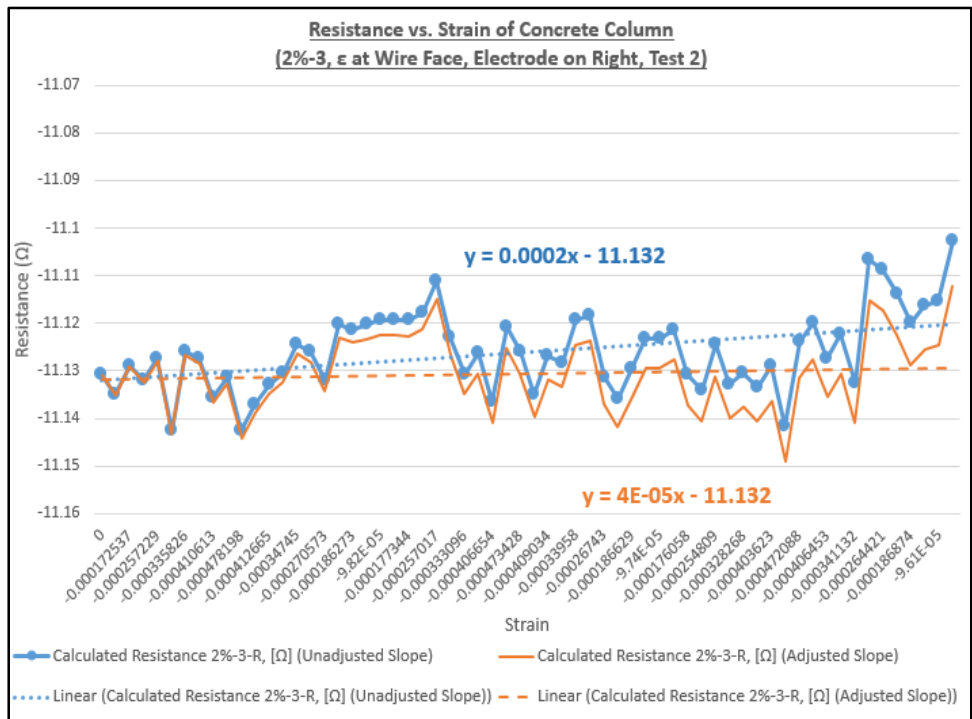
Figure F-106
Calculated Resistance (2%, Column 3, Test 2, Right Electrode Pair)

APPENDIX G: ELECTRO-ELASTIC TESTING OF CONCRETE COLUMN NUMBER
TWO WITH 2% CONCENTRATION OF RECYCLED STEEL RESIDUALS

The following includes plots for the testing on the concrete columns containing 2% concentration of recycled steel residuals. The specimen reported is number 2. The nomenclature is consistent with Appendix F such that 2%-2-W-M indicates that the measurements and/or calculations being reported are for column 2, with 2% recycled steel residuals, the strain is indicative of that measured on the wire face, and the middle pair of electrodes. Beyond the plots shown in Appendix F, this appendix provides additional analysis on the relationship between strain and elasto-electric parameters. As noted in Chapter 6, an elasto-electric factor is applied to the plots to correlate theoretical and experimental values. The elasto-electric factors used for the plots are indicated.

Static Resistance (RSR Concentration: 2%, Column 2)
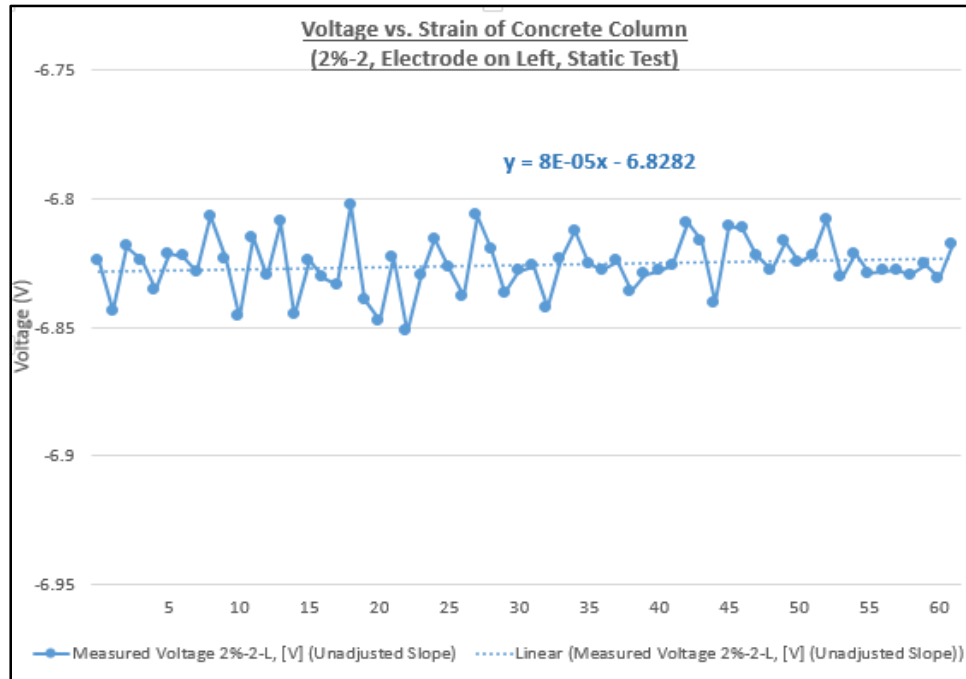
Figure G-1
Static Voltage Measurements (2%, Column 2, Left Electrode Pair)
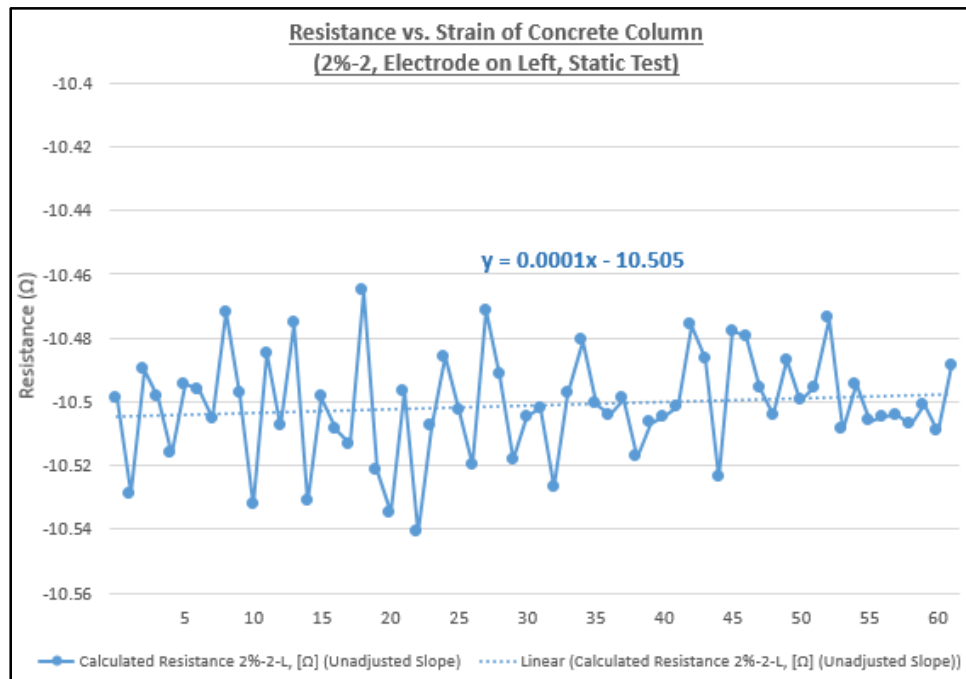
Figure G-2
Static Calculated Resistance (2%, Column 2, Left Electrode Pair)

302
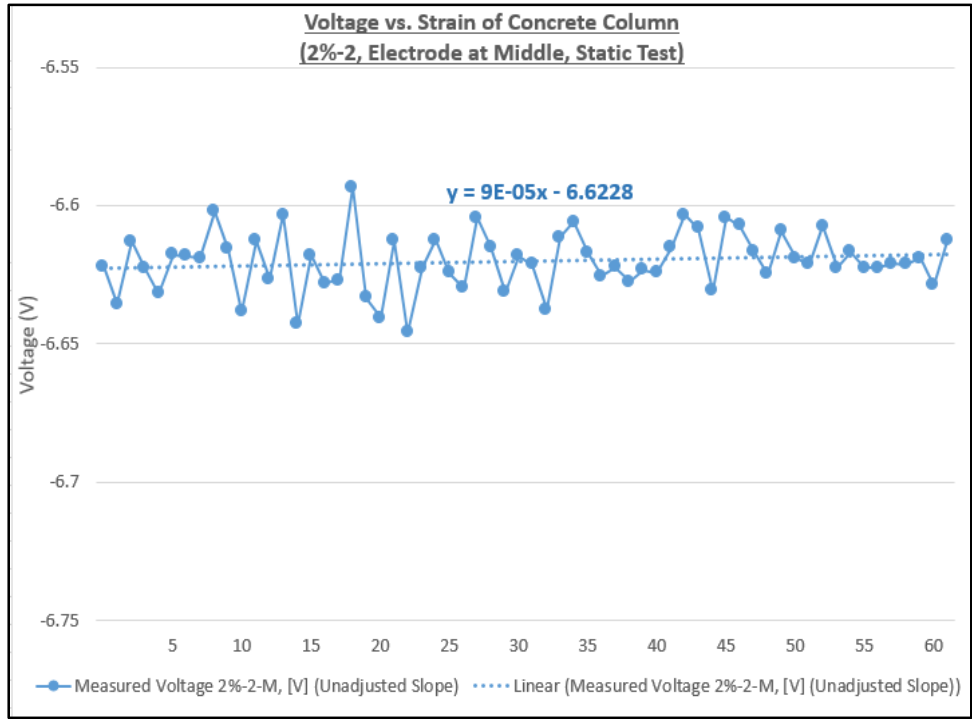
Figure G-3
Static Voltage Measurements (2%, Column 2, Middle Electrode Pair)
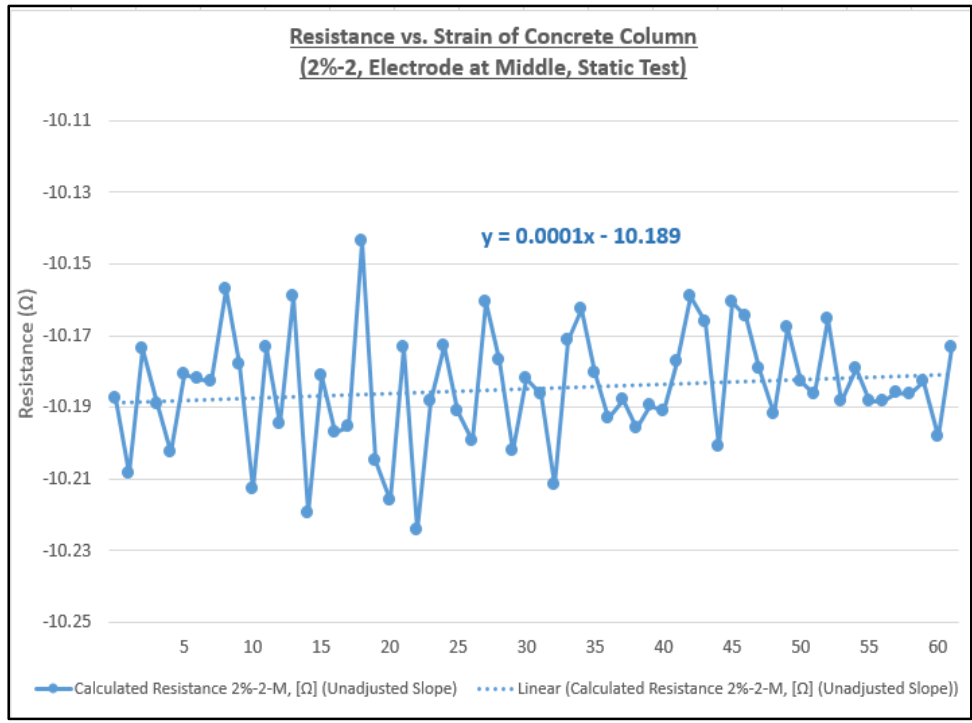
Figure G-4
Static Calculated Resistance (2%, Column 2, Middle Electrode Pair)
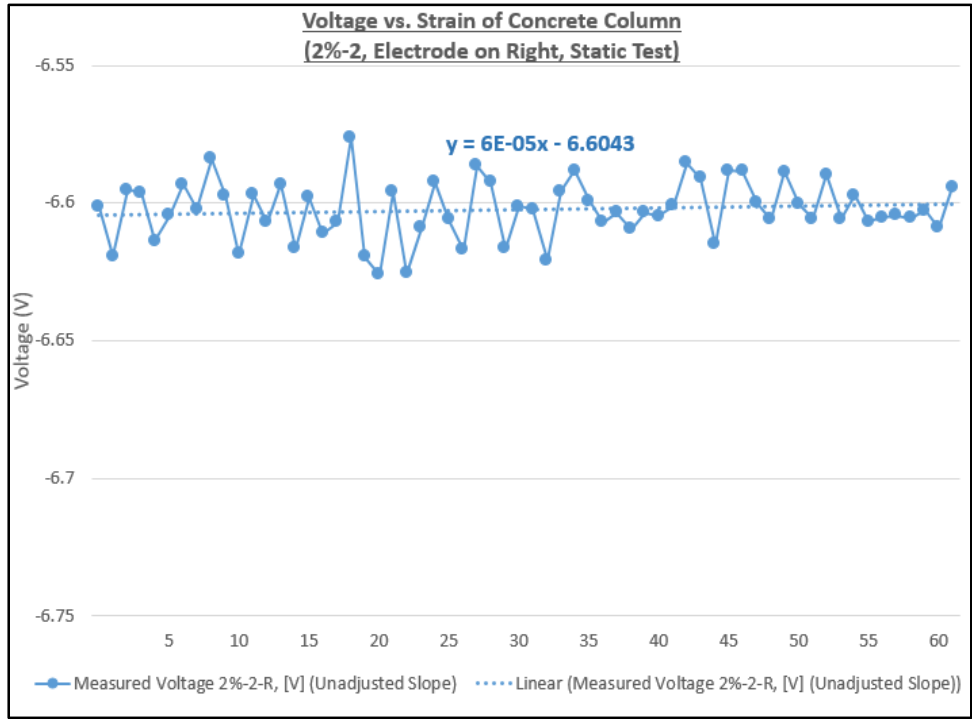
Figure G-5
Static Voltage Measurements (2%, Column 2, Right Electrode Pair)
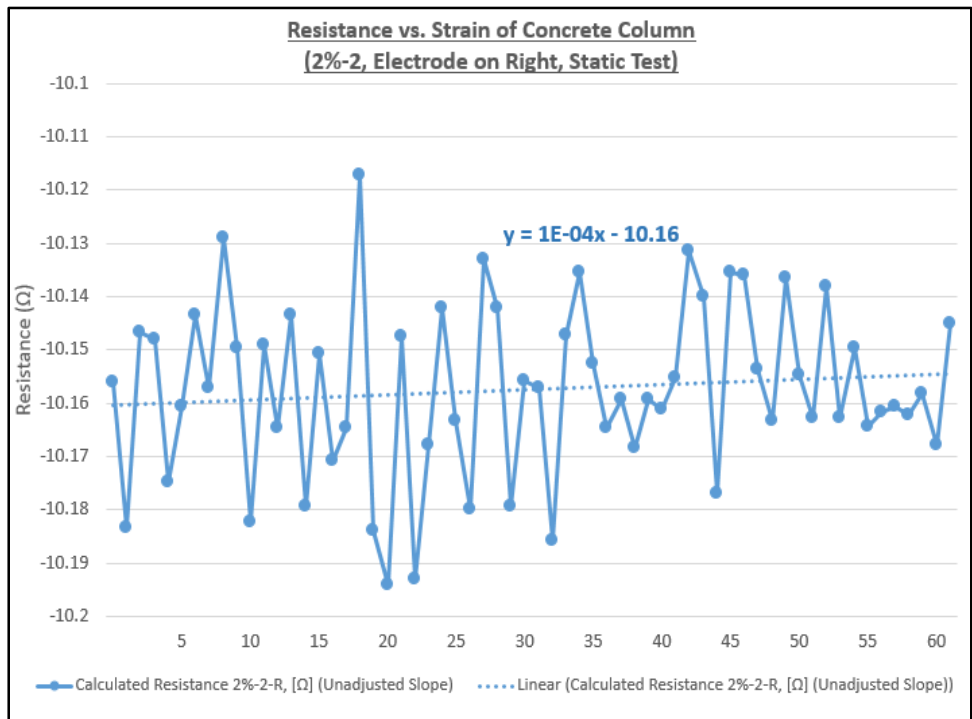
Figure G-6
Static Calculated Resistance (2%, Column 2, Right Electrode Pair)

Strain (RSR Concentration: 2%, Column 2, Test 1, Test 2, Test 3)
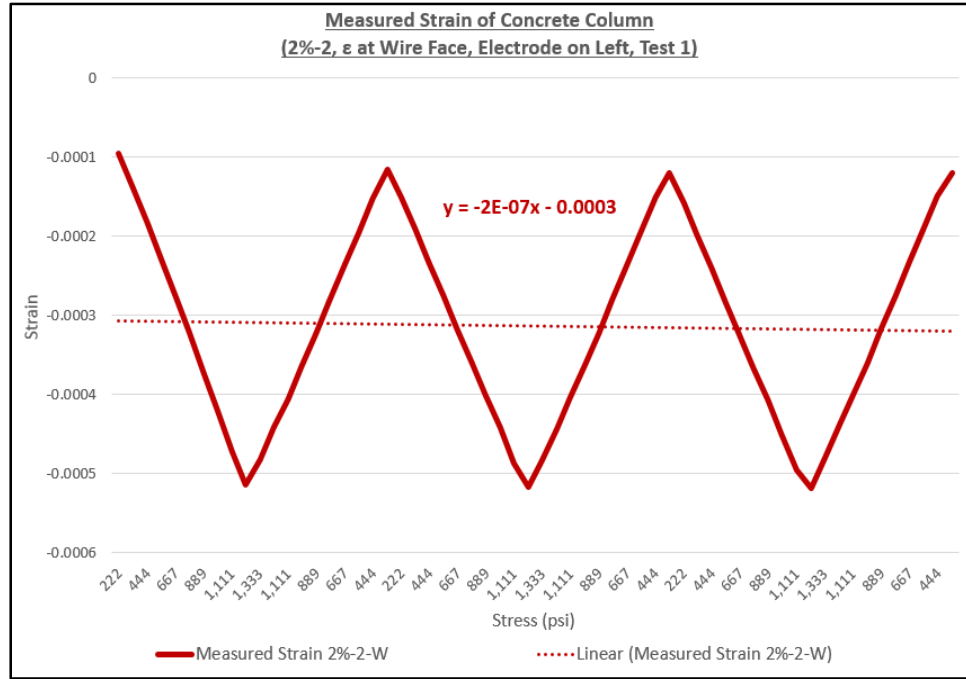
Figure G-7
Strain Measurements (2%, Column 2, Test 1, Wire Face)
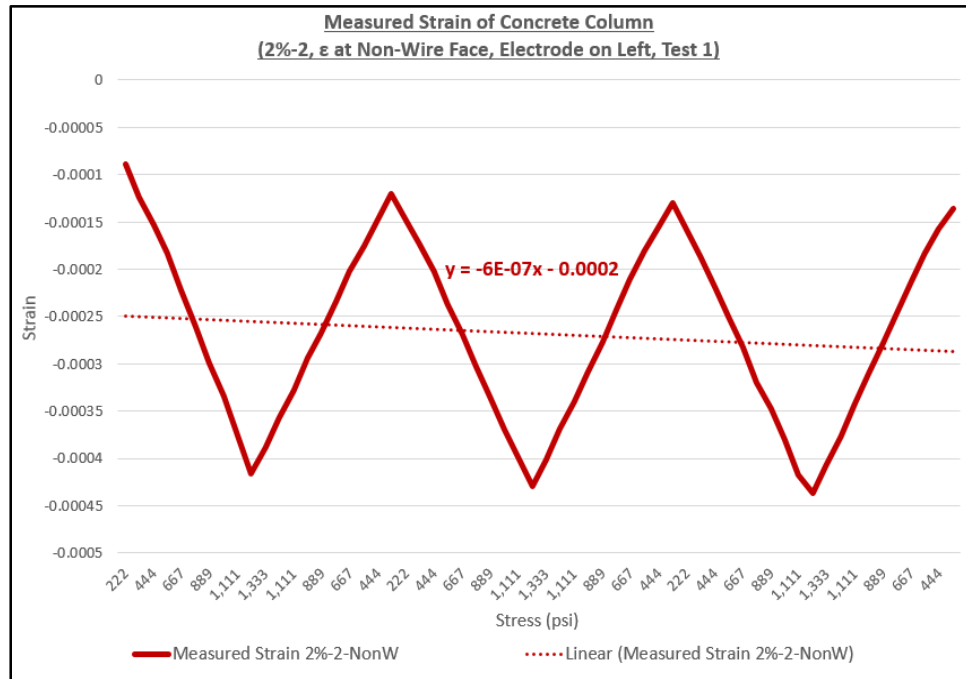
Figure G-8
Strain Measurements (2%, Column 2, Test 1, Non-Wire Face)

305
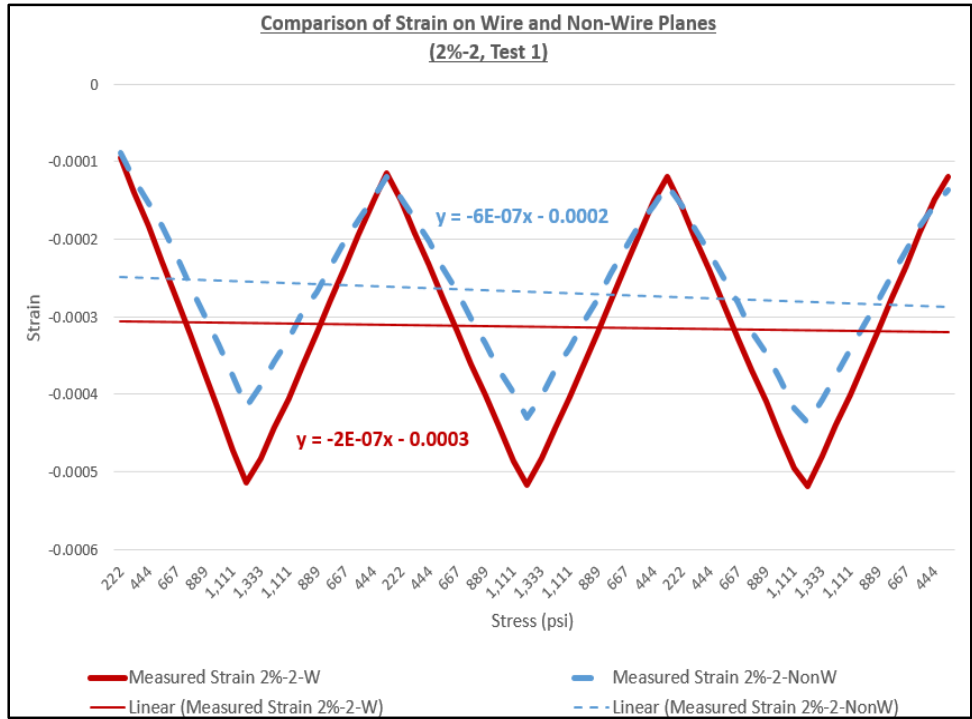
Figure G-9
Strain Comparison (2%, Column 2, Test 1)
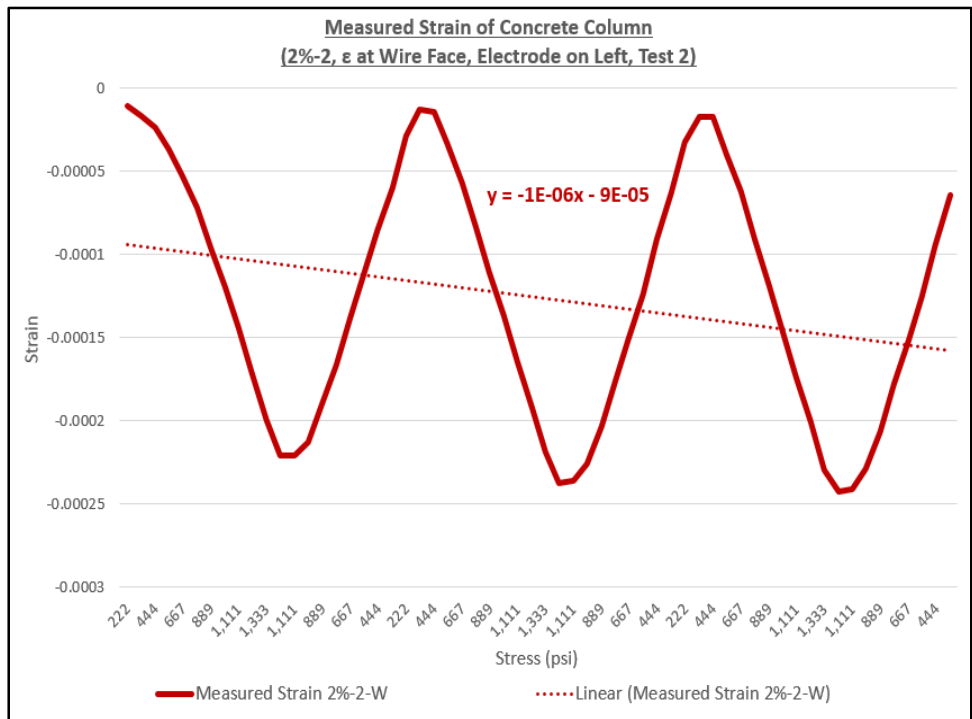
Figure G-10
Strain Measurements (2%, Column 2, Test 2, Wire Face)

306
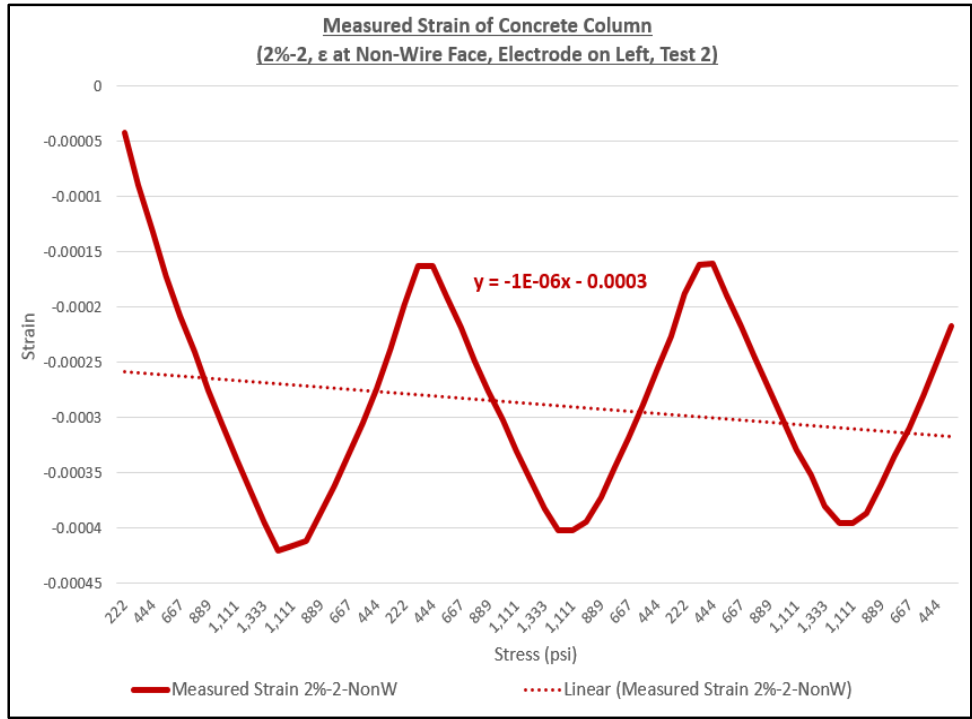
Figure G-11
Strain Measurements (2%, Column 2, Test 2, Non-Wire Face)
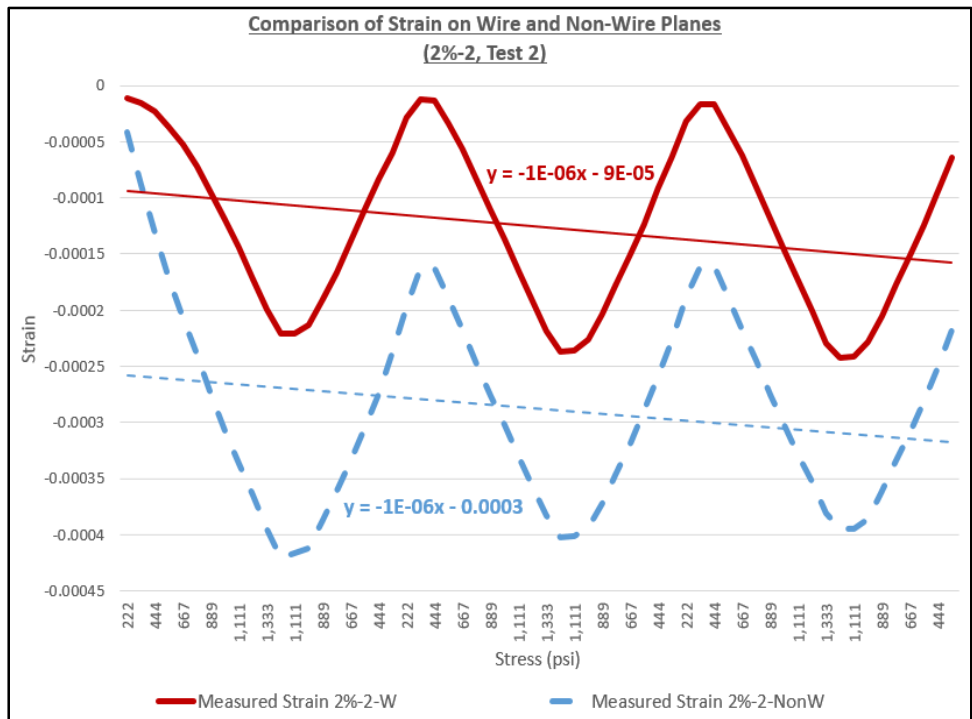
Figure G-12
Strain Comparison (2%, Column 2, Test 2)

307
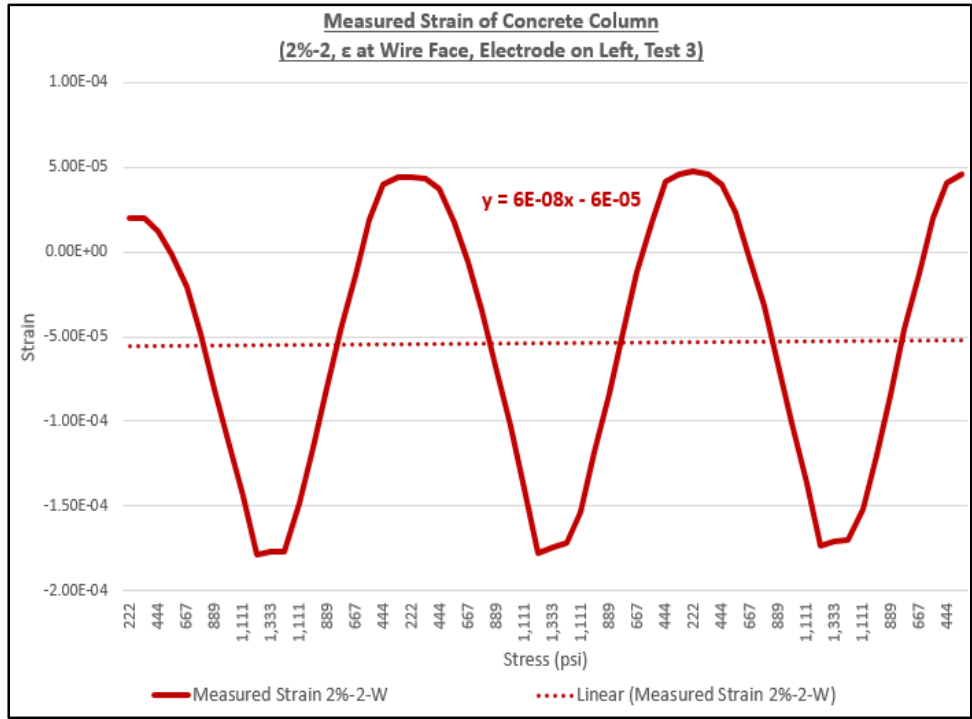
Figure G-13
Strain Measurements (2%, Column 2, Test 3, Wire Face)
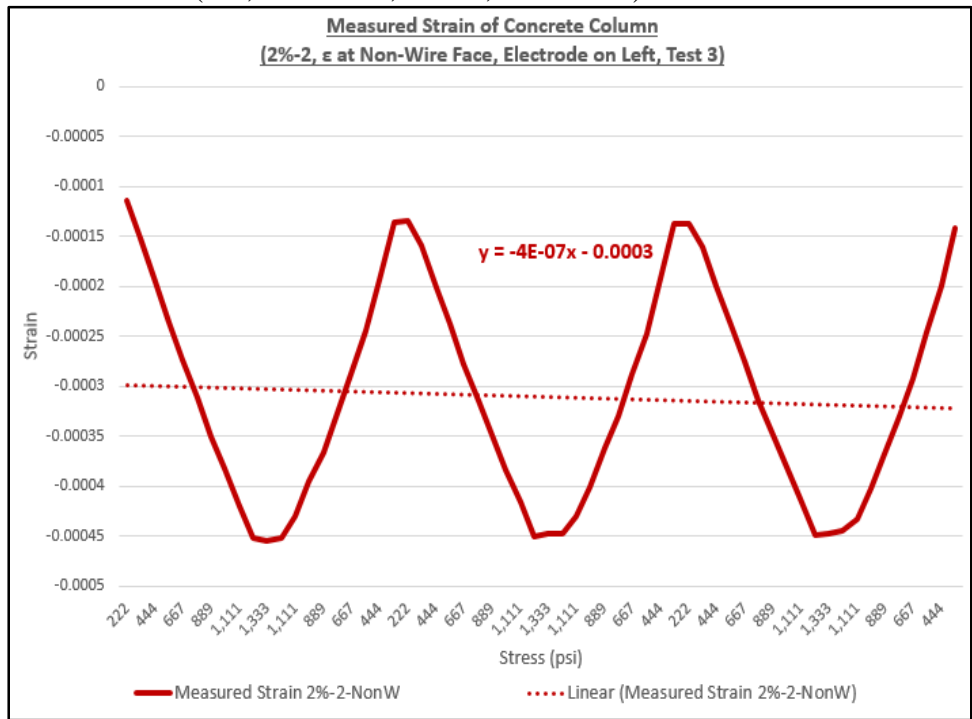
Figure G-14
Strain Measurements (2%, Column 2, Test 3, Non-Wire Face)

308
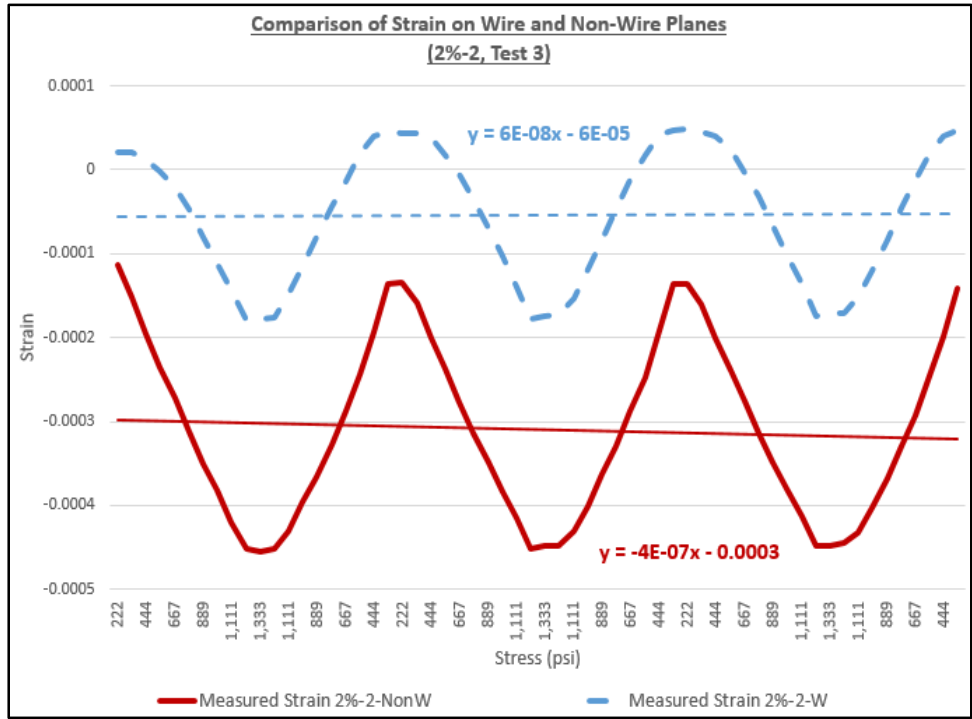
Figure G-15
Strain Comparison (2%, Column 2, Test 3)

Strain and Resistance (RSR Concentration: 2%, Column 2, Test 1)
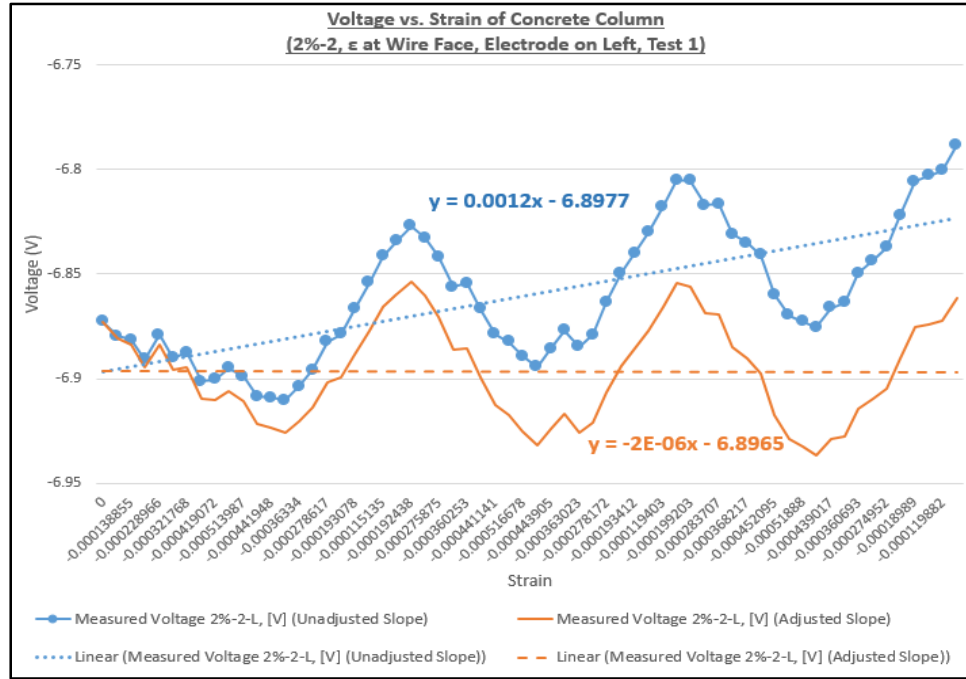
Figure G-16
Voltage Measurements (2%, Column 2, Test 1, Left Electrode Pair)
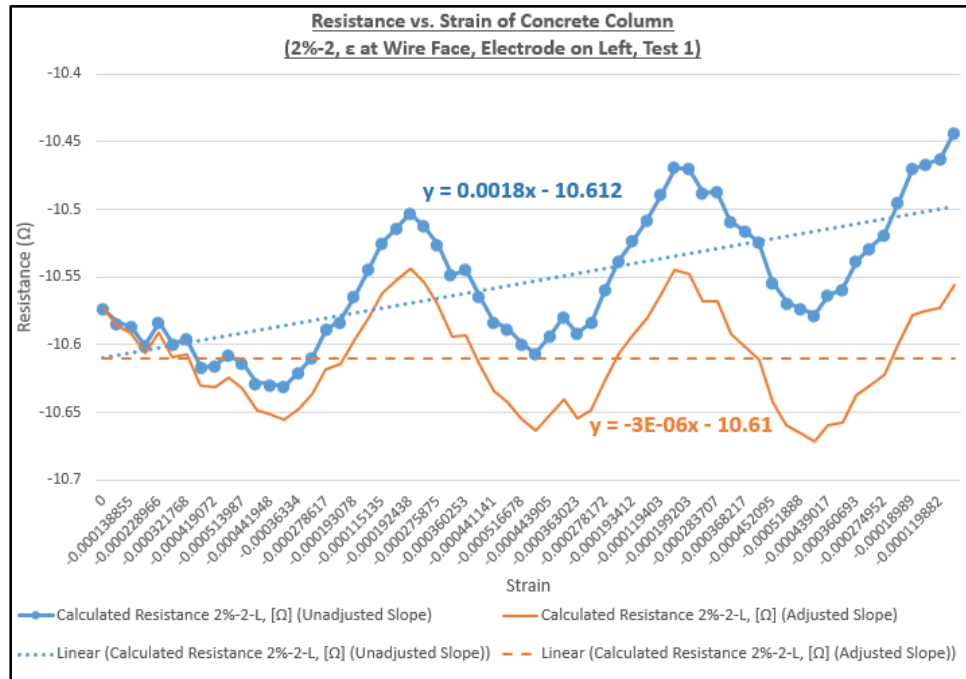
Figure G-17
Calculated Resistance (2%, Column 2, Test 1, Left Electrode Pair)
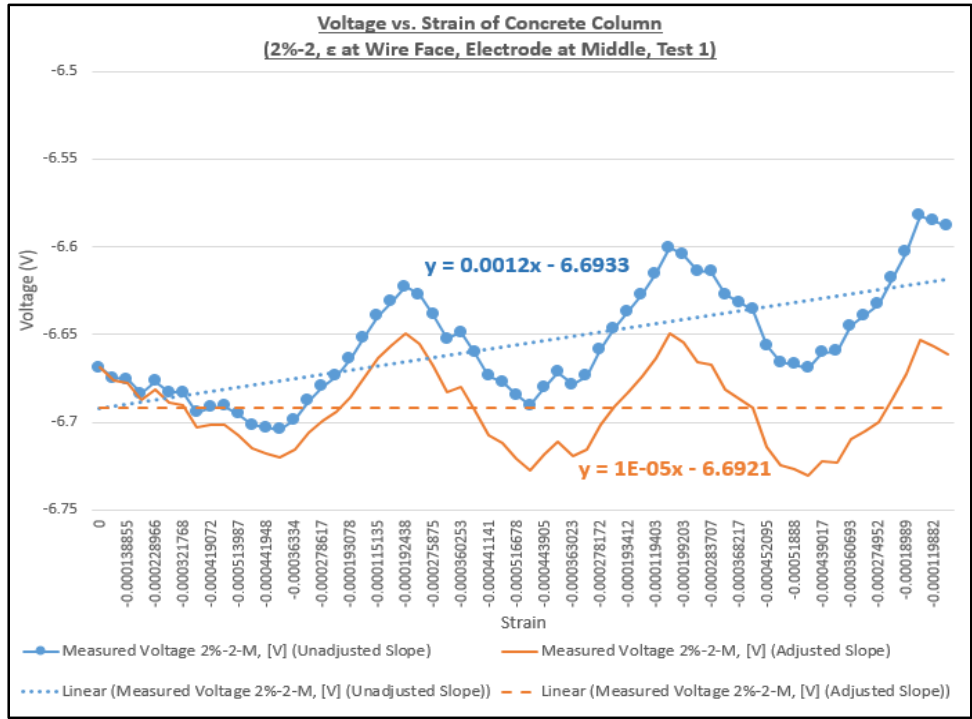
Figure G-18

Voltage Measurements (2%, Column 2, Test 1, Middle Electrode Pair)
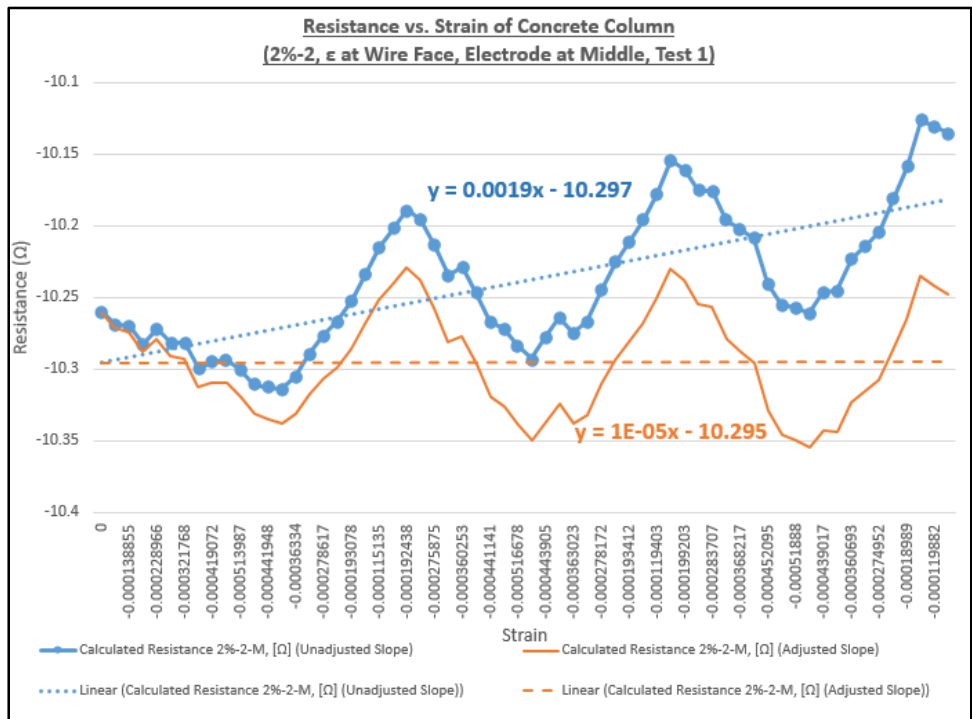
Figure G-19

Calculated Resistance (2%, Column 2, Test 1, Middle Electrode Pair)
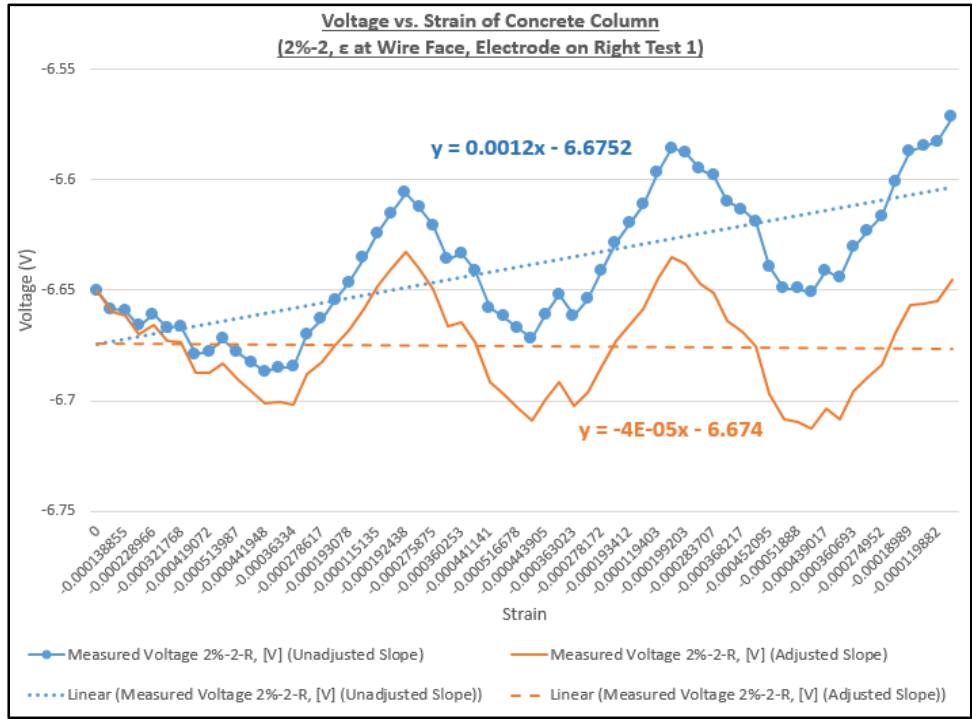
Figure G-20
Voltage Measurements (2%, Column 2, Test 1, Right Electrode Pair)
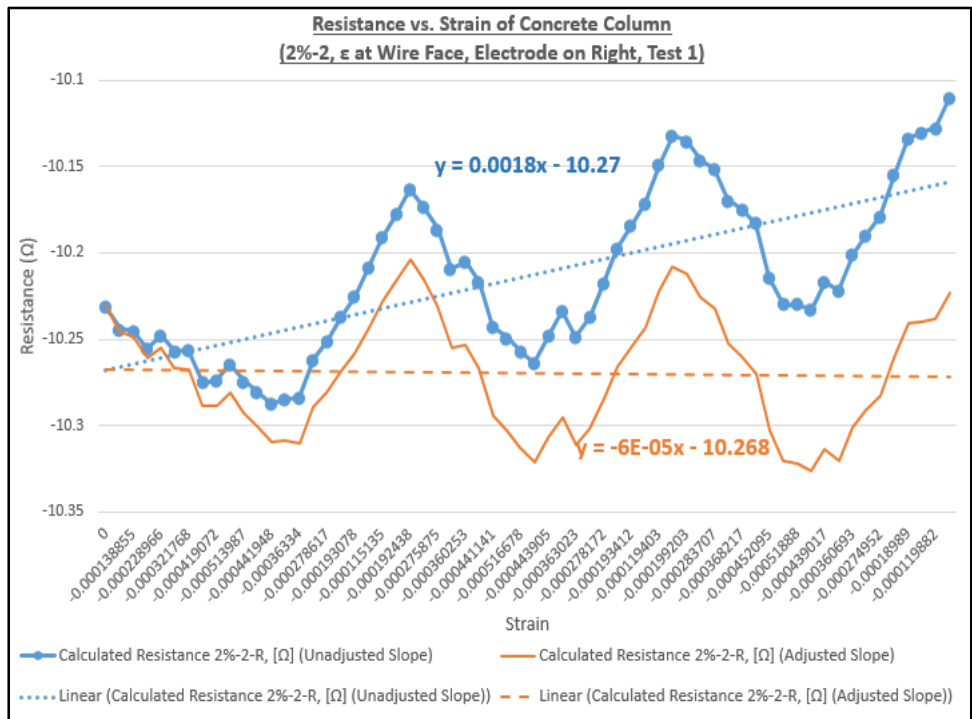
Figure G-21
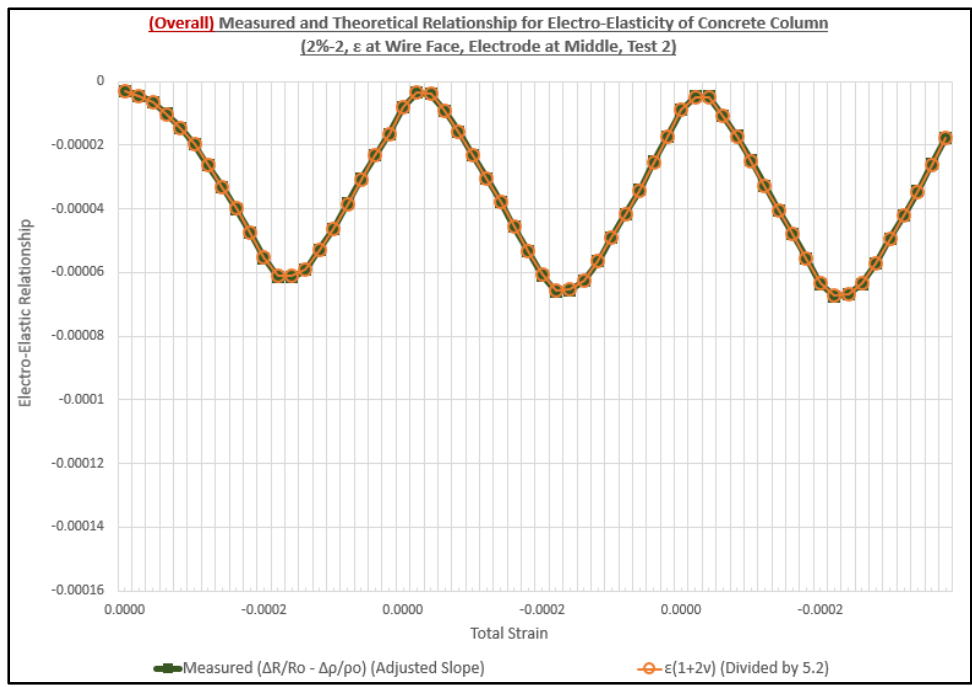Calculated Resistance (2%, Column 2, Test 1, Right Electrode Pair)

312
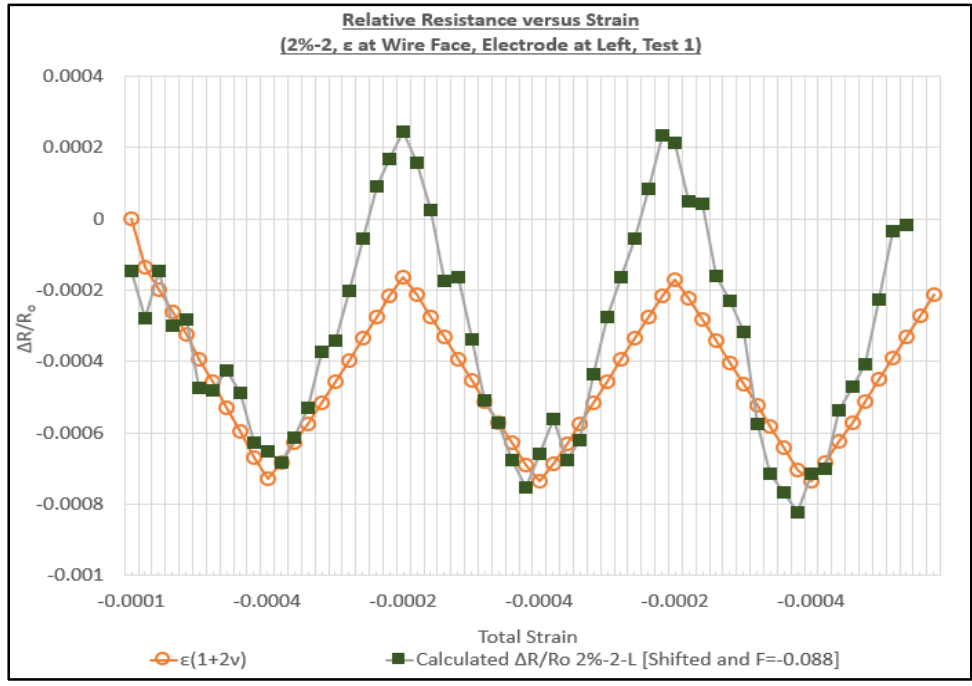
Figure G-22
Elasto-Electric Parameter Line Plot with Mechanical vs. Electrical Measurements (2%, Column 2, Strain at Wire Face, Test 1, Left Electrode Pair, Excluding Resistivity)
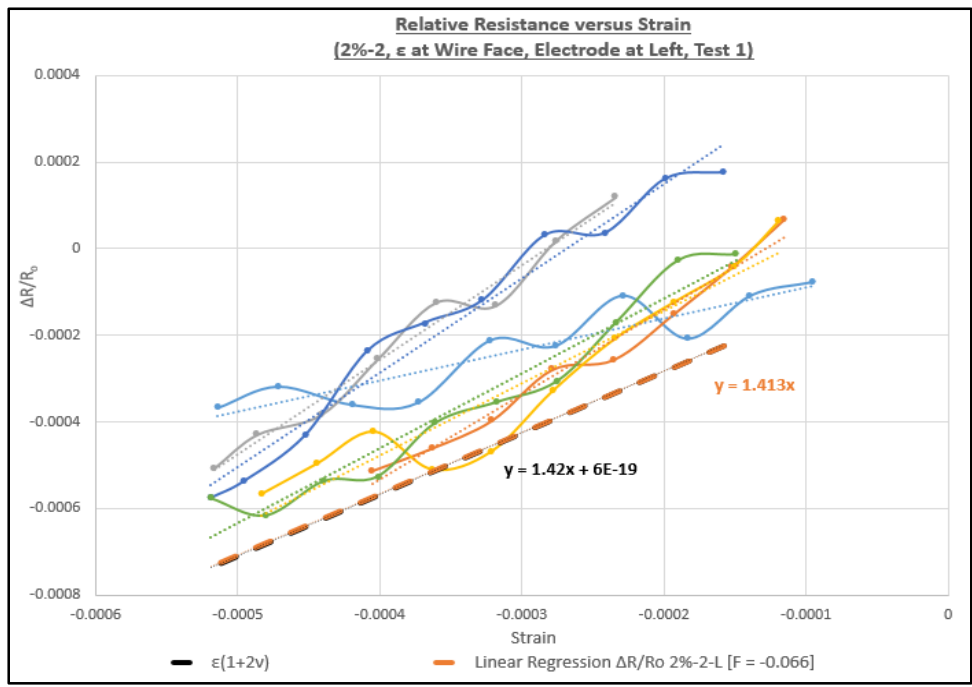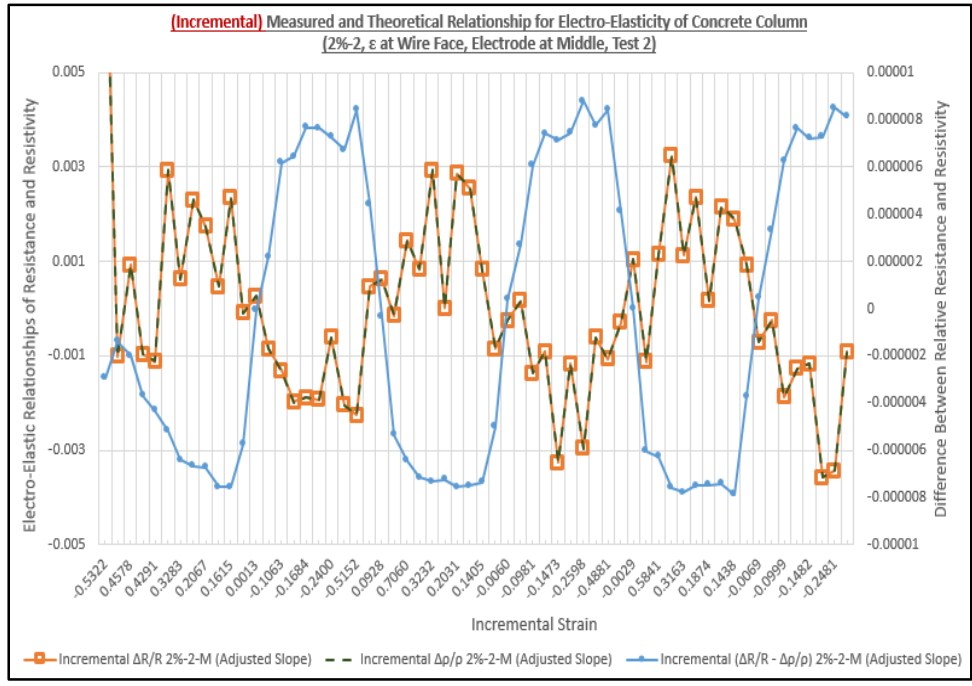

Figure G-23
Elasto-Electric Parameter X-Y Scatter Plot with Mechanical vs. Electrical Measurements (2%, Column 2, Strain at Wire Face, Test 1, Left Electrode Pair, Excluding Resistivity)

313
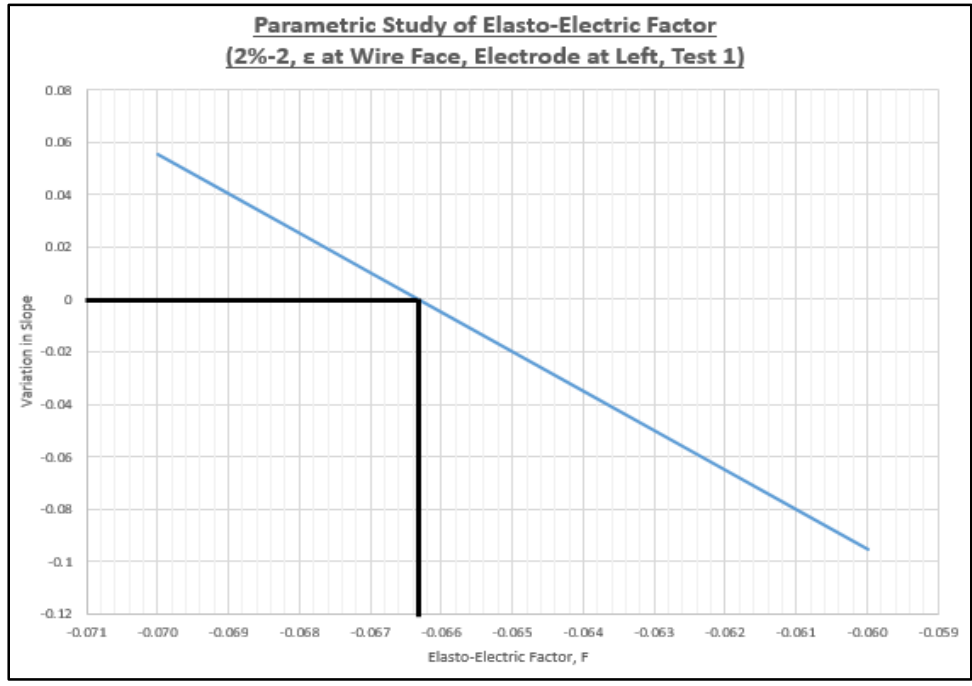
Figure G-24
Parametric Study of Elasto-Electric Factor (2%, Column 2, Strain at Wire Face, Test 1, Left Electrode Pair, Excluding Resistivity)
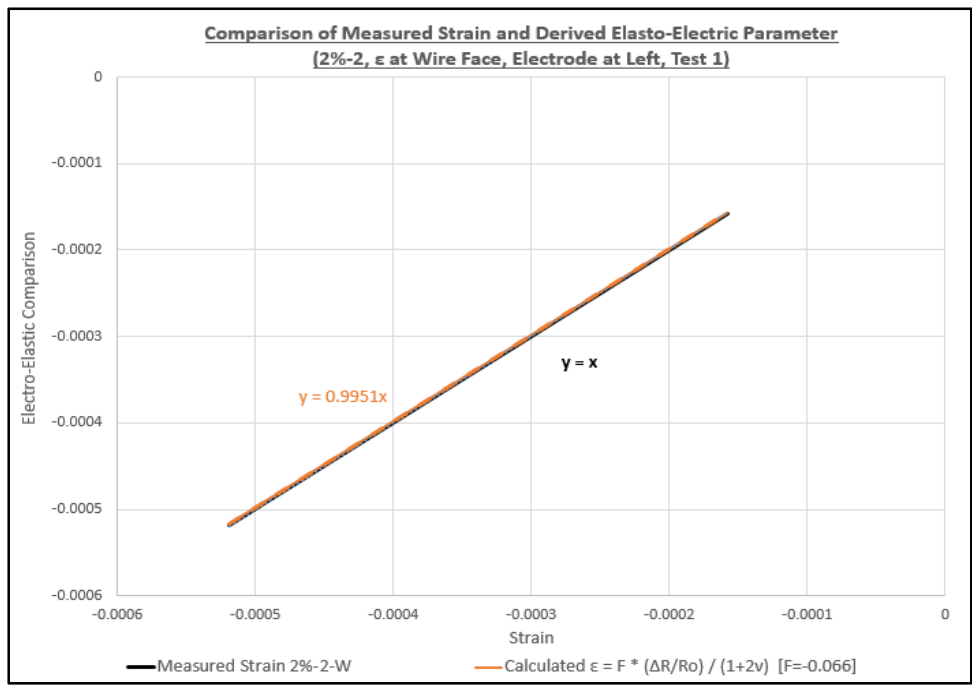
Figure G-25
Elasto-Electric Parameter (2%, Column 2, Strain at Wire Face, Test 1, Left Electrode Pair, Excluding Resistivity)

314
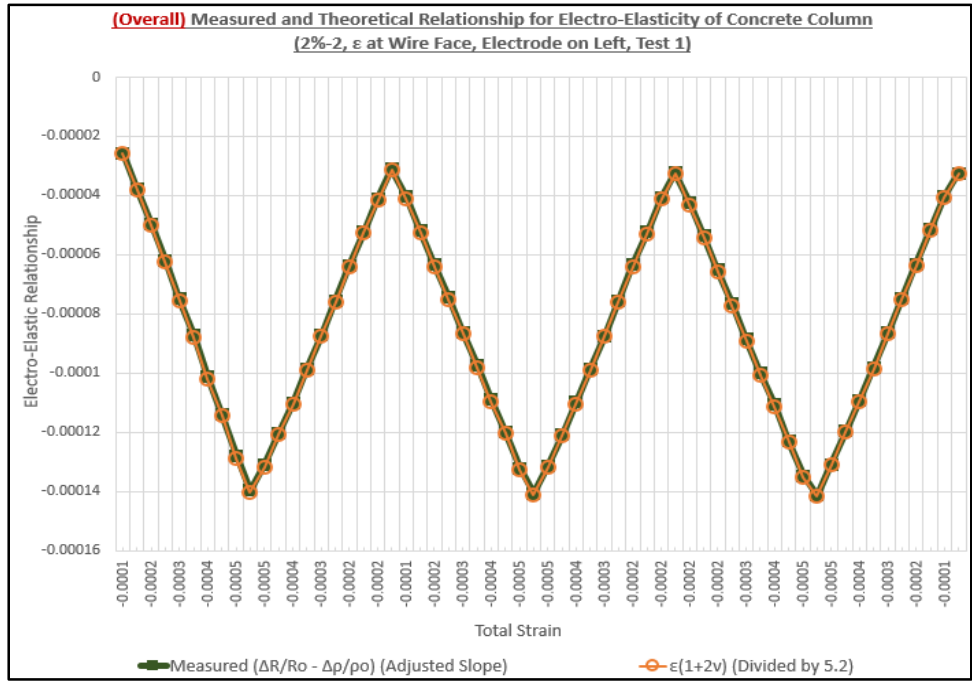
Figure G-26
Overall Elasto-Electric Parameter Line Plot with Mechanical vs. Electrical Measurements
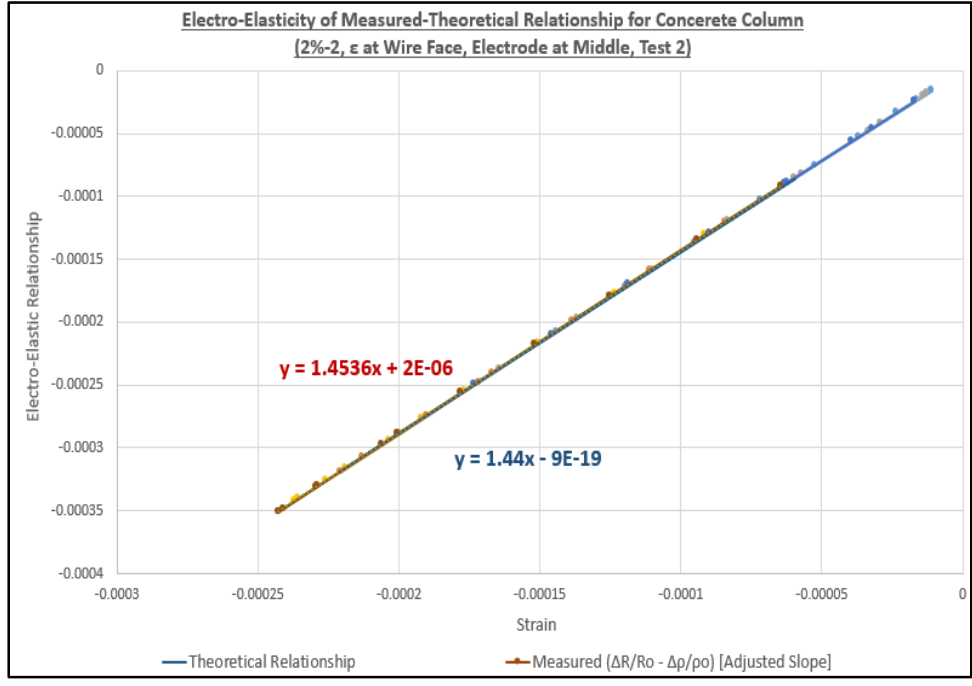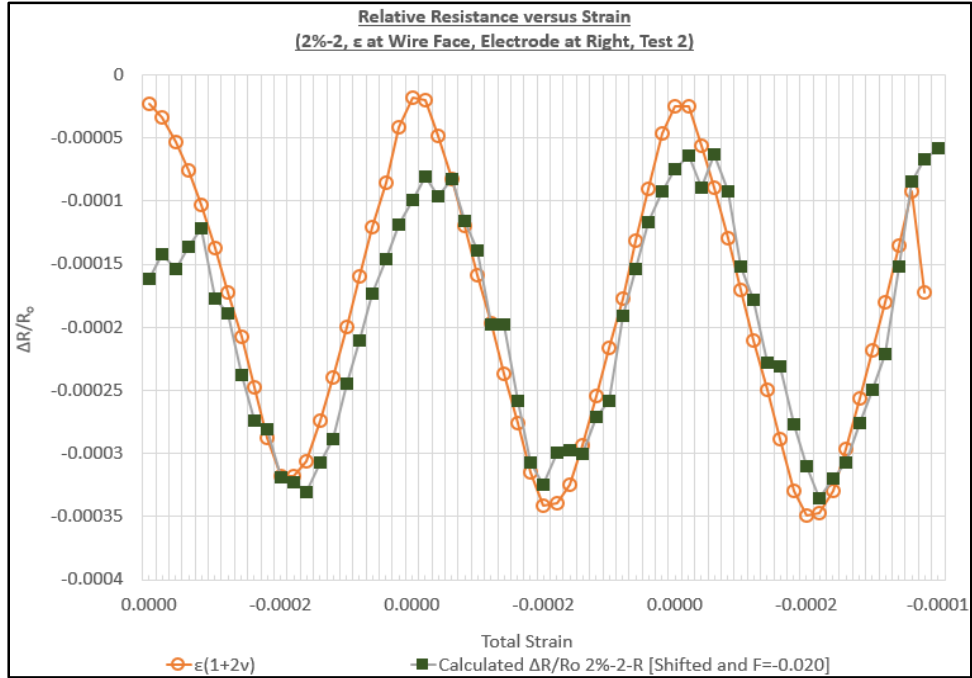(2%, Column 2, Strain at Wire Face, Test 1, Left Electrode Pair, Including Resistivity)
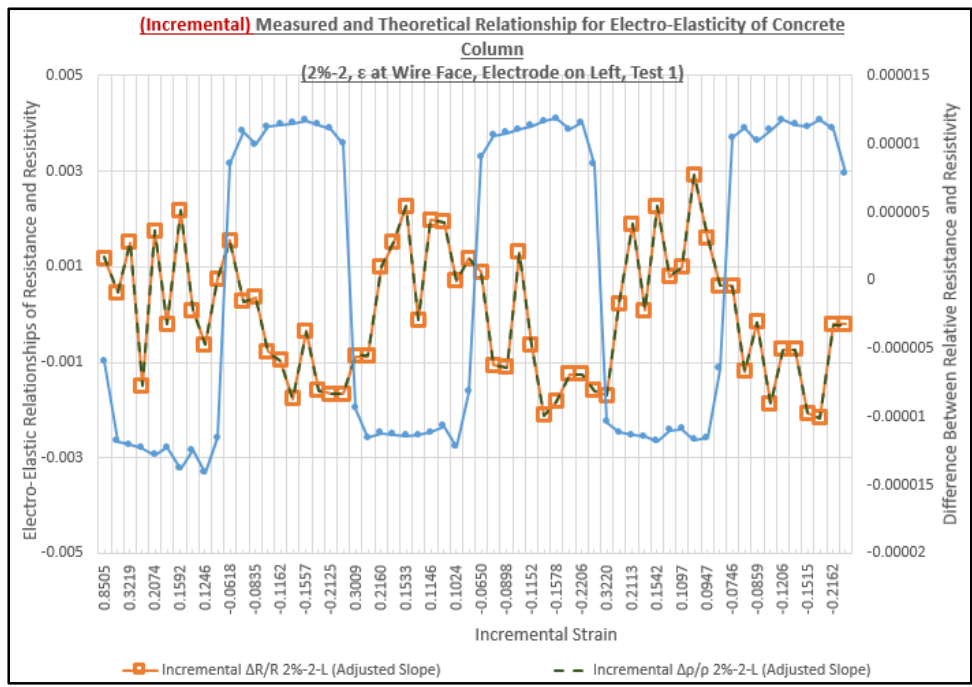
Figure G-27
Incremental Elasto-Electric Parameter X-Y Scatter Plot with Mechanical vs. Electrical
Measurements (2%, Column 2, Strain at Wire Face, Test 1, Left Electrode Pair, Including
Resistivity)
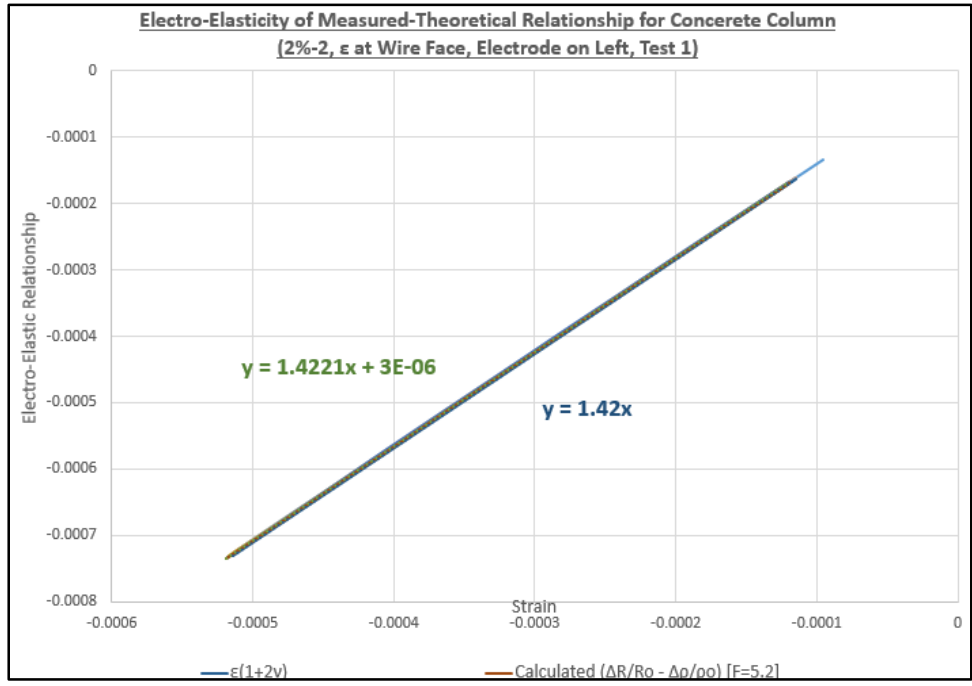
Figure G-28
Elasto-Electric Parameter (2%, Column 2, Strain at Wire Face, Test 1, Left Electrode Pair, Including Resistivity)
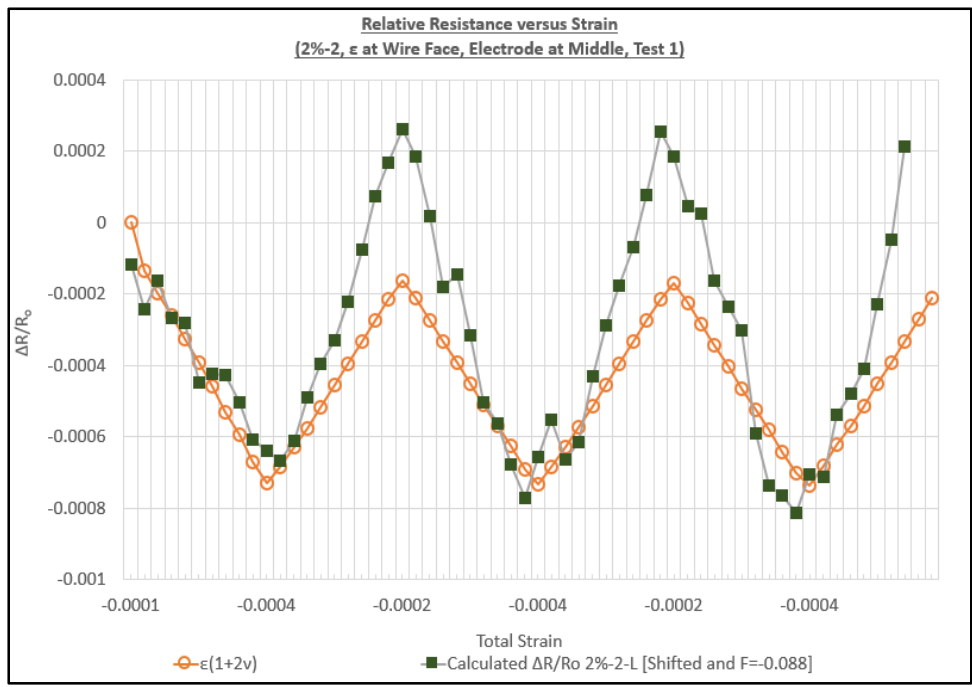
Figure G-29
Elasto-Electric Parameter Line Plot with Mechanical vs. Electrical Measurements (2%, Column 2, Strain at Wire Face, Test 1, Middle Electrode Pair, Excluding Resistivity)
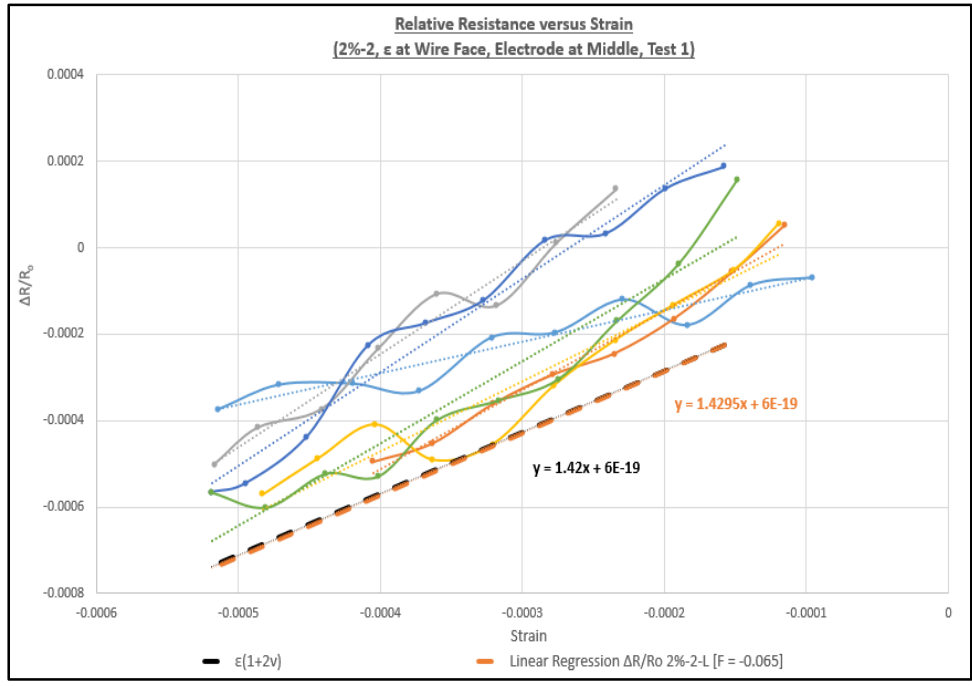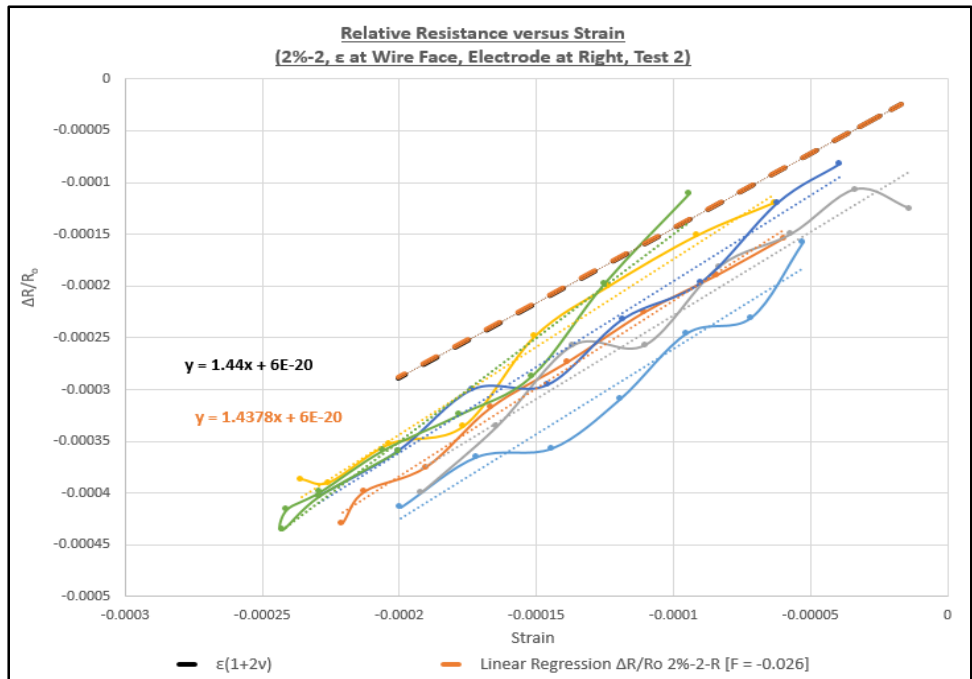
Figure G-30
Elasto-Electric Parameter X-Y Scatter Plot with Mechanical vs. Electrical Measurements
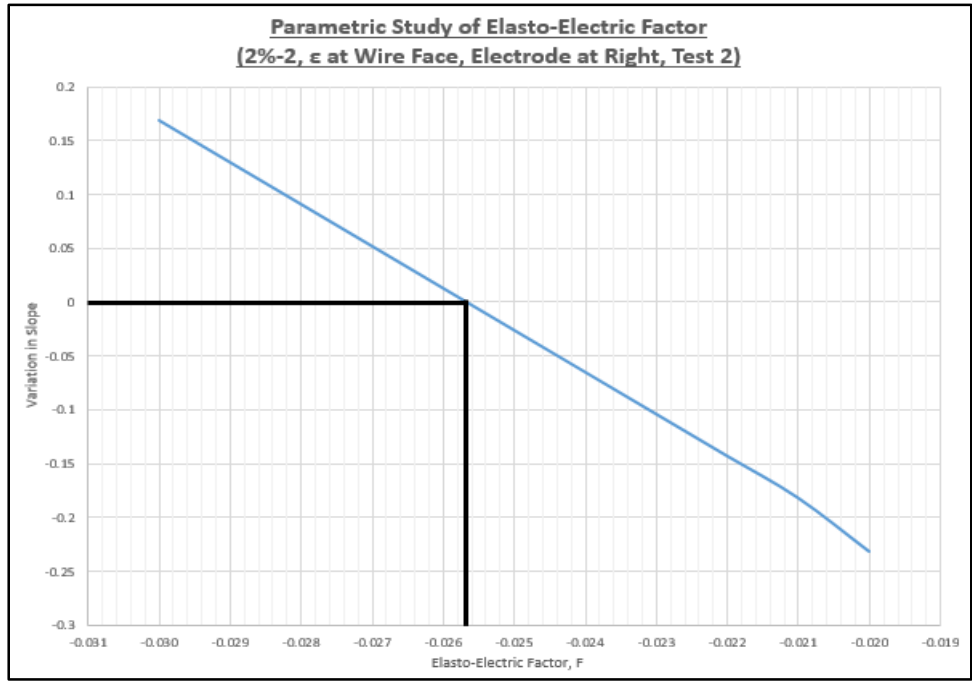(2%, Column 2, Strain at Wire Face, Test 1, Middle Electrode Pair, Excluding
Resistivity)
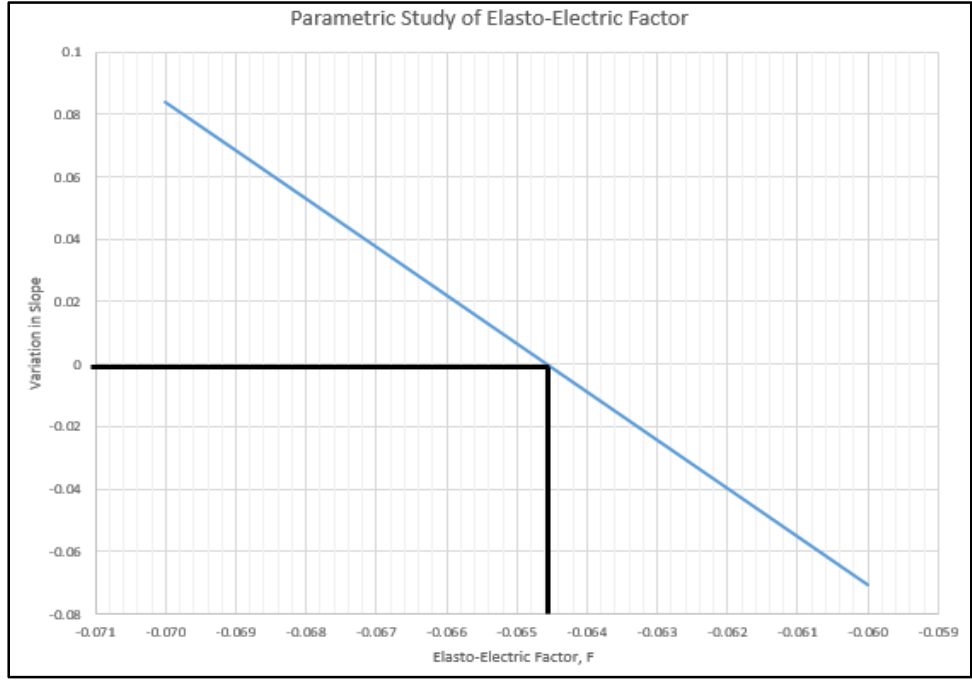
Figure G-31
Parametric Study of Elasto-Electric Factor (2%, Column 2, Strain at Wire Face, Test 1,
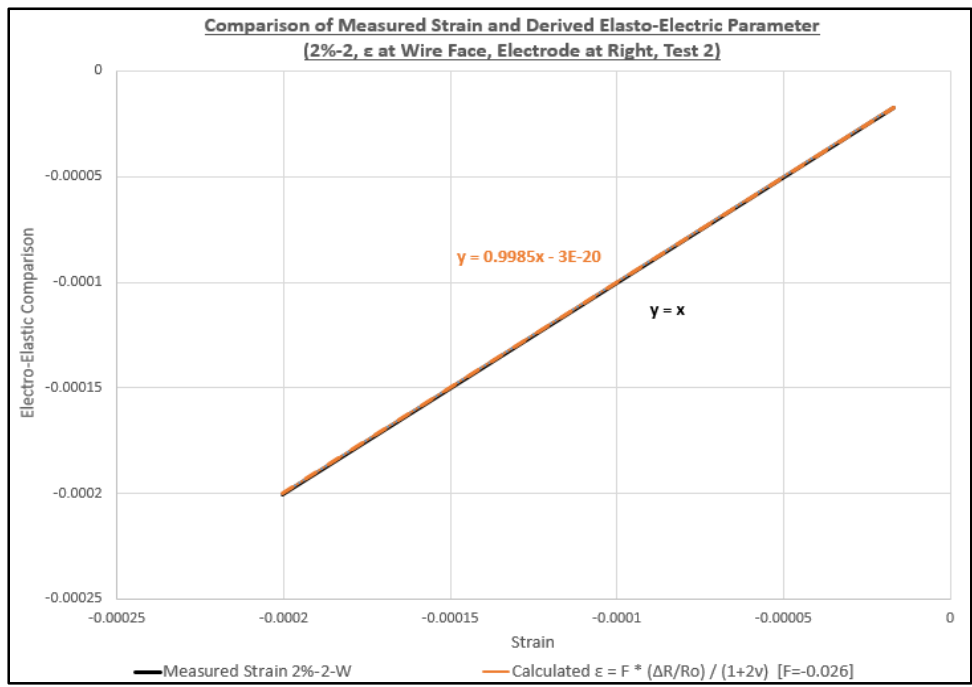Middle Electrode Pair, Excluding Resistivity)
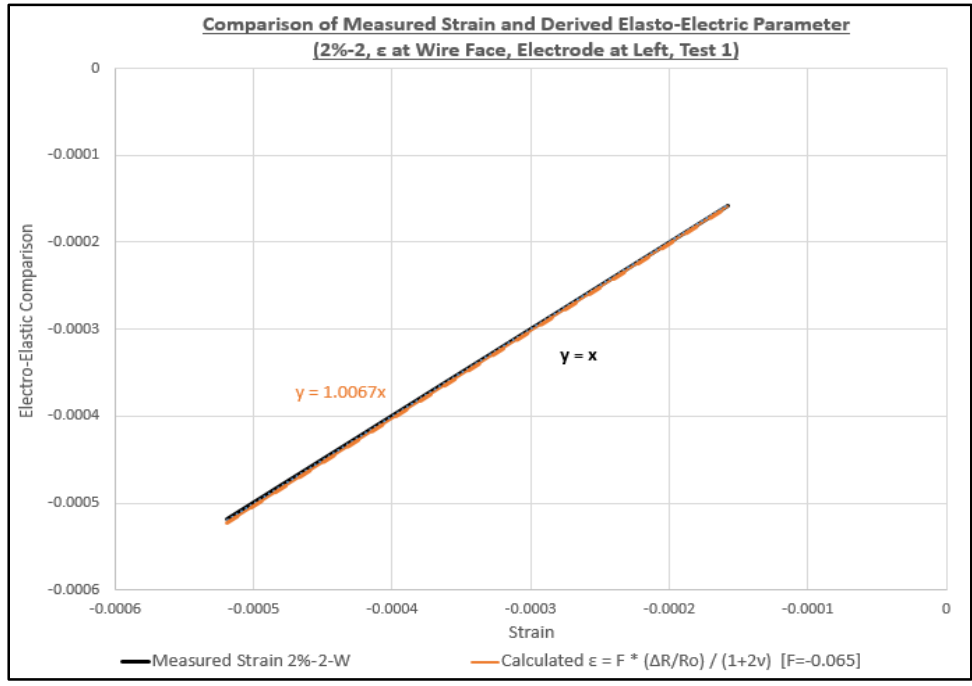
Figure G-32

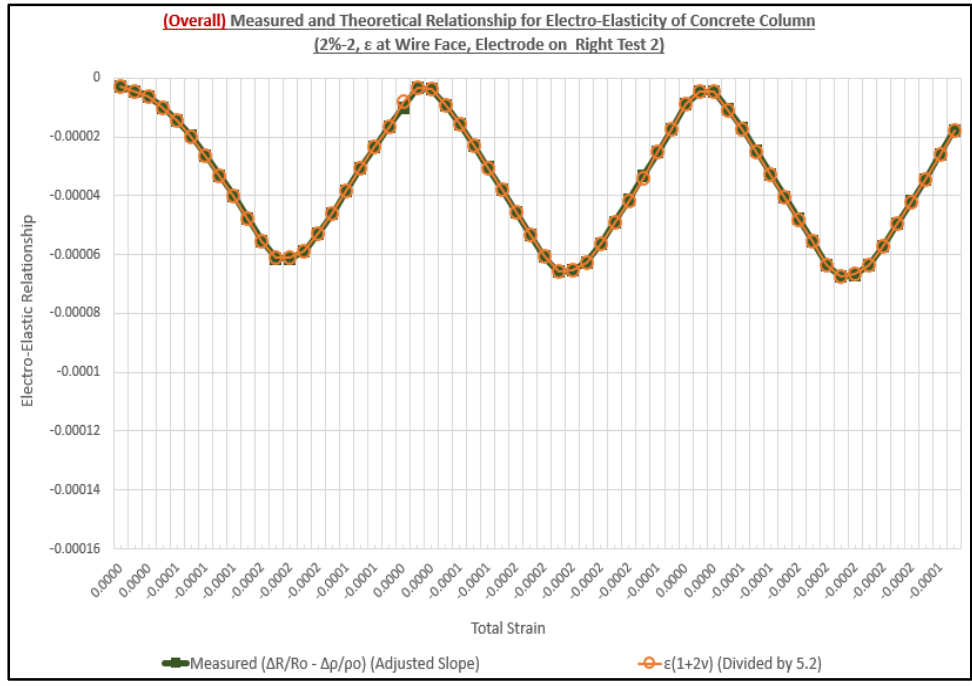Elasto-Electric Parameter (2%, Column 2, Strain at Wire Face, Test 1, Middle Electrode Pair, Excluding Resistivity)
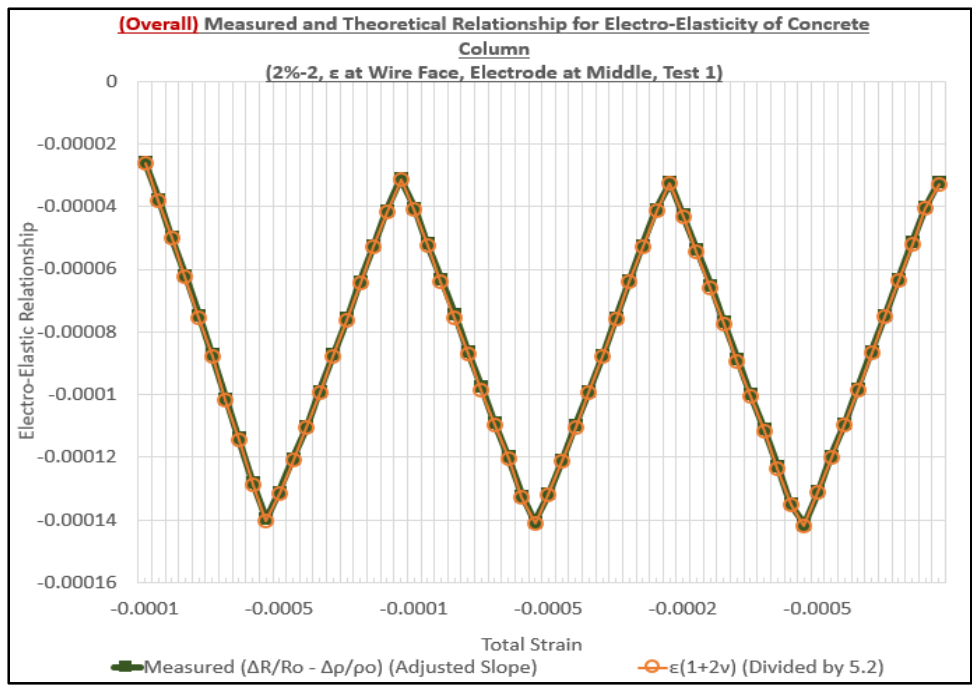
Figure G-33

Overall Elasto-Electric Parameter Line Plot with Mechanical vs. Electrical Measurements (2%, Column 2, Strain at Wire Face, Test 1, Middle Electrode Pair, Including Resistivity)
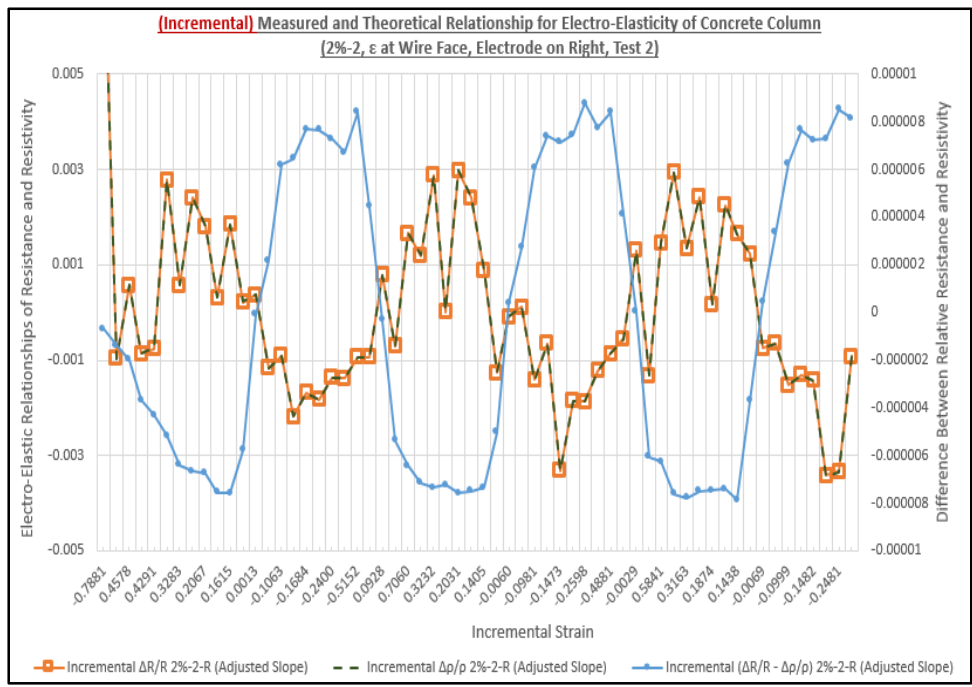
318
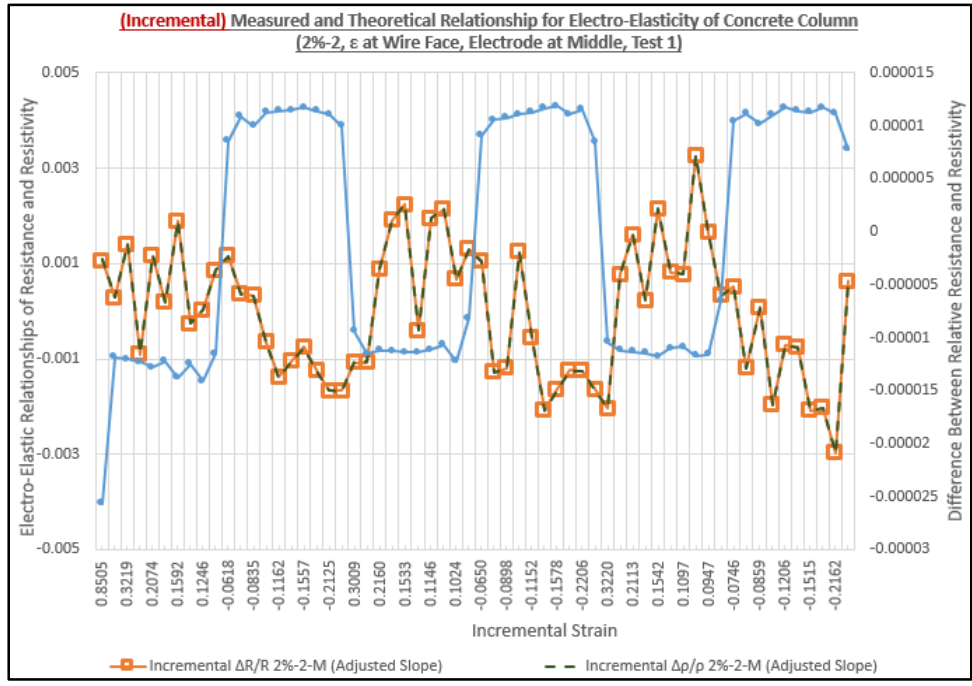
Figure G-34
Incremental Elasto-Electric Parameter X-Y Scatter Plot with Mechanical vs. Electrical
Measurements (2%, Column 2, Strain at Wire Face, Test 1, Middle Electrode Pair,
Including Resistivity)
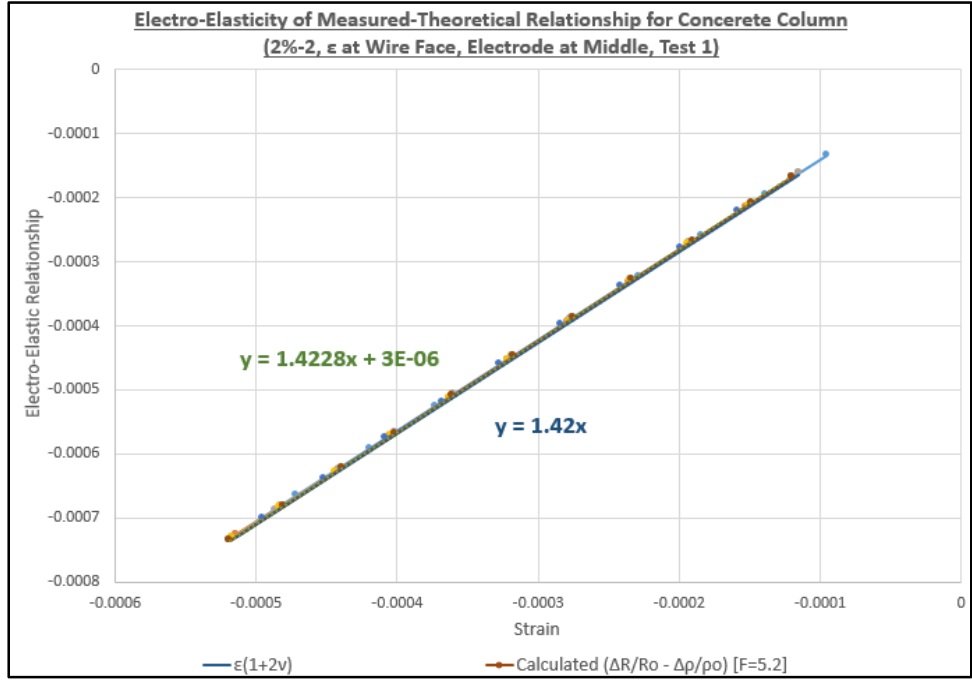
Figure G-35
Elasto-Electric Parameter (2%, Column 2, Strain at Wire Face, Test 1, Middle Electrode
Pair, Including Resistivity)

319
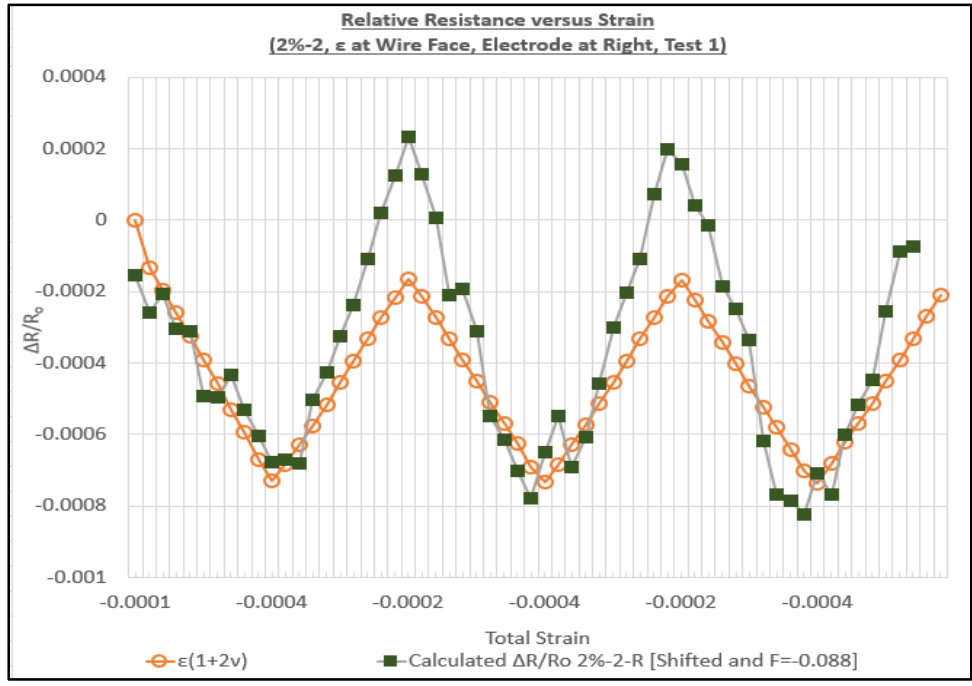
Figure G-36
Elasto-Electric Parameter Line Plot with Mechanical vs. Electrical Measurements (2%,
Column 2, Strain at Wire Face, Test 1, Right Electrode Pair, Excluding Resistivity)
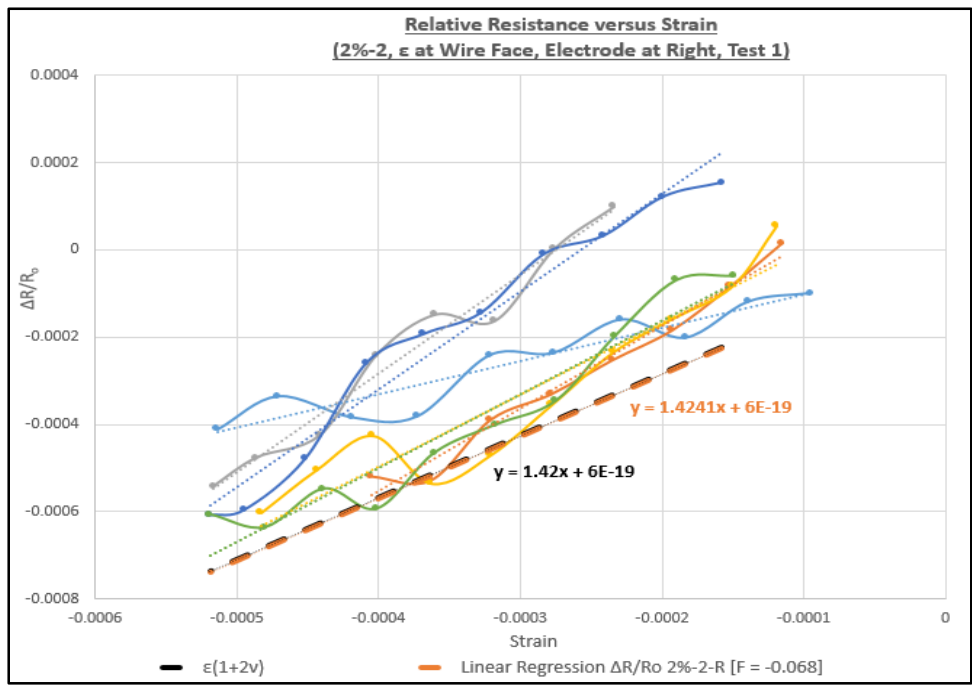
Figure G-37
Elasto-Electric Parameter X-Y Scatter Plot with Mechanical vs. Electrical Measurements
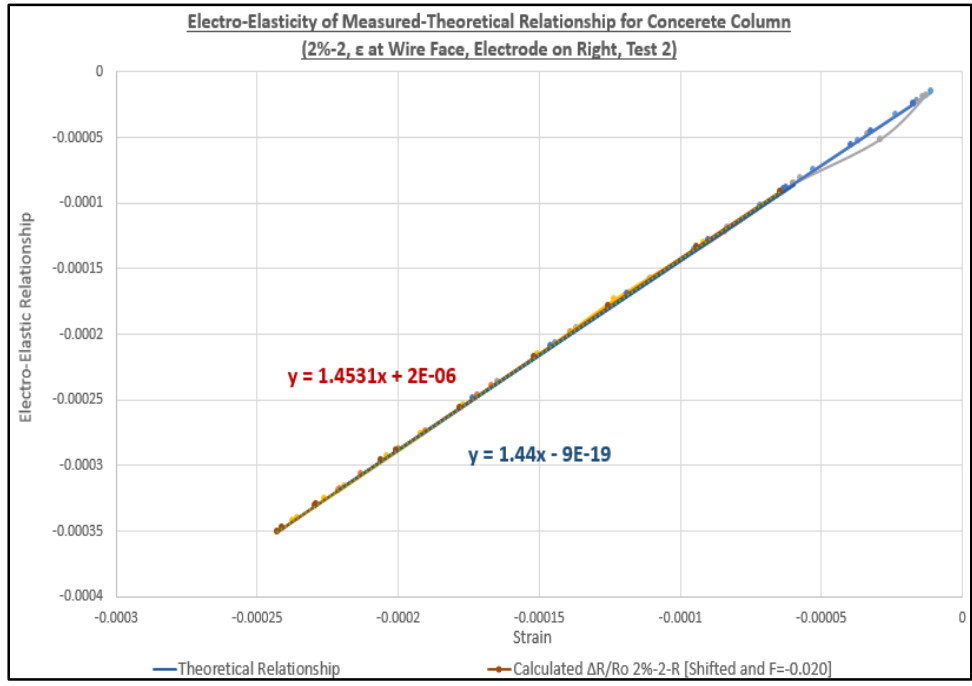(2%, Column 2, Strain at Wire Face, Test 1, Right Electrode Pair, Excluding Resistivity)
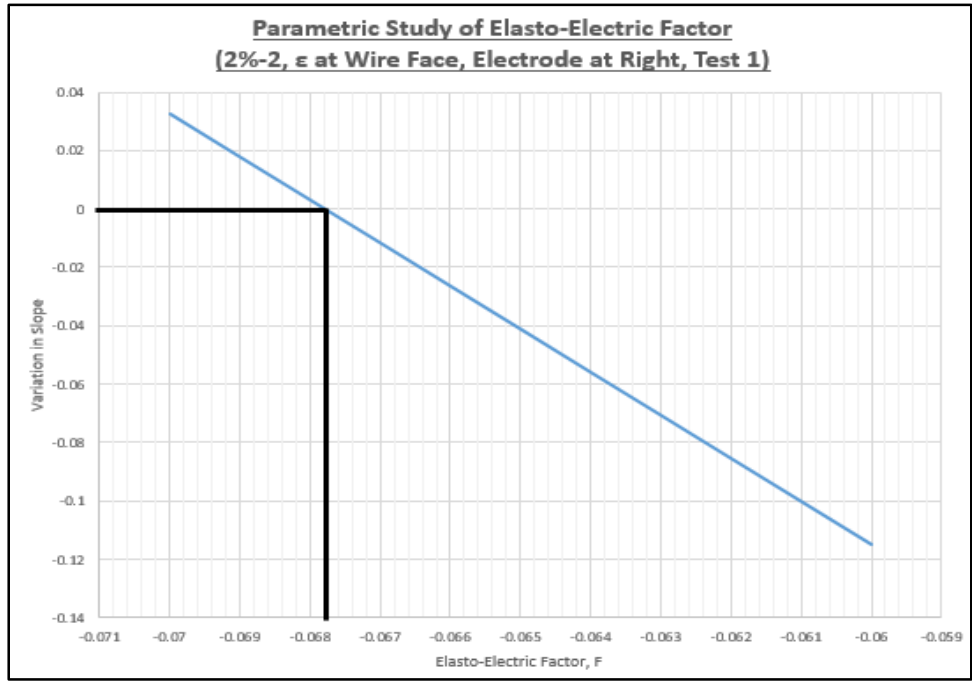
Figure G-38
Parametric Study of Elasto-Electric Factor (2%, Column 2, Strain at Wire Face, Test 1, Right Electrode Pair, Excluding Resistivity)
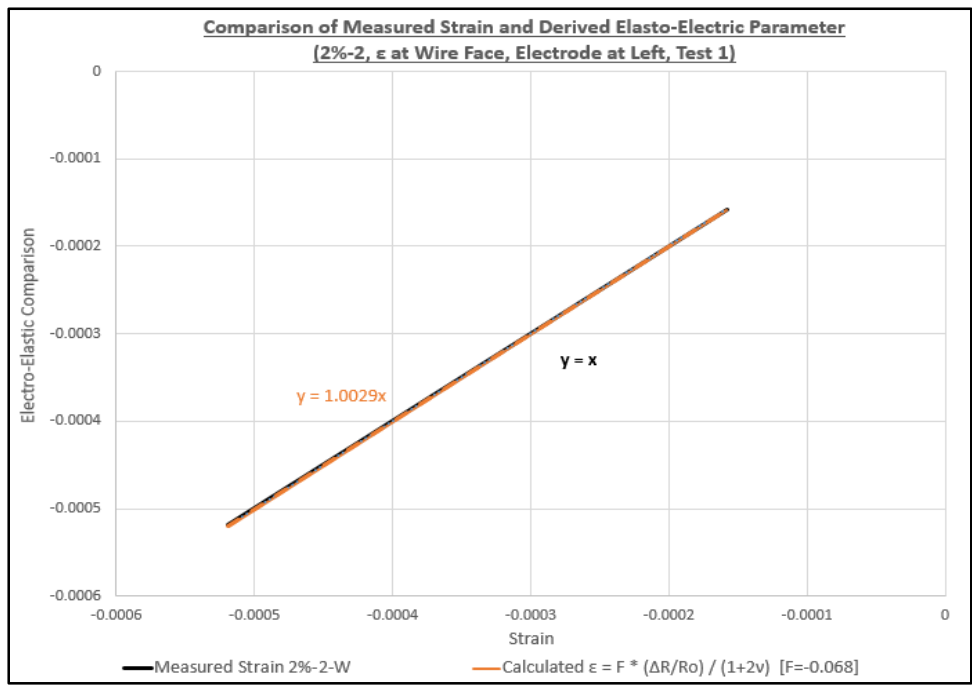
Figure G-39
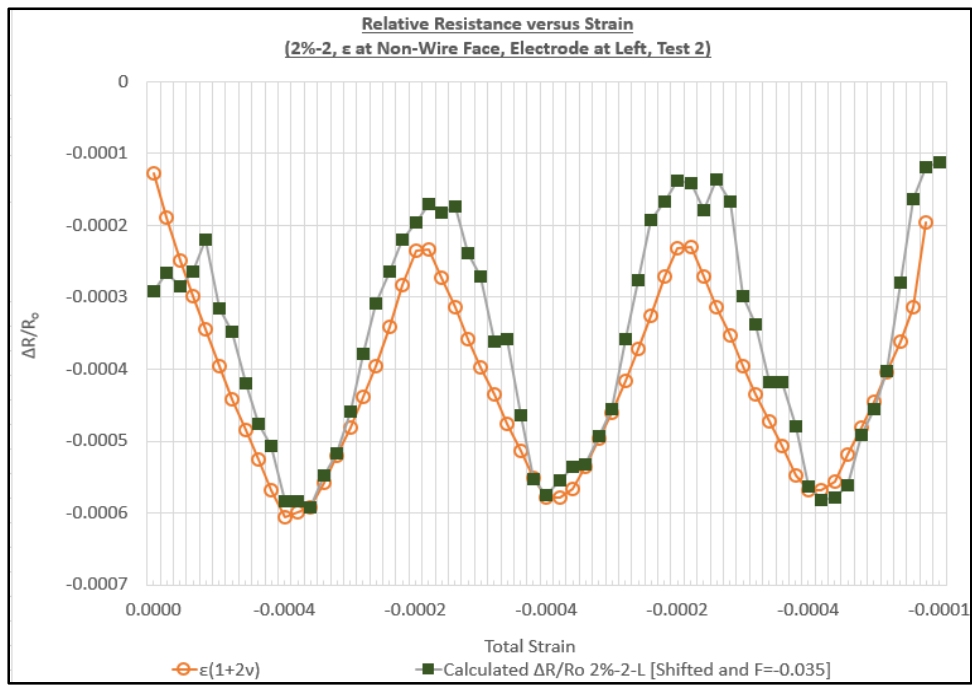Elasto-Electric Parameter (2%, Column 2, Strain at Wire Face, Test 1, Right Electrode Pair, Excluding Resistivity)

321
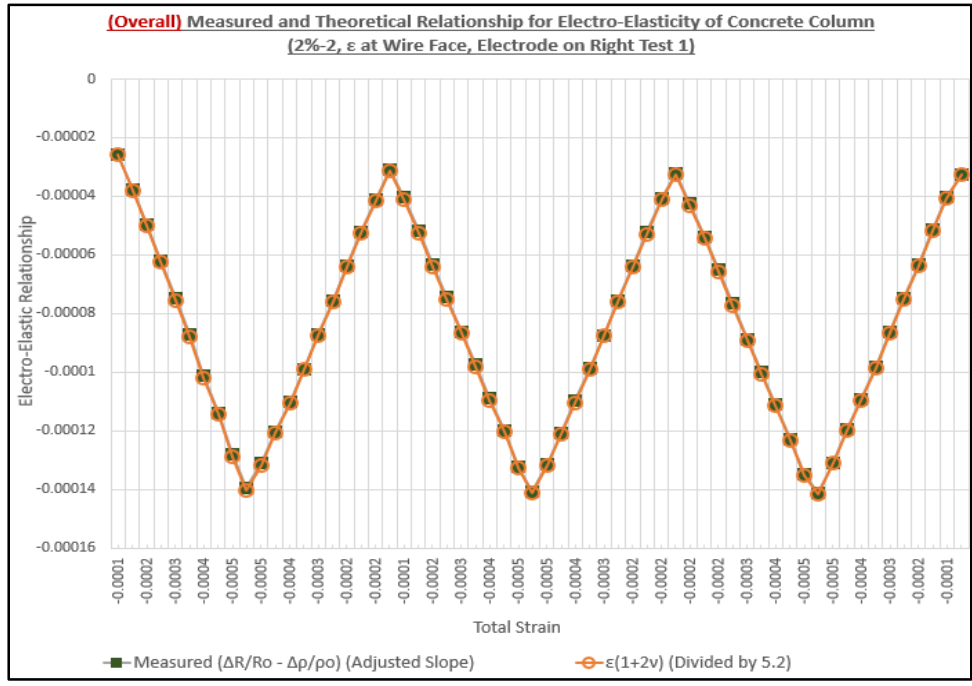
Figure G-40
Overall Elasto-Electric Parameter Line Plot with Mechanical vs. Electrical Measurements (2%, Column 2, Strain at Wire Face, Test 1, Right Electrode Pair, Including Resistivity)
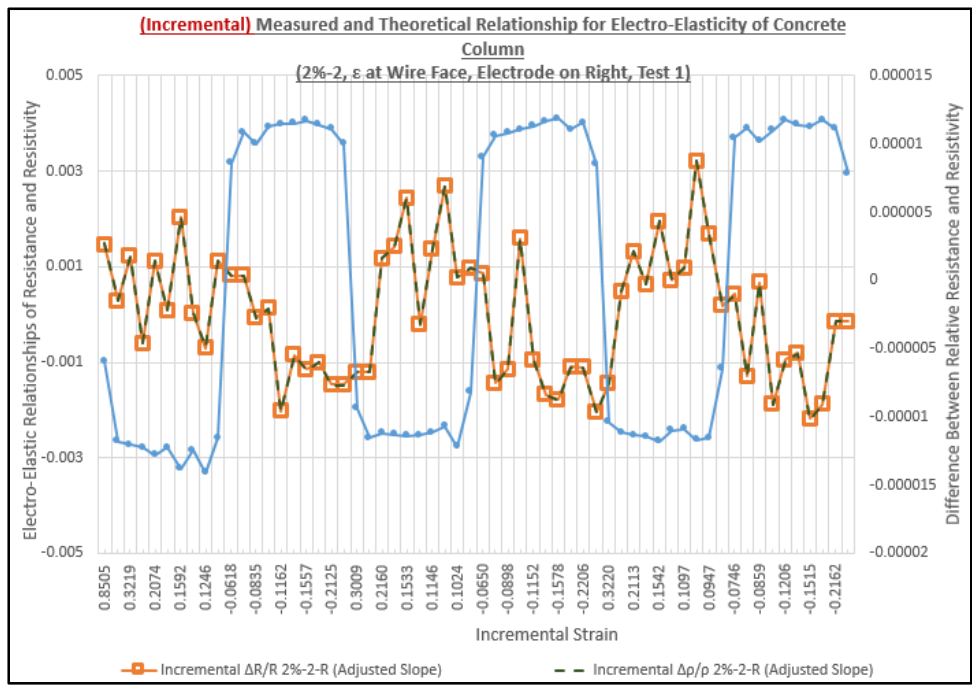
Figure G-41
Incremental Elasto-Electric Parameter X-Y Scatter Plot with Mechanical vs. Electrical Measurements (2%, Column 2, Strain at Wire Face, Test 1, Right Electrode Pair, Including Resistivity)
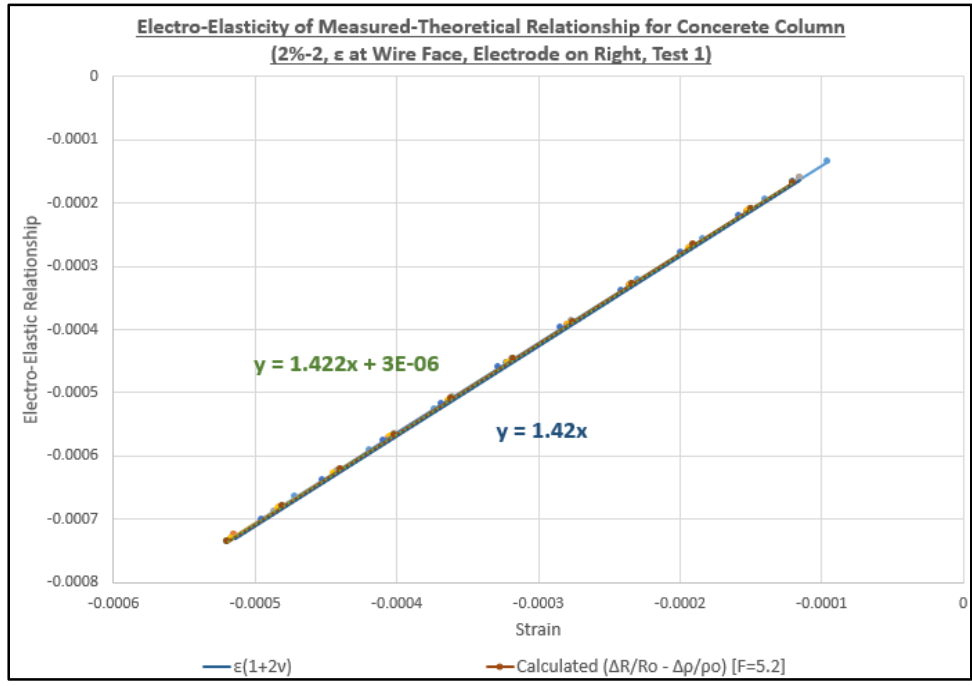
Figure G-42

Elasto-Electric Parameter (2%, Column 2, Strain at Wire Face, Test 1, Right Electrode Pair, Including Resistivity)
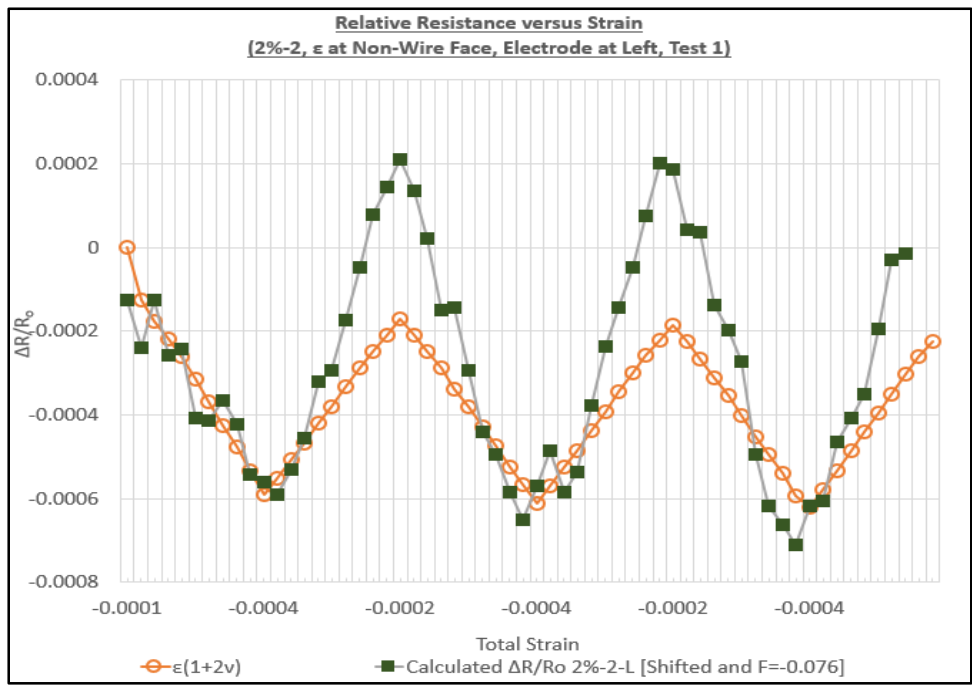
Figure G-43

Elasto-Electric Parameter Line Plot with Mechanical vs. Electrical Measurements (2%, Column 2, Strain at Non-Wire Face, Test 1, Left Electrode Pair, Excluding Resistivity)
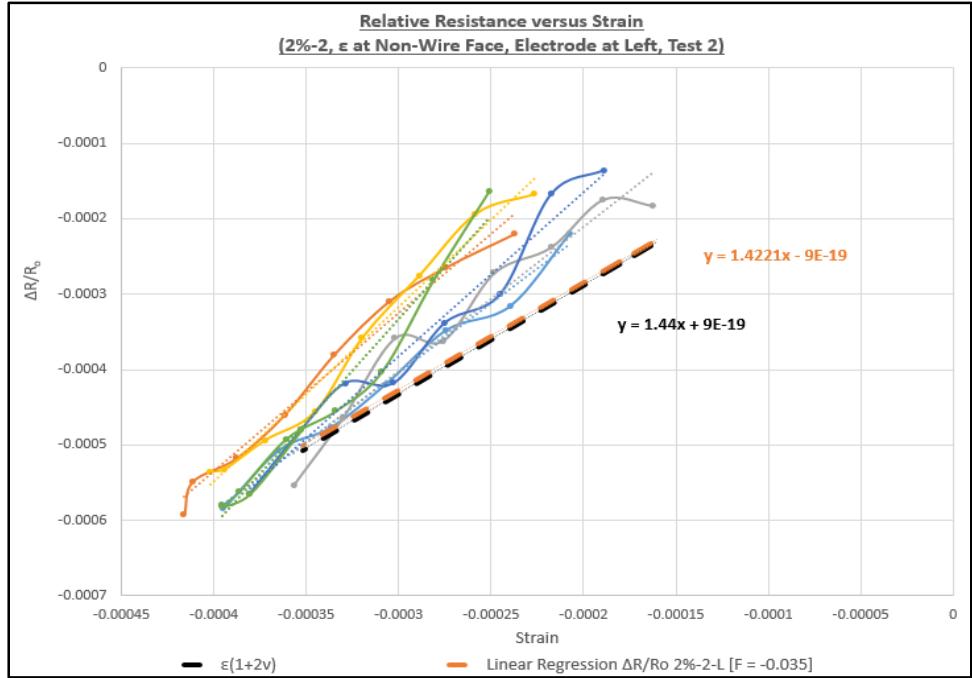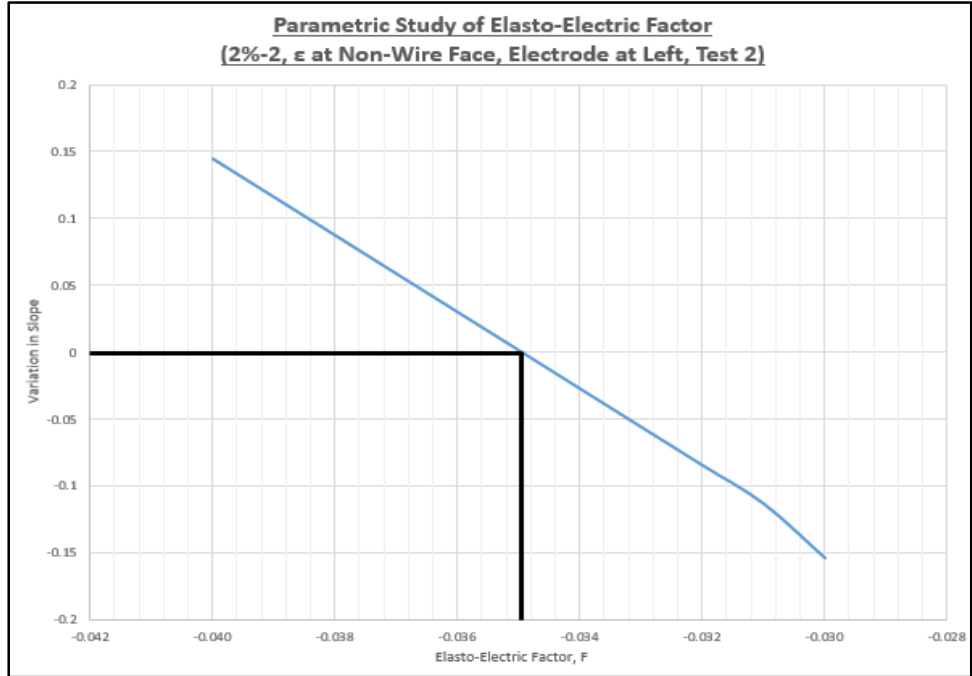
323
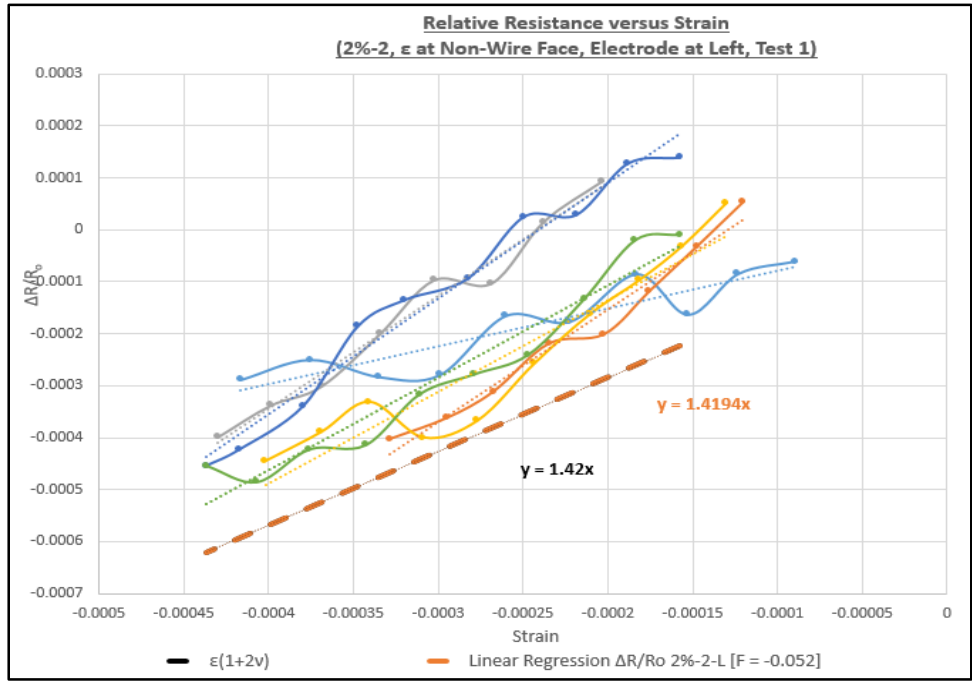
Figure G-44
Elasto-Electric Parameter X-Y Scatter Plot with Mechanical vs. Electrical Measurements (2%, Column 2, Strain at Non-Wire Face, Test 1, Left Electrode Pair, Excluding Resistivity)
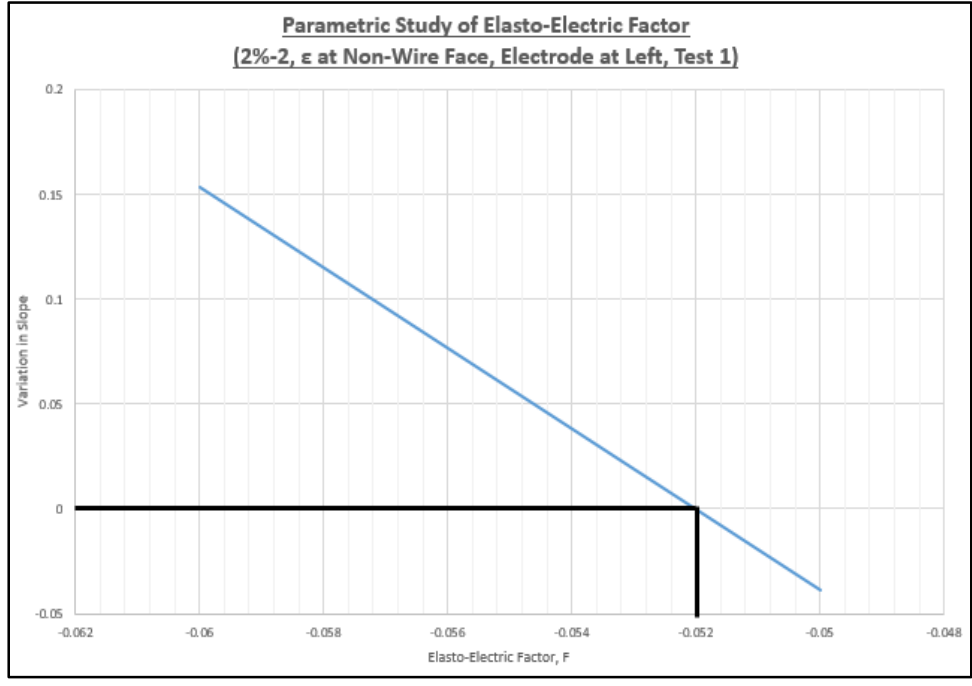
Figure G-45
Parametric Study of Elasto-Electric Factor (2%, Column 2, Strain at Non-Wire Face, Test 1, Left Electrode Pair, Excluding Resistivity)
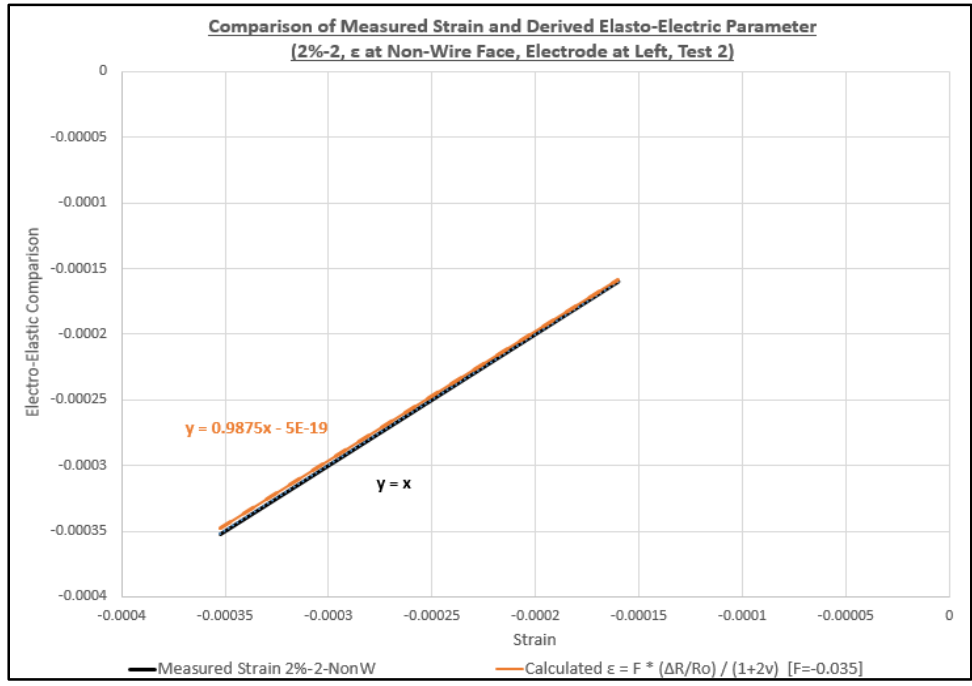
324
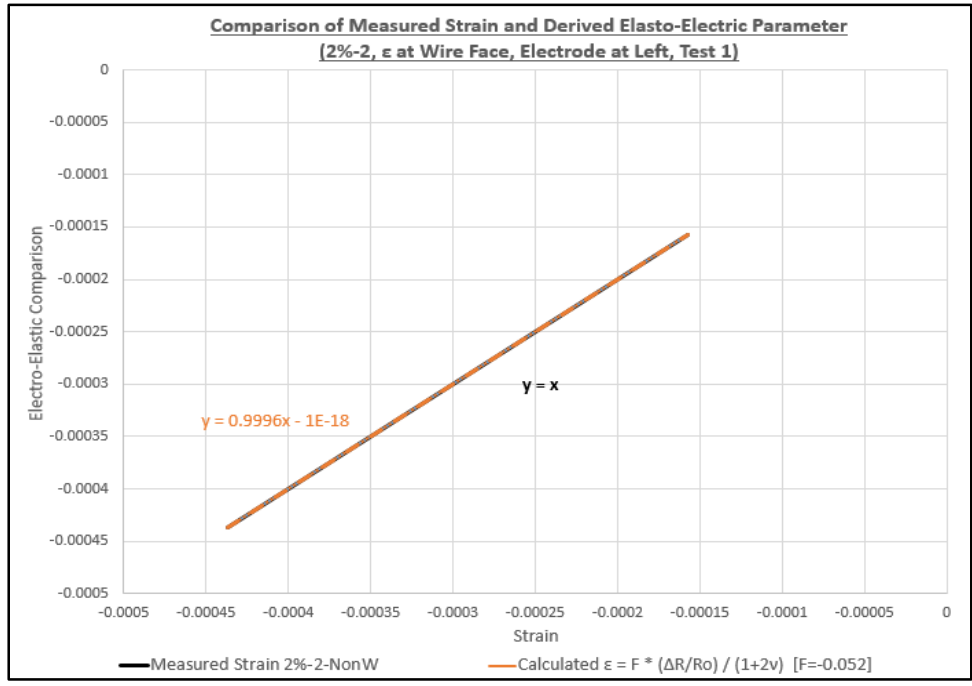
Figure G-46
Elasto-Electric Parameter (2%, Column 2, Strain at Non-Wire Face, Test 1, Left
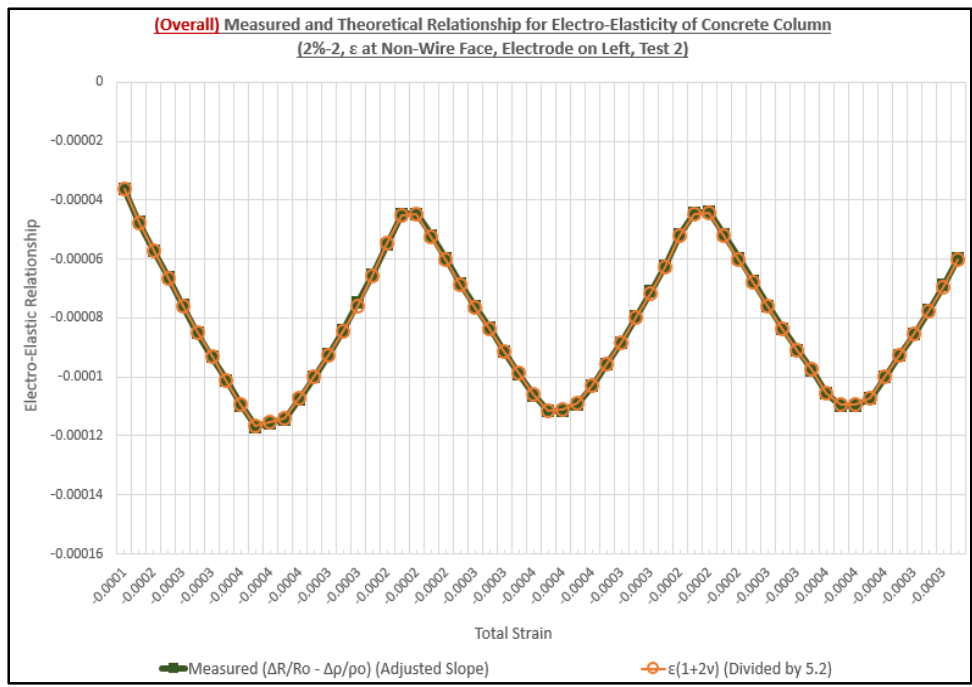Electrode Pair, Excluding Resistivity)
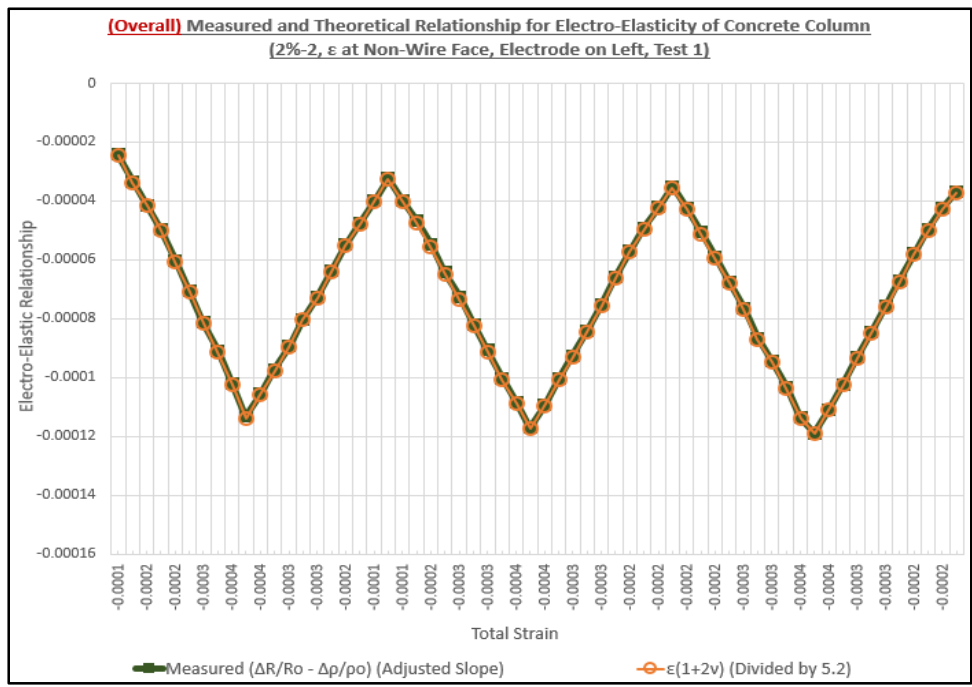
Figure G-47
Overall Elasto-Electric Parameter Line Plot with Mechanical vs. Electrical Measurements
(2%, Column 2, Strain at Non-Wire Face, Test 1, Left Electrode Pair, Including
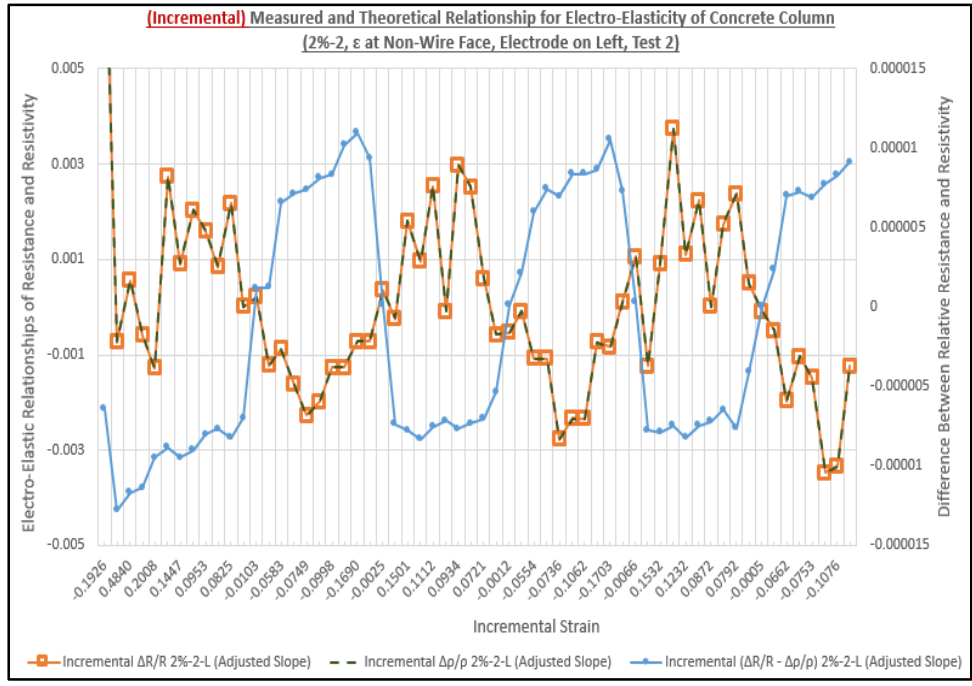Resistivity)
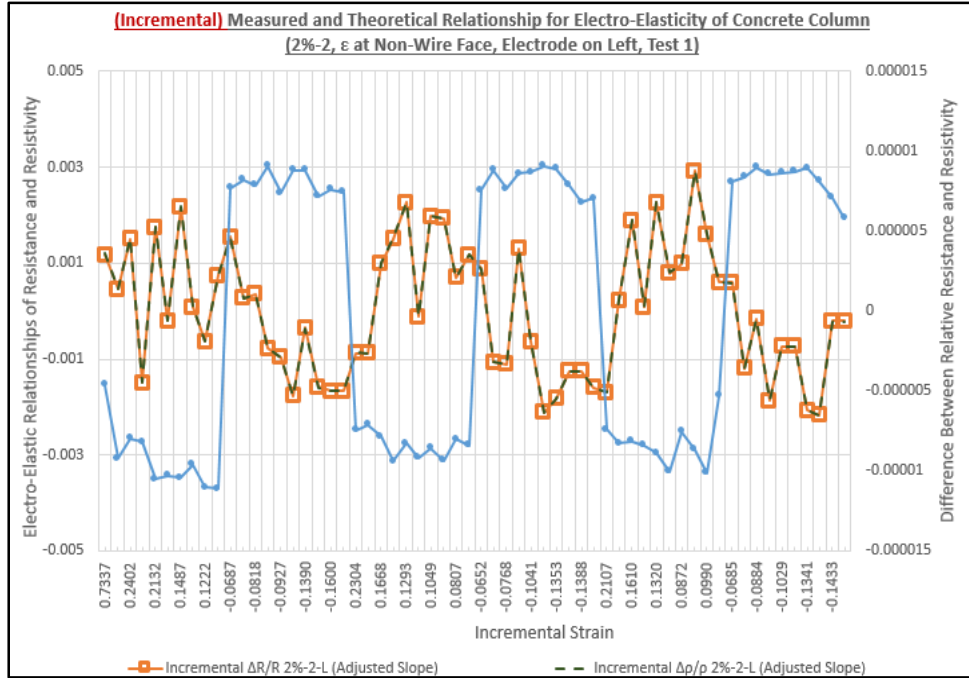
Figure G-48

Incremental Elasto-Electric Parameter X-Y Scatter Plot with Mechanical vs. Electrical Measurements (2%, Column 2, Strain at Non-Wire Face, Test 1, Left Electrode Pair, Including Resistivity)
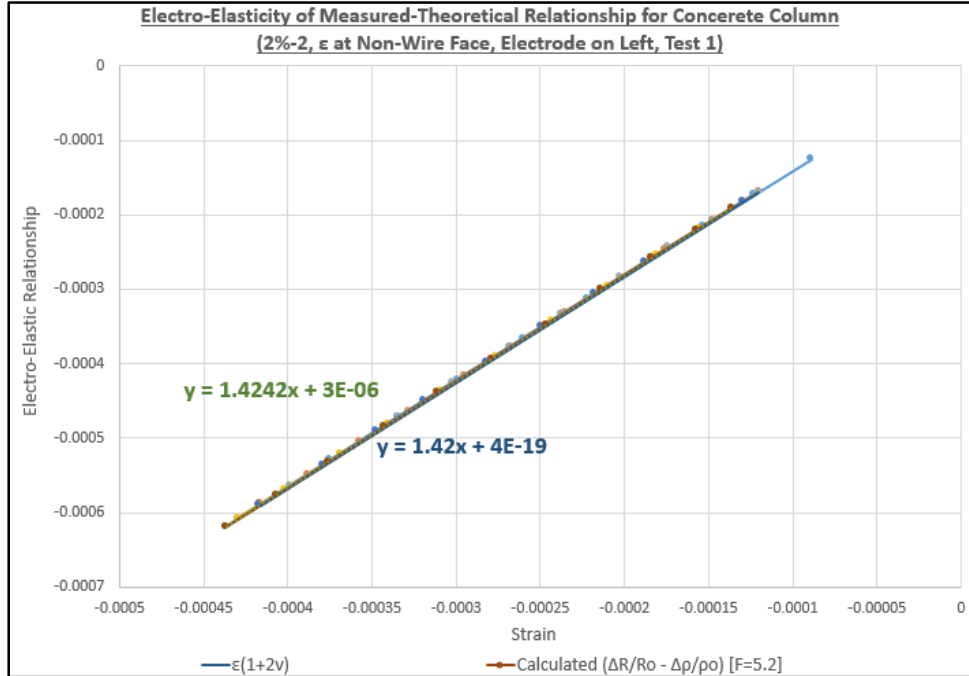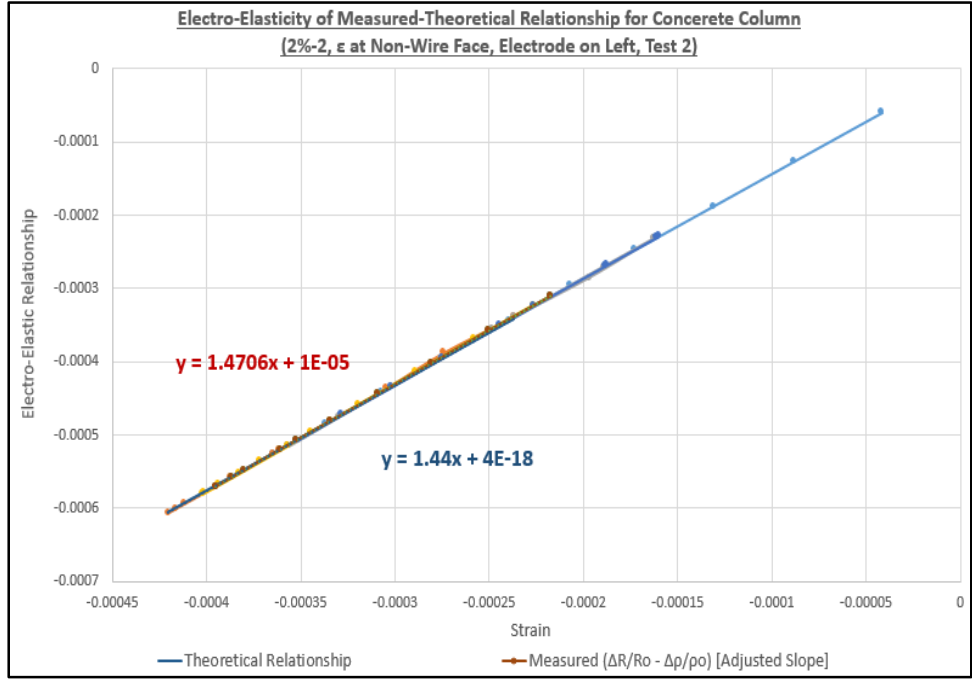

Figure G-49

Elasto-Electric Parameter (2%, Column 2, Strain at Non-Wire Face, Test 1, Left Electrode Pair, Including Resistivity)
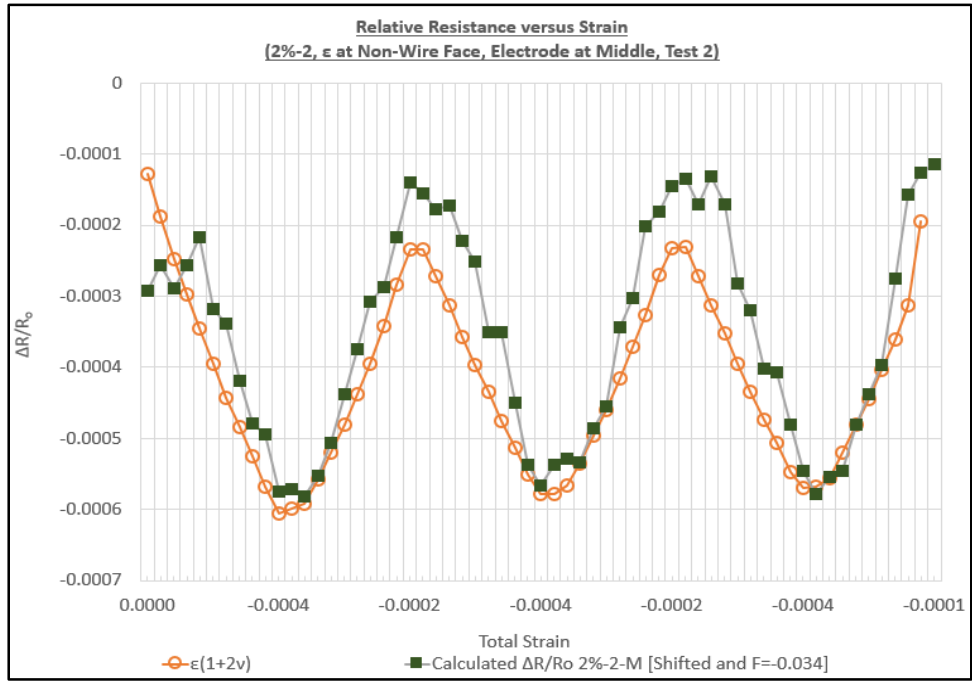
326
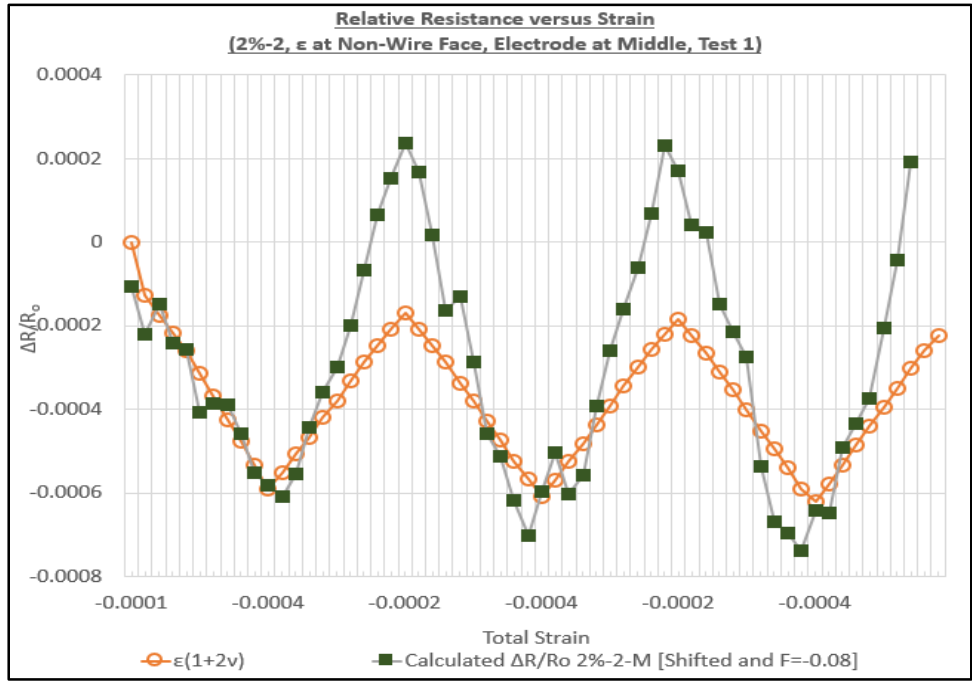
Figure G-50
Elasto-Electric Parameter Line Plot with Mechanical vs. Electrical Measurements (2%, Column 2, Strain at Non-Wire Face, Test 1, Middle Electrode Pair, Excluding Resistivity)
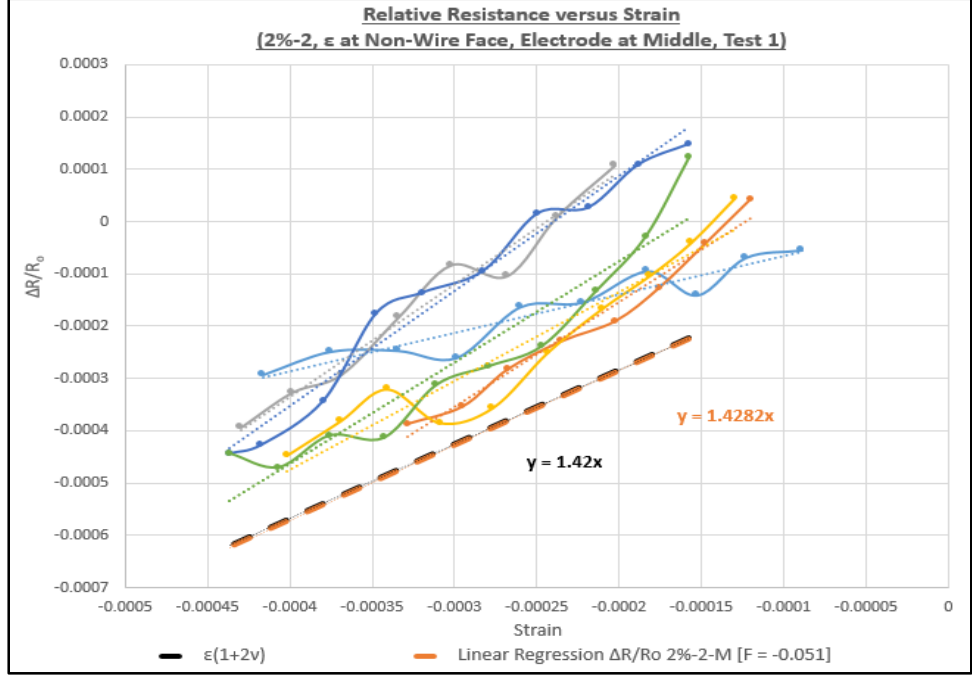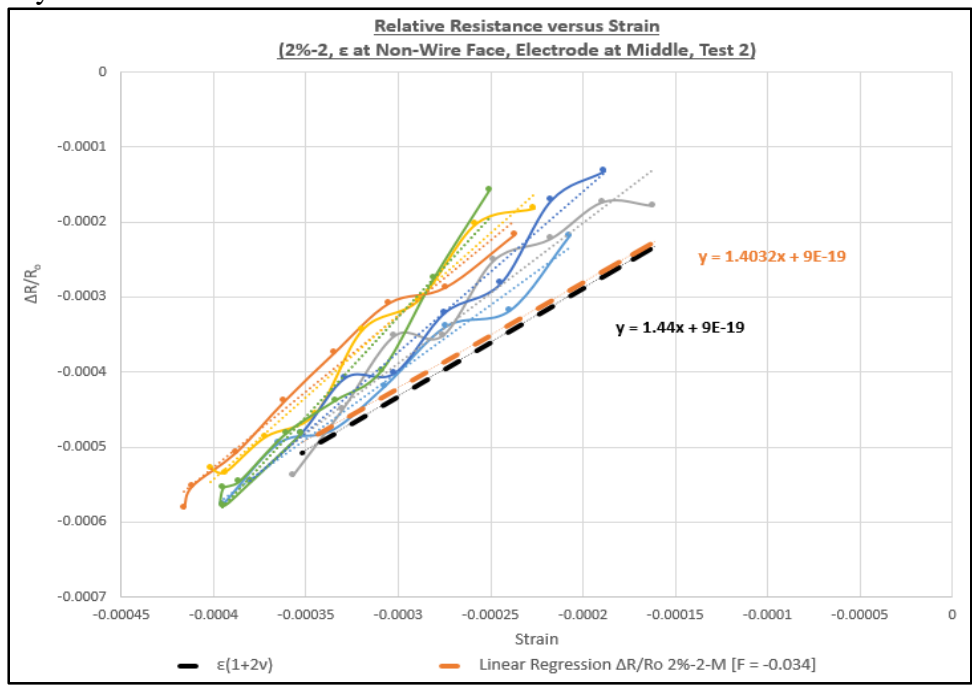

Figure G-51
Elasto-Electric Parameter X-Y Scatter Plot with Mechanical vs. Electrical Measurements (2%, Column 2, Strain at Non-Wire Face, Test 1, Middle Electrode Pair, Excluding Resistivity)
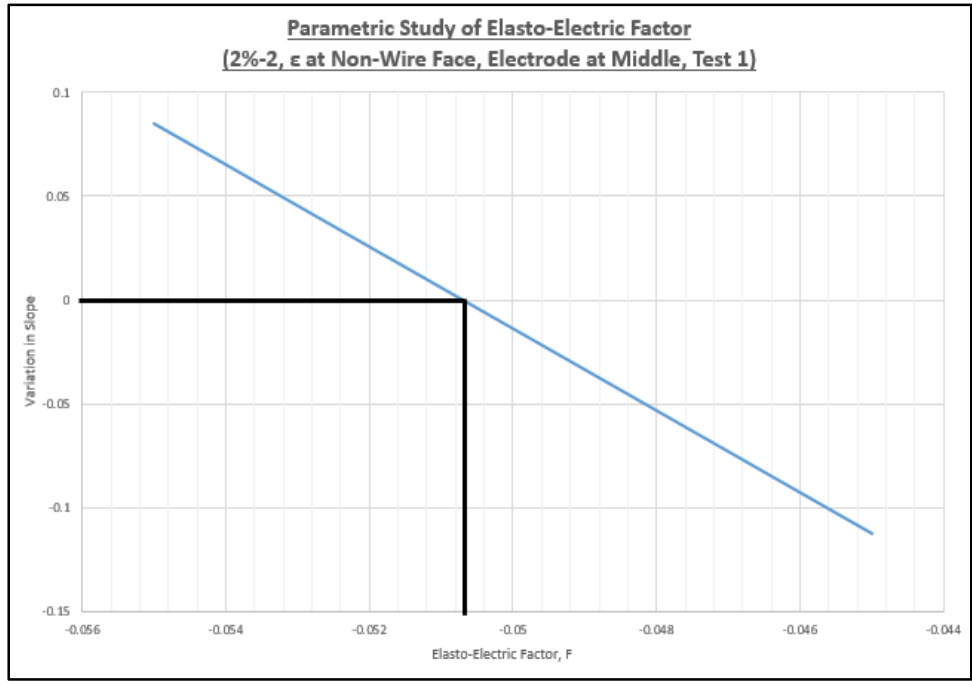
Figure G-52
Parametric Study of Elasto-Electric Factor (2%, Column 2, Strain at Non-Wire Face, Test 1, Middle Electrode Pair, Excluding Resistivity)
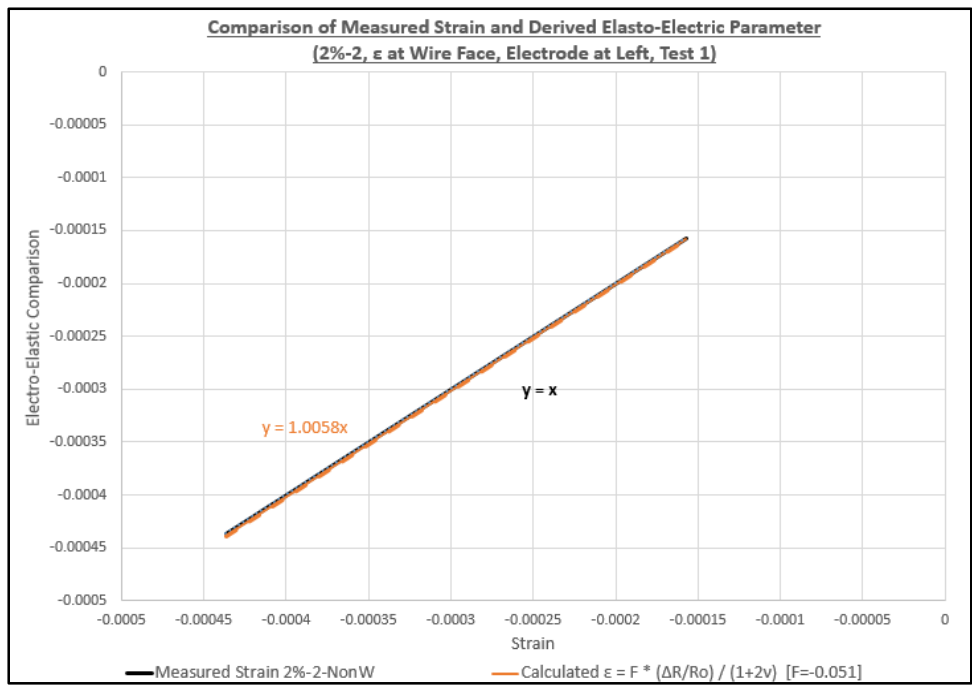
Figure G-53
Elasto-Electric Parameter (2%, Column 2, Strain at Non-Wire Face, Test 1, Middle Electrode Pair, Excluding Resistivity)
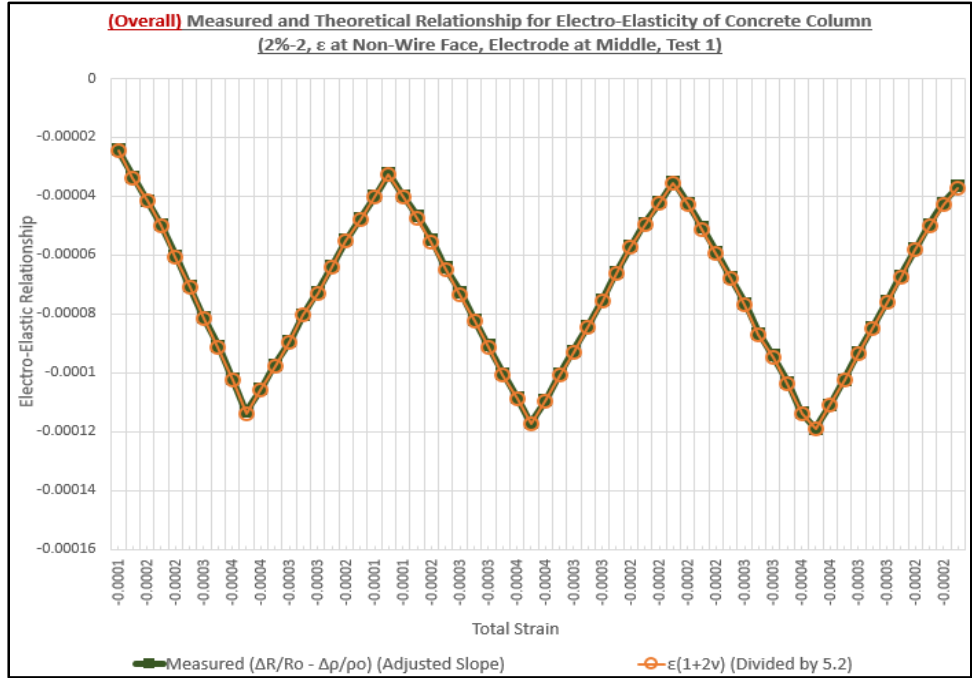
Figure G-54
Overall Elasto-Electric Parameter Line Plot with Mechanical vs. Electrical Measurements
(2%, Column 2, Strain at Non-Wire Face, Test 1, Middle Electrode Pair, Including
Resistivity)
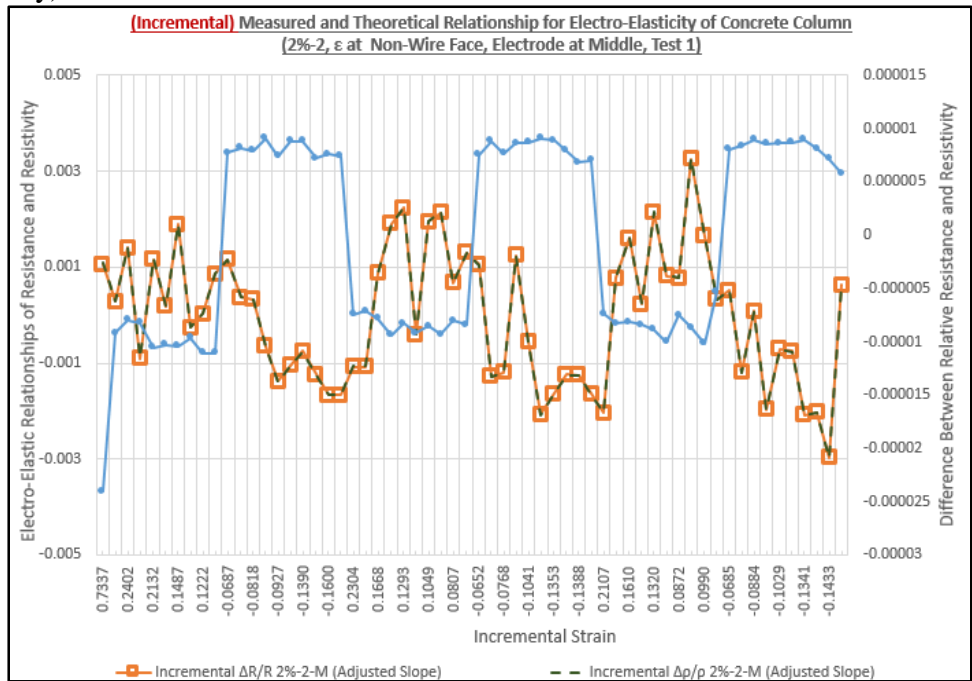
Figure G-55
Incremental Elasto-Electric Parameter X-Y Scatter Plot with Mechanical vs. Electrical
Measurements (2%, Column 2, Strain at Non-Wire Face, Test 1, Middle Electrode Pair,
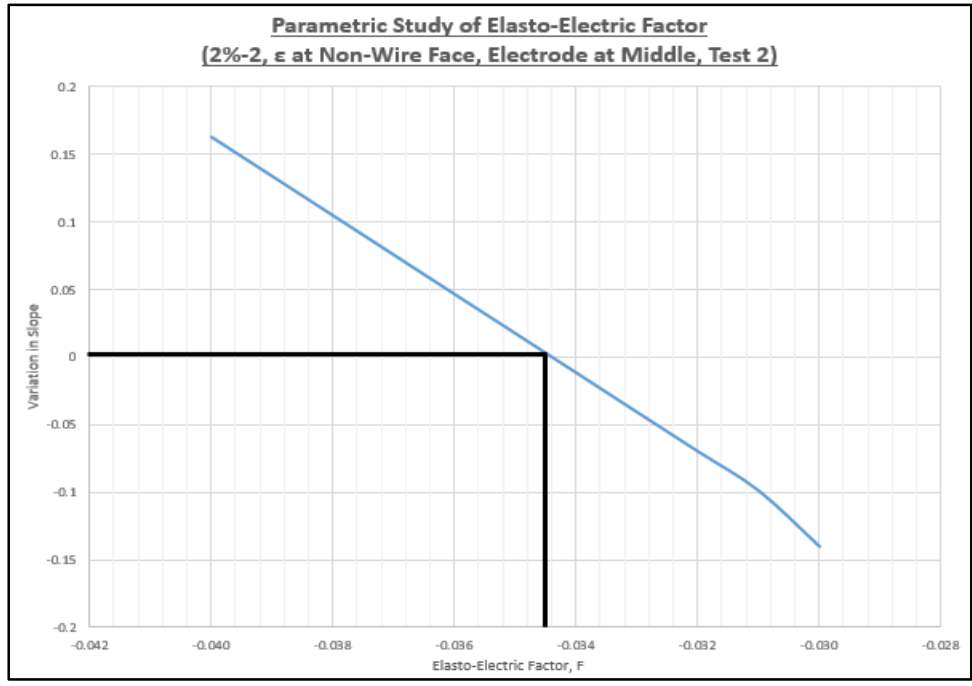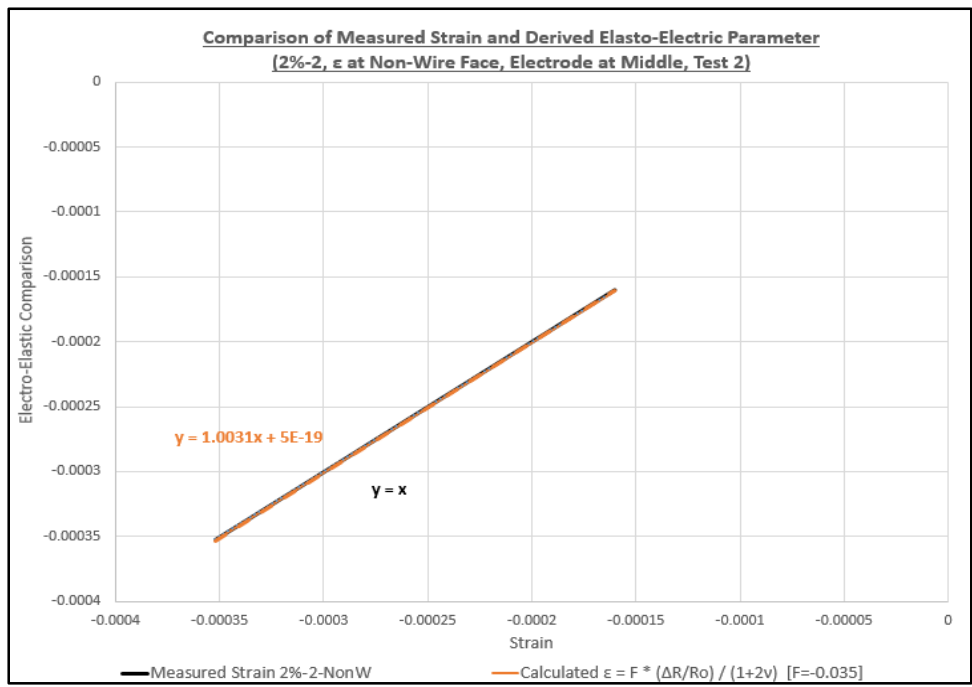Including Resistivity)
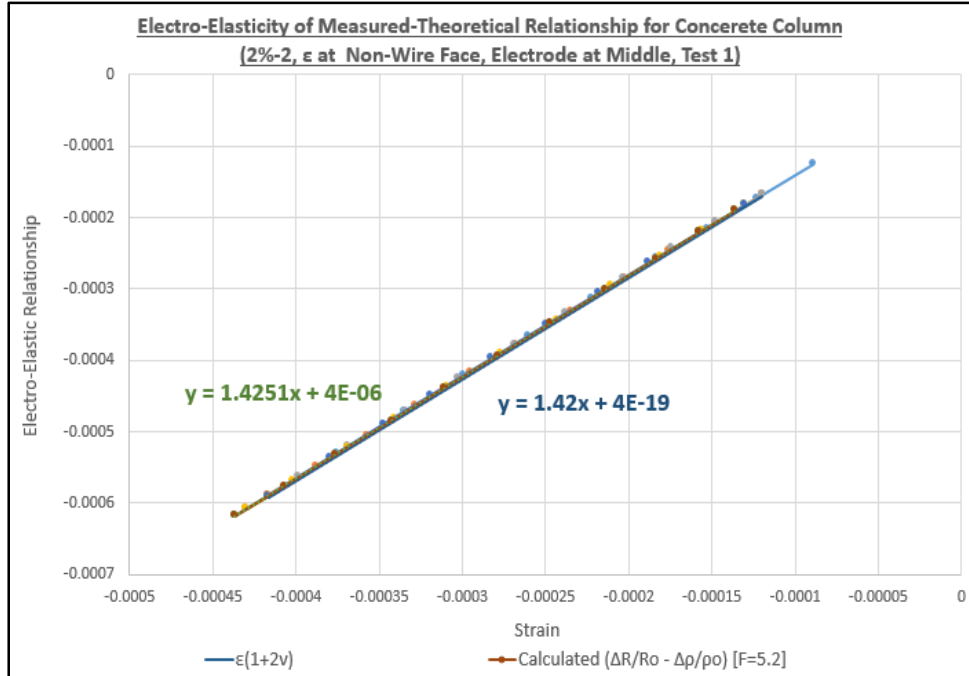
Figure G-56
Elasto-Electric Parameter (2%, Column 2, Strain at Non-Wire Face, Test 1, Middle
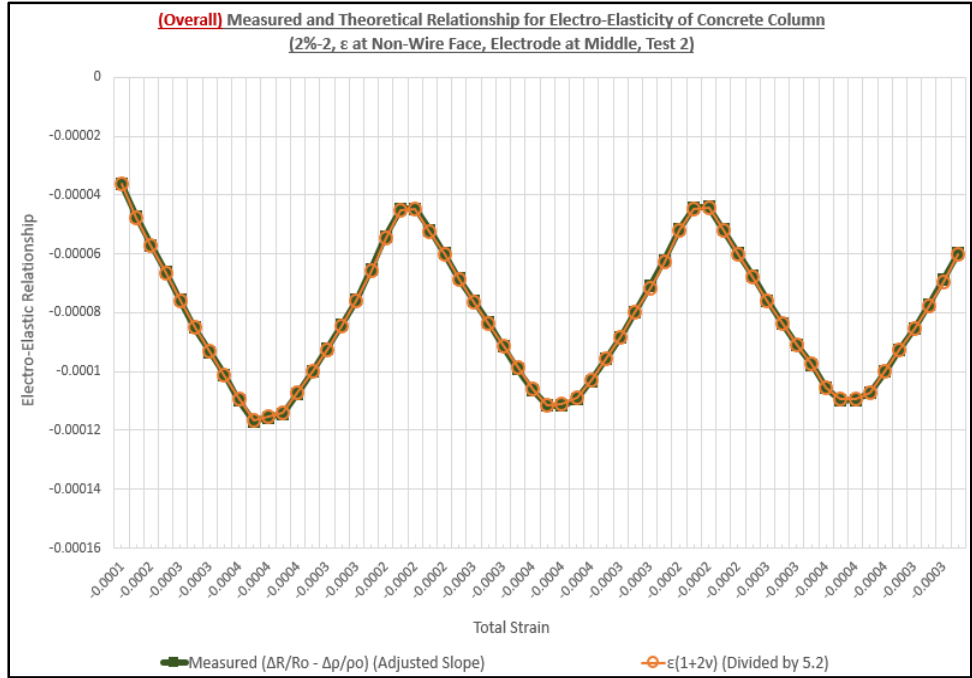Electrode Pair, Including Resistivity)
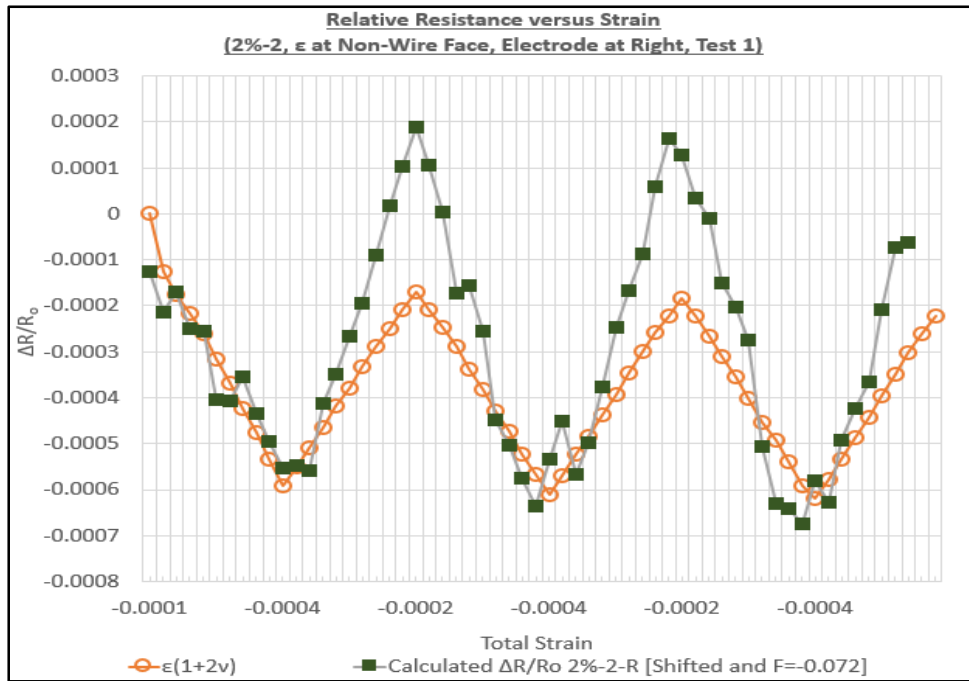
Figure G-57
Elasto-Electric Parameter Line Plot with Mechanical vs. Electrical Measurements (2%,
Column 2, Strain at Non-Wire Face, Test 1, Right Electrode Pair, Excluding Resistivity)

330
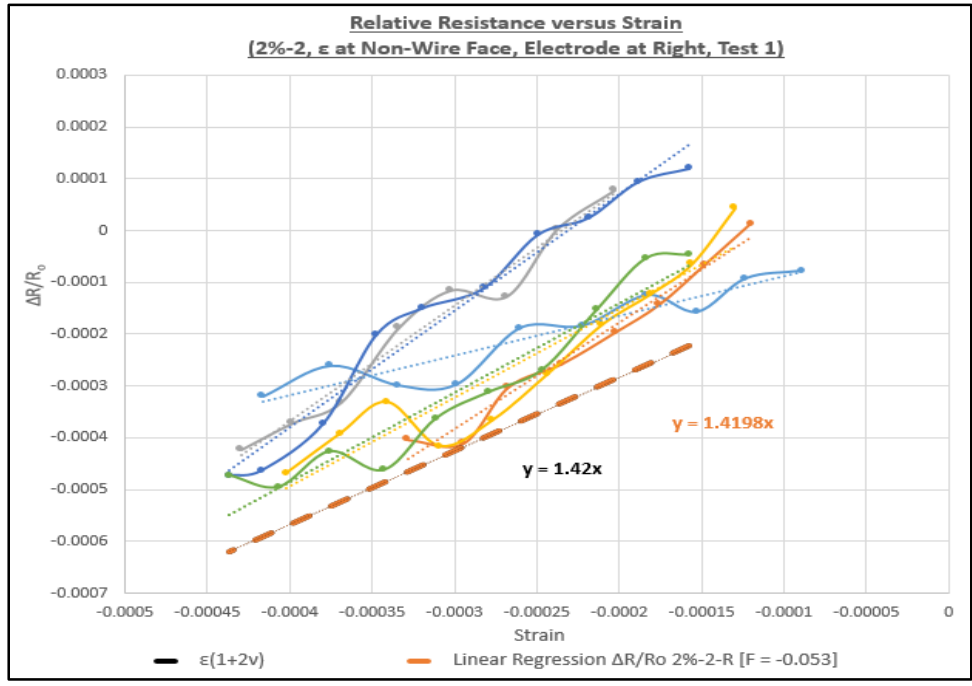
Figure G-58
Elasto-Electric Parameter X-Y Scatter Plot with Mechanical vs. Electrical Measurements
(2%, Column 2, Strain at Non-Wire Face, Test 1, Right Electrode Pair, Excluding
Resistivity)
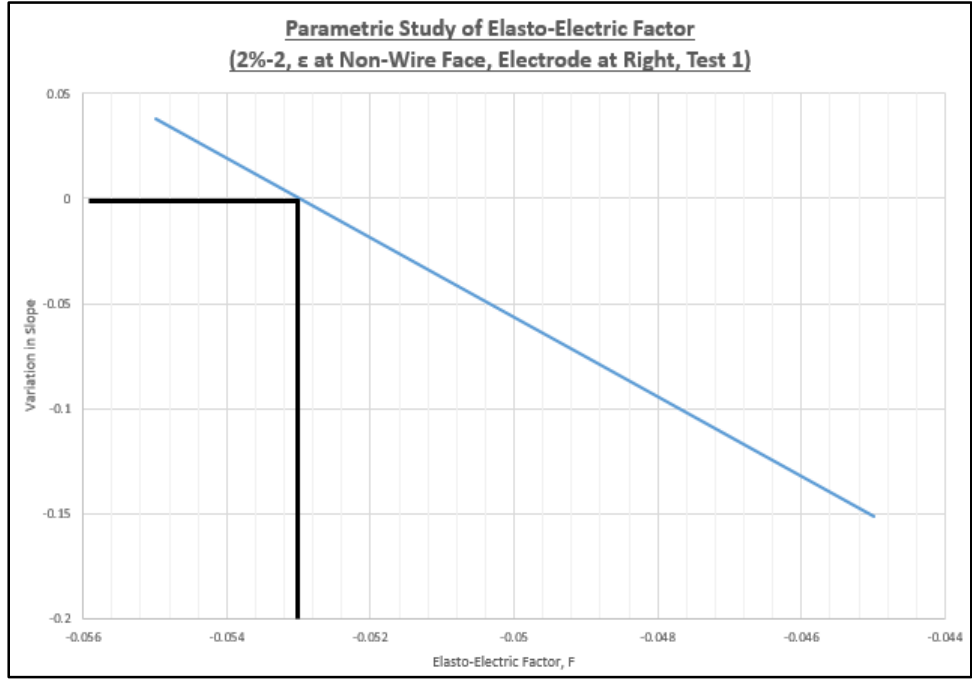
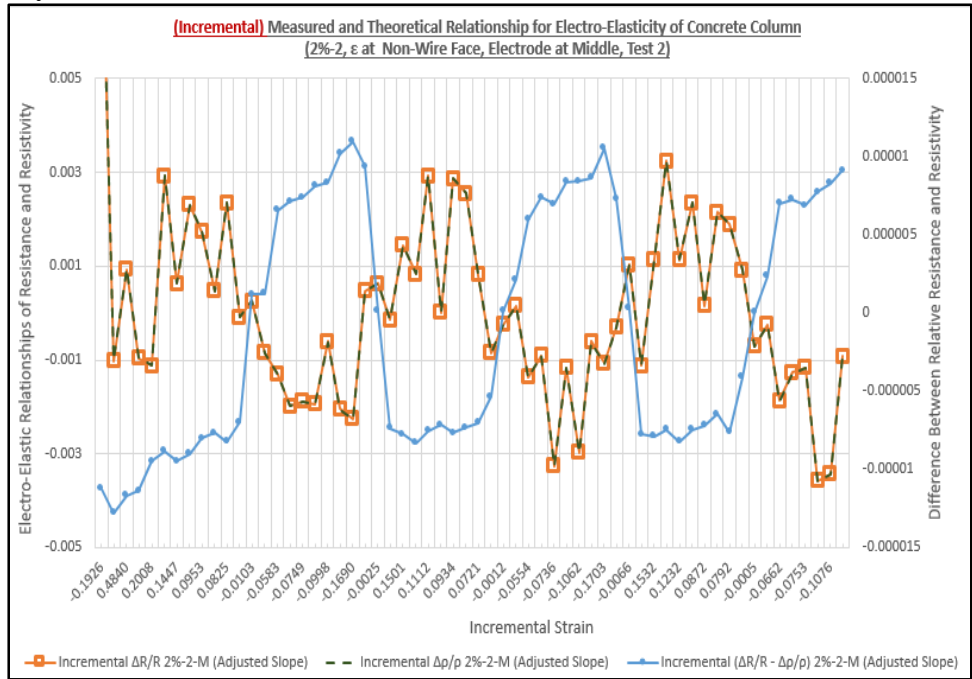Figure G-59
Parametric Study of Elasto-Electric Factor (2%, Column 2, Strain at Non-Wire Face, Test
1, Right Electrode Pair, Excluding Resistivity)

331
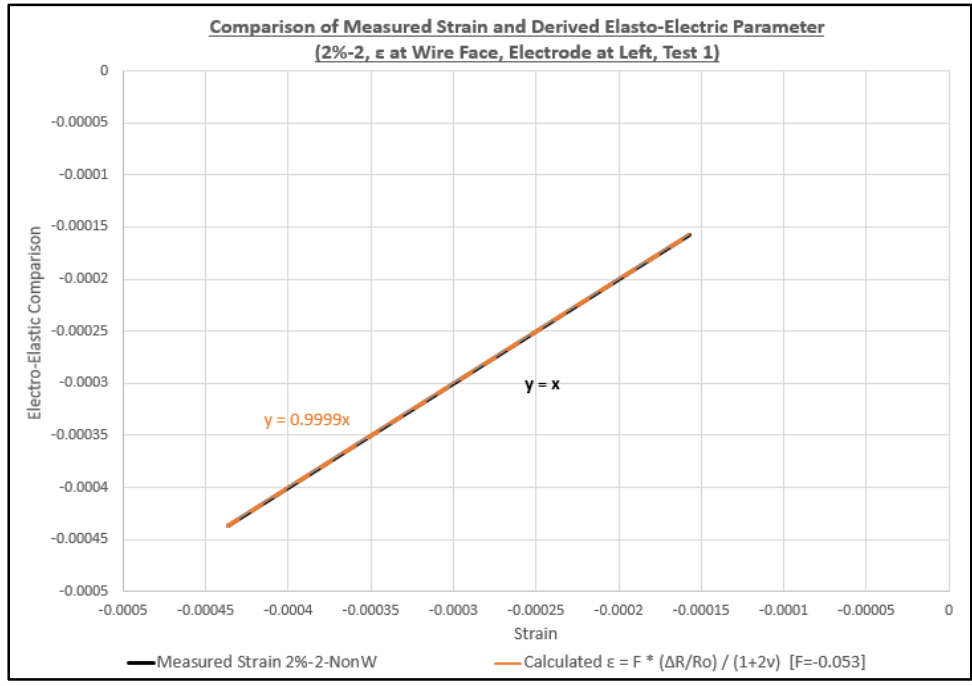
Figure G-60
Elasto-Electric Parameter (2%, Column 2, Strain at Non-Wire Face, Test 1, Right Electrode Pair, Excluding Resistivity)
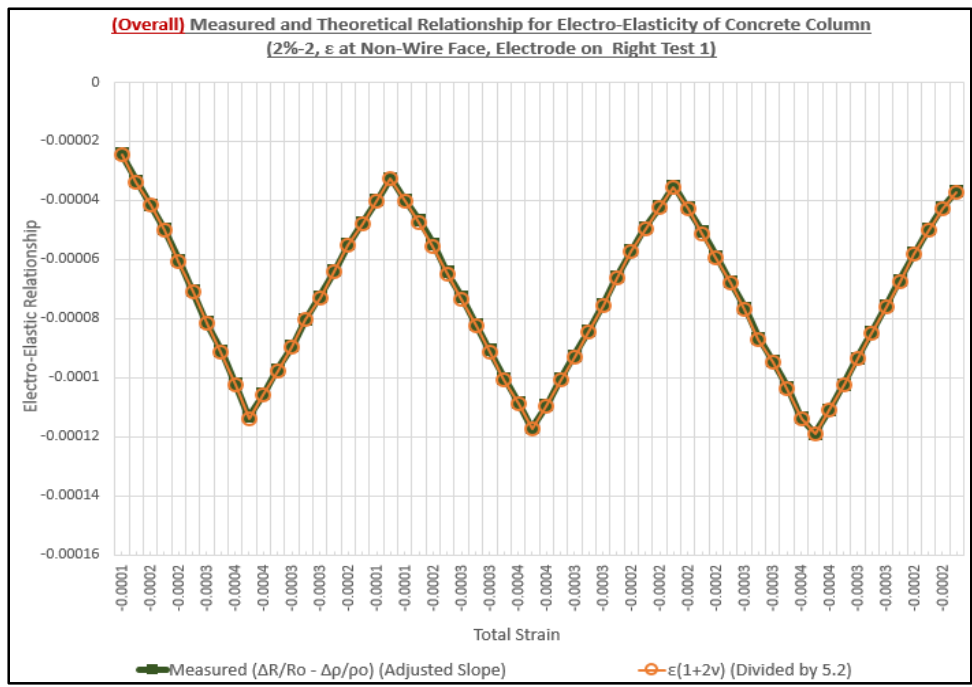
Figure G-61
Overall Elasto-Electric Parameter Line Plot with Mechanical vs. Electrical Measurements (2%, Column 2, Strain at Non-Wire Face, Test 1, Right Electrode Pair, Including Resistivity)
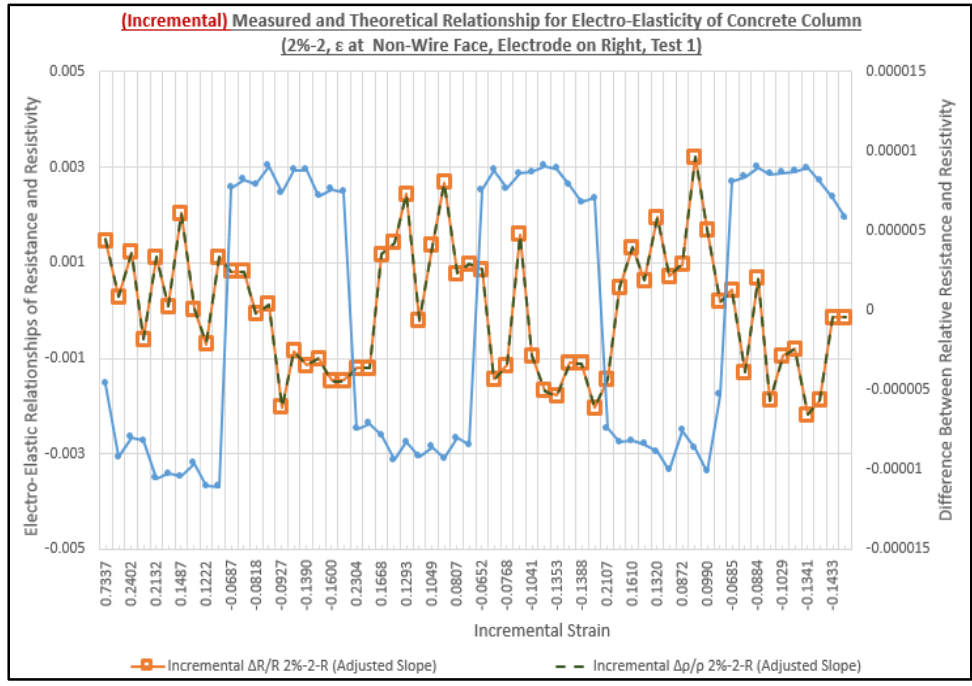
Figure G-62
Incremental Elasto-Electric Parameter X-Y Scatter Plot with Mechanical vs. Electrical Measurements (2%, Column 2, Strain at Non-Wire Face, Test 1, Right Electrode Pair, Including Resistivity)
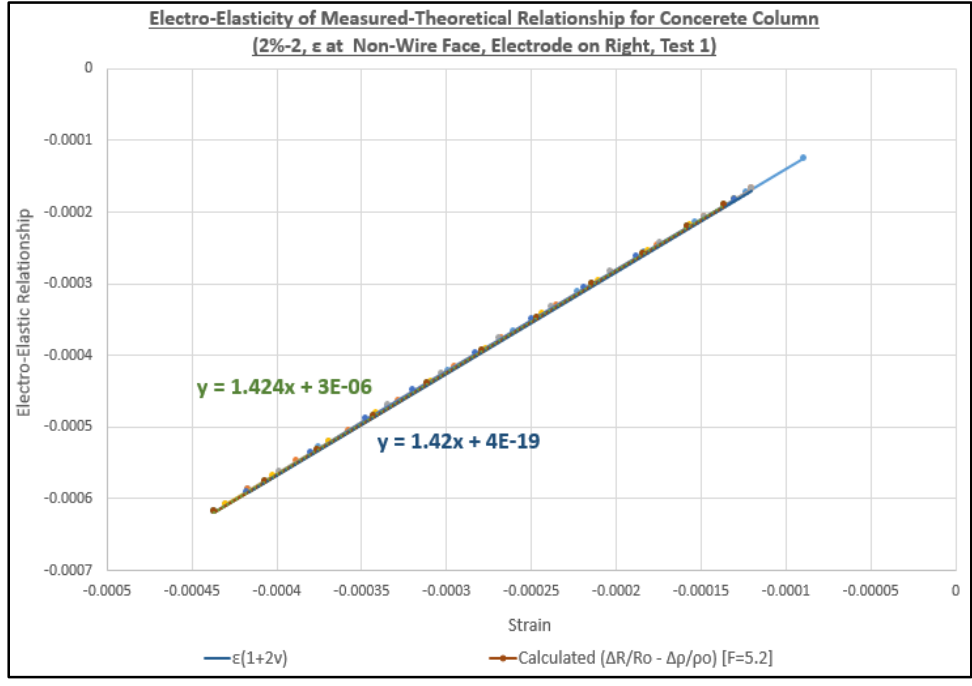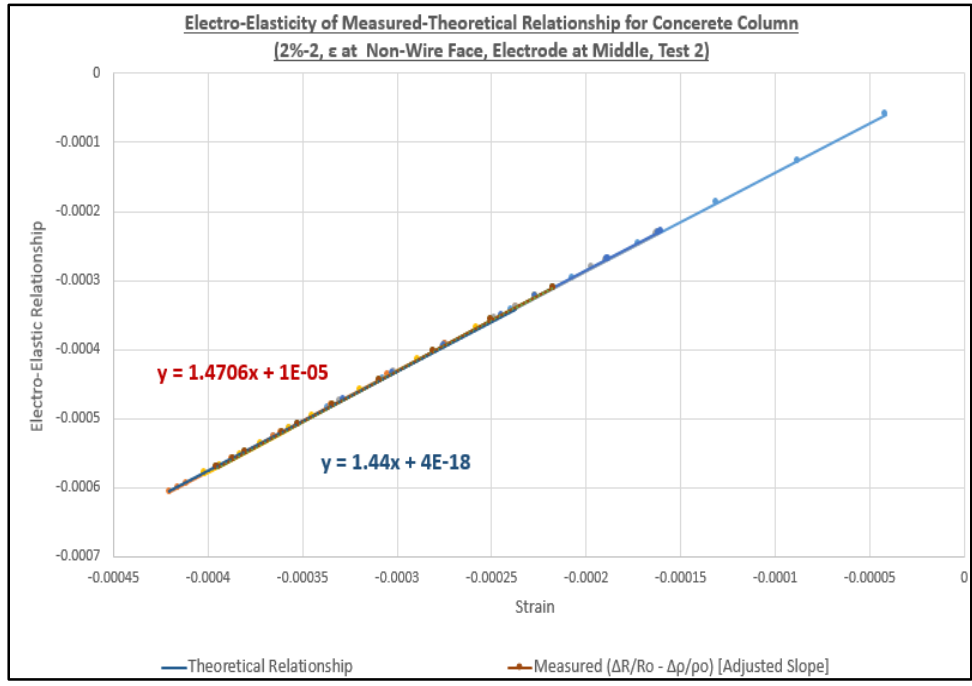

Figure G-63
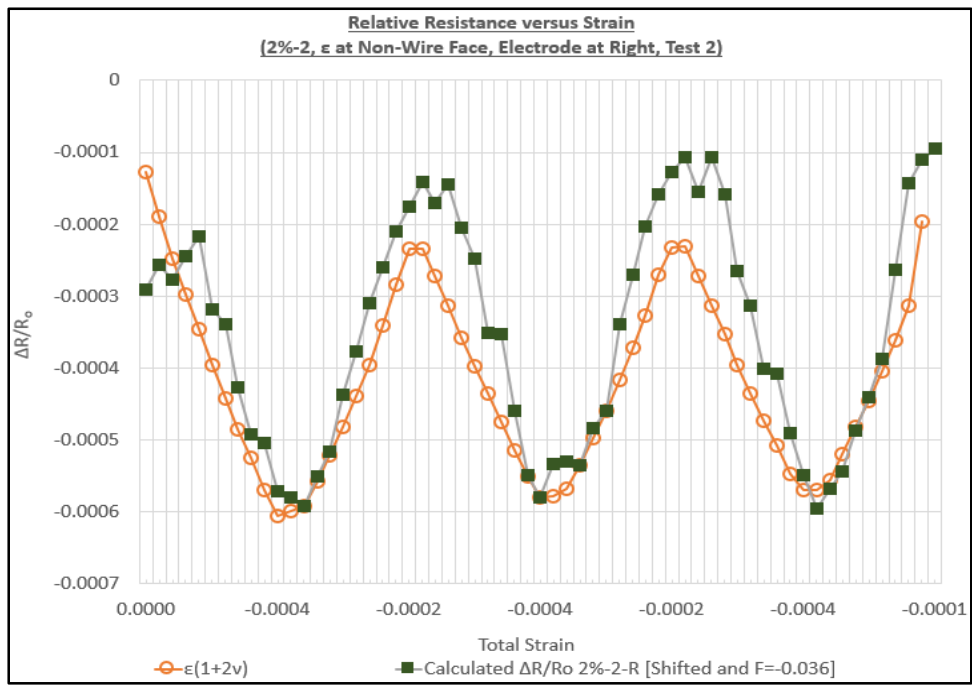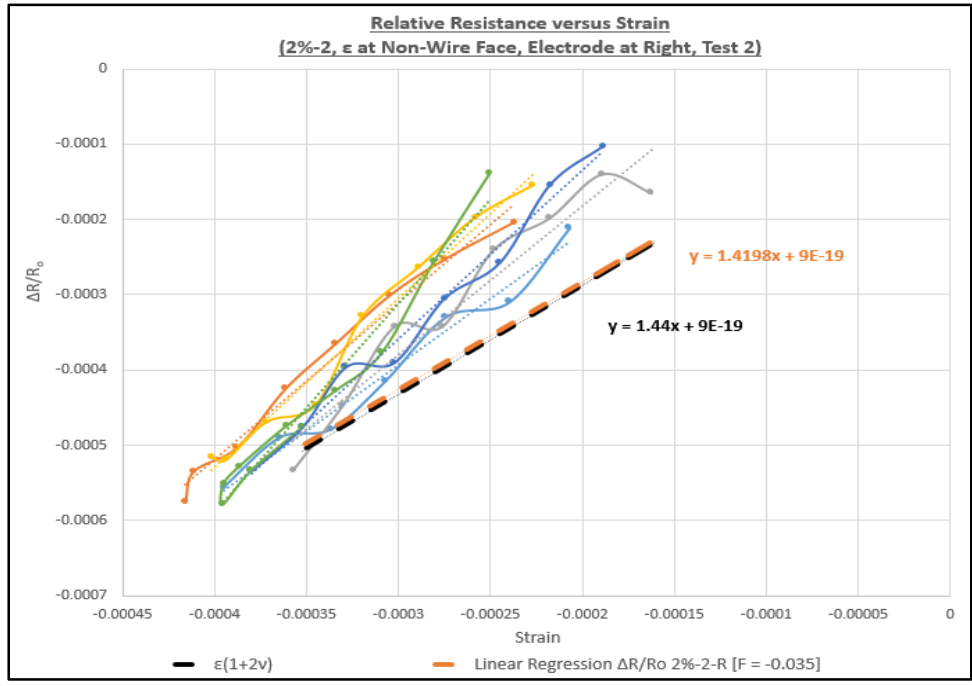Elasto-Electric Parameter (2%, Column 2, Strain at Non-Wire Face, Test 1, Right Electrode Pair, Including Resistivity)

333

Strain and Resistance (RSR Concentration: 2%, Column 2, Test 2)

Figure G-64
Voltage Measurements (2%, Column 2, Test 2, Left Electrode Pair)

Figure G-65
Calculated Resistance (2%, Column 2, Test 2, Left Electrode Pair)

Figure G-66
Voltage Measurements (2%, Column 2, Test 2, Middle Electrode Pair)

Figure G-67
Calculated Resistance (2%, Column 2, Test 2, Middle Electrode Pair)

335

Figure G-68
Voltage Measurements (2%, Column 2, Test 2, Right Electrode Pair)
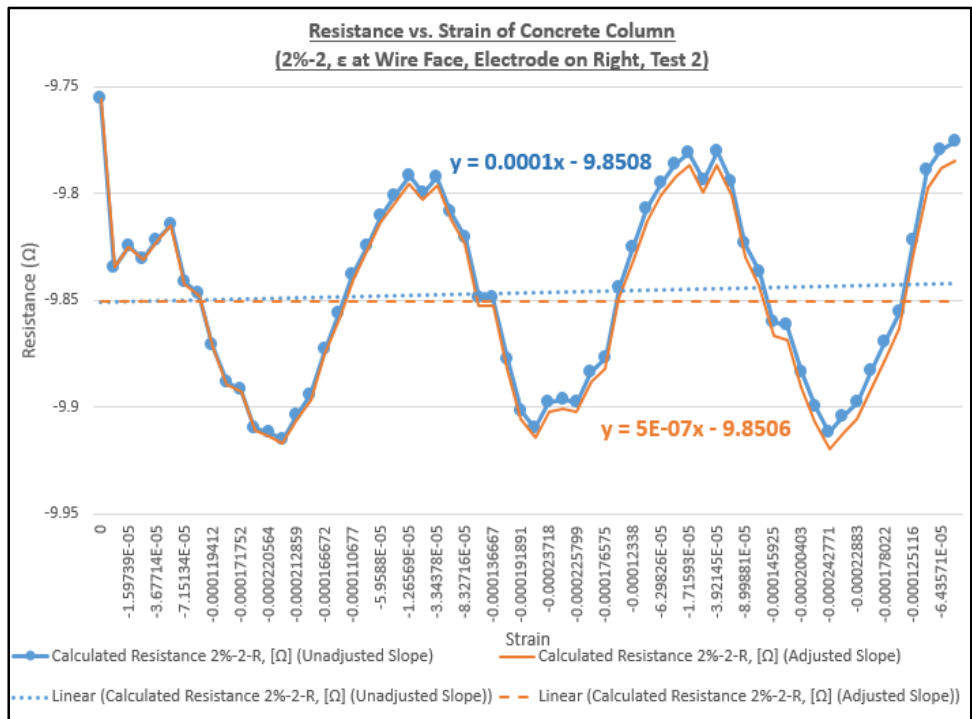
Figure G-69
Calculated Resistance (2%, Column 2, Test 2, Right Electrode Pair)

336
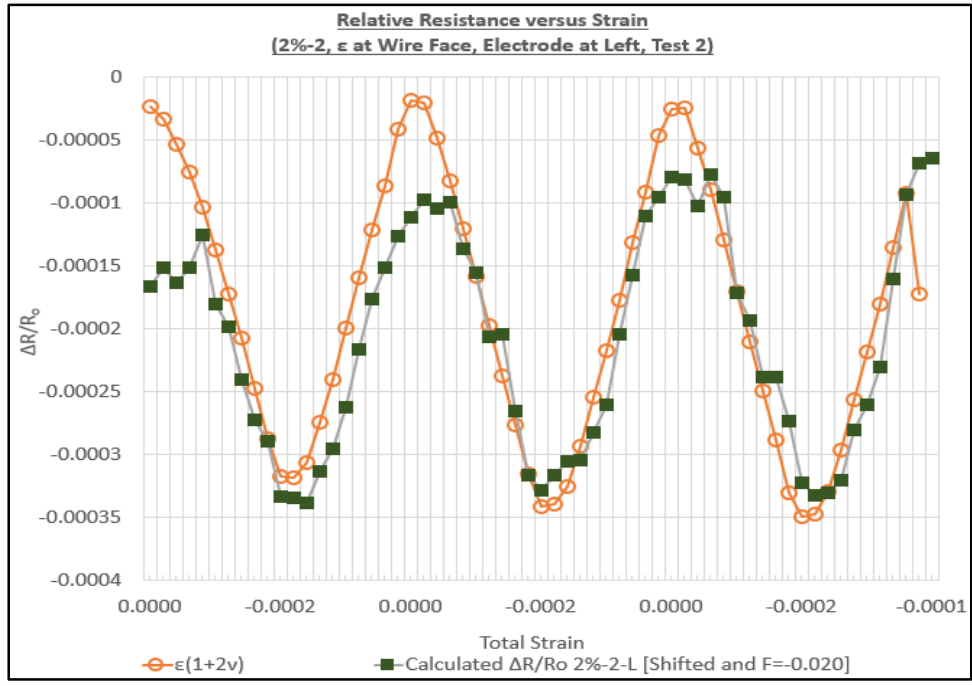
Figure G-70
Elasto-Electric Parameter Line Plot with Mechanical vs. Electrical Measurements (2%,
Column 2, Strain at Wire Face, Test 2, Left Electrode Pair, Excluding Resistivity)
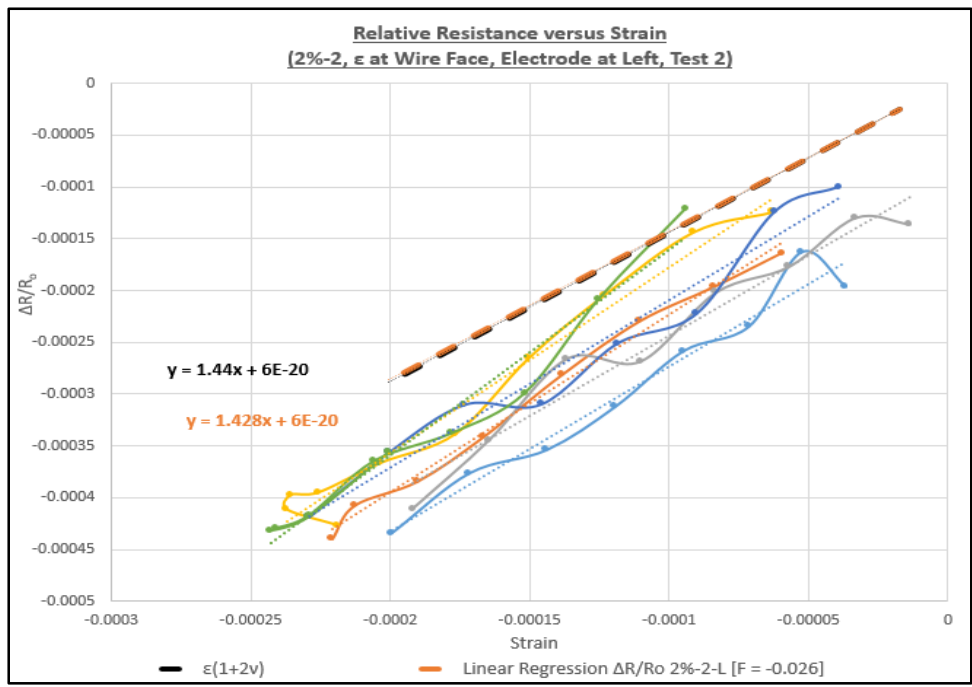
Figure G-71
Elasto-Electric Parameter X-Y Scatter Plot with Mechanical vs. Electrical Measurements
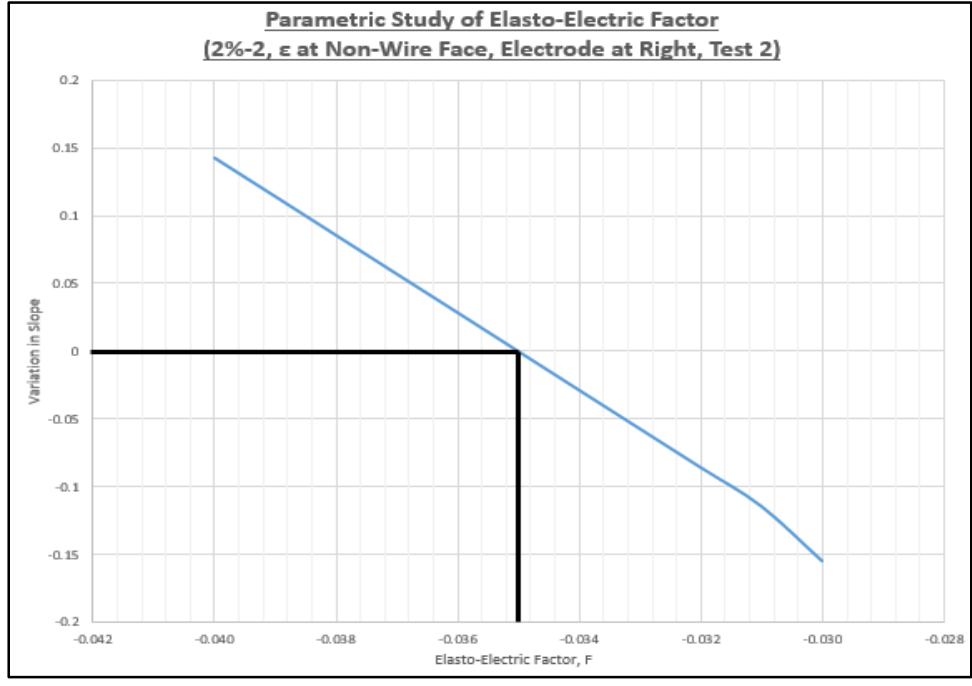(2%, Column 2, Strain at Wire Face, Test 2, Left Electrode Pair, Excluding Resistivity)

337
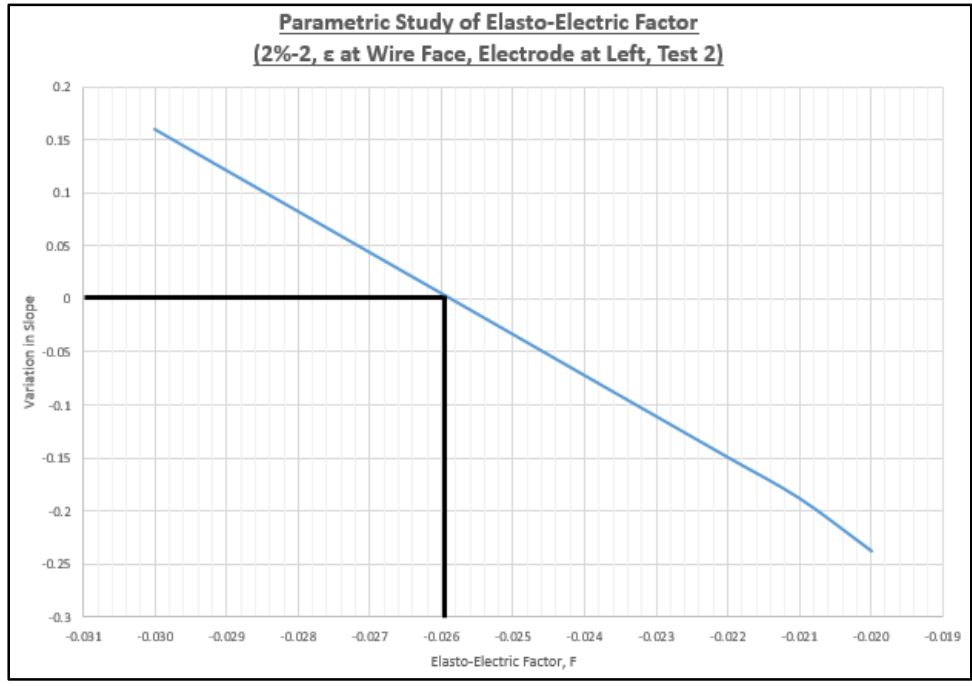
Figure G-72
Parametric Study of Elasto-Electric Factor (2%, Column 2, Strain at Wire Face, Test 2, Left Electrode Pair, Excluding Resistivity)
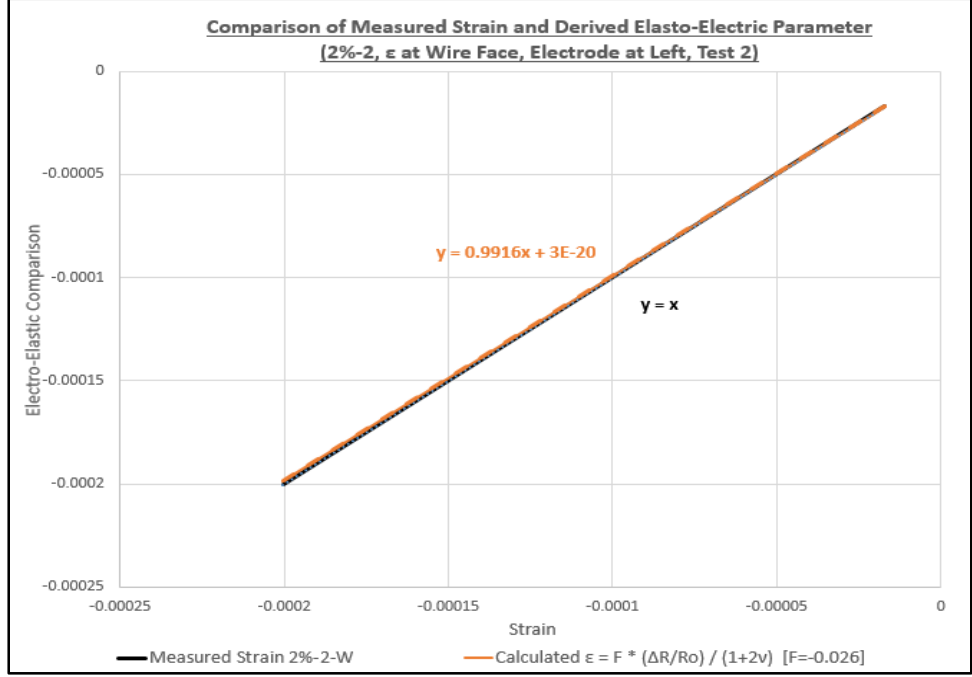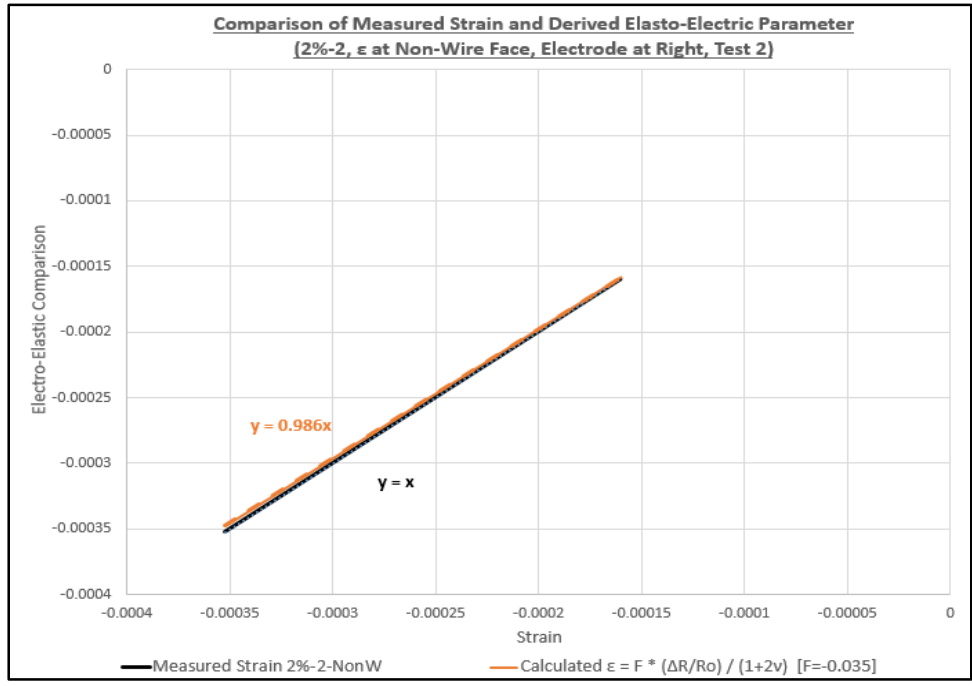

Figure G-73
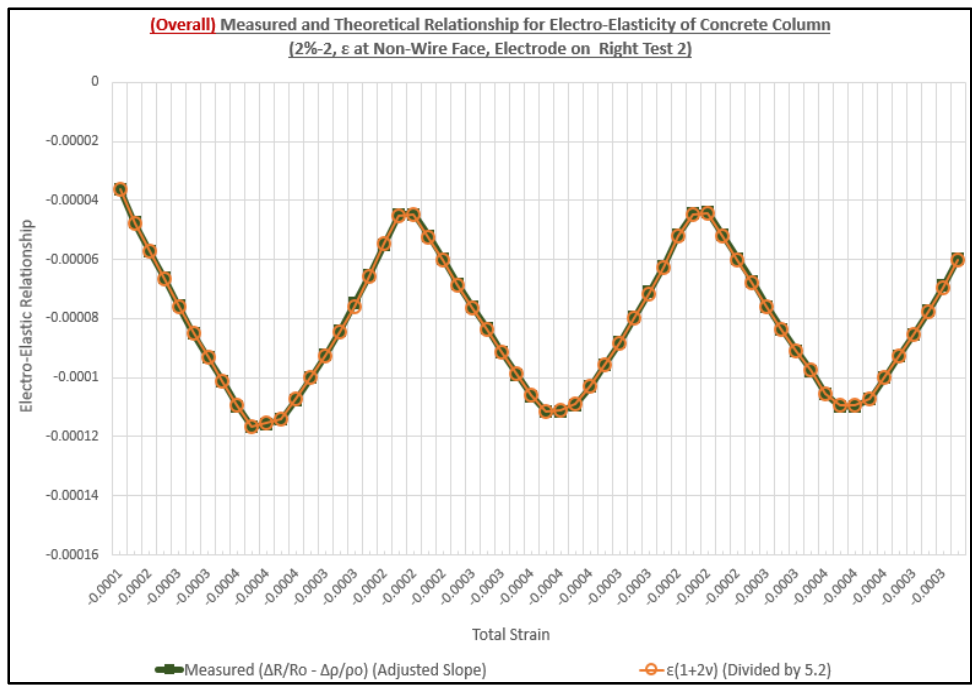Elasto-Electric Parameter (2%, Column 2, Strain at Wire Face, Test 2, Left Electrode Pair, Excluding Resistivity)

338
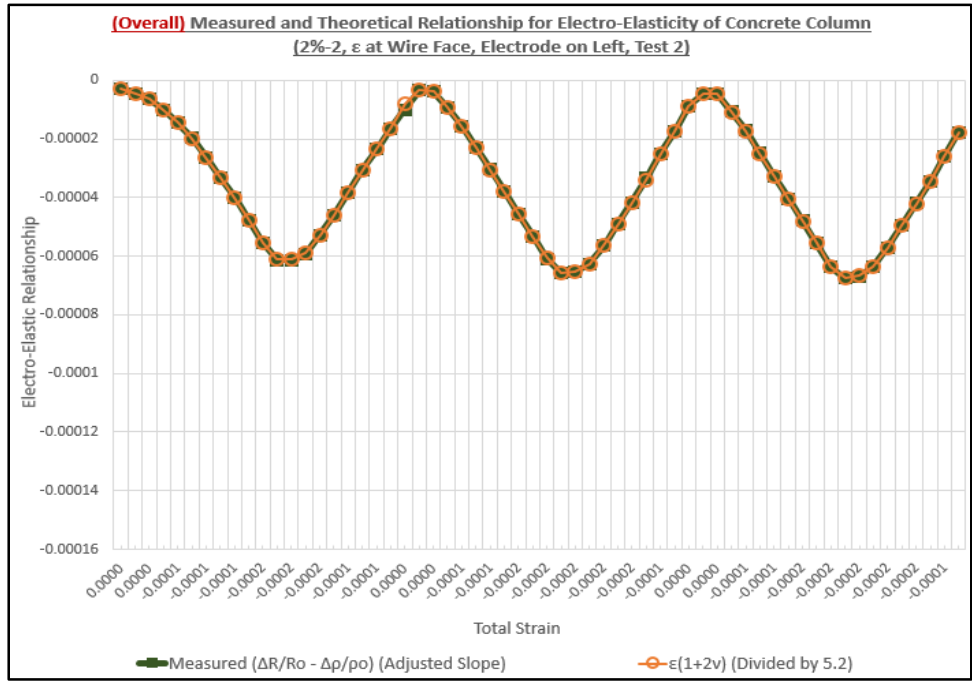
Figure G-74
Overall Elasto-Electric Parameter Line Plot with Mechanical vs. Electrical Measurements
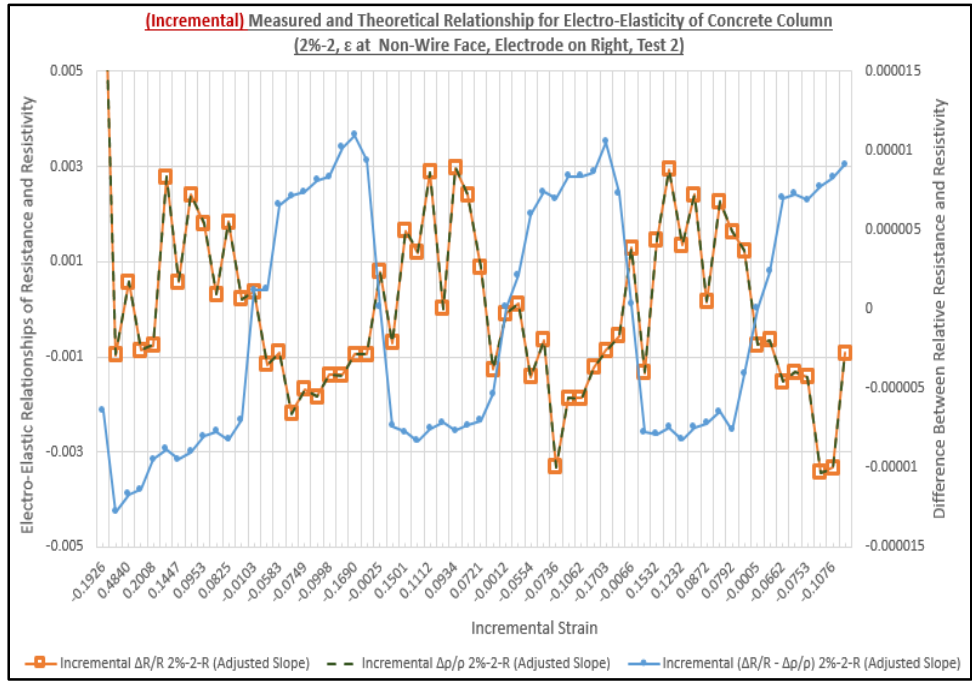(2%, Column 2, Strain at Wire Face, Test 2, Left Electrode Pair, Including Resistivity)
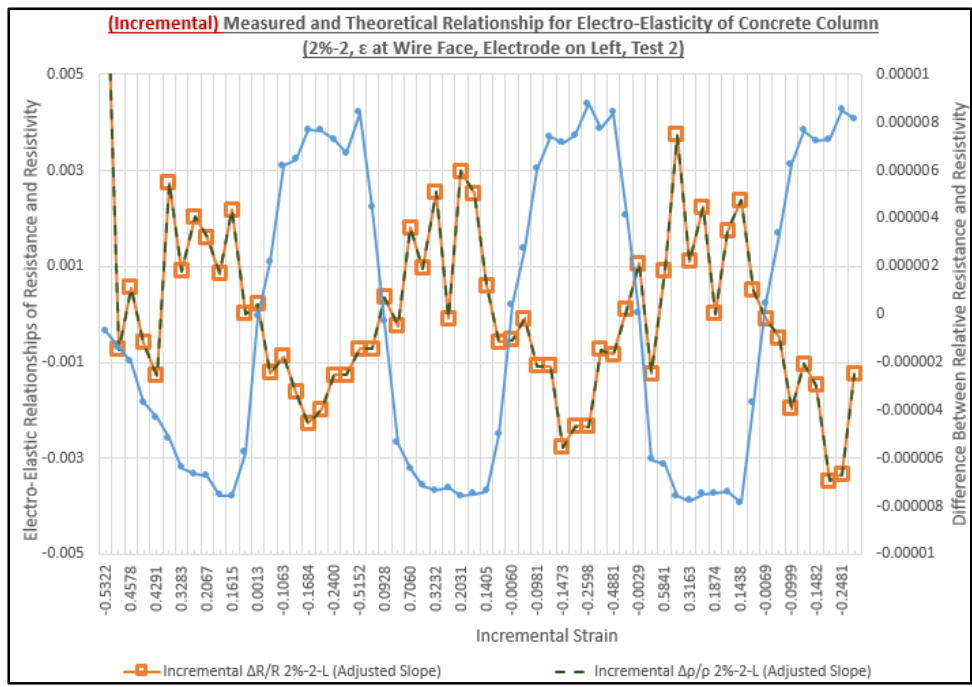
Figure G-75
Incremental Elasto-Electric Parameter X-Y Scatter Plot with Mechanical vs. Electrical
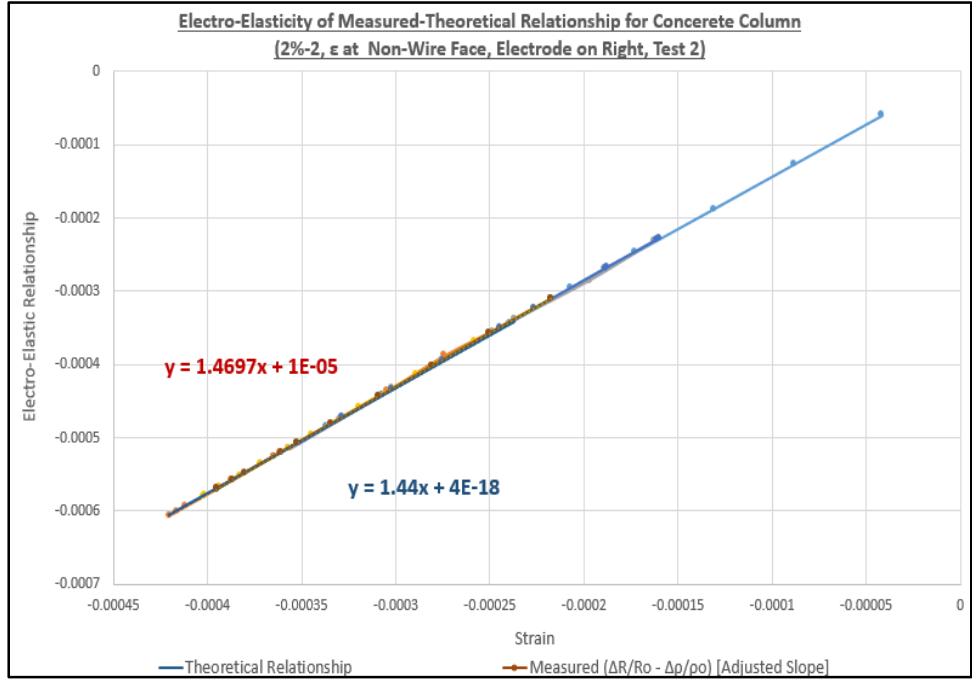Measurements (2%, Column 2, Strain at Wire Face, Test 2, Left Electrode Pair, Including
Resistivity)

339
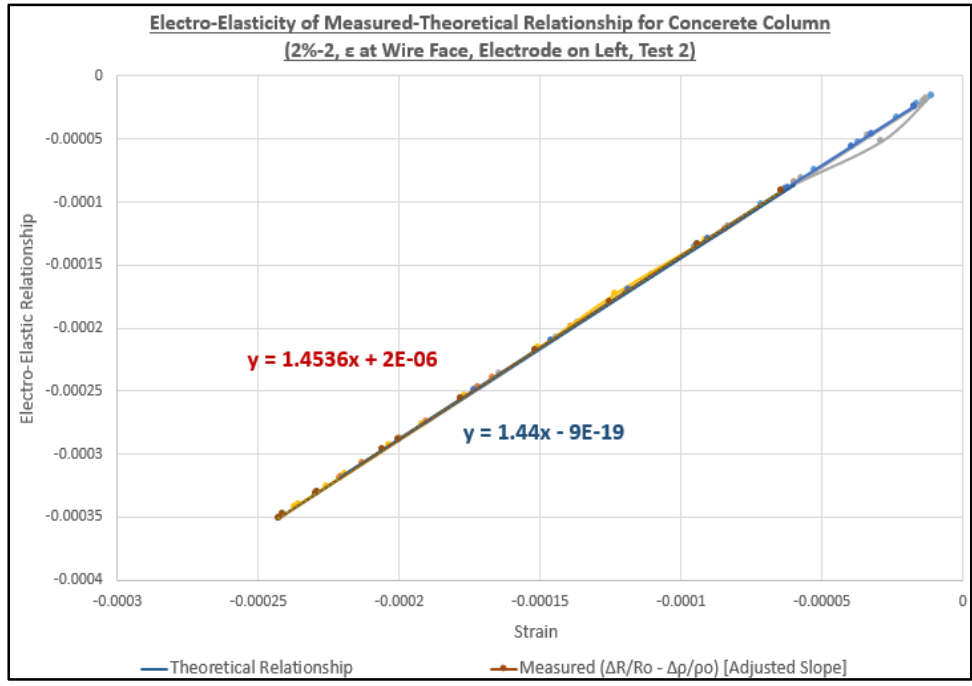
Figure G-76
Elasto-Electric Parameter (2%, Column 2, Strain at Wire Face, Test 2, Left Electrode Pair, Including Resistivity)
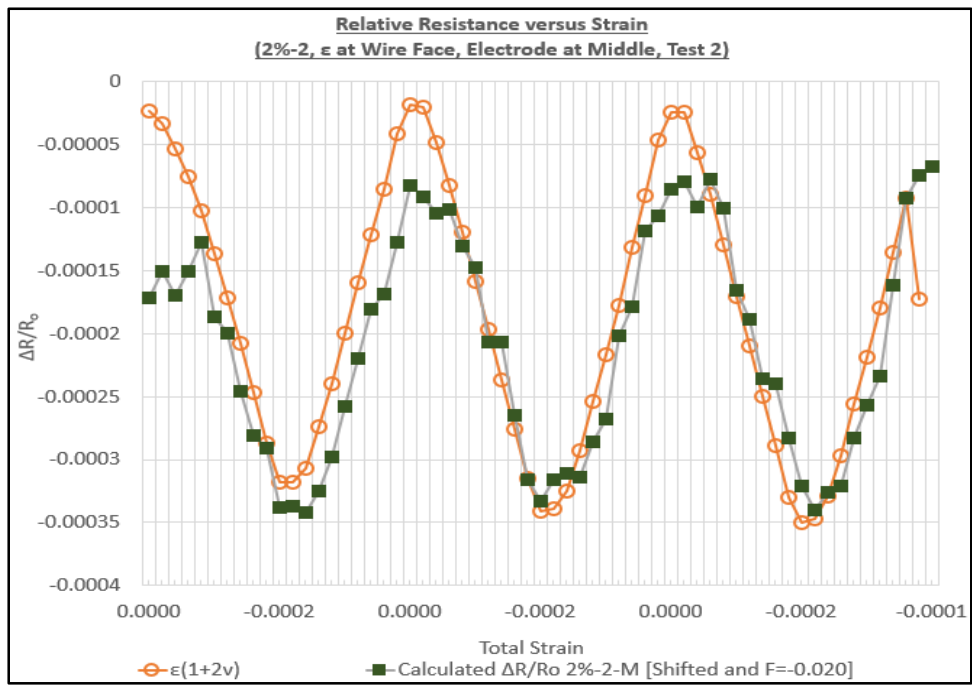
Figure G-77
Elasto-Electric Parameter Line Plot with Mechanical vs. Electrical Measurements (2%, Column 2, Strain at Wire Face, Test 2, Middle Electrode Pair, Excluding Resistivity)
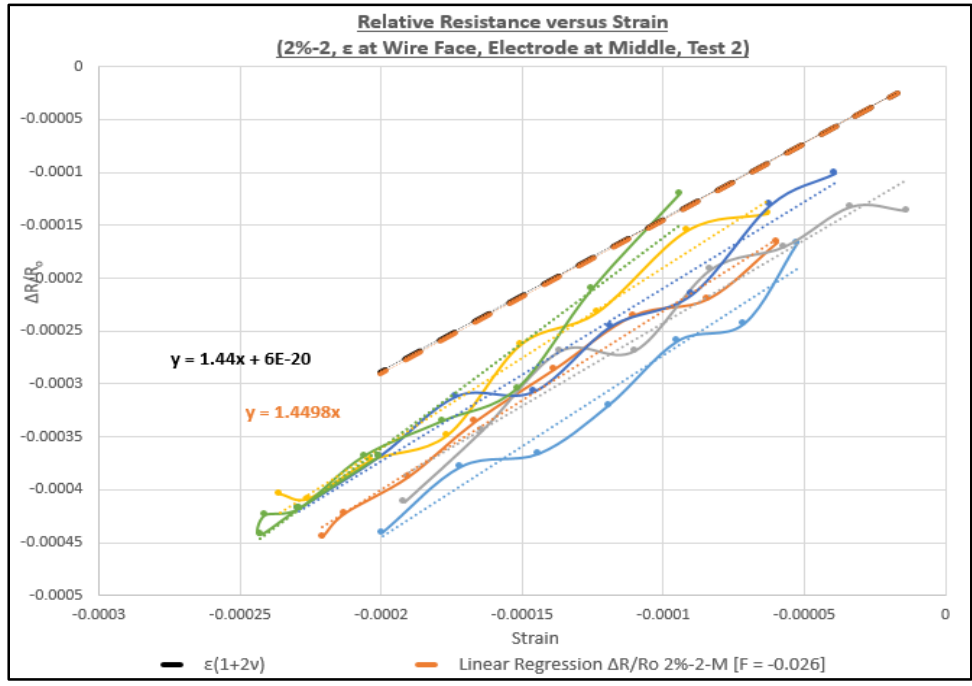
Figure G-78
Elasto-Electric Parameter X-Y Scatter Plot with Mechanical vs. Electrical Measurements
(2%, Column 2, Strain at Wire Face, Test 2, Middle Electrode Pair, Excluding
Resistivity)
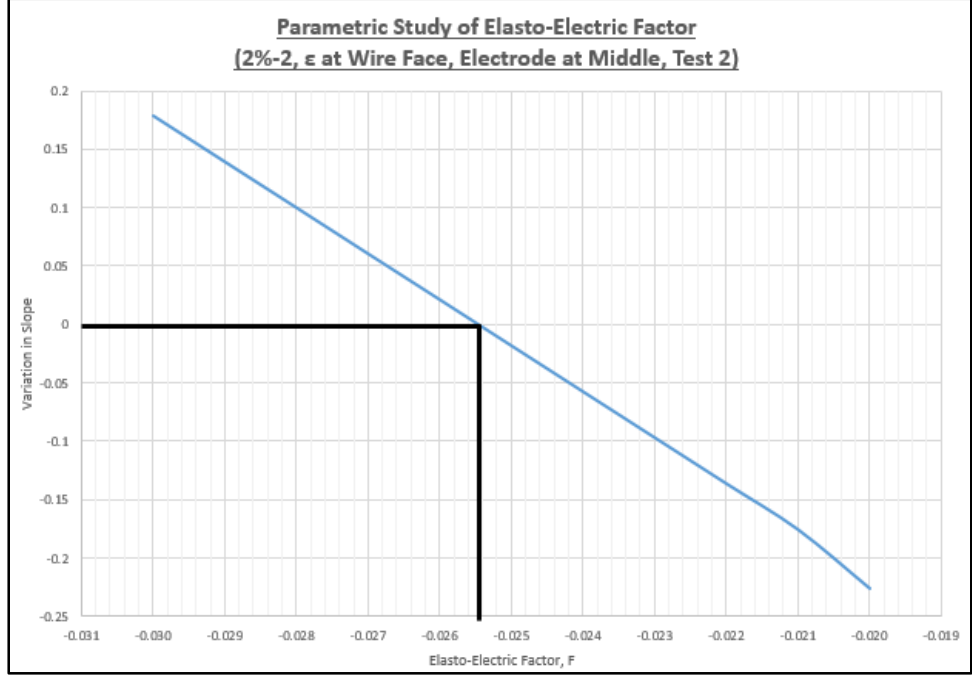
Figure G-79
Parametric Study of Elasto-Electric Factor (2%, Column 2, Strain at Wire Face, Test 2,
Middle Electrode Pair, Excluding Resistivity)

341
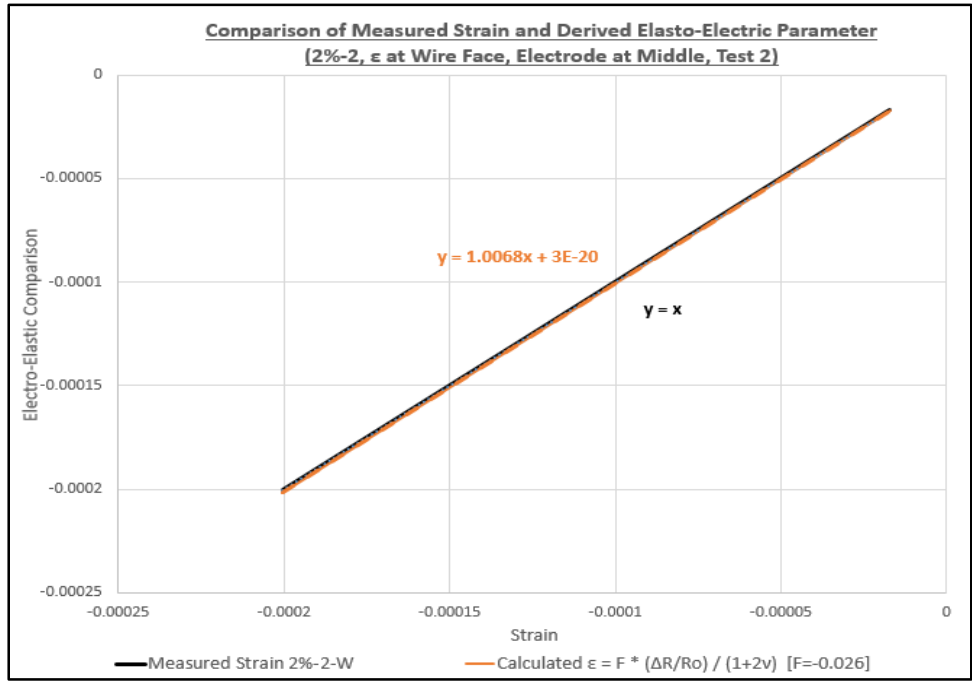
Figure G-80
Elasto-Electric Parameter (2%, Column 2, Strain at Wire Face, Test 2, Middle Electrode Pair, Excluding Resistivity)

Figure G-81
Overall Elasto-Electric Parameter Line Plot with Mechanical vs. Electrical Measurements (2%, Column 2, Strain at Wire Face, Test 2, Middle Electrode Pair, Including Resistivity)

Figure G-82
Incremental Elasto-Electric Parameter X-Y Scatter Plot with Mechanical vs. Electrical
Measurements (2%, Column 2, Strain at Wire Face, Test 2, Middle Electrode Pair,
Including Resistivity)

Figure G-83
Elasto-Electric Parameter (2%, Column 2, Strain at Wire Face, Test 2, Middle Electrode
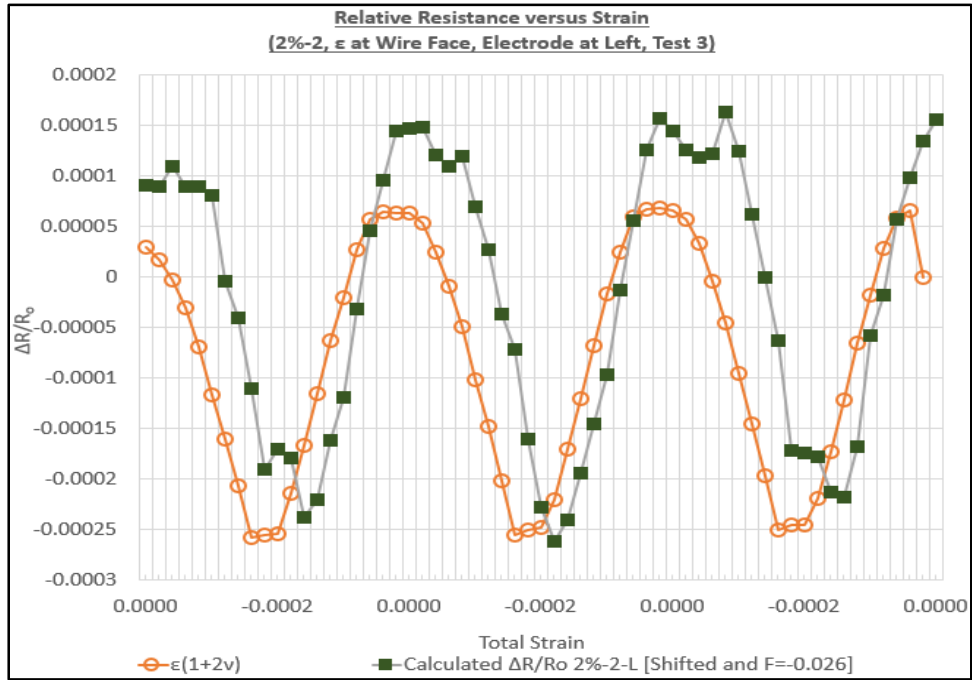Pair, Including Resistivity)

Figure G-84
Elasto-Electric Parameter Line Plot with Mechanical vs. Electrical Measurements (2%, Column 2, Strain at Wire Face, Test 2, Right Electrode Pair, Excluding Resistivity)

Figure G-85
Elasto-Electric Parameter X-Y Scatter Plot with Mechanical vs. Electrical Measurements (2%, Column 2, Strain at Wire Face, Test 2, Right Electrode Pair, Excluding Resistivity)

344

Figure G-86
Parametric Study of Elasto-Electric Factor (2%, Column 2, Strain at Wire Face, Test 2, Right Electrode Pair, Excluding Resistivity)

Figure G-87
Elasto-Electric Parameter (2%, Column 2, Strain at Wire Face, Test 2, Right Electrode Pair, Excluding Resistivity)

Figure G-88
Overall Elasto-Electric Parameter Line Plot with Mechanical vs. Electrical Measurements
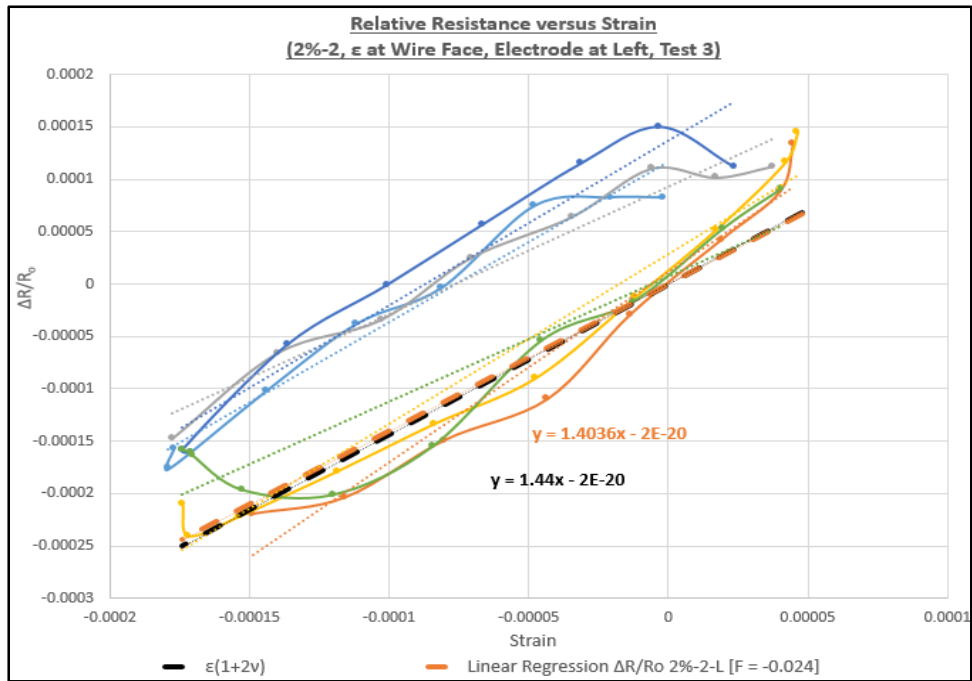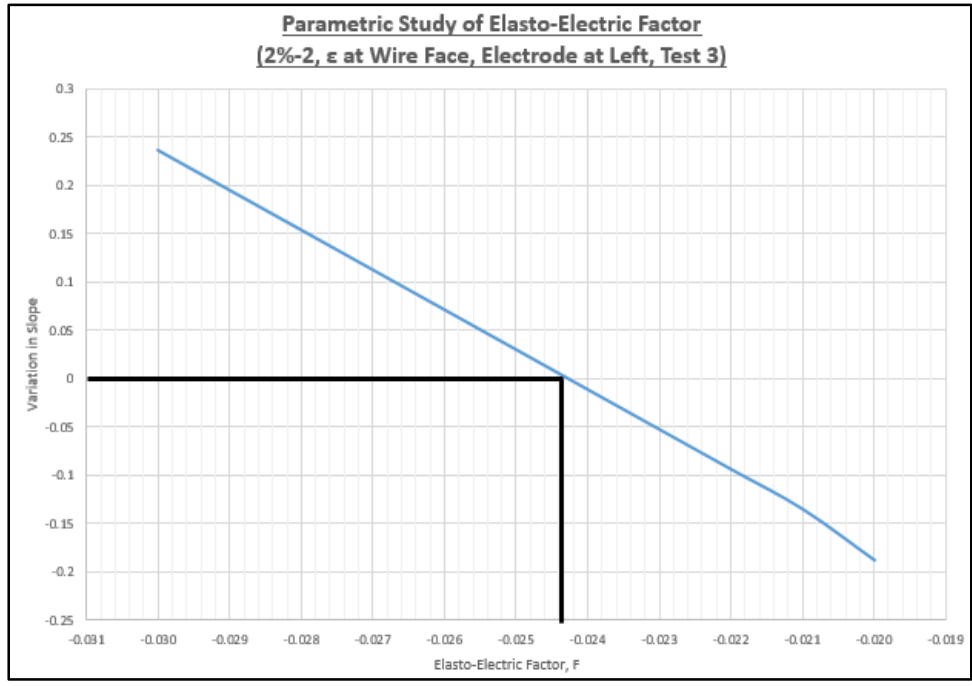(2%, Column 2, Strain at Wire Face, Test 2, Right Electrode Pair, Including Resistivity)

Figure G-89
Incremental Elasto-Electric Parameter X-Y Scatter Plot with Mechanical vs. Electrical
Measurements (2%, Column 2, Strain at Wire Face, Test 2, Right Electrode Pair,
Including Resistivity)

346

Figure G-90

Elasto-Electric Parameter (2%, Column 2, Strain at Wire Face, Test 2, Right Electrode Pair, Including Resistivity)

Figure G-91

Elasto-Electric Parameter Line Plot with Mechanical vs. Electrical Measurements (2%, Column 2, Strain at Non-Wire Face, Test 2, Left Electrode Pair, Excluding Resistivity)

347

Figure G-92
Elasto-Electric Parameter X-Y Scatter Plot with Mechanical vs. Electrical Measurements (2%, Column 2, Strain at Non-Wire Face, Test 2, Left Electrode Pair, Excluding Resistivity)

Figure G-93
Parametric Study of Elasto-Electric Factor (2%, Column 2, Strain at Non-Wire Face, Test 2, Left Electrode Pair, Excluding Resistivity)
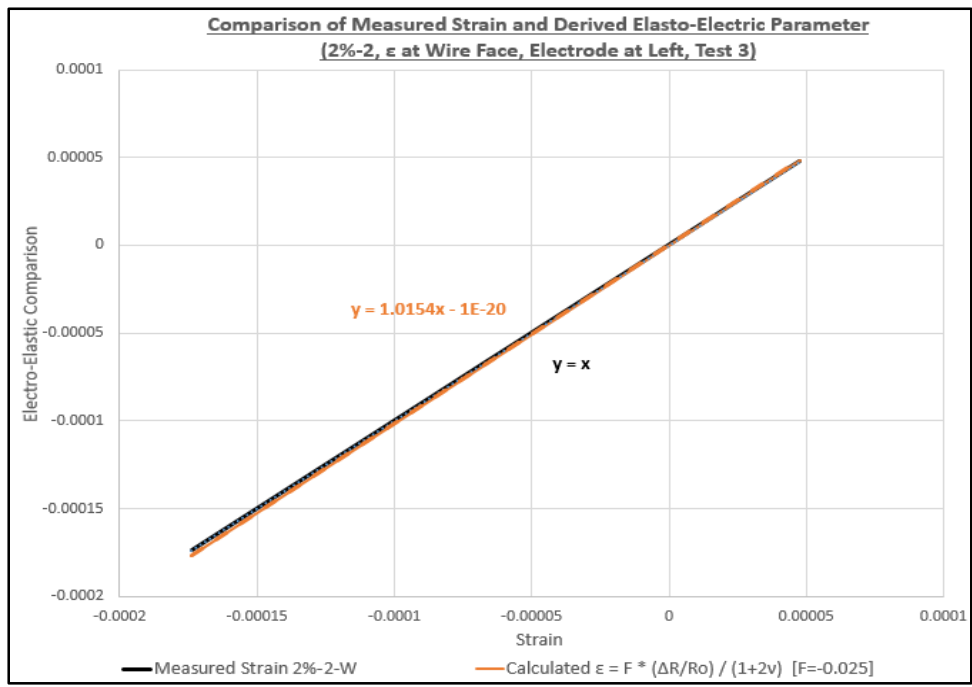
348

Figure G-94
Elasto-Electric Parameter (2%, Column 2, Strain at Non-Wire Face, Test 2, Left
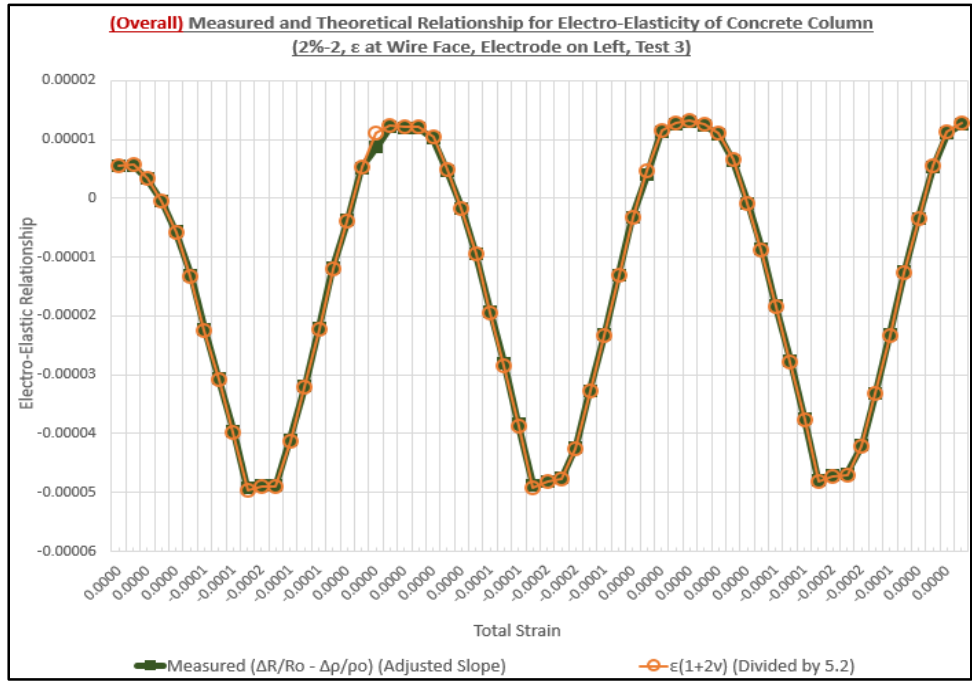Electrode Pair, Excluding Resistivity)

Figure G-95
Overall Elasto-Electric Parameter Line Plot with Mechanical vs. Electrical Measurements
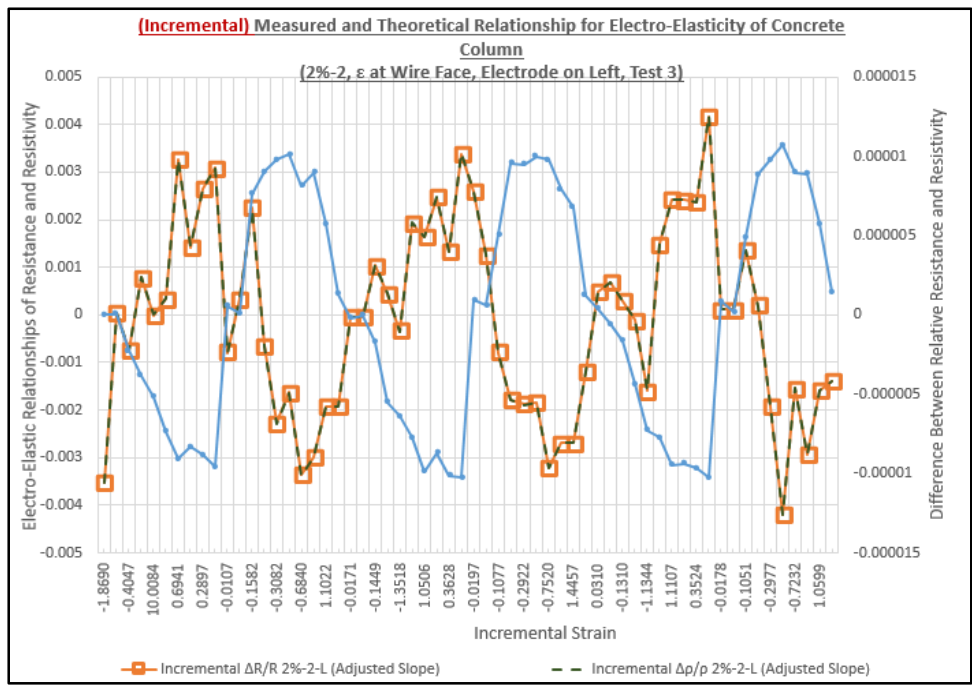(2%, Column 2, Strain at Non-Wire Face, Test 2, Left Electrode Pair, Including
Resistivity)

349

Figure G-96
Incremental Elasto-Electric Parameter X-Y Scatter Plot with Mechanical vs. Electrical
Measurements (2%, Column 2, Strain at Non-Wire Face, Test 2, Left Electrode Pair,
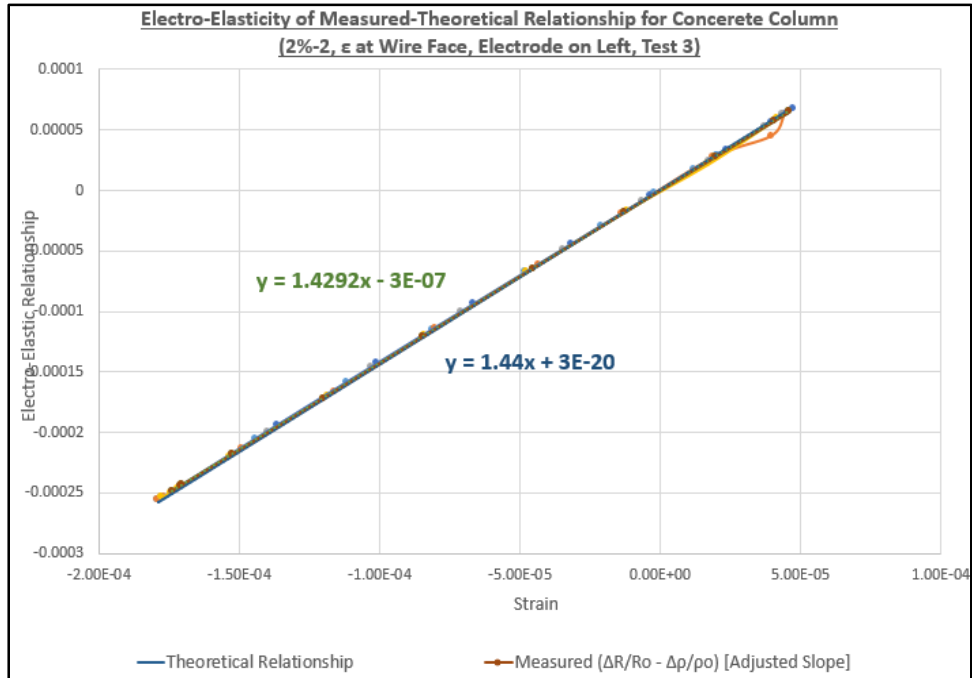Including Resistivity)

Figure G-97
Elasto-Electric Parameter (2%, Column 2, Strain at Non-Wire Face, Test 2, Left
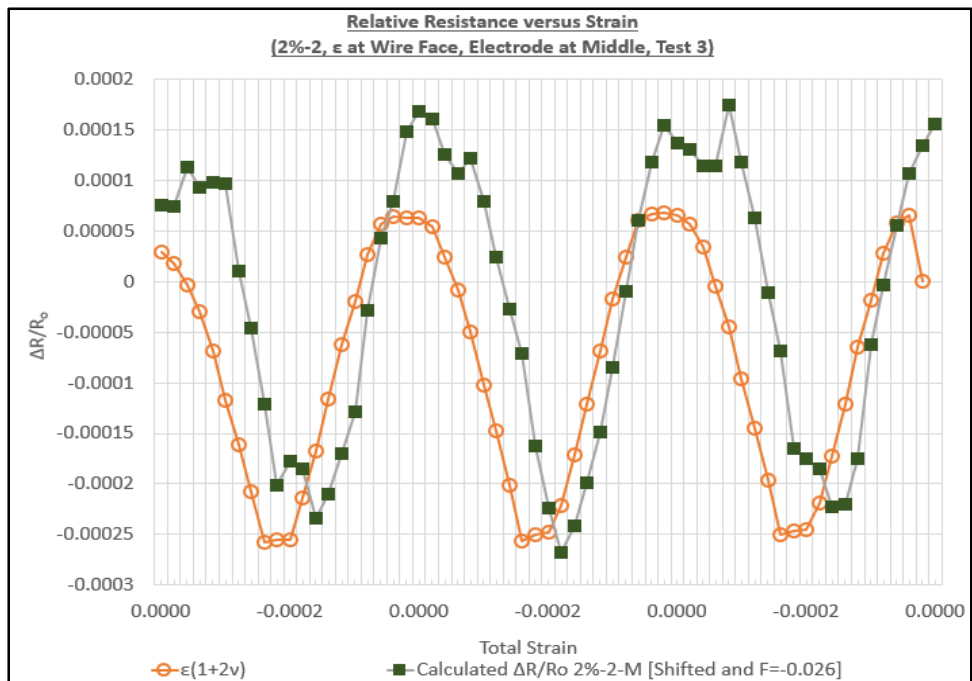Electrode Pair, Including Resistivity)

350

Figure G-98
Elasto-Electric Parameter Line Plot with Mechanical vs. Electrical Measurements (2%, Column 2, Strain at Non-Wire Face, Test 2, Middle Electrode Pair), Excluding Resistivity
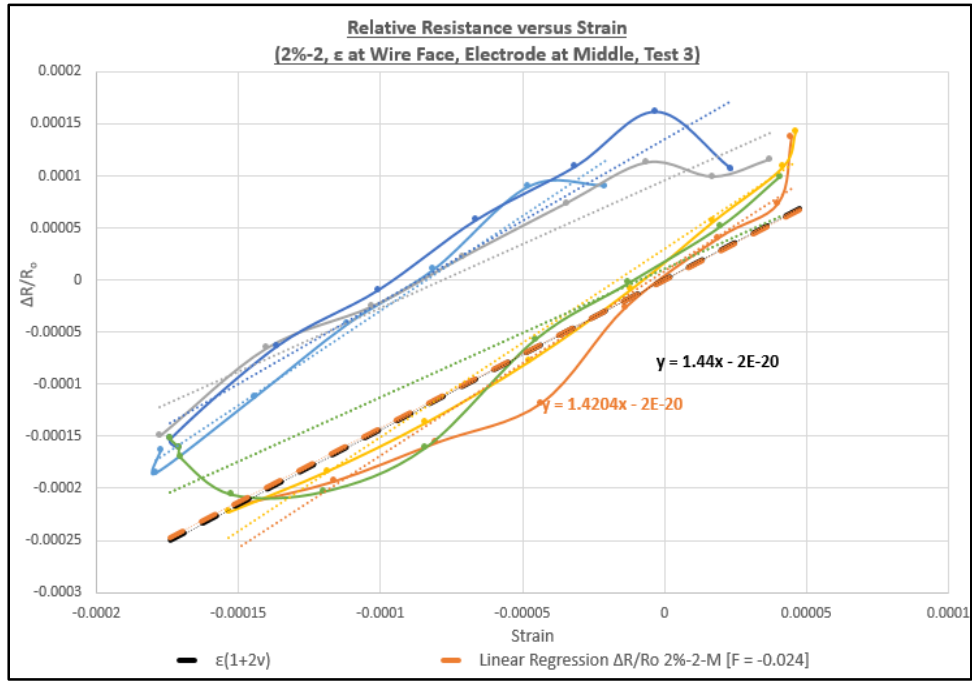

Figure G-99
Elasto-Electric Parameter X-Y Scatter Plot with Mechanical vs. Electrical Measurements (2%, Column 2, Strain at Non-Wire Face, Test 2, Middle Electrode Pair, Excluding Resistivity)
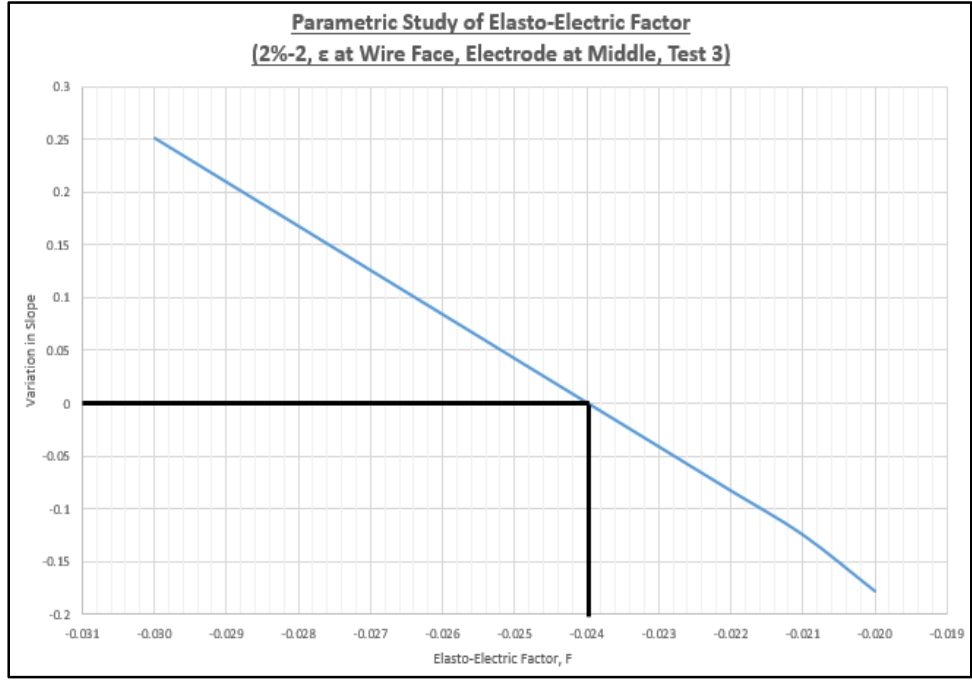
Figure G-100
Parametric Study of Elasto-Electric Factor (2%, Column 2, Strain at Non-Wire Face, Test 2, Middle Electrode Pair, Excluding Resistivity)
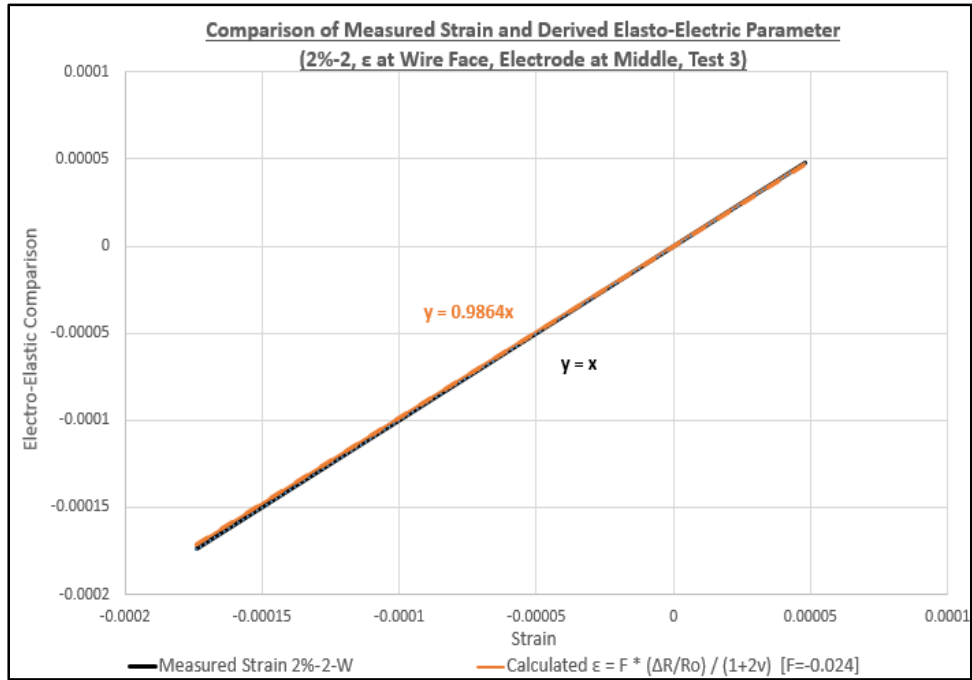

Figure G-101
Elasto-Electric Parameter (2%, Column 2, Strain at Non-Wire Face, Test 2, Middle Electrode Pair, Excluding Resistivity)

Figure G-102

Overall Elasto-Electric Parameter Line Plot with Mechanical vs. Electrical Measurements (2%, Column 2, Strain at Non-Wire Face, Test 2, Middle Electrode Pair, Including Resistivity)

Figure G-103

Incremental Elasto-Electric Parameter X-Y Scatter Plot with Mechanical vs. Electrical Measurements (2%, Column 2, Strain at Non-Wire Face, Test 2, Middle Electrode Pair, Including Resistivity)

353

Figure G-104
Elasto-Electric Parameter (2%, Column 2, Strain at Non-Wire Face, Test 2, Middle
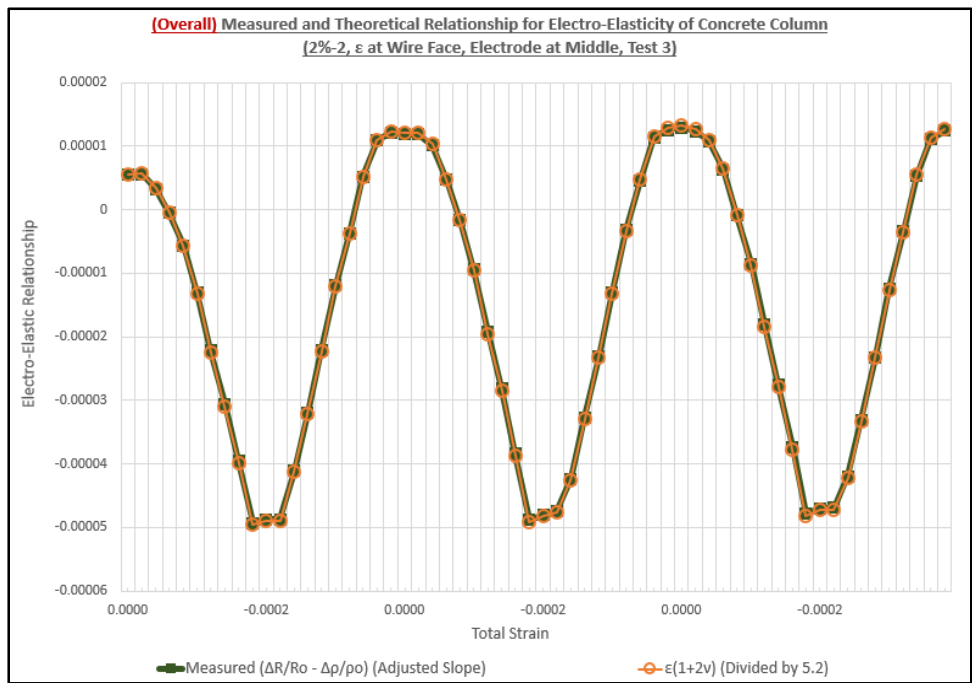Electrode Pair, Including Resistivity)

Figure G-105
Elasto-Electric Parameter Line Plot with Mechanical vs. Electrical Measurements (2%,
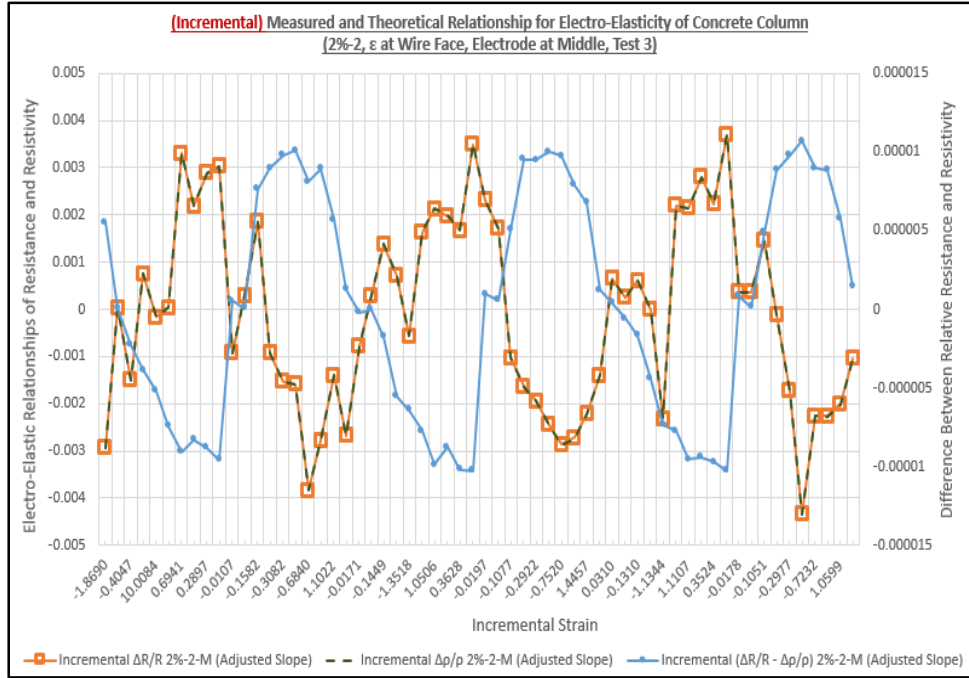Column 2, Strain at Non-Wire Face, Test 2, Right Electrode Pair, Excluding Resistivity)

354

Figure G-106
Elasto-Electric Parameter X-Y Scatter Plot with Mechanical vs. Electrical Measurements (2%, Column 2, Strain at Non-Wire Face, Test 2, Right Electrode Pair, Excluding Resistivity)

Figure G-107
Parametric Study of Elasto-Electric Factor (2%, Column 2, Strain at Non-Wire Face, Test 2, Right Electrode Pair, Excluding Resistivity)

Figure G-108

Elasto-Electric Parameter (2%, Column 2, Strain at Non-Wire Face, Test 2, Right
Electrode Pair, Excluding Resistivity)

Figure G-109

Overall Elasto-Electric Parameter Line Plot with Mechanical vs. Electrical Measurements
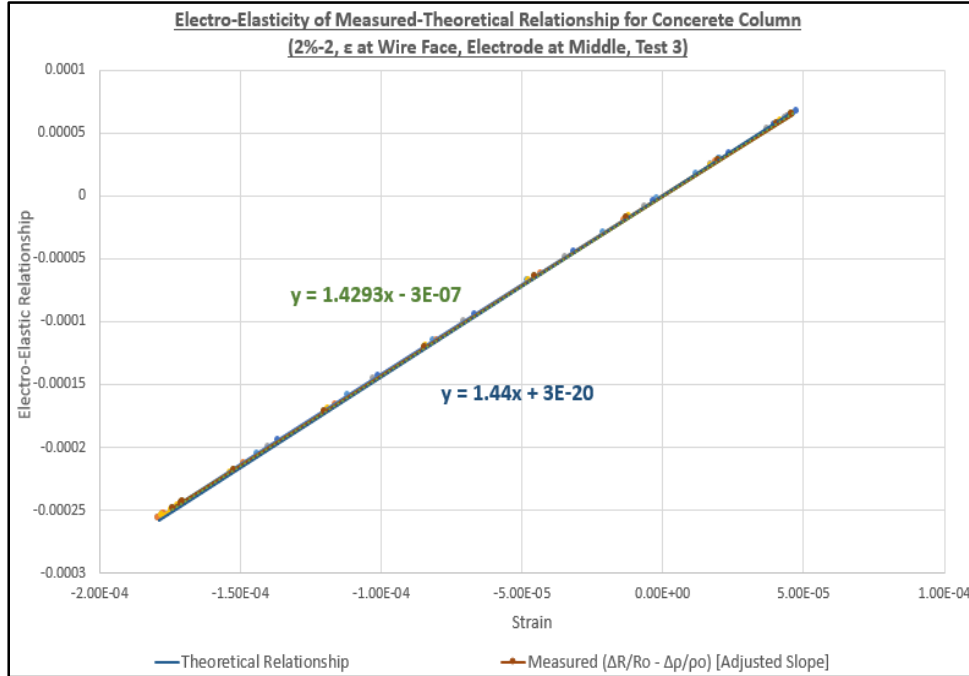(2%, Column 2, Strain at Non-Wire Face, Test 2, Right Electrode Pair, Including
Resistivity)

356

Figure G-110

Incremental Elasto-Electric Parameter X-Y Scatter Plot with Mechanical vs. Electrical
Measurements (2%, Column 2, Strain at Non-Wire Face, Test 2, Right Electrode Pair,
Including Resistivity)

Figure G-111

Elasto-Electric Parameter (2%, Column 2, Strain at Non-Wire Face, Test 2, Right
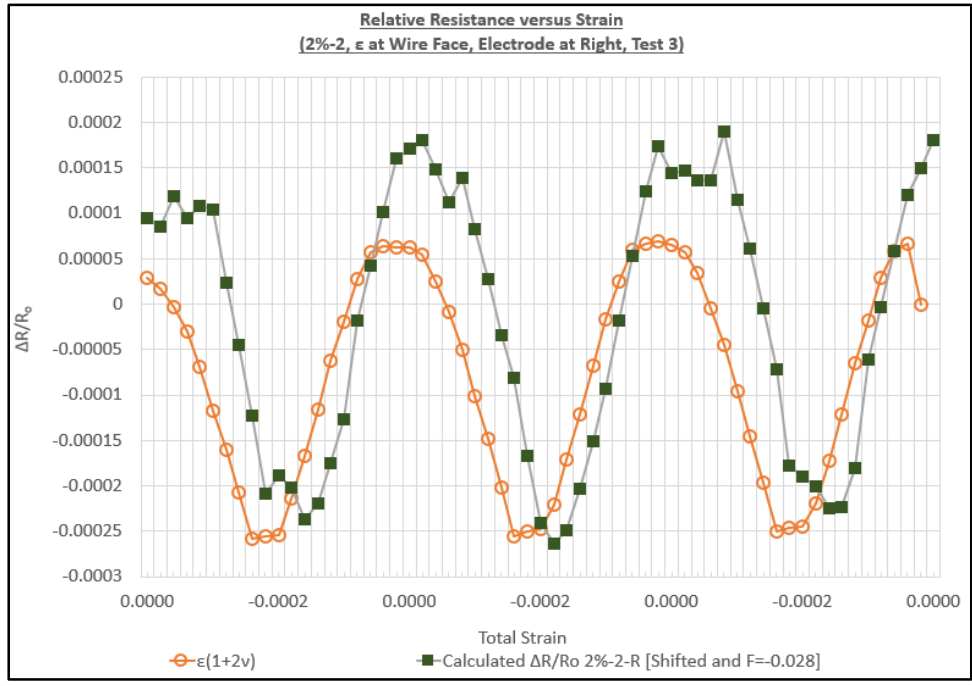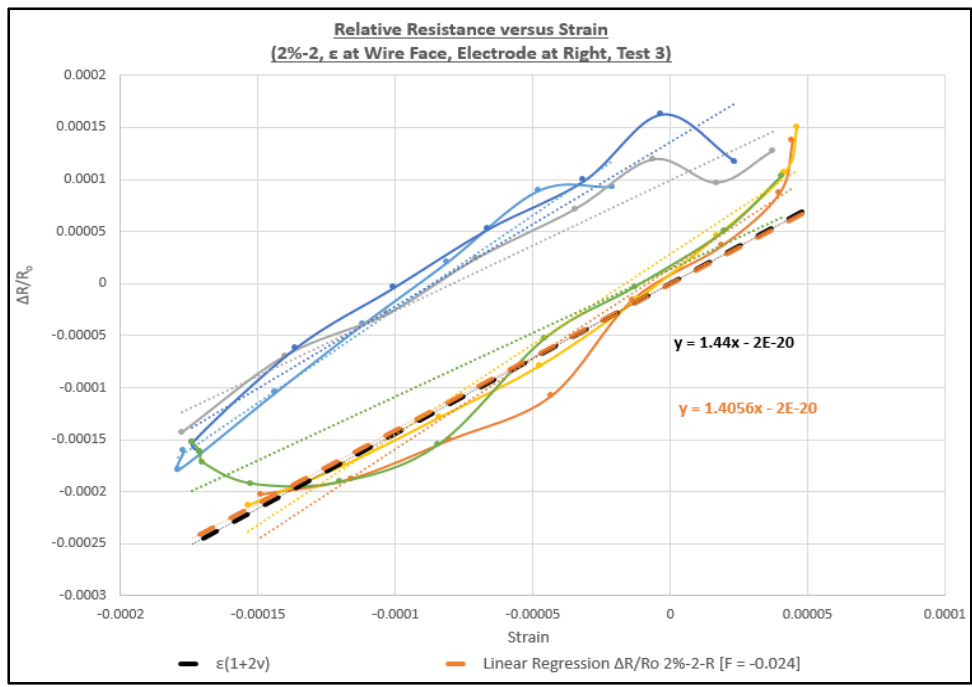Electrode Pair, Including Resistivity)

357

Strain and Resistance (RSR Concentration: 2%, Column 2, Test 3)
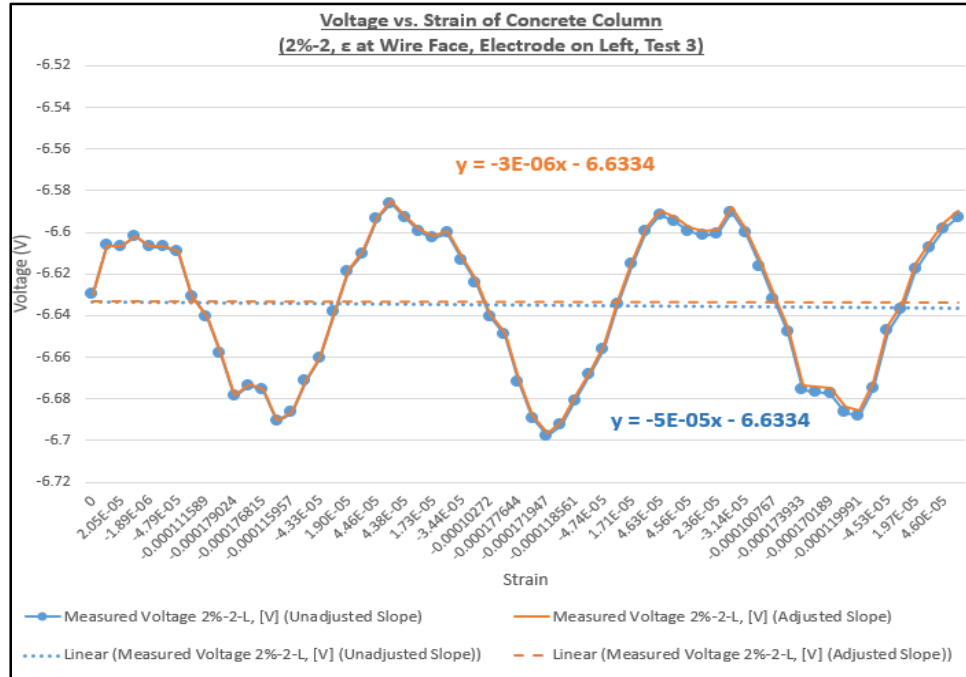
Figure G-112
Voltage Measurements (2%, Column 2, Test 3, Left Electrode Pair)
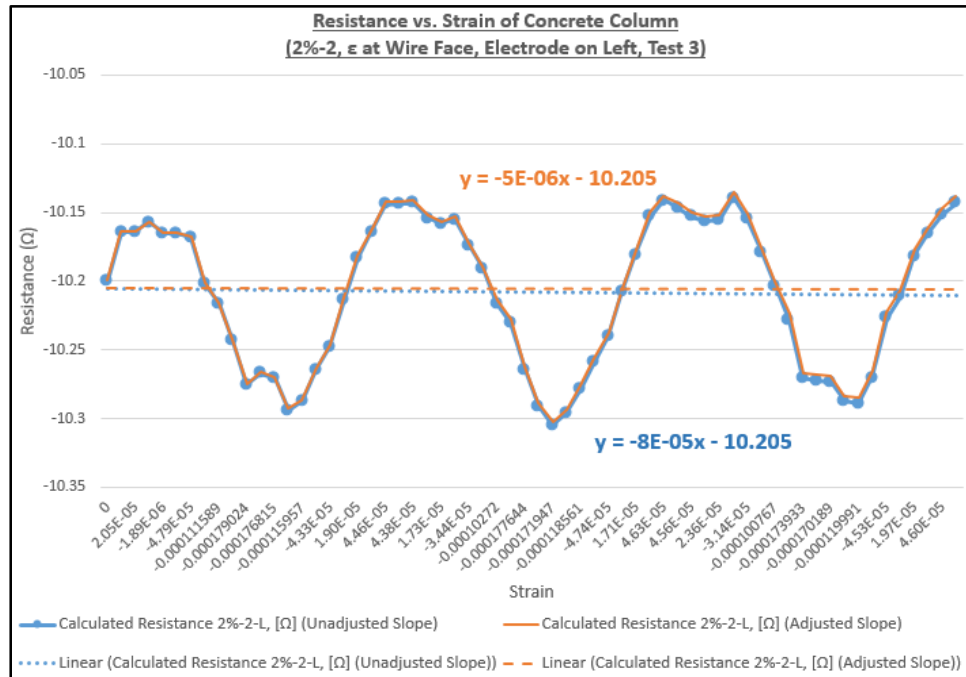
Figure G-113
Calculated Resistance (2%, Column 2, Test 3, Left Electrode Pair)
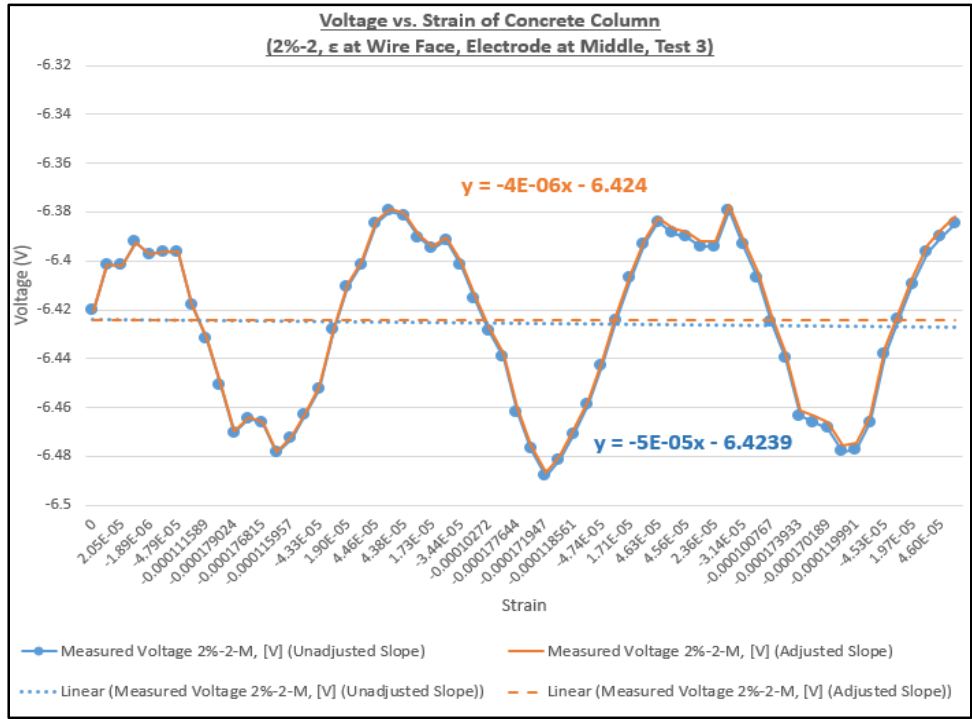
Figure G-114
Voltage Measurements (2%, Column 2, Test 3, Middle Electrode Pair)
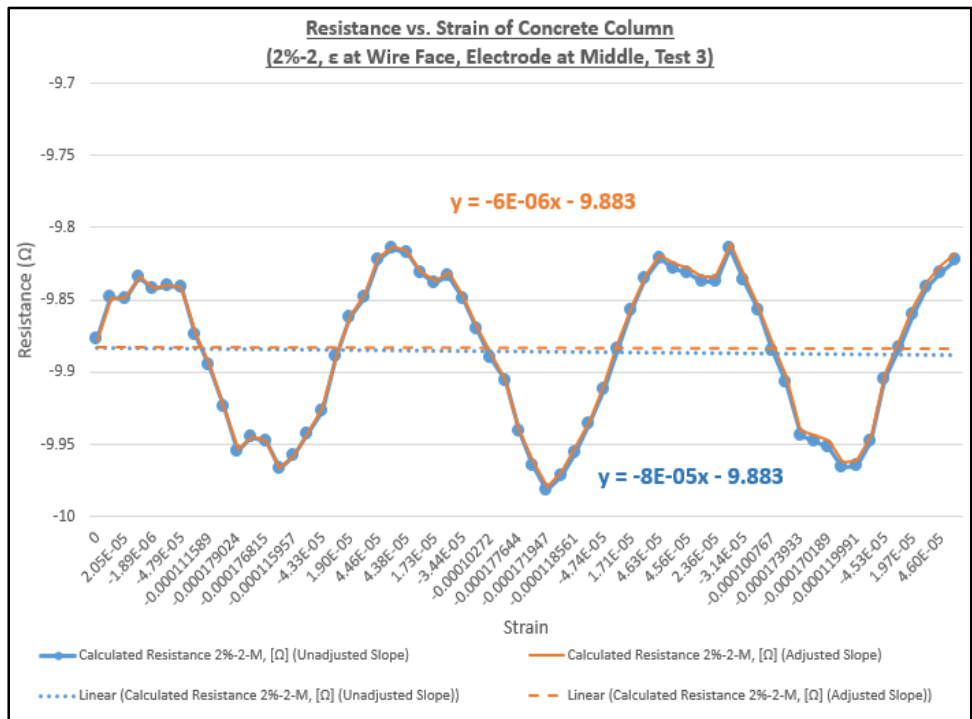
Figure G-115
Calculated Resistance (2%, Column 2, Test 3, Middle Electrode Pair)

359
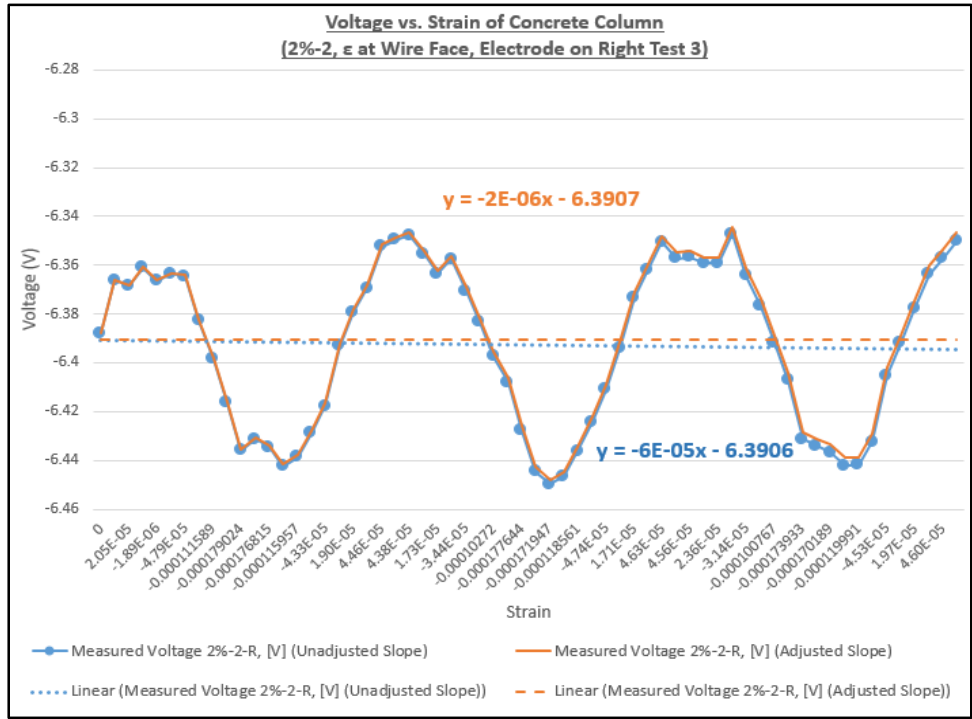
Figure G-116
Voltage Measurements (2%, Column 2, Test 3, Right Electrode Pair)
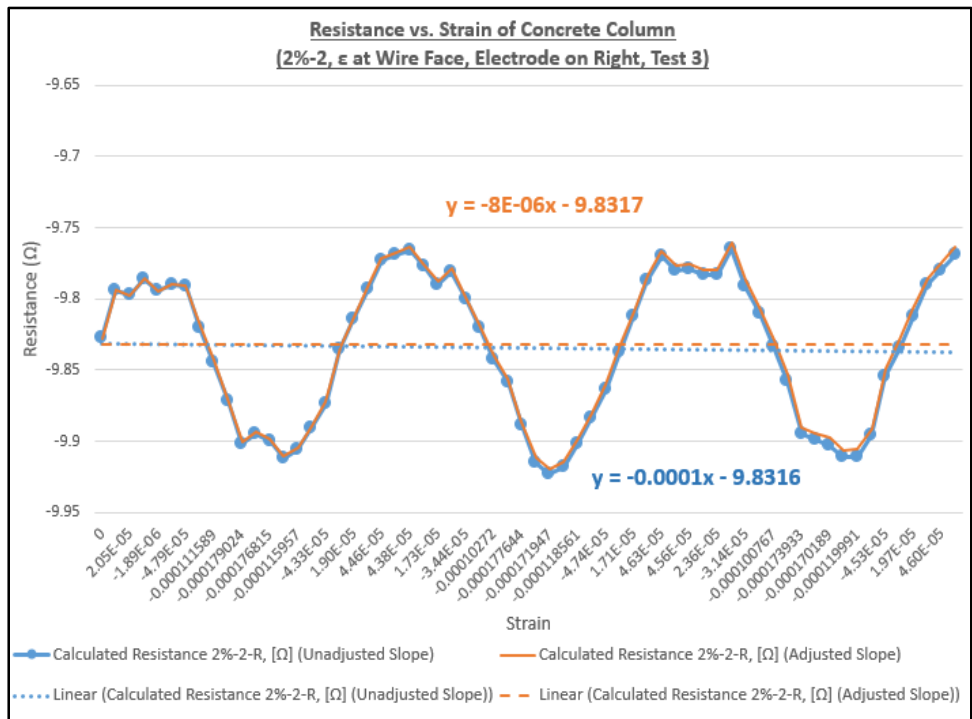
Figure G-117
Calculated Resistance (2%, Column 2, Test 3, Right Electrode Pair)

360

Figure G-118
Elasto-Electric Parameter Line Plot with Mechanical vs. Electrical Measurements (2%, Column 2, Strain at Wire Face, Test 3, Left Electrode Pair, Excluding Resistivity)

Figure G-119
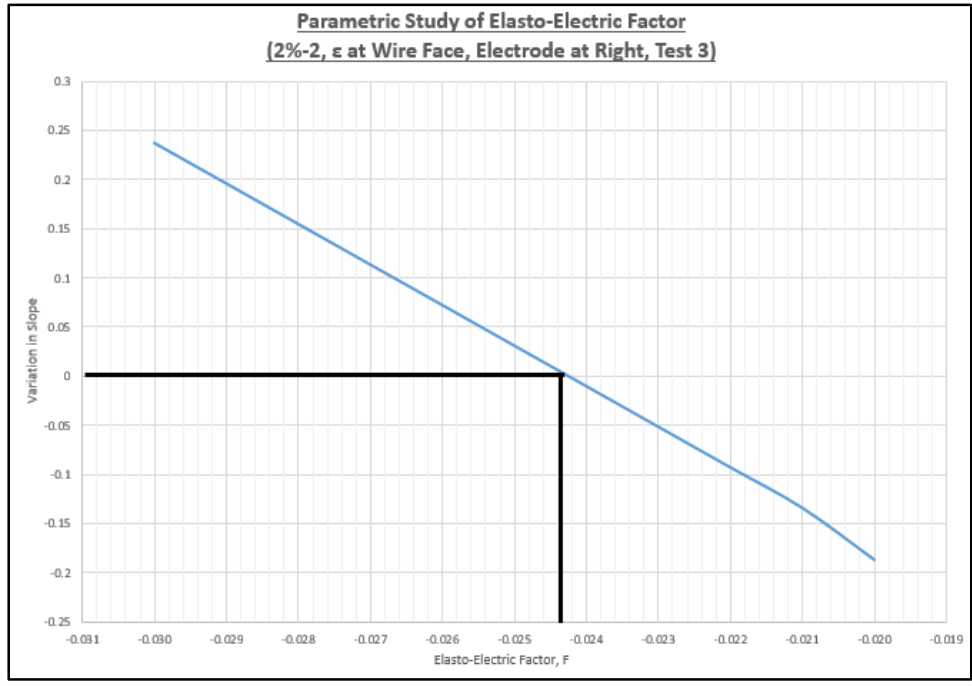Elasto-Electric Parameter X-Y Scatter Plot with Mechanical vs. Electrical Measurements (2%, Column 2, Strain at Wire Face, Test 3, Left Electrode Pair, Excluding Resistivity)

Figure G-120
Parametric Study of Elasto-Electric Factor (2%, Column 2, Strain at Wire Face, Test 3,
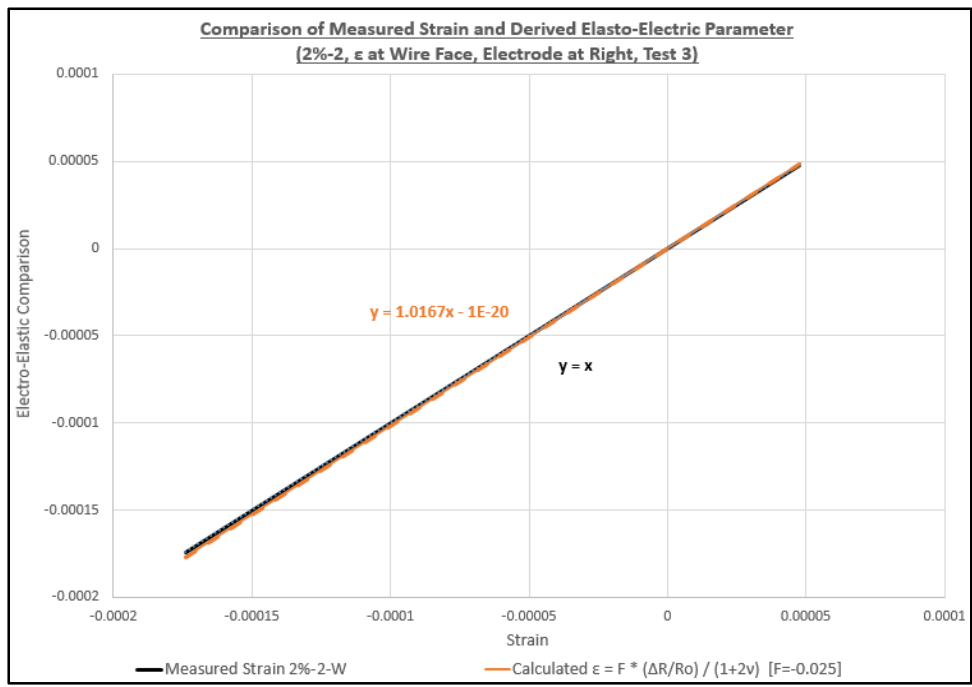Left Electrode Pair, Excluding Resistivity)

Figure G-121
Elasto-Electric Parameter (2%, Column 2, Strain at Wire Face, Test 3, Left Electrode
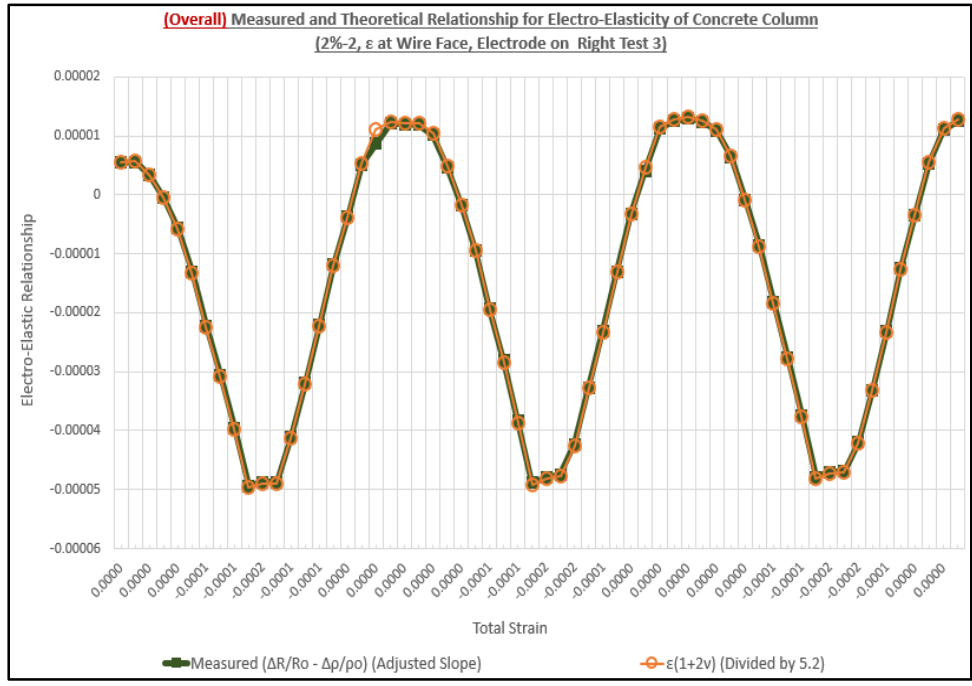Pair, Excluding Resistivity)

Figure G-122
Overall Elasto-Electric Parameter Line Plot with Mechanical vs. Electrical Measurements
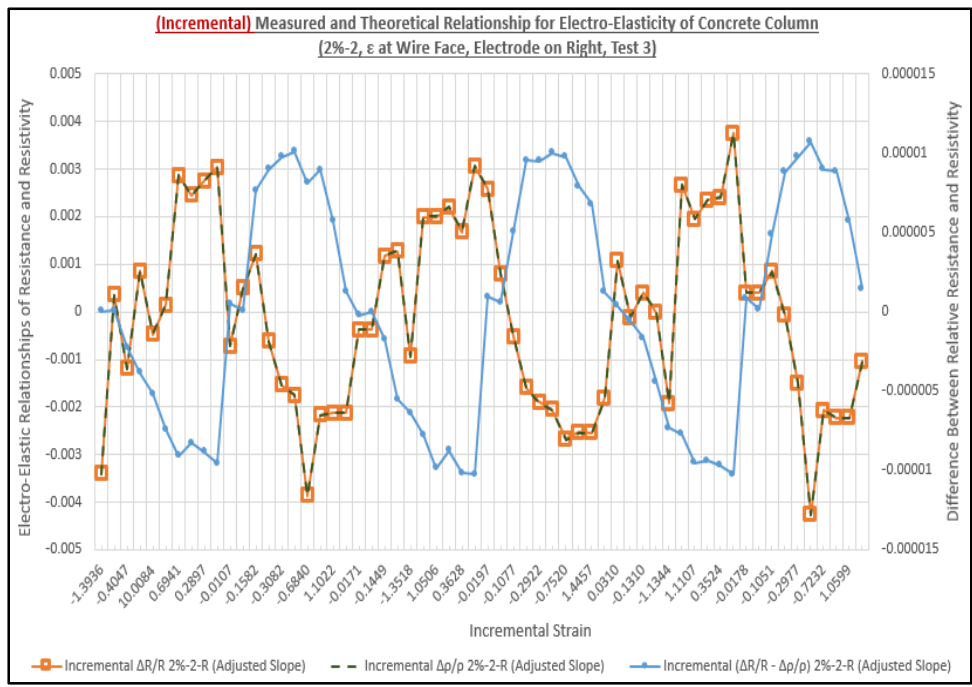(2%, Column 2, Strain at Wire Face, Test 3, Left Electrode Pair, Including Resistivity)

Figure G-123
Incremental Elasto-Electric Parameter X-Y Scatter Plot with Mechanical vs. Electrical
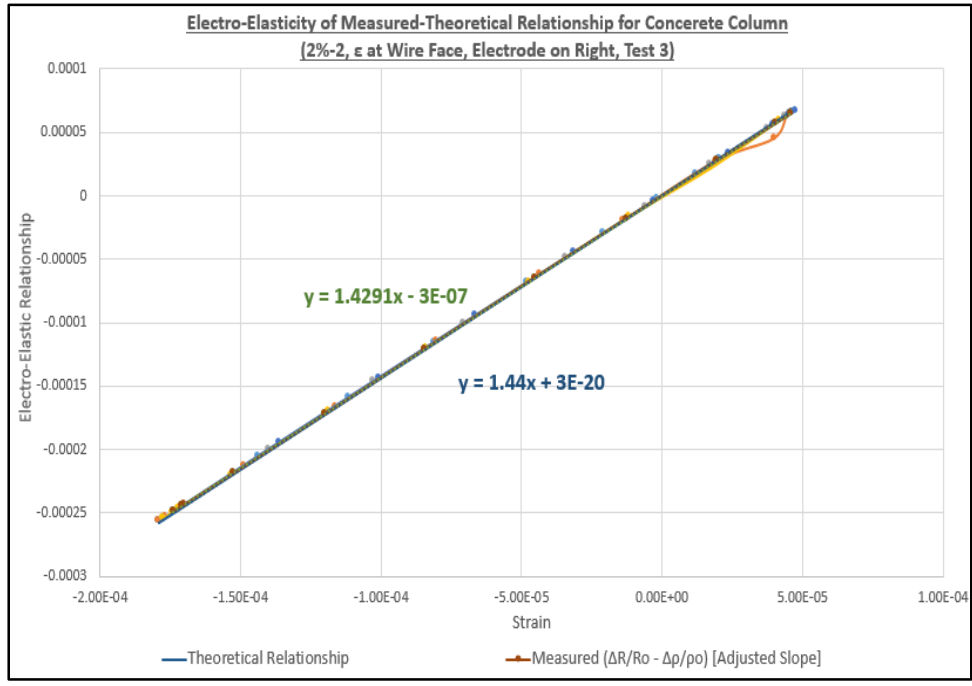Measurements (2%, Column 2, Strain at Wire Face, Test 3, Left Electrode Pair, Including
Resistivity)

Figure G-124
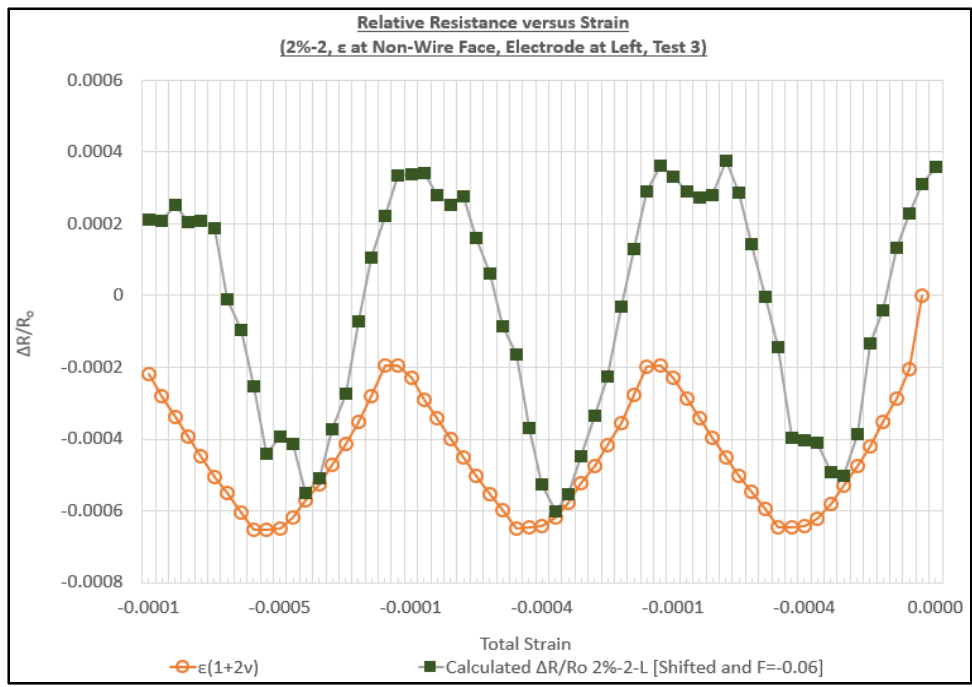Elasto-Electric Parameter (2%, Column 2, Strain at Wire Face, Test 3, Left Electrode Pair, Including Resistivity)

Figure G-125
Elasto-Electric Parameter Line Plot with Mechanical vs. Electrical Measurements (2%, Column 2, Strain at Wire Face, Test 3, Middle Electrode Pair, Excluding Resistivity)
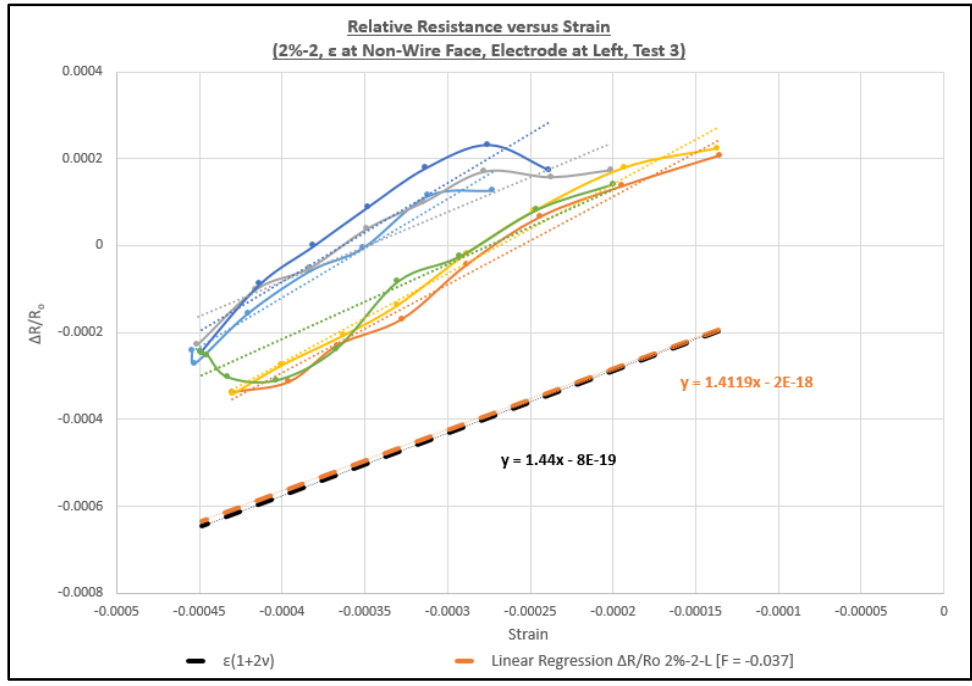
Figure G-126
Elasto-Electric Parameter X-Y Scatter Plot with Mechanical vs. Electrical Measurements
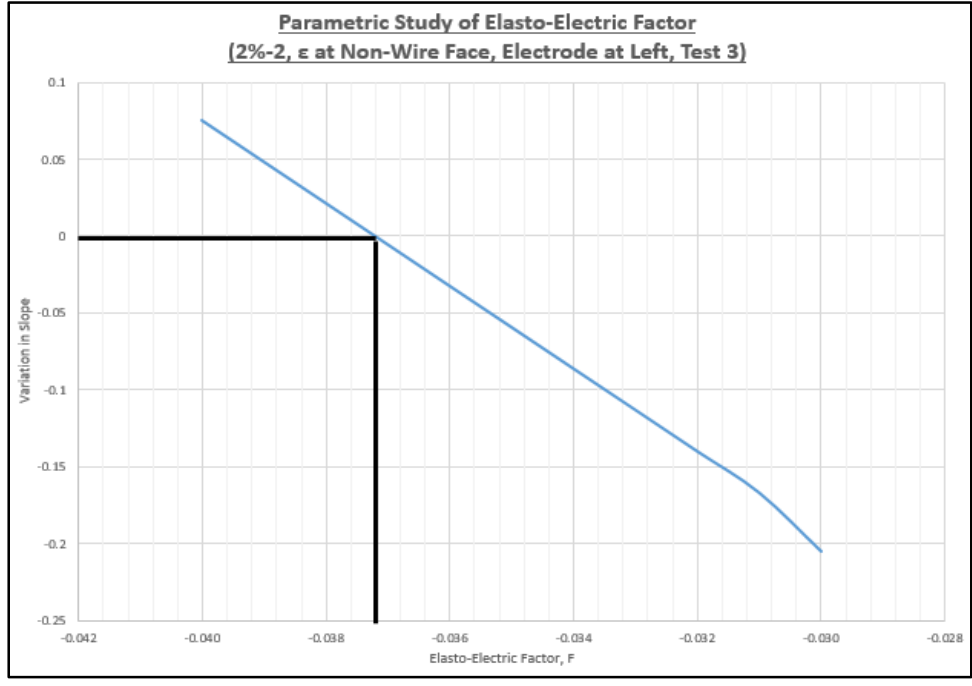(2%, Column 2, Strain at Wire Face, Test 3, Middle Electrode Pair, Excluding
Resistivity)

Figure G-127
Parametric Study of Elasto-Electric Factor (2%, Column 2, Strain at Wire Face, Test 3,
Middle Electrode Pair, Excluding Resistivity)

Figure G-128
Elasto-Electric Parameter (2%, Column 2, Strain at Wire Face, Test 3, Middle Electrode Pair, Excluding Resistivity)

Figure G-129
Overall Elasto-Electric Parameter Line Plot with Mechanical vs. Electrical Measurements (2%, Column 2, Strain at Wire Face, Test 3, Middle Electrode Pair, Including Resistivity)

Figure G-130
Incremental Elasto-Electric Parameter X-Y Scatter Plot with Mechanical vs. Electrical
Measurements (2%, Column 2, Strain at Wire Face, Test 3, Middle Electrode Pair,
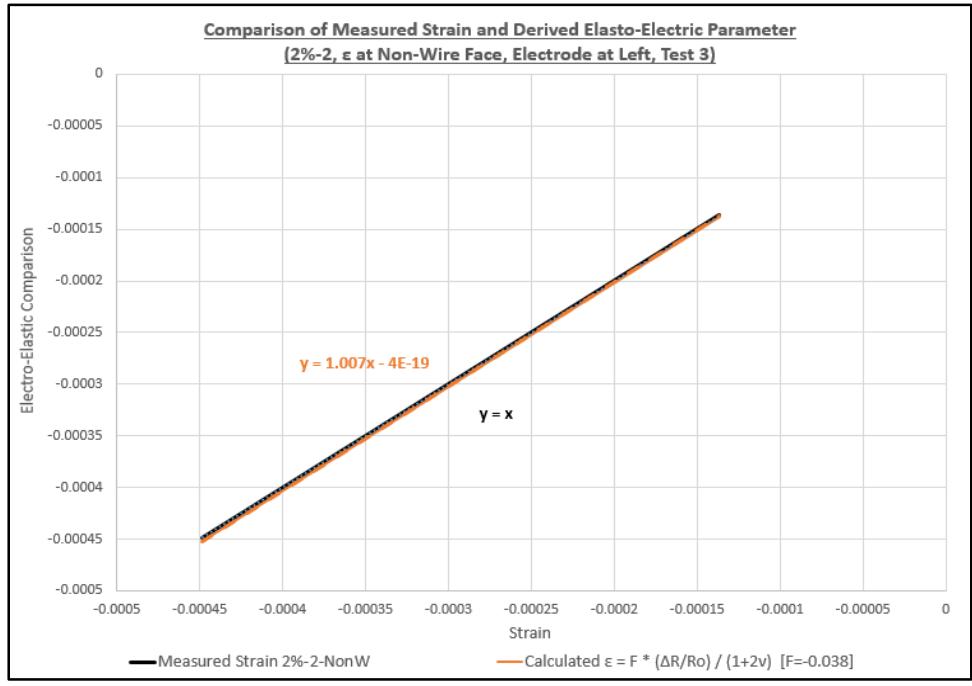Including Resistivity)

Figure G-131
Elasto-Electric Parameter (2%, Column 2, Strain at Wire Face, Test 3, Middle Electrode
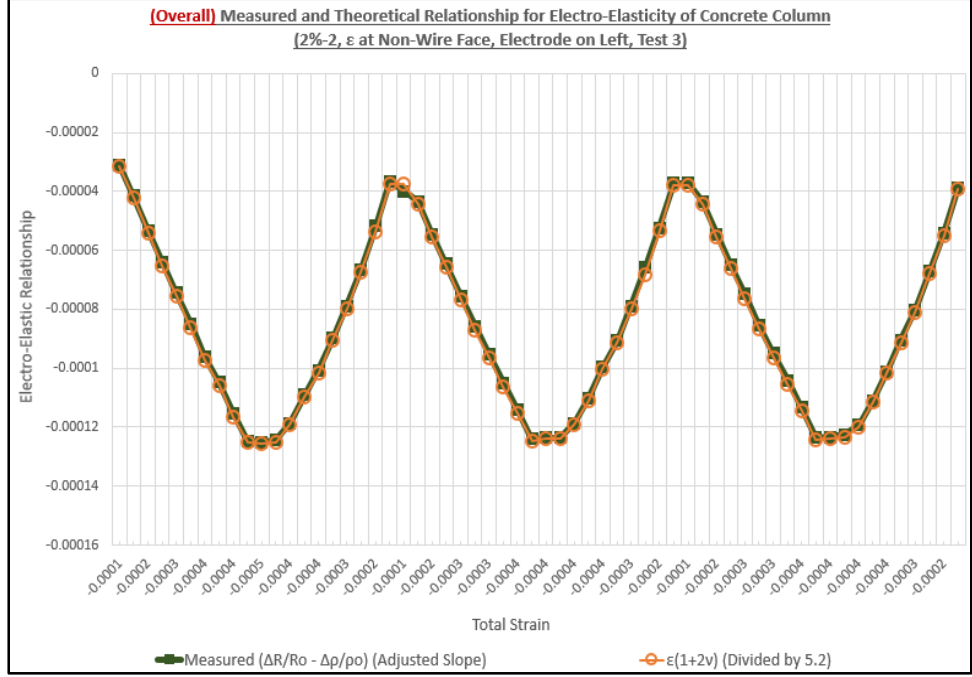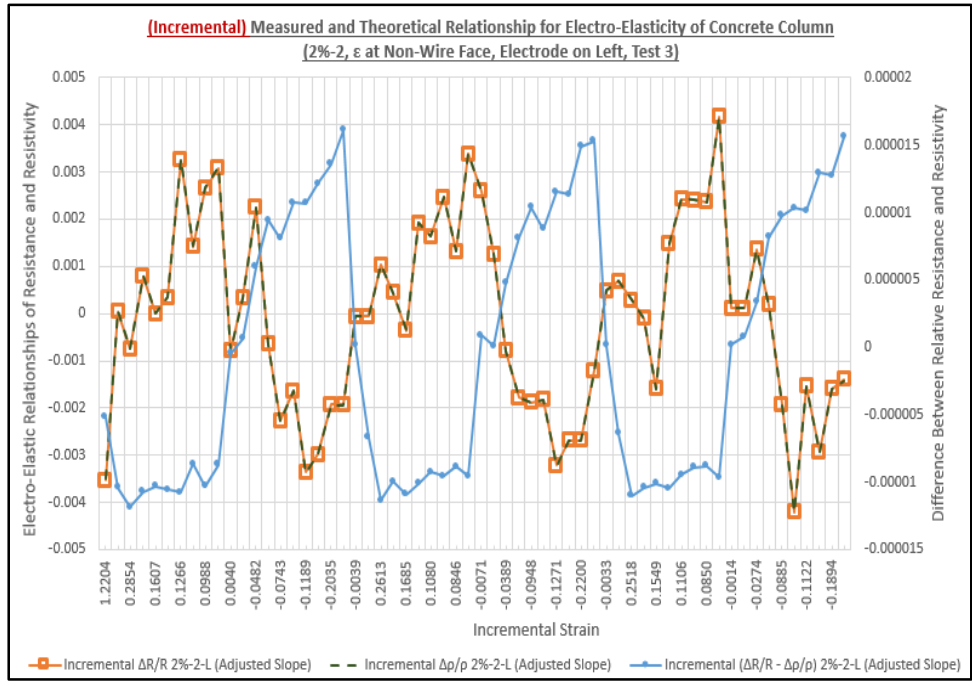Pair, Including Resistivity)

367

Figure G-132
Elasto-Electric Parameter Line Plot with Mechanical vs. Electrical Measurements (2%, Column 2, Strain at Wire Face, Test 3, Right Electrode Pair, Excluding Resistivity)

Figure G-133
Elasto-Electric Parameter X-Y Scatter Plot with Mechanical vs. Electrical Measurements (2%, Column 2, Strain at Wire Face, Test 3, Right Electrode Pair, Excluding Resistivity)

Figure G-134
Parametric Study of Elasto-Electric Factor (2%, Column 2, Strain at Wire Face, Test 3, Right Electrode Pair, Excluding Resistivity)

Figure G-135
Elasto-Electric Parameter (2%, Column 2, Strain at Wire Face, Test 3, Right Electrode Pair, Excluding Resistivity)

369

Figure G-136
Overall Elasto-Electric Parameter Line Plot with Mechanical vs. Electrical Measurements
(2%, Column 2, Strain at Wire Face, Test 3, Right Electrode Pair, Including Resistivity)

Figure G-137
Incremental Elasto-Electric Parameter X-Y Scatter Plot with Mechanical vs. Electrical
Measurements (2%, Column 2, Strain at Wire Face, Test 3, Right Electrode Pair,
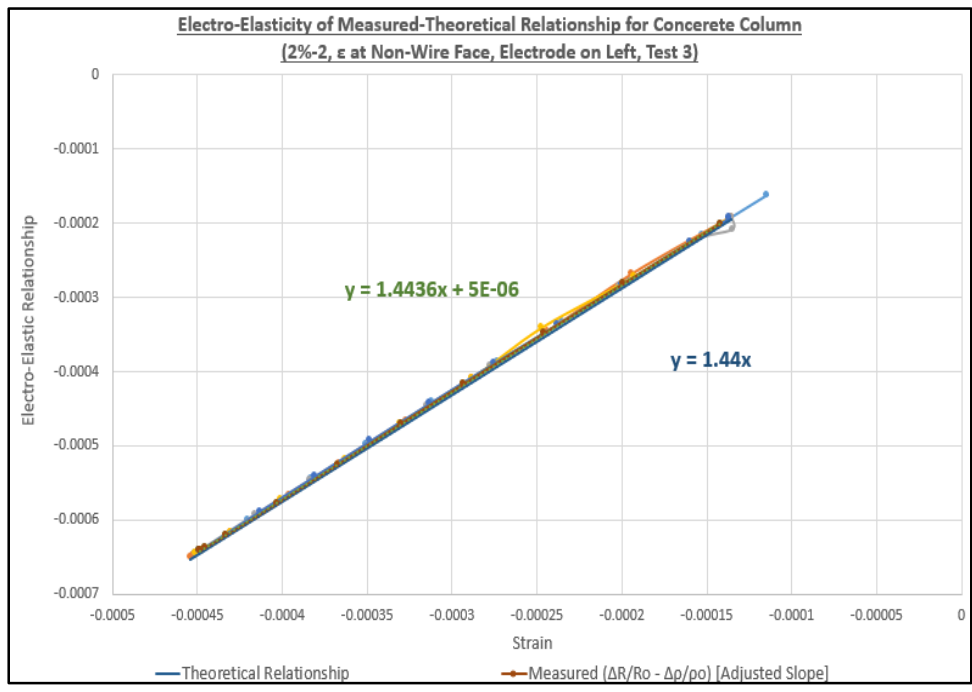Including Resistivity)

370

Figure G-138
Elasto-Electric Parameter (2%, Column 2, Strain at Wire Face, Test 3, Right Electrode Pair, Including Resistivity)

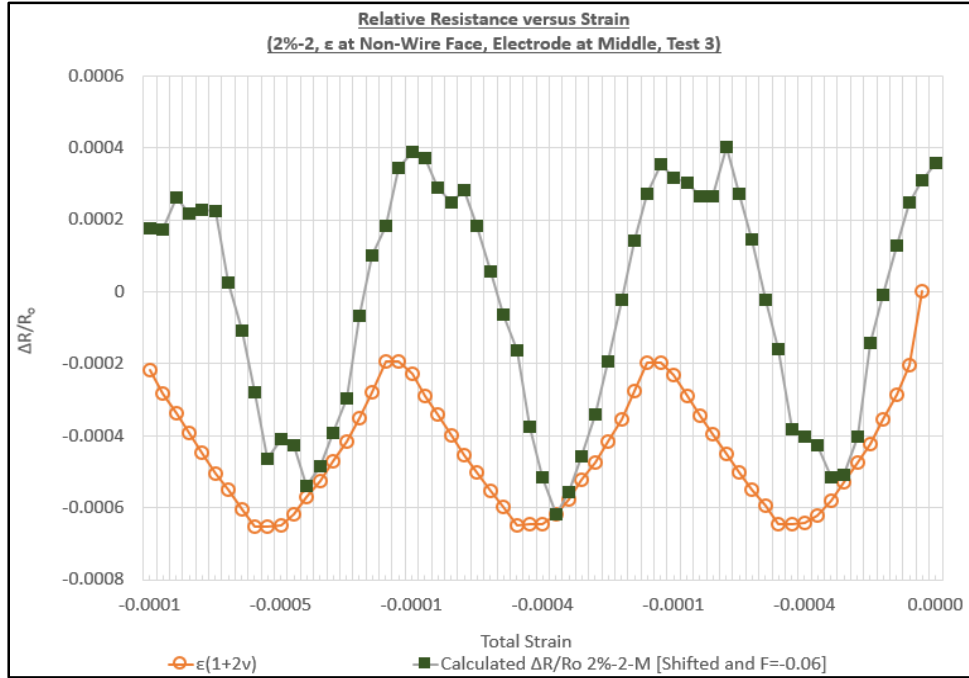Figure G-139
Elasto-Electric Parameter Line Plot with Mechanical vs. Electrical Measurements (2%, Column 2, Strain at Non-Wire Face, Test 3, Left Electrode Pair, Excluding Resistivity)
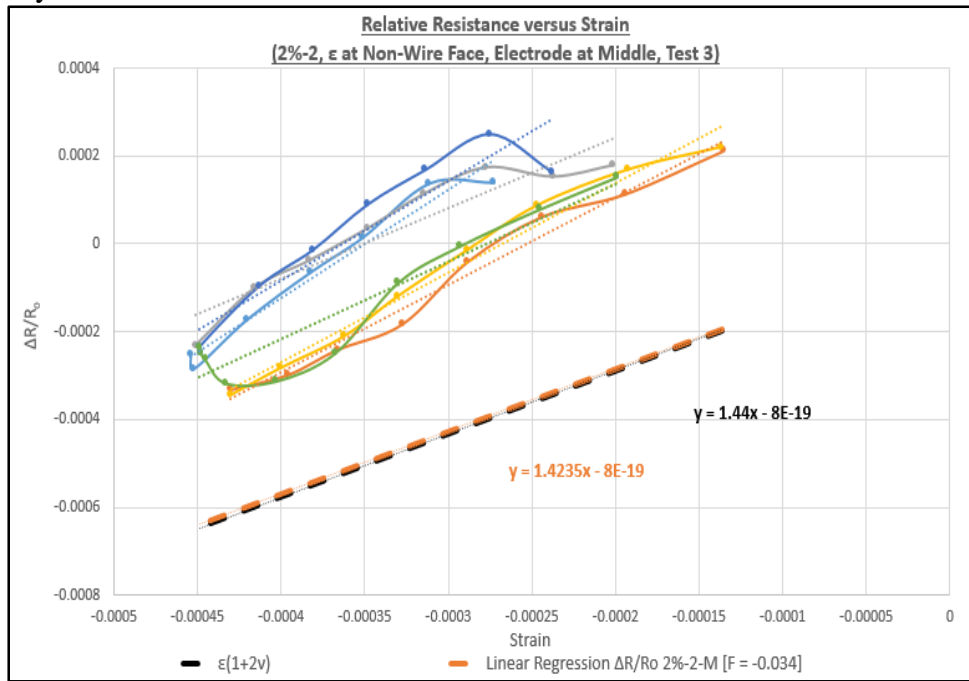
Figure G-140
Elasto-Electric Parameter X-Y Scatter Plot with Mechanical vs. Electrical Measurements
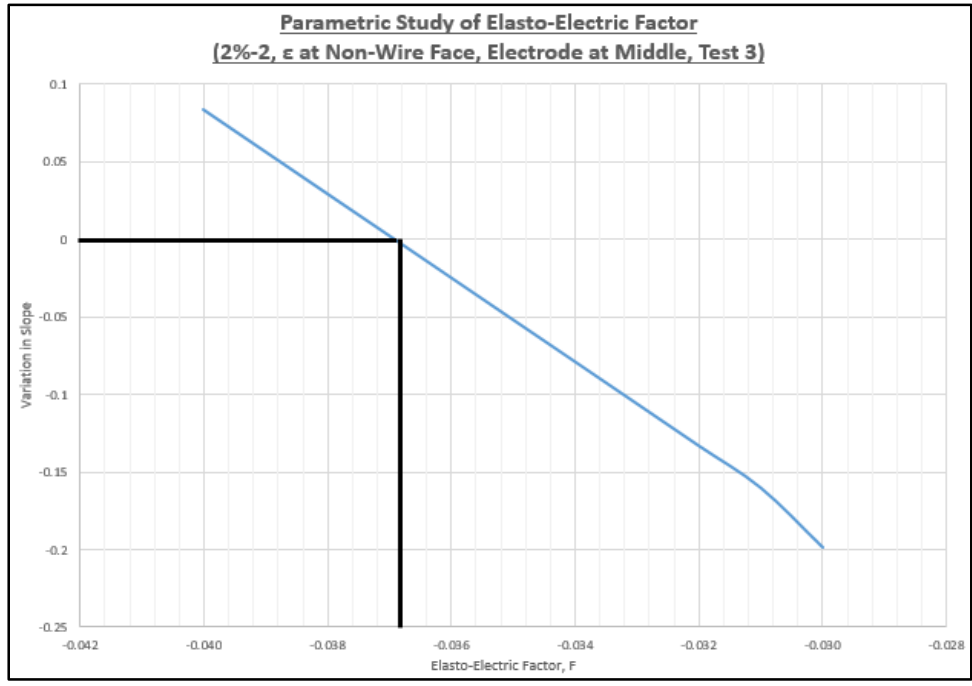(2%, Column 2, Strain at Non-Wire Face, Test 3, Left Electrode Pair, Excluding
Resistivity)

Figure G-141
Parametric Study of Elasto-Electric Factor (2%, Column 2, Strain at Non-Wire Face, Test
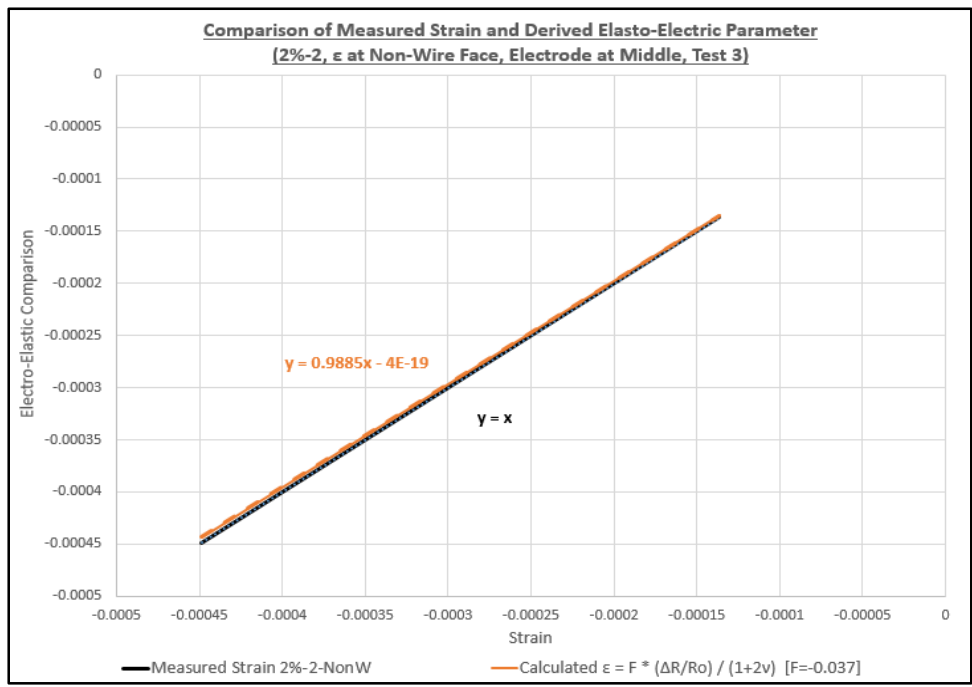3, Left Electrode Pair, Excluding Resistivity)

Figure G-142
Elasto-Electric Parameter (2%, Column 2, Strain at Non-Wire Face, Test 3, Left
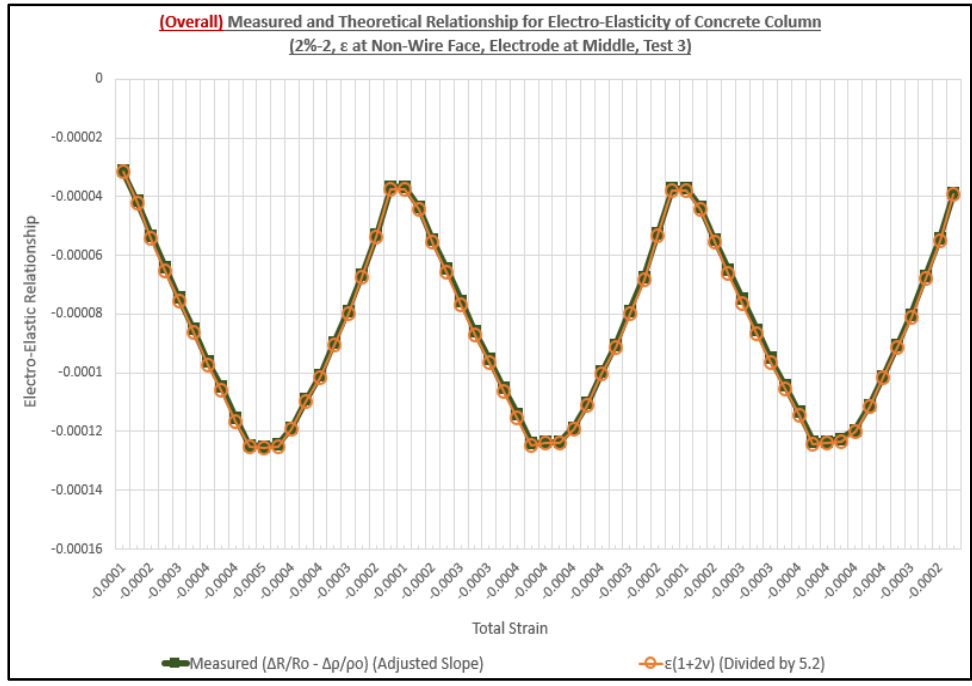Electrode Pair, Excluding Resistivity)

Figure G-143
Overall Elasto-Electric Parameter Line Plot with Mechanical vs. Electrical Measurements
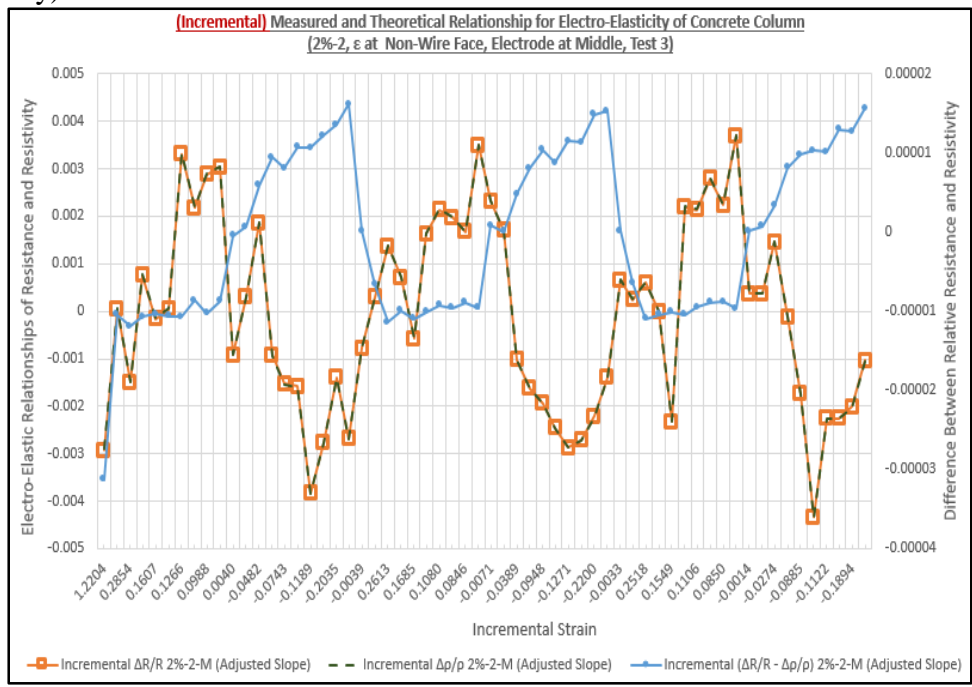(2%, Column 2, Strain at Non-Wire Face, Test 3, Left Electrode Pair, Including
Resistivity)

Figure G-144
Incremental Elasto-Electric Parameter X-Y Scatter Plot with Mechanical vs. Electrical
Measurements (2%, Column 2, Strain at Non-Wire Face, Test 3, Left Electrode Pair,
Including Resistivity)

Figure G-145
Elasto-Electric Parameter (2%, Column 2, Strain at Non-Wire Face, Test 3, Left
Electrode Pair, Including Resistivity)

374

Figure G-146
Elasto-Electric Parameter Line Plot with Mechanical vs. Electrical Measurements (2%, Column 2, Strain at Non-Wire Face, Test 3, Middle Electrode Pair), Excluding Resistivity

Figure G-147
Elasto-Electric Parameter X-Y Scatter Plot with Mechanical vs. Electrical Measurements (2%, Column 2, Strain at Non-Wire Face, Test 3, Middle Electrode Pair, Excluding Resistivity)
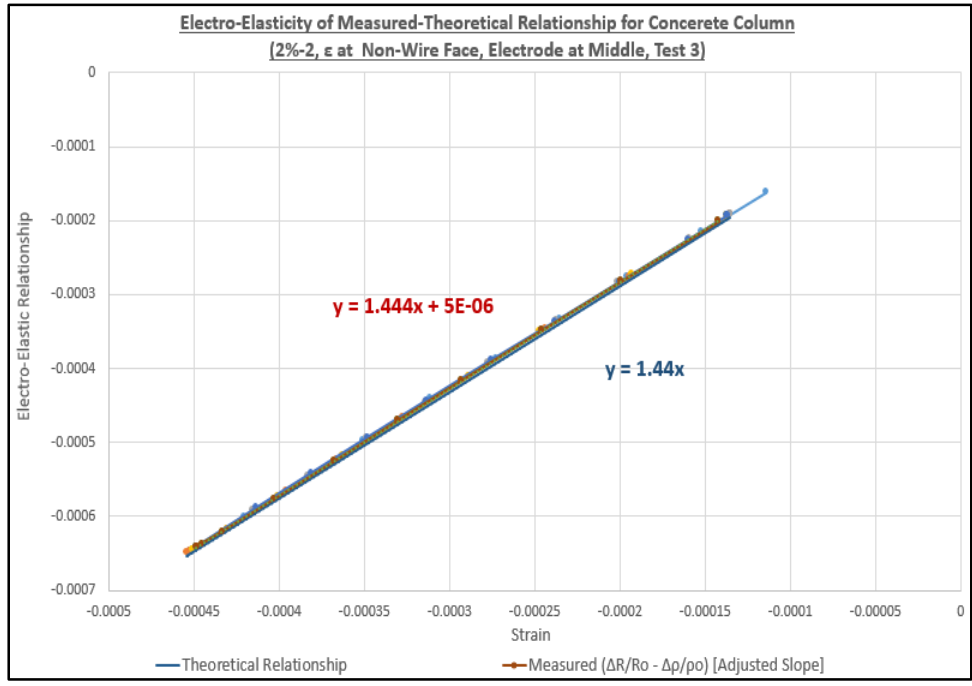
Figure G-148
Parametric Study of Elasto-Electric Factor (2%, Column 2, Strain at Non-Wire Face, Test 3, Middle Electrode Pair, Excluding Resistivity)

Figure G-149
Elasto-Electric Parameter (2%, Column 2, Strain at Non-Wire Face, Test 3, Middle Electrode Pair, Excluding Resistivity)
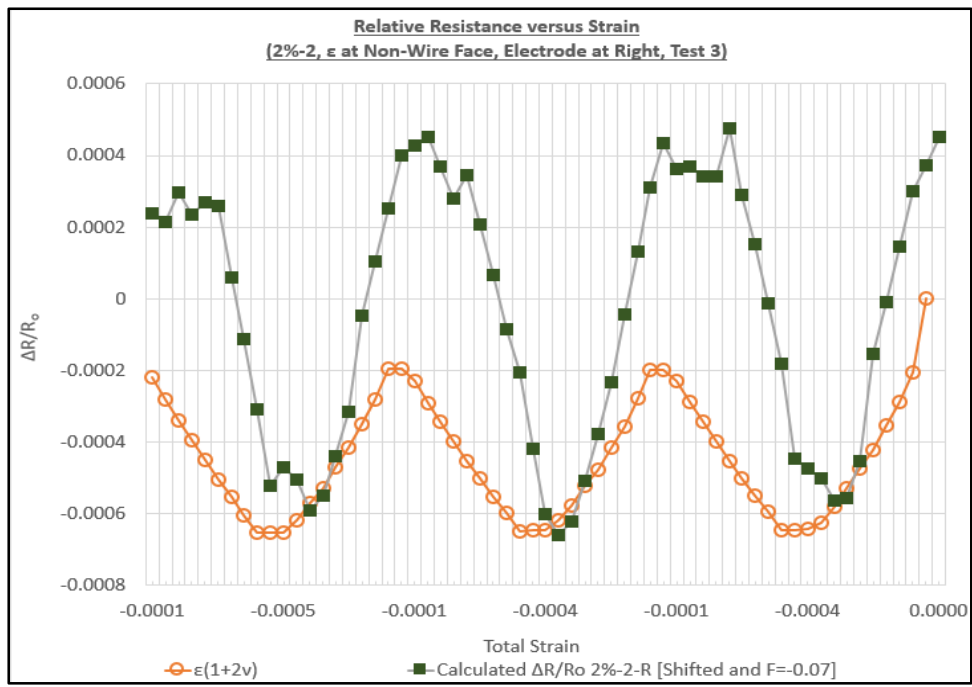
Figure G-150
Overall Elasto-Electric Parameter Line Plot with Mechanical vs. Electrical Measurements (2%, Column 2, Strain at Non-Wire Face, Test 3, Middle Electrode Pair, Including Resistivity)

Figure G-151
Incremental Elasto-Electric Parameter X-Y Scatter Plot with Mechanical vs. Electrical Measurements (2%, Column 2, Strain at Non-Wire Face, Test 3, Middle Electrode Pair, Including Resistivity)

377

Figure G-152
Elasto-Electric Parameter (2%, Column 2, Strain at Non-Wire Face, Test 3, Middle
Electrode Pair, Including Resistivity)

Figure G-153
Elasto-Electric Parameter Line Plot with Mechanical vs. Electrical Measurements (2%,
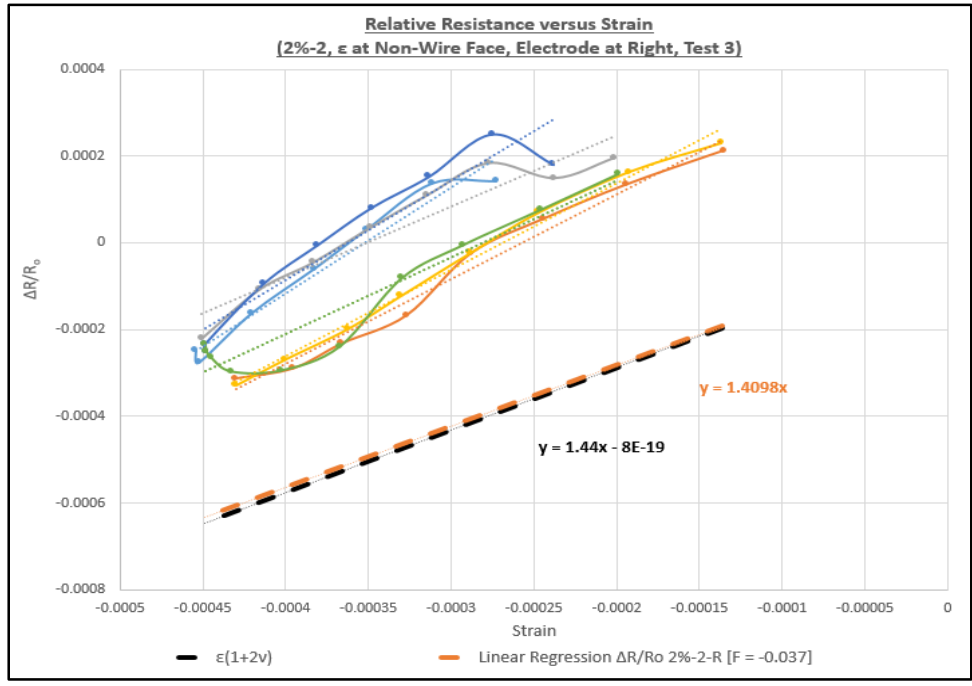Column 2, Strain at Non-Wire Face, Test 3, Right Electrode Pair, Excluding Resistivity)

Figure G-154
Elasto-Electric Parameter X-Y Scatter Plot with Mechanical vs. Electrical Measurements (2%, Column 2, Strain at Non-Wire Face, Test 3, Right Electrode Pair, Excluding Resistivity)
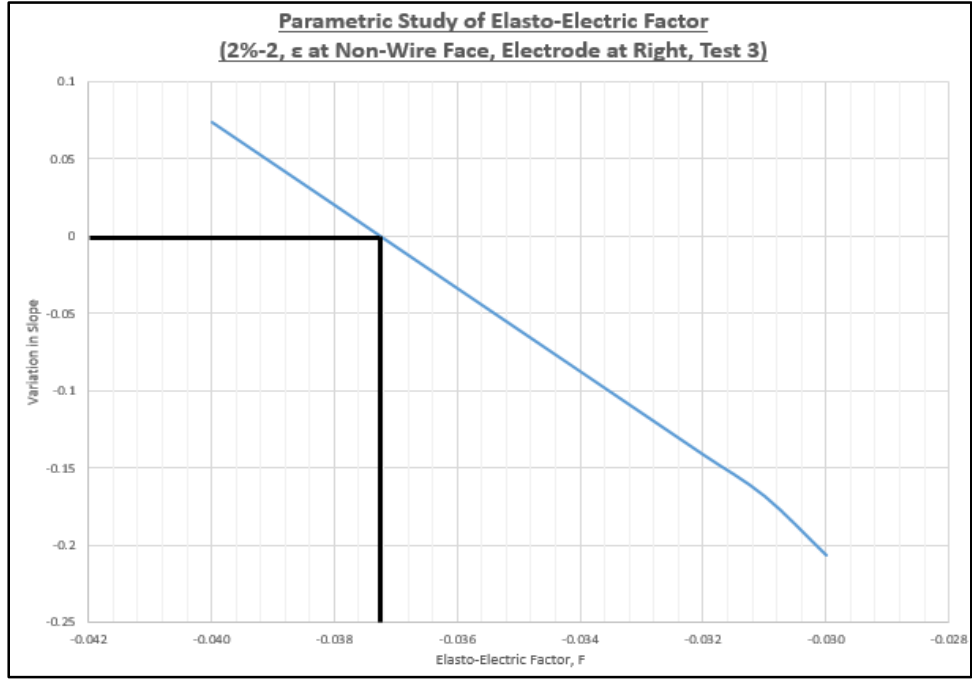

Figure G-155
Parametric Study of Elasto-Electric Factor (2%, Column 2, Strain at Non-Wire Face, Test 3, Right Electrode Pair, Excluding Resistivity)
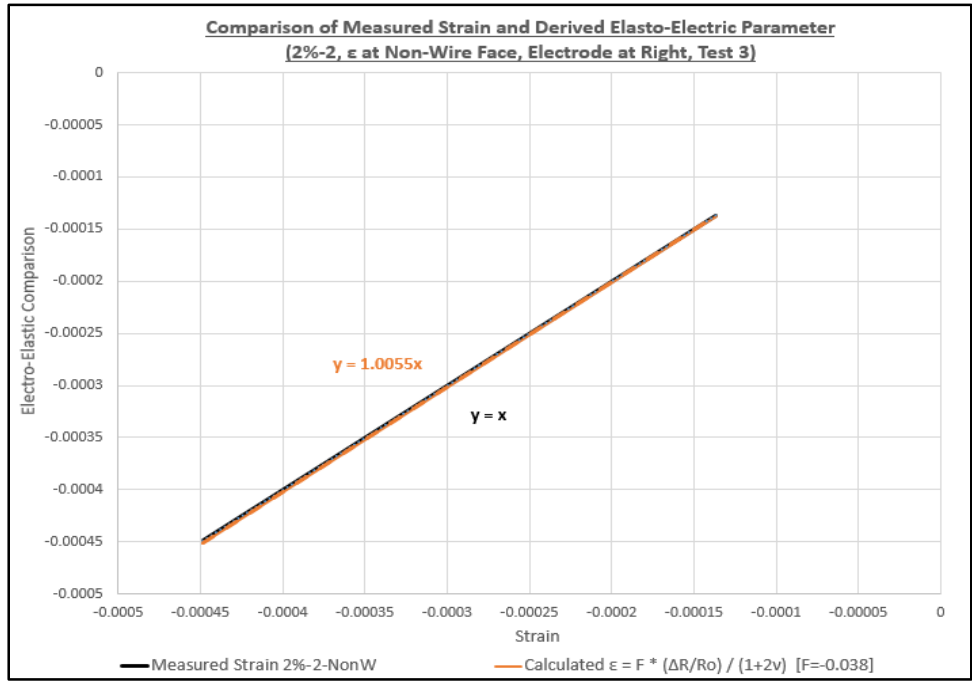
Figure G-156

Elasto-Electric Parameter (2%, Column 2, Strain at Non-Wire Face, Test 3, Right
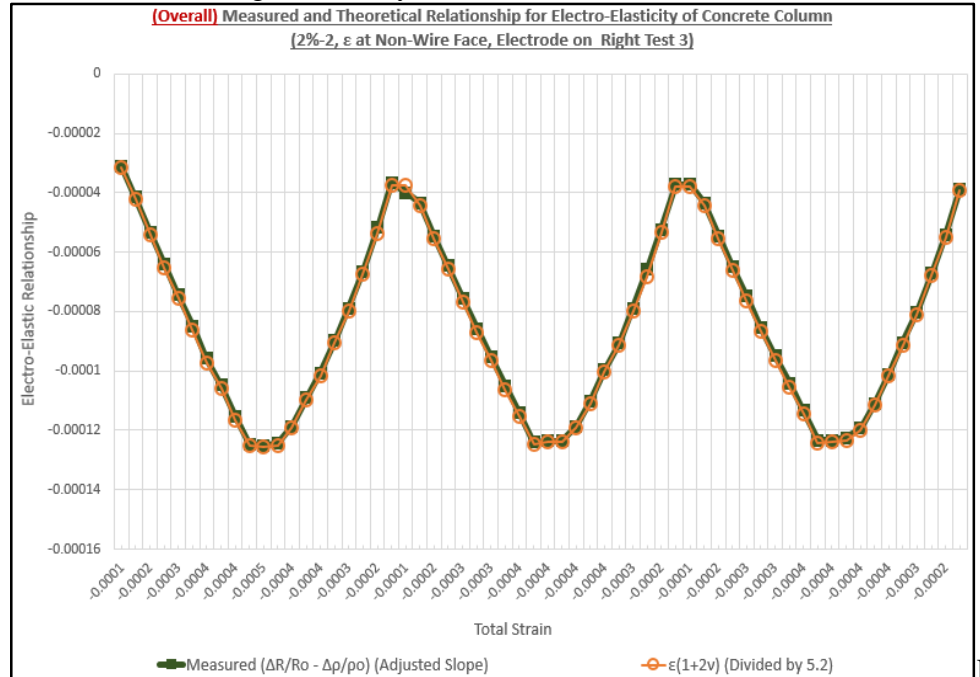Electrode Pair, Excluding Resistivity)

ure G-157

Overall Elasto-Electric Parameter Line Plot with Mechanical vs. Electrical Measurements
(2%, Column 2, Strain at Non-Wire Face, Test 3, Right Electrode Pair, Including
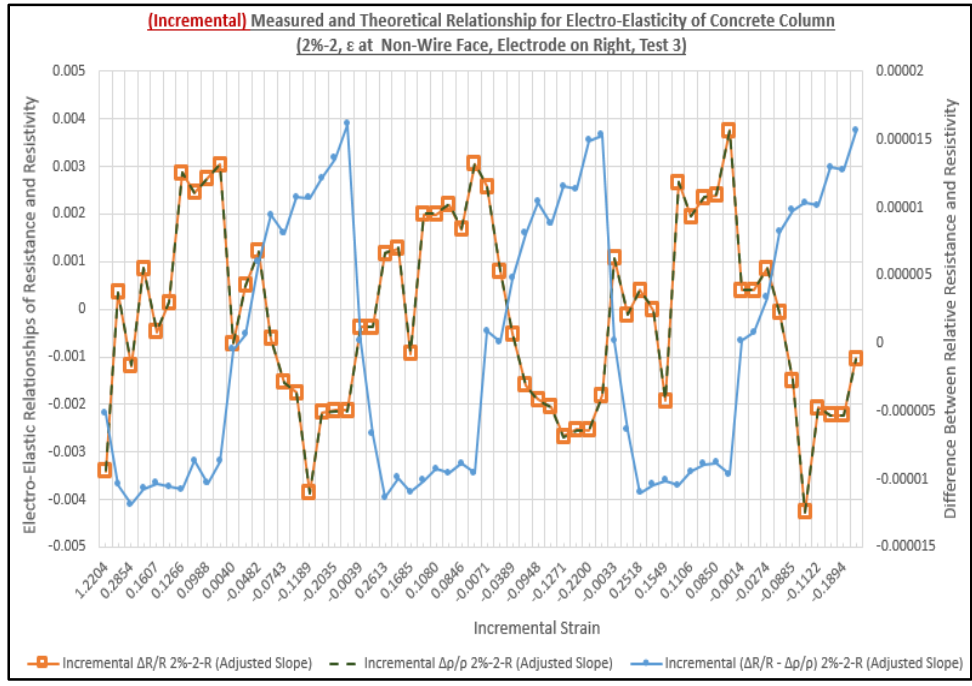Resistivity)

Figure G-158
Incremental Elasto-Electric Parameter X-Y Scatter Plot with Mechanical vs. Electrical
Measurements (2%, Column 2, Strain at Non-Wire Face, Test 3, Right Electrode Pair,
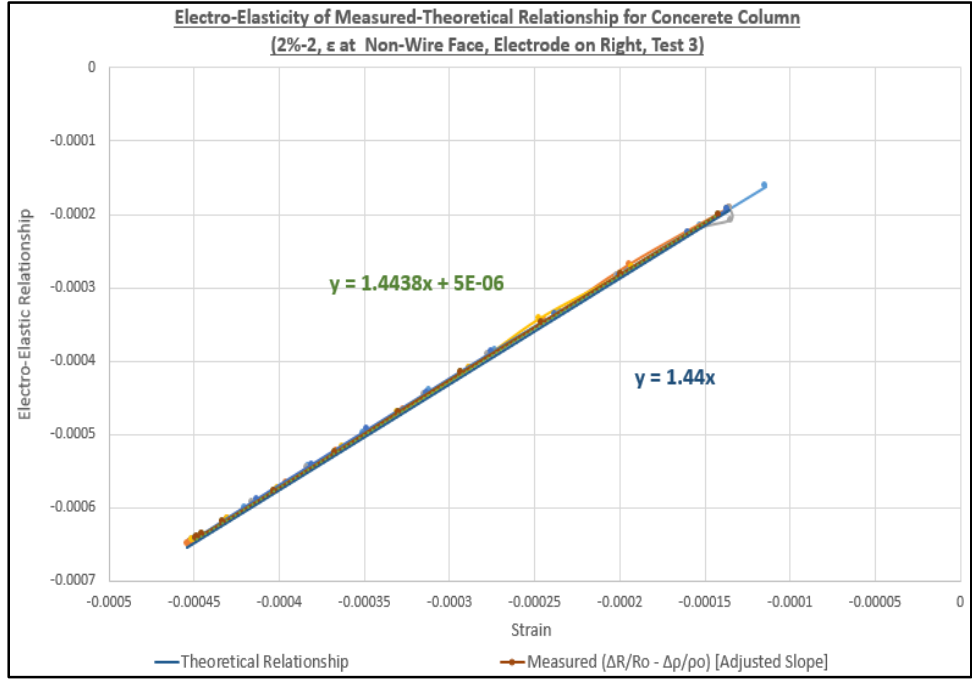Including Resistivity)

Figure G-159
Elasto-Electric Parameter (2%, Column 2, Strain at Non-Wire Face, Test 3, Right
Electrode Pair, Including Resistivity)

Statistical Review (RSR Concentration: 2%, Column 2, Test 1, Test 2, and Test 3)

Table G-1
Statistical Review (RSR Concentration: 2%, Column 2, Test 1, Test 2, and Test 3)

		Calculated $\Delta R/R_o$ 2%-2-R [Adjusted]			
		Elasto-Electric Factor	Standard Deviation	Coefficient of Variation	Linear Regression, R Squared Value
Test 1	**2%-2; W, L**	-0.066	0.000225	0.98	0.68
	2%-2; W, M	-0.065	0.000243	1.02	0.68
	2%-2; W, R	-0.068	0.000226	0.88	0.68
	2%-2; NonW, L	-0.052	0.000177	0.98	0.66
	2%-2; NonW, M	-0.051	0.000177	1.02	0.66
	2%-2; NonW, R	-0.053	0.000177	0.88	0.66
Test 2	**2%-2; W, L**	-0.026	0.000118	0.45	0.83
	2%-2; W, M	-0.026	0.000119	0.45	0.84
	2%-2; W, R	-0.026	0.000118	0.47	0.84
	2%-2; NonW, L	-0.035	0.000158	0.45	0.78
	2%-2; NonW, M	-0.034	0.000156	0.45	0.79
	2%-2; NonW, R	-0.035	0.000159	0.47	0.78
Test 3	**2%-2; W, L**	-0.024	0.000125	8.92	0.80
	2%-2; W, M	-0.024	0.000127	8.91	0.79
	2%-2; W, R	-0.024	0.000125	11.4	0.80
	2%-2; NonW, L	-0.037	0.000193	8.92	0.69
	2%-2; NonW, M	-0.037	0.000196	8.91	0.68
	2%-2; NonW, R	-0.037	0.000193	11.4	0.69